

UNCLASSIFIED

AD NUMBER
AD804723
NEW LIMITATION CHANGE
TO Approved for public release, distribution unlimited
FROM Distribution authorized to U.S. Gov't. agencies and their contractors; Administrative/Operational Use; 06 SEP 1966. Other requests shall be referred to Federal Aviation Agency, Office of Supersonic Transport Development Program, Washington, DC.
AUTHORITY
FAA notice, 3 Jul 1973

THIS PAGE IS UNCLASSIFIED

7

804723

ORIGINAL COPY

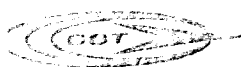
SUBJECT

TOPIC

DATE

BY

PHASE III PROPOSAL



U.S. AIR FORCE RESEARCH AND DEVELOPMENT COMMAND

SEPTEMBER 6 1966

⑥ ~~Supersonic Transport Development Program~~
Phase III Proposals
BOEING MODEL 2707.

Volume II-3.

AERODYNAMIC DESIGN
REPORT,

⑭ V2-B2707-3
September 6, 1966

DDC
RECORDED
JAN 13 1967
RESOLVED
BQ-

⑪ 6 Sep 66

⑫ 371 p.

PREPARED BY

Clarence S. Howell, Jr.

APPROVED BY

H. H. H. H.

⑩ Clarence S. Howell, Jr.

⑮
FA-SS-6-5

Prepared for
FEDERAL AVIATION AGENCY
Office of Supersonic Transport Development Program

"THIS DOCUMENT CONTAINS SENSITIVE, COMPETITIVE, AND PROPRIETARY DATA, AND IS NOT TO BE REPRODUCED OR RELEASED OUTSIDE OF YOUR ORGANIZATION OR USED FOR ANY PURPOSE OTHER THAN SUPERSONIC TRANSPORT EVALUATION WITHOUT THE WRITTEN PERMISSION OF EITHER THE FEDERAL AVIATION AGENCY, OFFICE OF SUPERSONIC TRANSPORT DEVELOPMENT, ATTENTION: SS-30, OR THE BOEING COMPANY, SUPERSONIC TRANSPORT DIVISION, ATTENTION: CONTRACT ADMINISTRATION."

402 977
THE **BOEING** COMPANY
SUPERSONIC TRANSPORT DIVISION

FAA

ISSUE NO 1-99

PAGES _____
ARE
MISSING
IN
ORIGINAL
DOCUMENT

FOREWORD

ENGINE AND AIRPLANE PERFORMANCE DATA

The engine and airplane performance provided in the main body of this document is based on engine performance data received prior to 15 July 1966.

The RFP provides for firm technical engine data to be submitted on 8 August 1966. The predicted effect of these data is of interest to the readers of this document. Accordingly, an addendum summarizing the effect of the 8 August 1966 engine performance on the B-2707 SST has been inserted into the following documents:

V2-B2707-3	Aerodynamic Design Report
V2-B2707-12	Propulsion Report - Part A
V4-B2707-1	Operational Suitability Report
V4-B2707-4	Airport and Community Noise Program

The performance information contained in the Summary document, the Model Specification, and the Statement of Work is based upon the 8 August 1966 firm technical data.

CONTENTS:

	<u>Page</u>
1.0 SUMMARY	1
1.1 CONFIGURATION DESCRIPTION	1
1.2 AIRPLANE PERFORMANCE	2
1.3 LIFT-TO-DRAG RATIO	11
1.4 STABILITY AND CONTROL	11
1.5 AEROELASTICITY	11
1.6 GROWTH	11
2.0 PERFORMANCE	17
2.1 MISSIONS	19
2.2 TAKEOFF PERFORMANCE	19
2.3 APPROACH AND LANDING PERFORMANCE	31
2.4 OFF-DESIGN AND EMERGENCY RANGE PAYLOAD PERFORMANCE	36
2.5 PERFORMANCE CALCULATION METHODS	40
3.0 PERFORMANCE SUBSTANTIATION	47
3.1 CRUISE CONFIGURATION	47
3.2 TAKEOFF AND LANDING CONFIGURATIONS	105
3.3 AEROELASTIC ANALYSIS METHODS	131
3.4 AERODYNAMIC DEVELOPMENT PROGRAM	137
4.0 STABILITY AND CONTROL	145
4.1 CONTROL AND TRIM	145
4.2 STATIC STABILITY	179
4.3 DYNAMIC STABILITY	210
4.4 CROSS-COUPLING CHARACTERISTICS	230
4.5 EMERGENCY OPERATIONS	231
5.0 FLIGHT CONTROLS AND STABILITY AUGMENTATION SYSTEM.	
5.1 PRIMARY FLIGHT CONTROL SYSTEM	245
5.2 SECONDARY FLIGHT CONTROL SYSTEM	254
5.3 STABILITY AUGMENTATION SYSTEM	254
SYMBOLS	275
REFERENCES	280
APPENDIX A CONFIGURATION DESCRIPTION	283
APPENDIX B ADDENDUM: SUMMARY REPORT - 8 AUGUST 1966 ENGINE PERFORMANCE DATA	

B-2707 PHASE III PROPOSAL DOCUMENTATION INDEX

VOLUME I	VOLUME III	VOLUME V
SUMMARY V1-B2707	ENGINE CONTRACTORS ONLY	MANAGEMENT MANUFACTURING V5-B2707
Phase III Proposal Summary -1		Configuration Management Plan -1
Boeing Model 2707 Warranties Program -2		Data Management Plan -2
		Master Program Plan -3
		Detail Work Plan -4
		Procurement Program -5
		Cost & Schedules Control Program -6
		Facilities Program -7
		Program Management -8
		Manufacturing Program -9
VOLUME II	VOLUME IV	VOLUME VI
AIRPLANE TECHNICAL REPORT V2-B2707	SYSTEM INTEGRATION V4-B2707	COST V6-B2707
System Engineering Report -1	Operational Suitability -1	Cost Baseline Report Summary Data -1
Mockup Plan -2	Sonic Boom Program -3	Cost Baseline Report Cost Support Data -2
Aerodynamic Design Report -3	Airport & Community Noise Program -4	
Airplane Performance (GE) -4	Internal Noise Program -5	
Airplane Performance (P&W) -5	System Safety Plan -6	
Airframe Design Report- -6-1	Training & Training Equipment Program -7	
Part A Weight & Balance	Human Engineering Program -8	
Airframe Design Report- -6-2	Test Integration & Management -10	
Part B Component Design	Integrated Test Program -11	
Airframe Design Report- -7	Simulation Program -12	
Part C	Flight Simulation Program -13	
Design Criteria	Flight Test Program -14	
Loads	Maintainability Program -15	
Aerodynamic Heating	Reliability Program -16	
Flutter	Quality Control Program -17	
Airframe Design Report- -8	Value Engineering Program -18	
Part D	Standardization Program -19	
Materials and Processes	Product Support Program -20	
Airframe Design Report- -9	Quality Assurance Program -21	
Part E		
Structural Tests		
Systems Report-Part A -10		
Environmental Control		
Electric		
Navigation and Communications		
Systems Report-Part B -11		
Hydraulics		
Landing Gear		
Auxiliary Systems		
Propulsion Report-Part A -12		
Engine, Inlet, & Controls		
Propulsion Report-Part B -13		
Engine Installation		
Fuel System		
Exhaust System		
Propulsion Report-Part C -14		
Engine Evaluation		

1.0 SUMMARY

1.1	CONFIGURATION DESCRIPTION	1
1.2	AIRPLANE PERFORMANCE	2
1.3	LIFT-TO-DRAG RATIO	11
1.4	STABILITY AND CONTROL	11
1.5	AEROELASTICITY	11
1.6	GROWTH	11

1.0 SUMMARY

Aerodynamic analysis of the B-2707 configuration is reported in three documents: Aerodynamic Design Report, V2-B2707-3, Airplane Performance (General Electric), V2-B2707-4, and Airplane Performance (Pratt & Whitney), V2-B2707-5. The documents are part of a series under Volume II, Airplane Technical Report, called for by the FAA Request for Proposal for Phase III of the Supersonic Transport Development Program.

The B-2707 configuration meets the FAA design objectives while providing a large increase in payload over previous supersonic transport configurations submitted by The Boeing Company. This improvement has been achieved without loss of aerodynamic efficiency and offers increased economy in airline operation as indicated by the payload-range curves shown in Fig. 1-1. The performance data shown in this figure and on the following pages are based on characteristics established for the production version of the airplane which is estimated to have a cruise lift-to-drag ratio of 8.2. Refinement of the B-2707 is expected to yield characteristics that are better than those quoted because only a modest 5 percent lift-to-drag improvement is assumed relative to the

current status; this is considerably less than would be indicated by past Boeing history for a comparable time span (Fig. 1-2).

Aerodynamic characteristics of the B-2707 airplane are based on wind tunnel test data corrected for scale effects and geometric differences between the full-scale and wind tunnel model configurations; they are adjusted for the expected improvement resulting from the design refinements of the planned programs. These programs include additional detailed studies of body shape, wing and horizontal tail camber and planform, the use of direct-lift control, and local boundary layer control. These programs are described in Secs. 3.0 and 4.0. Approximately 11,000 hours of wind tunnel testing have been devoted to aerodynamic research during Phase II; of these more than 2,000 hours have been used specifically for development of the B-2707 configuration.

1.1 CONFIGURATION DESCRIPTION

A three-view drawing of the B-2707 configuration is shown in Fig. 1-3. The design consists of a six-abreast body with a variable sweep wing and

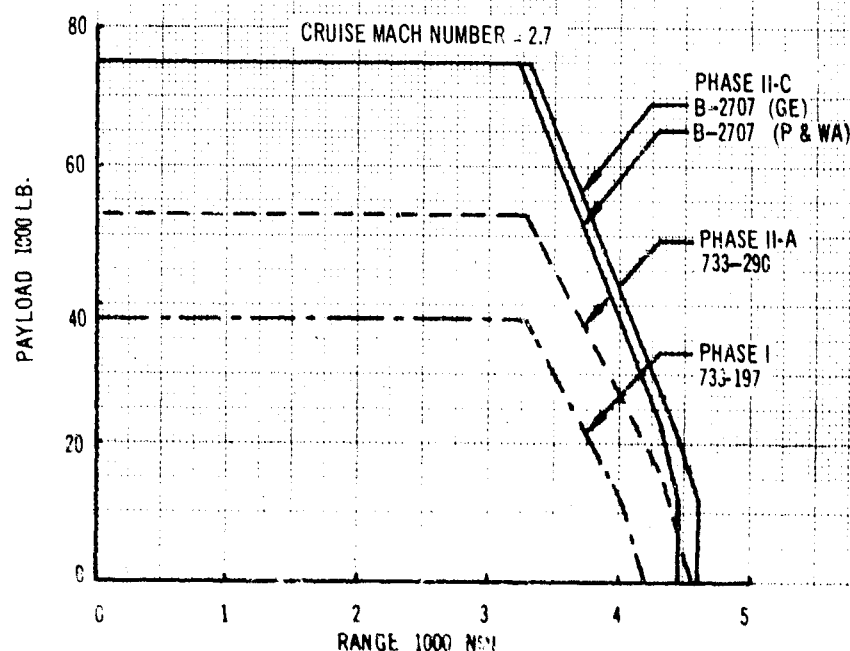


Figure 1-1. Payload Range Improvements

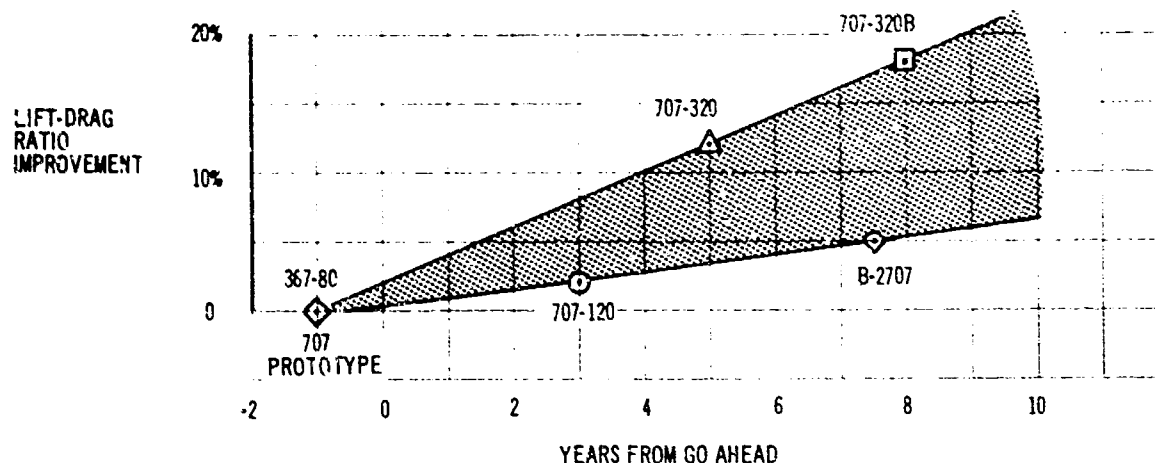


Figure 1-2. Aerodynamic Efficiency Improvements

four augmented engines (either General Electric GE4/J5P or Pratt and Whitney JTF17A-21B) located under the horizontal tail. The engines are mounted in individual nacelles near the trailing edge to provide favorable aerodynamic interference effects and an unobstructed area for the engine exhaust. Inlet foreign object ingestion is minimized by locating wing trailing edge flaps between the landing gear and the inlets. A vertical tail and ventral fin are incorporated in the design to achieve adequate directional stability.

A wing sweep of 30 degrees is used for takeoff and landing. During subsonic climb, acceleration, and cruise, the wing sweep is 42 degrees. At transonic and supersonic speeds the wing sweep is 72 degrees; the wing is joined to the horizontal tail in this position. The variable-sweep feature provides a high degree of operational flexibility. Principal dimensions, areas, and weights are given in Fig. 1-3, and a detailed description of the airplane geometry is given in Appendix A.

1.2 AIRPLANE PERFORMANCE

Payload range performance for the intercontinental version of the production airplane is shown in Figs. 1-4 and 1-5. The airplane is capable of carrying the following payloads:

	B-2707 (GE)	B-2707 (F&WA)
FAA Mission (4,000 Statute Miles)	66,000 lb	63,000 lb
New York - Paris	75,000 lb	74,000 lb
New York - Rome	55,000 lb	51,500 lb

The domestic airplane can carry a payload of 63,000 lb (B-2707 GE) or 62,500 lb (B-2707 P&WA) from New York to Los Angeles.

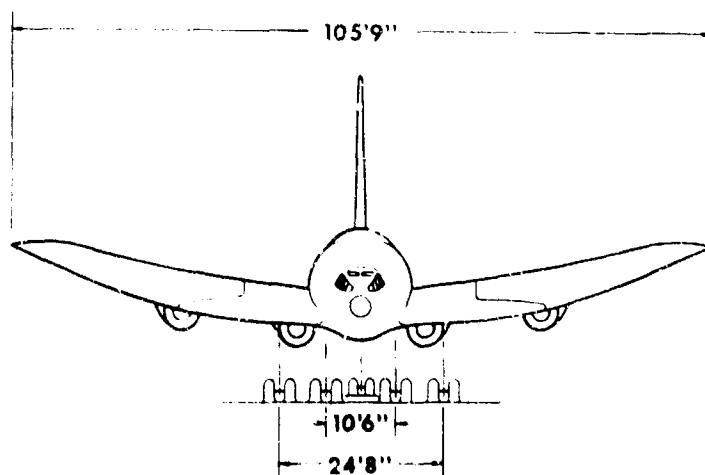
DATA MODEL B-2707

	G.E.	P&WA
POWER PLANTS (4)	G.E. 4/J5P	JTF 17A-21B
TOTAL ENGINE AIRFLOW	2480 LBS/SEC	2748 LBS/SEC
MAX. DESIGN TAXI WEIGHT	675,000 LBS	675,000 LBS
NOMINAL PAYLOAD	50,000 LBS	50,000 LBS
OPERATIONAL EMPTY WEIGHT	287,500 LBS	285,000 LBS
FUEL	374,700 LBS	374,700 LBS

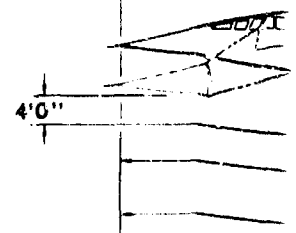
MAIN GEAR	16 - 45 x 19.2 TIRES TYPE VIII
NOSE GEAR	2 - 34 x 16 TIRES TYPE VIII
MAX. DESIGN TAXI WEIGHT C.G. - LIMITS, GEAR DOWN	
MOST FORWARD C.G.	59.5% REF. LENGTH - WINGS FWD
MOST AFT C.G.	64.0% REF. LENGTH - WINGS AFT

4 AIRPLANE

STA 200



SCALE (INCHES)



A

607 R25. LENGTH

AIRPLANE

163' 4"

15' 3"

STA. 1440

158' 1"
REF. LENGTH

STA. 200

294' 9"

STA.

MAX. GROSS WEIGHT C.G.

15' 7"

4' 0"

12' 6"

8' 3"

13' 11"

82' 5"

STA. 1189

122' 10"

306' 0"

500



(YES)

3

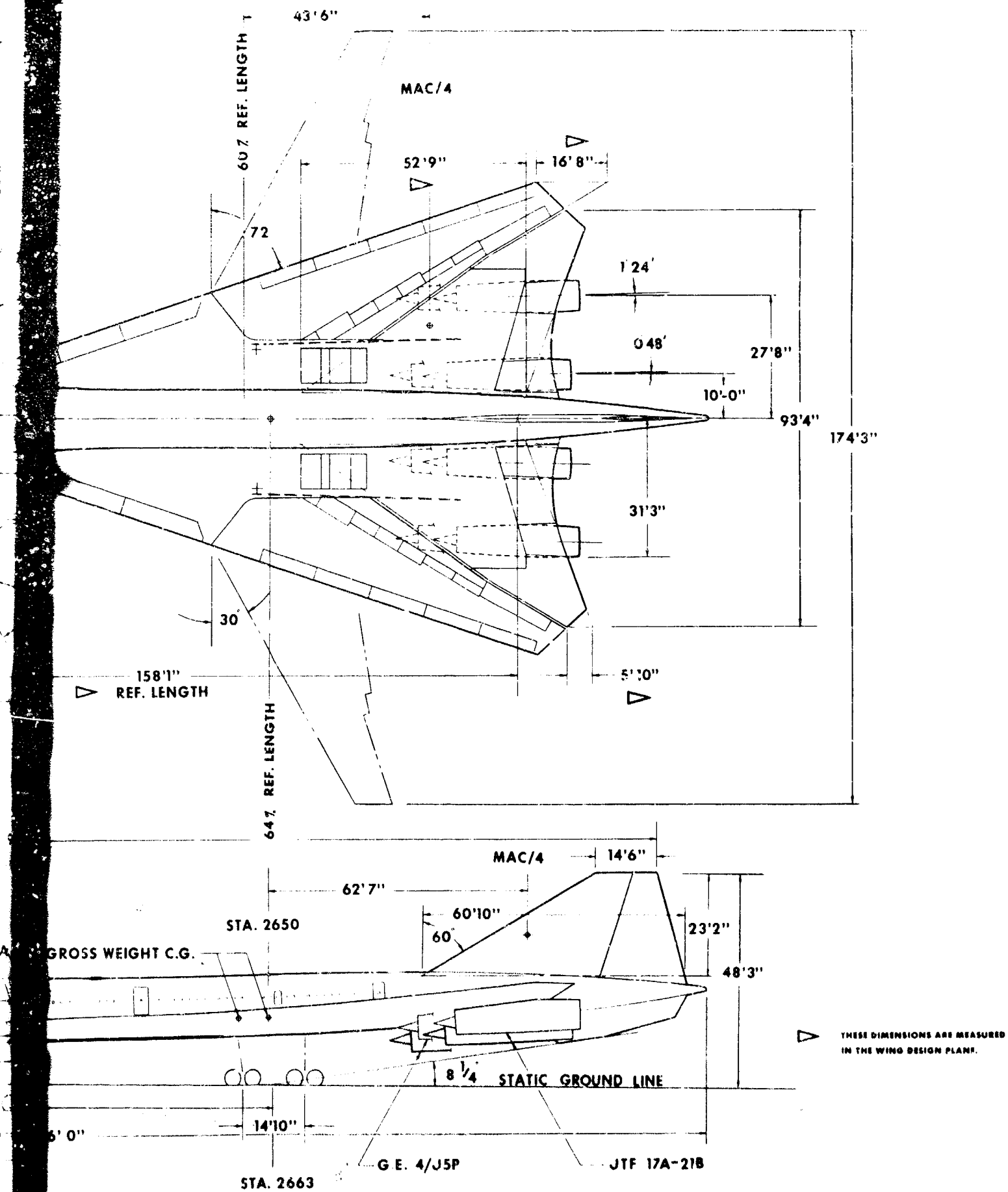


Figure 1-3. General Arrangement Model B2707

V2-B2707-3

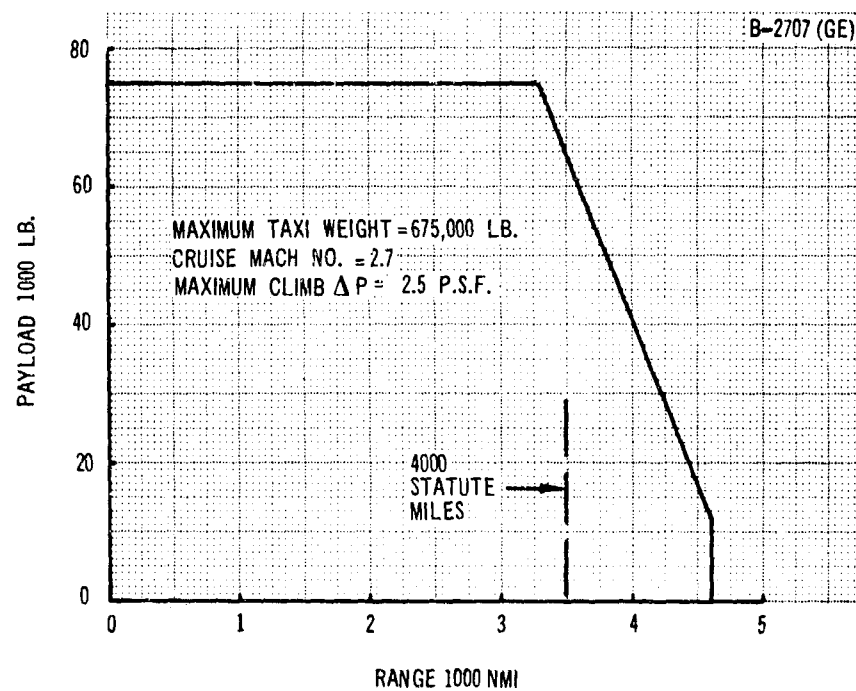


Figure 1-4. Payload Range Performance (GE)

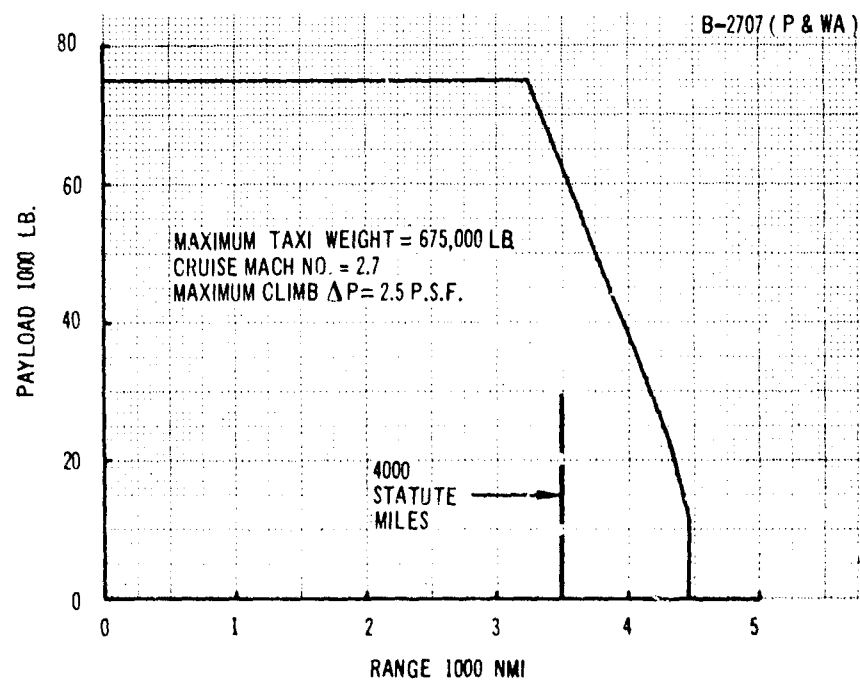


Figure 1-5. Payload Range Performance (P&WA)

The FAR takeoff field lengths, liftoff speeds, and community noise levels as a function of takeoff weight are shown in Figs. 1-6 and 1-7. The

B-2707 has the following takeoff performance at the maximum design taxi weight of 675,000 lb and maximum augmented thrust:

	<u>B-2707 (GE)</u>		<u>B-2707 (P&WA)</u>	
	0.595CR Forward	0.615CR Normal	0.595CR Forward	0.615CR Normal
Center of gravity location				
FAR takeoff field length (ft)	7,000	6,300	7,300	6,600
Liftoff speed, kn EAS	169	162	169	162
Airport noise, PNdb	121	121	117	117
Community noise, PNdb	100	99	105	104

The noise levels quoted above are those for the B-2707 with only the engine exhaust noise suppression systems provided by the engine manufacturer, and with a sonic throat in the inlet. Exhaust noise suppression systems under development by The Boeing Company offer even greater reductions in airport noise levels. With the Boeing suppressors, airport noise levels are reduced 9 PNdb for the GE engines and 4 PNdb for the P&WA

engines; community noise levels are reduced 1 to 2 PNdb for both engines.

Approach speeds, FAR landing field lengths, and approach noise levels as a function of landing weight are shown in Figs. 1-8 and 1-9. At maximum landing weight and with maximum flap deflection, the airplane has the following landing performance:

	<u>B-2707 (GE)</u>		<u>B-2707 (P&WA)</u>	
	0.595CR Forward	0.615CR Normal	0.595CR Forward	0.615CR Normal
Maximum landing weight (lb)	430,000		420,000	
Center of gravity location				
Approach speed, kn EAS	153	145	151	143
FAR landing field length (ft)	7,500	7,000	7,400	6,900
Constant velocity approach noise level, PNdb	112	111	115	114

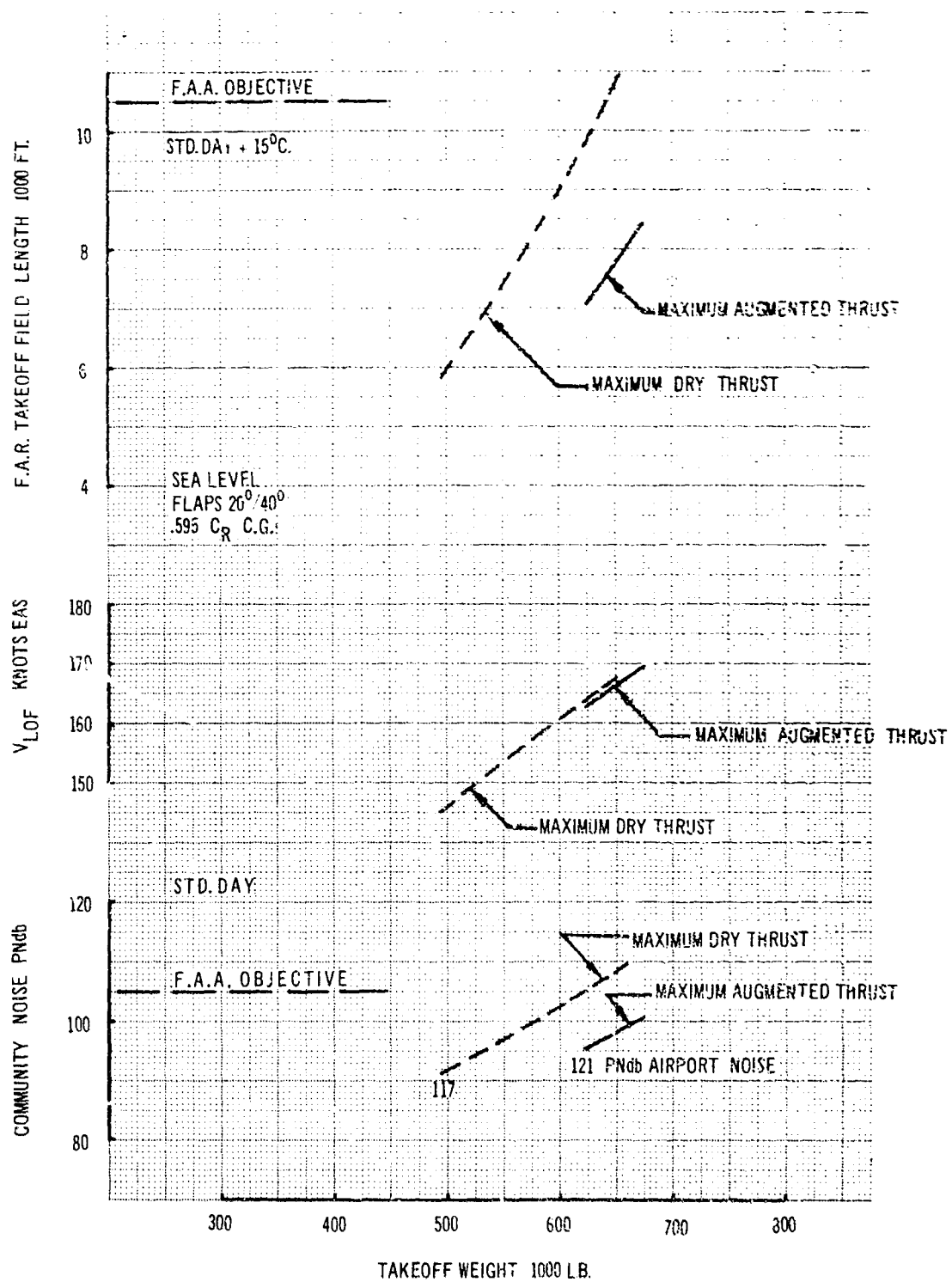


Figure 1-6. Takeoff Performance (GE)

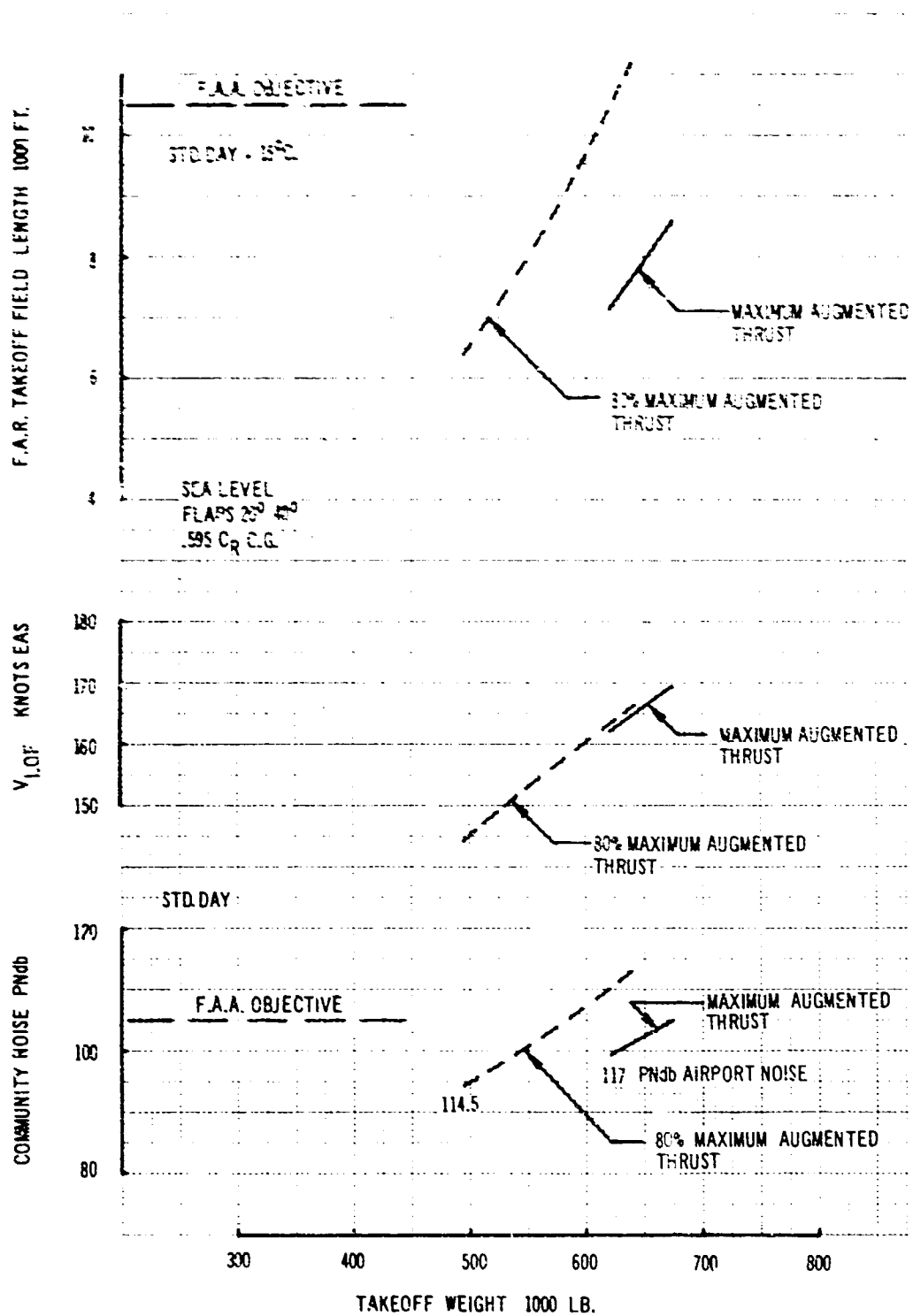


Figure 1-7. Takeoff Performance (P&WA)

V2-B2707-3

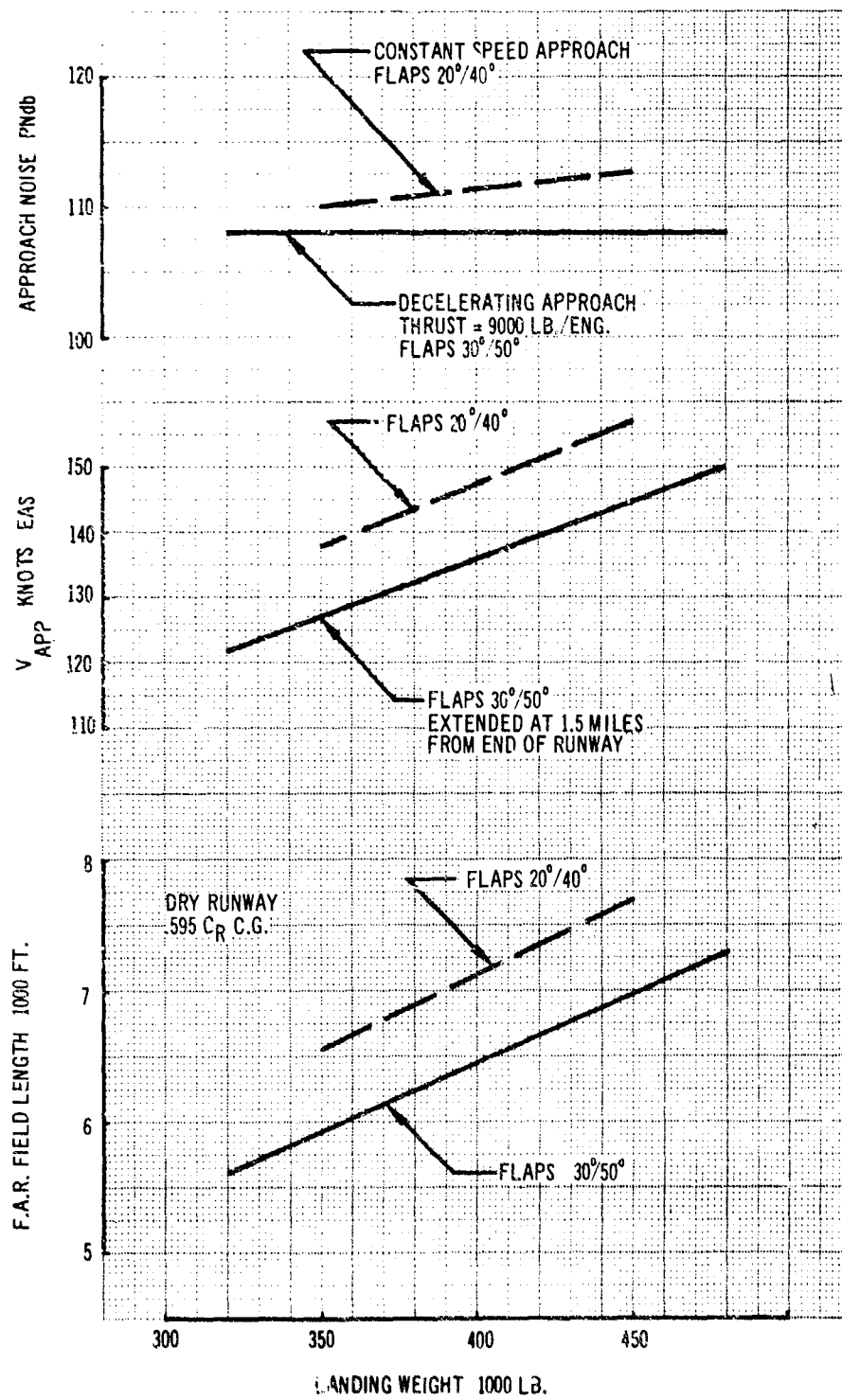


Figure 1-8. Landing Performance (GE)

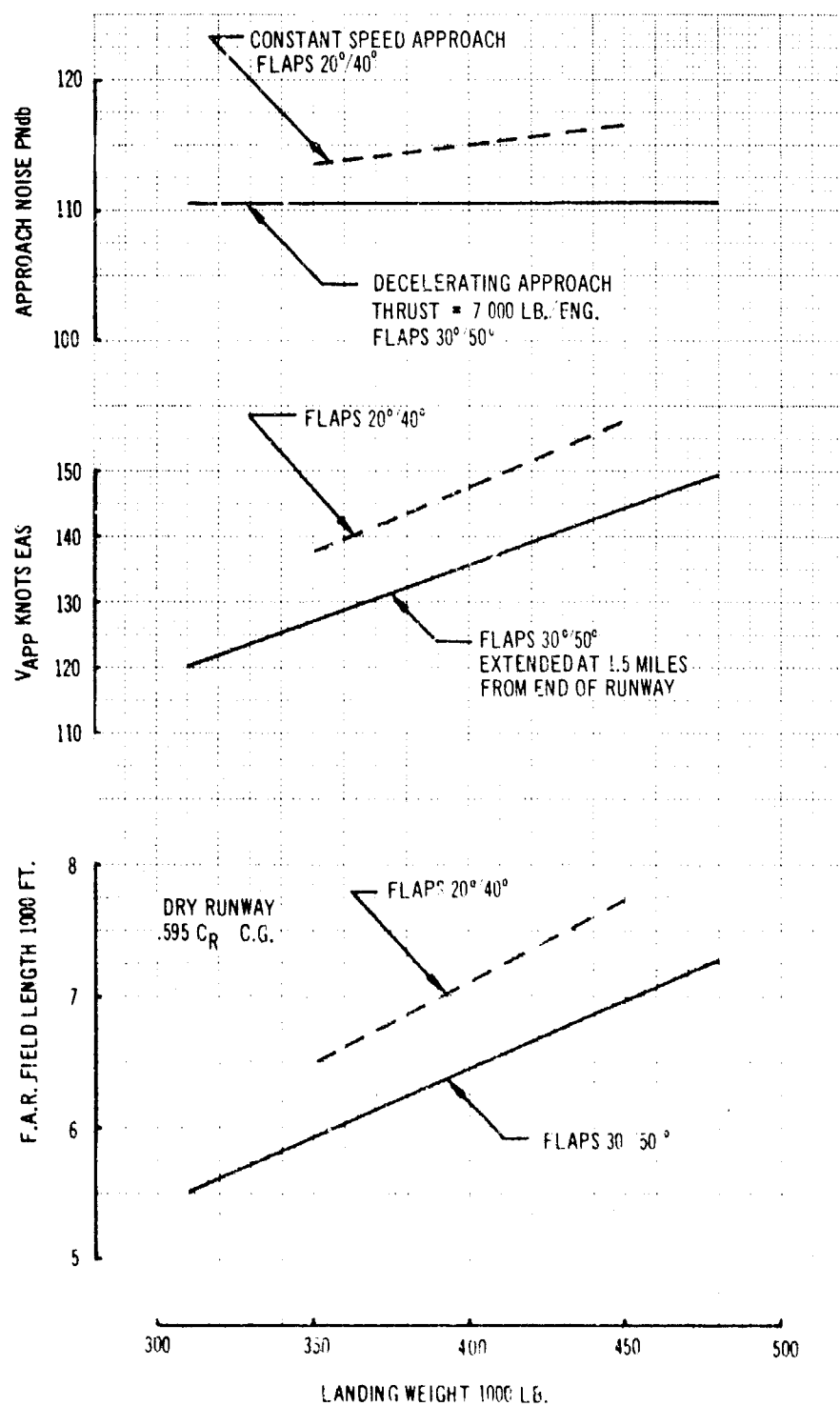


Figure 1-9. Landing Performance (P&WA)

1.3 LIFT-TO-DRAG RATIO

Current wind tunnel data indicate a Mach 2.7 maximum lift-to-drag ratio of 7.8 for the B-2707 configuration. Although achieved with a six-abreast body, this value is higher than that achieved with the previous five-abreast configuration. Refinements in the wing, body shape, cab design, and nacelle installation for the B-2707 have contributed to this high level of aerodynamic efficiency. The development of low drag nacelles having inlets aligned with the local flow, exit nozzles aligned for optimum thrust effects, and shape tailored to house the engine and accessories has been a major effort during the past two years. The wide variety of nacelle shapes which have been wind tunnel tested and have lead to the present design are shown in Fig. 1-10. All wind tunnel force and moment tests of complete configurations have been made with flow-type nacelles which properly duplicate the complete interference effects. Exploration of configuration refinements is continuing in order to ensure the best possible production airplane characteristics. This work is discussed in Sec. 3.0.

1.4 STABILITY AND CONTROL

A unique combination of stability and control surfaces is incorporated in the B-2707 design. The variable-sweep wing, in the forward position, permits longitudinal and lateral control of the airplane to be provided by separate and independent systems. This is a particularly desirable feature during gusty crosswind landings. Longitudinal control is provided by trailing edge elevators and tip elevons on the horizontal tail. Conventional ailerons near the wing tips and wing spoilers provide lateral control that is comparable to that on present jet transports. With the wings swept aft, longitudinal control is provided by the elevators and elevons with the elevons also providing lateral control. The four inboard segments of the wing spoilers also provide lateral control during high speed flight. Wind tunnel tests and theoretical analyses indicate that these systems,

with normal development, provide the good handling qualities and the high levels of safety necessary for commercial transport operation.

1.5 AEROELASTICITY

The development of accurate methods for predicting the effects of aeroelasticity on airplane aerodynamic characteristics has been a continuing program at Boeing for nearly 20 years. During the past eight years a number of analysis methods have been developed for determining airplane aeroelastic effects at subsonic, transonic, and supersonic speeds, and the results have been correlated with wind tunnel and flight test data. Typical correlations for a flexible wing model at Mach 2.7 are shown in Fig. 1-11 where initial lift curve slope, aerodynamic center location, and zero-lift pitching moment coefficient are shown for a range of dynamic pressures. Theoretical and experimental results for both a rigid and a scaled stiffness model are shown. The scaled stiffness model simulated the structural and geometric characteristics of the movable portion of a variable sweep configuration. Tests of a more sophisticated scaled stiffness model of the B-2707 configuration are scheduled for September, 1966. This model will provide the capability for testing both flexible and rigid wings, tails, and forward body sections.

1.6 GROWTH

Takeoff performance of the B-2707 configuration at gross weights greater than 675,000 lb is shown in Figs. 1-12 and 1-13. The gross weight of the basic configuration can be increased to 750,000 lb and at the same time meet the FAA objective of a 10,500-ft FAR takeoff field length, and the FAR second-segment climb gradient requirement on a hot day. Additional fuel volume can be provided by slight changes to the airplane's external contours, which will allow the space-limited payload of 75,000 lb to be carried a distance of 3,830 nmi (B-2707 GE) or 3,760 nmi (B-2707 P&WA) as shown in Figs. 1-14 and 1-15.



Figure 1-10. Flow Nacelle Development

V2-B2707-3

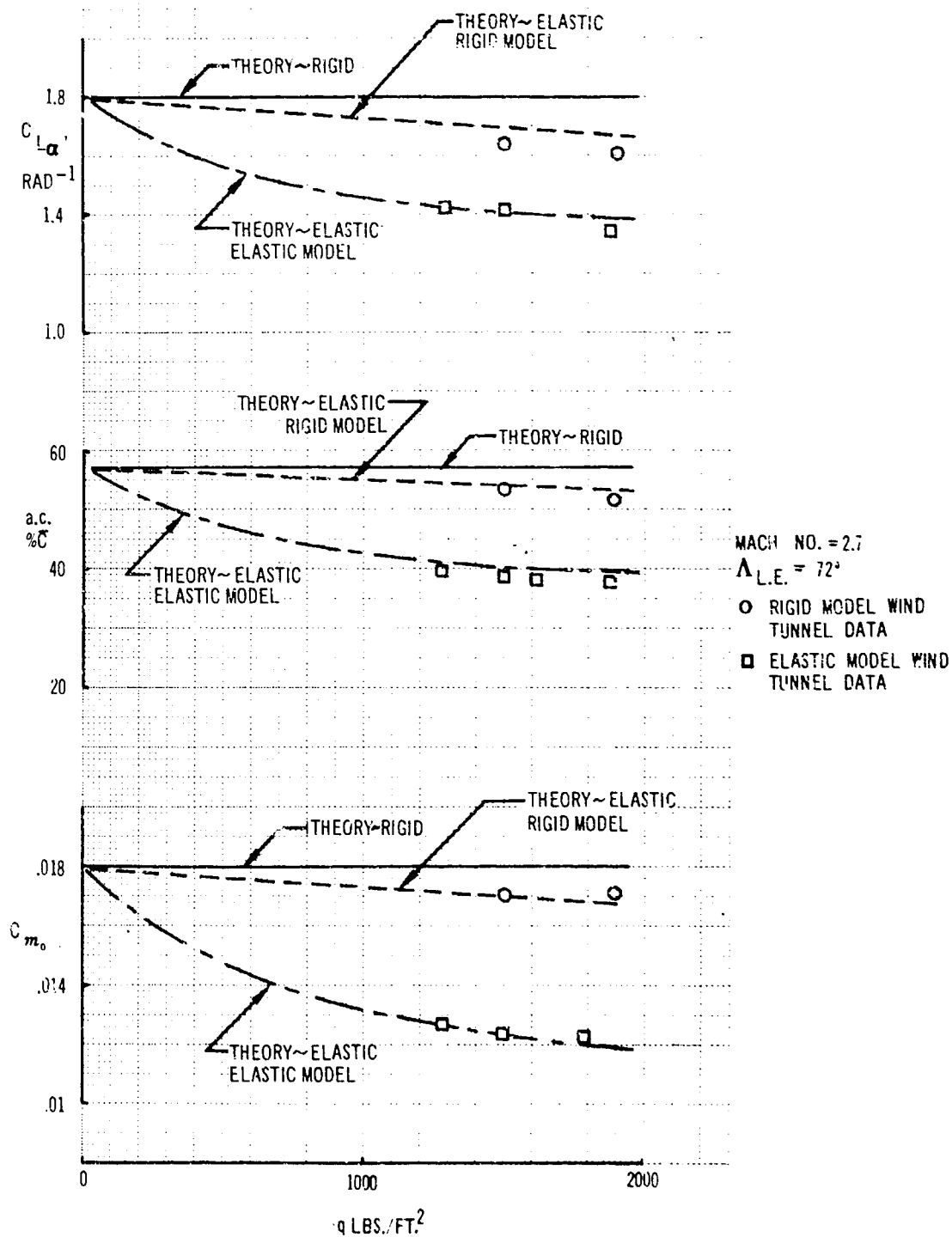


Figure 1-11. Effects of Aeroelasticity on Aerodynamic Characteristics

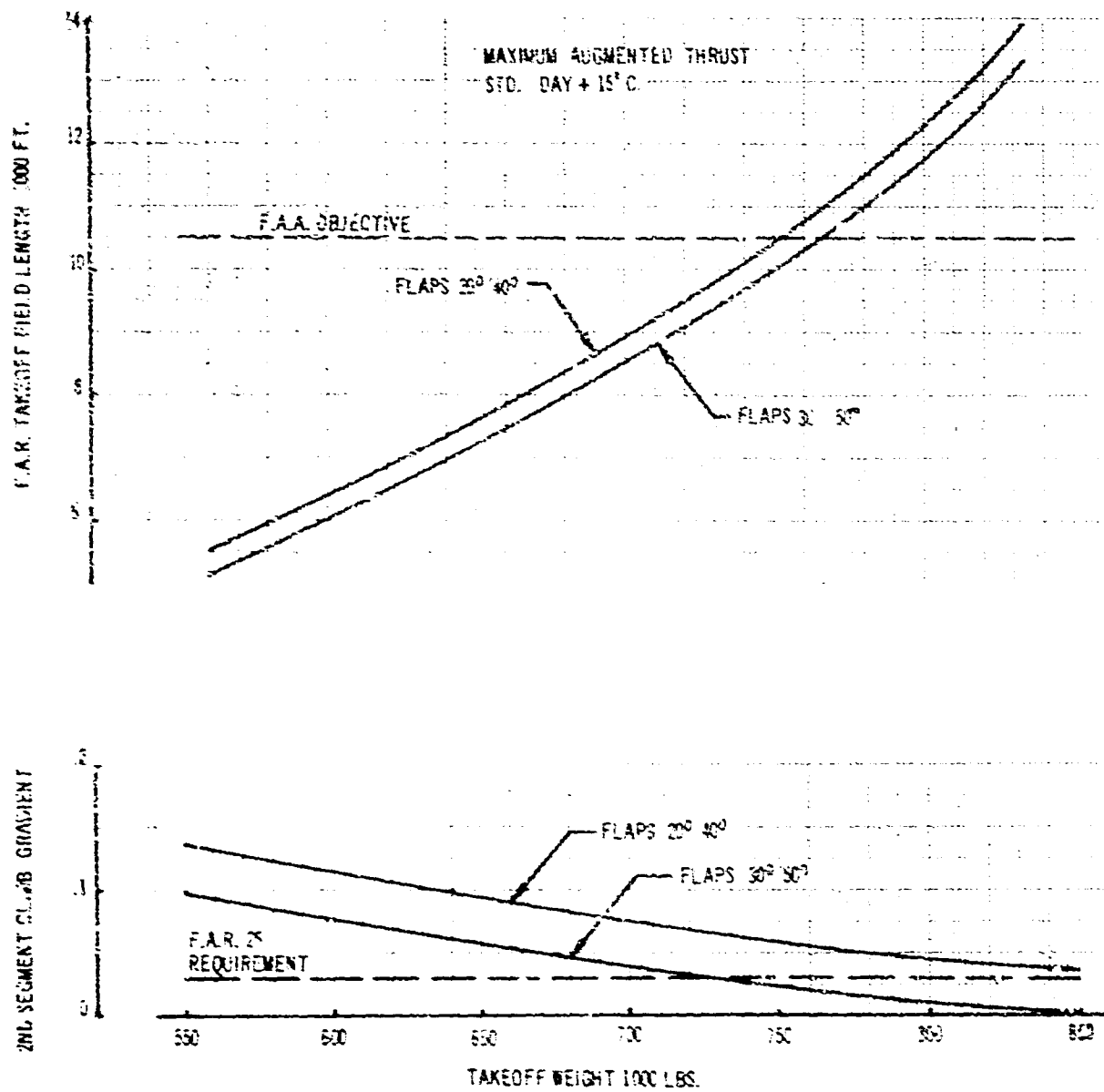


Figure 1-12. Growth Takeoff Performance (GE)

V2-B2707-3

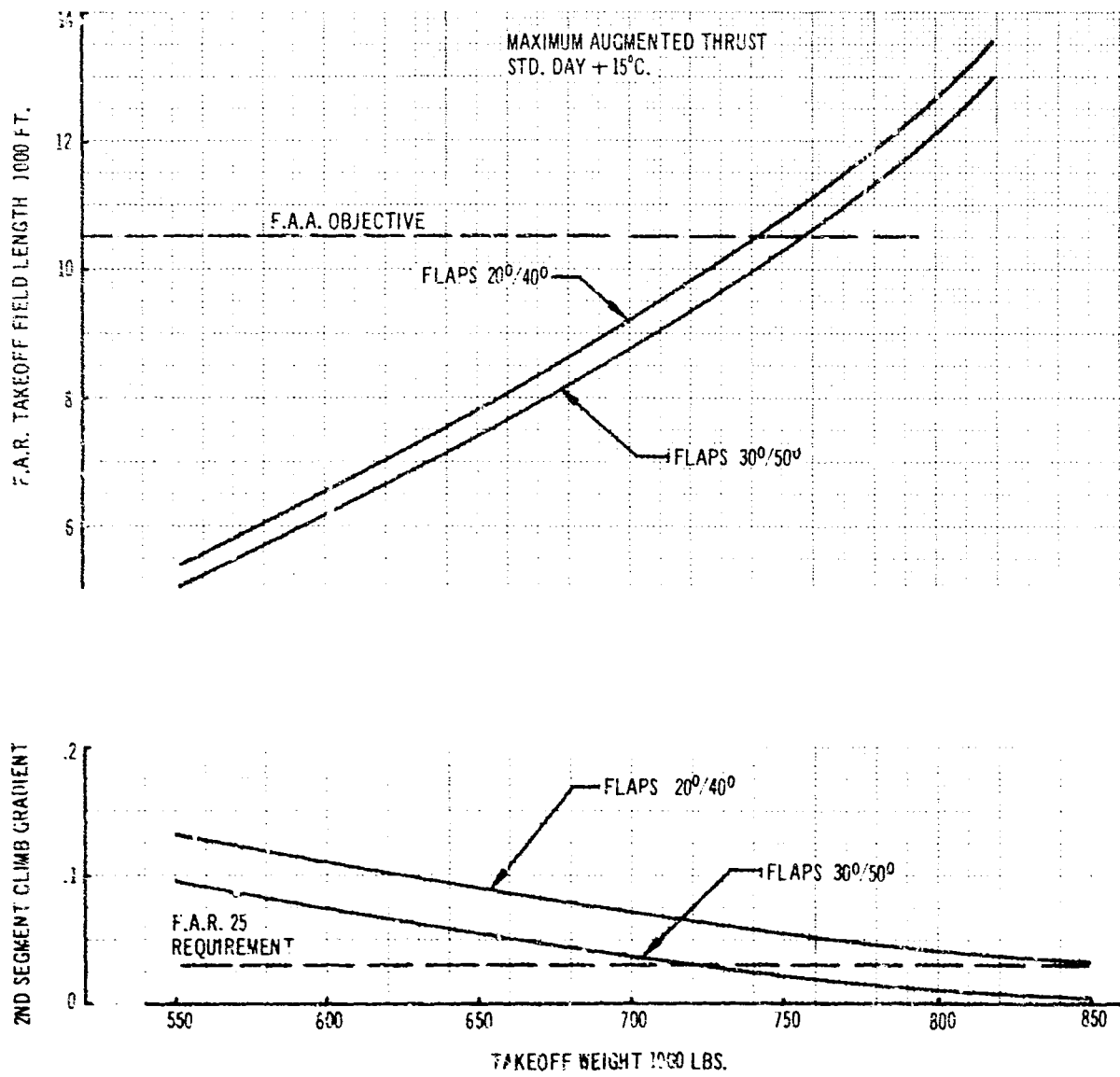


Figure 1-13. Growth Takeoff Performance (P&WA)

V2-B2707-3

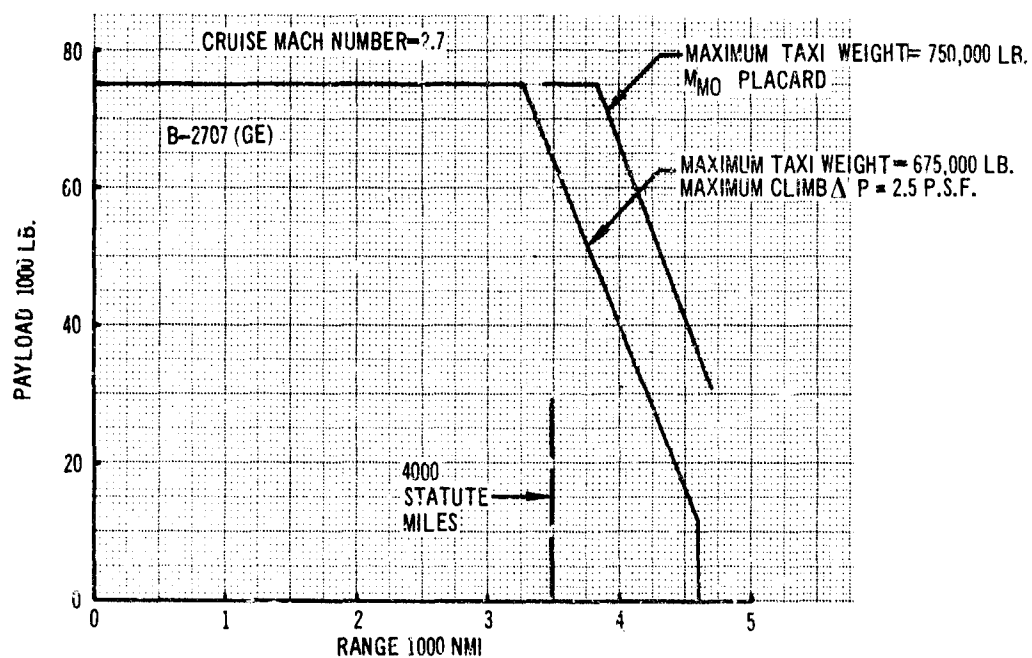


Figure 1-14. Growth Payload Range Performance (GE)

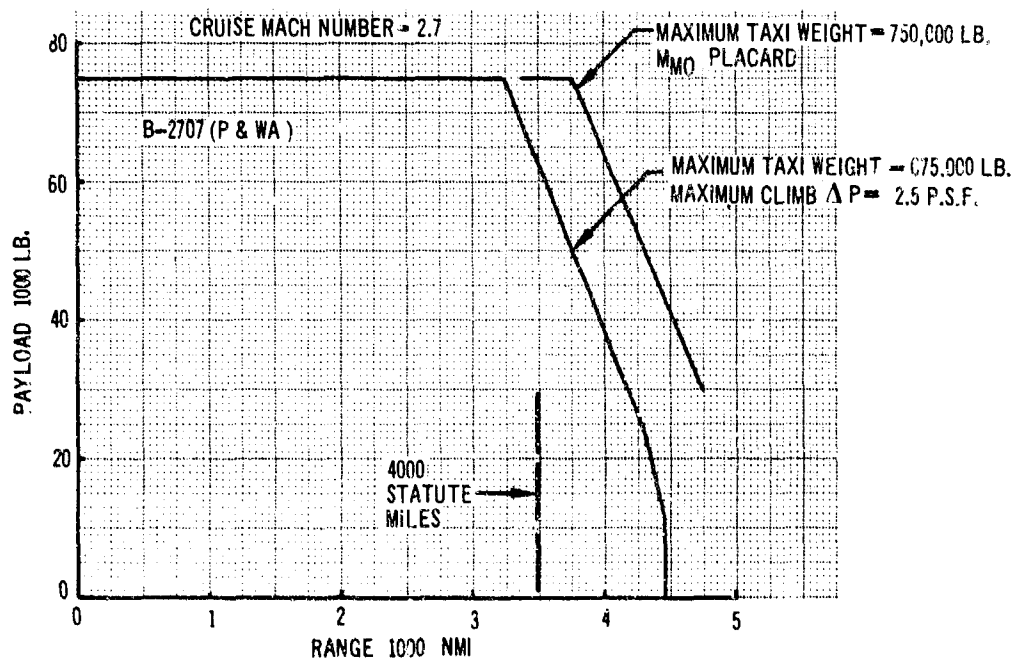


Figure 1-15. Growth Payload Range Performance (P&WA)

V2-B2707-3

2.0 PERFORMANCE

	Page
2.1 MISSIONS	19
2.2 TAKEOFF PERFORMANCE	19
2.3 APPROACH AND LANDING PERFORMANCE	31
2.4 OFF-DESIGN AND EMERGENCY RANGE PAYLOAD PERFORMANCE	36
2.5 PERFORMANCE CALCULATION METHODS	40

2.0 PERFORMANCE

This section presents a summary of the major performance capabilities of the Boeing Model 2707, powered with either General Electric or Pratt and Whitney engines. More detailed performance data, such as that required for airline route analyses and expansion upon all topics discussed here, are presented in Airplane Performance (General Electric Engines), V2-B2707-4, and Airplane Performance (Pratt and Whitney Engines), V2-B2707-5.

Evolution of the B-2707 has brought improved payload range capability, substantially greater than the Phase III objectives, while retaining good low speed performance and low community noise levels. The B-2707 has been designed in response to the airlines' desire for long range, high payload capacity with six-abreast passenger seating accommodations. Up to 354 passengers can be carried using an international tourist seating arrangement. In addition, use of the variable-sweep design results in exceptional operational versatility, for example, where mixed subsonic-supersonic missions are required.

The performance of the B-2707 airplane on international routes is summarized in Table 2-A. Comparative performance data on the B-2707 with four 620-lb/sec General Electric GE4/J5P engines and with four 687-lb/sec Pratt and Whitney JTF17A-21B engines are shown based upon engine data received before July 16, 1966. (See the foreword and Appendix B to this document for changes in performance caused by engine changes after July 15, 1966.) Especially noteworthy are: The excellent payload range capability with either engine—over 4,300 statute miles with 50,000 lb of payload; the low community noise values on landing approach—only 108 PNdb for the B-2707 (GE) and 111 PNdb for B-2707 (P&WA); and the excellent landing performance on dry or wet runways because of the high lift capabilities of the variable-sweep wing. Without the use of reverse thrust and including the 1.15 factor specified by the FAR, the wet-runway FAR landing field length is only 7,500 ft. Use of two engines with reverse thrust reduces the FAR wet-landing field length to only 6,200 ft.

The noise suppression characteristics used in the performance calculations are those offered by the engine manufacturers in their augmentation and exhaust nozzle systems plus the application of a sonic throat in the propulsion air inlet. Comparative performance and noise contour data are shown with a Boeing suppressor under development in noise research programs. The Boeing jet suppressor reduces the airport noise from 121 to 112 PNdb for the GE engine and from 117 to 113 PNdb for the P&WA engine. The engine data used in the performance calculations are given in Propulsion Report (V2-B2707-13). The engine noise data used are contained in Airport and Community Noise Program report (V4-B2707-4).

Landing approach noise has been calculated for a constant speed procedure and for a decelerating approach. Using the decelerating approach method reduces the community noise 4 PNdb. The decelerating approach only requires that the pilot extend the flaps to a higher angle setting as the community is approached. Trim and attitude changes are negligible. In the decelerating approach, the community noise is 108 PNdb for the B-2707 (GE) and 111 for the B-2707 (P&WA).

Sonic boom overpressures for the airplane performance are based upon the far-field calculation method. The method used is consistent with that established by the FAA and the NASA for Phases I, II-A, and II-C and is described in Ref. 1. To account for the effect of the atmosphere, the approximate correction factor $\sqrt{P_g/P_a}$ was used. Sonic boom overpressures using the near-field theory have also been calculated for the B-2707 and are shown in this section. Details are given in Sonic Boom Program, V4-B2707-3.

All performance data are based upon the U.S. Standard Atmosphere, 1962, at 45 degrees latitude, geometric altitude. Hot day performance has been computed for a modified standard atmosphere wherein the temperatures given by the U.S. Standard Atmosphere are increased +10 degrees C at all altitudes. The basis for computing performance during all phases of flight and the definition

Table 2-A. Performance Summary, International

Item	Configuration	*General Electric GE4/J5P	*Pratt & Whitney JTTF17A-21B	FAA Phase III objectives
<u>Weights</u>	Maximum design taxi weight (lb) Operational empty weight (lb) Maximum allowable payload (lb) Nominal payload (lb) Maximum landing weight (lb)	675,000 287,500 75,000 50,000 430,000	675,000 285,000 75,000 50,000 420,000	
<u>Range</u>	Range, M = 2.7, statute miles	4,380	4,300	
<u>Std day</u>	Maximum ΔP (PSF) of: climb/cruise/descent	2.50 1.88 1.66	2.50 1.87 1.65	2.5 1.7 1.5
P.L. = 50,000 lb	Range, M=0.85, statute miles	3,780	4,455	
<u>Std day</u> +10 deg C	Range, M = 2.6, statute miles	3,995	3,995	
	Maximum ΔP (PSF) of: climb/cruise/descent	2.50 1.85 1.64	2.50 1.83 1.63	
<u>Takeoff</u>	Thrust setting	Max. Aug.	Max. Aug.	
Max. design taxi wt.	FAR Field Length (ft) V_{LOF} Kn (equivalent air speed)	7,000 169	7,300 169	-----
S.L. Std. day	Airport noise (PNdb) Community noise (PNdb)	121 100	117 105	116 105
S.L. Std day +15° C	FAR Field Length (ft)	8,300	8,500	10,500
<u>Landing</u>	FAR Field Length (ft) (dry) FAR Field Length (ft) (wet) Community noise (using one Kn/sec decelerating approach) (PNdb)	7,500 7,600 108	7,400 7,500 111	----- 8,000 109
Max. ldg wt. S.L. Std day	Community noise (using constant velocity approach) (PNdb)	112	115	

*Based upon engine data received before July 16, 1966. See Appendix B to this volume for effects of subsequent changes in engine data. The data shown are without the Boeing jet noise suppressor.

of the nonstandard day atmosphere models used are described in Par. 2.5.

2.1 MISSIONS

2.1.1 Payload Range Capability

Figure 2-1 shows the payload-range capability of the B-2707, calculated using the FAA Supersonic Transport Economic Model Ground Rules (SST 66-3, dated June 30, 1966) for international missions. The special effects included in the payload range performance are those listed and calculated according to the instructions given in the Request for Proposal. The incremental range payload effects are given in Par. 2.5. Using these rules, the B-2707 has an international mixed seating capacity of 277 passengers. With this passenger payload, the M = 2.7 mission range is 3,720 nmi for the B-2707 (GE) and 3,640 nmi for the B-2707 (P&WA) when a climb schedule for a sonic boom overpressure of 2.5 psf is followed. Range payload capability is also shown for a climb procedure which follows MMO, the maximum operating Mach number schedule. Climb at MMO results in a maximum sonic boom overpressure of about 3.3 psf during climb and a range increase of 130 nmi for the B-2707 (GE) and 120 nmi for the B-2707 (P&WA). This climb procedure may be acceptable for overocean flights. For subsonic missions, the cruise Mach number is 0.85 and the wing leading edge sweep is 42 degrees. The all-subsonic mission range is 3,200 nmi for the B-2707 (GE) and 3,750 nmi for the B-2707 (P&WA). The detailed breakdown of time, fuel, and distance for these missions are presented in Airplane Performance (GE) V2-B2707-4 and Airplane Performance (P&WA) V2-B2707-5.

Figure 2-2 shows the payload range capability for standard day temperatures $\pm 10^{\circ}\text{C}$. The maximum sonic boom overpressure during climb is 2.5 psf. Stagnation temperature is limited to 500°F which results in a slight cruise Mach number reduction on hot days. A 50,000-lb payload can be carried 4,000 statute miles by the B-2707 with either engine installation on a standard $+10^{\circ}\text{C}$ day. A payload of 72,000 lb can be carried by the B-2707 (GE) and 75,000 lb by the B-2707 (P&WA) on a standard -10°C day.

A domestic airplane with a maximum taxi weight of 575,000 lb has been derived from the international version. It is identical in all respects with the 675,000-lb airplane except that the

operational empty weight (OEI) has been reduced 12,000 lb.

Payload range data are shown in Fig. 2-3 for domestic missions in which the climb and cruise overpressure objectives of 2.0 and 1.5 psf are met. The domestic mixed seating arrangement of the economic model ground rules results in a 261-passenger payload. At 575,000 lb maximum taxi weight and with this passenger payload, the domestic B-2707 (GE) has a range of 2,400 nmi; and the domestic B-2707 (P&WA) has a range of 2,380 nmi. Also shown are the trades of range payload capability if the sonic boom overpressures are allowed to increase slightly. The range is increased 380 nmi for the domestic B-2707 (GE), and 340 nmi for the domestic B-2707 (P&WA) for a 10 percent increase in climb overpressure.

2.1.2 Flight Profiles

A typical flight profile for the B-2707 for an international mission is shown in Fig. 2-4. Variations of far-field sonic boom overpressures under the flight path are shown. The far-field sonic boom overpressure calculation method is used for this proposal (Ref. 1). In descent the maximum overpressure reaches 1.65 psf. Descent schedules which meet the 1.5-psf objective are included in documents V2-B2707-4 and -5. The 1.5-psf descent schedule results in no range change but increases the descent time by approximately 3 minutes.

Figure 2-5 shows the effect of using the near-field theory for calculation of the sonic boom overpressures in climb. The overpressure values are up to 15 percent less during climb using the near-field method. Using near-field theory to calculate the $\Delta P = 2.5$ psf climb schedule gives a lower altitude Mach number schedule as compared to the far-field method. A range increase of 80 nmi for the B-2707 (GE) would result if near-field theory were used. A 100-nmi increase would occur for the B-2707 (P&WA).

2.2 TAKEOFF PERFORMANCE

The B-2707 has good takeoff performance using maximum augmented thrust for the maximum taxi weight of 675,000 lb. Equally good performance and reduced airport noise are possible for weights of 600,000 lb or less using maximum dry engine thrust for the B-2707 (GE) and 80-percent maximum augmented thrust for the B-2707 (P&WA).

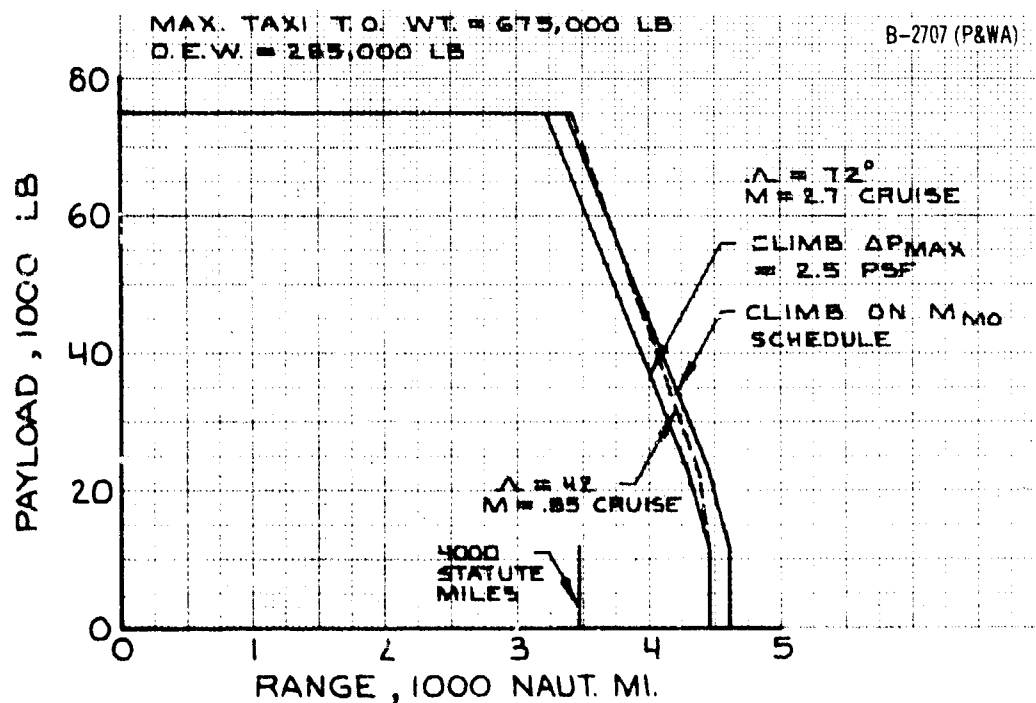
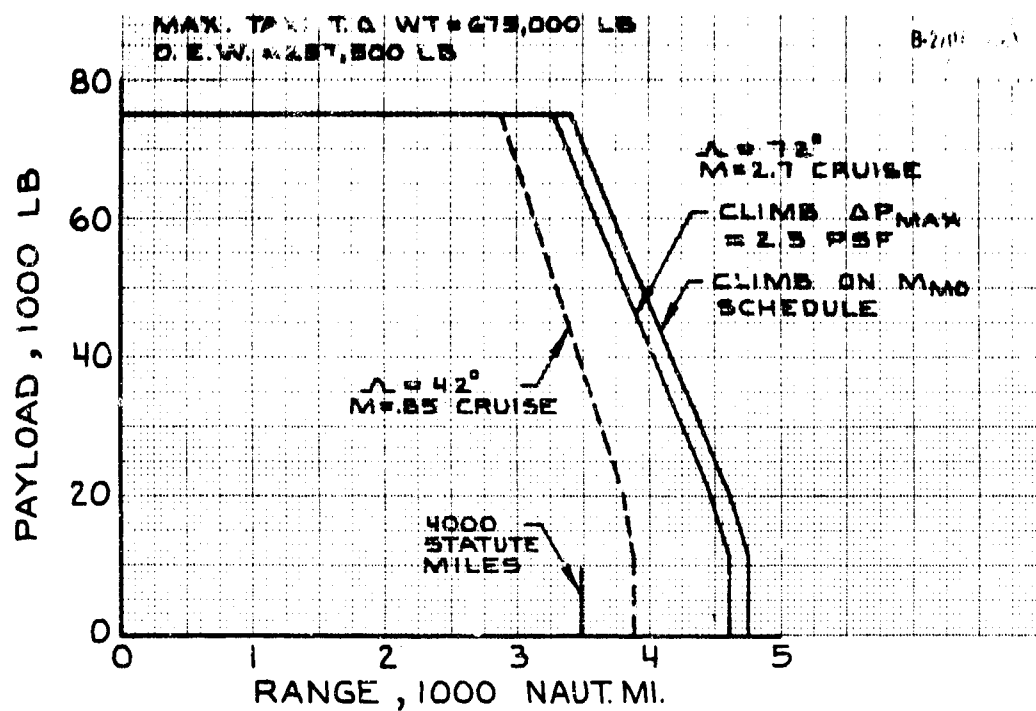


Figure 2-1. Payload Range, International Mission, Standard Day

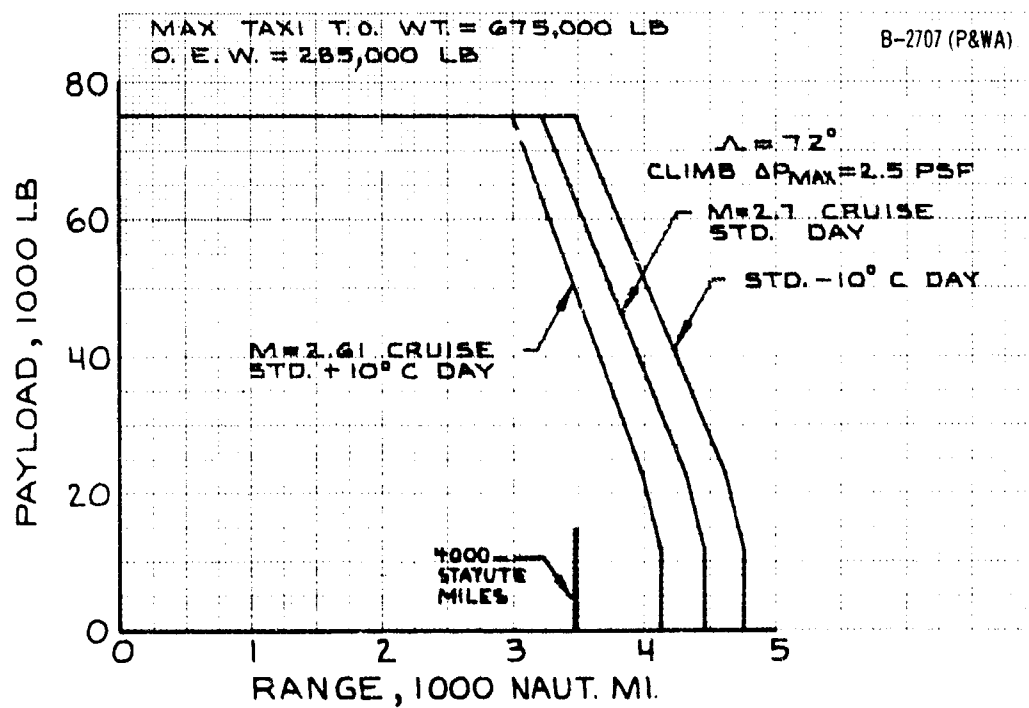
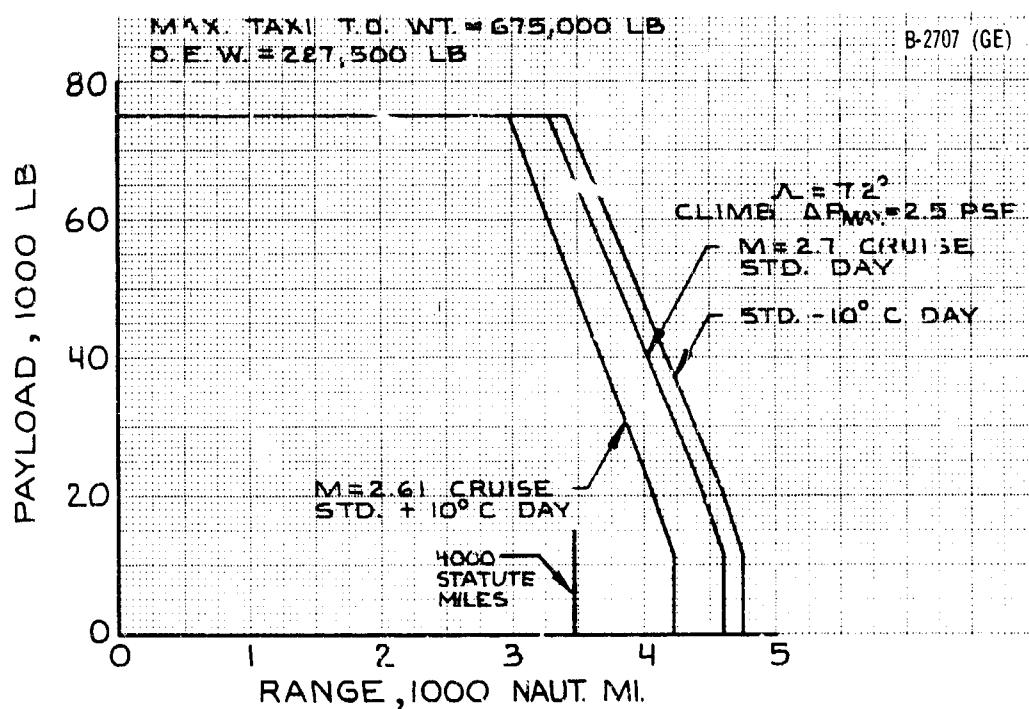


Figure 2-2. Payload Range, International Mission, Non Standard Day

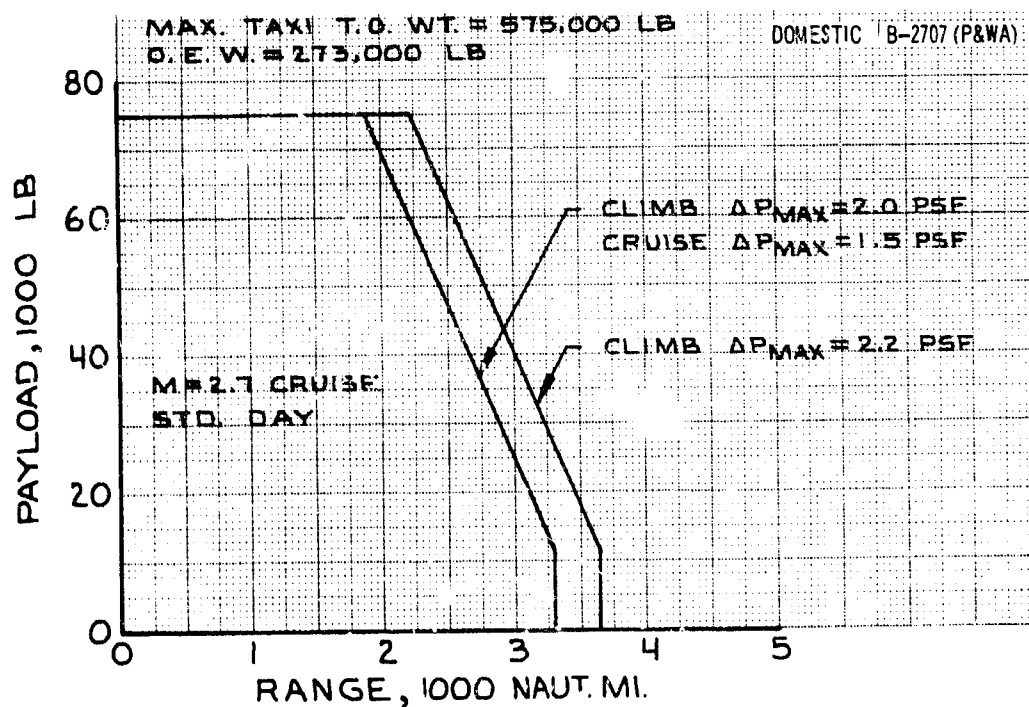
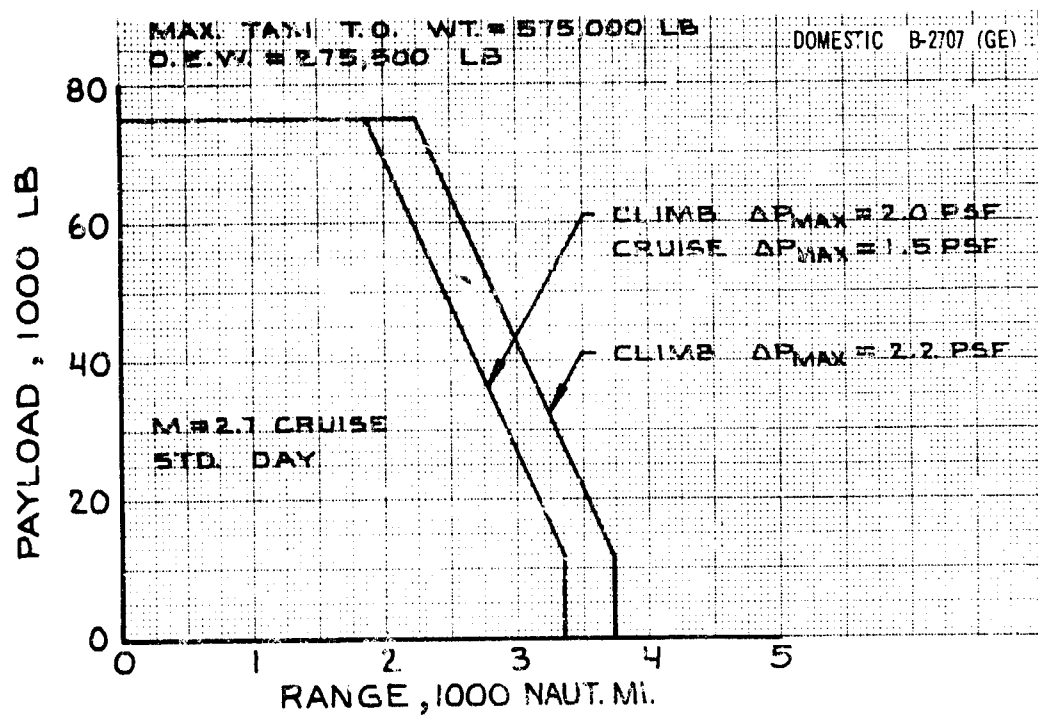


Figure 2-3. Payload Range, Domestic B-2707

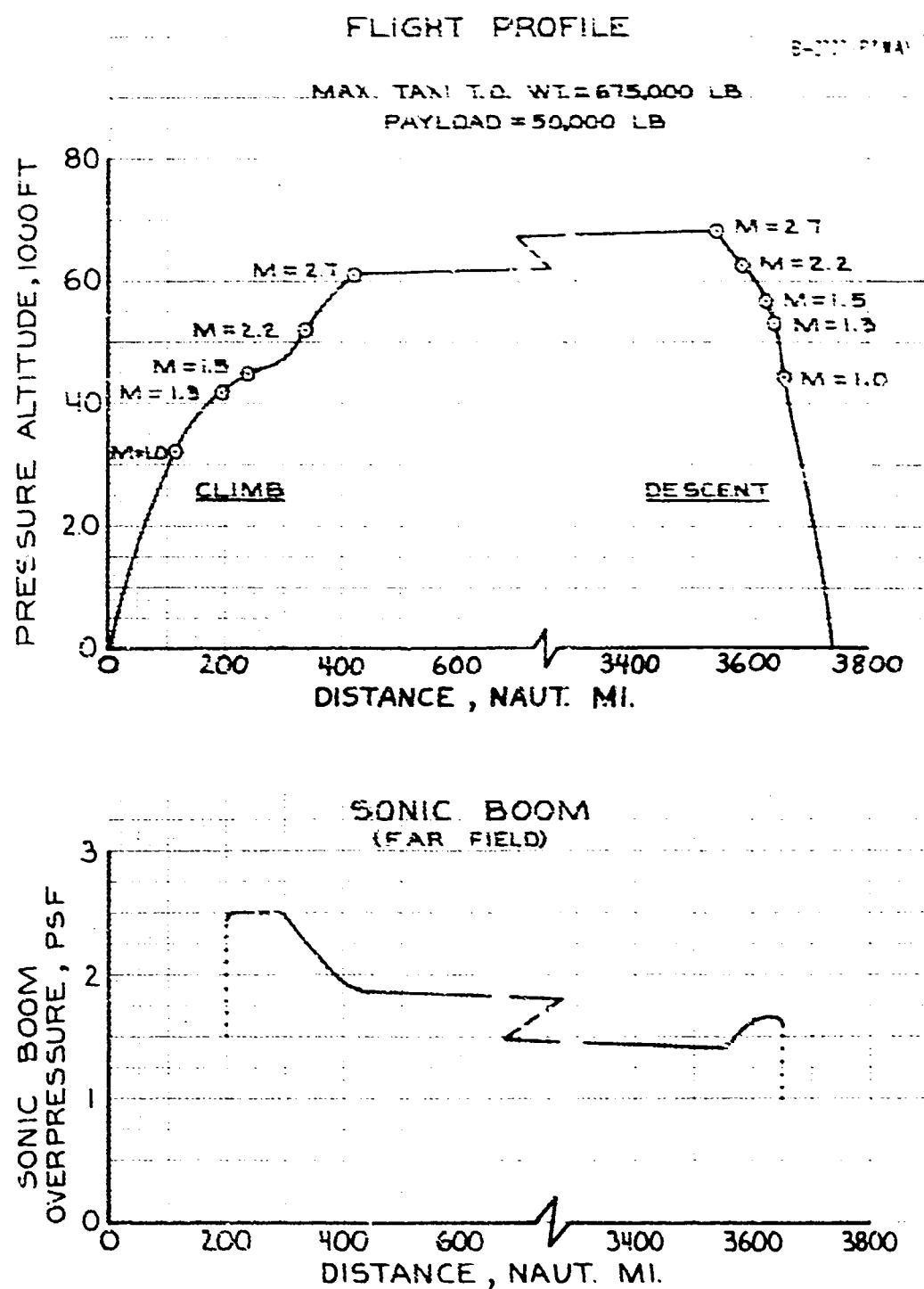


Figure 2-4. Far Field Sonic Boom Overpressures

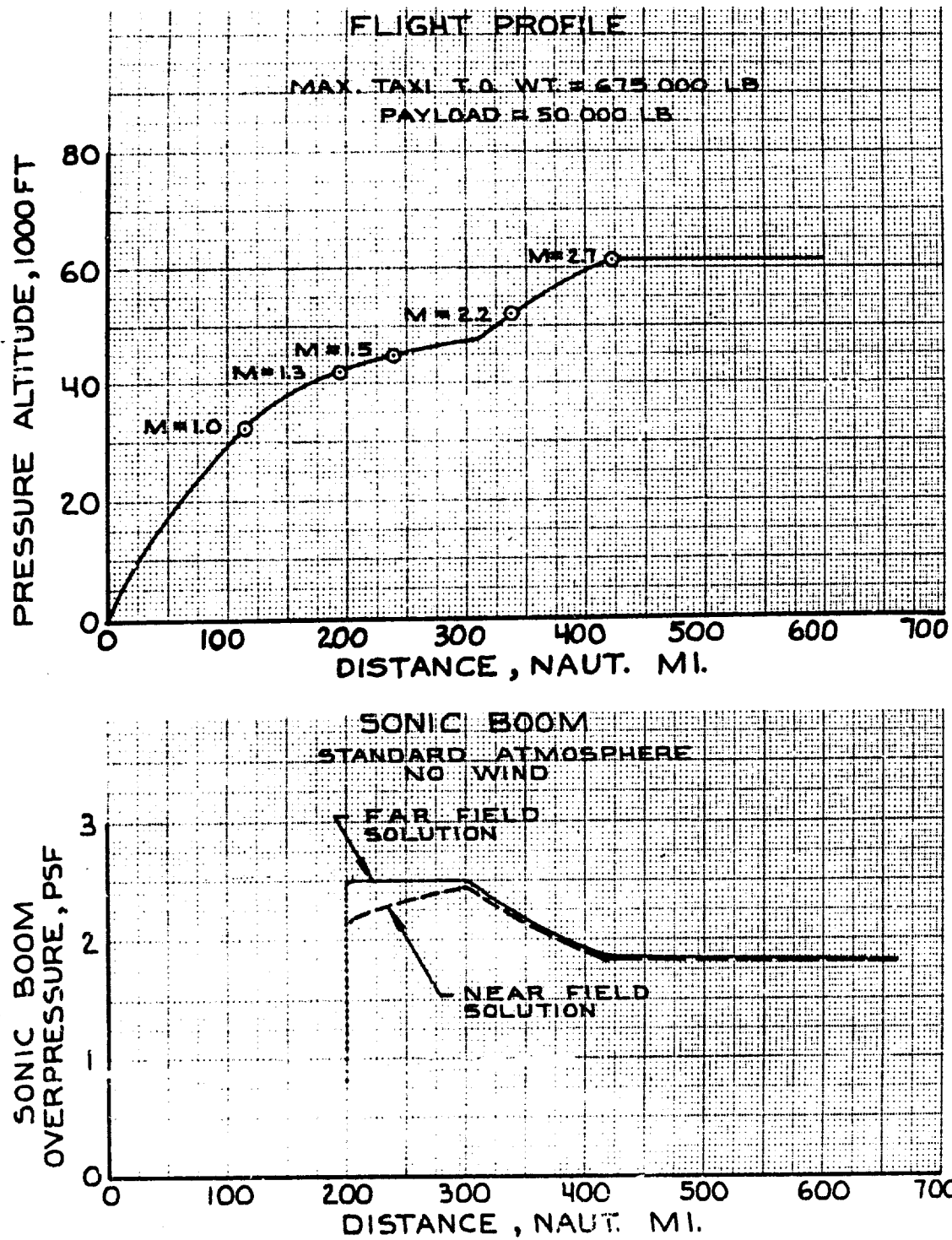


Figure 2-5. Sonic Boom Under Flight Track

A flap setting of 20/40 degrees was selected as the basic takeoff flap for the performance shown in the following paragraphs. This choice provides moderate liftoff speeds ($V_{LO} = 169$ kn at 675,000 lb) while meeting the FAA community noise objective of 105 PNdB. At the maximum taxi weight, liftoff speeds as low as 159 kn are possible using a 30/50-degree flap setting.

All takeoff performance shown is based on a forward cg location of 0.595 C_R . Most normal takeoffs will be accomplished at a cg location of 0.615 C_R which results in improved takeoff lift coefficient and improved climb out lift to drag ratio. At a gross weight of 675,000 lb on a standard day, the field length is reduced from 7,000 ft to 6,300 ft, the takeoff speed from 169 kn to 162 kn, and the community noise from 100 PNdB to 99 PNdB for the B-2707 (GE). The corresponding improvements for the B-2707 (P&WA) are: The field length is reduced from 7,300 to 6,600 ft, the takeoff speed from 169 kn to 162 kn, and the community noise from 105 PNdB to 104 PNdB.

2.2.1 Takeoff Field Lengths and Community Noise

FAR takeoff lengths are shown in Fig. 2-6 for a sea level standard +15°C day. At a weight of 675,000 lb, the FAR takeoff field length is 8,300 ft for the B-2707 (GE) and 8,600 ft for the B-2707 (P&WA). On a standard day the field lengths will be reduced to 7,000 ft for the GE and 7,150 for the P&WA engines. Data for maximum augmented thrust for both engines, dry thrust for the GE, and reduced augmentation for the P&WA are presented. Rotation, liftoff, and flare to climb altitude follow conventional practices as outlined in Federal Aviation Regulations Part 25. The FAR takeoff field length is determined by the all-engines-operating case. Comparisons with the balanced field lengths are given in documents V2-B2707-4 and -5.

Liftoff occurs at 169 kn after a ground roll of 4,800 ft. The flaps are retracted to 5/5-degree setting at an altitude of 400 ft. Noise abatement over the community is achieved with thrust reduction to the minimum consistent with a 500-ft-per-minute rate of climb. The takeoff speeds shown in Fig. 2-6 are based upon a body attitude of 10 degrees at liftoff. The liftoff

speeds are 10 percent greater than the nongeometry limited minimum unstick speeds in the current FAR. Airplane geometry prevents demonstration of minimum unstick speed in ground effect; however, the liftoff speeds are always at least 5 percent above the geometry-limited minimum speed.

All takeoff climb gradient requirements outlined in FAR 25.121 are easily met by the B-2707 with the critical engine inoperative. At sea level on a standard +15°C day, both the FAR requirement of 0.03 second segment gradient and the takeoff field length objective can be met at weights of 750,000 lb for the B-2707 (GE) and 740,000 lb for the B-2707 (P&WA) with a 20/40-degree flap setting.

2.2.2 Takeoff Noise

Community noise levels are shown in Fig. 2-7 corresponding to the takeoff performance shown in Fig. 2-6. Takeoff noise levels around the airport and community are presented in Fig. 2-8 for takeoff with maximum augmented thrust and taxi weight of 675,000 lb. The B-2707 (GE) is 1,750 ft over the community. The B-2707 (P&WA) is at 1,450 ft altitude. The noise characteristics shown reflect the jet noise levels of the two offered engines together with inlet noise suppression.

In addition to noise suppression studies using the nozzle ejector combinations offered by the engine manufacturers, Boeing has also conducted an intensive noise suppression research and development program to find methods of further improving the noise characteristics. This work is detailed in Propulsion Report, V2-B2707-12. The use of the Boeing jet noise suppressor, based on this research work, results in significant reductions in airport noise levels with only a slight increase in takeoff field lengths as shown in Table 2-B.

A comparison of the noise contours with the Boeing jet noise suppressor and inherent suppression is given in Fig. 2-9. The lateral spread of the 110-PNdB contours is reduced from more than 5,000 to less than 3,000 ft on the airport for the B-2707 (GE). Use of the Boeing jet noise suppressor results in essentially the same noise contours with either engine.

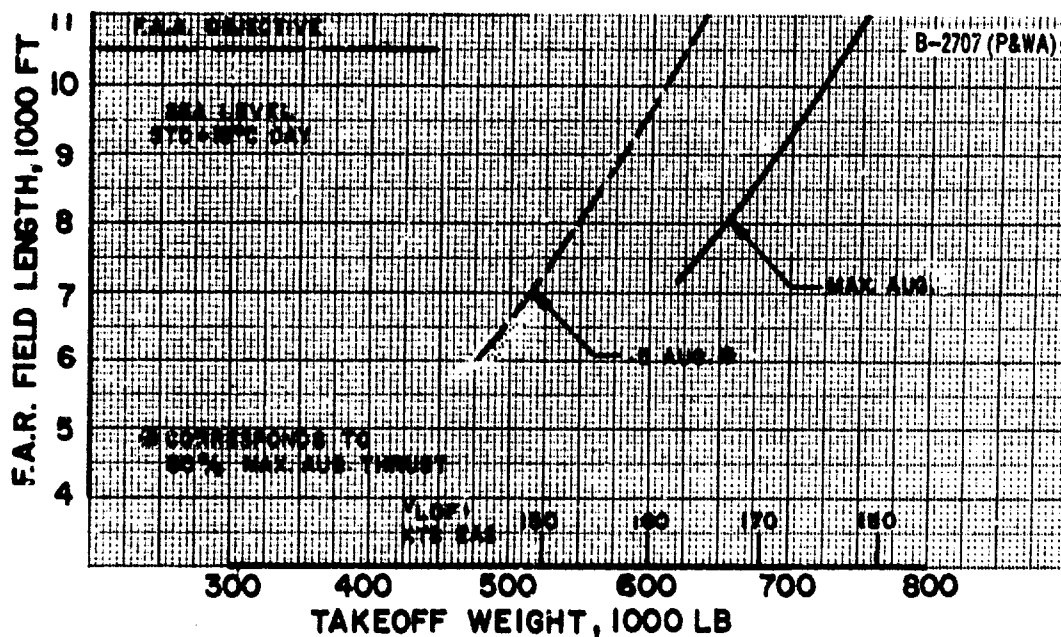
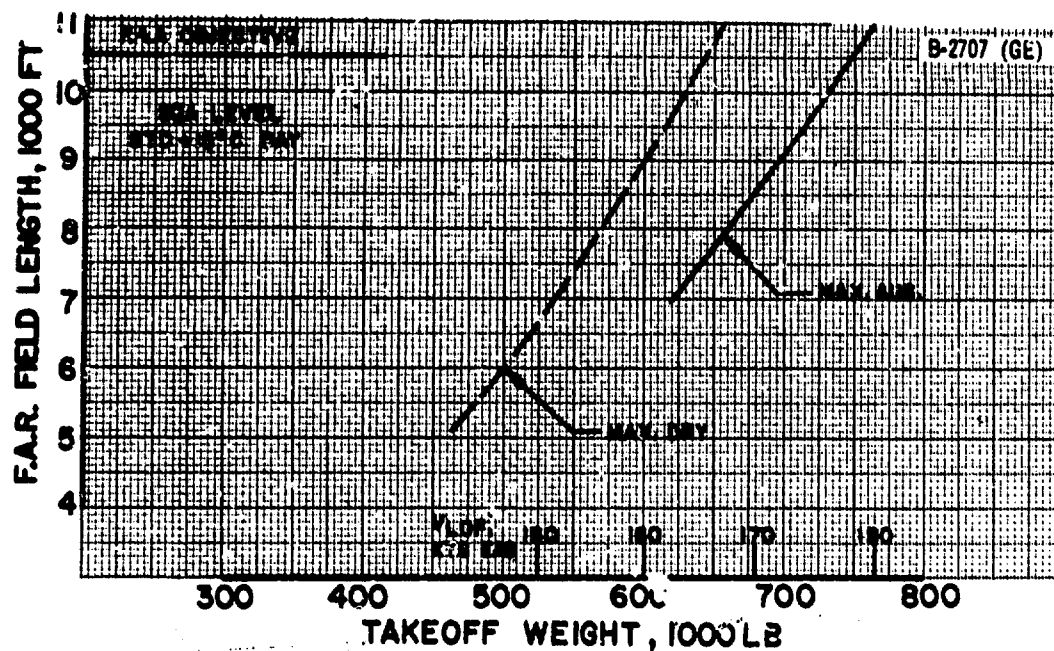


Figure 2-6. Takeoff Field Lengths and Speeds

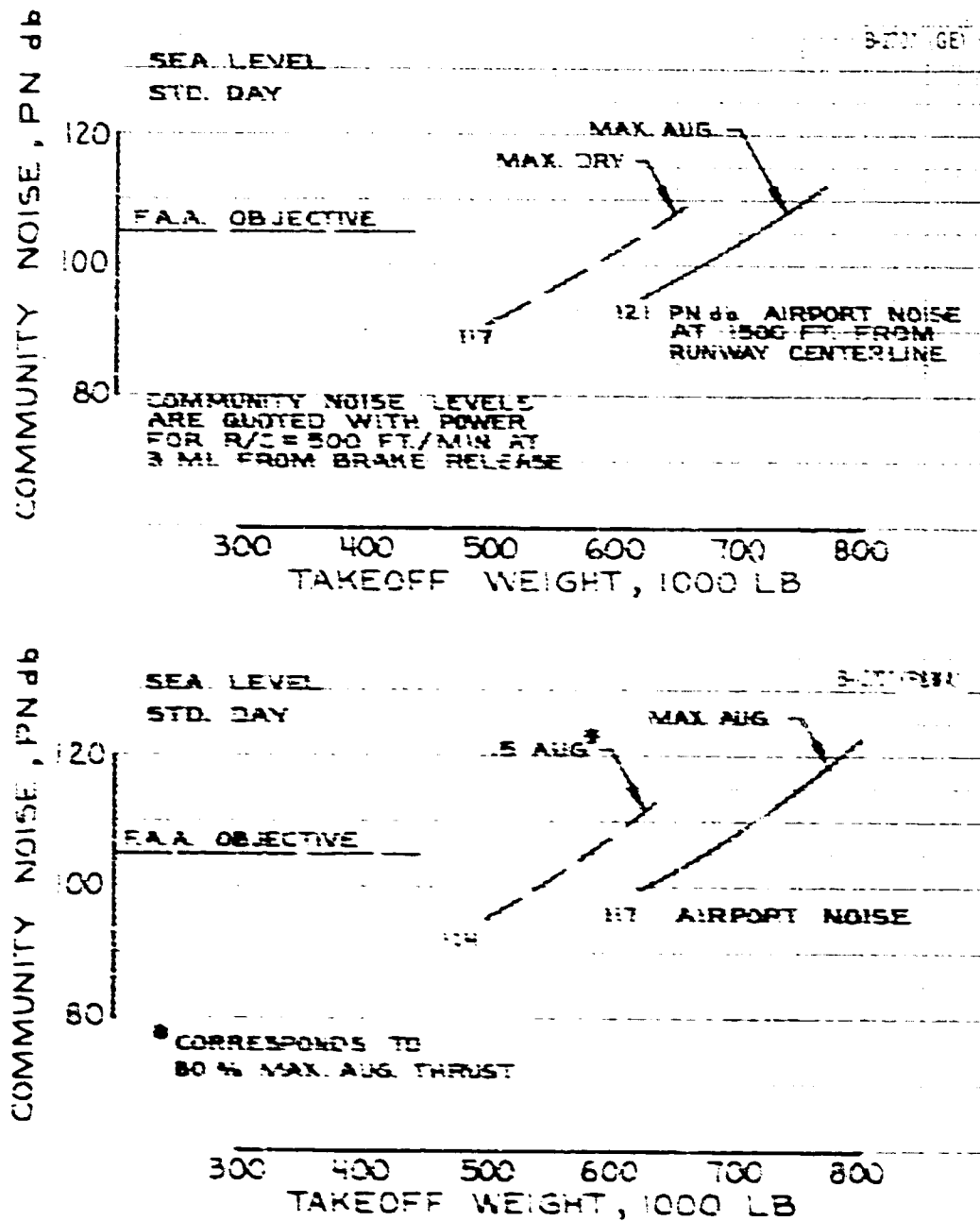
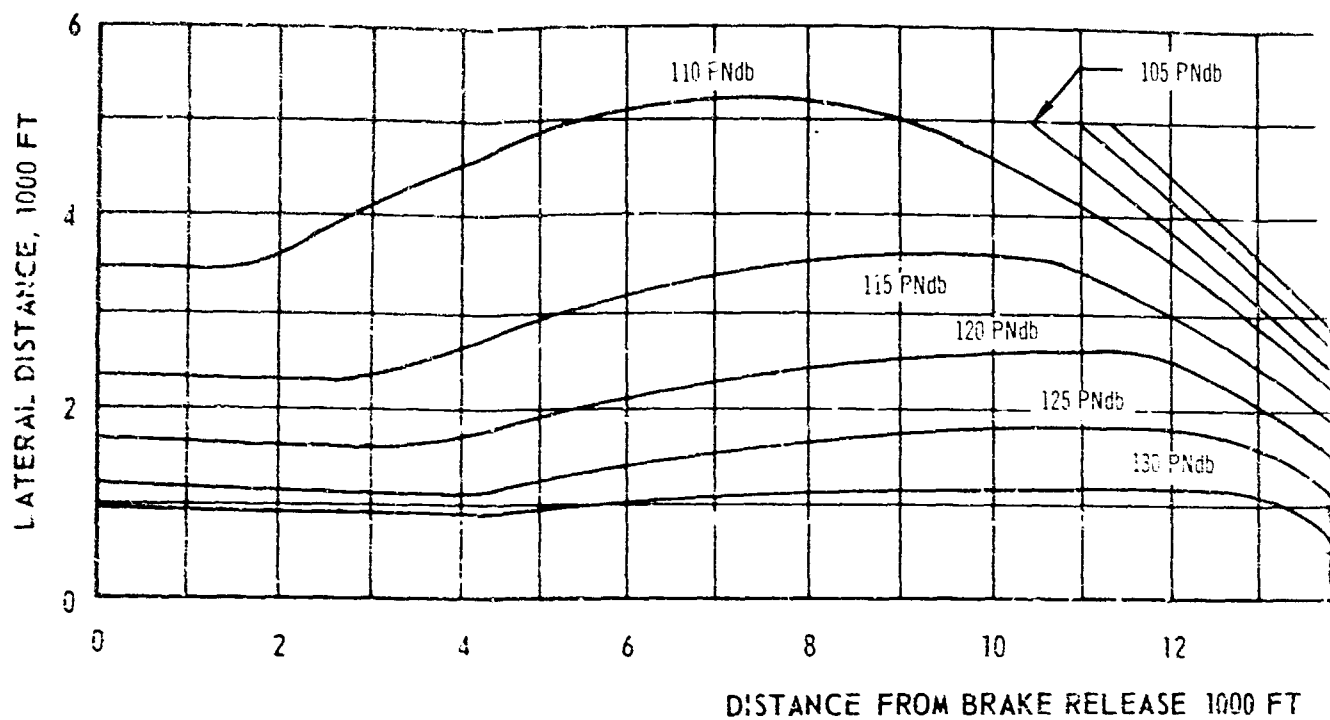
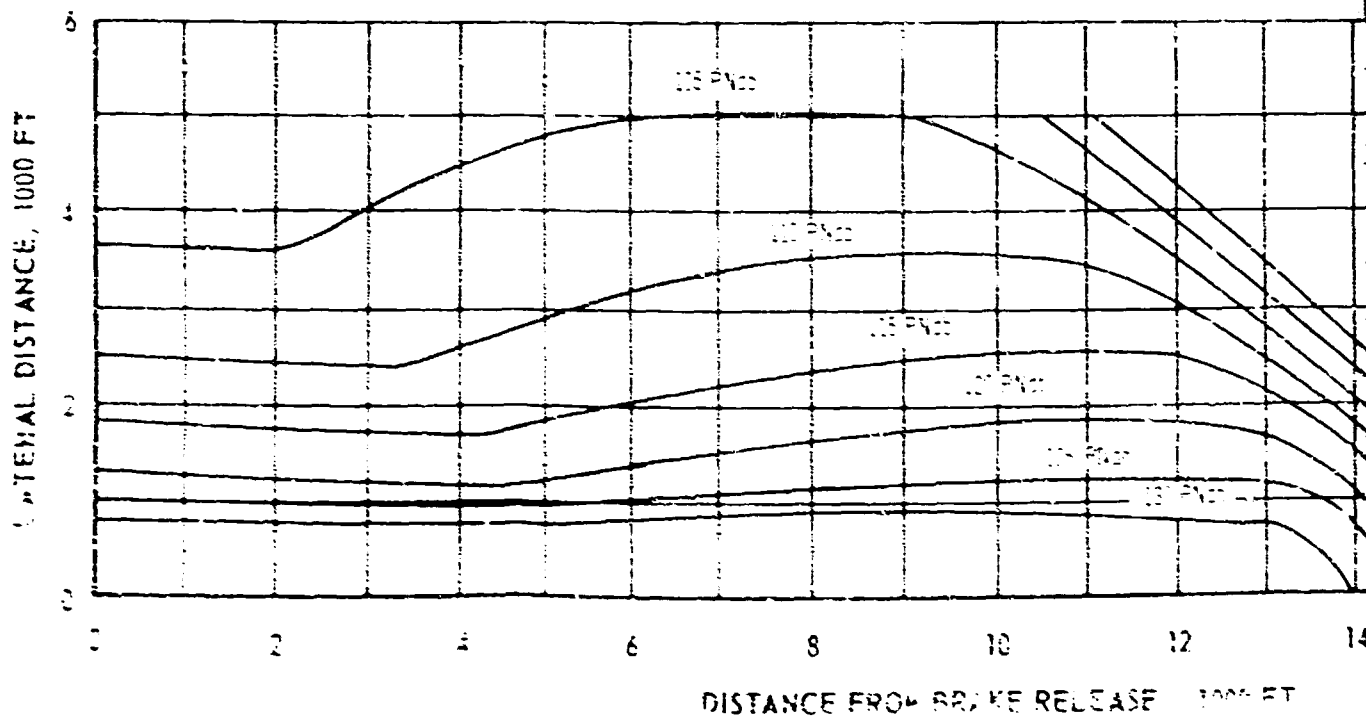
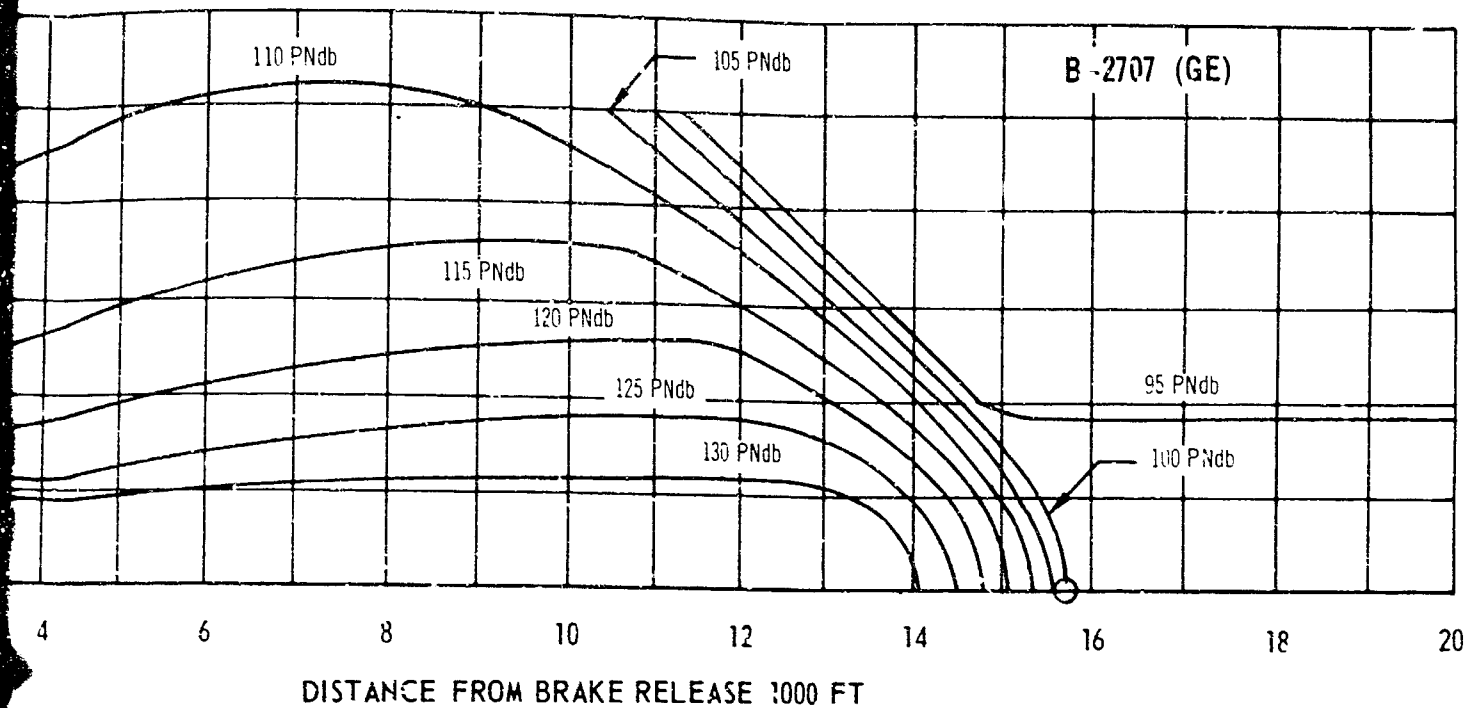


Figure 2-2. Takeoff Community Noise

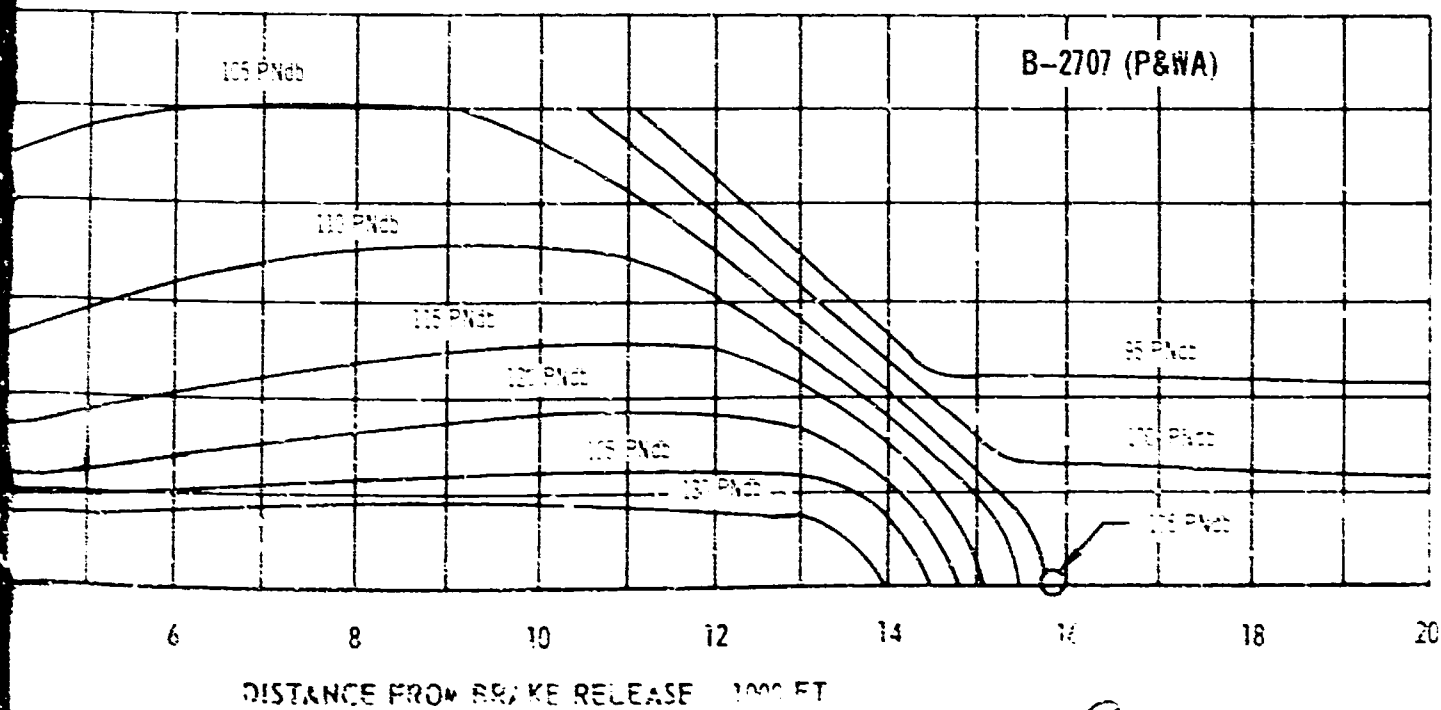


MAXIMUM TAXI WEIGHT 675,000 LB
 MAXIMUM AUGMENTED TAKEOFF THRUST
 STANDARD DAY





MAXIMUM TAXI WEIGHT 675,000 LB
 MAXIMUM AUGMENTED TAKEOFF THRUST
 STANDARD DAY



3
 Figure 2-2. Takeoff Noise Contours.

Table 2-B. Noise Comparison With Boeing Jet Noise Suppressor

Item	GE 4/J5P Engine	P&WA JTF17A-21B Engine
Airport noise, (PNdb)		
Inherent suppression	121	117
Boeing jet suppressor	112	113
Community noise (PNdb)		
Inherent suppression	100	105
Boeing jet suppressor	98	104
FAR takeoff field length (ft) on a standard day +15° C		
Inherent suppression	8,300	8,500
Boeing suppression	8,800	9,000

2.3 APPROACH AND LANDING PERFORMANCE

Landing field lengths, speeds, and approach noise levels are presented in this paragraph. The performance shown is based upon use of the 20/40-degree flap setting. This setting was selected as a compromise of attitude, approach noise, speed, and field length, giving an approach speed in excess of that required under present FAR 25.

Performance and noise trades for other flap settings are presented in documents V2-B2704-4 and -5.

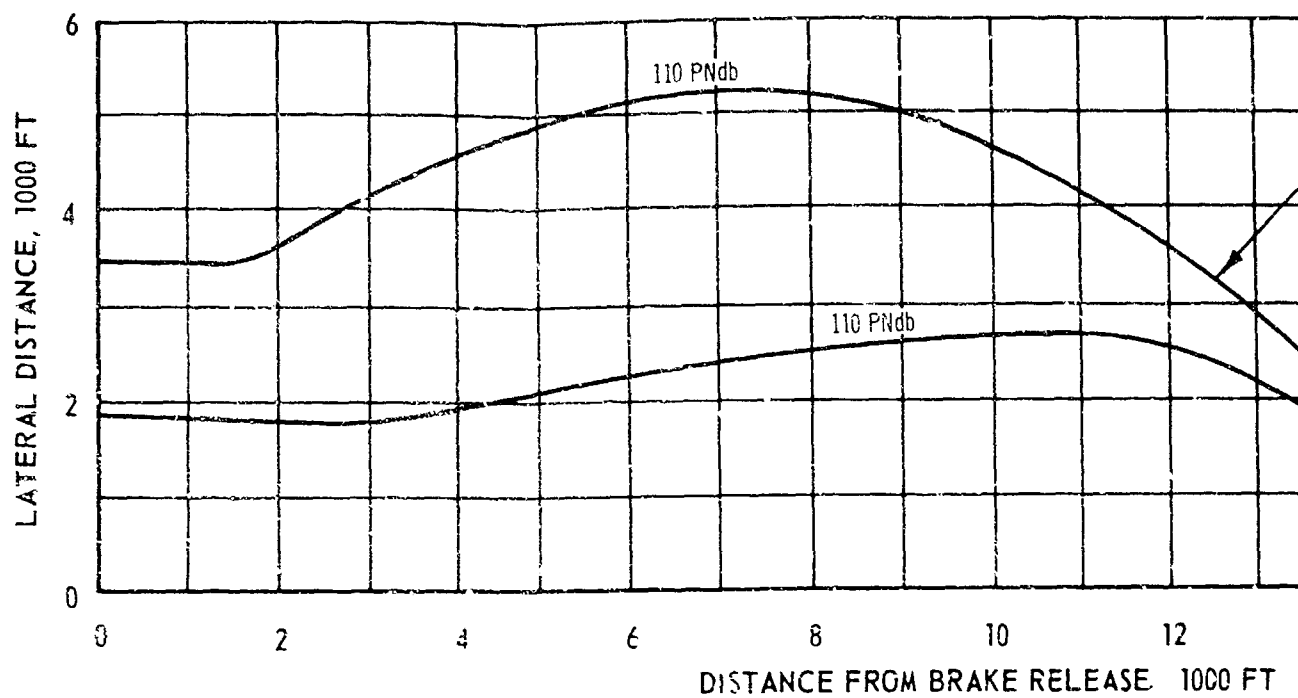
2.3.1 FAR Landing Field Lengths and Speeds

Figure 2-10 shows the FAR landing field lengths for a range of landing weights under wet and dry runway conditions. A 3-degree glide slope has been used to compute performance. Field lengths have been computed using brakes and spoilers only. The wet-runway field lengths have been computed using the alternate method of compliance according to FAA Advisory Circular 121.195 d-1 effective November 19, 1965. The wet runway FAR landing field lengths at maximum landing weight are 7,600 ft for the B-2707 (GE) and 7,500 ft for the B-2707 (P&WA). The use of a 30/50-degree flap setting would reduce the wet-runway FAR landing field length 500 ft. The use of two engines with reverse thrust and

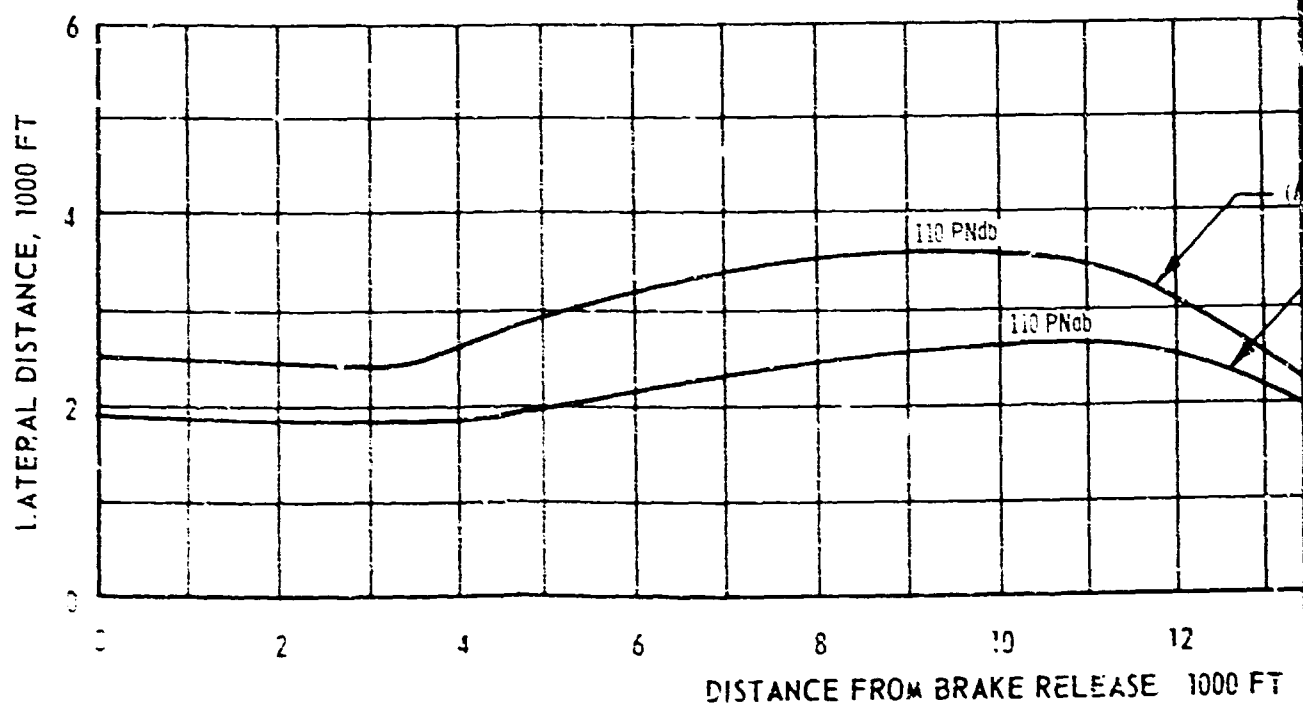
the 30/50-degree flap setting would result in a further reduction in FAR field length to 6,000 ft. Dry runway FAR landing field lengths are also shown in Fig. 2-10.

All landing approaches are made on the stable side of the thrust required curve. At maximum landing weights and using 20/40-degree flaps, the approach speed of the B-2707 (GE) is 153 kn while the B-2707 (P&WA) approaches at 151 kn. If lower approach speeds are desired, 30/50-degree flaps may be used resulting in approach speeds of 141 kn for the B-2707 (GE) and 140 kn for the B-2707 (P&WA). These speeds are only slightly above those of current subsonic jets. For example, a 707-300C airplane at a maximum landing weight of 258,000 lb approaches at 137 kn.

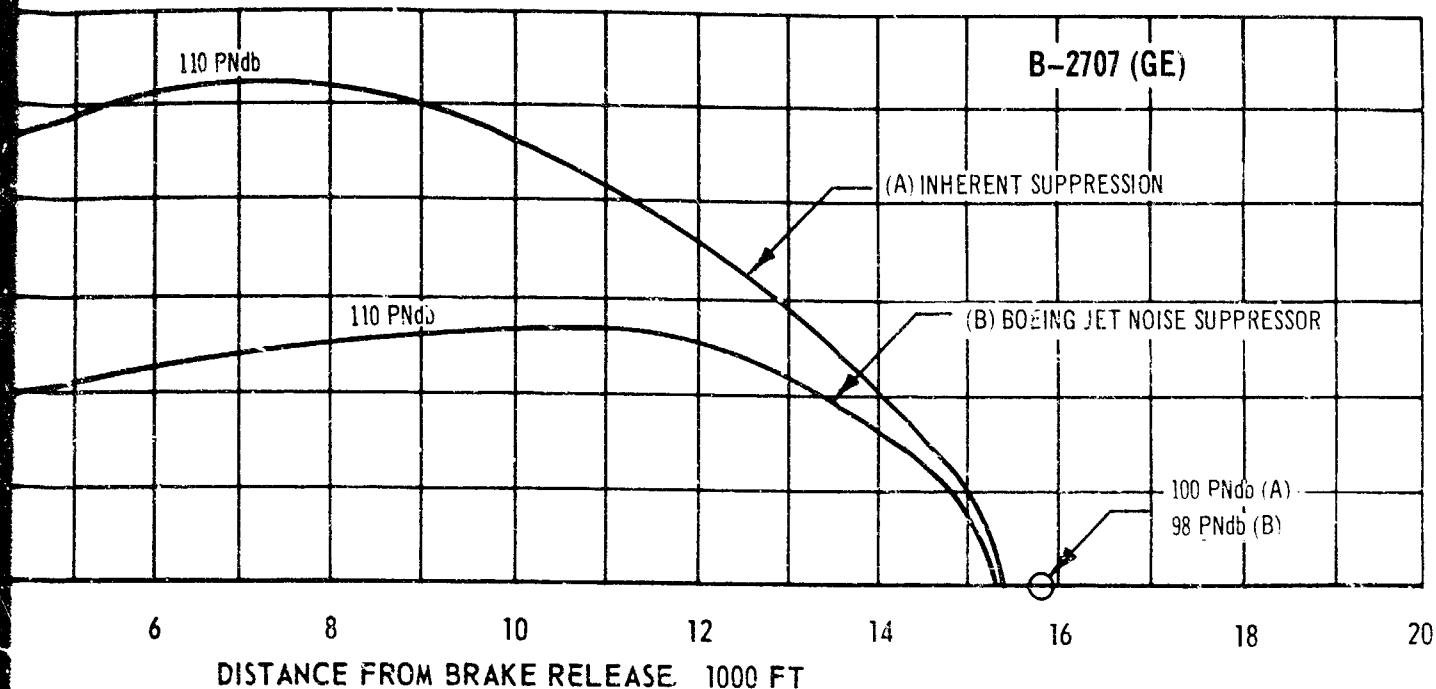
All landing performance is based on a forward cg location of 0.595 C_R corresponding to the maximum payload capacity. At smaller payloads, the cg's are more aft, resulting in improved approach lift-to-drag ratio and improved landing lift coefficients. With 50,000-lb payload at 0.615 C_R and a maximum landing weight of 430,000 lb, the FAR field length for a dry runway is reduced from 7,500 to 7,000 ft, the approach speed from 153 to 145 kn, and the community noise from 112 to 111 PNdb for the B-2707 (GE).



MAXIMUM TAXI WEIGHT 675,000 LB
 MAXIMUM AUGMENTED TAKEOFF THRUST
 STANDARD DAY



7



MAXIMUM TAXI WEIGHT 675,000 LB
 MAXIMUM AUGMENTED TAKEOFF THRUST
 STANDARD DAY

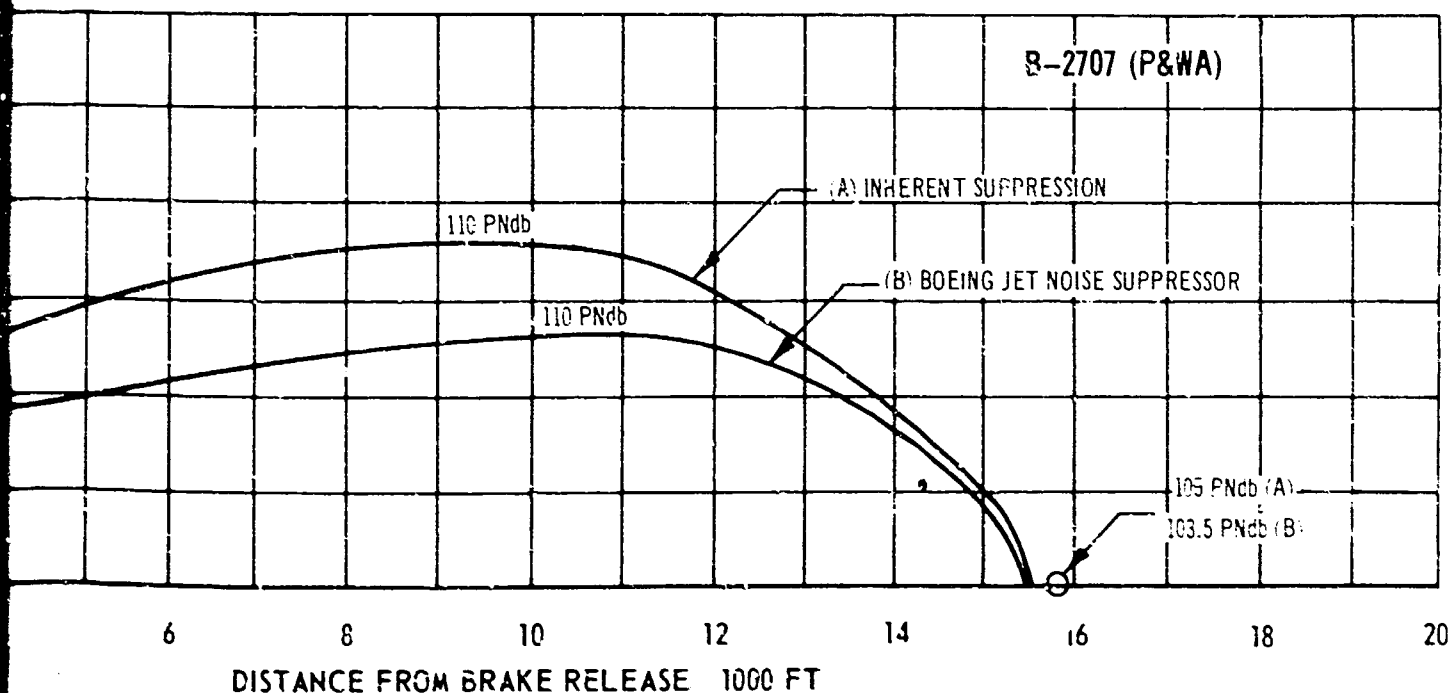


Figure 2-9. Boeing Jet Suppressor, Effect on Takeoff Noise

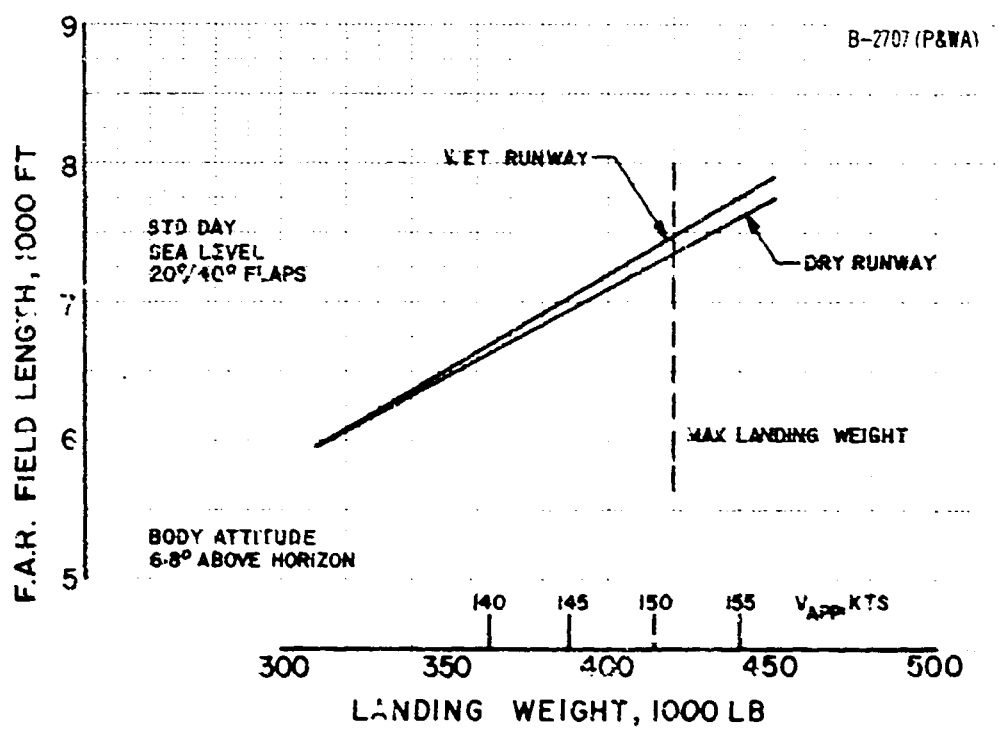
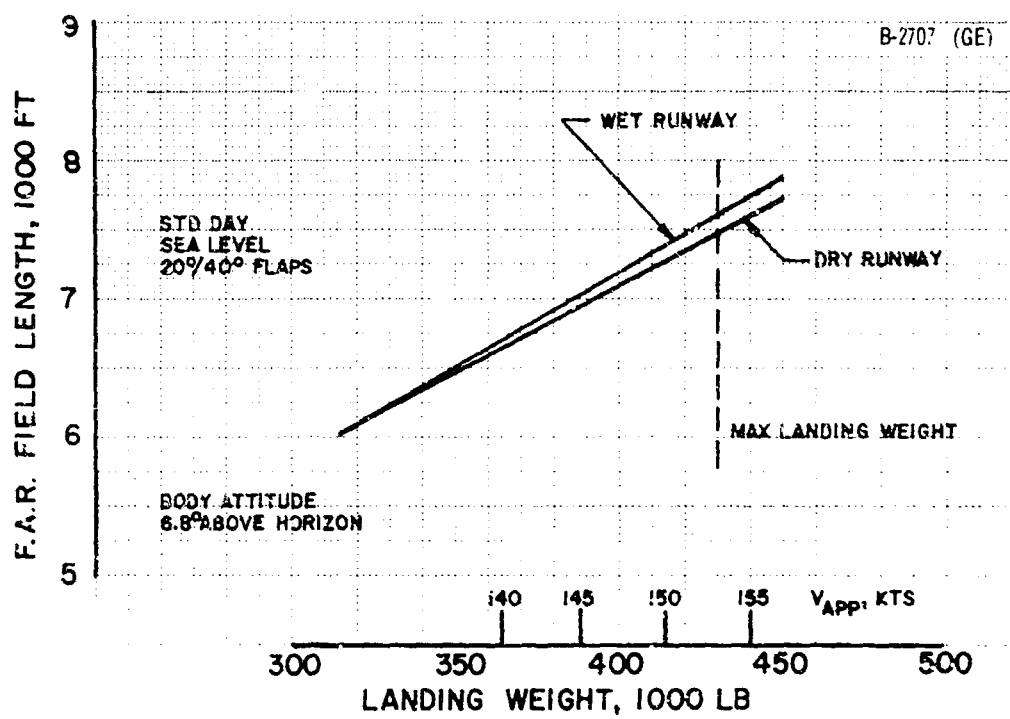


Figure 2-10. Landing Field Lengths and Speeds

The corresponding improvements for the B-2707 (P&WA) and a maximum landing weight of 420,000 lb are: The field length is reduced from 7,400 ft to 6,900 ft; the approach speed is reduced from 151 to 143 kn; and approach noise is reduced from 115 to 114 PNdb.

In the event of a go-around, 95 percent of maximum dry thrust is available in approximately 2.5 sec from the time the throttle is advanced. All landing and approach climb gradient requirements of FAR 25.119 and FAR 25.121 are easily met.

2.3.2 Approach Noise

Figure 2-11 shows the community noise levels 1 mi from the end of the landing runway, based on a constant speed and decelerating approach. For the constant speed approach, 20/40-degree flaps are used. A decelerating approach can be used to achieve lower noise levels than are possible with a normal constant speed approach. With this procedure the pilot extends the flaps to 30/50 degrees and reduces the engine thrust at 1.5 mi from the runway threshold. The pilot increases the thrust to maintain reference approach speed after passing over the community. During this maneuver the body attitude remains essentially constant and no trim change is required. The procedure is described in more detail in Operational Suitability (V4-B2707-1, Sec. 2.0).

The approach noise levels are based upon engine operation with a choked inlet which suppresses inlet noise and an open nozzle which provides low jet noise at low power settings. This is discussed in detail in Propulsion Report (V2-B2707-13) and Airport and Community Noise Program (V4-B2707-4).

2.3.3 Landing Field Length With Wing Sweep of 72 Degrees, Wet Runway

With a payload of 50,000 lb and fuel for a balked approach, the wings aft wet runway actual landing distance from a 50-ft obstacle is only 6,900 ft using four-engine reverse thrust at a weight of 350,000 lb for the B-2707 (GE). The wet runway landing distance is 7,400 ft for corresponding conditions using four-engine reverse thrust for the B-2707 (P&WA). The approach speed is 205 kn with a body attitude of 9 degrees.

2.4 OFF-DESIGN AND EMERGENCY RANGE PAYLOAD PERFORMANCE

2.4.1 Subsonic Cruise

Supersonic flight may possibly be prohibited over certain areas; in this event, subsonic cruise at the beginning or ending of a mission would be required. Figure 2-12 shows the capabilities of the B-2707 for such cases. The wing sweep is 42 degrees and the cruise Mach number is 0.85 for the subsonic cruise. For the B-2707 (GE) and for a 400-nmi subsonic cruise requirement, the total range would be reduced about 80 nmi; for a subsonic leg flown at the end of the mission, the total range would be reduced about 120 nmi. For the B-2707 (P&WA), there is no range reduction for a 400-nmi subsonic leg flown at the beginning of the mission; for a subsonic leg flown at the end of the mission, the total range would be reduced only 40 nmi.

2.4.2 Range With Engines Inoperative

The effects on the cruise performance and on the destination reserves of one and two engines being inoperative are shown in Fig. 2-13. The reserves remaining for a planned mission range of 4,000 statute miles (3,470 nmi) for a standard +10° C day is shown for supersonic cruise with one engine inoperative, subsonic cruise with one engine inoperative, and subsonic cruise with two engines inoperative. For the very severe condition of continuing subsonic cruise with two engines inoperative, only 1,500 lb of payload would have to be off loaded for the B-2707 (GE). For cruise with a single engine inoperative for either the subsonic or supersonic cases, about three times the FAR reserve requirements would be remaining after reaching the planned destination.

It is necessary to off load 5,000 lb of payload for the B-2707 (P&WA) to permit the airplane to continue a 4,000-statute-mile mission subsonically with two engines inoperative on a standard +10° C day. For the single-engine-inoperative subsonic or supersonic cases, the planned destination of 4,000 statute miles could be reached with a minimum of three times the FAR reserve requirements remaining.

The effect of enroute engine failures for the domestic B-2707 has been studied for standard and standard +10° C day conditions. The destination reserve remaining following a two-engine failure at the midpoint and then continuing cruise at $M = 0.80$ is about twice the minimum 15-minute holding allowance on a hot day. In the case of an engine failure prior to reaching

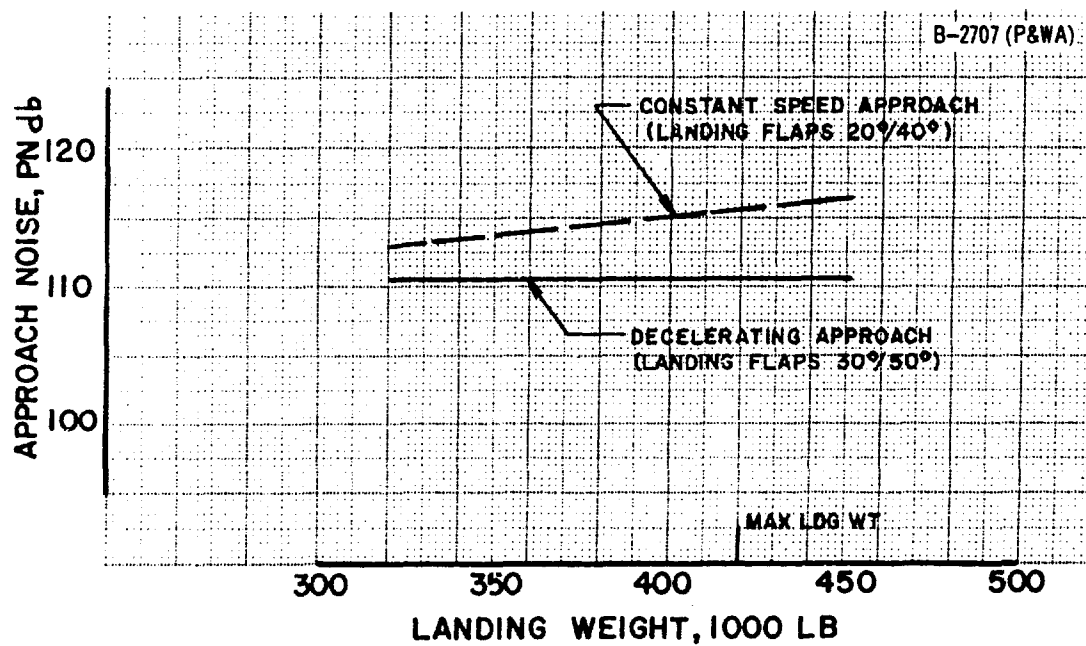
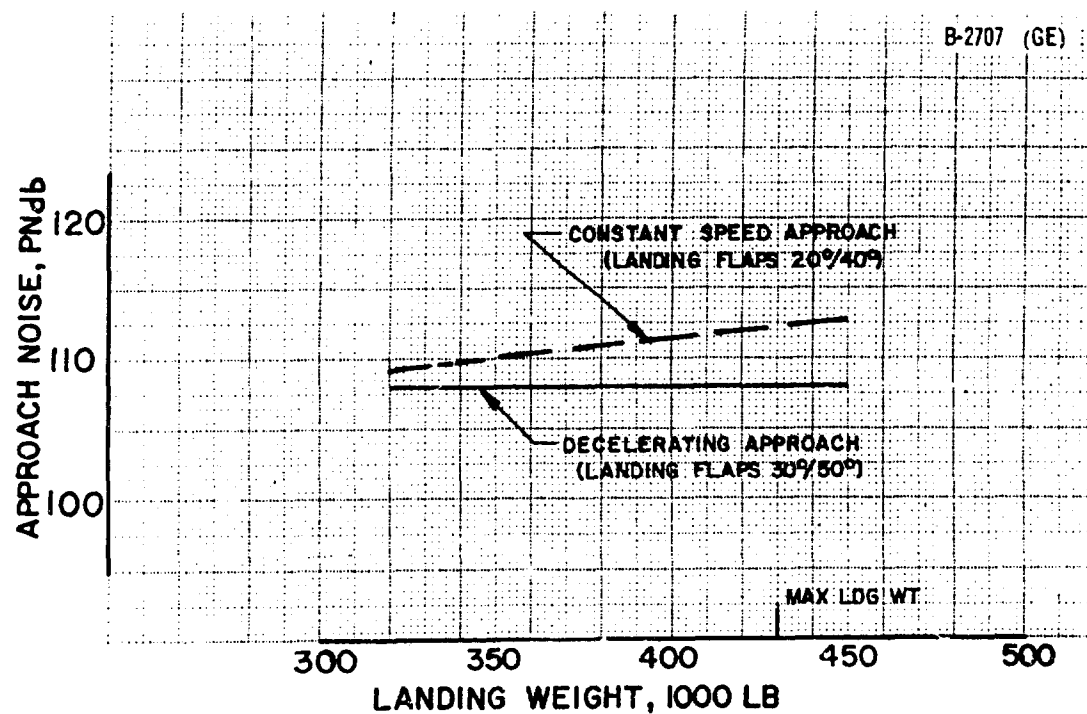


Figure 2-11. Landing Approach Noise

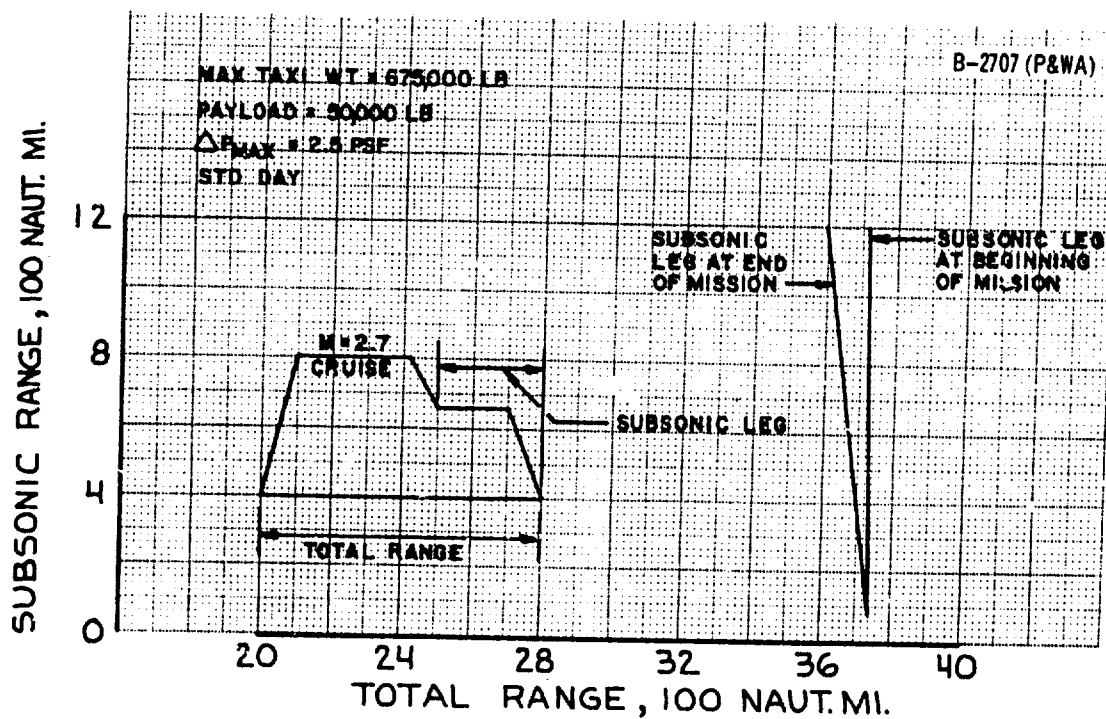
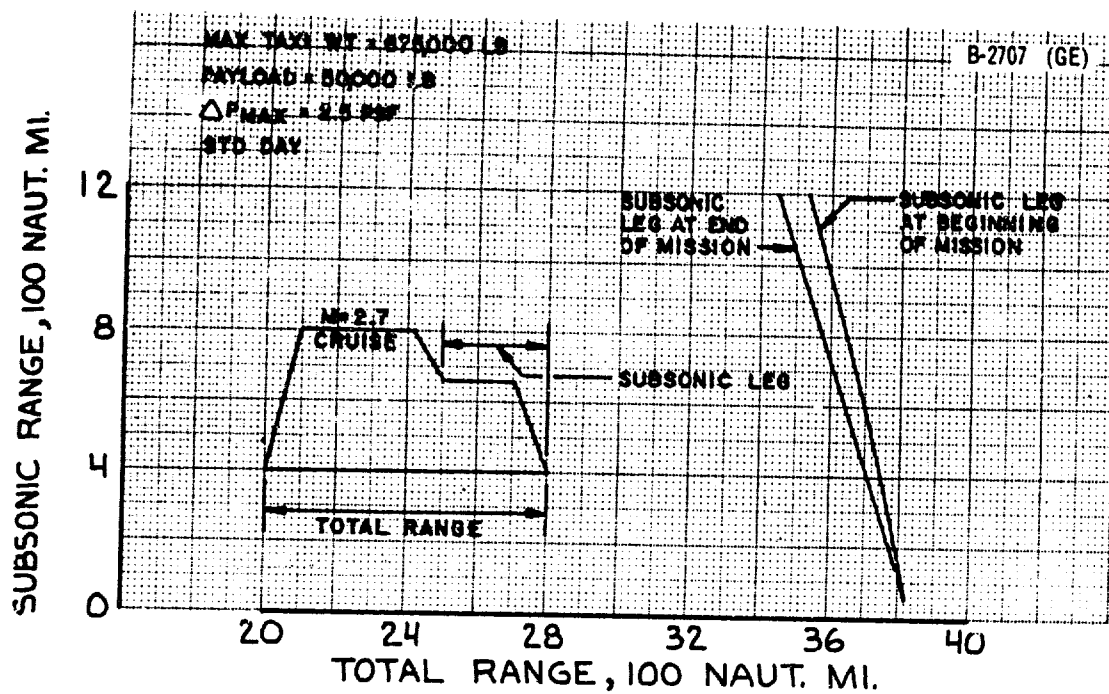
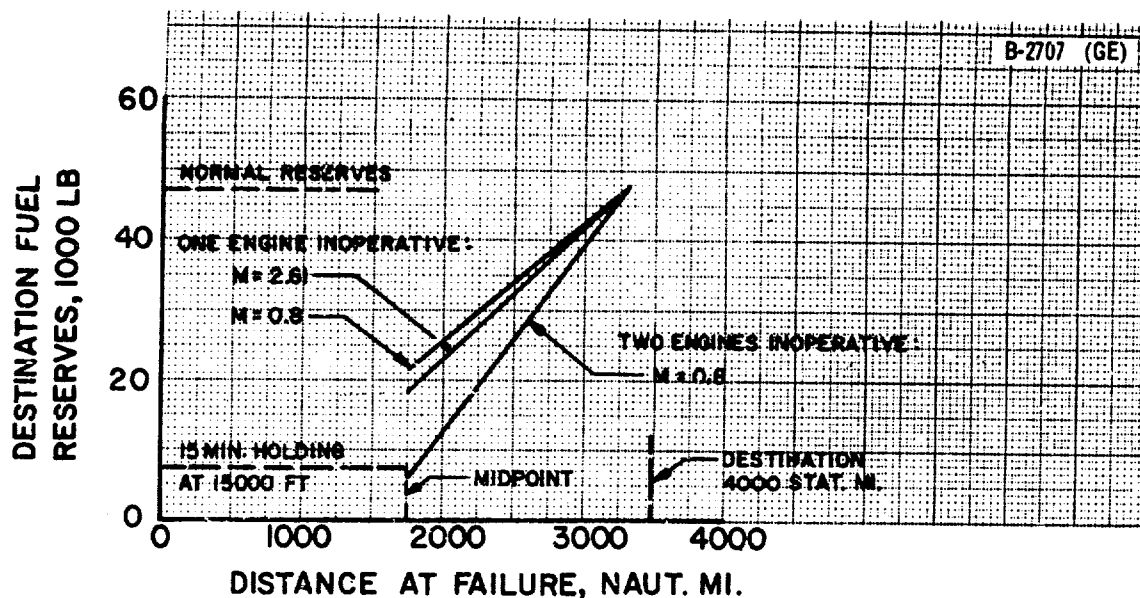


Figure 2-12. Operational Versatility, Subsonic Legs



MAX TAXI WT = 675,000 LB
 RANGE = 3470 NAUT. MI.
 PAYLOAD = 50000 LB
 STD+10°C DAY
 MAX CLIMB $\Delta P = 2.5$ PSF

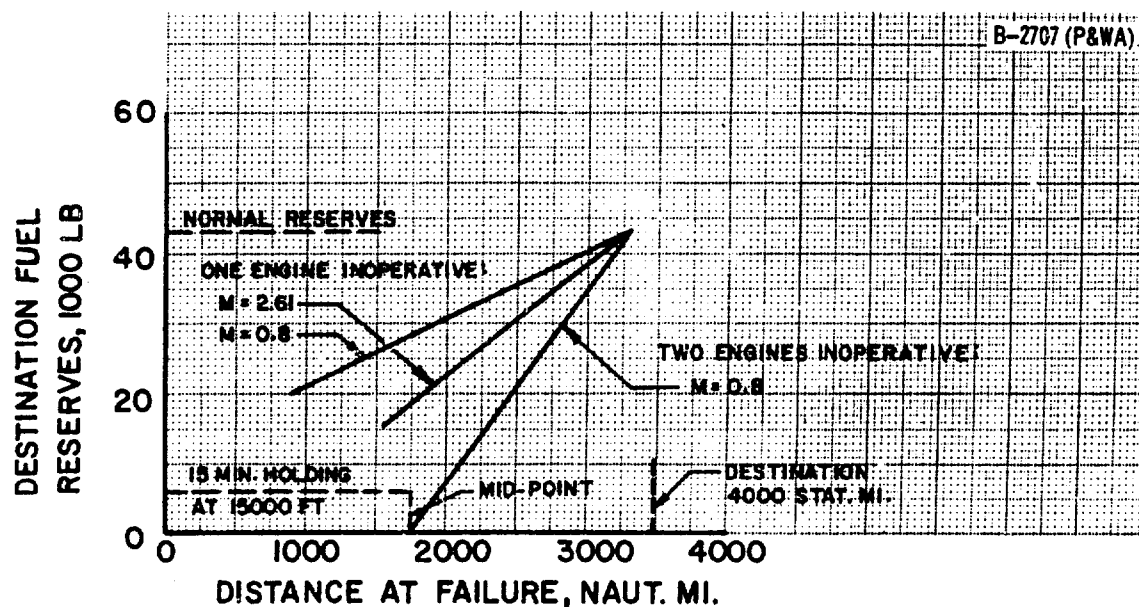


Figure 2-13. Operational Reliability and Safety, International,
 STD+10°C Day

transonic acceleration altitude, missions involving supersonic cruise would be cancelled.

2.4.3 Range With Augmentors Inoperative

Range payload performance has been studied for 1, 2, 3, or 4 augmentors inoperative. Figure 2-14 shows the destination fuel reserves remaining for augmentor failures as a function of distance to failure for a $M = 2.7$ international mission on a standard day. For the worst case, i.e. four augmentors inoperative at midpoint, the B-2707 (GE) would cruise at $M = 0.85$, wing sweep 42 degrees, and could complete the mission with destination fuel reserves of 21,700 lb. Sufficient cruise thrust would be available to continue cruise at $M = 2.7$ at ranges beyond 2,300 nmi. The destination reserves would be 43,000 lb.

The planned destination would be reached with 32,000 lb of fuel reserves remaining if 4 augmentors failed at the midpoint on the B-2707 (P&WA).

2.5 PERFORMANCE CALCULATION METHODS

The FAA Supersonic Transport Economic Model Ground Rules for Phase III (SST 66-3, dated June 30, 1966) were used in calculating the mission performance.

All performance data are based upon the U.S. Standard Atmosphere, 1962, at 45 degrees latitude, geometric altitude. Hot day performance has been computed for a modified standard atmosphere wherein the temperature is increased 10°C at all altitudes. A similar procedure was used in defining the atmosphere for the cold day performance. The characteristics for the nonstandard atmospheres are shown in Fig. 2-15. Cruise speed with a stagnation temperature limit of 500°F is shown in Fig. 2-16.

The following special effects are included in the mission performance and have been computed according to the instructions given in the Request for Proposal:

- a. Centrifugal force, computed for non-rotating earth
- b. Gravitational change with altitude
- c. Thrust inclination effect on lift and drag
- d. Increase in range required because of arc length at altitude

e. Cabin air weight

- f. Effect of increased thrust required because of climbing cruise procedure.

Table 2-C shows the detailed effect of these items on the basic international mission for the B-2707 (GE) and B-2707 (P&WA) in the form requested by the RFP.

2.5.1 Mission Calculations

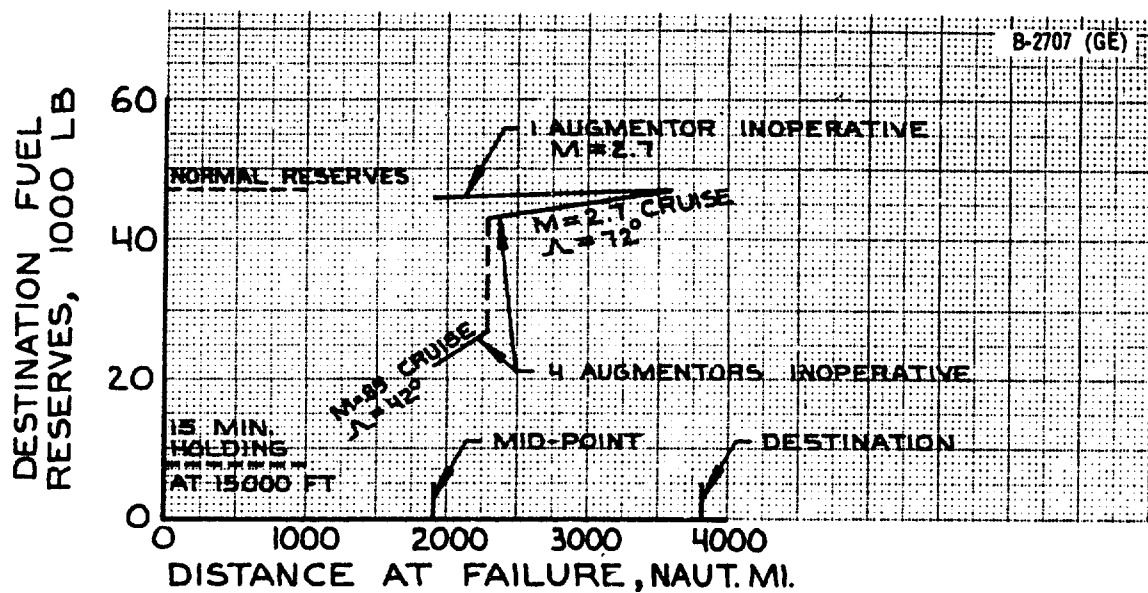
The methods used in calculating the basic performance are the same as those used in Phase I, Volume A-V, Aerodynamics (D6-2400-11, B.3.9). Breakdowns of the time, fuel, and distances for typical missions are given in documents V2-B-2707-4 and -5, Figs. 1-5 and 1-6. A 4-minute air maneuver allowance following takeoff and a 5-minute allowance before landing are made with no distance credit. The reserve fuel consists of 5 percent of the block fuel plus fuel for a missed approach, then climb to 1,500 ft above sea level, then a climb, cruise, and descent to sea level at an alternate airport 300 statute miles away; and finally a 20-minute hold at 15,000 ft over the alternate airport. The alternate cruise altitude and Mach number are selected to minimize the total fuel required for the 300-statute-mile distance.

2.5.1.1 The engine thrust settings used are as follows:

- a. Takeoff, maximum dry or maximum augmented
- b. Climb, maximum dry from V_2 to Mach 0.85, maximum augmented Mach 1.0 to 2.7 for GE maximum dry, V_2 to Mach 0.8, maximum augmented, Mach 1.0 to 2.7 for P&WA
- c. Cruise, optimum
- d. Descent, flight idle, Mach 2.7 to Mach 0.3 at 1,500 ft
- e. Reserves, throttled from maximum dry as required by airplane weight, altitude and speed.

2.5.1.2 The wing sweep schedules used in the mission are as follows:

- a. Takeoff, leading edge sweep = 30 degrees
- b. Departure air maneuver, leading edge sweep = 42 degrees



MAX. TAXI WT. = 675,000 LB
 PAYLOAD = 50,000 LB
 STD. DAY
 MAX CLIMB $\Delta P = 2.5$ PSF

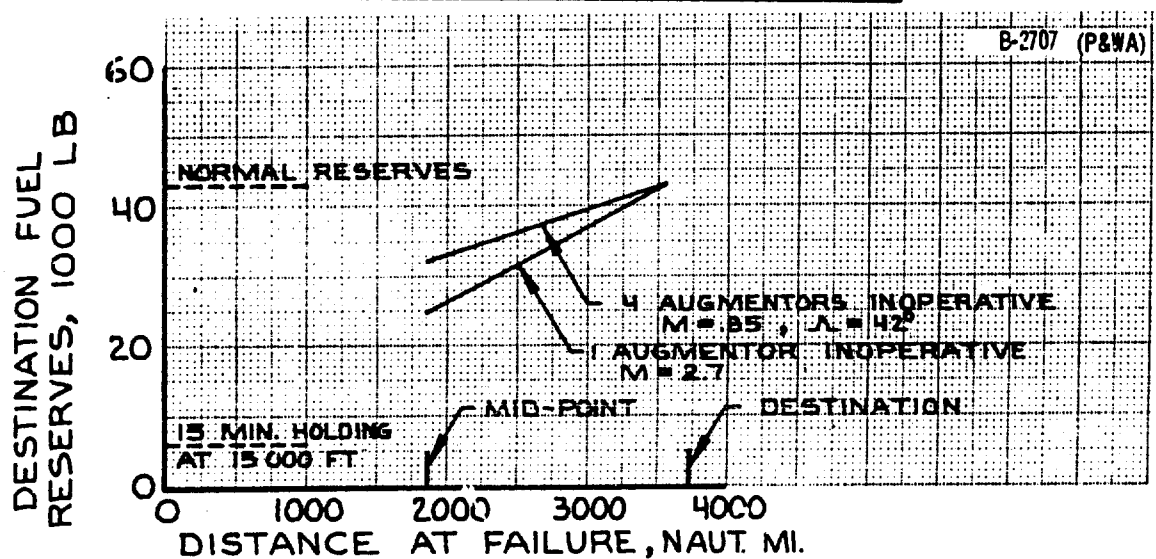


Figure 2-14. Range Capability With Augmentor Failure, Standard Day

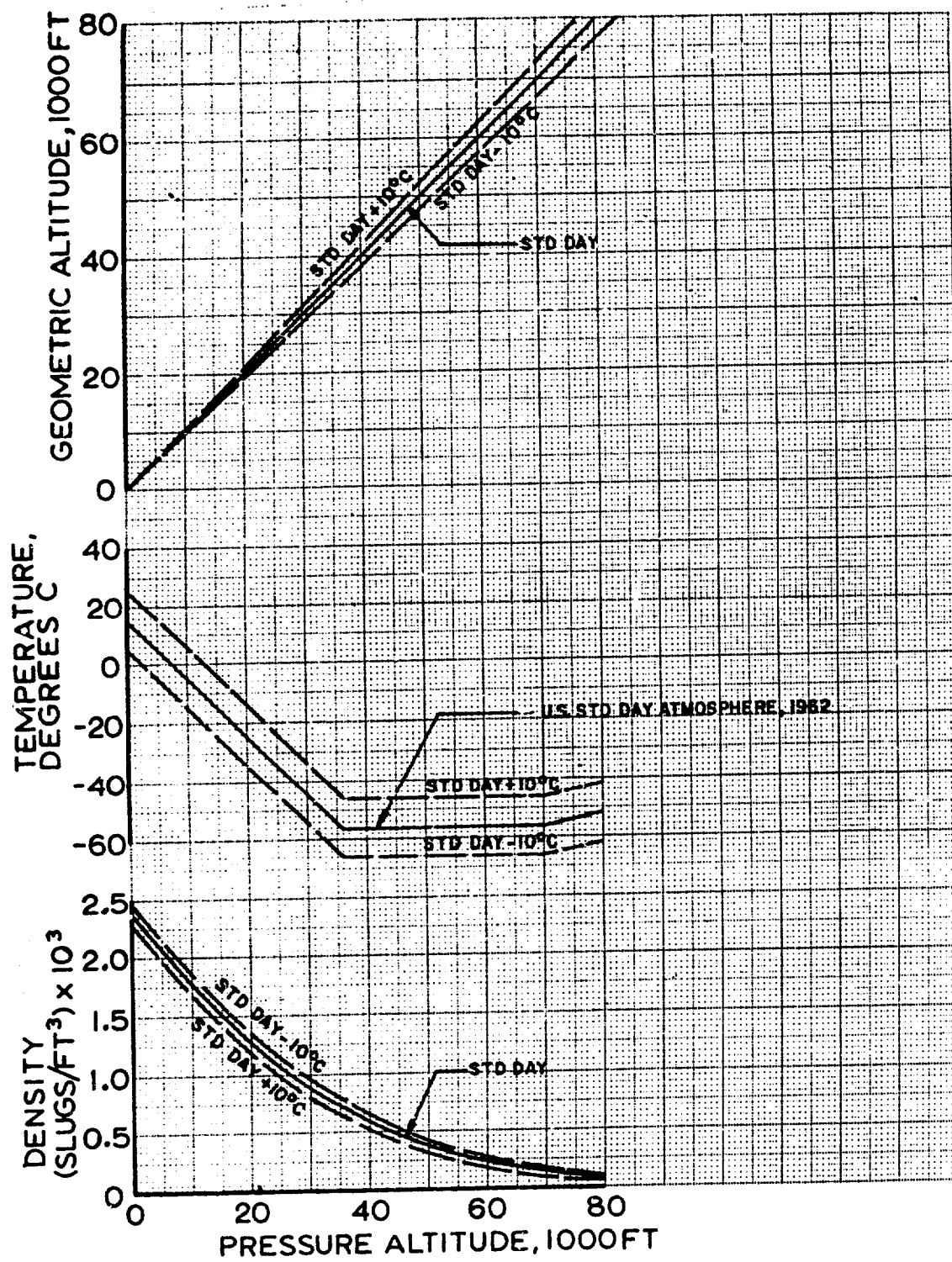


Figure 2-15. Nonstandard Day Atmosphere Definitions

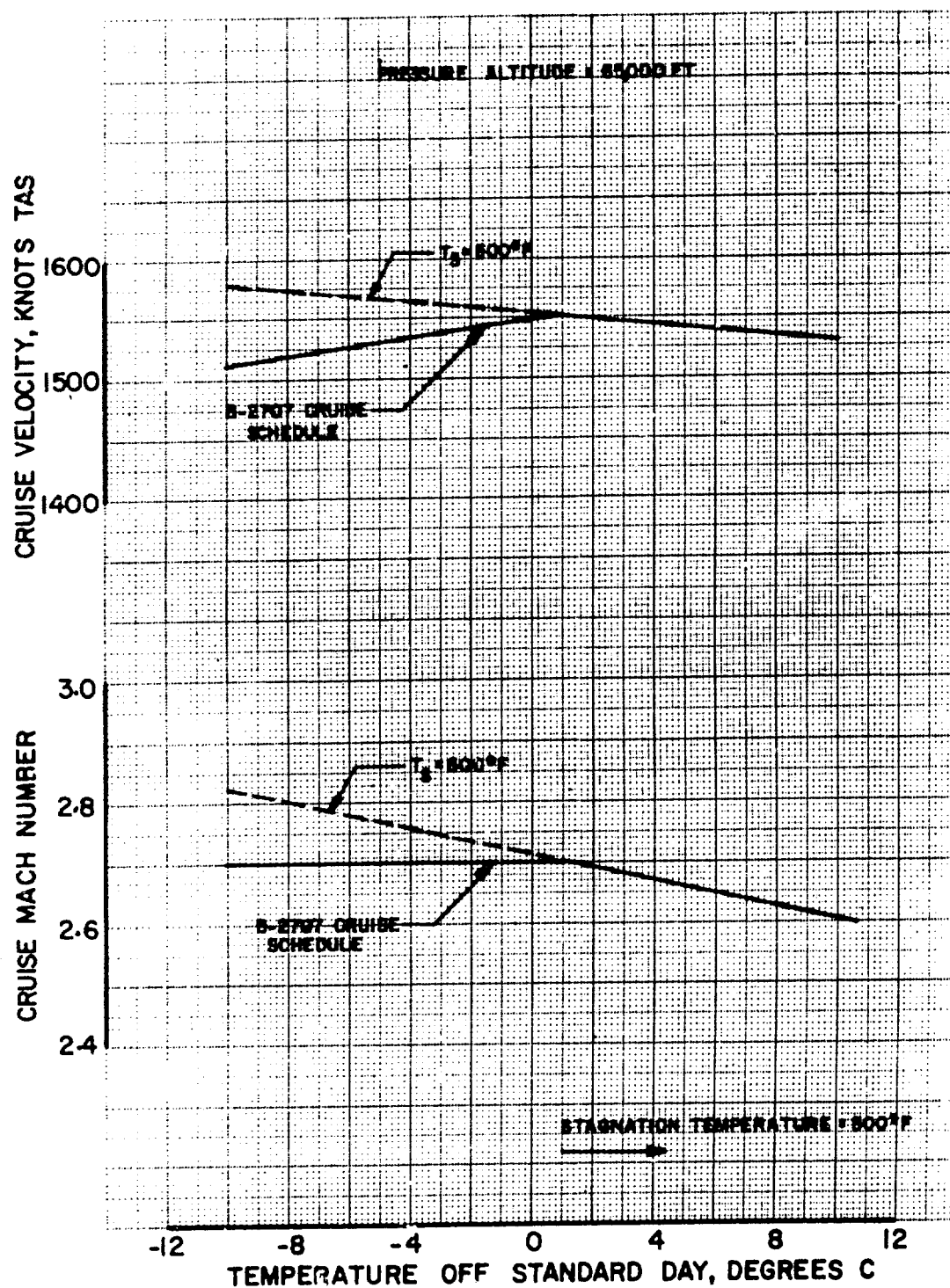


Figure 2-16. B-2707 Cruise Speed and Mach Number

Table 2-C. Special Effects on Mission Performance

Item	Range, (nmi) (For a fixed pay- load of 50,000 lb)		Payload (lb) (For a fixed range of 4,000 statute miles)	
	General Electric GE4/J5P	Pratt & Whitney JTF17A-21B	General Electric GE4/J5P	Pratt & Whitney JTF17A-21B
Basic mission (excluding all special effects)	3,751	3,670	62,872	59,750
Effect of				
Centrifugal force only	36	36	1,656	1,721
g/g ₀ only	13	18	828	860
Thrust effects on lift and drag, only "T sin α"	50	45	2,300	2,151
Arc length at altitude only	-10	-10	-460	-478
Cabin air weight only	-11	-9	-506	-430
Cruise climb only	-15	-12	-690	-574
Basic Mission (Including all special effects)	3,819	3,738	66,000	63,000

c. Climb, Fig. 4-24, V2-B-2707-4, -5

d. Cruise, leading edge sweep = 72 degrees

e. Descent, Fig. 6-1, V2-B2707-4, -5

f. Destination air maneuver, leading edge
sweep = 30 degrees

2.5.1.3 Spoilers are used during the normal and high-speed descents to prevent the cabin rate of descent from exceeding 300 fpm. The normal descent uses full spoilers (45 degrees) below 10,000 ft altitude. The high-speed descent and landing uses full spoilers below 40,000 ft altitude for the B-2707 (GE) and 34,500 ft altitude for the B-2707 (P&WA). Full spoilers are used throughout the emergency descent. The spoiler drags used are as follows:

$M = 0.32$ to $M = 0.85$, wing sweep =
42 degrees, $\Delta C_D = 0.0150$

Below $M = 1.0$, wing sweep = 72 degrees,
 $\Delta C_D = 0.0020$

$M = 1.1$ to 2.7 , wing sweep = 72 degrees,
 $\Delta C_D = 0.0077$ to 0.0028 (linear variation
with Mach number)

2.5.2 Takeoff and Landing Distance

Takeoff and landing field lengths have been calculated by the flight manual performance methods used for the certification of present Boeing jet transports, as described in Phase I (Volume A-V, Aerodynamics) with the exception of flare time. The method for computing takeoff flare is the same as that used in the Phase II-A and II-C studies. Rotation capability was based on a maximum angular velocity of 2.5 degrees per second and an angular acceleration of 2 degrees per second per second. The load factor increment applied during the air distance from liftoff was limited to 0.2 g. Angle of attack was reduced above the 35-ft altitude level when necessary to maintain this load factor limit. Airspeed increases from the speed at 35 ft to the steady state climb speed which is held until power cut-back 1 statute mile beyond the end of the runway.

A load factor of 1.15 was used for the landing flare calculations. Speed at brake application is approximately 0.90 V_{app} . The time delays

and thrust decay factors used during landing and refused takeoff are shown in Table 2-D.

Table 2-D. Time Delays and Thrust Settings, Takeoff and Landing

Item	Time delay (sec.)	Engine thrust
<u>Refused takeoff</u>		
Engine failure recognition and start of throttles back to brakes on	0.4	95 percent takeoff power
Brakes on to throttles back	1.4	80 percent takeoff power
Throttles back to spoilers up	2.0	10 percent takeoff power
Start of throttles back to start of reverse thrust windup	2.4	
Start of reverse thrust windup to full-reverse thrust		
a. GE engine	3.0	Maximum dry power
b. P&W engine	3.5	80 percent maximum dry power
<u>Landing</u>		
Nose gear touchdown to brakes on	.4	Idle
From the beginning of engine windup to reverse thrust power setting		
a. GE engine	6.0	Maximum dry power
b. P&W engine	6.0	80 percent maximum dry power
Full reverse thrust to 60 kn	---	Full percent maximum reverse thrust
60 kn to full stop	---	Full reverse thrust to idle reverse thrust

3.0 PERFORMANCE SUBSTANTIATION

	Page
3.1 CRUISE CONFIGURATION	47
3.2 TAKEOFF AND LANDING CONFIGURATIONS	105
3.3 AEROELASTIC ANALYSIS METHODS	131
3.4 AERODYNAMIC DEVELOPMENT PROGRAM	137

3.0 PERFORMANCE SUBSTANTIATION

The aerodynamic characteristics of the B-2707 are substantiated in this section. The substantiation is based on wind tunnel results, corrected to full-scale flight conditions, and on well-proved analytical methods. There are two parts to this section, Pars. 3.1 and 3.2, where the characteristics of the cruise configuration and the takeoff and landing characteristics are discussed respectively. Supersonic airplanes are particularly sensitive to aeroelastic effects; in Par. 3.3 aeroelastic studies are discussed comprehensively. The aerodynamic development program is presented in Par. 3.4.

3.1 CRUISE CONFIGURATION

The aerodynamic data for the calculation of airplane performance have been prepared taking into account refinement and improvements that will be made to the design in the following phases. Improvements in aerodynamic efficiency that were obtained during the 707 jet transport development are presented in Fig. 3-1. Continuous design refinement has led to significant improvements. Accordingly, a performance level has been selected for the production Model B-2707 which includes a modest 5 percent improvement in maximum lift-to-drag ratio.

To ensure that the development of the airplane will benefit from continuous advances in the state of the art, an aerodynamic development program has been prepared; all possibilities of drag improvement will be examined during refinement of the design to determine worth and cost of each.

As a part of that program, well-defined targets have been set for the components of drag, such as wave drag, friction drag, etc. In order to be sure that the targets were achievable, an aerodynamic development model was designed. It retained the general B-2707 geometric features, volumes, surface thicknesses, and arrangements but incorporated a large number of individual configuration variations; many or all could be reflected in the production airplane configuration without compromising the benefits of the prototype program. The variations incorporated were based on NASA and Boeing research activities. The limited extent of the variations can be seen by comparing Figs. 3-2 and 3-3 for the B-2707

and the aerodynamic development model respectively.

All of the features exhibited by the aerodynamic development model will be examined for incorporation into the B-2707 refinement work. High-speed wind tunnel tests of this configuration have just been completed. Photographs of this model and a model of the B-2707 are shown in Fig. 3-4. Based on the results of the first series of tests, a full-scale maximum lift drag ratio in excess of 8.7 has been obtained at Mach 2.7. The comparable current lift drag ratio for the B-2707 is 7.8 and the basis of performance has been set at 8.2; a conservative estimate for the production airplane in light of the extensive prototype and production development programs. In Fig. 3-5 the corresponding drag polars based on a continuing series of wind tunnel tests are compared with the lift drag characteristics that have been defined for performance calculations.

Aerodynamic characteristics that have been defined for performance calculations are tabulated for various flight conditions in Par. 3.1.1. Drag characteristics for installations of both GE and P&WA engines have been examined. Although differences in wetted area and in engine bleed characteristics have a perceptible effect on incremental drag, the drag difference is well inside the accuracy of drag determination. Tabulated drag characteristics have been prepared for airplanes with GE and P&WA engines so that performance calculations will reflect the small drag difference. For purposes of substantiation however, the two installations are considered to be equivalent in drag and only one set of data, applicable to both installations, is considered. Test data obtained with wind tunnel models for both installations are presented and discussed in Par. 3.1.3.5.

Detailed discussion of performance substantiation for the cruise configuration is presented in the following paragraphs:

- Lift drag characteristics of the B-2707
- Theoretical drag analysis
- Wind tunnel test results

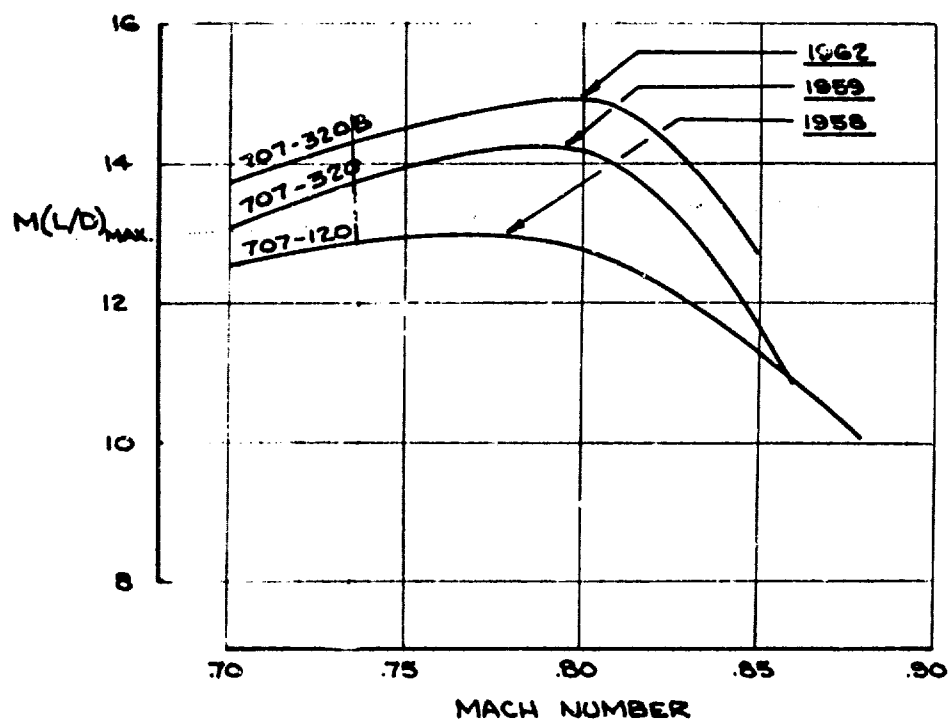


Figure 3-1. Boeing Jet Transport Efficiency Improvement

DATA

L.E. SWEEP	72°
WING AREA	9,000 FT ²
WING SPAN	105' 9"
REF. CHORD	158' 1"
WING T/C	2.26%
ROOT	2.85%
WING-SPAN	3%
TIP	306' 9"
FUSELAGE LENGTH	

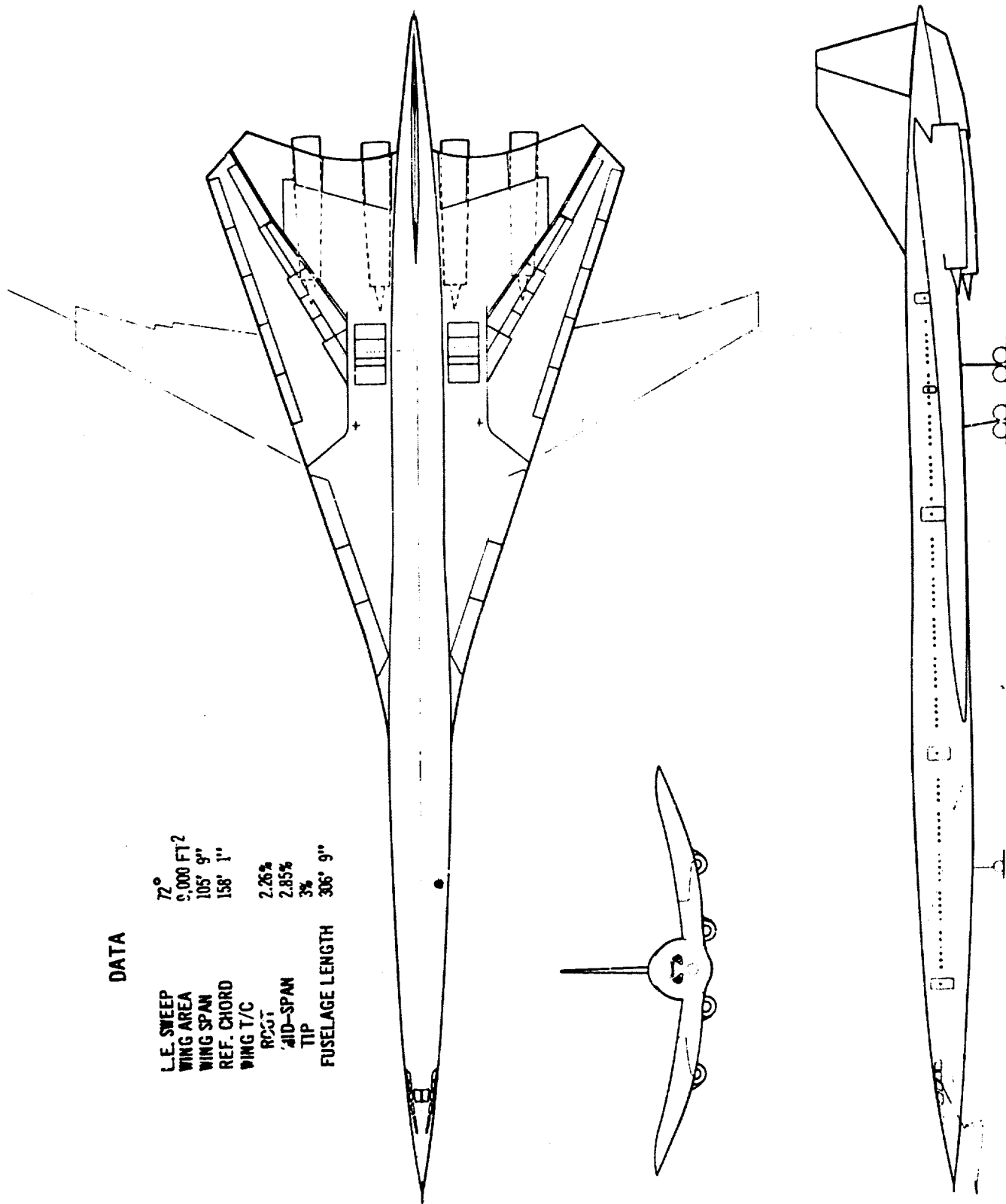
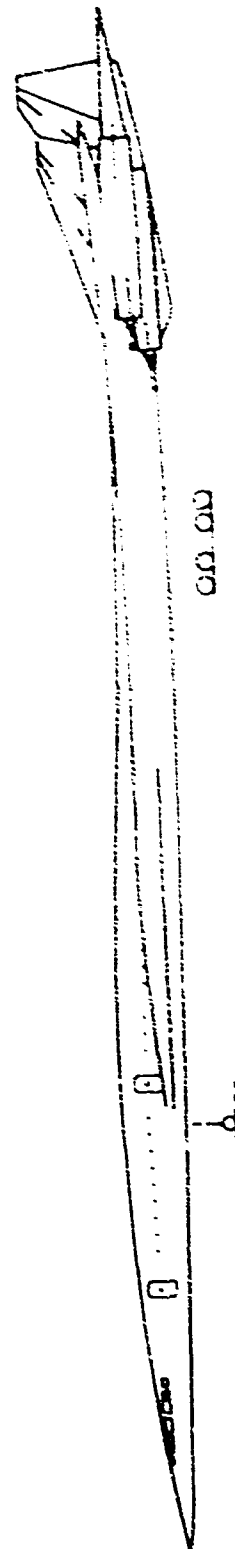
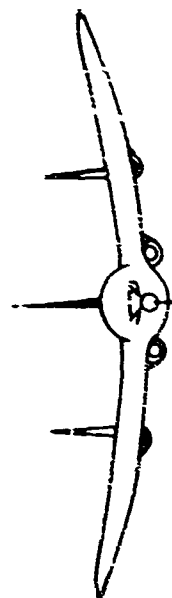
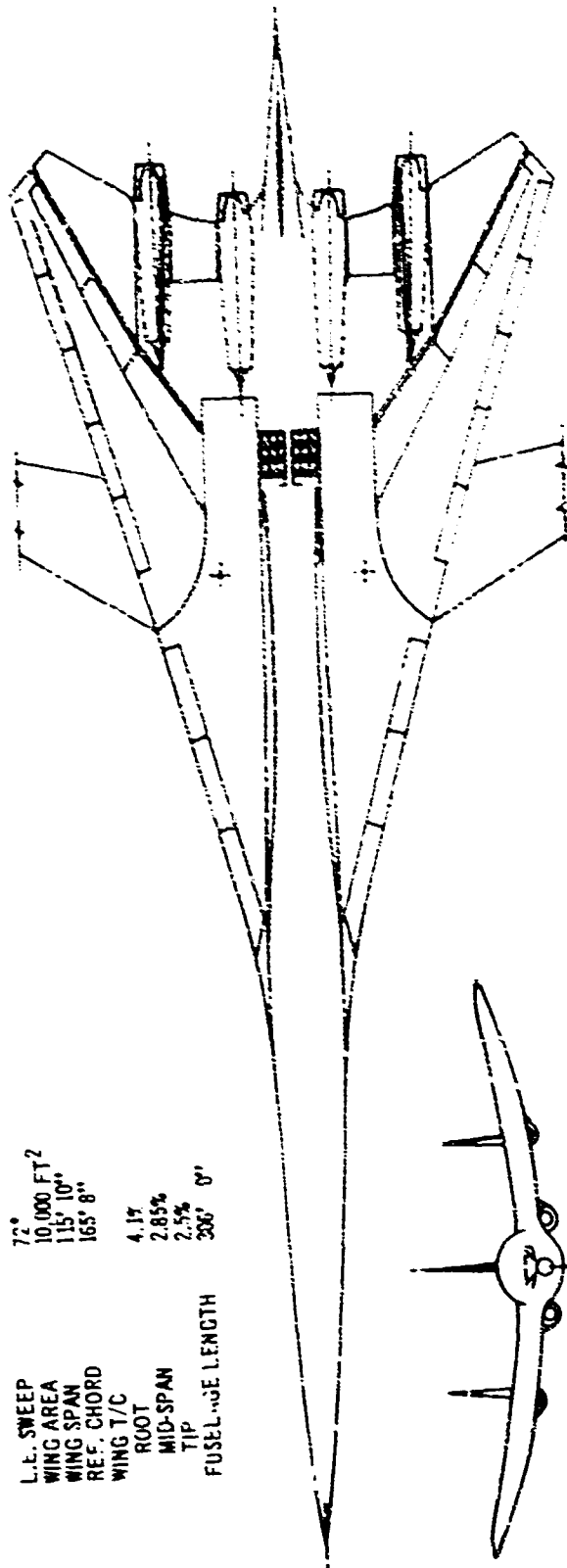


Figure 3-2. B-2707 General Arrangement

DATA

L.E. SWEEP	72°
WING AREA	10,000 FT ²
WING SPAN	115' 10"
REF. CHORD	165' 8"
WING T/C	4.1%
ROOT	2.85%
MID-SPAN	2.5%
TIP	300' 0"
FUSELAGE LENGTH	



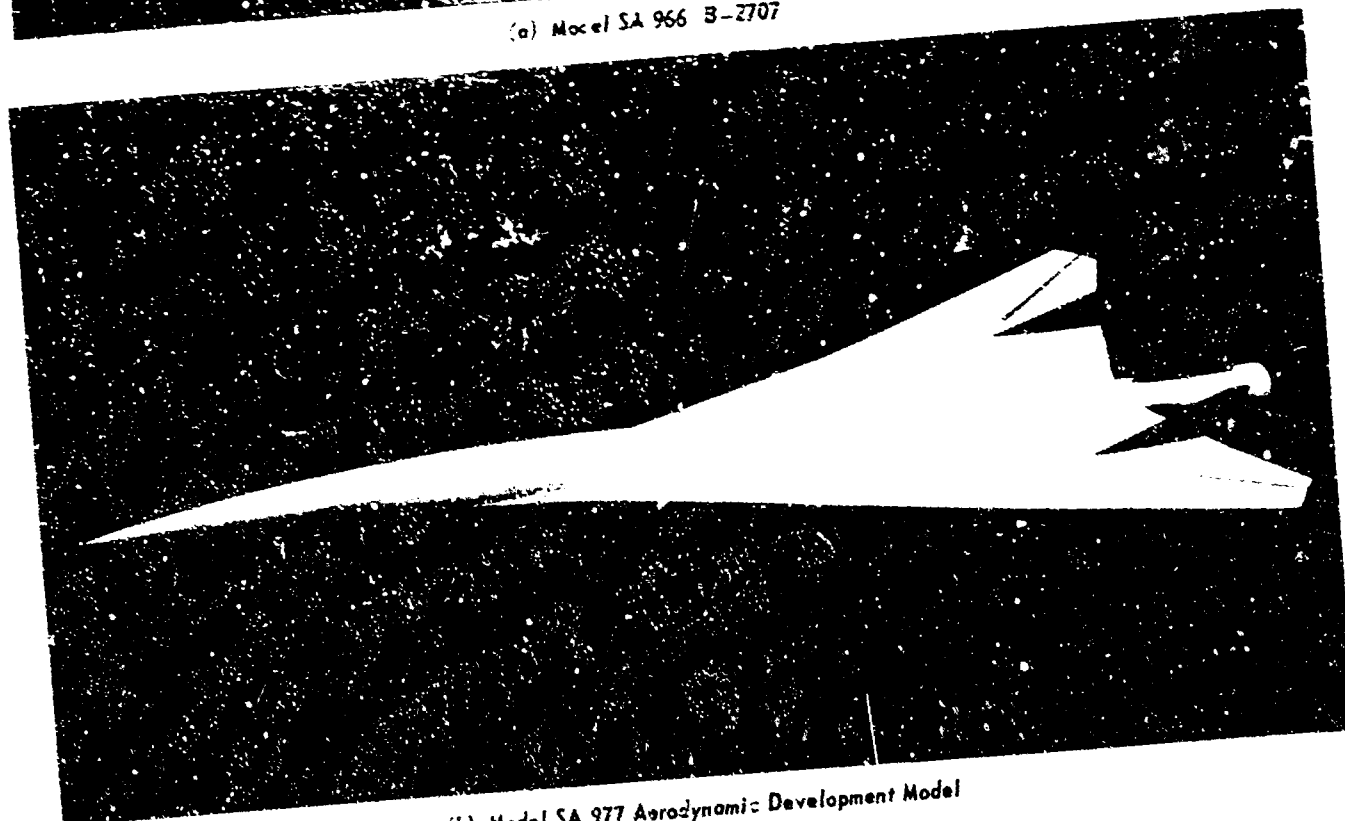
00.00

Figure 3-3. Aerodynamic Development Model

V2-B2707-3



(a) Model SA 966 B-2707



(b) Model SA 977 Aerodynamic Development Model

Figure 3-4. Photographs of Supersonic Wind Tunnel Models

V2-32737-3

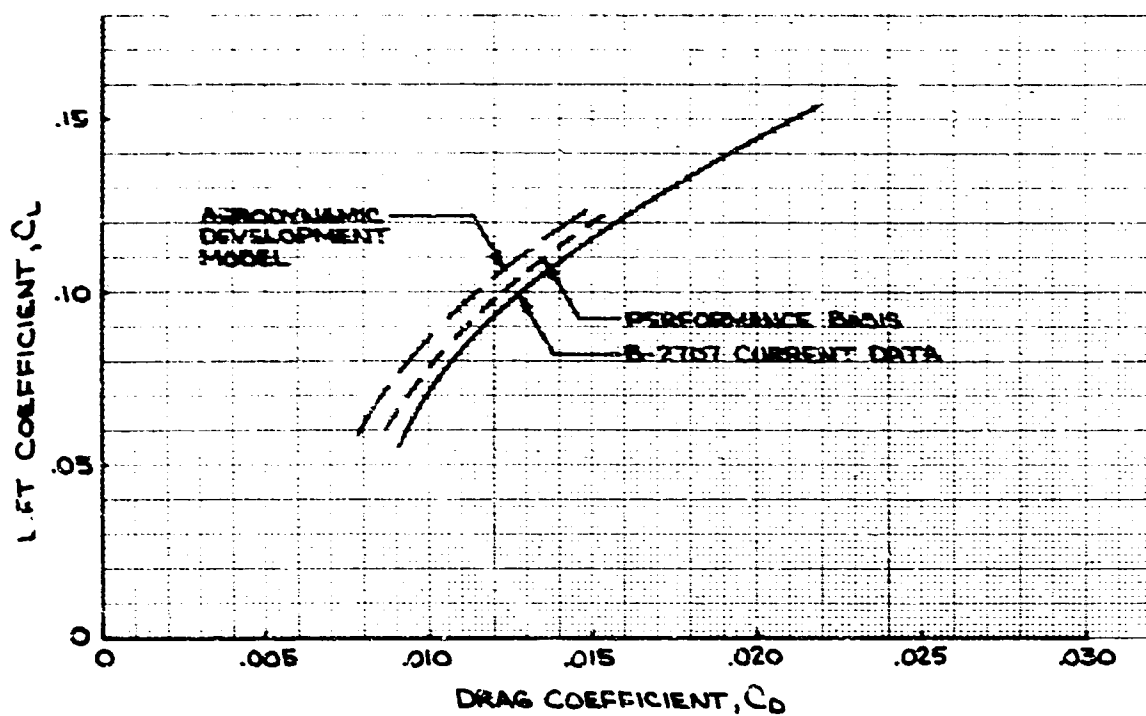


Figure 3-5. (a) B-2707 Lift Drag Characteristics - Mach 2.7

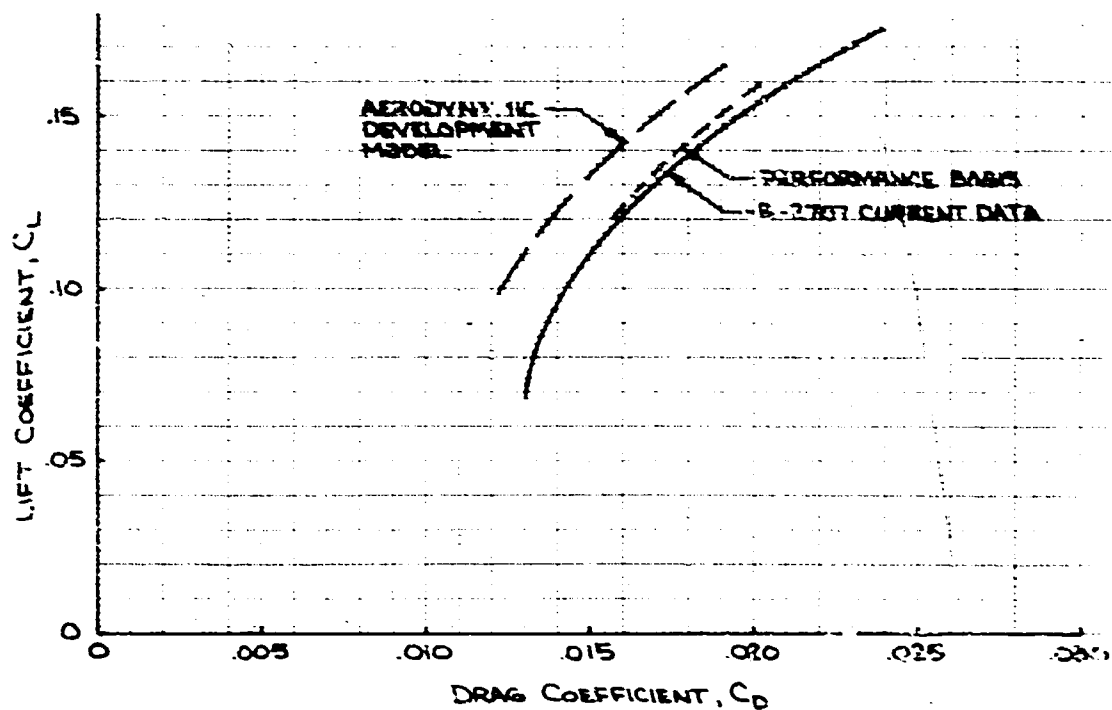


Figure 3-5 (b) B-2707 Lift Drag Characteristics - Mach 1.5

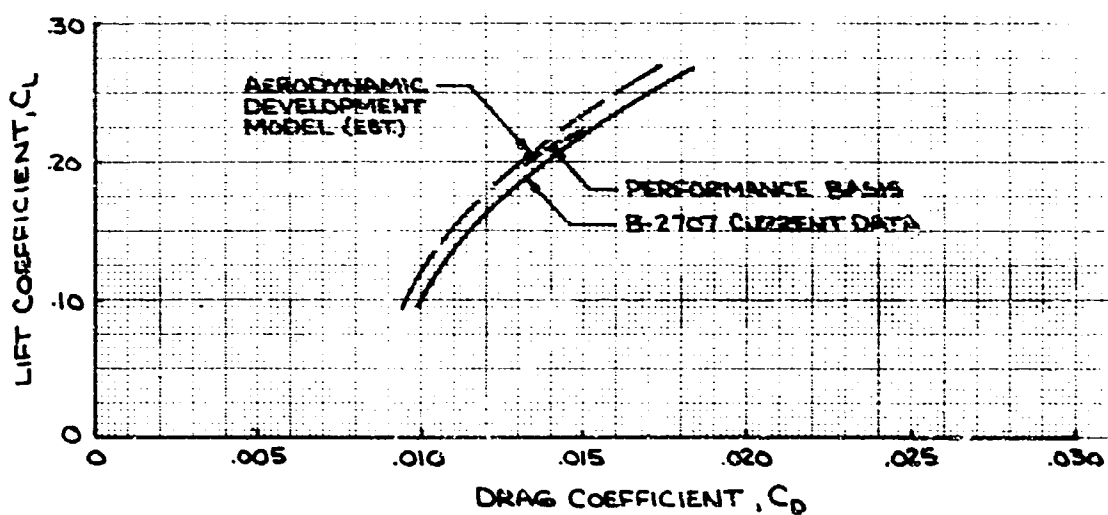


Figure 3-5 (c) B-2707 Lift Drag Characteristics - Mach 0.85

3.1.1 Lift Drag Characteristics of the B-2707
For performance calculations, the variation of airplane drag, C_D , with lift, C_L , is described by the following expression:

$$C_D = C_{D_{min}} + K(C_L - C_{L_0})^2$$

where:

$C_{D_{min}}$ Minimum drag coefficient

K An asymmetric drag due to lift factor

C_{L_0} Lift coefficient corresponding to $C_{D_{min}}$

The terms of this equation are tabulated as a function of altitude (H), and Mach number in Tables 3-A to 3-H. In addition, the lift slope C_{L_α} , the lift coefficient at zero body reference angle of attack C_{L_0} , and the rate of change of

skin friction drag with altitude $\frac{\Delta C_{D_F}}{\Delta H}$ are shown.

The data are tabulated separately for airplanes powered by GE and P&WA engines. The tabulations are for the nominal mission profile as well as at $\pm 10,000$ ft except where operating criteria, such as limiting angle of attack or maximum operating Mach number (M_{MO}), limit the operation.

The tabulations differentiate between the following cases: climb cruise, takeoff and landing air maneuvers, holding, and cruise to alternate. The climb cruise flight schedules are shown in Fig. 3-6 and the angles of leading edge sweep for all flight conditions are shown in Fig. 3-7.

3.1.2 Theoretical Drag Analysis

Theoretical analyses have been carried out to:

a. Determine incremental drag items such as wave drag, friction drag, etc.

b. Define increments to be applied to the wind tunnel model drag level in order to extrapolate this drag to the airplane flight conditions.

c. Evaluate the performance of the wind tunnel models, using the theoretical drag level as a yardstick, to determine that the design objectives of the wind tunnel models have been achieved.

3.1.2.1 Skin Friction Drag

At supersonic Mach numbers the skin friction drag has been calculated assuming fully turbulent, equivalent flat plate conditions. At subsonic Mach numbers an increment of form drag is added to the flat plate friction drag. The procedure used to calculate the equivalent flat plate turbulent skin friction drag is an application of the reference temperature method of Sommer and Short and the Karman-Schoenherr incompressible formula. Each component of the airplane is considered separately and the wing is further subdivided into chordwise strips. The calculations have been carried out with a digital computer program.

The effect of heat transfer on skin friction has been considered but found to be negligible. A skin emissivity of 0.2 and a solar absorptivity of 0.7 were used in the calculations. The effects of thermal conduction into the airplane, radiation heat input and output, and convective heat transfer by Reynolds analogy were considered. The skin friction drag along the flight schedule indicated in Fig. 3-6, is shown in Fig. 3-8. The wetted area breakdown of the B-2707 is tabulated in Tables 3-I and 3-J. A second wetted area breakdown of the aerodynamic development model is given in Tables 3-K and 3-L. Increments in skin friction drag for flight profiles that are slightly different from the one shown in Fig. 3-6 are shown in Table 3-M.

Table 3-A. B-2707 (G.E.) Performance Inputs (Reference Altitude)

MACH	H _{REF} (ft)	C _D _{MIN} x10 ⁴	K	C _L ₀	C _L _α	C _L _{α=0}	ΔC _D _{F/ΔH} x10 ⁸
.26	35	631.3	.142	0.20	.0460	.1170	2.50
.40	1,501	81.7	.202	0.035	.0502	-.1060	2.29
.60	7,500	78.7	.189	0.035	.0537	-.1295	2.40
.80	23,000	84.3	.190	0.035	.0572	-.1315	2.55
.85	26,000	86.3	.190	0.035	.0580	-.1340	2.74
.90	28,200	96.9	.350	0.0	.0345	-.1135	2.65
.95	30,400	103.1	.324	0.0	.0342	-.1065	2.71
1.00	32,500	125.8	.304	0.0	.0336	-.0965	2.89
1.05	34,500	147.7	.297	0.0	.0327	-.0860	3.00
1.10	36,000	154.3	.300	0.0	.0316	-.0795	3.08
1.15	38,000	151.8	.305	0.0	.0308	-.0750	3.16
1.20	39,500	144.3	.317	0.0	.0299	-.0725	3.21
1.40	43,750	118.1	.340	0.0	.0281	-.0655	3.30
1.60	45,750	102.4	.370	0.0	.0267	-.0585	3.26
1.80	46,700	95.5	.400	0.0	.0250	-.0485	3.16
2.00	47,500	81.1	.432	0.0	.0236	-.0435	3.03
2.20	52,000	75.2	.470	0.0	.0225	-.0405	2.88
2.40	55,700	70.0	.509	0.0	.0218	-.0390	2.82
2.60	59,300	65.7	.556	0.0	.0212	-.0385	2.80
2.70	61,000	63.6	.579	0.0	.0211	-.0385	2.88
2.70	61,169	63.6	.580	0.0	.0211	-.0385	2.88
2.70	68,427	65.6	.580	0.0	.0211	-.0385	2.88

Table 3-B. B-2707 (P & WA) Performance Inputs (Reference Altitude)

MACH	H _{REF} (ft)	C _D _{MIN} x10 ⁴	K	C _L ₀	C _L _α	C _L _{α=0}	ΔC _D _{F/AH} x10 ⁸
.26	35	630.1	.142	0.20	.0460	.1170	2.50
.40	1,501	80.6	.202	0.035	.0592	-.1060	2.29
.60	7,500	77.5	.187	0.035	.0537	-.1205	2.40
.80	23,000	78.5	.190	0.035	.0572	-.1315	2.55
.85	26,000	79.1	.191	0.035	.0580	-.1340	2.74
.90	28,200	87.8	.350	0.0	.0345	-.1135	2.65
.95	30,400	91.4	.324	0.0	.0342	-.1065	2.71
1.00	32,500	110.5	.304	0.0	.0336	-.0965	2.89
1.05	34,500	139.0	.300	0.0	.0327	-.0860	3.00
1.10	36,000	144.0	.300	0.0	.0316	-.0795	3.08
1.15	38,000	142.0	.305	0.0	.0308	-.0750	3.16
1.20	39,500	139.0	.315	0.0	.0299	-.0725	3.21
1.40	43,750	116.1	.340	0.0	.0281	-.0655	3.30
1.60	45,750	102.2	.370	0.0	.0267	-.0585	3.26
1.80	46,700	93.2	.401	0.0	.0250	-.0485	3.16
2.00	47,500	80.2	.432	0.0	.0236	-.0435	3.03
2.20	52,000	74.4	.470	0.0	.0225	-.0405	2.88
2.40	55,700	69.7	.509	0.0	.0218	-.0390	2.82
2.60	59,300	65.3	.554	0.0	.0212	-.0385	2.80
2.70	61,000	63.5	.580	0.0	.0211	-.0385	2.88
2.70	61,111	63.6	.580	0.0	.0211	-.0385	2.88
2.70	69,314	65.8	.580	0.0	.0211	-.0385	2.88

Table 3-C. B-2707 (GE) Performance inputs (Reference Altitude +10,000 Ft)

MACH	H ft	$C_{D_{MIN}}$ $\times 10^4$	K	C_{L_0}	C_{L_α}	$C_{L_{\alpha=0}}$	$\Delta C_{DF}/\Delta H$ $\times 10^8$
.26	10,035	633.8	.141	0.20	.0460	.1170	2.50
.40	11,000	83.8	.204	0.035	.0502	-.1060	2.29
.60	17,500	81.2	.198	0.035	.0537	-.1205	2.40
.80	33,000	87.0	.201	0.035	.0572	-.1315	2.55
.85	36,000	89.0	.201	0.035	.0580	-.1340	2.74
.90	37,370	99.3	.367	0.0	.0345	-.1135	2.65
.95	40,000	105.7	.350	0.0	.0342	-.1065	2.71
1.00	40,000	128.1	.335	0.0	.0336	-.0965	2.89
1.05	40,100	149.4	.324	0.0	.0327	-.0860	3.00
1.10	40,700	155.7	.320	0.0	.0316	-.0795	3.08
1.15	41,500	152.9	.317	0.0	.0308	-.0750	3.16
1.20	42,700	145.3	.319	0.0	.0299	-.0725	3.21
1.40	48,200	119.6	.360	0.0	.0281	-.0655	3.30
1.60	52,200	104.5	.405	0.0	.0267	-.0585	3.26
1.80	55,000	98.1	.445	0.0	.0250	-.0485	3.16
2.00	57,500	84.1	.480	0.0	.0236	-.0435	3.03
2.20	62,000	78.1	.520	0.0	.0225	-.0405	2.88
2.40	65,700	72.7	.555	0.0	.0218	-.0390	2.82
2.60	69,200	68.4	.585	0.0	.0212	-.0385	2.80
2.70	70,400	66.3	.605	0.0	.0211	-.0385	2.88
2.70	71,169	66.4	.610	0.0	.0211	-.0385	2.88
2.70	78,427	68.6	.590	0.0	.0211	-.0385	2.88

Table 3-D. B-2707 (P & WA) Performance Inputs (Reference Altitude +10,000 FT)

MACH	H (ft)	$C_{D_{MIN}}$ $\times 10^4$	K	C_{L_0}	C_{L_α}	$C_{L_{\alpha=0}}$	$\Delta C_{D_{FAH}}$ $\times 10^8$
.26	10,035	632.6	.141	0.20	.0460	.1170	2.50
.40	11,000	82.8	.204	0.035	.0502	-.1060	2.29
.60	17,500	79.9	.198	0.035	.0537	-.1205	2.40
.80	33,000	81.1	.201	0.035	.0572	-.1315	2.55
.85	36,000	81.8	.201	0.035	.0580	-.1340	2.74
.90	37,370	90.3	.367	0.0	.0345	-.1135	2.65
.95	40,000	94.0	.350	0.0	.0342	-.1065	2.71
1.00	40,000	112.7	.335	0.0	.0336	-.0965	2.89
1.05	40,100	140.7	.324	0.0	.0327	-.0860	3.00
1.10	40,700	145.4	.320	0.0	.0316	-.0795	3.08
1.15	41,500	143.1	.317	0.0	.0308	-.0750	3.16
1.20	42,700	140.0	.319	0.0	.0299	-.0725	3.21
1.40	48,200	117.6	.360	0.0	.0281	-.0655	3.30
1.60	52,200	104.3	.405	0.0	.0267	-.0585	3.26
1.80	55,000	95.8	.445	0.0	.0250	-.0485	3.16
2.00	57,500	83.2	.480	0.0	.0236	-.0435	3.03
2.20	62,000	77.3	.520	0.0	.0225	-.0405	2.83
2.40	65,700	72.4	.555	0.0	.0218	-.0390	2.82
2.60	69,200	68.0	.585	0.0	.0212	-.0385	2.80
2.70	70,400	66.2	.605	0.0	.0211	-.0385	2.88
2.70	71,111	66.4	.610	0.0	.0211	-.0385	2.88
2.70	79,314	69.0	.590	0.0	.0211	-.0385	2.88

Table 3-E. B-2707 (GE) Performance Inputs (Minimum Altitude)

MACH	H (ft.)	C_{DMIN} $\times 10^4$	K	C_{L0}	$C_{L\alpha}$	$C_{L\alpha=0}$	$\Delta C_{DF}/\Delta H$ ($\times 10^8$)
.26	35	631.3	.142	0.20	.0460	.1170	2.50
.40	1,501	81.7	.202	0.035	.0502	-.1060	2.29
.60	7,500	78.7	.189	0.035	.0537	-.1205	2.40
.80	23,000	84.3	.190	0.035	.0572	-.1315	2.55
.85	25,000	86.1	.186	0.035	.0580	-.1340	2.74
.90	25,000	96.2	.340	0.0	.0345	-.1135	2.65
.95	25,000	101.8	.318	0.0	.0342	-.1065	2.71
1.00	26,400	124.3	.300	0.0	.0336	-.0965	2.89
1.05	27,900	146.1	.297	0.0	.0327	-.0860	3.00
1.10	28,900	152.6	.300	0.0	.0316	-.0795	3.08
1.15	30,100	149.8	.305	0.0	.0308	-.0750	3.16
1.20	31,200	142.0	.312	0.0	.0299	-.0725	3.21
1.40	35,300	115.4	.340	0.0	.0281	-.0655	3.30
1.60	39,000	100.2	.370	0.0	.0267	-.0585	3.26
1.80	43,200	94.5	.400	0.0	.0250	-.0485	3.16
2.00	47,500	81.1	.432	0.0	.0236	-.0435	3.03
2.20	52,000	75.2	.470	0.0	.0225	-.0405	2.88
2.40	55,700	70.0	.509	0.0	.0218	-.0390	2.82
2.60	59,300	65.7	.556	0.0	.0212	-.0385	2.80
2.70	61,000	63.6	.579	0.0	.0211	-.0385	2.88
2.70	61,169	63.6	.580	0.0	.0211	-.0385	2.88
2.70	68,427	65.6	.580	0.0	.0211	-.0385	2.88

Table 3-5 S-277 F3WA Performance Inputs Minimum Altitude

MACH	H ft	C _D MIN X10 ⁻³	K	C _L 0	C _L 2	C _L 4	10 ³ D _{FA} X10 ³
.35	35	630.1	.342	1.22	.0469	-.1177	1.31
.40	1,501	60.6	.300	1.035	.0542	-.1286	1.19
.45	7,500	77.5	.287	1.035	.0637	-.1278	1.40
.50	23,000	78.5	.283	1.035	.0672	-.1311	1.53
.55	25,000	78.9	.287	1.035	.0660	-.1347	1.74
.60	25,000	87.0	.340	0.0	.0345	-.1135	1.65
.65	25,000	90.1	.318	0.0	.0342	-.1065	1.71
1.00	36,400	109.0	.300	0.0	.0335	-.0935	2.39
1.05	27,000	132.0	.297	0.0	.0327	-.0860	3.00
1.10	29,900	142.3	.300	0.0	.0316	-.0795	3.04
1.15	30,100	139.5	.305	0.0	.0309	-.0750	3.16
1.20	31,200	136.7	.312	0.0	.0299	-.0725	3.21
1.40	35,300	113.5	.340	0.0	.0281	-.0655	3.30
1.60	39,000	100.2	.370	0.0	.0257	-.0585	3.26
1.80	43,200	92.3	.401	0.0	.0250	-.0495	3.16
2.00	47,500	80.2	.432	0.0	.0236	-.0435	3.03
2.20	52,000	74.4	.470	0.0	.0225	-.0405	2.88
2.40	55,700	69.7	.509	0.0	.0218	-.0390	2.82
2.60	59,300	65.3	.554	0.0	.0212	-.0385	2.80
2.70	61,000	62.5	.580	0.0	.0211	-.0385	2.88
2.70	61,111	63.6	.580	0.0	.0211	-.0385	2.88
2.70	69,314	65.8	.580	0.0	.0211	-.0385	2.88

Table 3-G. B-2707 (GE) Lift-Drag Characteristics 30 & 42 Degrees Sweep

MACH	H _{REF}	C _{DMIN}	K	C _{LO}	C _{Lα}	C _{Lα=0}	$\Delta CDF/\Delta H$ $\times 10^8$	SWEEP	CONFIGURATION
.414	5,000	.01590	.200	.10	.0502	-.106	2.29	42° T.O	SLATS AIR MANEUVER
.414	5,000	.00832	.186	.04	.0540	-.033	2.31	30°	CLEAN LANDING AIR MAN.
.500	15,000	.00837	.180	.04	.0554	-.034	2.63	30°	CLEAN HOLDING
.850	36,150	.00899	.183	.035	.0580	-.134	3.50	42°	CLEAN CRUISE TO ALTERNATE
.850	33,300	.00890	.196	.035	.0580	-.134	3.50	42°	CLEAN SUBSONIC CRUISE

Table 3-H. B-2707 (P & WA) Lift-Drag Characteristic 30 & 42 Degrees Sweep

MACH	H _{REF}	C _{DMIN}	K	C _{LO}	C _{Lα}	C _{Lα=0}	$\Delta CDF/\Delta H$ $\times 10^8$	SWEEP	CONFIGURATION
.414	5,000	.01580	.200	.10	.0502	-.106	2.29	42° T.O.	SLATS AIR MANEUVER
.414	5,000	.00821	.184	.04	.0540	-.033	2.31	30°	CLEAN LANDING AIR MAN.
.500	15,000	.00826	.180	.04	.0554	-.034	2.63	30°	CLEAN HOLDING
.850	36,150	.00825	.184	.035	.0580	-.134	3.50	42°	CLEAN CRUISE TO ALTERNATE
.850	33,150	.00825	.195	.035	.0580	-.134	3.50	42°	CLEAN SUBSONIC CRUISE

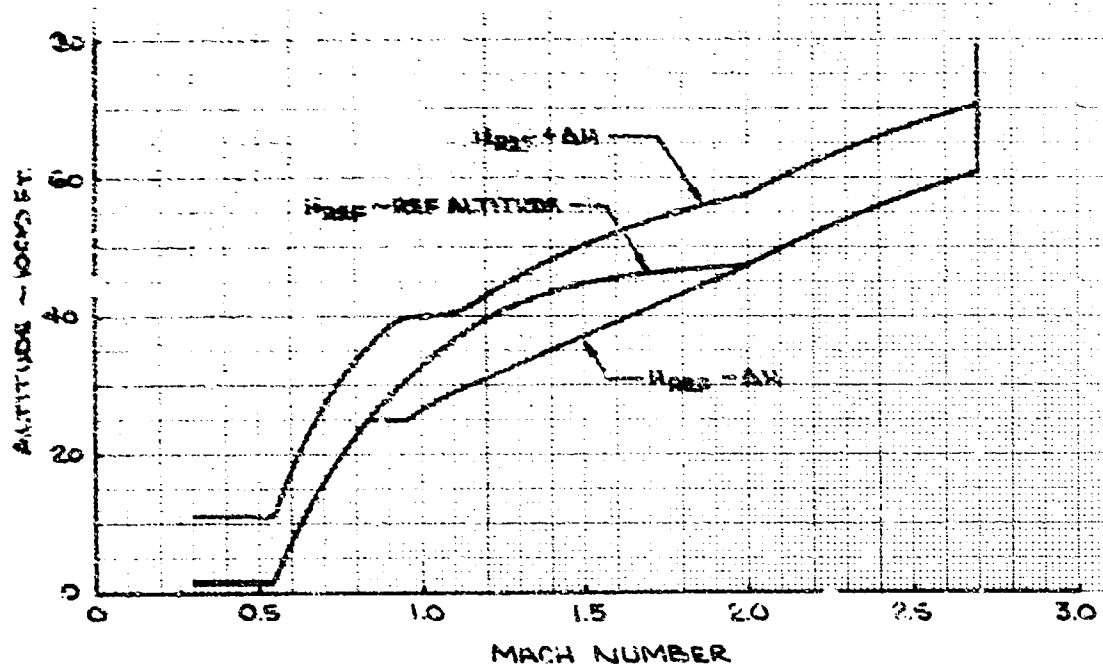


Figure 3-6. S-2707 Climb Profiles

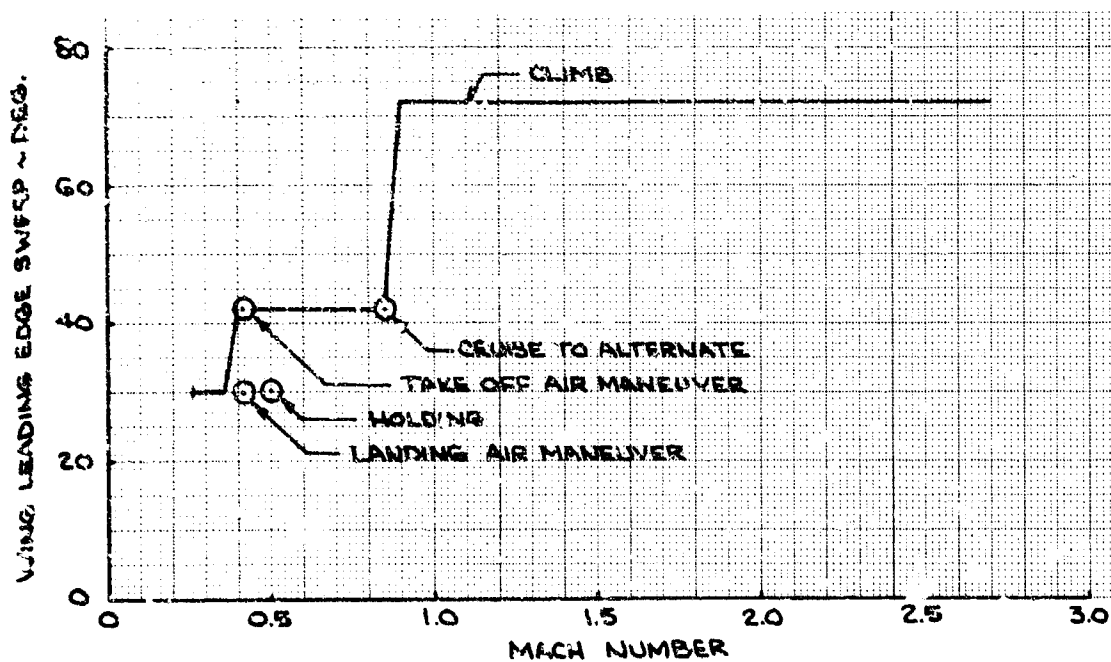


Figure 3-7. S-2707 Sweep Schedules

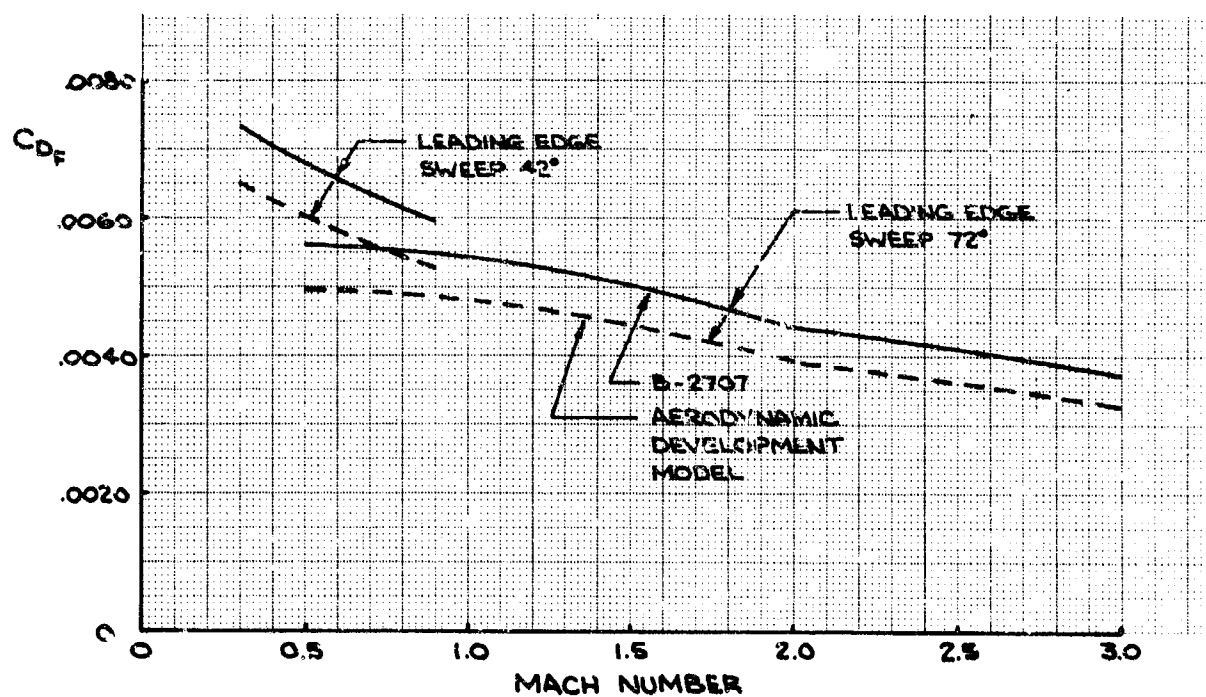


Figure 3-8. Skin Friction Drag

Table 3-I. B-2707 Wetted Areas - Leading Edge Sweep - 72 Degrees

COMPONENT	WETTED AREA (Sq Ft)		CHARACTERISTIC LENGTH (Ft)	
	GE	P&W	GE	P&W
Body	9885	9885	306	306
Wing	14970	15047	93	93
Nacelles	2700	2300	35.9	28.7
Horizontal Tail	(Included in Wing)			
Vertical Tail	1750	1750	40	40
Ventral	402	402	40	40
Fences	226	276	40	50
Total	29933	29660		

Table 3-J. B-2707 Wetted Areas - Leading Edge Sweep - 42 Degrees

COMPONENT	WETTED AREA (Sq Ft)		CHARACTERISTIC LENGTH (Ft)	
	GE	P&W	GE	P&W
Body	9885	9885	306	306
Wing	12720	12797	58	58
Nacelles	2700	2300	35.9	28.7
Horizontal Tail	3085	3085	29	29
Vertical Tail	1750	1750	40	40
Ventral	402	402	40	40
Fences	226	276	40	50
Total	30768	30495		

Table 3-K. Aerodynamic Development Model Wetted Areas Leading Edge Sweep 72 Degrees

COMPONENT	WETTED AREA (Sq Ft)		CHARACTERISTIC LENGTH (Ft)	
	GE	P&W	GE	P&W
Body	8850	8850	306	306
Wing	16470	16550	95	96
Nacelles	2600	2300	35.9	28.7
Horizontal Tail		(Included in Wing)		
Wing-Mounted Vertical Tails (2)	1170	1170	35	35
Body-Mounted Vertical Tail (1)	650	650	25	25
Ventral	280	280	75	75
Total	30020	29700		

Table 3-L. Aerodynamic Development Model Wetted Areas Leading Edge Sweep 42 Degrees

COMPONENT	WETTED AREA (Sq Ft)		CHARACTERISTIC LENGTH (Ft)	
	GE	P&W	GE	P&W
Body	8850	8850	306	306
Wing	13996	14076	61	61
Nacelles	2600	2300	35.9	28.7
Horizontal Tail	3390	3390	30	30
Wing-Mounted Vertical Tails (2)	1170	1170	35	35
Body-Mounted Vertical Tail (1)	650	650	25	25
Ventral	280	280	75	75
Total	30936	30616		

Table 3-M. Friction Drag Characteristics at 100 FT

Mach Number	$\Delta C_{DF} \Delta H$
.4	2.29×10^{-5}
.6	2.55×10^{-5}
1.0	2.89×10^{-5}
1.2	3.21×10^{-5}
2.0	3.03×10^{-5}
2.7	2.58×10^{-5}

At subsonic Mach numbers, the flat plate skin friction drag has to be increased by an increment of form drag due to thickness effects. The form drag increments for the B-2707 are listed in Table 3-N. Form drag increments have been obtained using the published data sheets of the Royal Aeronautical Society.

Table 3-N. B-2707 Form Drag

Mach Number	ΔC_D	
	42° Sweep	72° Sweep
.4	.00060	.00035
.6	.00056	.00033
.8	.00052	.00033

3.1.2.2 Roughness and Miscellaneous Drag

The calculations of skin friction drag have been based on the assumption that the skin of the airplane is smooth. A drag increment has been added to include the effects of:

- Surface waviness and manufacturing roughness.

- Miscellaneous protuberances not simulated on the wind tunnel models.
- Ram pressure and thrust recoveries of secondary air used for cooling, environmental control, etc.

Reference 2 contains a detailed description of the size and location of roughness items due to manufacturing tolerances, miscellaneous protuberances, and vents. The calculation of the drag for surface roughness and protuberances was based on test data for typical roughness elements. The general procedure was similar to that described in Ref. 3 which includes an extensive bibliography on test data for roughness elements. Since the publication of Ref. 3, more test data have become available and additional data from Refs. 4 to 7 have been used for the estimates of roughness drag. A summary of the surface roughness drag increments at Mach 2.70 is presented in Table 3-O. Detailed calculations for other Mach numbers are available. The drag, at Mach 2.7, of miscellaneous protuberances is listed in Table 3-P.

The drag of the environmental system is defined as the drag of that inlet air discharged from all areas other than the engine nozzles. External and internal air properties were determined for each exhaust nozzle, and these data were used to calculate ideal and estimated thrust recoveries. The ideal thrust recovery values were obtained by assuming isentropic flow. These values were then corrected using secondary air injection test data (Refs. 8 through 10), and skin friction increments due to the formation of secondary air boundary layers in the vicinity of each nozzle. In addition, drag components of the normal forces on inclined surfaces due to shock wave formation at supersonic Mach numbers (Refs. 11 through 13) were included in calculation of the estimated thrust recoveries. Total drag increments were obtained by subtracting ideal and estimated thrust recoveries from the ram drag of each inlet streamtube. An itemized summary of these calculations for Mach 2.7 is shown in Table 3-Q. Similar summaries and detailed calculations for other Mach numbers will be available.

The total drag increment for roughness, miscellaneous items, protuberances, etc., as a function of Mach number is shown in Fig. 3-9.

Table 3-0. Manufacturing Roughness Increment Drag Coefficients at Mach 2.7

ITEMS	
Wing	$\Delta C_{D_R} \times 10^4$
Surface Waves	.1424
Pivot Fairing Mismatch	.0165
Pivot Access Doors	.0022
Main Landing Gear Doors	.0058
Wing Access Doors	.0043
Skin Butt Joints	.0504
Leading Edge Main Slat to Wing	.0225
Leading Edge Fore Slat to Main Slat	.0100
Leading Edge Slat Ends	.0133
Trailing Edge Flaps to Wing	.0187
Ailerons to Wing	.0083
Spoilers to Wing	.0103
Aft Flap to Stabilizer	.0288
Inboard Flap Doors	.0137
Flap and Aileron Ends	.0107
Fuselage	
Surface Waves	.2216
Cargo Doors	.0036
Nose and Main Landing Gear Doors	.0122
Entry and Galley Doors	.0190
Escape Hatch and Doors	.0100
Body Fuel Tank Doors	.0017
Equipment Access Panels	.0008
Auxiliary Drive System Door	.0020
Hydraulic System Access Door	.0008
Skin Butt Joints	.0289
Cabin Windows	.0102
Air Traffic Control Antenna	.0002
Radome	.0010
Canopy Windows	.0035
Canopy Fairing	.0053
Horizontal Tail	
Surface Waves	.0462
Access Doors	.0017
Thrust Reverser Doors	.0072
Air Conditioning Access Panel	.0014
Elevator to Horizontal Tail	.0021
Skin Butt Joints	.0267
Elevon Actuator Access Panels	.0036
Auxiliary Drive System Panels	.0007
Elevons to Horizontal Tail	.0072
Vertical Tail	
Surface Waves	.0178
Access Doors	.0009
Skin Butt Joints	.0230
Rudder to Vertical Tail	.0105
Ventral Fin	
Skin Butt Joints	.0041
Surface Waves	.0032
Propulsion Pods	
Surface Waves (GE)	(.2398)
(P&W)	(.1550)
Power Take-Off Drive System Access Doors	.0013
Oil Tank Filler Doors	.0014
Skin Butt Joints	.0050
Thrust Reverser Access Panels	.0021
Diverter Doors	.0007
Inlet By-Pass Doors	.0006
Secondary Air/Thrust Reverser Doors (P&W)	(.0540)
Secondary Air Doors (GE)	(.0210)
Thrust Reverser Doors (GE)	(.0320)
Pressure Relief & Burnout Doors (GE)	(.0030)
(P & W)	(.0029)

Table 3-P. Miscellaneous Protuberance Incremental Drag Coefficients at Mach 2.70

Protuberances	$\Delta C_{D_R} \times 10^4$
Nose Pitot Static Probe	.0639
Keel Beam Chords	.0652
Total Air Temperature Probes	.0649
Galley Door Guide Plates	.0096
VHF Antennae	.0530
Fuselage Pitot Probes	.0148
Angle of Attack Sensors	.0182
Wing Fuel Tank Vent	.0001
Vertical Tail Fuel Tank Vent	.0001
Fuel Computer Pitot Probes	.0079
Tail Cone Fuel Jettison Nozzle	.0226
Precipitation Static Dischargers (Blade Type)	.0400
Precipitation Static Dischargers (Rod Type)	.0013
Protuberances on the Wind Tunnel Model	
Actuator Fairings on Horizontal Tail	
Wing Pivot Fairings	
Landing Gear Fairings (on Fuselage and Wing)	
All Fences	
Wing Tip Fairings	
Wing Upper Surface Grooves	
Wing-Body Fairings	

Table 3-Q. Itemized Cooling Air-Quantities and Drags at Mach 2.7

ITEM	WEIGHT FLOW lb/min	IDEAL DRAG COEFFICIENT $\times 10^4$	ESTIMATED DRAG COEFFICIENT $\times 10^4$
Ram Drag	*	1.228	1.228
ACM Bearing & Separator Drain	9.2	-0.018	-0.013
Uncontrolled Leakage	48.6	0	0
Nose Wheel Well Cooling Air	3.0	-0.003	0.003
Main Wheel Well Cooling Air	16.0	-0.016	0.014
Accessory Drive System Cooling Air	8.0	-0.008	0.009
Cabin Intrawall Air Exhaust (Inbd)	152.2	-0.262	-0.188
Cabin Intrawall Air Exhaust (Outbd)	152.2	-0.262	-0.188
Totals	389.2*		$\Delta C_D = 0.865$

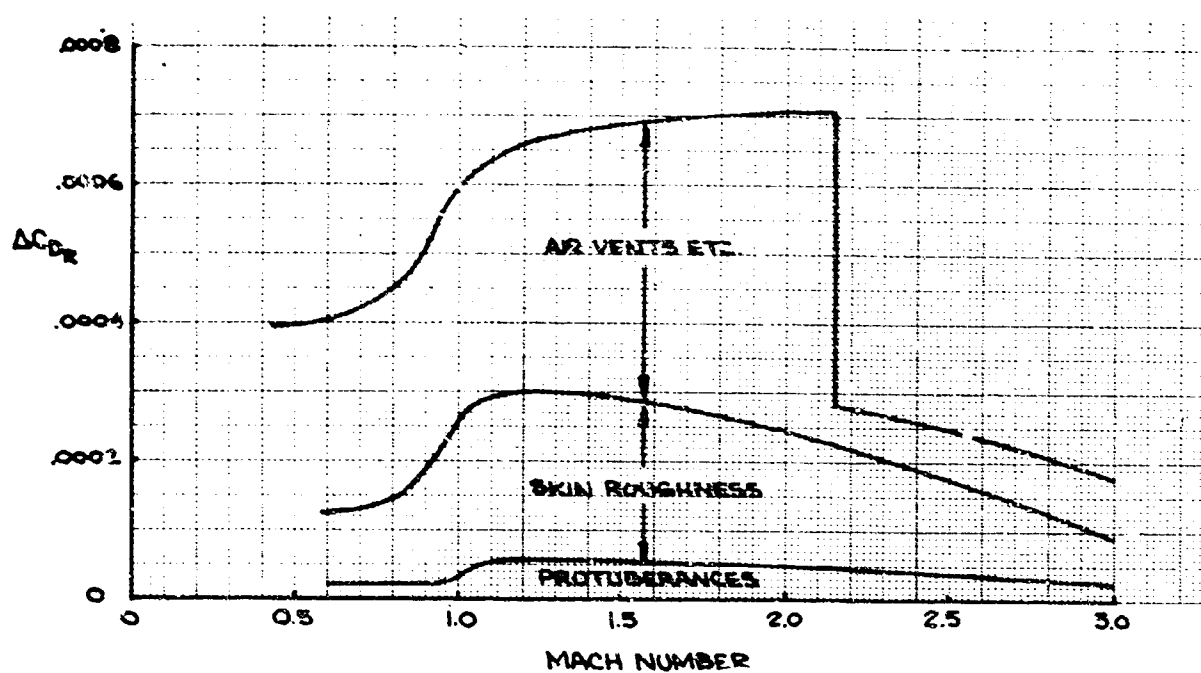


Figure 3-9. Roughness and Miscellaneous Drag

3.1.2.3 Wave Drag

The procedure used to calculate wave drag is an application of slender body theory in combination with the supersonic area rule. The geometric input data for the NASA Langley Computer Program P 7129 are given in Tables 3-R and 3-S. The computer program input tables indicate different inputs for GE and P&WA propulsion pods but since the calculated wave drag difference is well within the accuracy of the theory, only one drag level, applicable to both pods, has been shown in Fig. 3-10. The wing has a blunt base from wing buttock line 375 to wing buttock line 434. The drag increment shown on Fig. 3-11 has been estimated assuming that two-dimensional base pressure exists (Refs. 14 and 15).

3.1.2.4 Drag Due to Propulsion System Operation

The propulsion system increments for bleed drag, boattail drag, and additive drag, with the substantiation for these increments, are presented in Sec. 3 of Propulsion Report, Part A (V2-B2707-12). The propulsion drag increments and the corresponding engine airflow curves are repeated in Figs. 3-12 and 3-13. The greater part of the drag difference is caused by the accounting of nozzle boattail drag. For the P&WA engine, the drag of the nozzle is in the internal performance.

The effect of engine thrust on lift, drag, and pitching moment is shown in Fig. 3-14. The corrections are caused by the nonalignment of the thrust force with the thrust drag axis, as a function of airplane angle of attack, and for the moment changes caused by these forces. The propulsion pods have been designed with canted nozzles so that the thrust has a small component in the lift direction; this has a beneficial effect on drag. Particular care has been taken to simulate this feature on the pods of the wind tunnel models so the effect of thrust has also been included in the drag polars.

3.1.2.5 Aeroelastic Corrections and Trim Drag

Aeroelastic corrections are necessary because the theoretical drag analysis and the rigid model test data do not include the effects of airplane flexibility. The wind tunnel model duplicates the correct shape of the airplane at the design condition at Mach 2.7. Under all other conditions aeroelastic corrections have to be applied; these

corrections have been calculated using linearized theory. The calculations have been programmed for a digital computer and the method is discussed in Par. 3.3.

Because the mission is carried out at near unit load factor, it has been assumed that, at each Mach number, lift coefficient is varied by changing altitude at unit load factor. Thus, each lift coefficient, at constant Mach number, corresponds to a particular altitude.

The corrections have been applied as follows:

The rigid pitching moment C_{M_R} is corrected to a flexible moment C_{M_F} , at each lift coefficient, by the application of an increment ΔC_M such that

$$C_{M_F} = C_{M_R} + \Delta C_M$$

In Fig. 3-15, ΔC_M is shown plotted as a function of Mach number for various lift coefficients.

The aeroelastic corrections to angle of attack and drag are also a function of the elevator angle that is required to trim the flexible airplane (for simplicity, the elevon and elevator system are referred to as the elevator). The elevator angle is calculated from the equation:

$$\delta = \frac{C_{M_F}}{C_{M_{\delta_F}}}$$

where

$$C_{M_{\delta_F}} = \frac{C_{M_{\delta_F}}}{C_{M_{\delta_R}}} C_{M_{\delta_R}}$$

= Flexible Elevator Efficiency

The ratio $C_{M_{\delta_F}} / C_{M_{\delta_R}}$ is shown in Fig. 3-18.

The rigid elevator effectiveness has been obtained from experiment; it is shown in Fig. 3-17 and discussed in Par. 3.1.1.3. Once δ is known, at any lift coefficient, the corrected angle of attack is obtained from:

$$\alpha_F = \alpha_R + \Delta\alpha + \frac{d\alpha}{d\delta} \delta$$

where

α_R = Rigid airplane angle of attack with undeflected elevator

α_F = Flexible airplane angle of attack with undeflected elevator

$$\Delta\alpha = (\alpha_F - \alpha_R) / \delta = 0$$

$\frac{d\alpha}{d\delta}$ = Rate of change of flexible airplane angle of attack with elevator angle.

The quantities $\Delta\alpha$ and $\frac{d\alpha}{d\delta}$ are shown in Figs. 3-18 and 3-19.

The drag coefficient of the trimmed flexible airplane, C_{D_F} , is determined in a similar way:

$$C_{D_F} = C_{D_R}(0) + \Delta C_{D_F} + \Delta C_{D_{TRIM}}$$

$C_{D_R}(0)$ is the drag of the rigid airplane with zero elevator deflection obtained from wind tunnel tests and/or theory. $C_{D_R}(\delta)$ is the drag at an elevator deflection δ .

$$\Delta C_{D_F} = C_{D_F}(\delta) - C_{D_R}(\delta)$$

The elastic correction ΔC_{D_F} is shown in Fig. 3-20. The trim drag increment $\Delta C_{D_{TRIM}}$ is defined as the increment between the drag coefficient at zero elevator deflection $C_D(0)$ and the drag with the elevator deflected to the trimmed condition, lift coefficient being held constant. No attempts have been made to calculate the trim

drag increment theoretically, and experimentally determined increments have been used to define the analytical drag polars. Trim drag increments are presented in Par. 3.1.3.

3.1.2.6 Drag Due to Lift

Drag due to lift has been calculated using several computer programs varying in complexity from the NASA-Ames program for the complete wing body (Ref. 16) to one which solves only the planar, thin wing problem. The latter method has been extended to subsonic speeds using ideas described in Ref. 17. This method is in agreement with NASA program 916.C (Ref. 18) at supersonic speeds and with vortex lattice methods in incompressible flow.

Figure 3-21 shows the proportion of theoretical leading edge thrust which has been included in the drag due to lift estimates; it varies from 0 at Mach 2.7 to 90 percent at low subsonic speeds. Figure 3-21 is based on test data presented in Refs. 19 and 20.

The nacelles on the model B-2707 have been designed to produce favorable lifting interference with the wing. The nacelle pressure field has been calculated by a method based upon the analysis described in Ref. 21.

Figure 3-22 shows the drag due to lift, reduced to symmetric envelope form and compared to flat wing and optimum surface envelopes.

The camber and twist is defined in Table 3-T in a form suitable for input to NASA Langley Computer Program 916C.

3.1.2.7 Theoretical Drag Polars

The drag polars resulting from the analytical buildup are compared with drag polars obtained by the extrapolation of wind tunnel data in Fig. 3-23. It is seen that the experimental polars show higher drag than the theory. Although the test data have not been corrected for boundary layer trip drag and for bluntness of the wind tunnel model nacelle lips and vertical tail leading edge, it is obvious that the full potential predicted by the theory has yet to be achieved. Further work is indicated, particularly on the drag due to lift; this is discussed in Par. 3.4.

Table 3-R. B-2707 Wave Drag Program Inputs

0.0	2.5	10.0	25.0	40.0	50.0	60.0	75.0	90.0	100.0	X/C
92.10	5.625	-4.0	179.05							W1
129.39	9.86	-3.5	140.36							W2
141.0	12.24	-3.2	128.83							W3
151.03	15.5	-2.8	118.55							W4
164.93	20.0	-2.4	105.2							W5
197.53	31.25	-1.1	73.54							W6
190.56	31.26	-1.1	47.10							W7
214.65	36.17	-0.5	39.03							W8
248.10	47.04	0.8	24.52							W9
266.0	52.87	1.5	0.0							W10
0.0	0.24	0.55	0.88	1.07	1.13	1.11	0.87	0.36	0.0	Z/C-1
0.0	0.41	0.87	1.40	1.57	1.46	1.28	0.88	0.35	0.0	Z/C-2
0.0	0.45	1.02	1.70	1.75	1.60	1.35	0.90	0.36	0.0	Z/C-3
0.0	0.45	0.89	1.40	1.75	1.75	1.50	0.87	0.35	0.0	Z/C-4
0.0	0.44	0.87	1.28	1.40	1.39	1.29	0.88	0.35	0.0	Z/C-5
0.0	0.44	0.87	1.28	1.40	1.39	1.29	0.88	0.35	0.0	Z/C-6
0.0	0.51	1.10	1.69	2.00	2.12	2.17	2.18	2.06	1.88	Z/C-7
0.0	0.46	0.91	1.34	1.49	1.50	1.44	1.12	0.54	0.0	Z/C-8
0.0	0.46	0.91	1.34	1.49	1.50	1.44	1.12	0.54	0.0	Z/C-9
0.0	0.46	0.91	1.34	1.49	1.50	1.44	1.12	0.54	0.0	Z/C-10
0.0	10.0	20.0	30.0	40.0	50.0	60.0	70.0	80.0	90.0	XFUS
100.0	110.0	120.0	130.0	140.0	150.0	160.0	170.0	180.0	190.0	XFUS
200.0	210.0	220.0	230.0	240.0	250.0	260.0	270.0	280.0	306.0	XFUS
0.0	11.0	27.0	46.0	63.0	90.0	113.0	134.0	151.0	166.0	FUSA
176.0	12.0	183.0	178.0	169.0	159.0	152.0	147.0	144.0	143.0	FUSA
144.0	143.0	141.0	132.0	118.0	99.0	79.0	58.0	18.0	0.0	FUSA
0.0	12.0	24.0	25.0	26.0	27.0					XACT
0.0	1.026	0.0	0.0	0.0	0.0					ACTR
240.1	0.0	4.16	60.8	280.2	0.0	26.83	14.5			FINLOC
0.0	30.0	70.0	100.0							FIN X/C
0.0	1.50	1.50	0.0							FIN Z/C
246.33	31.25	-1.0	26.70	270.33	45.00	0.50	7.75			CANLOC
0.0	37.5	62.5	100.0							CAN X/C
0.0	1.50	1.50	0.0							CAN Z/C

G.E. NACELLES

236.6	9.58	-8.0	239.3	27.3	-5.75	248.5*	32.5*	0.0*		PODLOC
0.0	19.166	25.499	28.0	31.80	35.915					XPOD
2.592	3.40	3.54	3.54	3.47	3.092					PODR
0.0	19.166	25.499	28.0	31.80	35.915					XPOD
2.592	3.40	3.54	3.54	3.47	3.092					PODR

P & WA NACELLES

245.4	9.67	-8.0	247.2	27.1	-5.75	248.5*	32.5*	0.0*		PODLOC
0.0	12.083	17.00	22.00	25.00	28.667					XPOD
2.813	3.341	3.540	3.65	3.58	3.333					PODR
0.0	12.083	17.00	22.00	25.00	28.667					XPOD
2.813	3.341	3.540	3.65	3.58	3.333					PODR

NOTE: Actuator Fairing Input As a Nacelle.

* Actuator Origin

Table 3-S. Wave Drag Program Inputs for the Aerodynamic Development Model (GE)

0.0	2.5	10.0	25.0	40.0	50.0	60.0	75.0	90.0	100.0	X/C
83.03	6.67	0.0	180.95							W1
114.53	10.33	0.8	150.82							W2
127.73	12.83	1.0	138.56							W3
192.01	31.25	4.5	81.44							W4
192.03	31.26	4.5	49.49							W5
224.07	41.67	6.2	35.88							W6
247.51	49.28	7.5	25.69							W7
258.83	52.96	8.2	20.76							W8
274.08	57.92	9.0	0.0							W9
0.0	0.85	1.60	2.01	2.03	1.95	1.72	1.18	0.50	0.0	Z/C-1
0.0	0.35	0.88	1.34	1.49	1.49	1.35	0.98	0.43	0.0	Z/C-2
0.0	0.36	0.85	1.30	1.43	1.40	1.29	0.92	0.42	0.0	Z/C-3
0.0	0.44	0.88	1.28	1.40	1.39	1.29	0.90	0.35	0.0	Z/C-4
0.0	0.58	1.12	1.74	2.08	2.21	2.27	2.28	2.21	2.06	Z/C-5
0.0	0.44	0.78	1.15	1.25	1.25	1.21	0.95	0.46	0.0	Z/C-6
0.0	0.44	0.78	1.15	1.25	1.25	1.21	0.95	0.46	0.0	Z/C-7
0.0	0.44	0.78	1.15	1.25	1.25	1.21	0.95	0.46	0.0	Z/C-8
0.0	0.44	0.78	1.15	1.25	1.25	1.21	0.95	0.46	0.0	Z/C-9
0.0	10.0	20.0	30.0	40.0	50.0	60.0	70.0	80.0	90.0	XFUS
100.0	110.0	120.0	130.0	140.0	150.0	160.0	170.0	180.0	190.0	XFUS
200.0	210.0	220.0	230.0	240.0	250.0	260.0	270.0	290.0	306.0	XFUS
0.0	9.0	25.0	44.0	62.0	80.0	98.0	115.0	132.0	146.0	FUSA
154.0	158.0	157.0	155.0	151.0	145.0	139.0	133.0	128.0	124.0	FUSA
119.0	115.0	111.0	105.0	97.0	82.0	61.0	42.0	9.0	0.0	FUSA
237.0	10.0	-3.33	242.5	27.10	-0.58					PODLOC
0.0	19.166	25.449	28.0	31.8	35.915					XPOD
2.46	3.315	3.54	3.56	3.47	3.092					PODR
0.0	19.166	25.449	28.0	31.8	35.915					XPOD
2.46	3.315	3.54	3.56	3.47	3.092					PODR
237.0	26.0	4.83	40.0	274.0	26.0	17.33	6.67			FINLOC
0.0	37.5	62.5	100.0							FIN X/C
0.0	1.0	1.0	0.0							FIN Z/C
243.51	31.25	4.5	29.64	277.70	50.92	7.8	5.96			CANLOC
0.0	37.5	62.5	100.0							CAN X/C
0.0	1.5	1.5	0.0							CAN Z/C

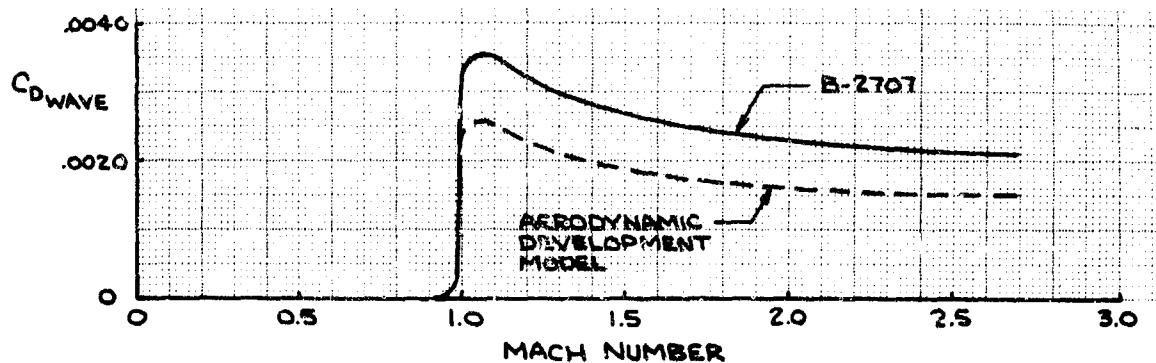


Figure 3-10. Variation of Wave Drag with Mach Number

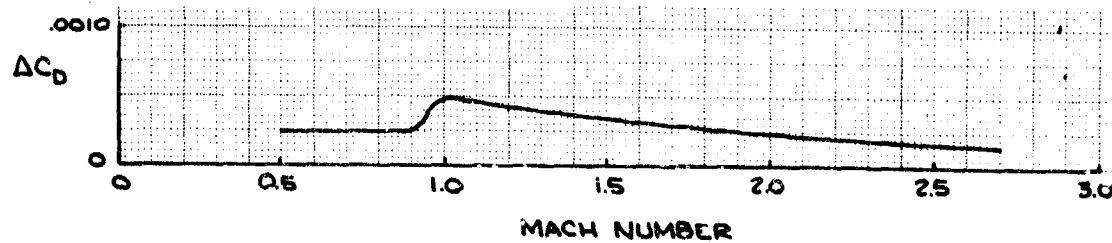


Figure 3-11. Variation of Wing Gap Drag with Mach Number

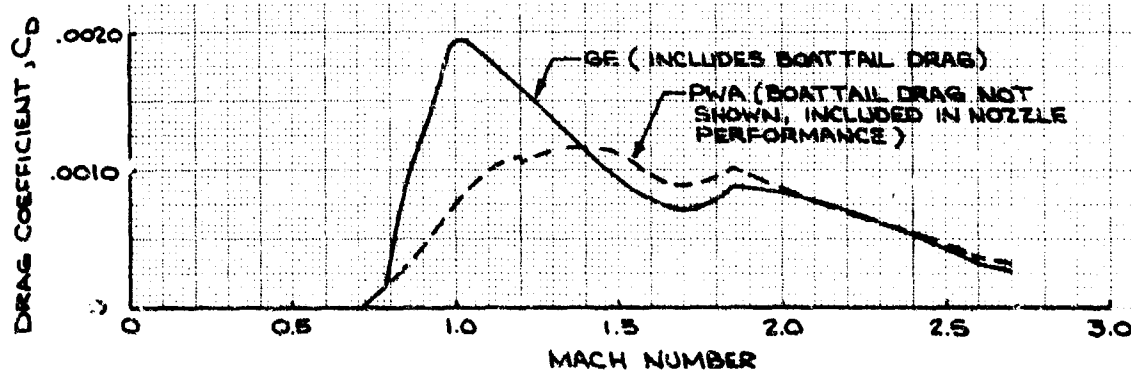


Figure 3-12. Drag Due to Propulsion System

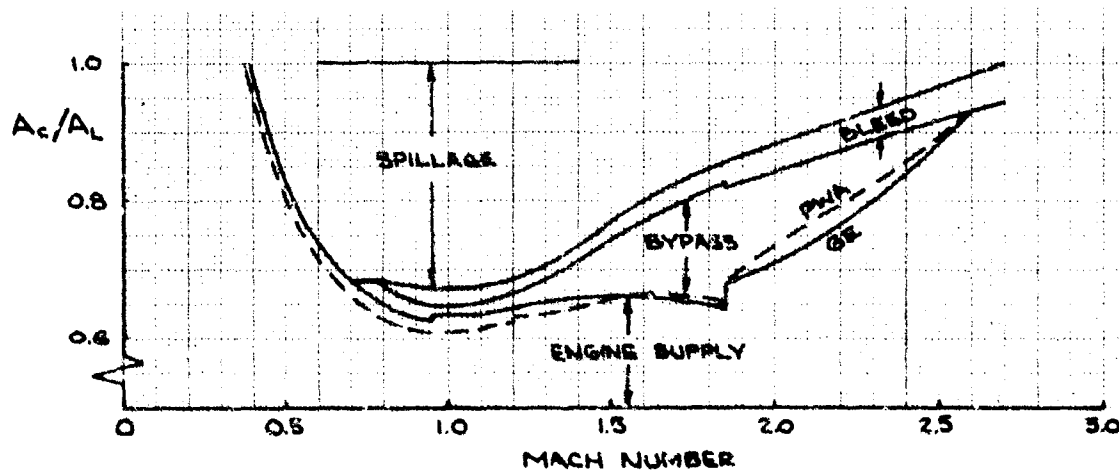


Figure 3-13. Inlet Airflow Characteristics

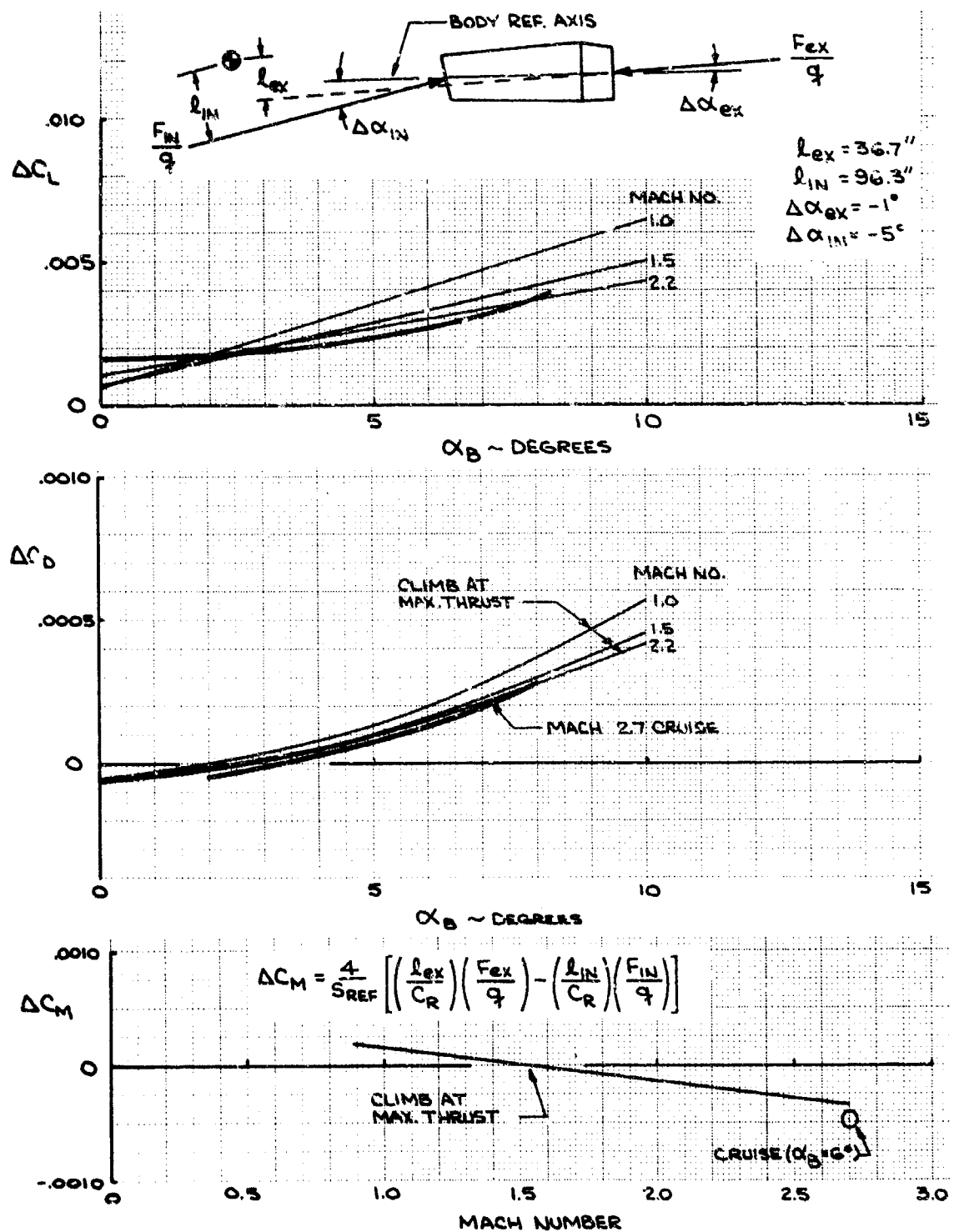


Figure 3-14. Effect of Thrust on Aerodynamic Data

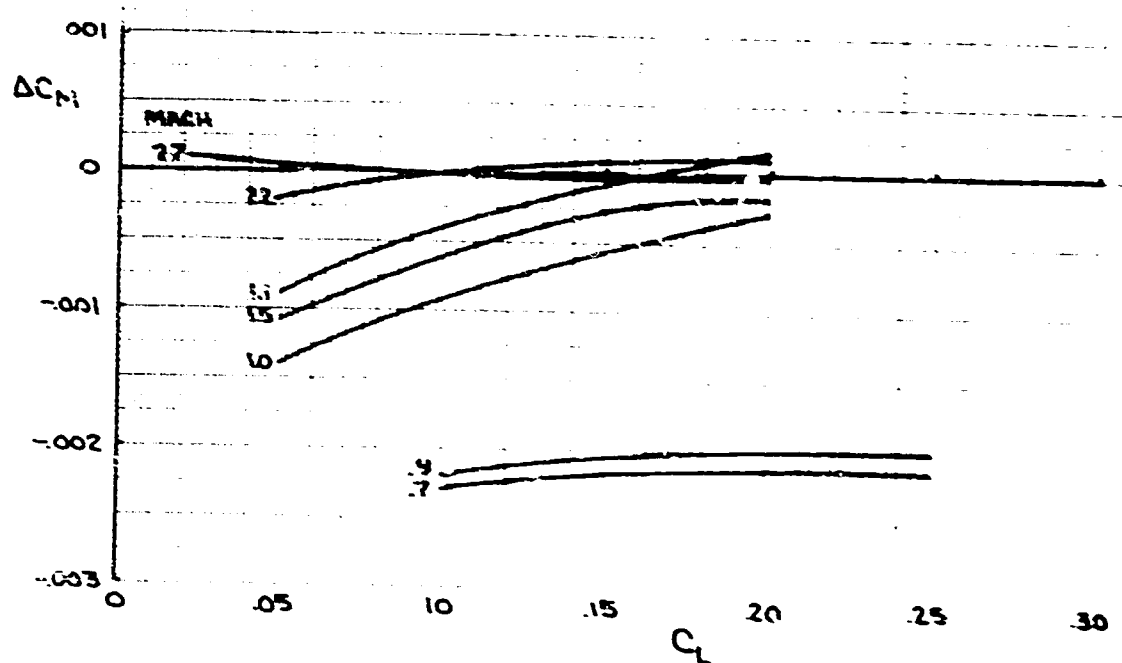


Figure 3-15. (a) Aeroelastic Corrections to Rigid Pitching Moment Data - 72 Degrees Leading Edge Sweep

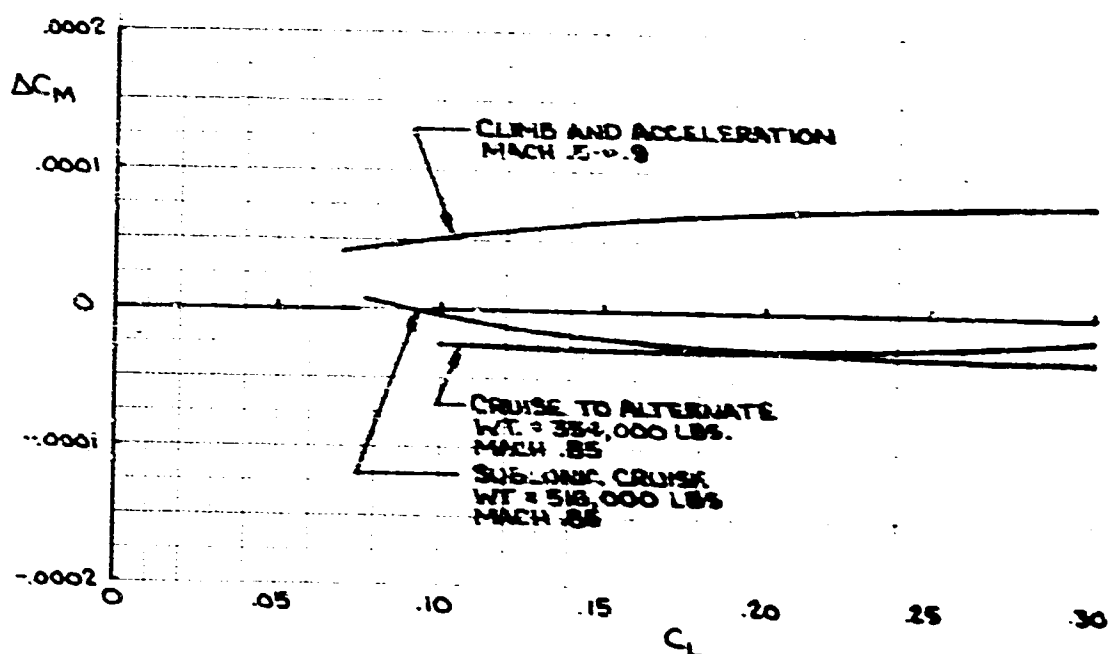
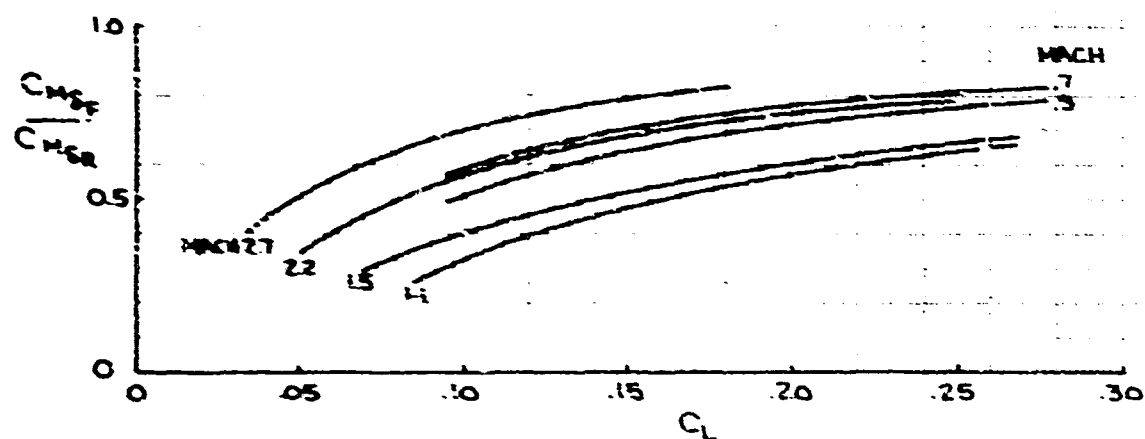
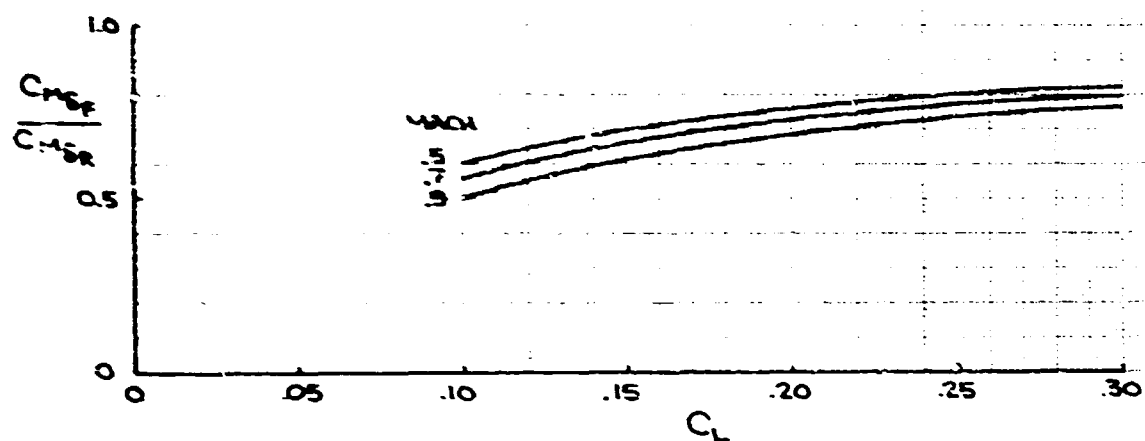


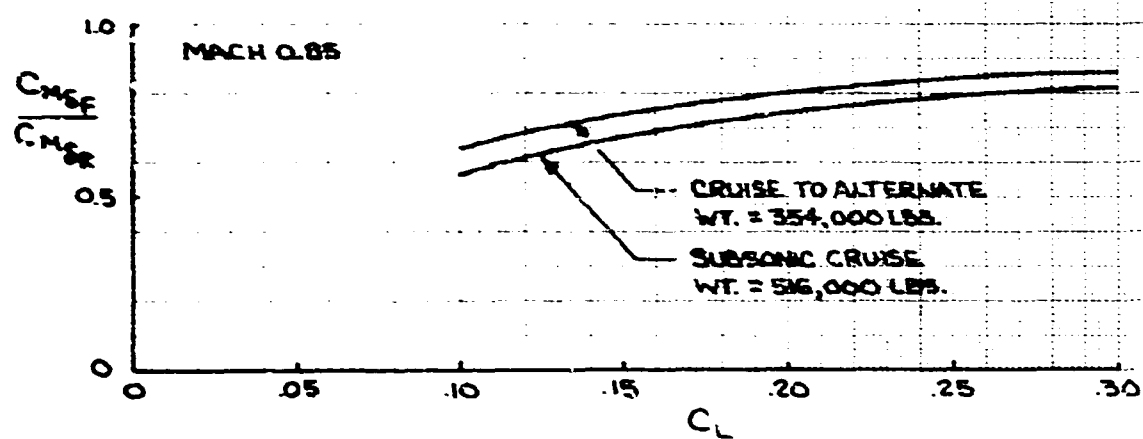
Figure 3-15. (b) Aeroelastic Corrections to Rigid Pitching Moment Data - 42 Degrees Leading Edge Sweep



(a) 72 Degrees Leading Edge Sweep



(b) 42 Degrees Leading Edge Sweep - Climb and Acceleration



(c) 42 Degrees Leading Edge Sweep - Subsonic Missions

Figure 3-16. Flexible Elevator Effectiveness

V2-B2701-3

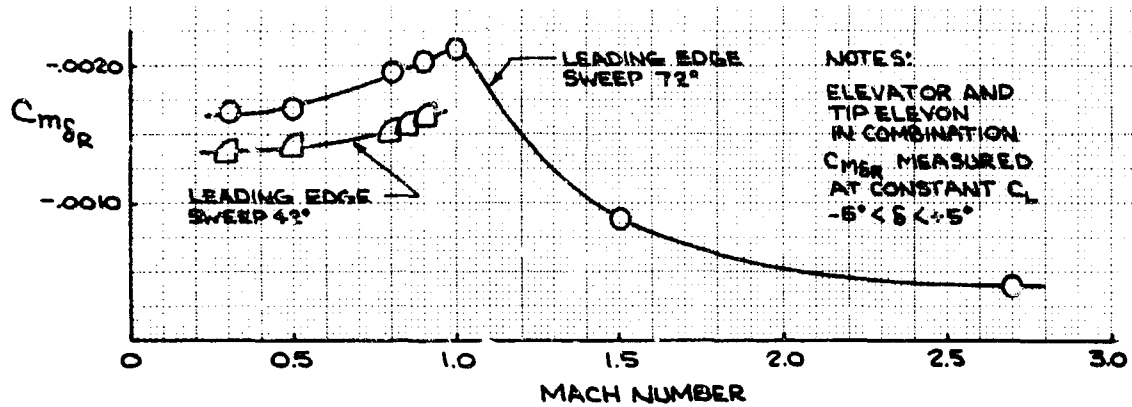


Figure 3-17. Rigid Elevator Effectiveness

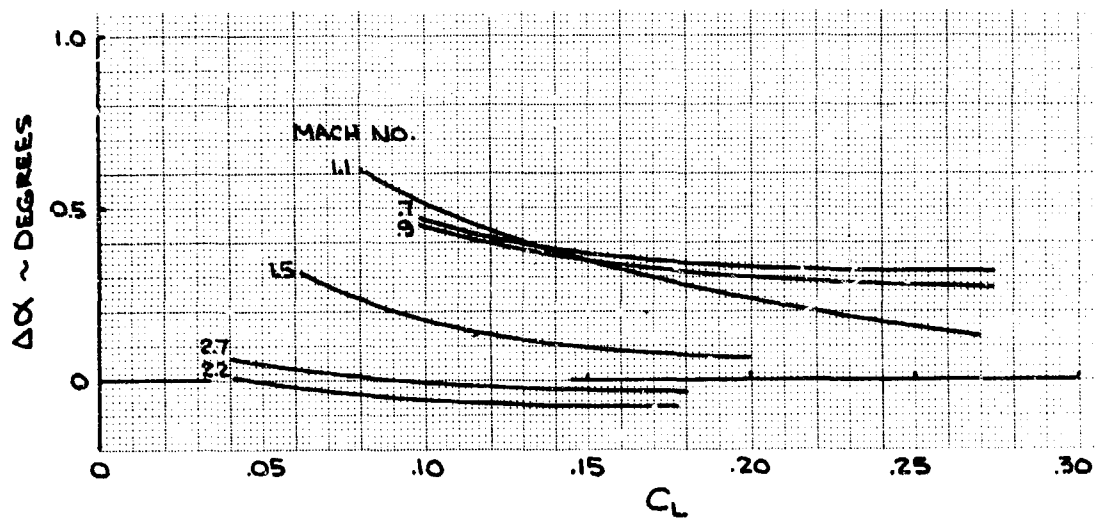


Figure 3-18. Effect of Flexibility on Incidence - Leading Edge Sweep - 72 Degrees

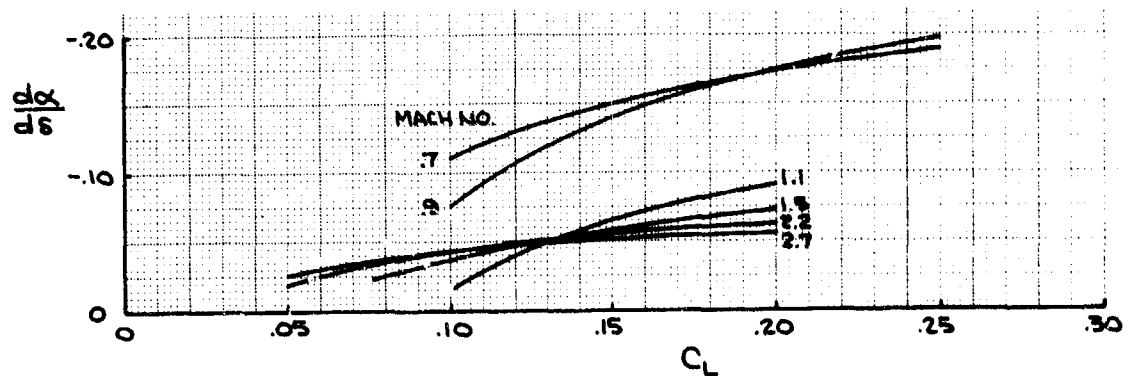


Figure 3-19. Effect of Elevator Angle on Incidence - Leading Edge Sweep - 72 Degrees

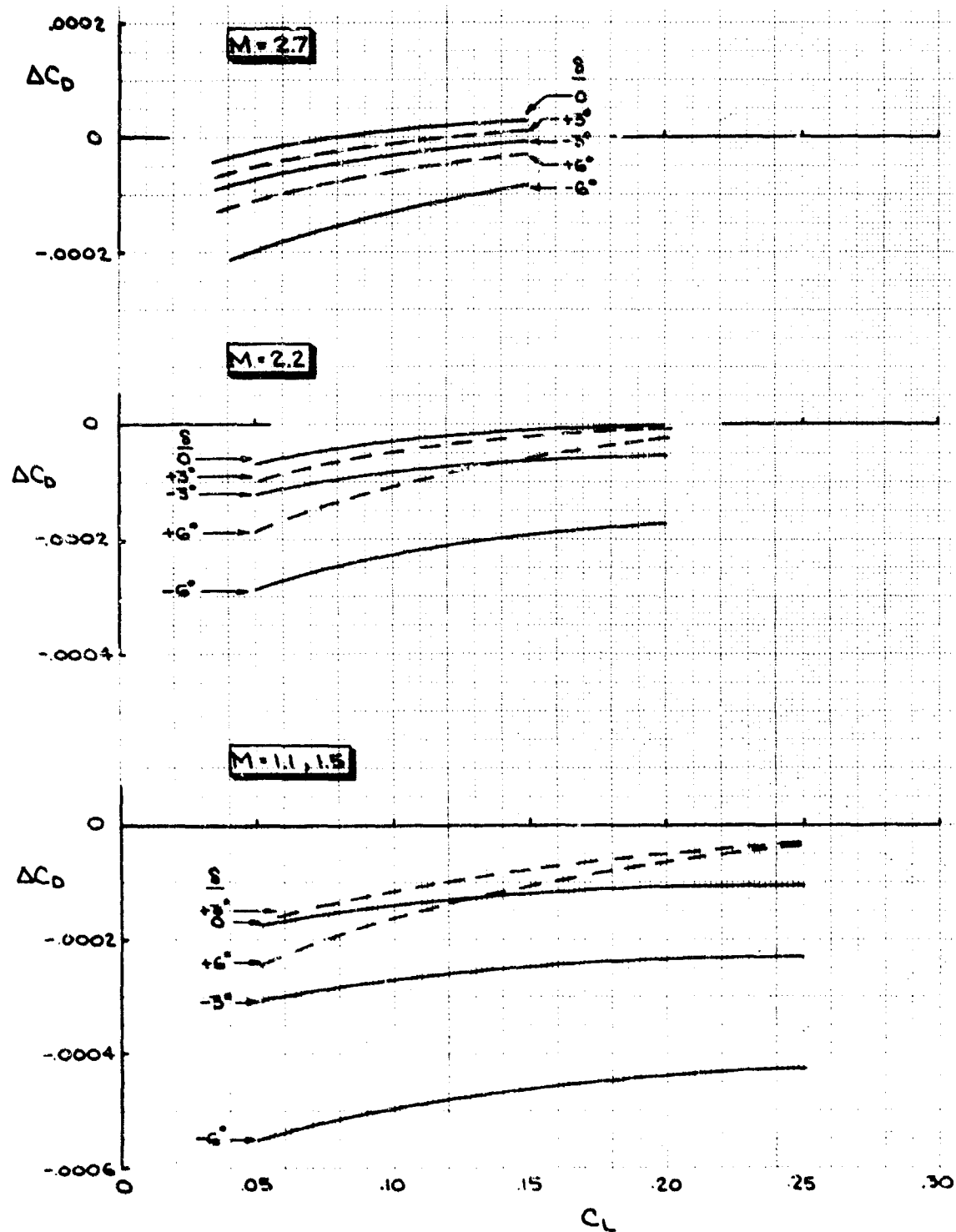


Figure 3-70. Flexibility Correction to Drag

V2-B2707-3

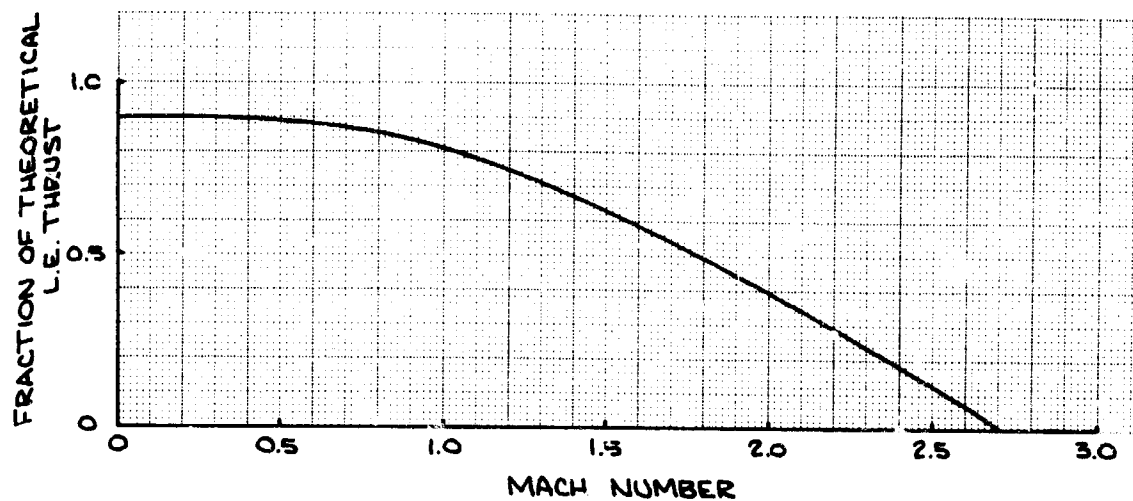


Figure 3-21. Variation of Leading Edge Thrust with Mach Number at 72 Degrees Leading Edge Sweep

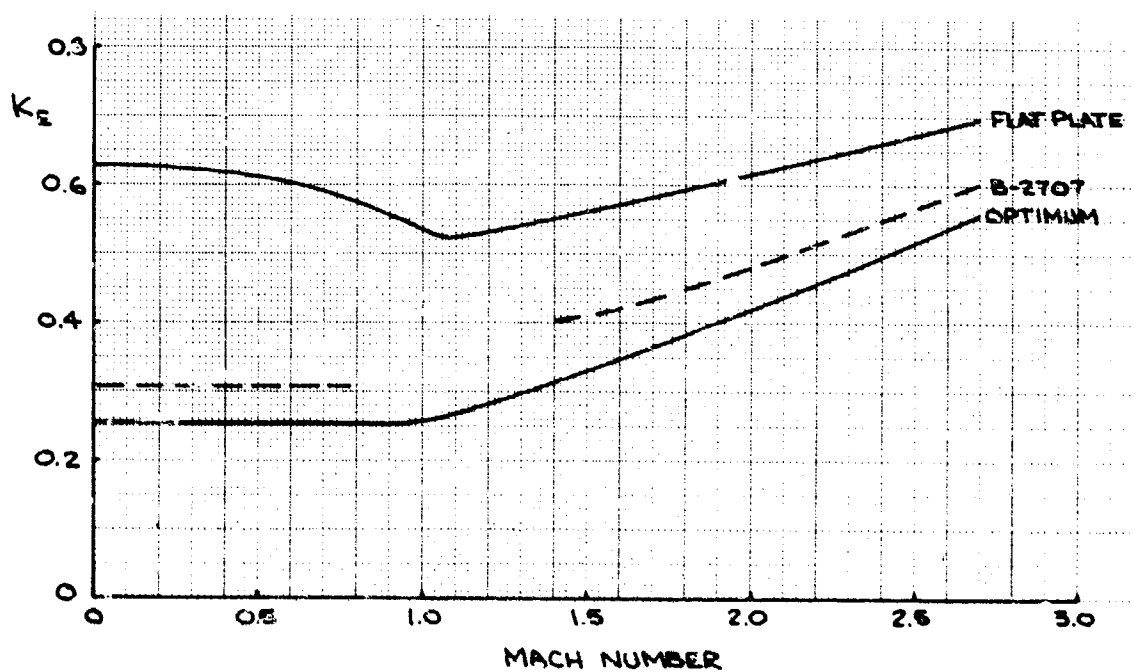


Figure 3-22. B-2707 Symmetric Drag Due to Lift Variation

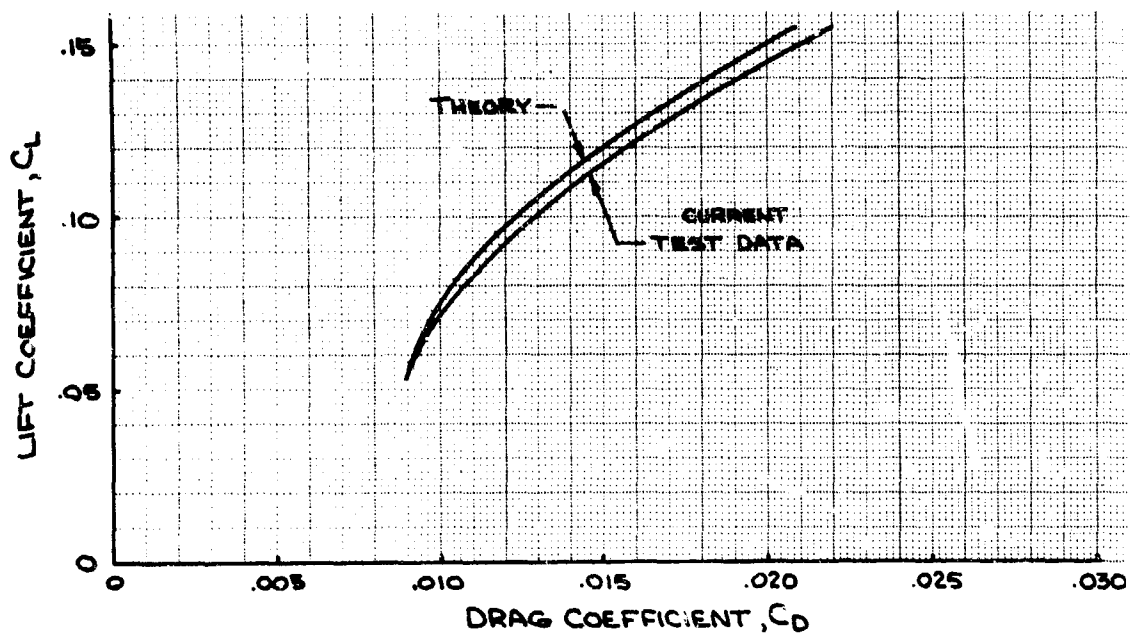


Figure 3-23. (a) Comparison of Theory and Test -- B-2707 -- Mach 2.7

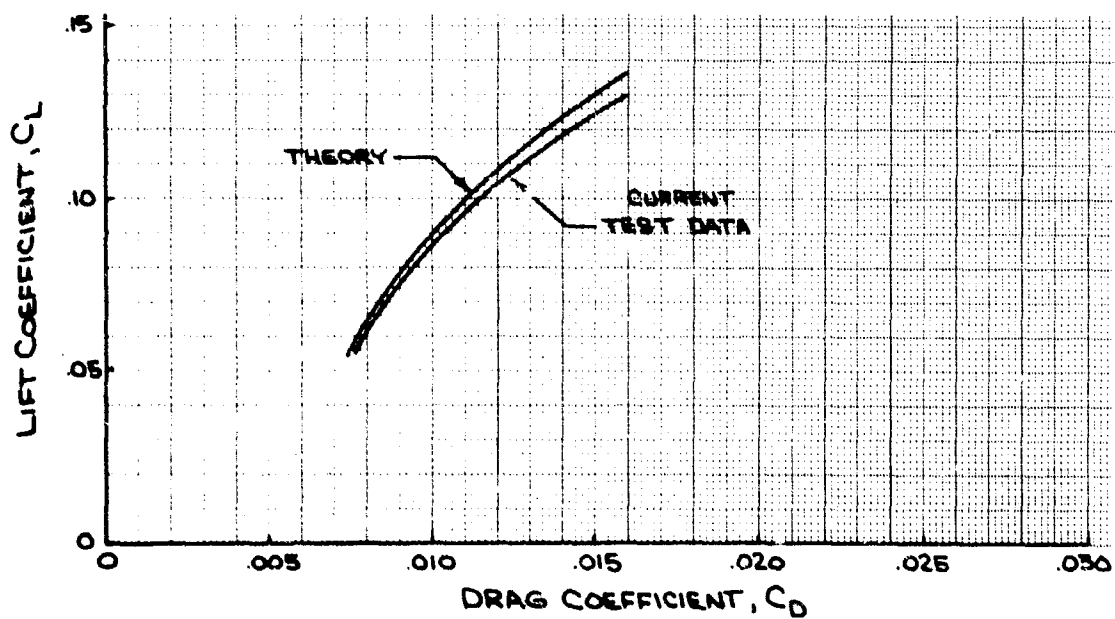


Figure 3-23. (b) Comparison of Theory and Test -- Aerodynamic Development Model -- Mach 2.7

3.1.3 Wind Tunnel Results

3.1.3.1 Wind Tunnel Models

The substantiation of the lift drag characteristics is based on wind tunnel results obtained with three wind tunnel models. For the range of Mach numbers from 0.9 to 2.7, where the airplane operates at a fixed 72 degrees of sweep, models SA-966 and SA-977 were used to represent the B-2707 and aerodynamic development model respectively. A reduced sweep of 42 degrees is used for lower Mach numbers and model SA-856 has been used to obtain transonic data for the B-2707. Model photographs are shown in Figs. 24 and 25. Three other force models of the B-2707, models SA-981, -983, and -984, together with relevant drawings and data, will be supplied to the FAA for evaluation. Although these models have been tested at Boeing, time did not permit incorporating the analysis of the data into this report; but this analysis will be available for evaluators' onsite inspection.

3.1.3.2 Test Procedures

The wind tunnel data were obtained in the Boeing 4- by 4-ft supersonic and 8- by 12-ft transonic wind tunnels. Nominal test conditions have been shown in Fig. 4-9 of Ref. 3. Standard test procedures have been used. Models are fitted with sparse transition trips to ensure turbulent boundary layers over all the surfaces of the model, but drag corrections are not applied for trip drag. The data are corrected for chamber and base pressures and also for internal nacelle drag. The models have been tested with nacelles of the correct external shape including a correct simulation of the boundary layer diverter. These nacelles are bent at the nozzle, in order to obtain a favorable thrust component in flight, but the internal ducts are straight and circular, so that the internal drag is an axial force transmitted to the model through shear stresses.

3.1.3.3 Extrapolation of Wind Tunnel Results to Full-Scale Flight Conditions

The full-scale drag polars have been obtained by adjusting the wind tunnel measurements to full-scale conditions. The corrections applied to the model data, to account for differences between the model and the airplane, are listed and described as follows:

- Scale effect corrections
- Drag due to surface roughness and miscellaneous items

- Wave drag
- Corrections due to propulsion system operation
- Aeroelastic corrections and trim drag

a. Scale Effect Corrections

The methods used to calculate skin friction and form drag have been discussed in Par. 3.1.2. These methods have been used to determine the corrections for the measured drag levels to account for the differences between the skin friction drag of the wind tunnel model at the test conditions, and that of the full-scale aircraft at the flight conditions. The corrections for the nominal mission are shown in Fig. 3-26 for a wing sweep of 72 degrees. The corrections for the wing sweep of 42 degrees are:

Mach Number	Height (ft)	C_D
0.5	30,000	0.0039
0.8	30,000	0.0038
0.9	30,000	0.0037

A correction has been applied, for scale effect, to the polar shape at subsonic speeds. This correction has been defined, in terms of a parameter S , in Ref. 20. It was shown that S , which is a measure of the amount of leading edge suction, is a unique function of the Reynolds number of the leading edge. The variation of this Reynolds number as a function of Mach number in the wind tunnel (for the SA-856 model) and for the airplane is shown in Fig. 3-27. The parameter S is defined by the following equation:

$$S = \frac{C_L \tan \alpha - (C_D - C_{Dmin})}{C_L \tan \alpha - A \sqrt{Re_d} \left(\frac{y}{b/2} \right)}$$

It is the experimentally measured leading edge suction in percent of the total theoretical suction. With no suction the drag due to lift is $C_L \tan \alpha$; the drag due to lift for 100 percent suction is the second term in the denominator and for an elliptically loaded wing this would be $C_L^2 / \pi A$, where A is the aspect ratio; the measured drag due to lift is $C_D - C_{Dmin}$. The parameter S was determined from the test data and an increment applied



Figure 3-24. Transonic Wind Tunnel Model SA-836

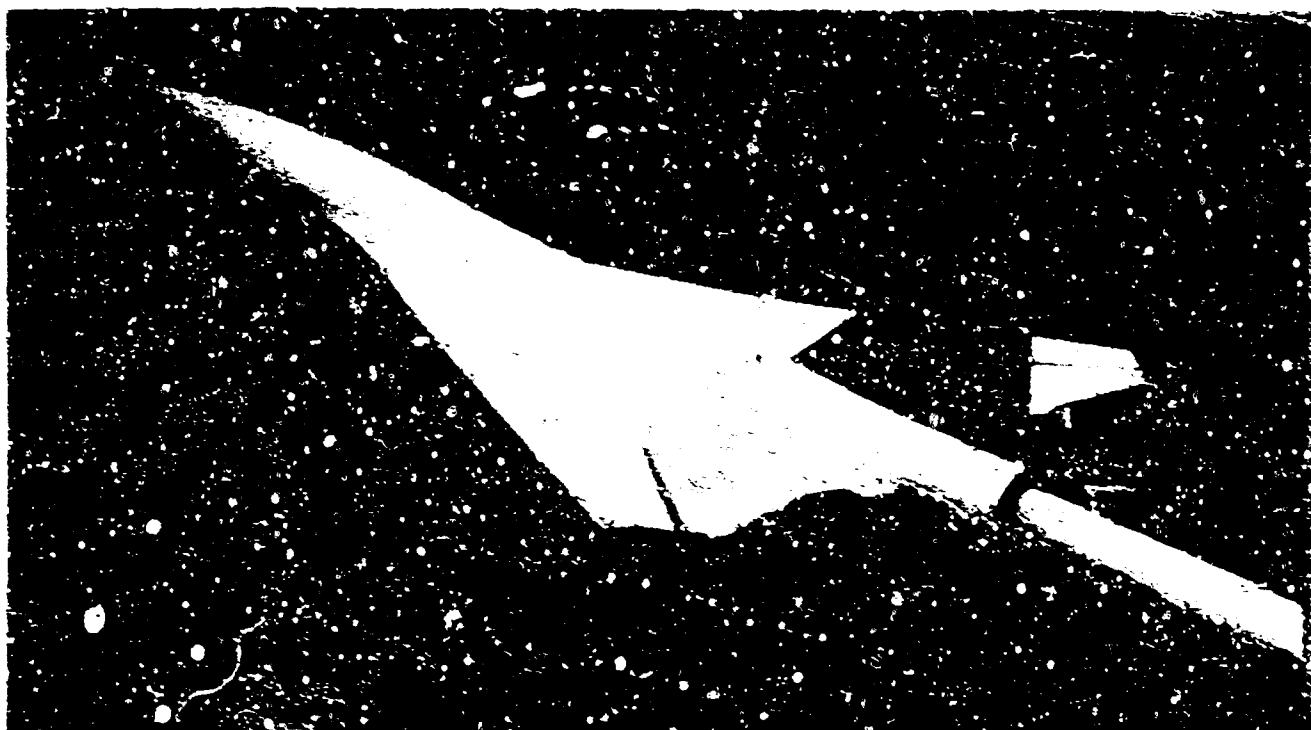


Figure 3-25. Supersonic Wind Tunnel Model SA-966

V2-E9707-3

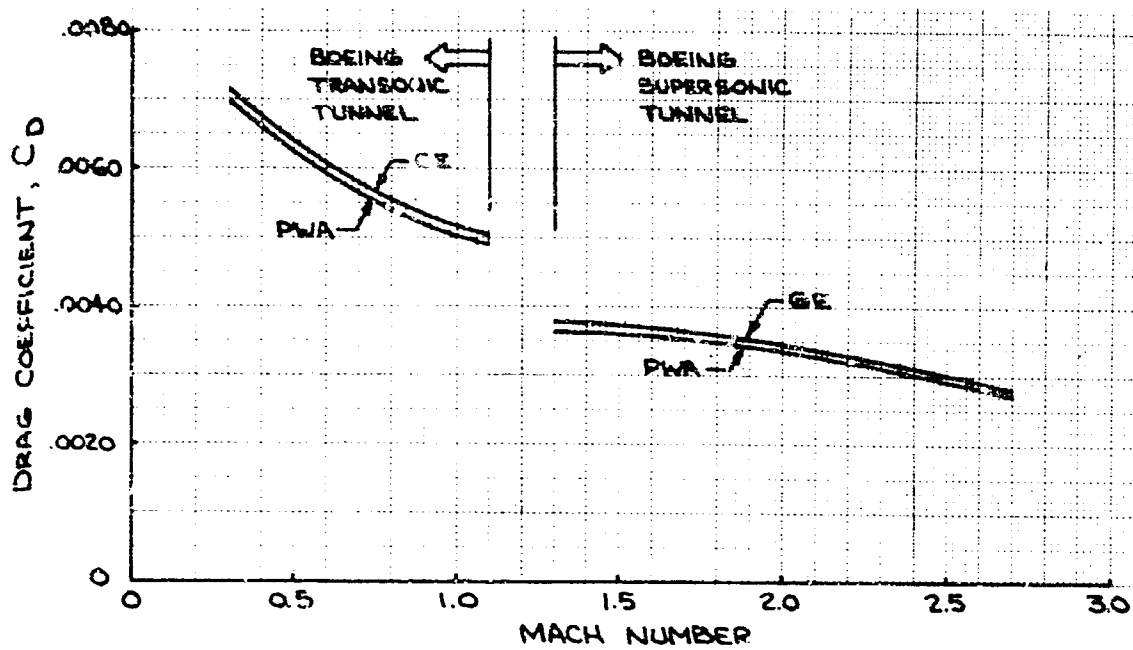


Figure 3-26. Skin Friction Drag Correction

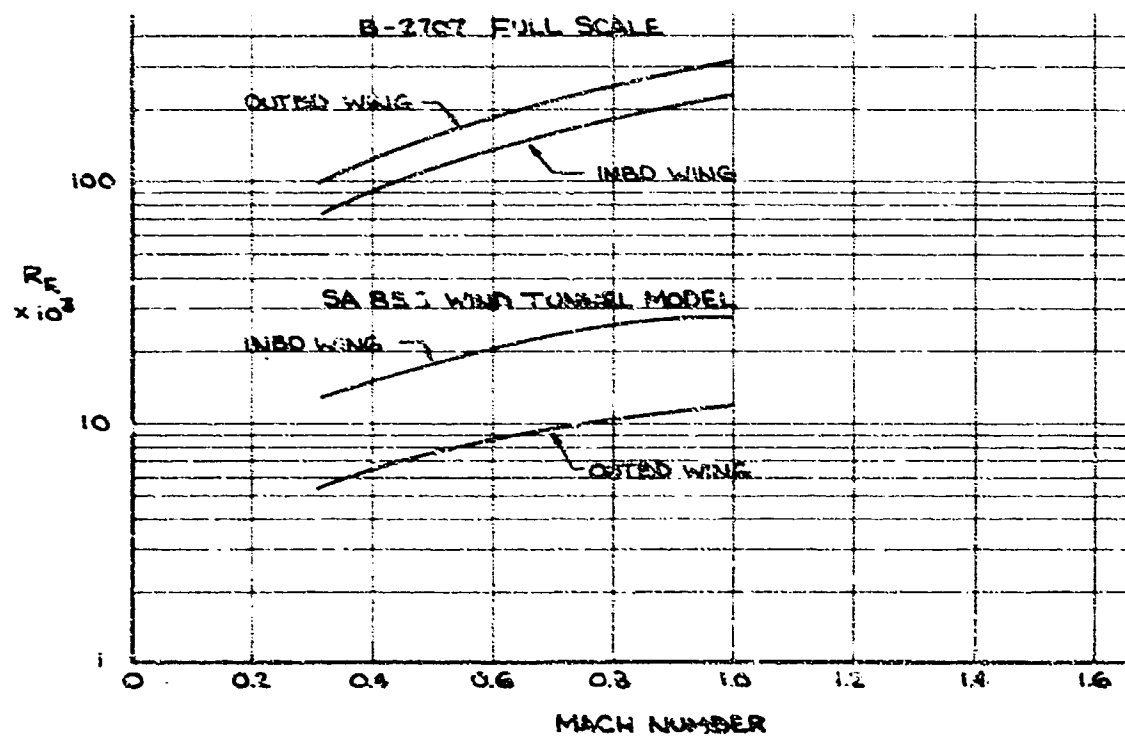


Figure 3-27. Leading Edge Reynolds Number

to it, for scale effect, based on the data shown in Fig. 7 of Ref. 20. The increment was obtained by entering that figure with the leading edge Reynolds Number for the average radius of the inboard wing portion, 72-degrees sweep, and also the average radius for the outboard wing portion, 42 degrees of sweep; and then averaging the two values of S that were obtained. The data in Fig. 7 of Ref. 20 were obtained at very small Mach numbers. Rather than assume that these would be valid at all Mach numbers, Fig. 3-28 was used to adjust them for Mach number; it being assumed that the probability of achieving an improvement in leading edge suction, due to scale effect, diminishes with increasing Mach number. The results are:

Mach	S (Wind tunnel)	ΔS (From Ref. 19)	S (Full scale)
0.5	74.	12.	86.
0.7	74.	9.	83.
0.9	46.	7.	53.

The effect on the drag polar at Mach 0.85 is shown in Fig. 3-29.

b. Drag Due to Surface Roughness and Miscellaneous items

The drag increments given in Par. 3.1.2.2 have been applied to the wind tunnel model drag level to account for surface roughness and the miscellaneous items listed and analyzed in Par. 3.1.2.2.

c. Wave Drag Corrections

A wave drag correction has been applied to the wind tunnel drag level to account for differences between the wind tunnel models and the aircraft. The major difference is in the afterbody, on the models, to accommodate a sting support system. The wave drag estimation procedure has been described in Par. 3.1.3 and the aircraft geometries in Tables 3-R, 3-S, and 3-T. Tables 3-U and 3-V define the geometry of the wind tunnel models. The thickness ratio of the wing of the SA 966 model is somewhat greater than on the airplane. The wave drag increments to be applied to the measured model drag coefficients are shown in Fig. 3-30. The geometry difference between the wind tunnel model and the airplane is the cause of a small change in aerodynamic center; the airplane being slightly less stable than the model. The data in Ref. 24 have been used to

estimate this effect and the results are shown in Fig. 3-31.

d. Propulsion System Drag

The increments given in Par. 3.1.3 have been applied to the lift, drag, and pitching moment measured in the wind tunnel.

e. Aeroelastic Corrections and Trim Drag

The aeroelastic corrections presented in Figs. 3-15 to 3-20, Par. 3.1.2.5, have been applied to the wind tunnel lift, drag, and moment data. Trim drag was determined as follows:

(1) Data were transferred to the appropriate center of gravity position obtained from Fig. 3-32.

(2) Wind tunnel pitching moment data were corrected for engine thrust from Fig. 3-14.

(3) Wind tunnel data were corrected for fuselage aft closure from Fig. 3-31.

(4) Wind tunnel data were corrected for airplane flexibility as previously described (Fig. 3-15).

(5) Fig. 3-17 was used at the appropriate Mach number to determine the rigid elevator effectiveness. This has been obtained directly from test data at constant lift coefficients appropriate to the nominal flight profile; it is valid for small deflections (± 5 degrees) only.

(6) Figure 3-16 was used at the appropriate Mach number and lift coefficient, to determine the ratio of flexible to rigid elevator effectiveness, to obtain the flexible elevator effectiveness.

(7) The deflection for trim was then determined by dividing the moment to trim by the flexible elevator effectiveness.

(8) Figures 3-33 and 3-34 present experimentally determined drag increments due to elevator deflections. Trim drag was obtained by entering these figures at the appropriate Mach number and lift coefficient, with the elevator deflection δ determined in preceding step (7).

Trim drag results for the airplane are shown in Figs. 3-35 to 3-38. The trim drag increment and elevator deflection, for the nominal mission, are shown in Figs. 3-35 to 3-36 as a function of Mach number. The effect of cg on the lift drag

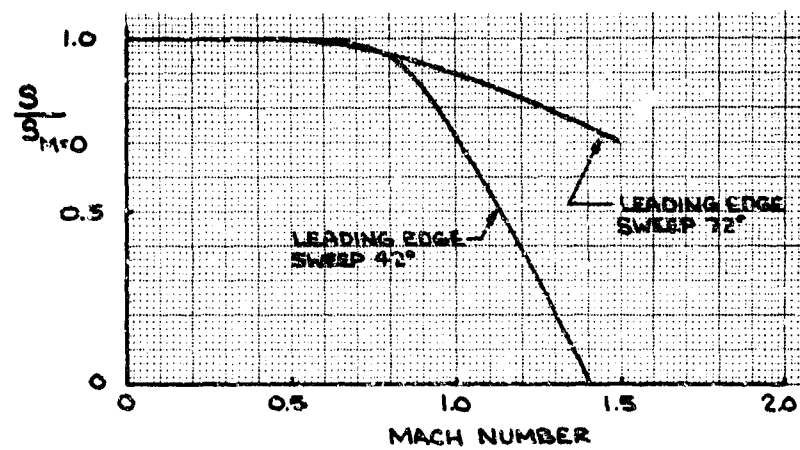


Figure 3-28. Effect of Mach Number on Leading Edge Thrust

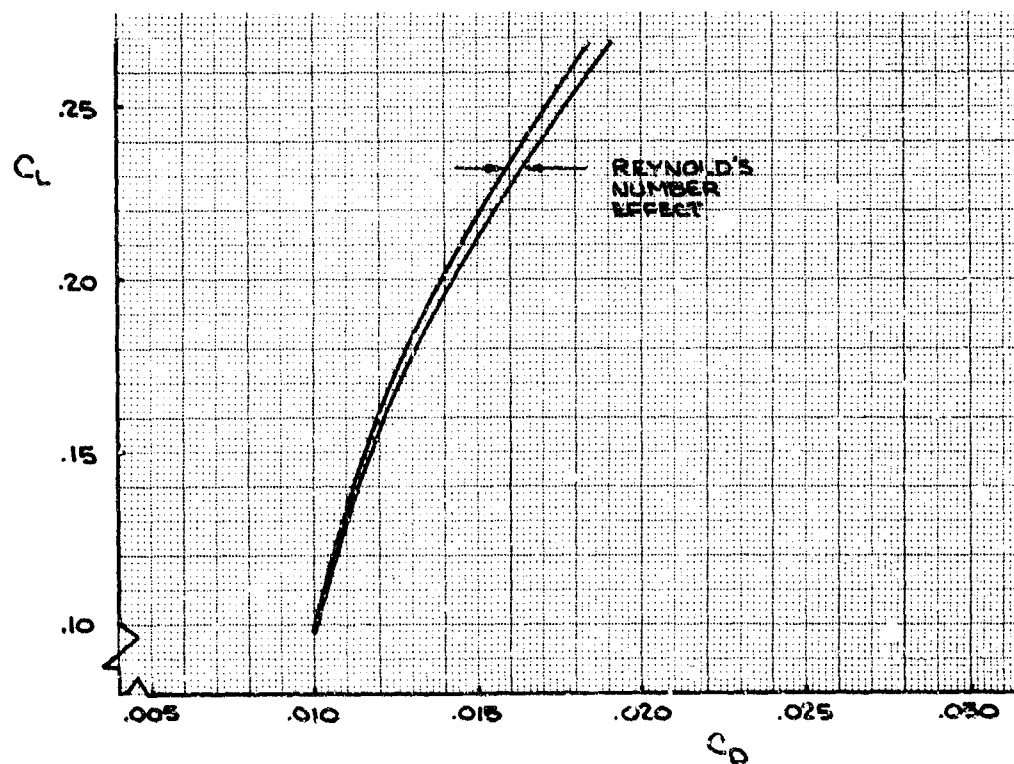


Figure 3-29. Reynolds Number Effect on Drag Due to Lift at Mach .85

Table 3-T. 3-2707 Camber Line Ordinates (% Chord)

Percent Span Percent Chord	10.6	14.6	18.6	23.2	29.3	39.1	47.4	51.6	54.4	59.1	69.9	81.1	87.3
0	1.69	1.44	1.19	.85	.44	-.28	-.64	-.71	-.85	-.85	-.30	1.50	3.57
5	1.73	1.53	1.33	1.00	.64	-.023	-.32	-.38	-.54	-.52	.04	1.91	4.02
10	1.68	1.50	1.32	1.04	.70	.15	-.15	-.20	-.35	-.30	.29	2.24	4.37
15	1.56	1.38	1.195	.925	.68	.15	-.08	-.11	-.24	-.16	.46	2.50	4.62
20	1.36	1.18	1.0	.725	.58	.11	-.78	-.08	-.15	-.10	.58	2.70	4.85
30	.78	.62	.46	.25	.12	-.105	-.185	-.15	-.19	-.08	.74	3.01	5.25
40	.08	-.045	-.17	-.29	-.35	-.42	-.41	-.31	-.31	-.125	.82	3.24	5.53
50	-.72	-.78	-.83	-.88	-.85	-.785	-.63	-.48	-.42	-.17	.88	3.42	5.81
60	-1.44	-1.12	-1.39	-1.38	-1.31	-1.10	-.87	-.65	-.53	-.21	.92	3.57	6.06
70	-2.02	-1.94	-1.86	-1.76	-1.63	-1.33	-1.01	-.85	-.61	-.26	.95	3.69	6.28
80	-2.42	-2.31	-2.27	-2.06	-1.87	-1.49	-1.14	-1.09	-.69	-.31	.98	3.79	6.49
90	-2.64	-2.52	-2.74	-2.23	-2.02	-1.60	-1.18	-1.37	-.71	-.34	1.02	3.86	6.67
100	-2.70	-2.59	-3.27	-2.30	-2.11	-1.65	-1.25	-1.70	-.77	-.36	1.05	3.93	6.88

PLANFORM GEOMETRY								
X (FT)	0	17.2	30.5	47.4	62.1	76.8	131.5	162.7
Y (FT)	0	5.625	9.86	15.5	20.68	25.0	42.7	52.9
CHORD (FT)	169.75	150.5	136.1	118.7	103.4	90.6	42.5	0 (15.1)

Table 3-U. Model SA 966 Wave Drag Program Inputs

0.	2.5	10.	25.	40.	50.	60.	75.	90.	100.	X/C
16.832	1.028	-.731	32.723							W1
23.647	1.802	-.640	25.652							W2
25.769	2.237	-.585	23.545							W3
27.602	2.833	-.512	21.566							W4
30.143	3.655	-.439	19.226							W5
36.466	5.711	-.201	13.440							W6
36.472	5.713	-.201	8.608							W7
39.229	6.610	-.091	7.133							W8
45.343	8.597	.146	4.481							W9
48.614	9.663	.274	0.0							W10
0.0	0.25	0.56	0.88	1.10	1.18	1.17	0.93	0.43	0.0	Z/C-1
0.0	0.40	0.98	1.47	1.64	1.53	1.39	1.0	0.44	0.0	Z/C-2
0.0	0.44	1.04	1.74	1.80	1.65	1.45	1.03	0.44	0.0	Z/C-3
0.0	0.45	0.92	1.45	1.81	1.80	1.61	1.02	0.44	0.0	Z/C-4
0.0	0.46	0.91	1.34	1.49	1.50	1.44	1.12	0.54	0.0	Z/C-5
0.0	0.46	0.91	1.34	1.49	1.50	1.44	1.12	0.54	0.0	Z/C-6
0.0	0.58	1.15	1.76	2.09	2.25	2.32	2.34	2.28	2.14	Z/C-7
0.0	0.46	0.91	1.34	1.49	1.50	1.44	1.12	0.54	0.0	Z/C-8
0.0	0.46	0.91	1.34	1.49	1.50	1.44	1.12	0.54	0.0	Z/C-9
0.0	0.46	0.91	1.34	1.49	1.50	1.44	1.12	0.54	0.0	Z/C-10
0.0	2.0	4.0	6.0	8.0	10.0	12.0	14.0	16.0	18.0	XFUS
20.0	22.0	24.0	26.0	28.0	30.0	32.0	34.0	36.0	38.0	XFUS
40.0	42.0	44.0	46.0	48.0	50.0	52.0				XFUS
0.0	0.341	1.00	1.77	2.57	3.37	4.11	4.875	5.450	5.88	FUSA
6.08	6.12	5.95	5.58	5.23	5.01	4.84	4.81	4.82	4.81	FUSA
4.75	4.41	4.20	4.0	3.78	3.55	3.35				FUSA
0.0	2.193	4.386	4.569	4.751	4.934					XACT
0.0	0.186	0.0	0.0	0.0	0.0					ACTR
44.502	0.0	1.127	8.401	50.387	0.0	6.077	2.100			FINLOC
0.0	37.5	62.5	100.0							FIN X/C
0.0	1.5	1.5	0.0							FIN Z/C
45.019	5.711	-0.183	4.880	49.406	8.224	0.091	1.416			CANLOC
0.0	37.5	62.5	100.0							CAN X/C
0.0	1.50	1.50	0.0							CAN Z/C

G.E. NACELLES

43.241	1.751	-1.462	43.734	4.989	-1.051	45.416	5.940	0.0	PODLOC
0.0	3.503	4.660	5.117	5.812	6.56				XPOD
0.474	0.621	0.647	0.647	0.634	0.565				PODR
0.0	3.503	4.660	5.117	5.812	6.56				XPOD
0.474	0.621	0.647	0.647	0.634	0.565				PODR

P & WA NACELLES

44.849	1.767	-1.462	45.178	4.953	-1.051	45.416	5.940	0.0	PODLOC
0.0	2.208	3.107	4.021	4.569	5.239				XPOD
0.514	0.611	0.647	0.667	0.654	0.609				PODR
0.0	2.208	3.107	4.021	4.569	5.239				XPOD
0.514	0.611	0.647	0.667	0.654	0.609				PODR

Table 3-V. Model SA 977 Wave Drag Program Inputs

0.0	2.5	10.0	25.0	40.0	50.0	60.0	75.0	90.0	100.0	X/C
14.94	1.20	0.0	32.57							W1
20.62	1.859	0.144	27.15							W2
22.99	2.309	0.180	24.94							W3
34.56	5.625	0.810	14.66							W4
34.56	5.626	0.810	8.908							W5
40.33	7.501	1.116	6.458							W6
44.55	8.870	1.350	4.624							W7
46.59	9.533	1.476	3.737							W8
49.33	10.426	1.620	0.0							W9
0.0	0.85	1.60	2.01	2.03	1.95	1.72	1.18	0.50	0.0	Z/C-1
0.0	0.35	0.88	1.34	1.49	1.49	1.35	0.98	0.43	0.0	Z/C-2
0.0	0.36	0.85	1.30	1.43	1.40	1.29	0.92	0.42	0.0	Z/C-3
0.0	0.44	0.88	1.28	1.40	1.39	1.29	0.90	0.35	0.0	Z/C-4
0.0	0.58	1.12	1.74	2.08	2.21	2.27	2.28	2.21	2.06	Z/C-5
0.0	0.44	0.78	1.15	1.25	1.25	1.21	0.95	0.46	0.0	Z/C-6
0.0	0.44	0.78	1.15	1.25	1.25	1.21	0.95	0.46	0.0	Z/C-7
0.0	0.44	0.78	1.15	1.25	1.25	1.21	0.95	0.46	0.0	Z/C-8
0.0	0.44	0.78	1.15	1.25	1.25	1.21	0.95	0.46	0.0	Z/C-9
0.0	1.80	3.60	5.40	7.20	9.00	10.8	12.6	14.4	16.2	XFUS
18.0	19.8	21.6	23.4	25.2	27.0	28.8	30.6	32.4	34.2	XFUS
36.0	37.8	39.6	41.4	43.2	45.0	46.8	48.6	52.2	55.08	XFUS
0.0	0.292	0.81	1.426	2.009	2.592	3.175	3.726	4.277	4.730	FUSA
4.990	5.119	5.086	5.022	4.892	4.698	4.536	4.406	4.309	4.212	FUSA
4.115	3.985	3.856	3.726	3.499	3.370	3.240	3.175	3.143	3.143	FUSA
42.66	4.68	0.869	7.20	49.32	4.68	3.119	1.201			FINLOC
0.0	37.5	62.5	100.0							FIN X/C
0.0	1.0	1.0	0.0							FIN Z/C
43.832	5.625	0.810	5.335	49.986	9.166	1.404	1.073			CANLOC
0.0	37.5	62.5	100.0							CAN X/C
0.0	1.5	1.5	0.0							CAN Z/C
42.66	1.800	-0.599	43.83	4.88	-0.10					PODLOC
0.0	3.450	4.59	5.04	5.72	6.46					XPOD
0.443	0.597	0.637	0.641	0.625	0.556					PODR
0.0	3.450	4.59	5.04	5.72	6.46					XPOD
0.443	0.597	0.637	0.641	0.625	0.556					PODR

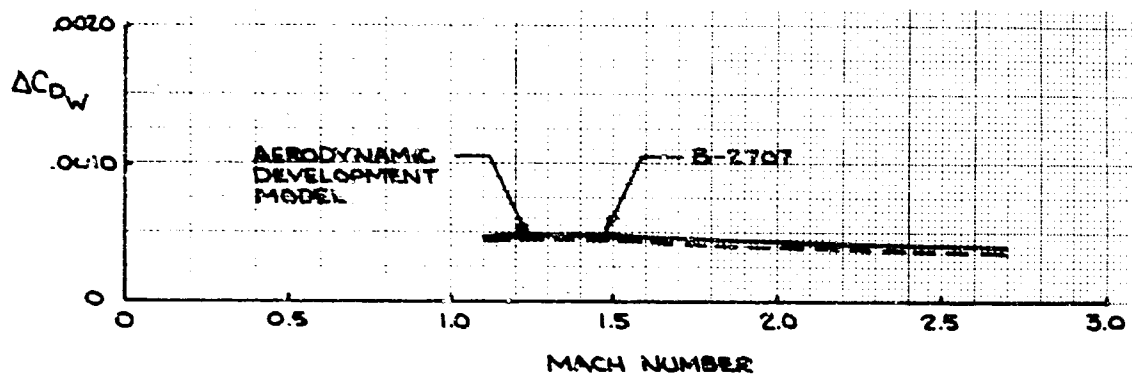


Figure 3-30 Wave Drag Correction

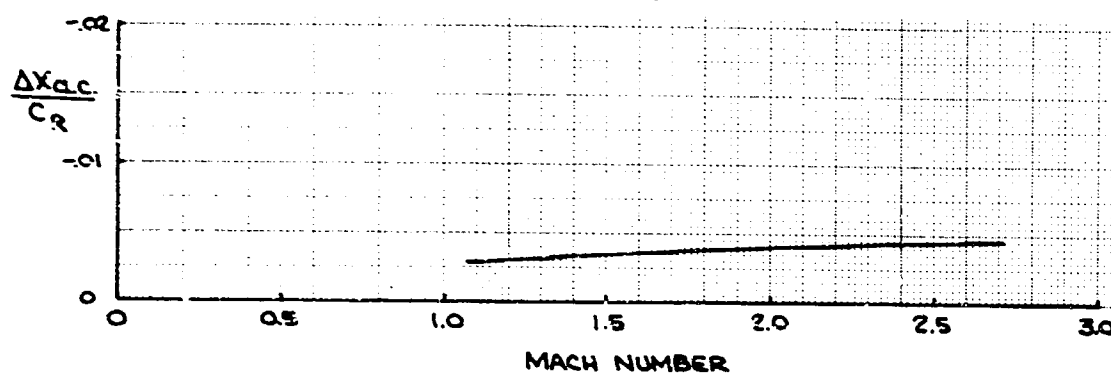


Figure 3-31. Effect of Wind Tunnel Model Body Closure on Aerodynamic Center

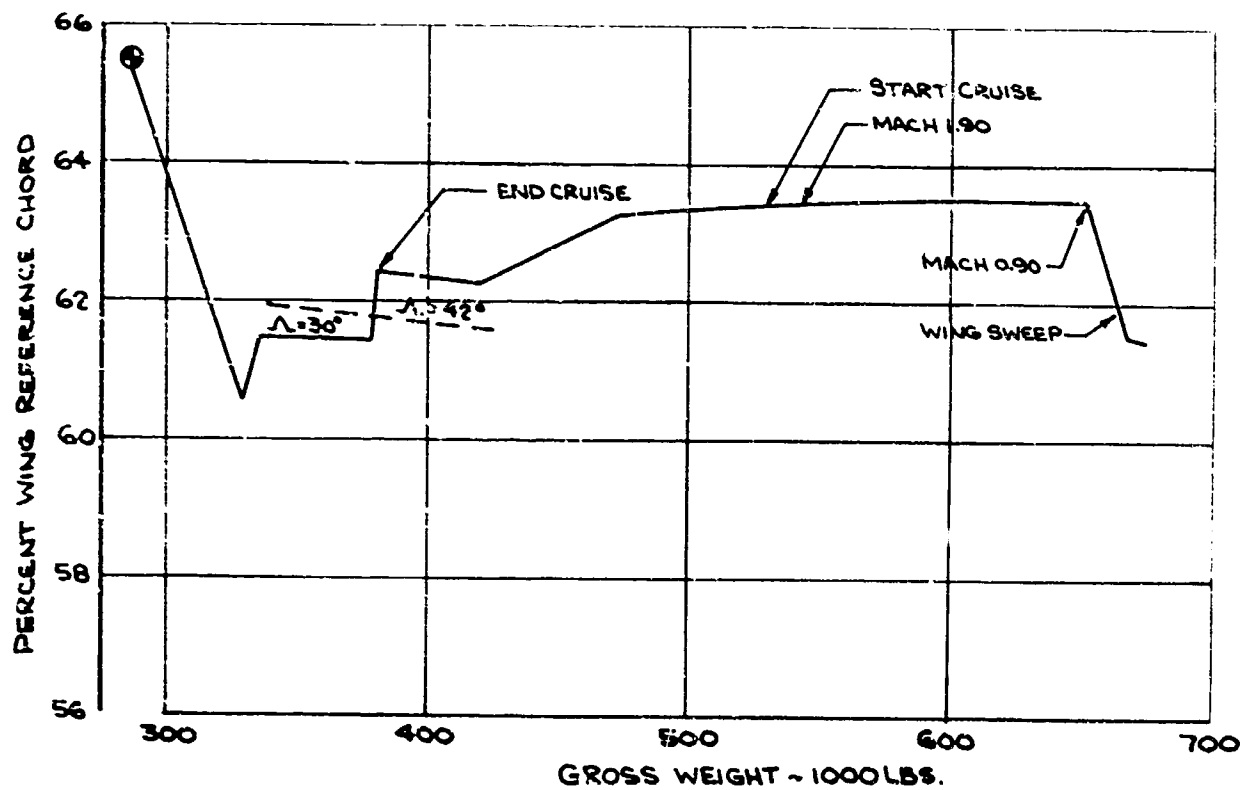


Figure 3-32. B-2707 Center of Gravity Location as a Function of Weight

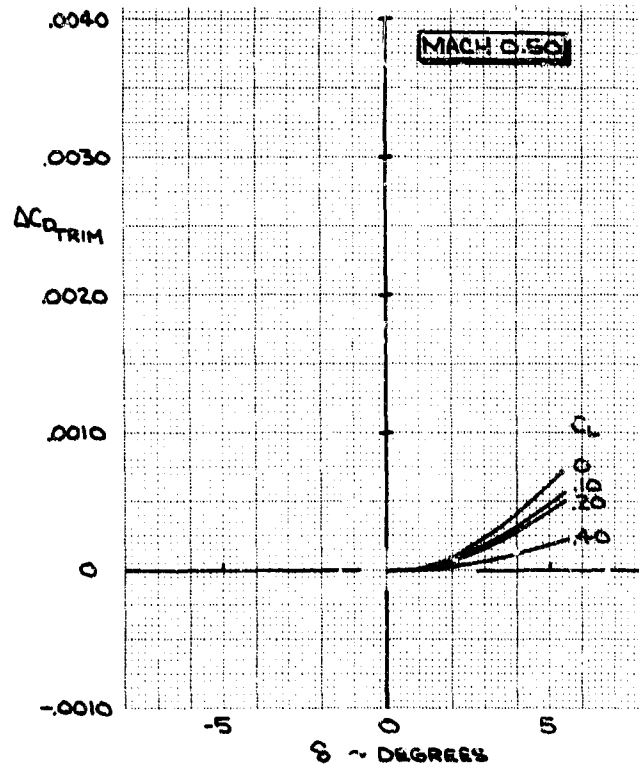
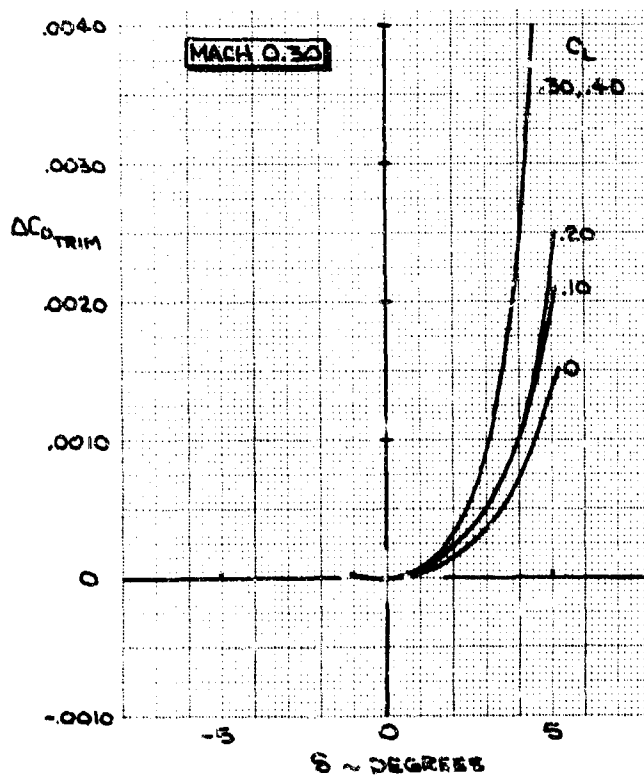
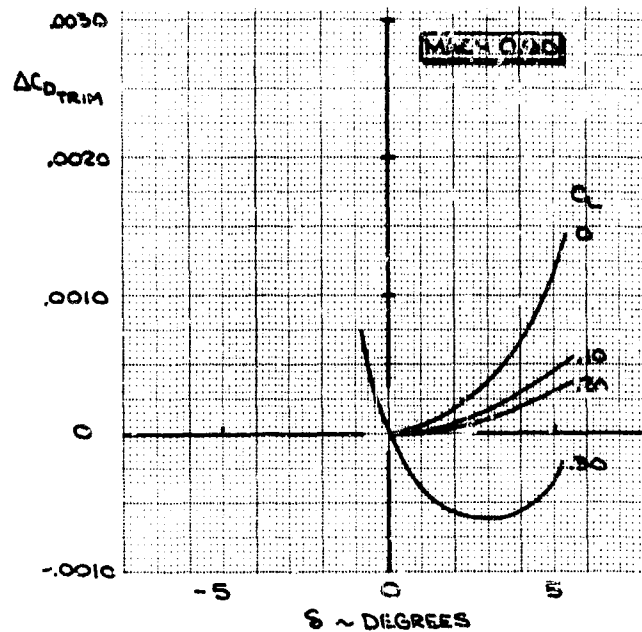
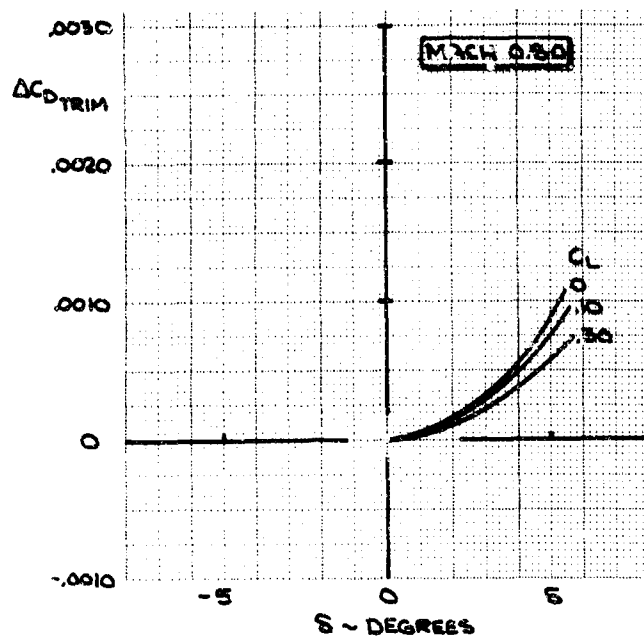


Figure 3-33. Trim Drag at 42 Degrees Leading Edge Sweep

V2-B2707-3

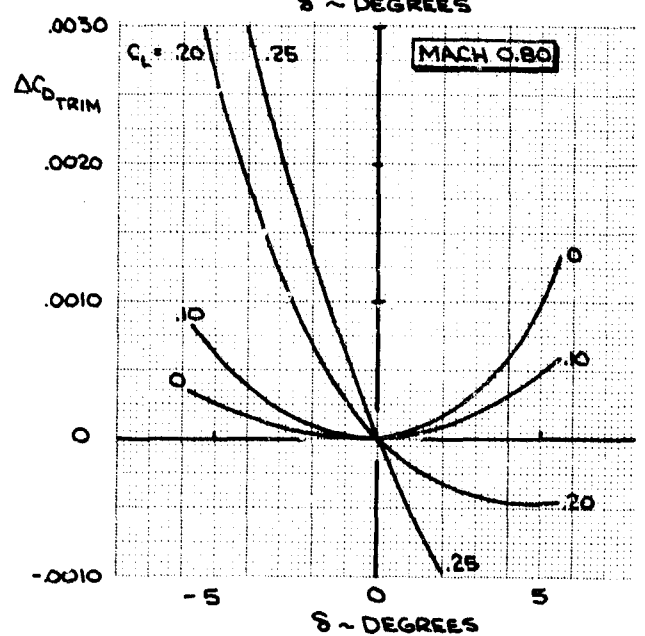
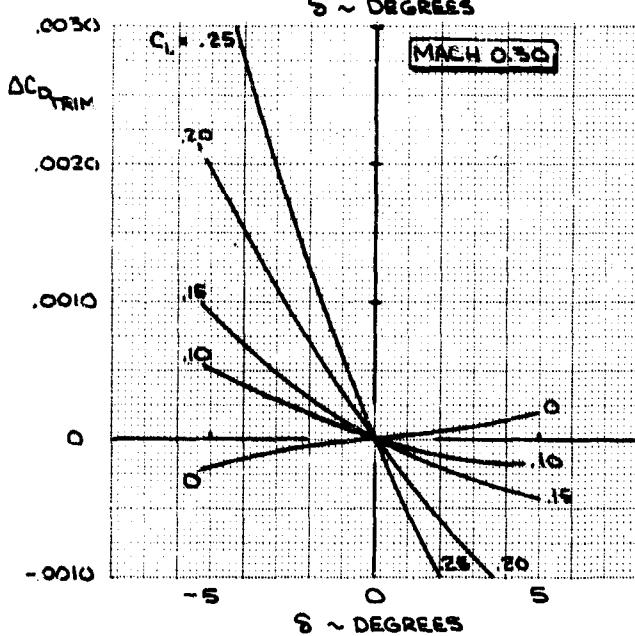
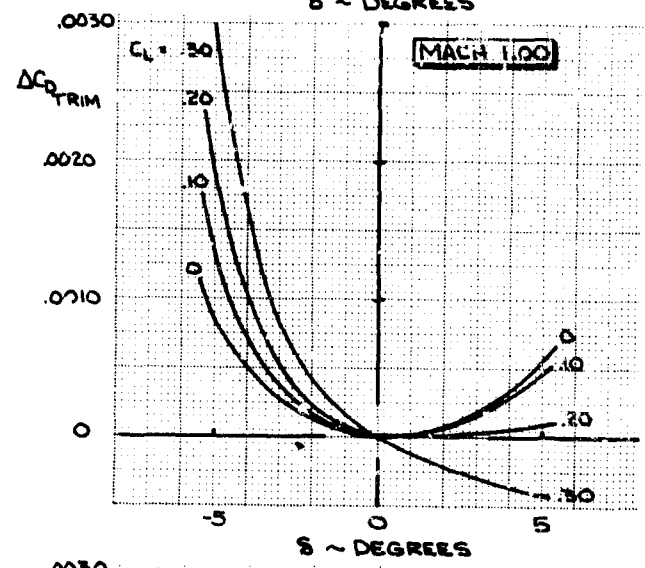
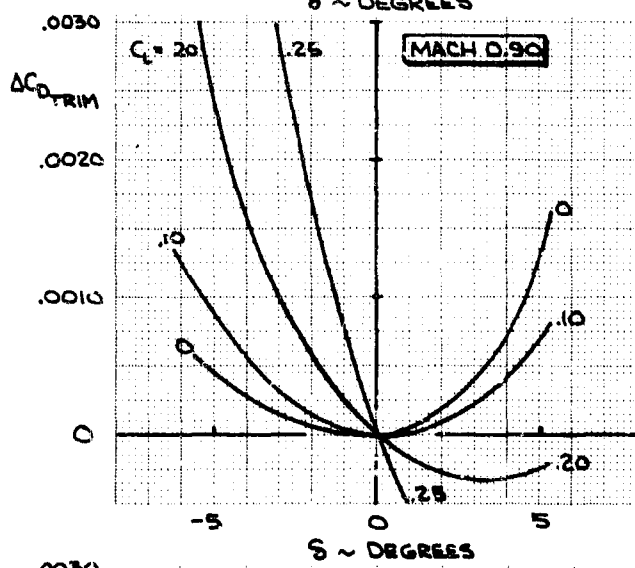
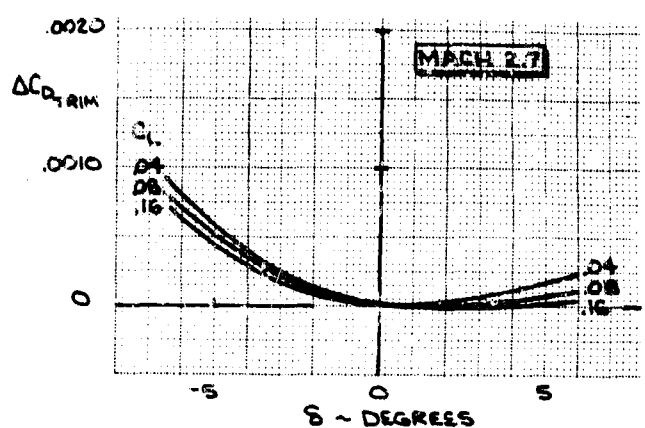
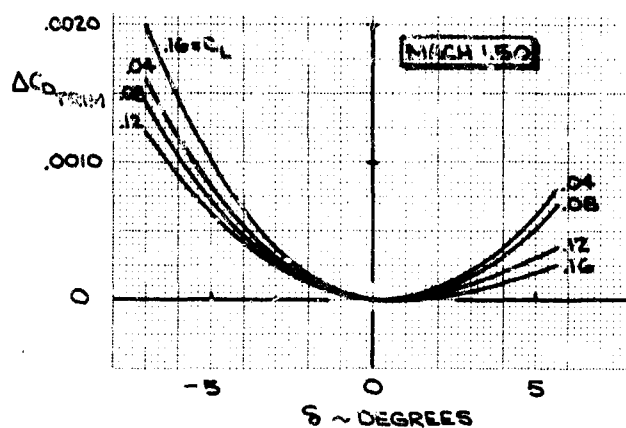
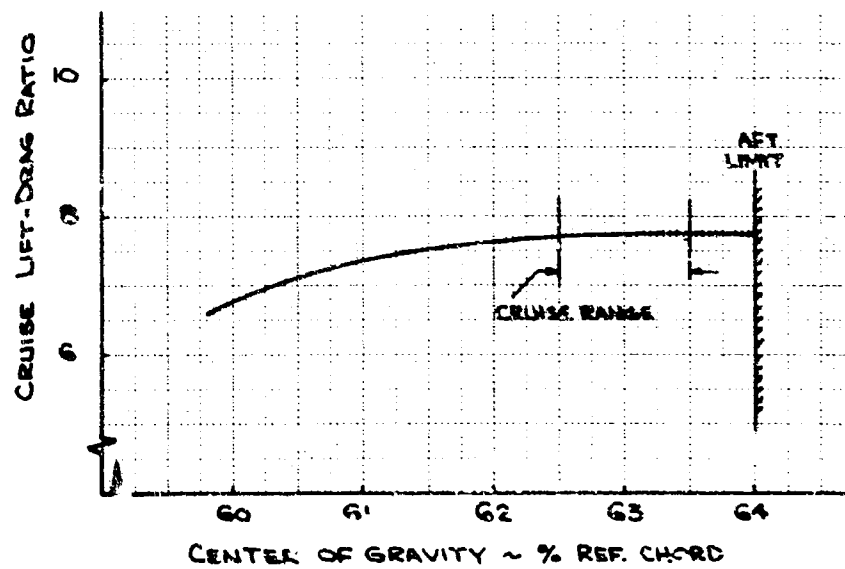
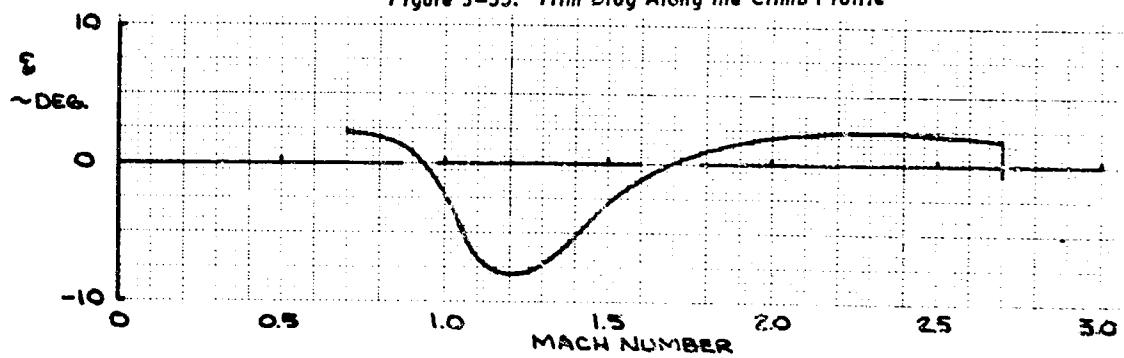
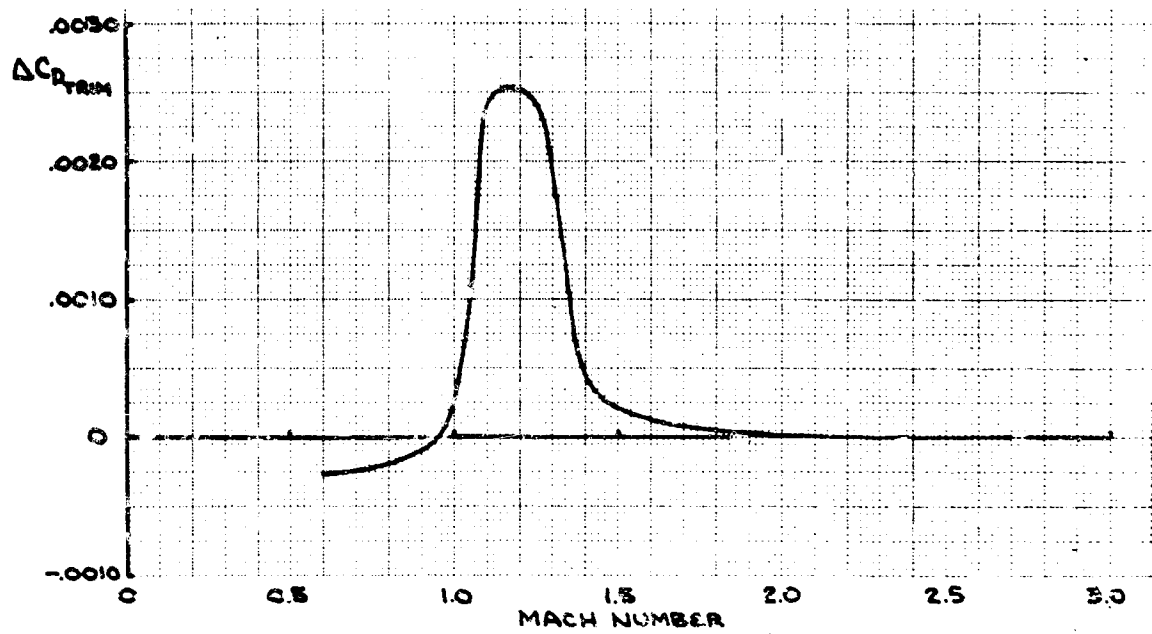


Figure 3-34 Trim Drag at 72 Degrees Leading Edge Sweep



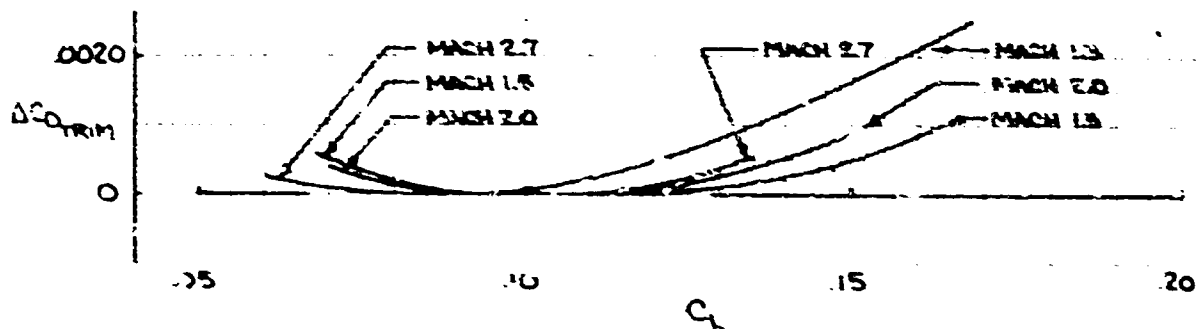


Figure 3-38. (a) Effect of Lift Coefficient on Trim Drag - Mach 1.3 to 2.7

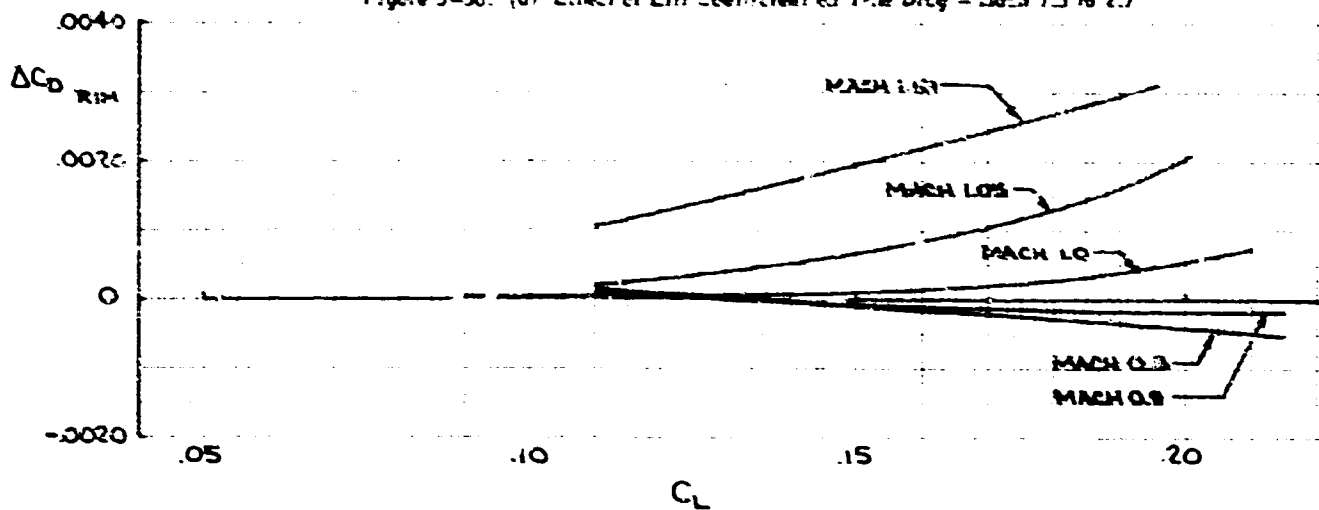


Figure 3-38. (b) Effect of Lift Coefficient on Trim Drag - Mach .8 to 1.1

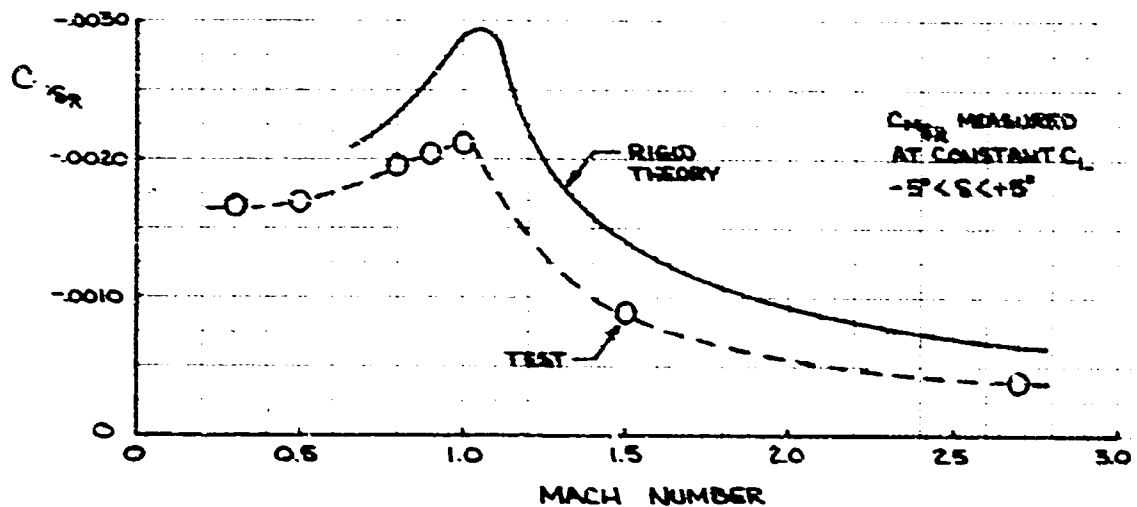


Figure 3-39. Comparison of Measured Elevator Effectiveness with Theory

ratio, at Mach 2.7 is shown in Fig. 3-37 and the effect of lift coefficient on trim drag is shown in Fig. 3-38 at various Mach numbers.

In Fig. 3-39 the theoretically calculated values of $C_{M\delta R}$ are compared with the experimental values shown in Fig. 3-17. The poor agreement is surprising, particularly in the light of similar comparisons obtained during other Boeing and NASA tests. The reason for this is not fully understood now, and the measured value of $C_{M\delta R}$ have been used for trim drag calculations although this has resulted in trim drag penalties. Some measurements of the flexibility of the wind tunnel model have been made; they have indicated that the experimental values of $C_{M\delta R}$ might be

small because of model flexibility. If this is verified, smaller deflections would be required to trim the airplane and further refinement of the wing camber and twist would be desirable.

3.1.3.4 Full-Scale Lift Drag Characteristics
The drag corrections itemized in the preceding paragraphs have been applied to the model data to account for differences between model and airplane conditions. Trimmed data for the flight profile of Fig. 3-6 are shown in Figs. 3-40 through 3-45. One set of data, applicable to both engines, is shown.

3.1.3.5 Comparisons of Installed Propulsion Pod Drag

A comparison has been made, at Mach 2.7, of the drag of GE and P&WA nacelle installations on the SA 966 wind tunnel model. Photographs are shown in Figs. 3-46 through 3-49. The design of the nacelles was based on information received from the engine manufacturers before July 1. Prior to that a careful survey had been carried

out on the flow field below the wing of the model, to determine local flow directions, local Mach number, local boundary layer thickness, and the variation of these with angle of attack. The following criteria were applied to the design:

- a. Inlet aligned into the local flow.
- b. Boundary layer diverter deep enough to ensure that no boundary layer will enter the inlets and wide enough to enclose volume requirements.
- c. Nozzle size determined by taking into account: internal efficiency, interference drag, skin friction drag, transonic boattail drag, and weight.
- d. Nozzle exit flow direction determined by consideration of thrust, lift, sonic boom, and landing gear length considerations.
- e. The nacelle had to enclose all volume requirements and the installation had to allow for thrust reverser operations.

Within these constraints the installations were designed for best drag. The design was based on analytical studies and augmented by development work in the wind tunnel. The wings of the wind tunnel models were so designed that the part affected by the interference from the nacelles was detachable; different wing designs were tested in the presence of GE and P&WA nacelles, respectively. Drag polars obtained for GE and P&WA installations are shown in Fig. 3-50. Because skin friction drag is accounted for separately, the drag data have been corrected by subtracting the skin friction drag. It is apparent that the drag difference between the engines, if any, is within the accuracy of the measurements.

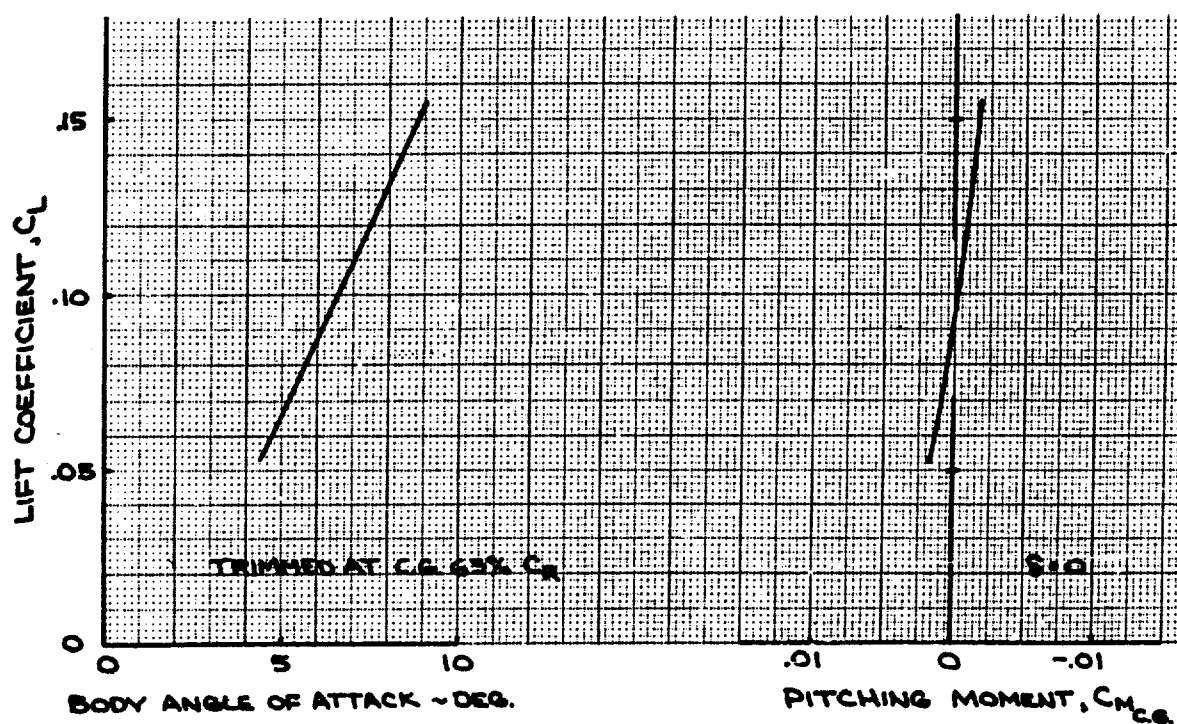
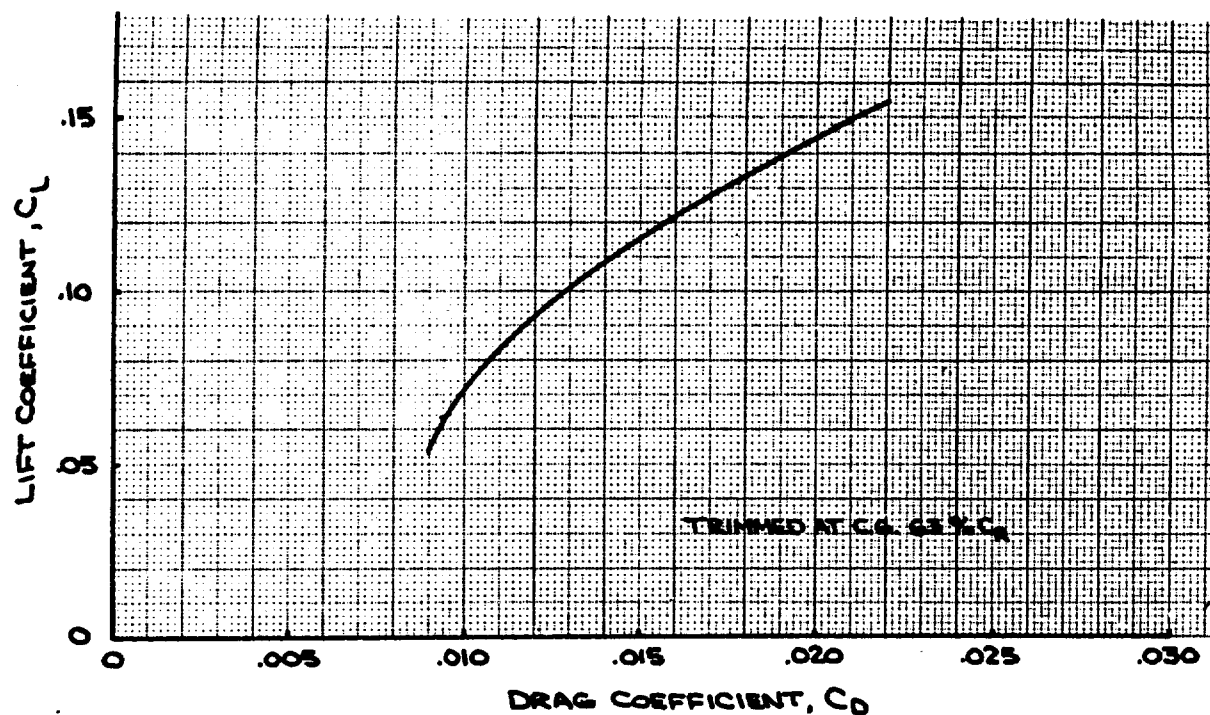


Figure 3-40. Mach 2.7 B-2707 Aerodynamic Characteristics Leading Edge Sweep 72 Degrees - Current Data

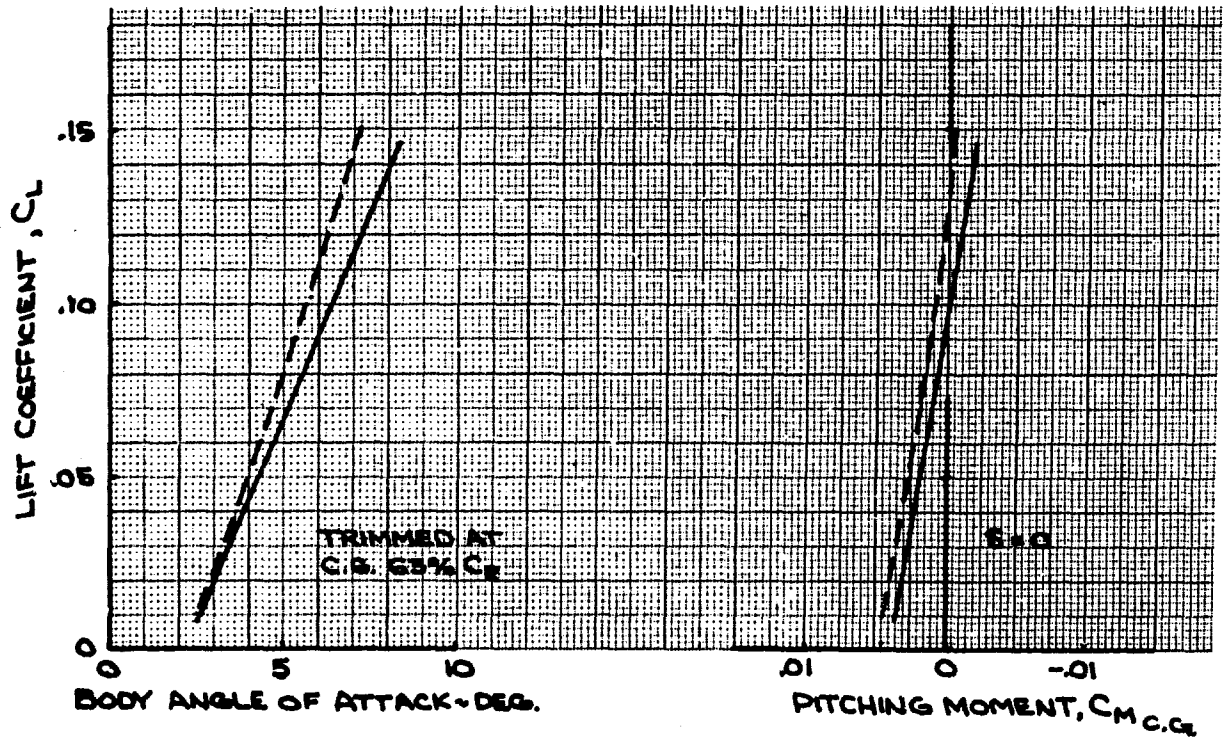
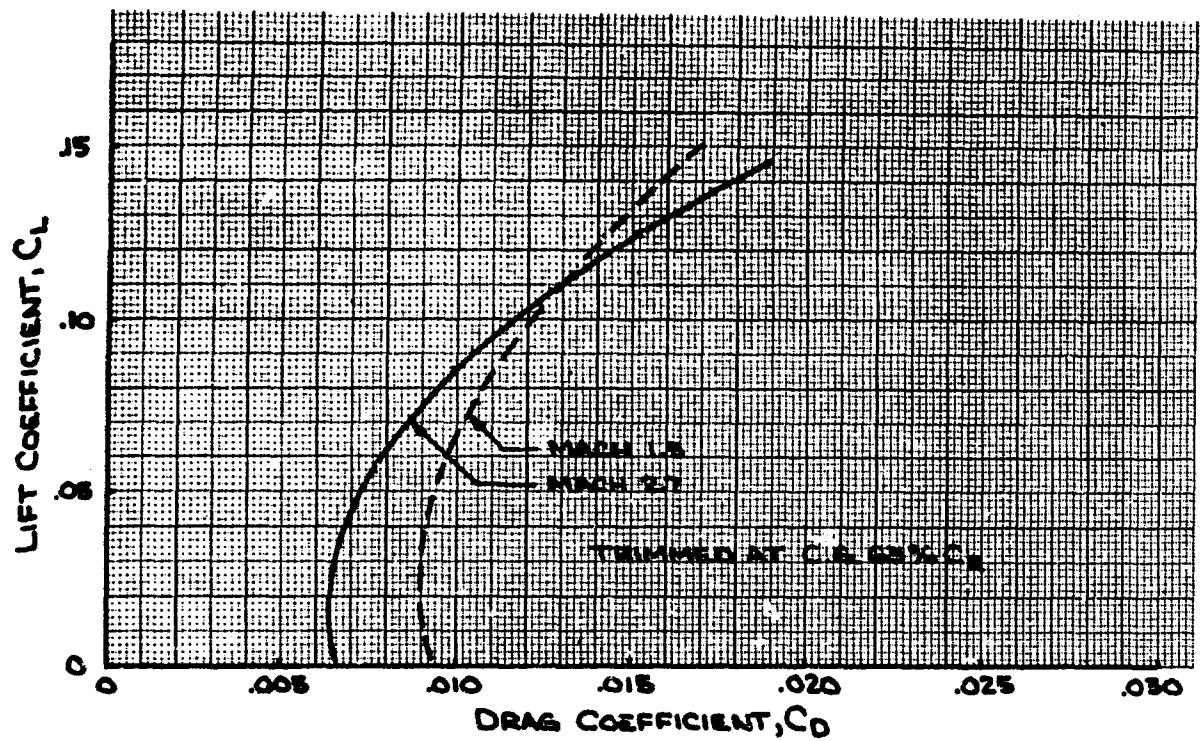


Figure 3-41. Aerodynamic Development Model Aerodynamic Characteristics ; Leading Edge Sweep- 72 Degrees

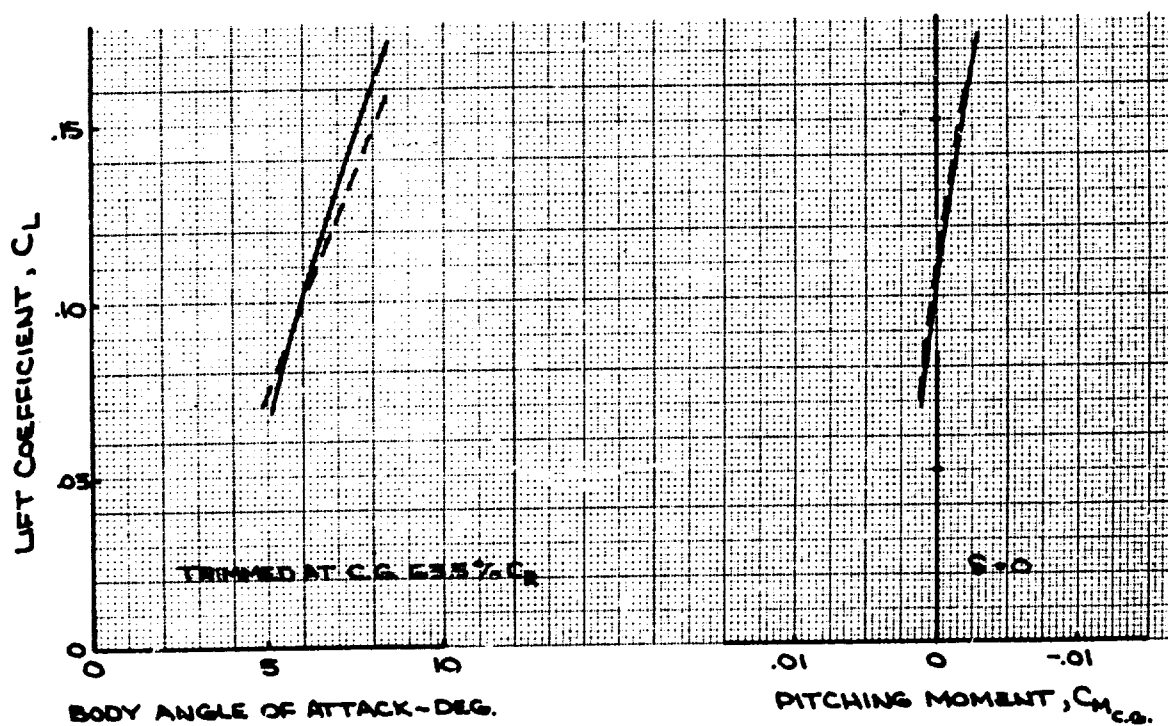
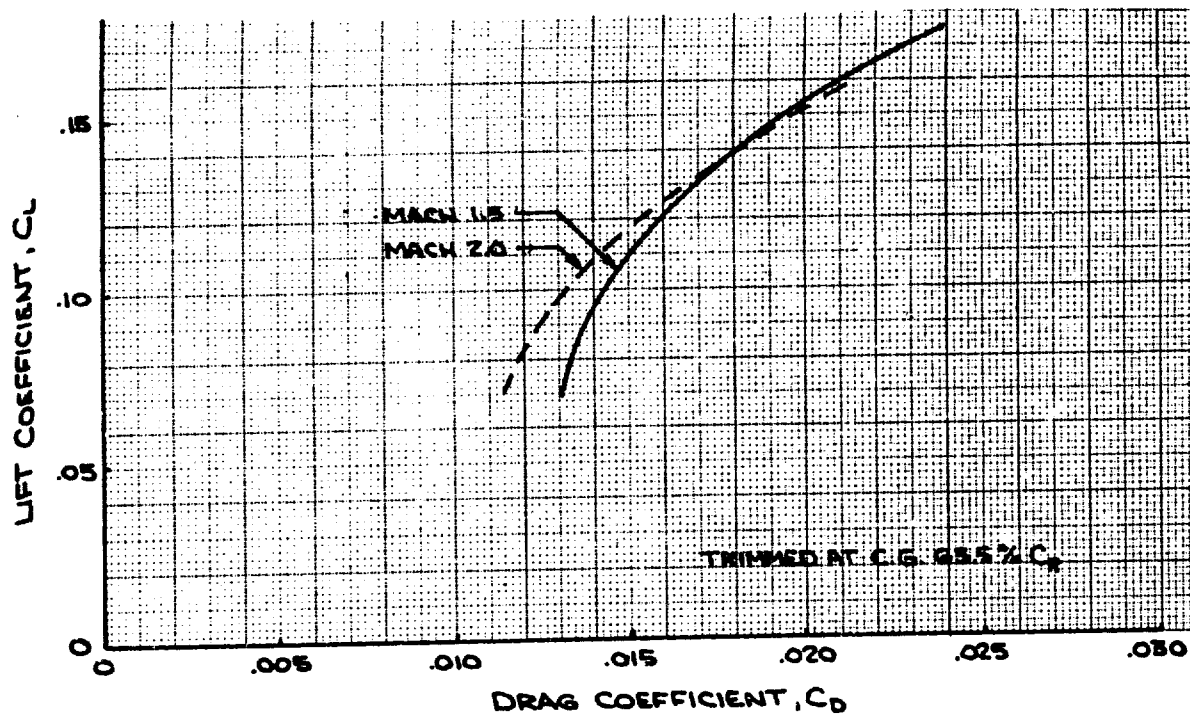


Figure 3-42. B-2707 Configuration, Leading Edge Sweep 72 Degrees ,
Mach Numbers 2.0 and 1.5 Current Data

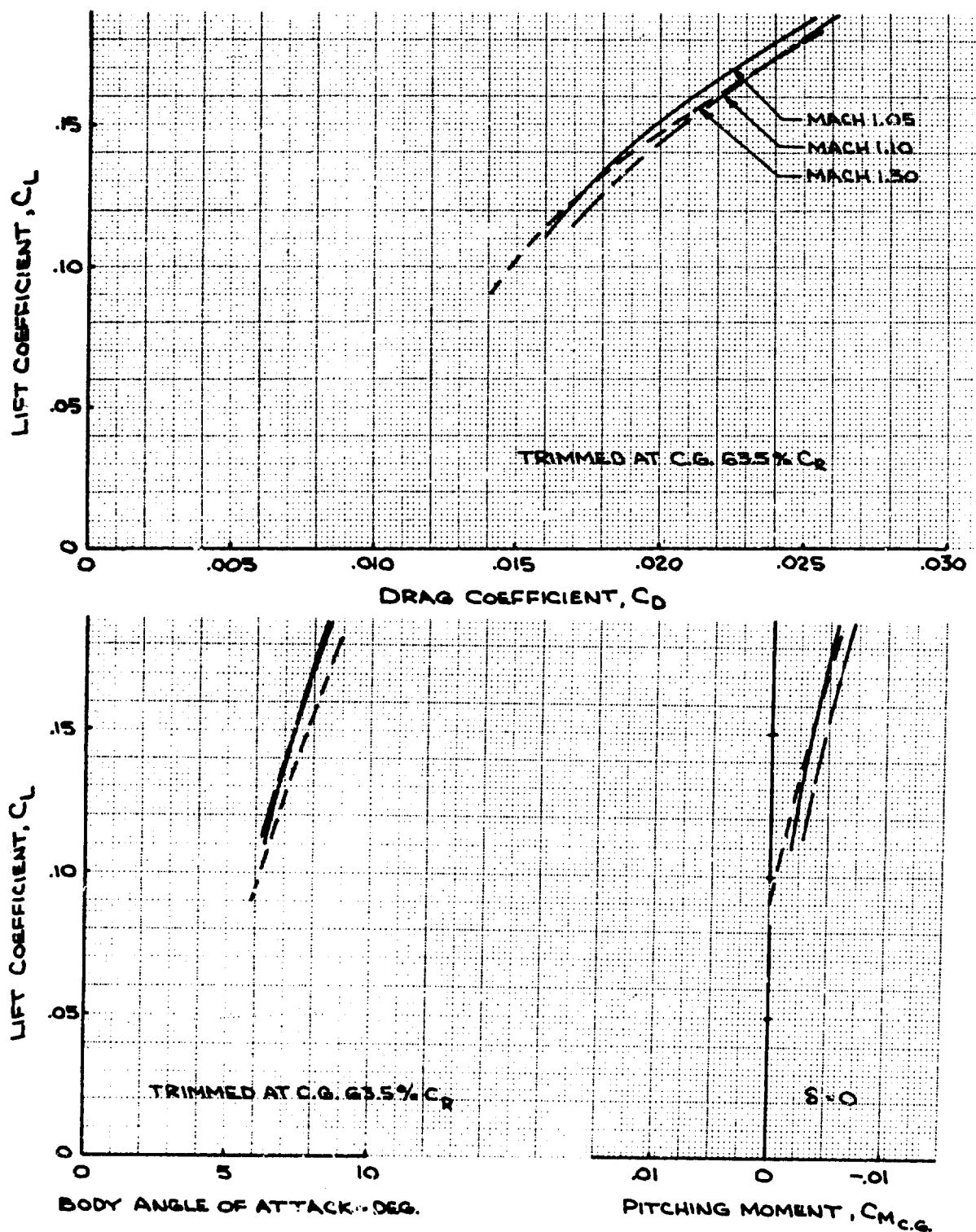


Figure 3-43. B-2707 Configuration, Leading Edge Sweep 72 Degrees, Mach Numbers 1.3, 1.1, and 1.05 Current Data

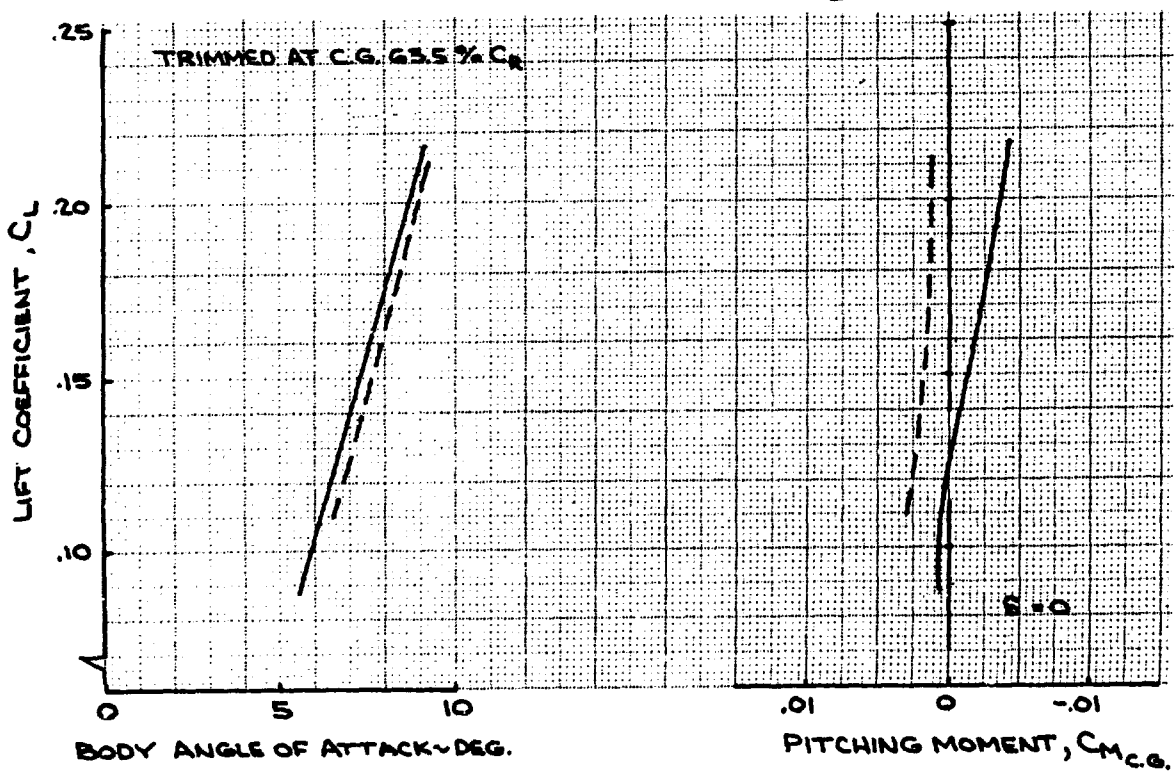
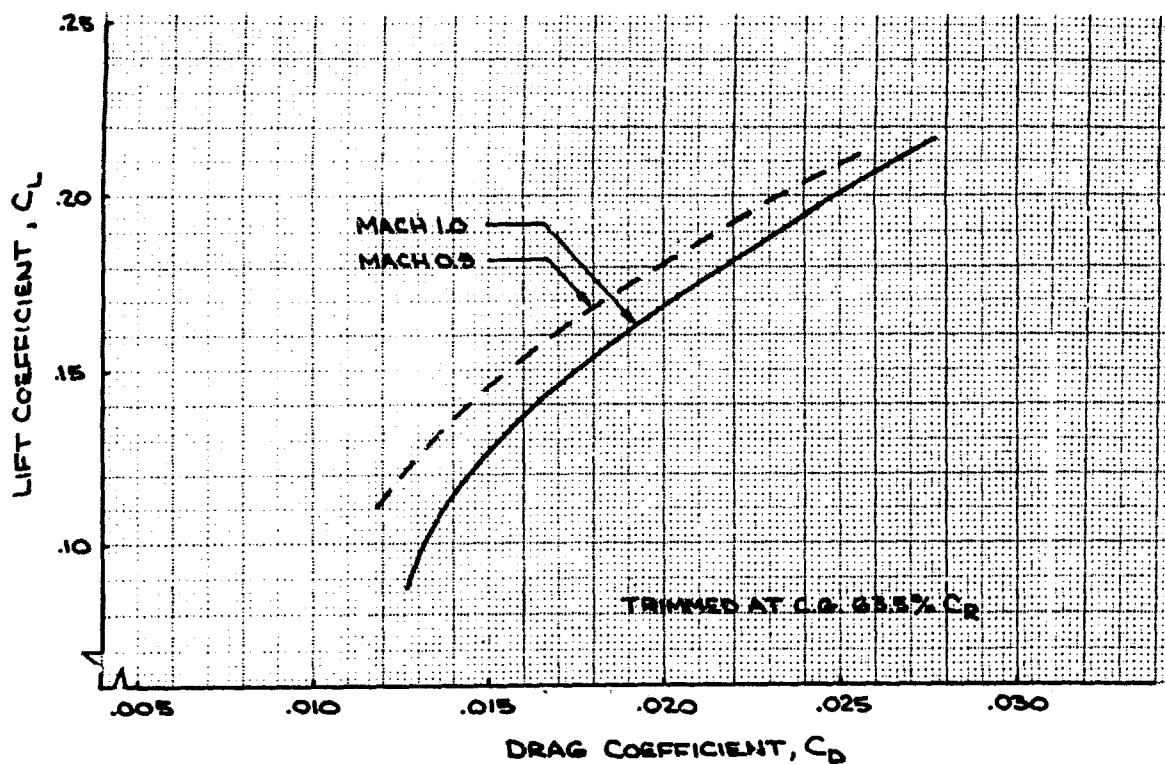


Figure 3-44. B-2707 Configuration, Leading Edge Sweep 72 Degrees, Mach Numbers 1.0, .9 Current Data

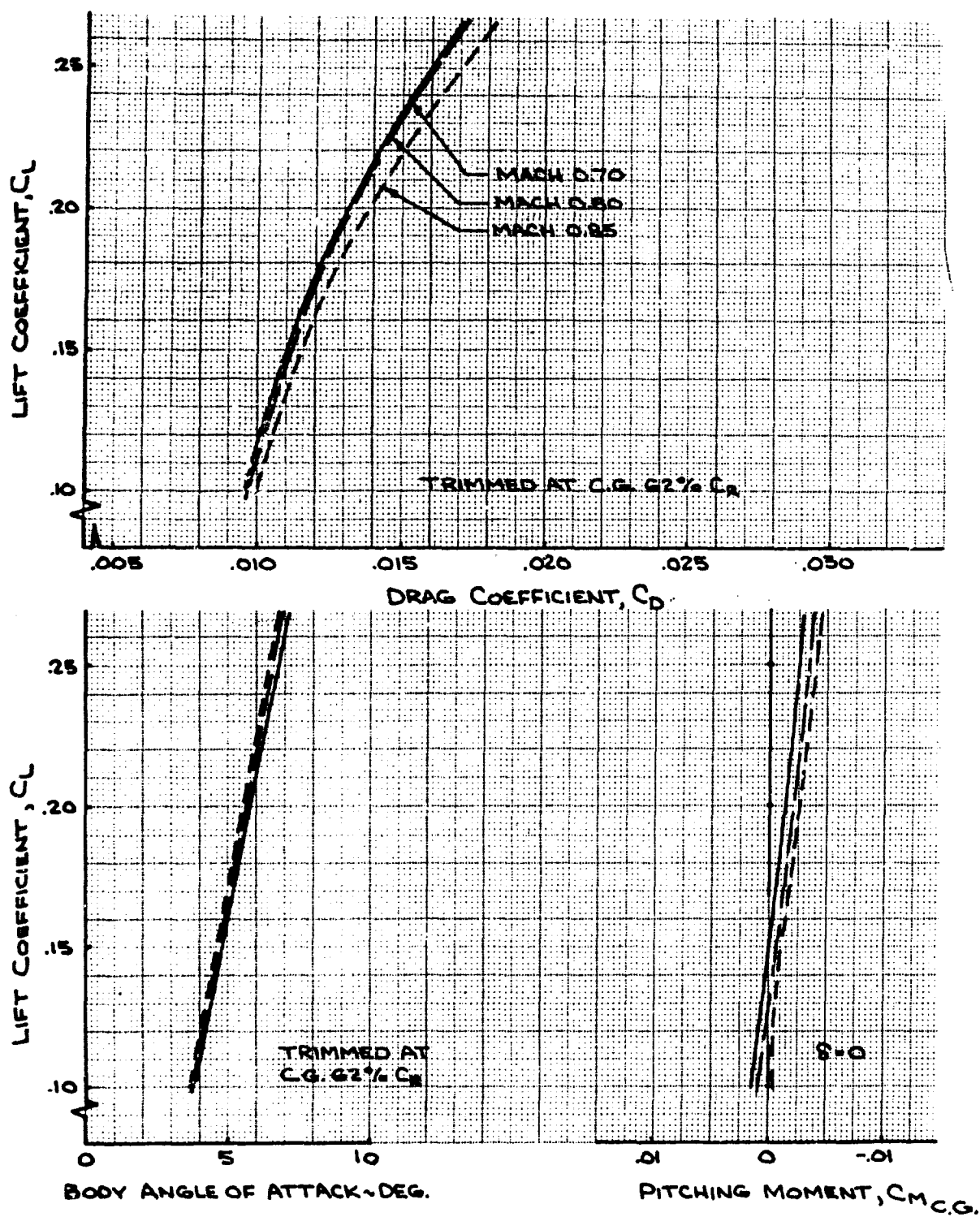


Figure 3-45. B-2707 Configuration, Leading Edge Sweep 42 Degrees, Mach Numbers .7, .8, and .85, Current Data



Figure 3-46. Supersonic Wind Tunnel Model
GE Outboard Pod

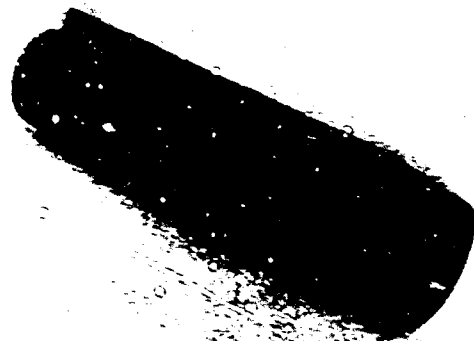


Figure 3-47. Supersonic Wind Tunnel Model
P & WA Inboard Pod



Figure 3-48. Thrust Reverser Simulation on
Supersonic Model

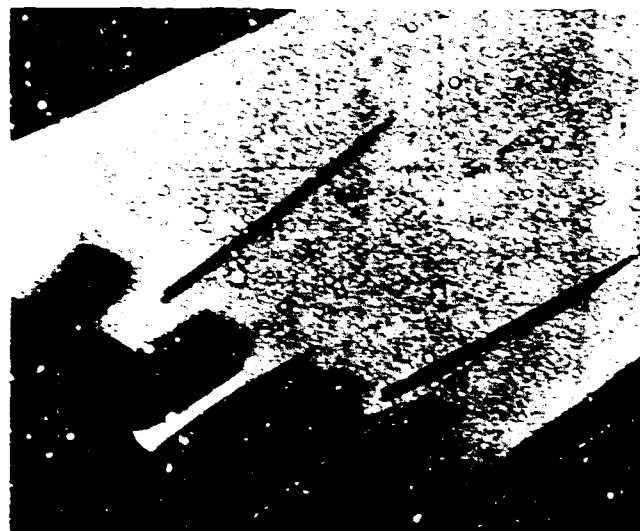


Figure 3-49. Nacelle Installation on SA 966
Supersonic Model

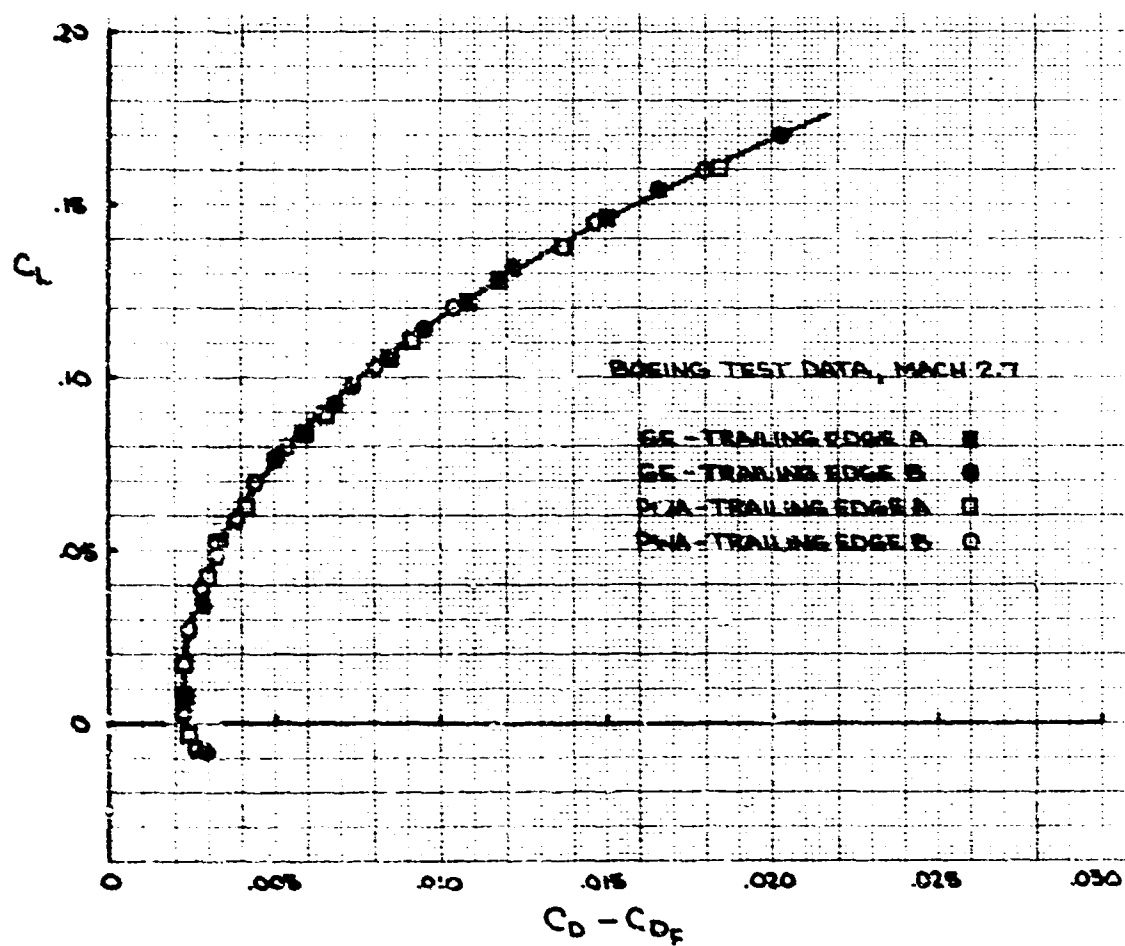


Figure 3-50. Wind Tunnel Comparison of Installed Engine Drag

3.2 TAKEOFF AND LANDING CONFIGURATIONS

Lift and drag of the model B-2707 applicable to takeoff and landing operations are substantiated in this paragraph. The close-coupled horizontal tail and longitudinal trim system in the low speed configuration at 30 degrees wing sweep call for a new approach to optimization. Analysis of preliminary test data leads to the conclusion that considerable improvements in trimmed lift and drag can be effected by design refinements, especially at the forward cg; these are being intensively studied. An estimate of the performance capabilities of the airplane with refinements has been made and has been used in calculating the takeoff and landing performance of the B-2707 airplane (shown in Sec. 2). Figure 3-51 is a summary plot comparing the aerodynamic characteristics

with the current status. The estimated flight characteristics are based on preliminary wind tunnel model tests, with scale corrections and adjustments for geometry differences based on proven analytical techniques.

3.2.1 Airplane Geometry

3.2.1.1 Wing Geometry

Takeoff and landing operations are programmed using a wing leading edge sweepback angle of 30 degrees. The wing pivot location is chosen to give a favorable wing twist distribution at the 30-degree sweep angle.

Figure 3-52 shows a plan view of the airplane at the takeoff and landing wing sweepback angle of

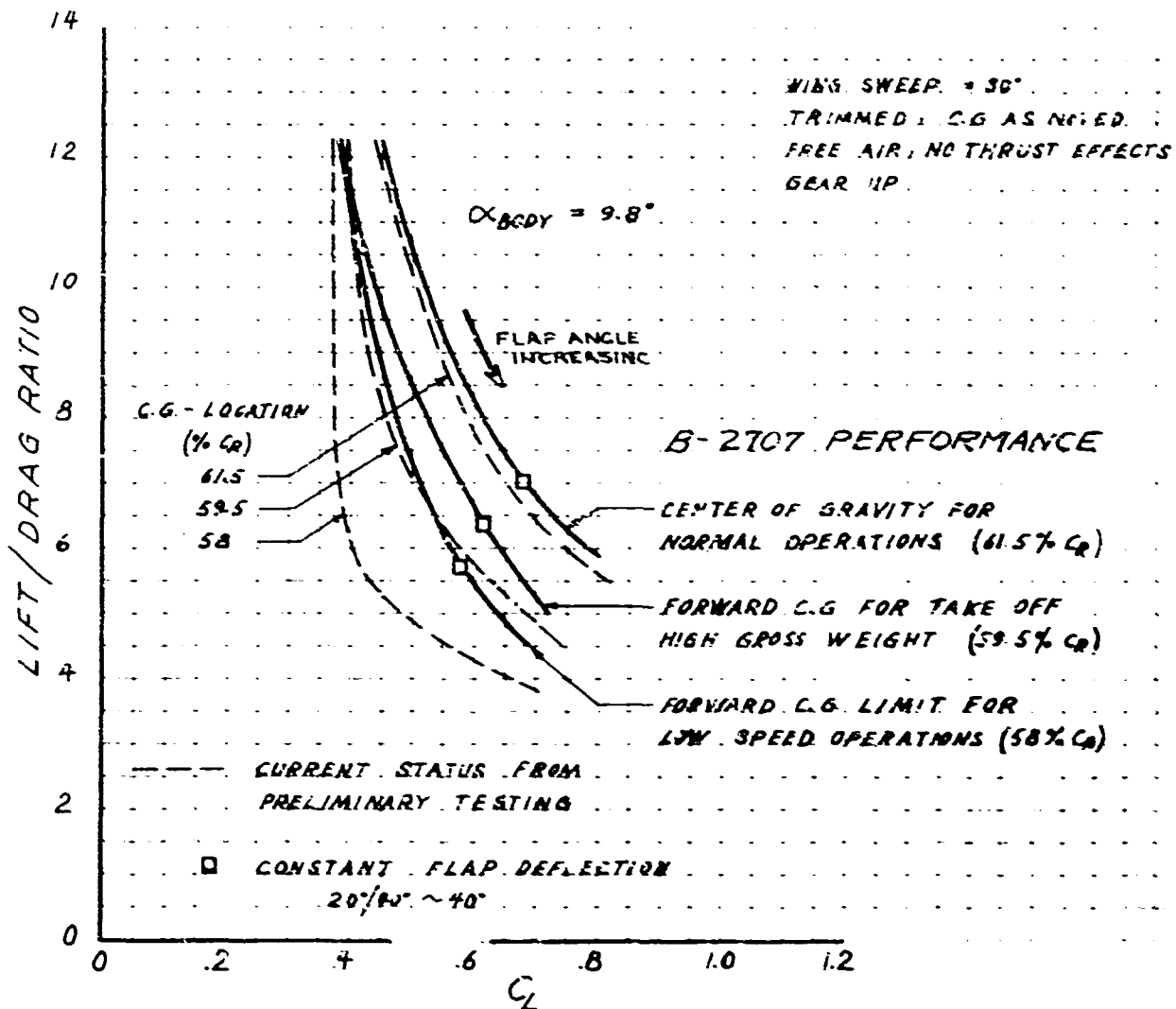


Figure 3-51. Performance Summary

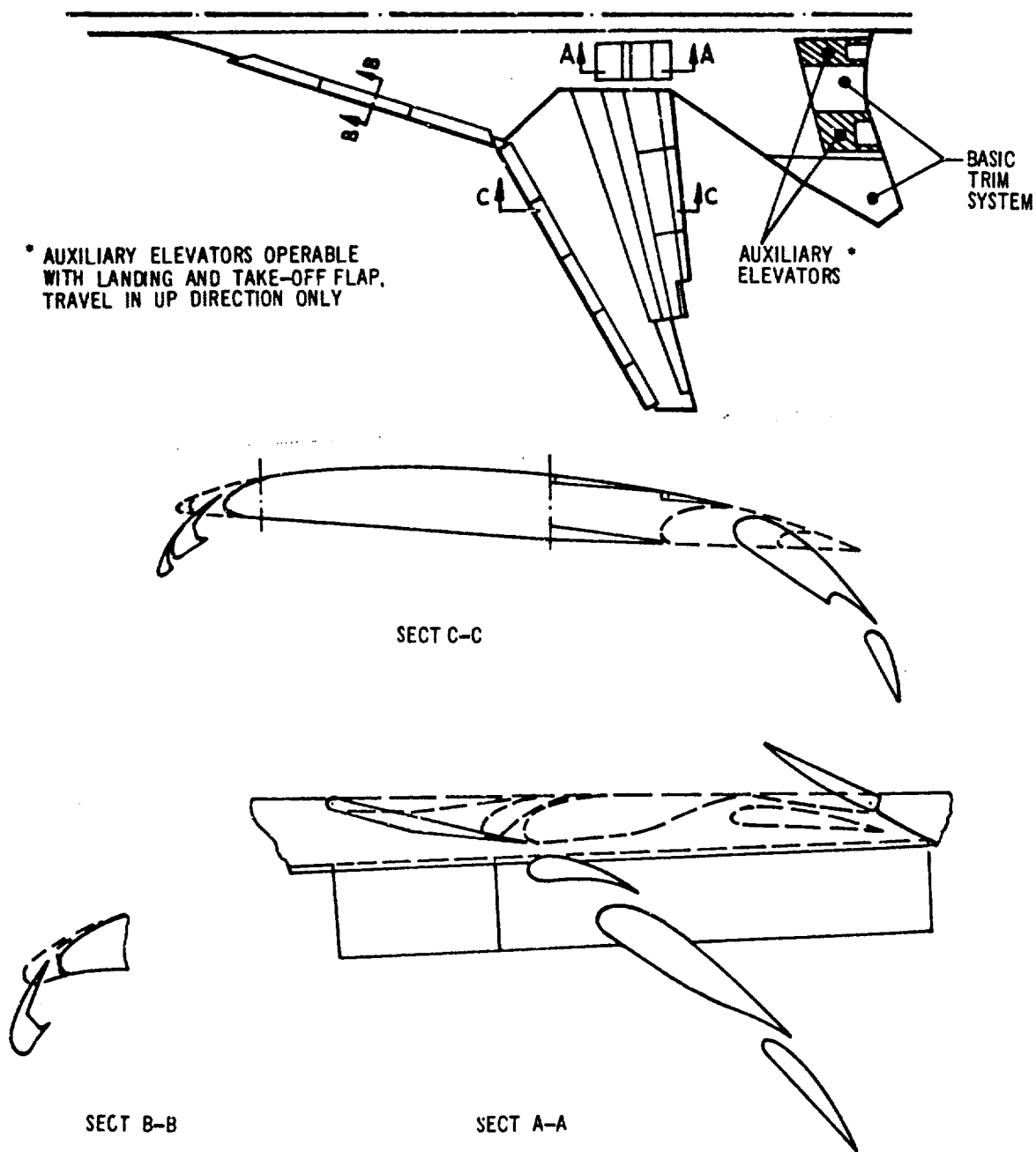


Figure 3-52. Wing Flap and Slat Geometry

30 degrees with section views depicting the slats and flaps.

The spanwise wing twist distribution at a typical 1-g takeoff climb condition is shown in Fig. 3-53. This is similar to that of the model 733-390, giving the same zero-lift angle, flaps up.

3.2.1.2 High Lift Devices

Development work on flaps and slats during Phases I and II has produced the very effective high lift system used on the B-2707 airplane. Trailing edge flaps on the outboard wing portion are double slotted for low drag. This flap was perfected in a NASA test program on the 1/5 scale model. Wing slats have a drooped nose to increase their efficiency. Inboard flaps are triple slotted like the powerful 727 airplane flaps. The leading edge slat on the fixed portion of the wing controls vortex development, increasing longitudinal stability, maximum lift coefficient, and lift to drag ratio.

Table 3-W lists the flap and slat deflections appropriate to takeoff and landing operations.

3.2.2 Airplane Characteristics

3.2.2.1 Performance Inputs

Lift and drag characteristics which have been used to calculate performance are estimated values which are well within the potential of the B-2707 airplane concept. These, or better levels of aerodynamic efficiency will be obtained through refinements to the configuration geometry in Phase III of the SST program. Trimmed lift and drag characteristics are affected by cg location, which can vary with loading according to the mission to be flown. It is convenient to quote representative takeoff and landing performance values, neglecting the many intricate loading variations which can have small effects on the numbers quoted. All generalized performance shown in Sec. 2.0 is based on the lift and drag curves of Figs. 3-54 and 3-55, applicable to a forward cg location of 59.5 percent C_{R} . All normal takeoffs and landings will be accomplished at cg locations

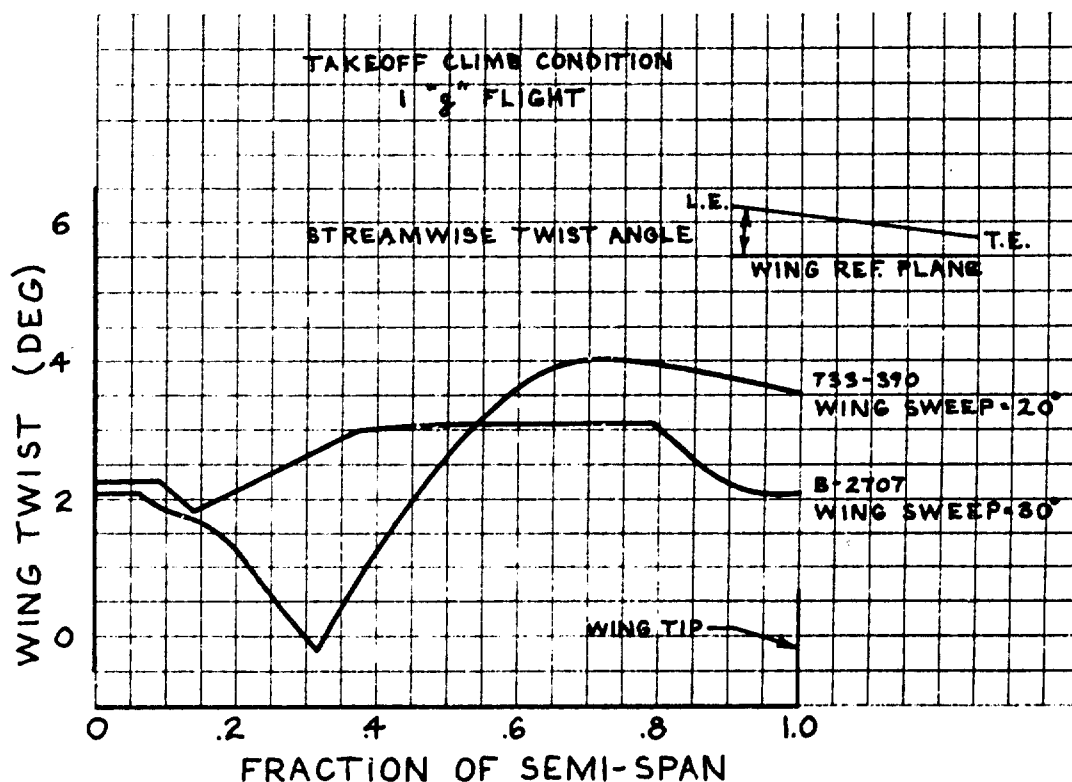
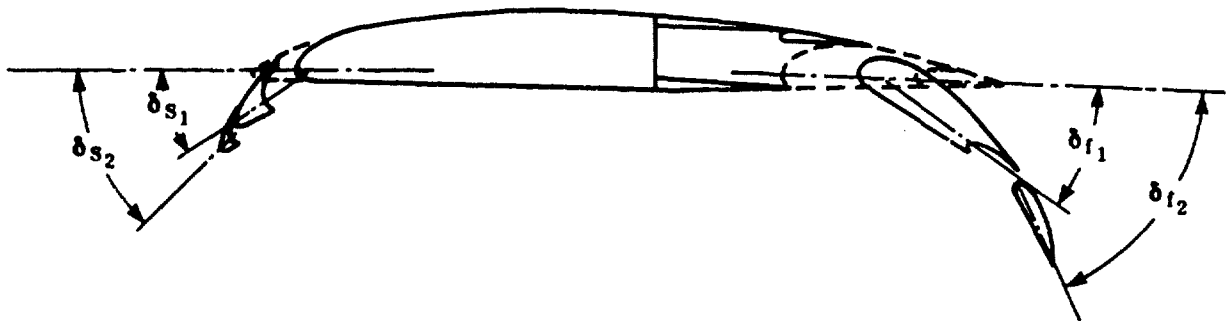


Figure 3-53. Wing Twist at 30° Sweep

Table 3-W. Flap and Slat Angles for Low Speed Operations

FLIGHT MODE	TRAILING EDGE FLAPS		LEADING EDGE SLATS	
	INBOARD FLAP	OUTER WING FLAPS	FIXED WING	OUTER WING
TAKEOFF & LANDING	21°/40°/60°	20°/40°	35°	20°/37.5°
ALTERNATE TAKEOFF	Up	10°/20°	28.5°	11°/19.5°
CLIMB	UP	5°/5°	25°	6°/10°
ALTERNATE LANDING	21°/40°/60°	30°/50°	35°	30°/55°
LANDING, WING SWEEP 72°	Up	Up	25°	Nested Up

NOTE: Flap and slat segment deflections are measured from the up datum, as shown below.



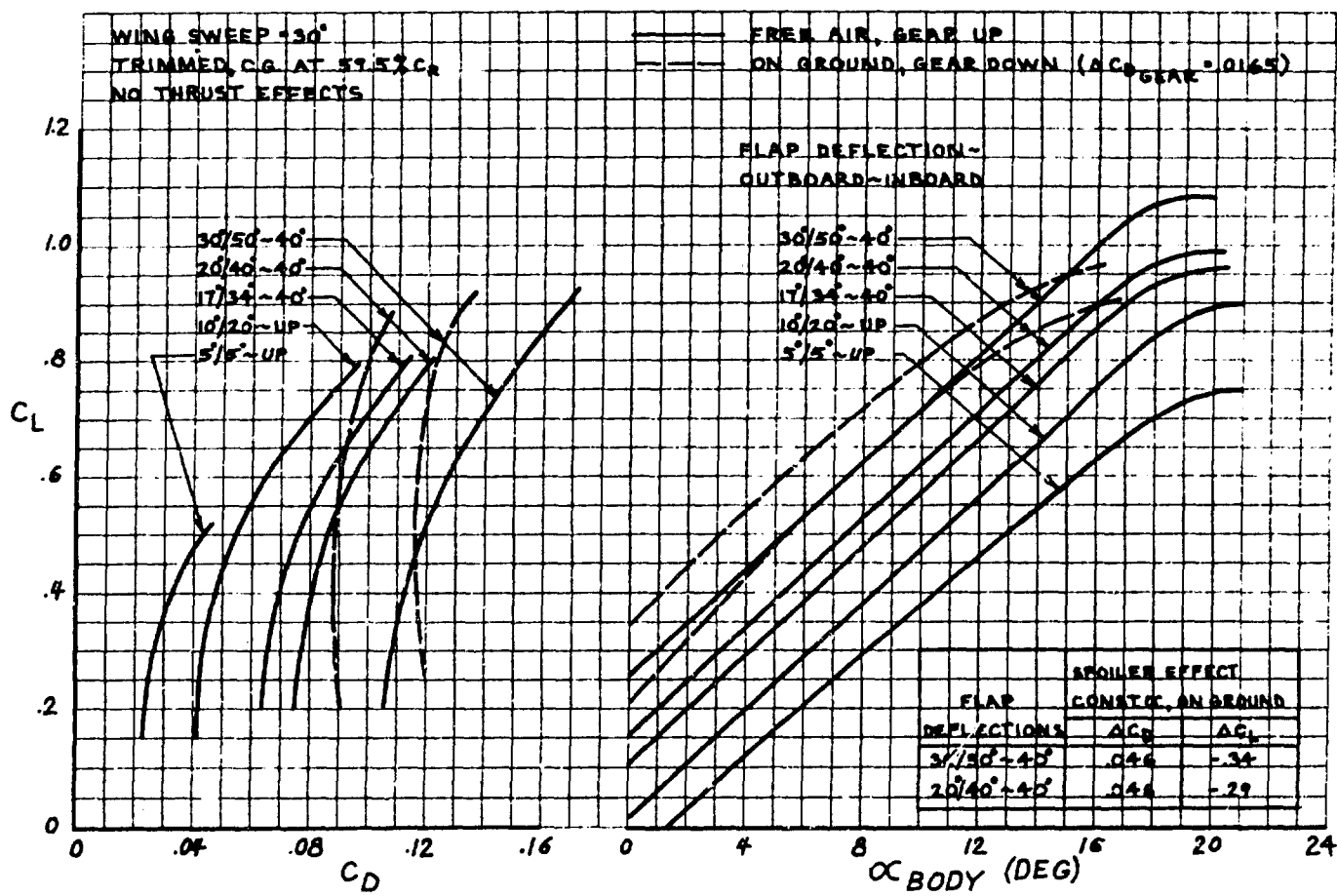


Figure 3-54. B2707 Lift and Drag

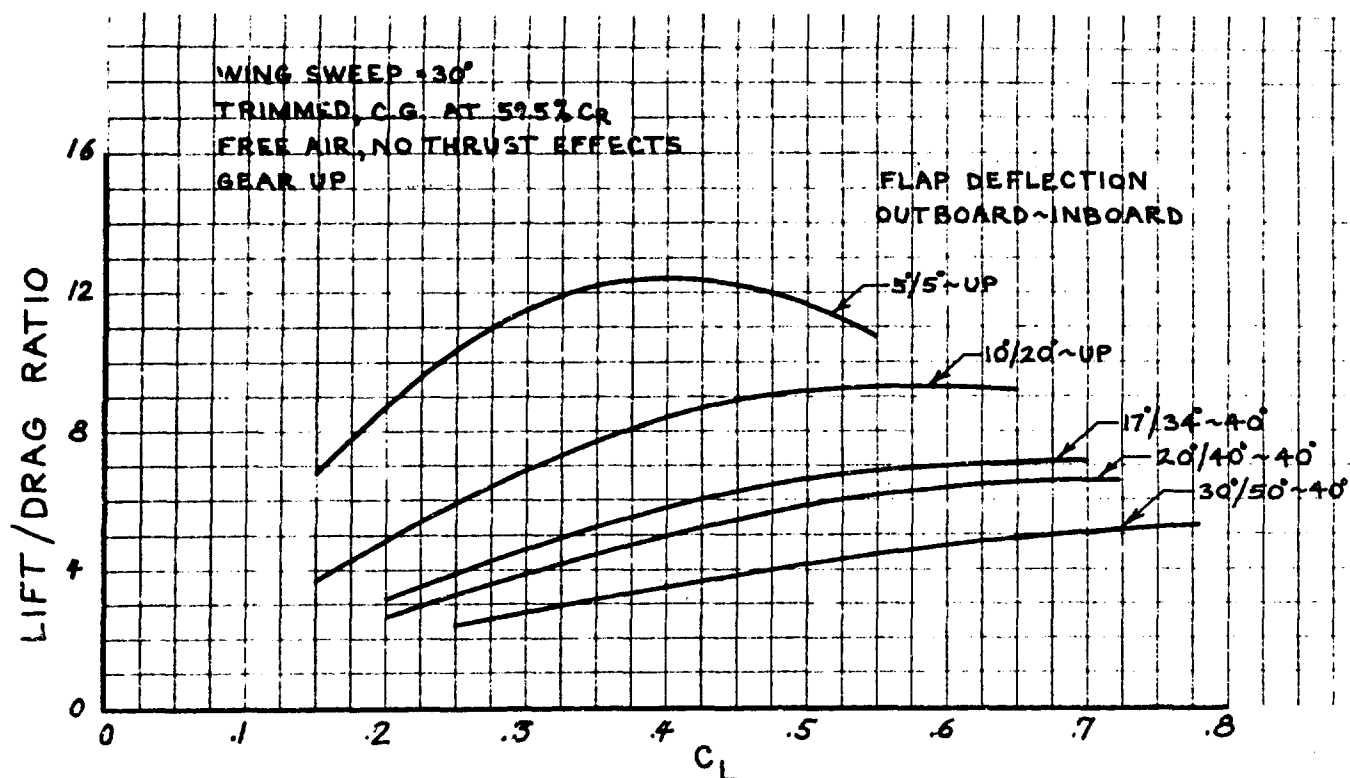


Figure 3-55. B2707 Lift to Drag Ratio Curves

of about 61.5 percent root chord, so the trades with varying cg location are illustrated for typical takeoff climb and landing approach angles of attack in Fig. 3-56.

Small friction drag differences between the GE and P&WA engine installations are within the accuracy to which the drag with flaps down can be determined, and have been ignored.

Thrust effects on lift and drag, which are not included in the graphical data are accounted for by solving for the lift coefficient in terms of angle of attack, normal load factor, and thrust to weight ratio, using equations shown in Fig. 3-57.

Table 3-X lists representative lift, drag, and angle of attack values used for takeoff and landing; these have been selected to provide adequate margins for controllability, maneuvering, gust encounters, inadvertent speed changes and abuse.

Stalling characteristics of the B-2707 in the takeoff and landing configurations will be similar to those of many jet airplanes now in service. The airplane characteristics will be entirely conventional. It will be possible to establish both the decelerating stall speed ($\frac{dv}{dt} = -1$ kn/sec) used as reference in the current FAR regulations, and the 1-g load factor minimum speed under essentially steady state conditions. This latter will occur at the angle of attack for $C_{L_{Max}}$, about 20 degrees, and will be about 5 percent faster than the stall speed, as it is on present airplanes.

Because of the conventional angle of attack at which the minimum and stall speeds will be reached, the minimum demonstrated speed for operations in the sense of Ref. 23 will be the stall speed. In the discussions which follow, operating speeds are related to either the stall speed or the 1-g minimum speed as appropriate.

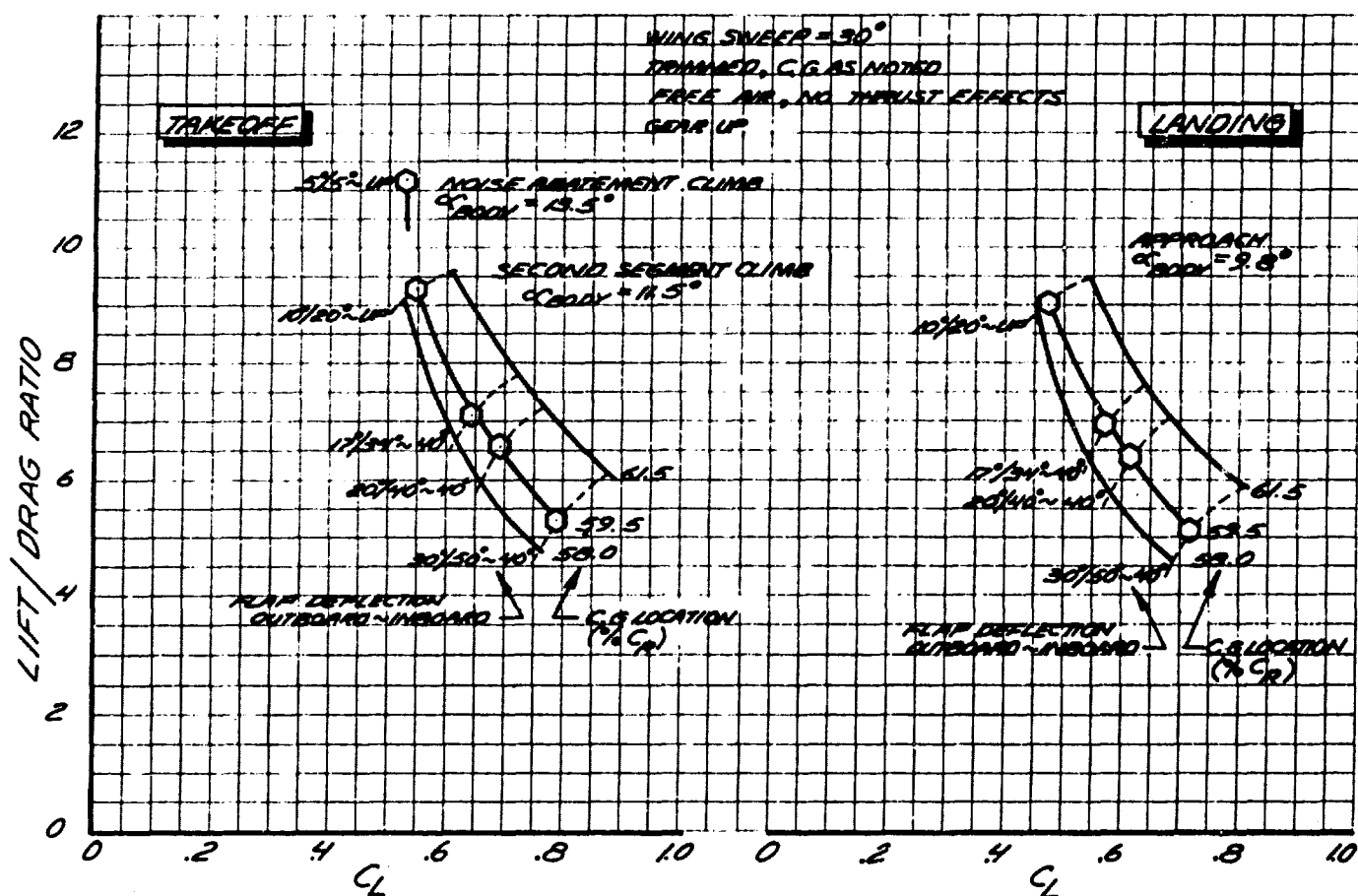
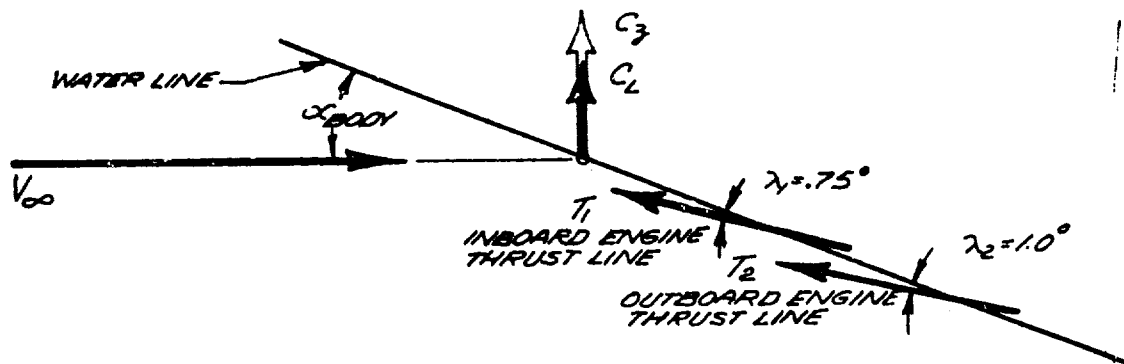


Figure 3-56. Effect of C.G. Location on B2707 Lift and Drag



$$C_z = C_L + \frac{T_1}{gS} \sin(\alpha_B - \lambda_1) + \frac{T_2}{gS} \sin(\alpha_B - \lambda_2)$$

ALSO

$$C_z gS = nW$$

ELIMINATING gS

$$C_z = C_L + \left[\frac{T_1}{nW} \sin(\alpha_B - \lambda_1) + \frac{T_2}{nW} \sin(\alpha_B - \lambda_2) \right]$$

FINALLY

$$\frac{C_z}{C_L} = \frac{1}{\left[1 - \frac{T_1}{nW} \sin(\alpha_B - \lambda_1) - \frac{T_2}{nW} \sin(\alpha_B - \lambda_2) \right]}$$

EQUATION NEGLECTS;
(a) DIFFERENCE IN LINE
OF ACTION OF INLET AND
GROSS THRUST VECTORS.
I.E. T_1 AND T_2 ARE NET
THRUST VECTORS
(b) 1.1° (AVERAGE) TOE-IN OF
THE GROSS THRUST AXIS
IN THE PLANVIEW

WHERE

C_L = LIFT COEFFICIENT = LIFT/ gS

T_1 = NET THRUST VECTOR OF INBOARD ENGINES

T_2 = NET THRUST VECTOR OF OUTBOARD ENGINES

α_B = BODY ANGLE OF ATTACK

λ_1 AND λ_2 = INCLINATION OF THRUST AXES WITH REFERENCE TO WATER LINE

n = NORMAL LOAD FACTOR

W = AIRPLANE WEIGHT

FOR EQUILIBRIUM CONDITIONS, WINGS LEVEL

$$n = \cos \gamma + \frac{V \dot{\theta}}{g} = 1 \text{ FOR LEVEL FLIGHT}$$

WHERE

γ = FLIGHT PATH ANGLE

$\dot{\theta}$ = PITCH RATE

g = ACCELERATION OF GRAVITY

Figure 3-57. Lift Coefficient with Thrust Effects

Table 3-X. B2707 Takeoff and Landing Operation

Flight Condition	T/W	Flap Deflection Outboard ~ Inboard (Deg)	α Body (Deg)	C_L C_D		C_L Including Thrust Effects
				No Thrust Effects		
Lift Off In ground effect Gear down	.308 *	20/40 ~ 40	10	.725	.0945	.76
Approach Free Air Gear Down	—	20/40 ~ 40	9.8	.615	.1130	—
		30/50 ~ 40	9.8	.710	.1565	—
Touchdown In ground effect Gear down	—	20/40 ~ 40	8.4	.650	.0905	—
		30/50 ~ 40	8.4	.750	.1200	—

* MAX. AUG. THRUST, SEA LEVEL ~ 86°F, TAKEOFF
AT MAX. DESIGN TAXI WEIGHT, 675,000 LB.

3.2.2.2 Takeoff

The primary takeoff flap angle for most airports is 20/40 degrees. Larger and smaller deflections will be defined to meet unique airport requirements such as high-altitude airports, or runways where normal standards for field length and community noise require further optimization. In all cases a liftoff attitude of 10 degrees (body reference water line) is recommended. Liftoff speed for the maximum taxi weight of 675,000 lb is 169 kn estimated airspeed (EAS) using the primary flap setting.

Maximum pitch attitude, with gear oleos fully extended and the tail skid touching the runway is 11.5 degrees, so that an early rotation to tail skid contact will permit liftoff at about 96 percent of the normal speed. Rotation characteristics are described in Par. 4.1.1.1.

Table 3-Y shows some of the significant minimum operating margins achieved during takeoff for the chosen operating mode. Minimum requirements of the current Federal Aviation Regulations are shown in parentheses where applicable.

Figure 3-58 illustrates the takeoff operating speeds in more detail, showing their variation with thrust-to-weight ratio. Margins are equal to or greater than the current minima in all cases.

Airworthiness standards for application to supersonic transport operations are under continuous review, with the objective of ensuring satisfactory operating margins in all circumstances, together with a high degree of efficiency. Comparing the presently proposed operating margins with the current regulations is, therefore, largely a matter of convenience. Future changes may be made in operating procedures when found to be desirable.

3.2.2.3 Landing

The flap angle to be used for landing must be a compromise determined by the requirements for good visibility, low speed, and an acceptable noise level throughout the approach. Maximum flap deflection is 30/50 degrees.

Table 3-Y. Minimum Operating Margins - Takeoff

OPERATING MARGIN	NORMAL LIFTOFF $\alpha_{\text{BODY}} = 10^\circ$		MINIMUM LIFT OFF SPEED, $\alpha_{\text{BODY}} = 11.5^\circ$ Tail Skid Contacting Runway	
	Ground Effect	Free Air	Ground Effect	Free Air
$\Delta \alpha$ to 1 "g" stall at V_{LOF}	6°	10°	4.5°	8.5°
Increment in normal load factor to 1 "g" stall Δn Minimum, liftoff to 35 ft	0.28	—	0.12	—
Increment in normal load factor to 1 "g" stall Δn 2nd Segment climb	.35 (0.3 typical)			
$\frac{V_2}{V_{\text{LOF}}}$ Critical engine inoperative, most adverse loading	1.043			
$\frac{V_2}{V_{\text{S.F.A.R.}}}$ Critical engine inoperative, most adverse loading	1.225 (1.2)			
$\frac{V_2}{V_{\text{MIN LEVEL FLIGHT}}}$ Critical engine inoperative, most adverse loading, gear extended	1.21			

Values in Parentheses Result From Meeting Current F.A.R. Operating Minimums

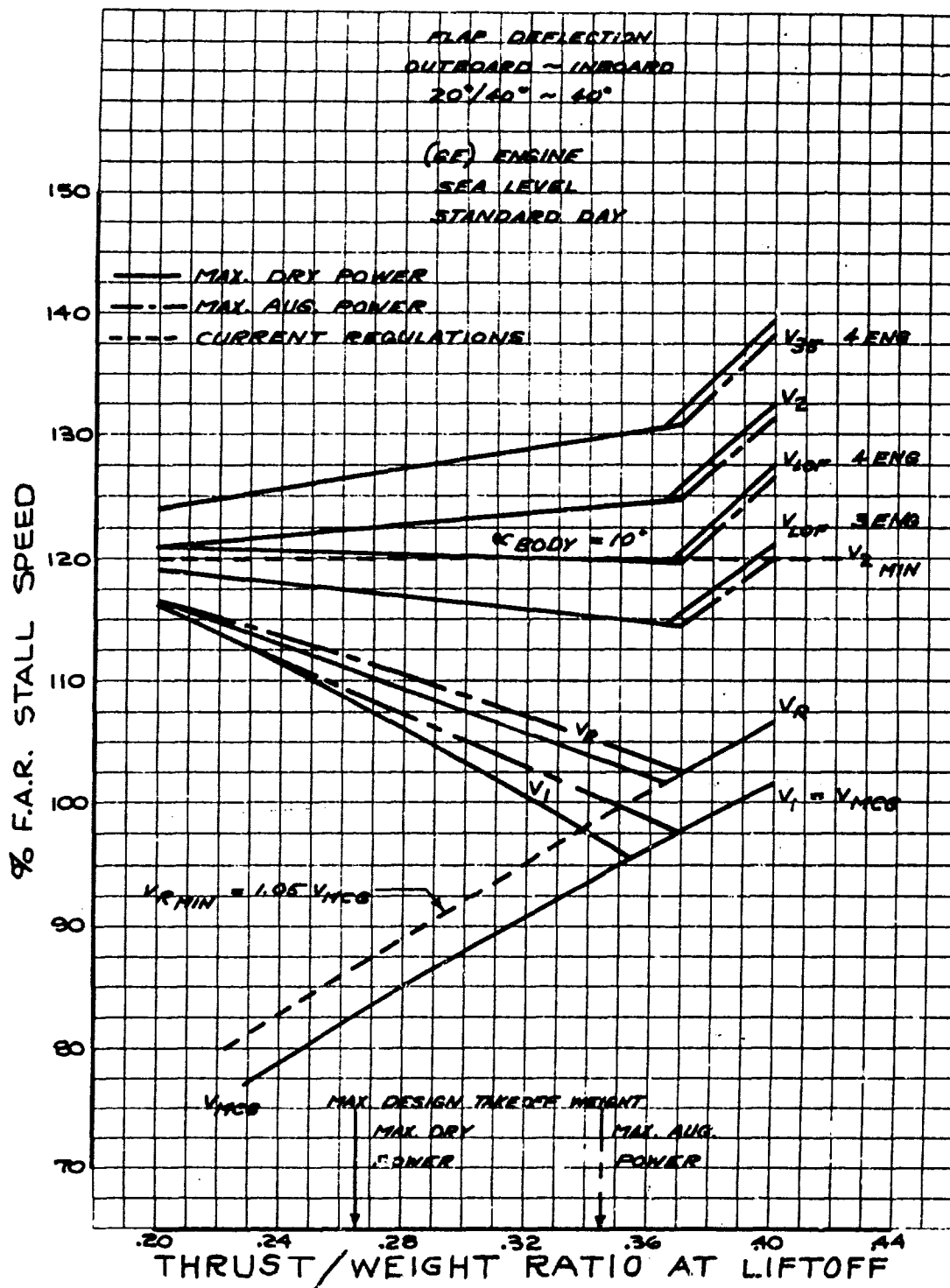


Figure 3-58. Takeoff Speeds

A representative approach condition is flaps 20/40 degrees, angle of attack 9.8 degrees measured to the reference body water line. (This gives a body attitude of 6.8 degrees nose up when descending with a 3-degree glide slope.) The approach speed will be $1.35 V_{SFAR}$ at a C_L of

0.62 leaving a margin of 0.6-g incremental normal acceleration to the 1-g stall for maneuvering. Body attitude at landing will be about 8.4 degrees. Tail drag angle is 11.5 degrees, leaving a normal clearance of 3.1 degrees of pitch rotation (42 inches actual clearance to the tail skid).

3.2.2.4 Landing With 72-Degrees Wing Sweep
In low speed flight at 72 degrees of wing sweep, the inboard wing portion leading edge slat (the strake slat) will be deflected 25 degrees down. This provides satisfactory pitch stability with an aft cg limit of 64 percent root chord. The wing high lift flaps cannot be used at this sweep angle.

Trimmed lift and drag curves are shown Fig. 3-59 for a representative cg position of 62 percent C_R .

An approach speed of 205 kn has been recommended to ensure good handling characteristics. This results in an approach attitude of 9 degrees at 350,000 lb weight, using a 3-degree glide slope. Body attitude at touchdown will be just over 10 degrees.

Future improvements in control and stability characteristics could permit the approach speed to be reduced to about 185 kn with a body attitude of 10.5 degrees. Touchdown would then be about 176 kn at 11.5 degrees body attitude, the tail skid scrape angle.

3.2.3 Wind Tunnel Tests and Results

The test data used to derive preliminary estimates of takeoff and landing performance were obtained on a 0.0371 scale model, closely simulating the proposal configuration in all important respects except wing twist. Tests were made in the University of Washington Aeronautical Laboratory 8- by 12-ft wind tunnel, at a Reynolds number of 4.87×10^6 , based on the model root chord reference length. Photographs of the model are shown in Figs. 3-60 and 3-61.

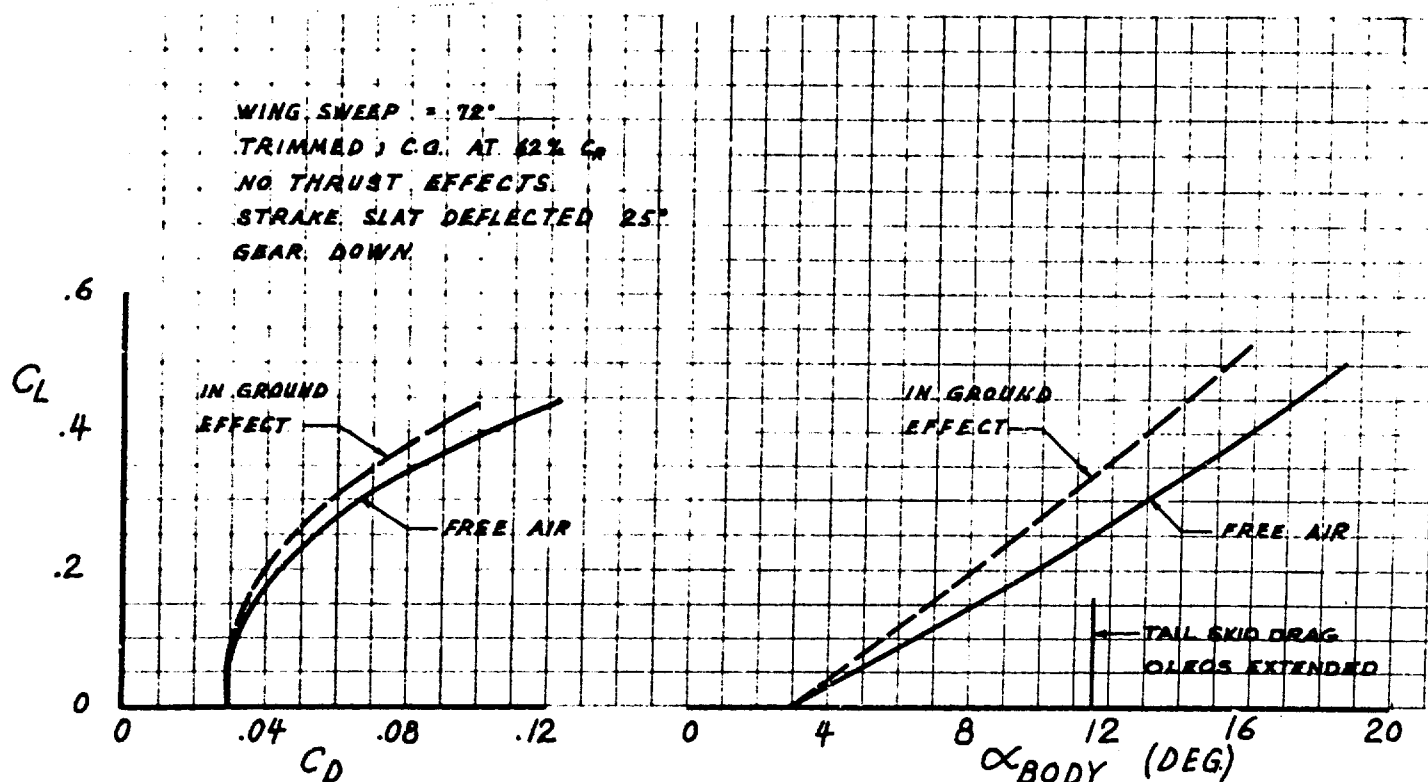


Figure 3-59. Lift and Drag for Landing, Wing Sweep 72 Degrees



TAKEOFF CONFIGURATION



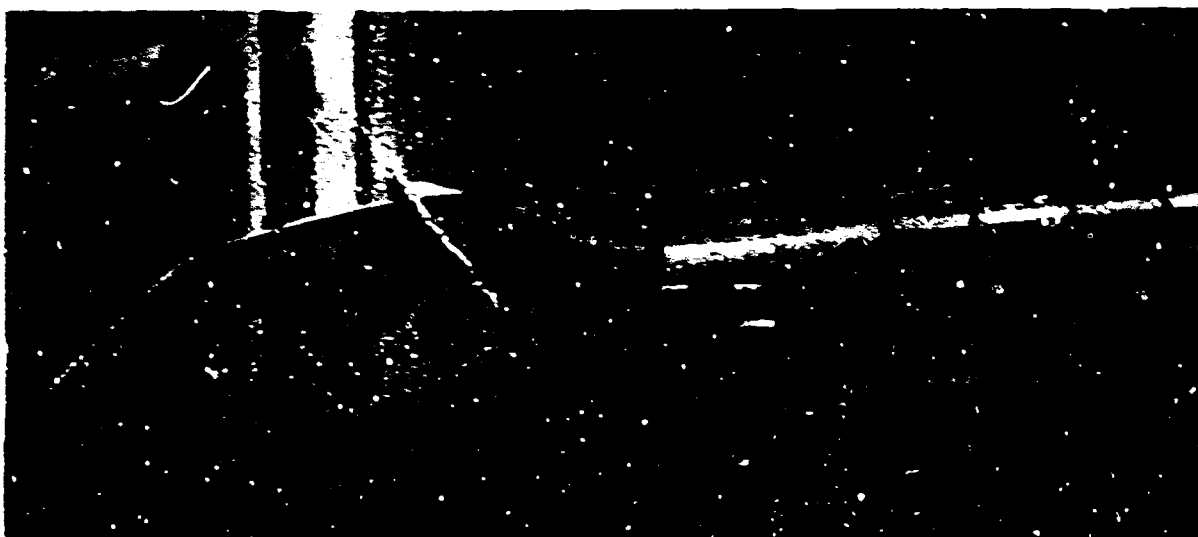
WING SWEEP 72°

Figure 3-60. Low Speed Wind Tunnel Model

V2-E2707-3



MODEL CONFIGURATION



CLOSEUP OF LEADING
EDGE SLATS

Figure 3-61. Low Speed Wind Tunnel Model

V2-B2707-3

A new low-speed configuration development model of the B-70 has been constructed. It will be submitted to the FAA for evaluation testing by the NASA. A continuing program using this and other

models will be used to explore configuration refinements. A photograph of the FAA evaluation model is Fig. 3-62.



Figure 3-62. FAA Evaluation Model

The preliminary model twist distribution resulted from an adaption of a 733-390 model to the new configuration, expediting development testing. Lifting surface theory has been used to estimate corrections for the wing twist differences. These corrections have been applied to the test data, making it representative of the proposal airplane, and are as follows:

$$\Delta \alpha_{\text{BODY}} = -2.37'$$

$$\Delta C_M = -0.0055$$

$$\Delta C_{\text{Tail}} = -1' \text{ per } C_L$$

All these are applicable with tail off, at 30-degrees wing sweep, and corresponding corrections have been added to data obtained with tail on. Drag values have been further adjusted by $\Delta C_D = -0.0116$, allowing for mounting tares and Reynolds effect on skin friction.

Test data, including these adjustments, are shown in Fig. 3-62 (with tail off) and Fig. 3-64 (tail on) for a range of wing flap angles. Moment data is given in Fig. 3-65.

Model data used to analyze landings with 72-degrees wing sweep, shown in Fig. 3-66, are taken from tests in the Boeing Transonic Wind Tunnel. The model has a representative wing twist distribution, but the data have been corrected for wing incidence setting on the body and for tare and Reynolds effect on drag:

$$\Delta \alpha_{\text{BODY}} = -0.5'$$

$$\Delta C_D = -0.0020$$

Trimmed lift and drag curves for landing at 72-degree wing sweep, shown in Fig. 3-59 were derived from further tests with the elevator angle varying. Trimmed performance curves

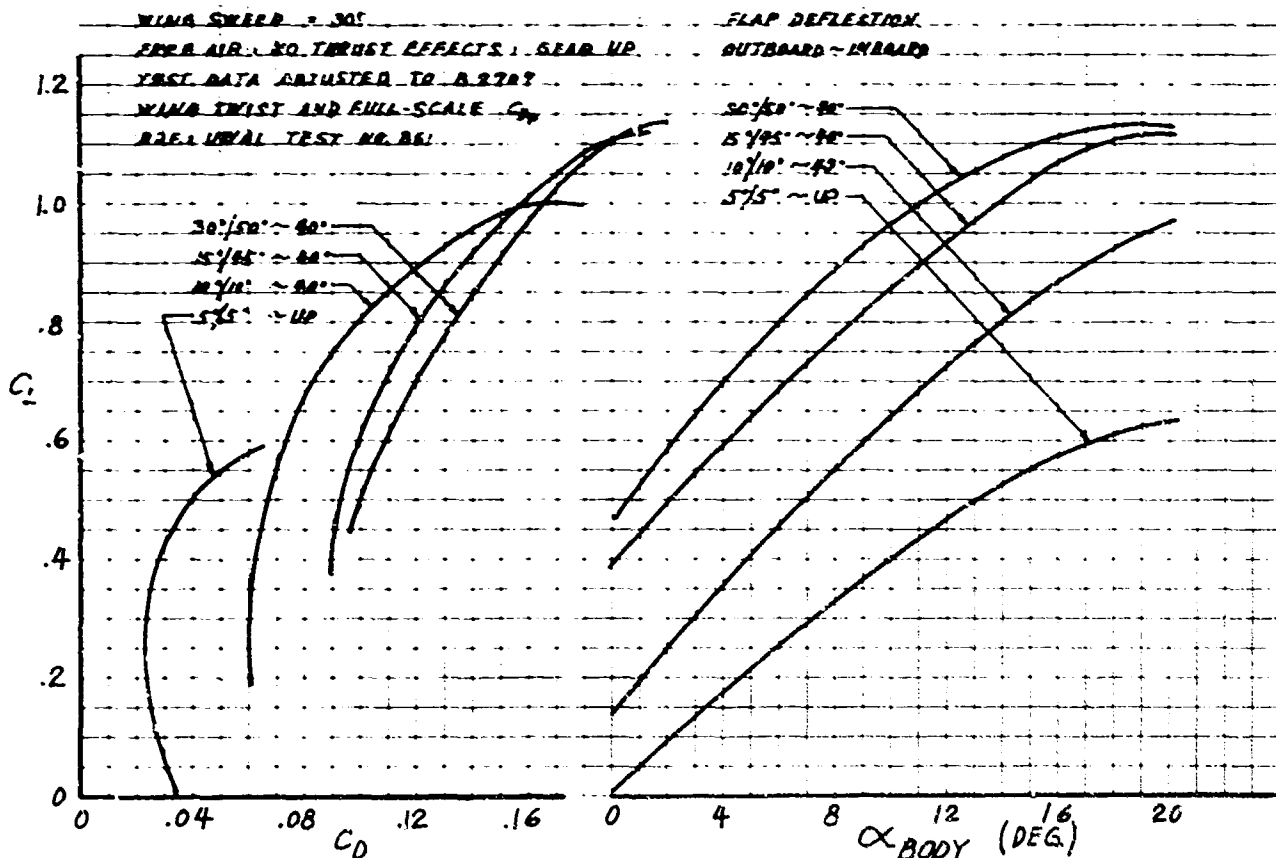


Figure 3-63. Preliminary Test Lift and Drag - Tail Off

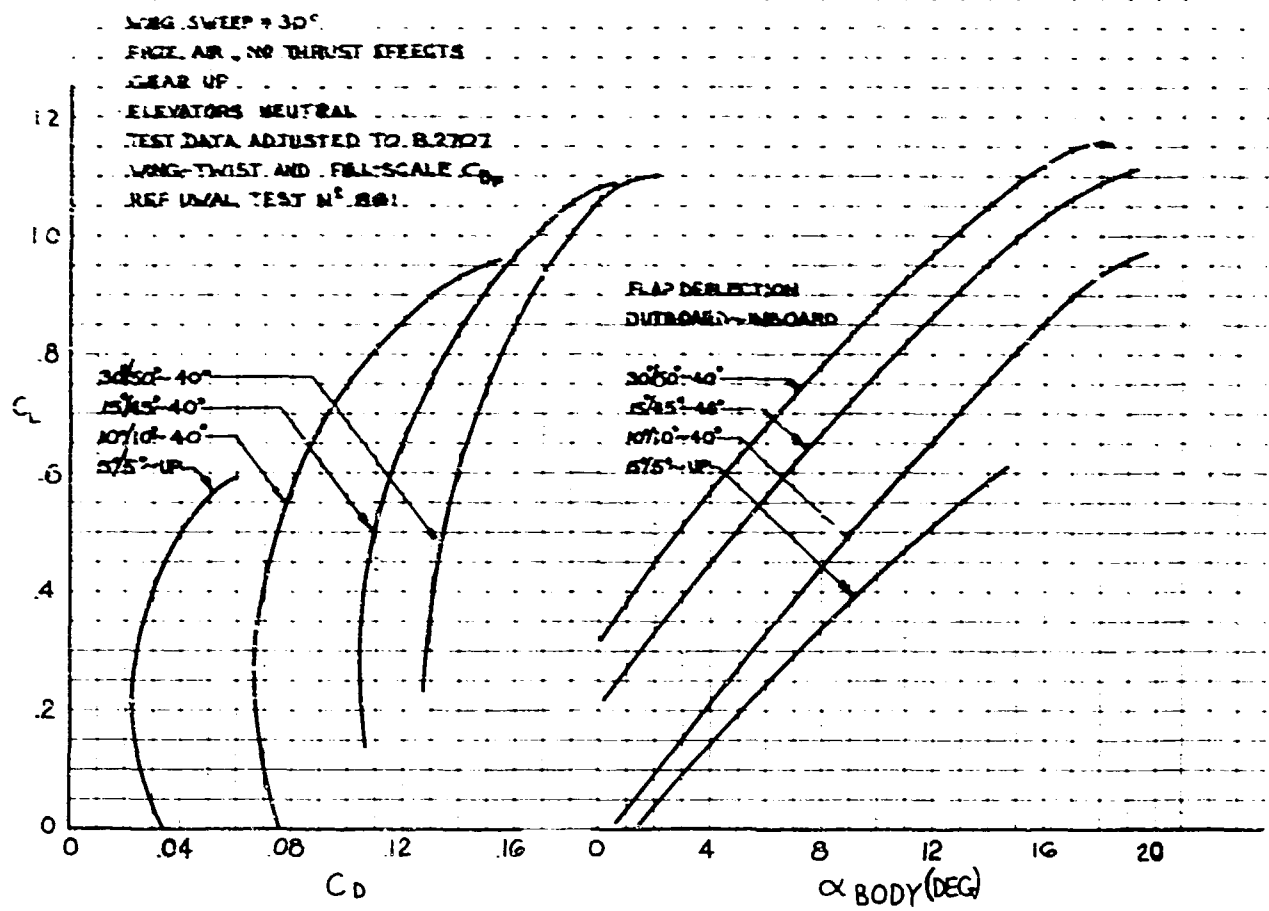


Figure 3-64. Preliminary Test Lift and Drag - Tail On

TEST DATA ADJUSTED TO B-2707 WING TWIST
REF. UVAL TEST 661

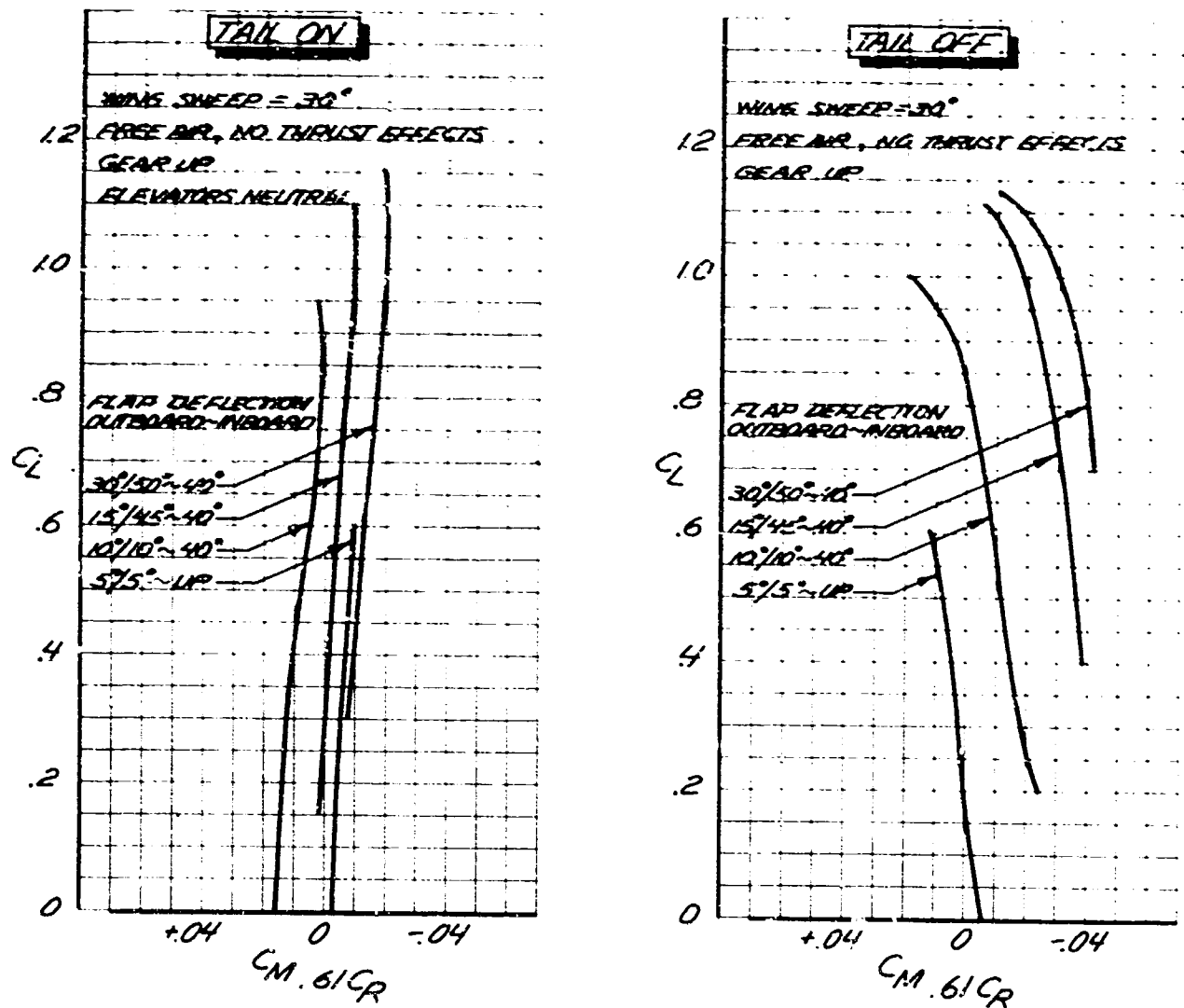


Figure 3-65. Preliminary Test Pitching Moments

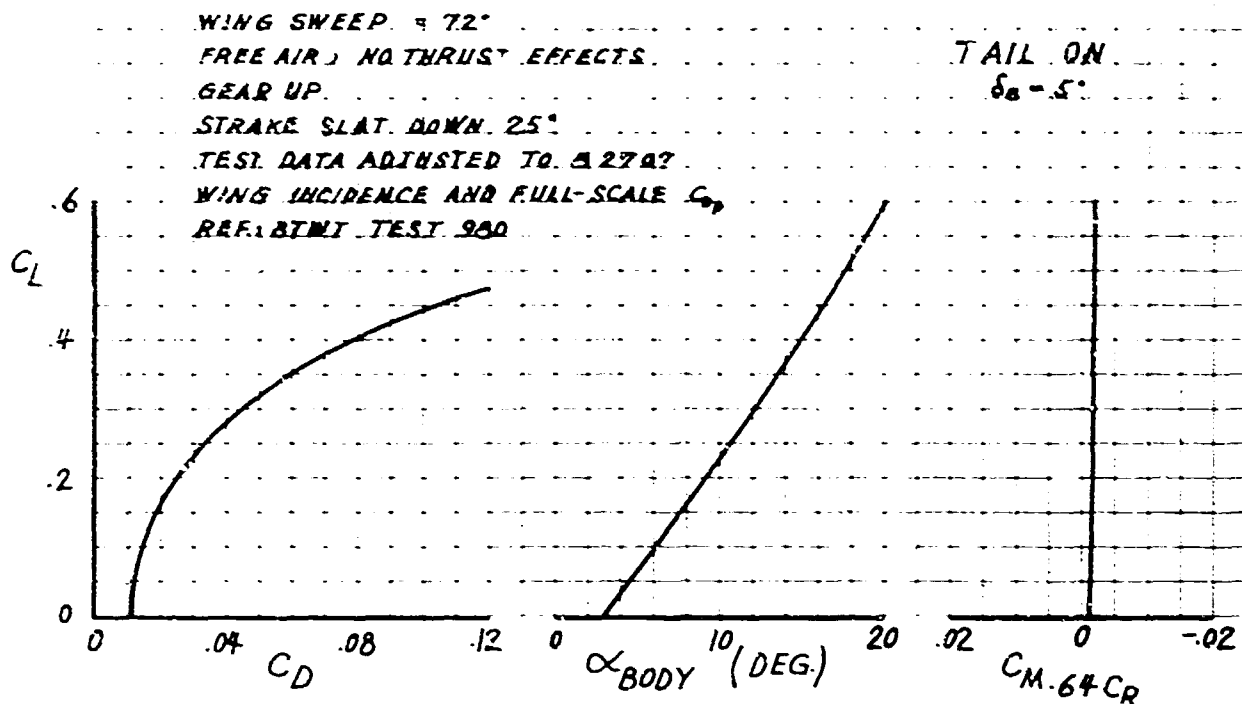


Figure 3-66. Wind Tunnel Data, Wing Sweep 72 Degrees

for 30-degree wing sweep were also derived, and are shown for the takeoff and landing forward center-of-gravity limits in Figs. 3-67 and 3-68. An analysis of the lift and drag increments for trim is made in Par. 3.2.5 to define the configuration features that are amenable to refinement. The performance levels of the B-2707 airplane include the effects of such refinements.

3.2.4 Aeroelastic and Scale Corrections

3.2.4.1 Lift

Previous proposal documents used empirical corrections to lift in developing full-scale airplane characteristics from small-scale model test data. This use is justified because of the basic similarity between the SST and present day jet transports in the takeoff and landing configurations. The so called scale effects established empirically are, in fact, the sum of two effects:

- Viscous effects on lift slope due to the large difference between model and flight Reynolds numbers.
- Wing, flap, and control surface deflections relative to the test model geometry, varying

with the airloads applied to the airplane, and affecting the lift at any given angle of attack.

The airplane lift slope, at 1-g flight conditions, is increased by the corrections for these effects. The flap and control installations are designed to eliminate adverse blow back effects on lift for the chosen design condition.

Pending completion of aeroelastic design studies on the B-2707 (see Par. 3.3), the empirically derived 7-percent factor on lift slope and $C_{L_{MAX}}$.

(Phase I Proposal, Par. C6.2.5 Volume A-V, D6-2400-11) gives a good indication of the probable effect. Figure 3-69 shows the estimated scale and aeroelastic effects on rigid model data for a representative flap angle. The most significant scale effect is that on the maximum lift coefficient, which is the only one included in the present estimates of the B-2707 airplane performance.

3.2.4.2 Drag

Full-scale airplane drag is estimated by the buildup technique explained in Par. 3.1.2. Table 3-Z shows the drag elements for a rep-

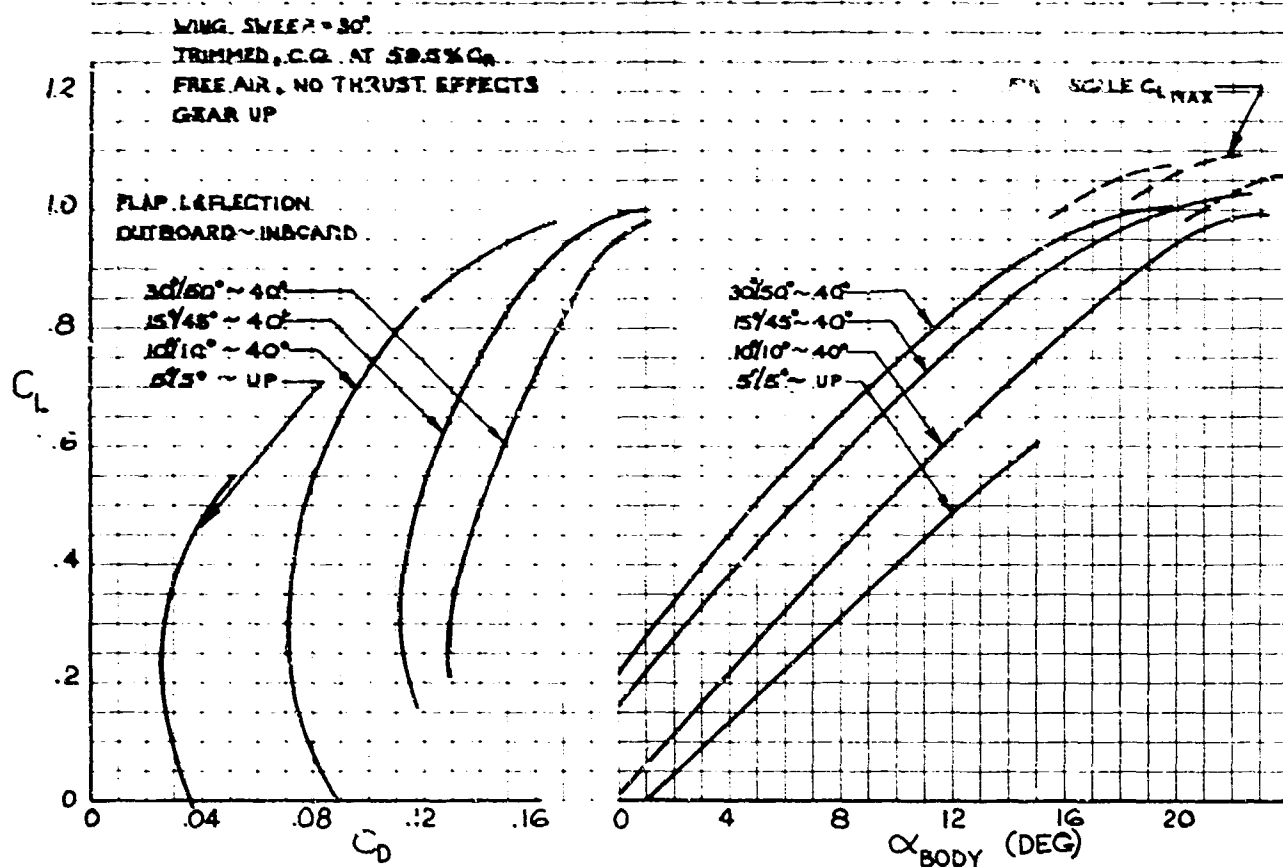


Figure 3-67. B2707 Performance—Current Status, C. G. at 59.5% C_R

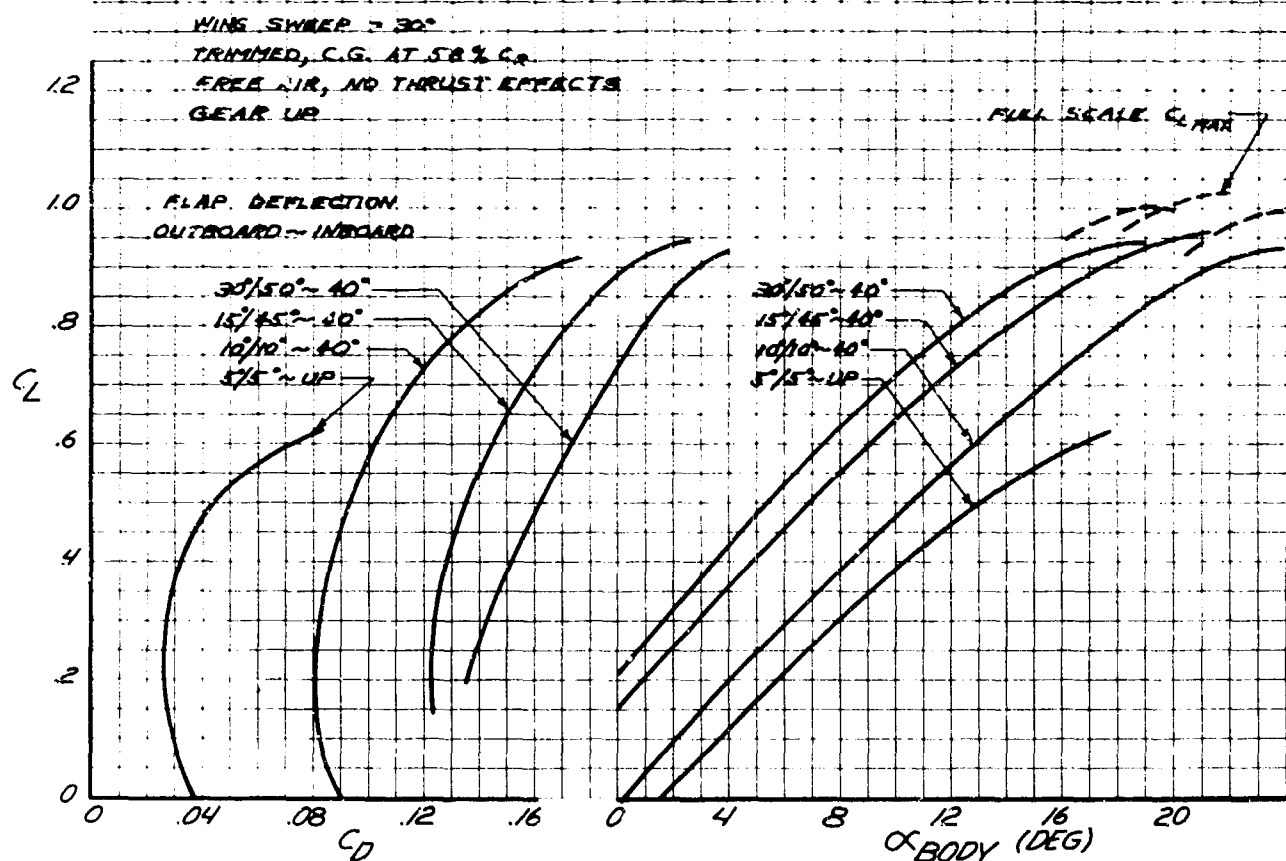


Figure 3-68. B2707 Performance—Current Status, C. G. at 58% C_R

representative low-speed flight condition for the clean airplane. Small differences are apparent in the drags with the GE and the P&WA engines.

The tare and scale correction to wind-tunnel model drag values, ΔC_D of the previous section, was the difference between the model $C_{D\text{MIN}}$

and the estimated full-scale value.

3.2.5 Analysis of Performance

A highly effective double slotted wing flap system has been adopted for the airplane, with leading edge slats for stall control. These high lift devices have been developed by wind-tunnel testing at Boeing and at the NASA. The triple-slotted inboard flap is of similar design to that of the 727 airplane.

Analysis of model test data to date reveals certain areas for potential improvement in the trimmed lift and drag, especially at the forward cg. The pitch trim system is the key to better performance. The data points to two factors susceptible to improvement by refinements in design:

a. An interference between the closely-coupled wing and tail, giving a small effective

tail arm for trimming the wing body pitching moments.

b. High tail drags, indicating near zero leading edge suction on the tail; this feature is sensitive to Reynolds number as well as tail section geometry.

3.2.5.1 Effective Tail Arm and Trim Lift Loss
With a conventional small tail set well behind the wing, the tail lift force which trims the airplane in pitch has a center of pressure at, or slightly behind, the tail quarter chord point. For a large tail like that of the B-2707, the center of lift depends upon the spanwise loading, which in turn is determined by the wing downwash distribution, the dynamic pressure distribution, and the tail twist. Since the tail is a low aspect ratio surface, and because the trimming is accomplished by elevators and elevons, the design goal is to place the point of action of the trim lift to be behind the tail quarter chord point. Preliminary testing shows that the tail lift is centered forward of this point, as shown in Fig. 3-70. From this it can be surmised that much of the download induced on the tail from the wing downwash field, is inboard, near the body and consequently centered well forward. The wing chordwise loadings might also be affected by the close-coupled tail.

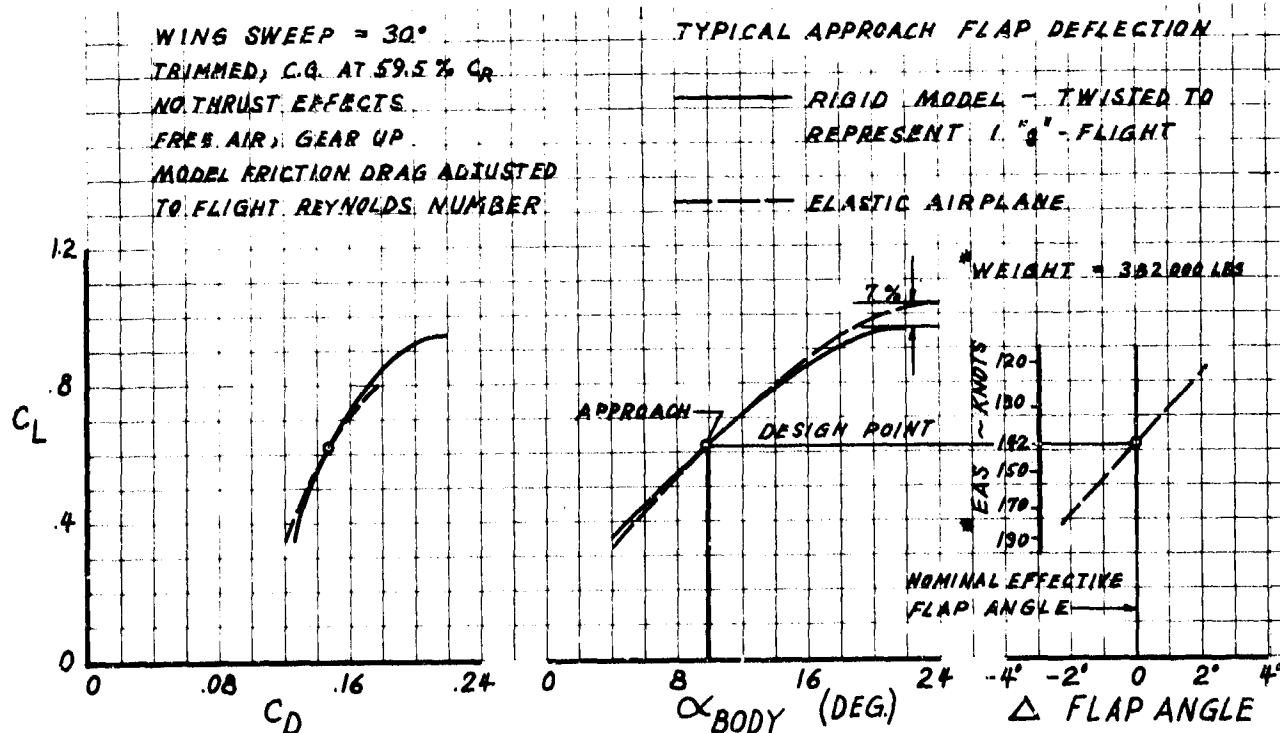


Figure 3-69. Typical Scale Effects

Table 3-Z. Airplane Minimum Parasite Drag

$(\Lambda = 30^\circ, S_{ref} = 9000 \text{ ft}^2)$ AVERAGE TAKEOFF AND LANDING FLIGHT CONDITION $V = 150 \text{ Kn, Sea Level, } Re/\text{Foot} = 1.5 \times 10^6$ Flaps and Slats Up						
ITEM	WETTED AREA (Ft ²)		λC_f		Δf (Ft ²)	
BODY	9885		.00178		17.60	
WING	12800		.00254		32.50	
HORIZ. TAIL	3085		.00259		8.00	
VERT. TAIL	1890		.00249		4.70	
VENTRAL	355		.00245		0.87	
SURFACE GAPS					5.96	
INTERFERENCE					4.98	
MISCELLANEOUS					3.87	
ENGINE	(GE)	(P&WA)	(GE)	(P&WA)	(GE)	(P&WA)
NACELLES	2700	2300	.00229	.00233	6.18	5.36
FENCES	226	276	.00245	.00238	0.55	0.66
TOTAL	31,018	30,668			85.20	84.50
$C_{DPMIN} =$.00947	.00939

Figure 3-70 shows:

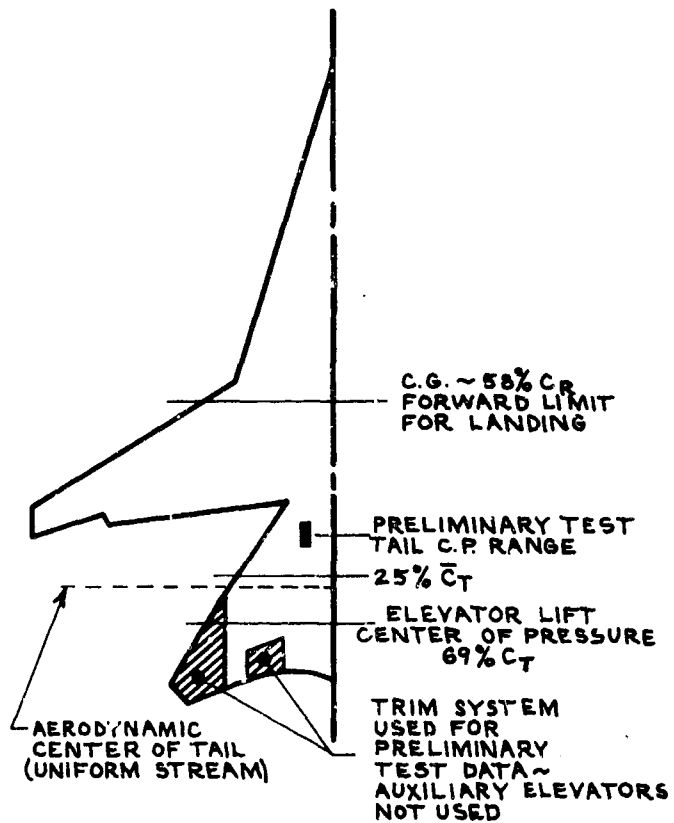
a. The tail lift center of pressure range determined experimentally, the quarter MAC and pitch-trim load centers of pressure estimated for a flat surface in a uniform stream.

b. Actual effective value of tail arm ratio $\frac{C_R}{l_t}$ for several flap angles. This quantity is defined by the approximation

$$\Delta C_{L_{to \text{ trim}}} = C_{M_{to \text{ be trimmed}}} \times \left(\frac{C_R}{l_t} \right)$$

c. Numerical values of the trimming lift loss as a function of wing flap angle.

It is concluded that the lift loss in trimming the wing pitching moments is unexpectedly large in the current configuration data. This may be reduced considerably by design refinements. An aerodynamic development program described in Par. 3.4.2 is underway to study means of improving trim lift and drag. Some refinements that appear likely to increase the effective tail arm are:



PRELIMINARY WIND TUNNEL TEST DATA

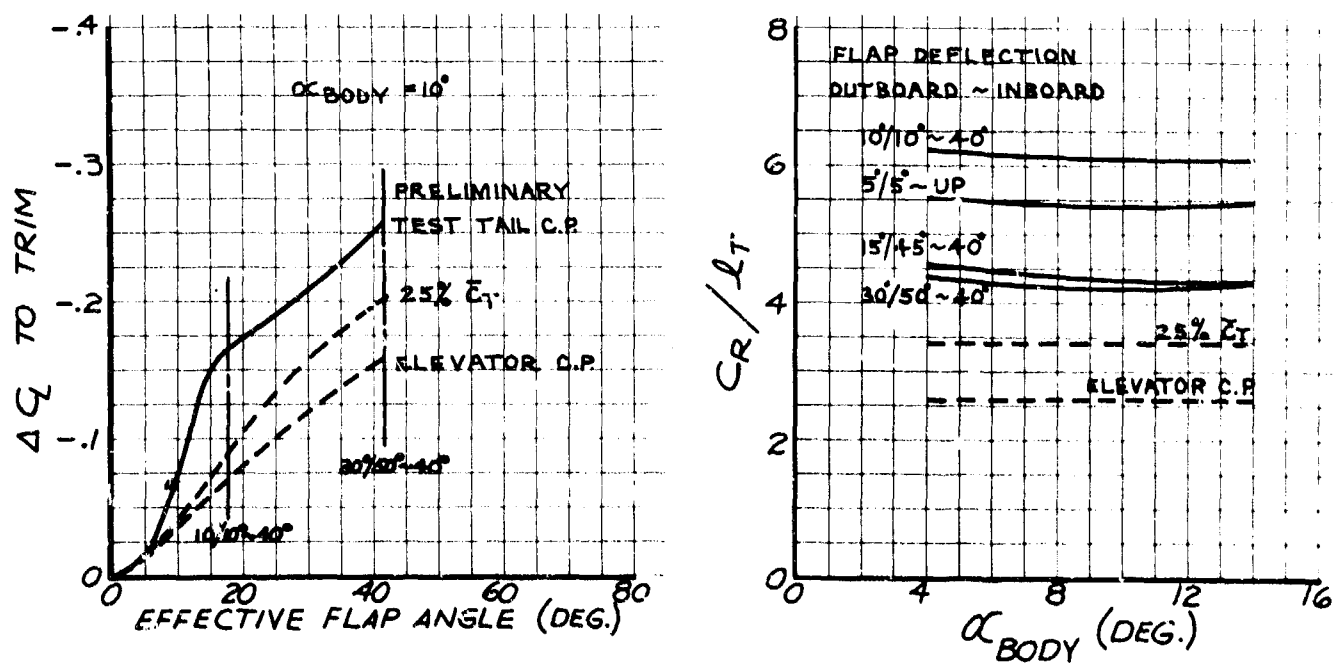


Figure 3-70. Trim Lift and Tail Center of Pressure

- Changing the relative main flap and aft flap deflection angles, thus changing the downwash and wake characteristics.
- Spanwise grading of the flap angles.
- Nose camber (leading edge up) in the tail.
- More trailing edge reflex in the tail.
- Increased washout toward the tail tips.

It is necessary to reconcile any geometry changes to the tail with the requirements for wing-to-tail closure and efficient supersonic and subsonic cruise; nevertheless, it is believed that much may be done to improve the tail efficiency during takeoff and landing. Figure 3-73 shows large potential performance gains.

3.2.5.2 Tail Drag

Tail on and tail off data have been analyzed using the equations shown in Fig. 3-71 to determine the mean downwash angles, tail lift, and tail drag

relationships, which are shown in Fig. 3-72. Tail lift and drag in this figure are referred to the wing reference area, 9,000 sq ft, for convenience. These quantities may be multiplied by 3.63 to refer them to the exposed tail area of 2,478 sq ft. The downwash at the tail is practically independent of flap angle when plotted against wing lift coefficient. The tail lift and drag curves vary in normal fashion with pitch control angle δ_e , the deflection of the elevator and elevon surfaces. Reference to the plot of C_D tail against $(C_L)^2$ tail, on which lines of

$\frac{(C_L)^2}{\pi A F}$ and $\frac{(C_L)^2}{C_{L\alpha}}$ have been drawn representing full leading edge suction and zero suction respectively, shows that very little suction is being realized.

The apparent leading edge suction force on the tail surface is, of course, related to the lift distribution on the tail, and it is doubtful if the ideal value could ever be realized, even with optimum

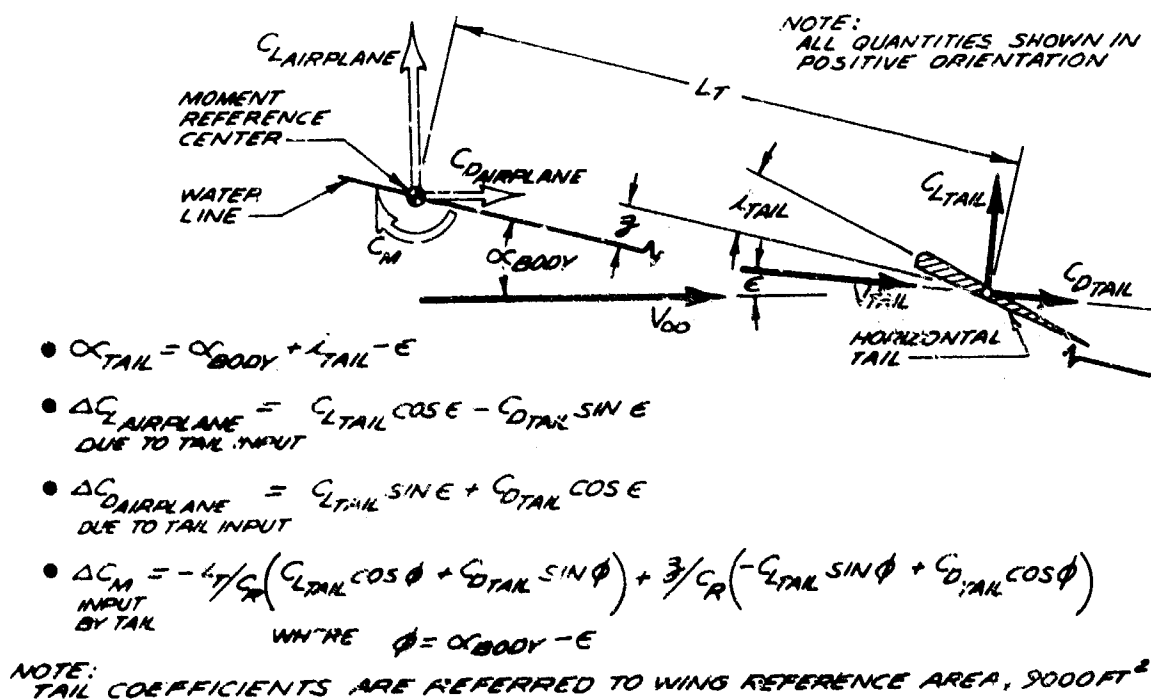


Figure 3-71. Horizontal Tail Force and Moment Equations

COEFFICIENTS REFERRED TO 9000 FT.² AREA
TAIL EXPOSED AREA EQUALS 2478 FT.²

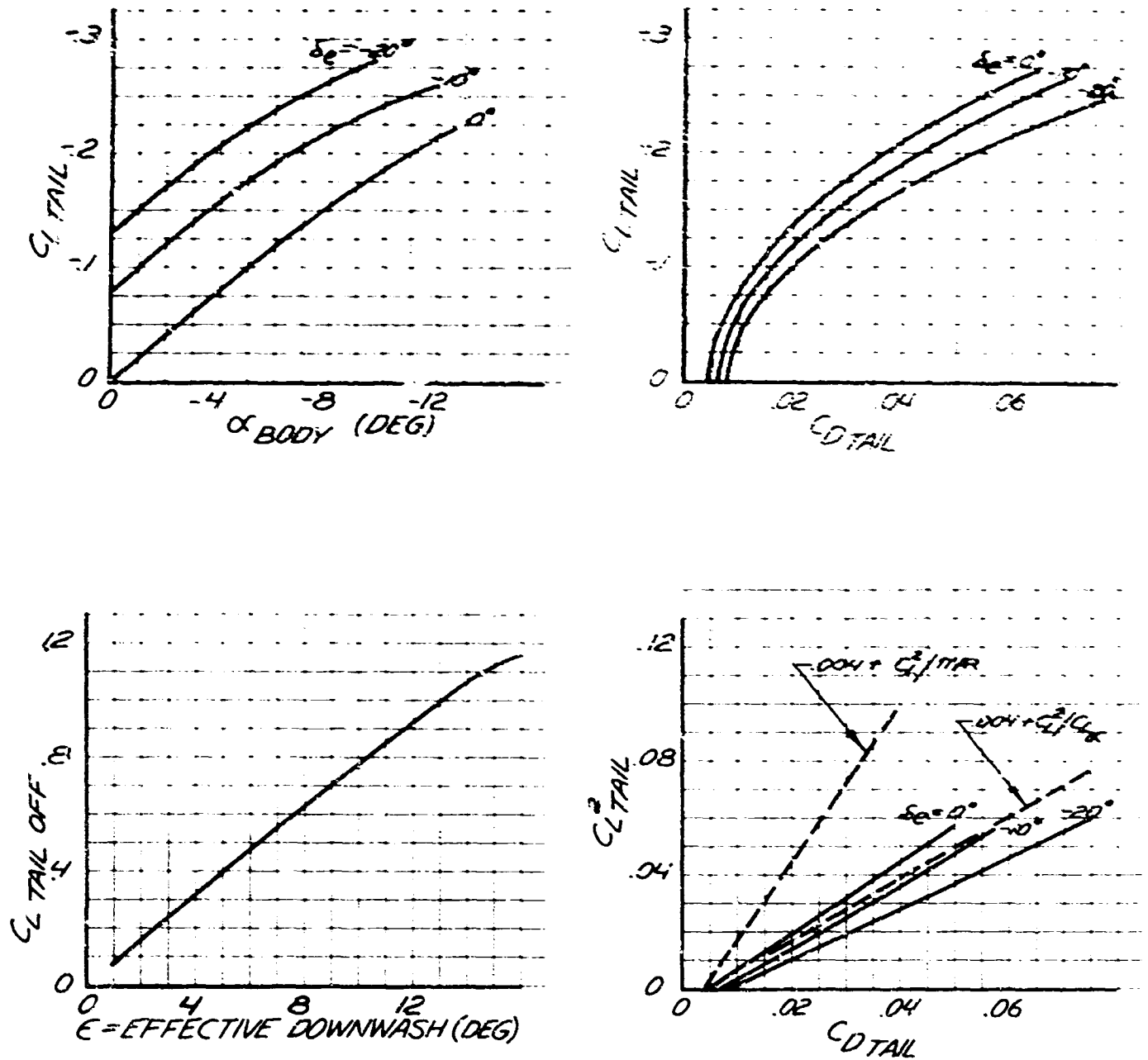


Figure 3-72. Model Tail Lift and Drag Characteristics

section geometry. However, two factors hold promise for improved values at full scale on a refined version of the airplane. These are:

a. Leading edge suction force improves sharply on swept wings having rounded leading edges as Reynolds number is increased. This has been proved by NASA tests. (See Ref. 20.) The model test Reynolds number was below the critical value defined in that reference. The same paper also shows considerable drag reductions from judicious use of twist and leading edge camber. A design goal of 40 percent theoretical suction appears reasonable.

b. The wing tail design study discussed in Par. 3.4.2 will show where the greatest drag benefits accrue from appropriate local section changes; a larger effective tail arm, once realized, ensures large reductions in tail drag by reducing tail lift and trim control deflections required.

3.2.6 Effects of Tail Refinements

Figure 3-73 illustrates potential low-speed performance improvement from refinements to the horizontal stabilizer and pitch trim system design. It shows airplane lift and drag effects from moving the effective tail trim force center of pressure aft. The illustration is for one flap angle and one angle of attack for clarity; similar improvements occur for other conditions. Effects are shown for two tail center-of-pressure positions:

- a. At the exposed tail quarter mean aerodynamic chord, believed to be readily attainable.
- b. At 69 percent of the tail mean aerodynamic chord, a position which pertains if all the trim force is generated by the elevator and moving tip.

3.2.7 Influence of cg Position and of cg Margin
Trimmed lift and drag are directly influenced by fore and aft location of the airplane center of gravity. The best usable performance is obtained when the center of gravity is as far aft as airplane handling considerations will allow.

The variable-sweep wing offers another means to control the cg margin. If wing sweep programming is carefully correlated with airplane load distribution, it is possible to ensure takeoff and landing operations with small cg margins under all conditions.

The effects of cg position on L/D ratio and C_L are shown in Fig. 3-74 for a 10-degree angle of attack, representative of takeoff and landing operations. If the cg margin is controlled by reducing wing sweep angle, the performance gains will be somewhat increased because of the increased wing span.

Figure 3-75 summarizes the performance for all flap deflections, as affected by cg margin and effective tail arm. This shows the tremendous performance potential of the B-2707 airplane configuration, and supports the input lift and drag levels used to estimate production airplane take-off and landing performance.

3.3 AEROELASTIC ANALYSIS METHODS

Careful consideration has been given to aeroelastic effects in the development of the B-2707 configuration. Extensive analyses, trade studies, and experimental programs have supported the design. While the aeroelastic effects are very important, none has been found to pose a serious problem; however, it is essential that the effects can be accurately calculated. Having this capability, aeroelasticity becomes a routine design consideration.

The calculations principally are made to:

- a. Determine aeroelastic effects on the lift, drag, stability, and control characteristics of the airplane.
- b. Define a manufacturing jig shape for the structure such that the desired flight shape is attained while the airplane deflects under normal flight loads.
- c. Determine flexibility corrections to the rigid model wind-tunnel test data.

In the paragraphs following, analytical and experimental methods are discussed and some typical test data presented. Specific, detailed flexibility effects on the B-2707 lift, drag, stability, and control characteristics are found in Par. 3.1 and Sec. 4.

3.3.1 Analytical Methods

Aeroelastic deflections and resulting incremental air loads are caused by aerodynamic and inertia (including gravity) loads on the airplane. Schematic loading situation is shown in Fig. 3-76.

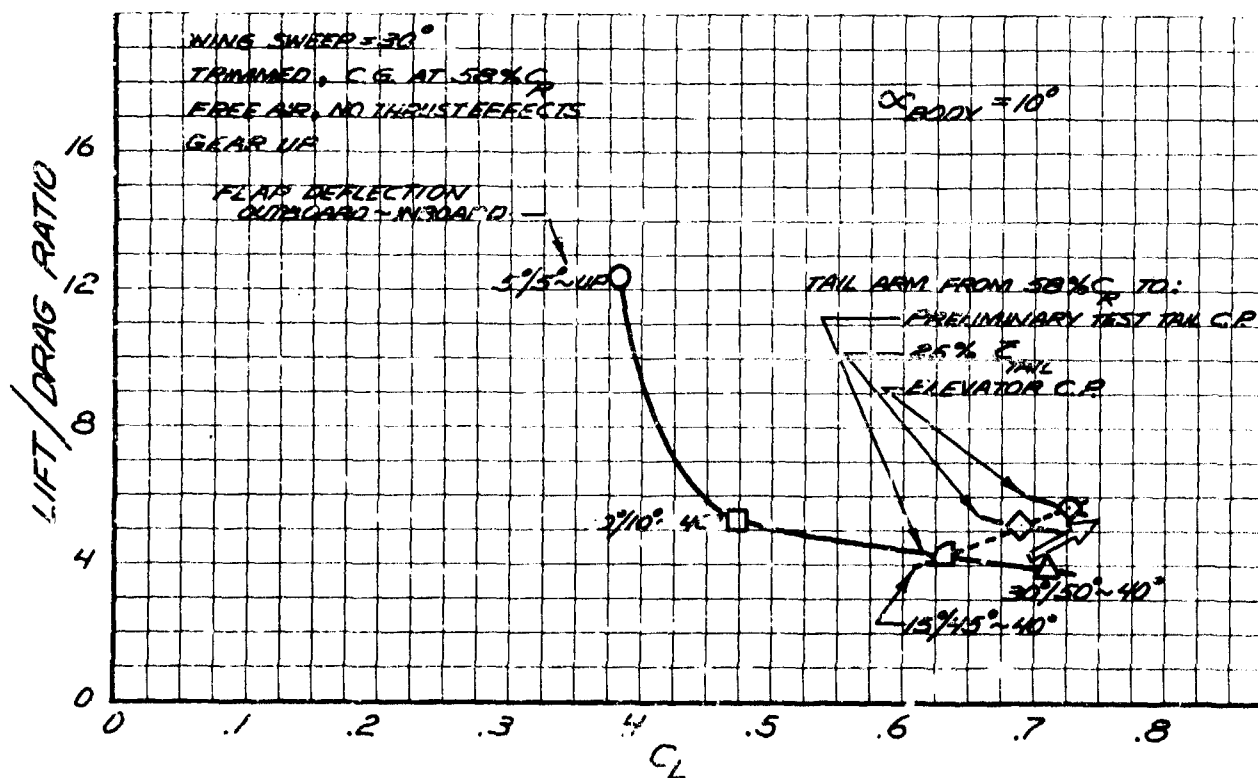
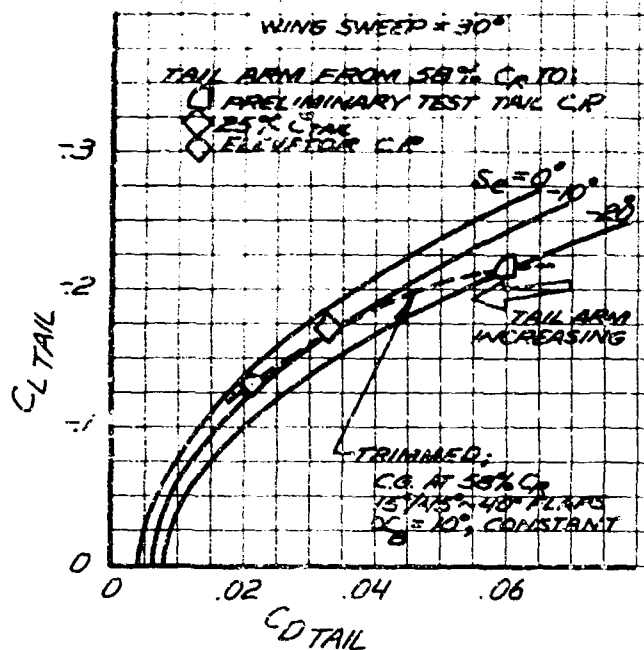


Figure 3-73. Tail Arm Effect on Lift and Drag

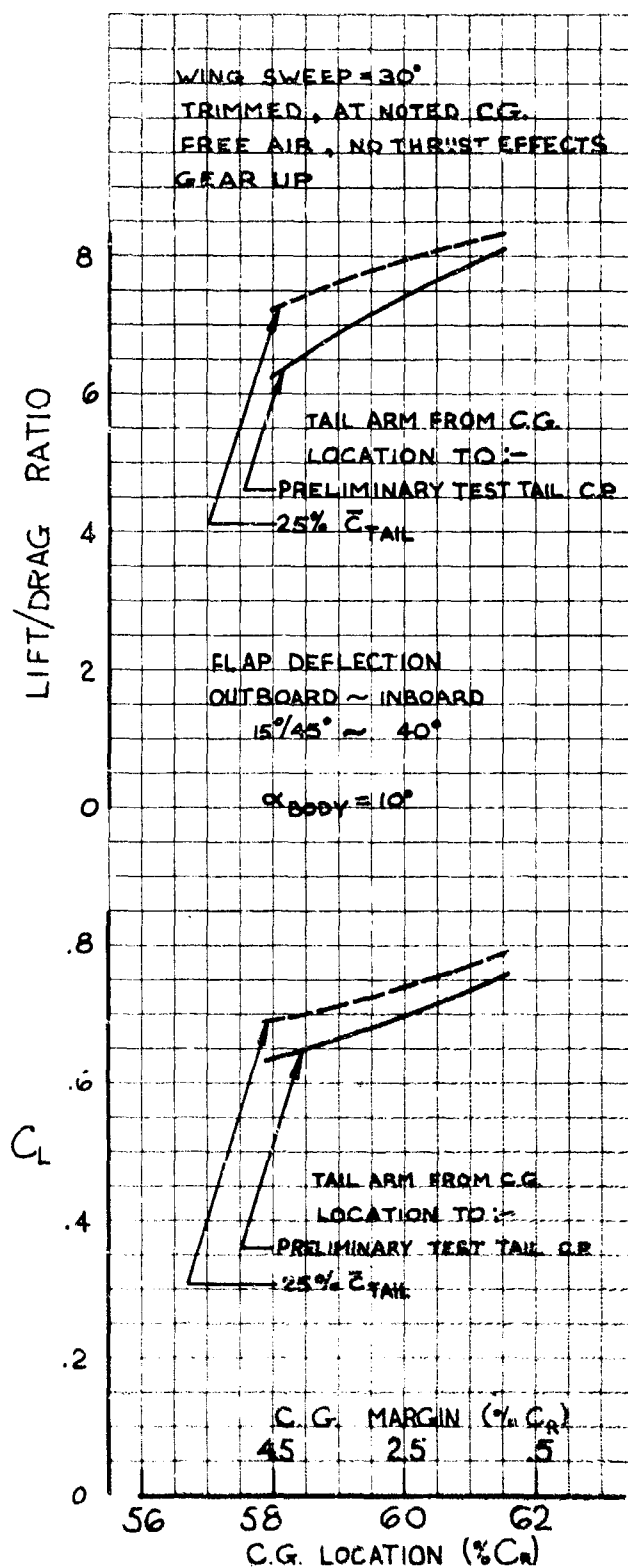


Figure 3-74. C. G. Effect on Lift and Drag

The overall flexibility effects depend on the structural stiffness and on the magnitude and distribution of loads over the complete airplane. For illustrative purposes it is convenient to think of the total aeroelastic effect as the sum of effects of each airplane component: forebody, aftbody, wing, and tail.

Consider the forebody deflections as indicated in Fig. 3-77. Air loads tend to bend the forebody upward, increasing its angle of attack and lift by an incremental amount. On the other hand, inertia loads tend to bend the forebody downward, decreasing its angle of attack and lift. The combined loading results in some intermediate position. Often for the forebody, inertia dominates, so that Case II in the figure is representative. For this case, as the airplane angle of attack increases during a maneuver, the incremental loss in lift due to forebody flexibility results in a nose down pitching moment increasing airplane stability. The other components can be viewed in a similar manner to study their individual effects.

No general statement can be made as to whether the aeroelastic effects of the various components will be stabilizing or destabilizing. Wing and tail can go either way or change with Mach number and airplane loading. The forebody and aftbody are usually, but not always, stabilizing. To determine effects accurately, a careful aeroelastic analysis for each situation is essential, taking into account the airplane geometry, structural characteristics, Mach number, loading condition, and other pertinent factors.

Current methods of aeroelastic analysis have evolved from experience gained in the company's subsonic military and commercial airplane programs, and from the supersonic IM99 which was investigated in considerable detail, including longitudinal and lateral stability and control effects. While the fundamental approach has not changed appreciably, there has been a continuous improvement in the accuracy of methods. This is a result of better aerodynamic pressure distribution prediction methods and of more accurate and complete structural representation of the airplane. To use the better and more detailed aerodynamic and structural data, computer programs have been developed which process the lengthy and involved calculations rapidly.

It is anticipated that improvement in analysis methods will continue; for example, Boeing is

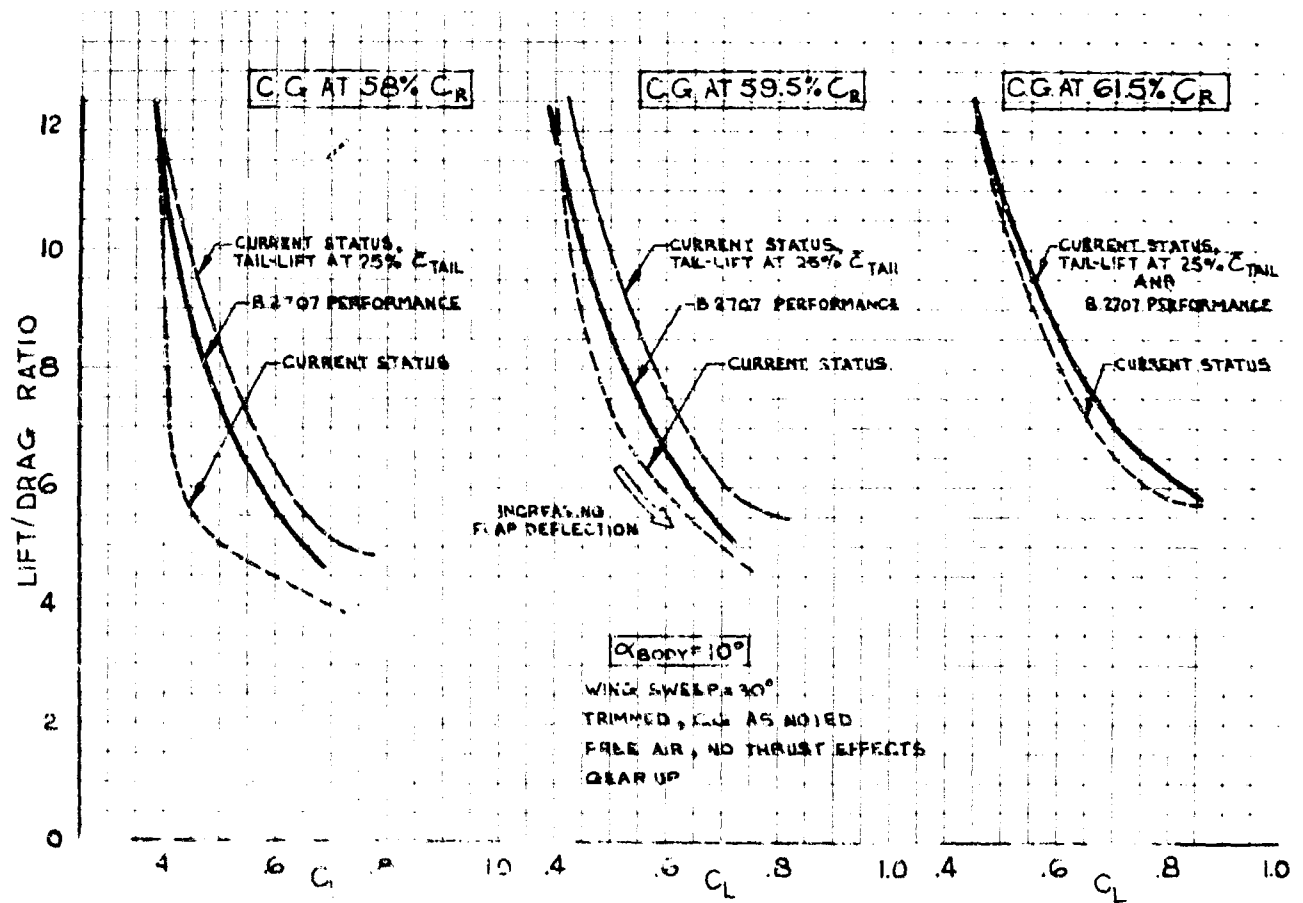


Figure 3-75. Developed Performance Potential of B2707

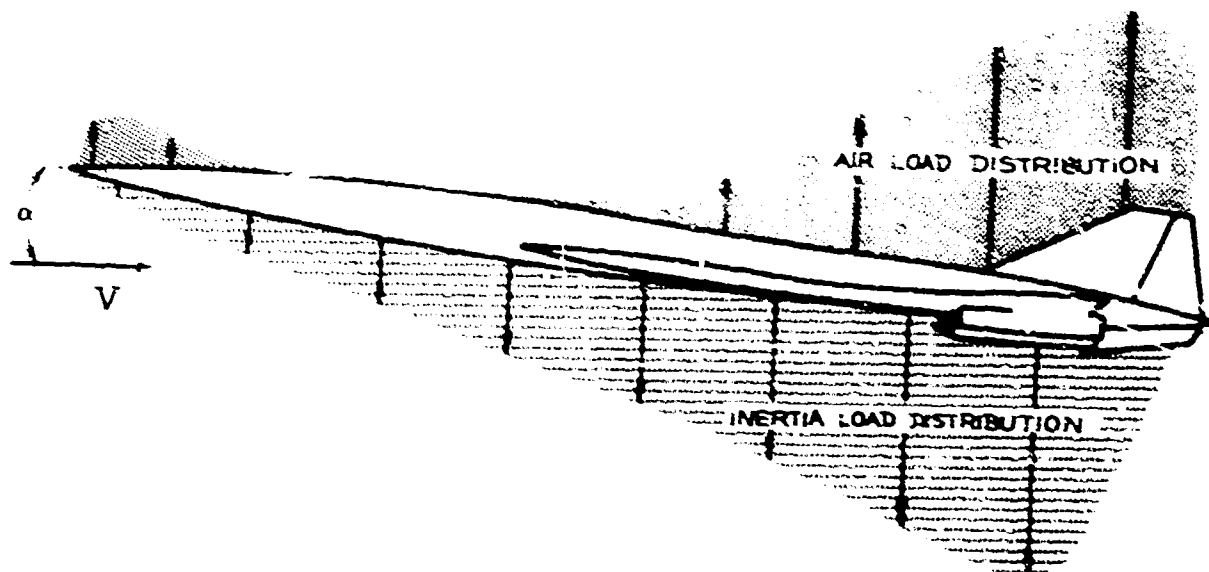


Figure 3-76. Schematic Air and Inertia Loads on a Rigid Airplane

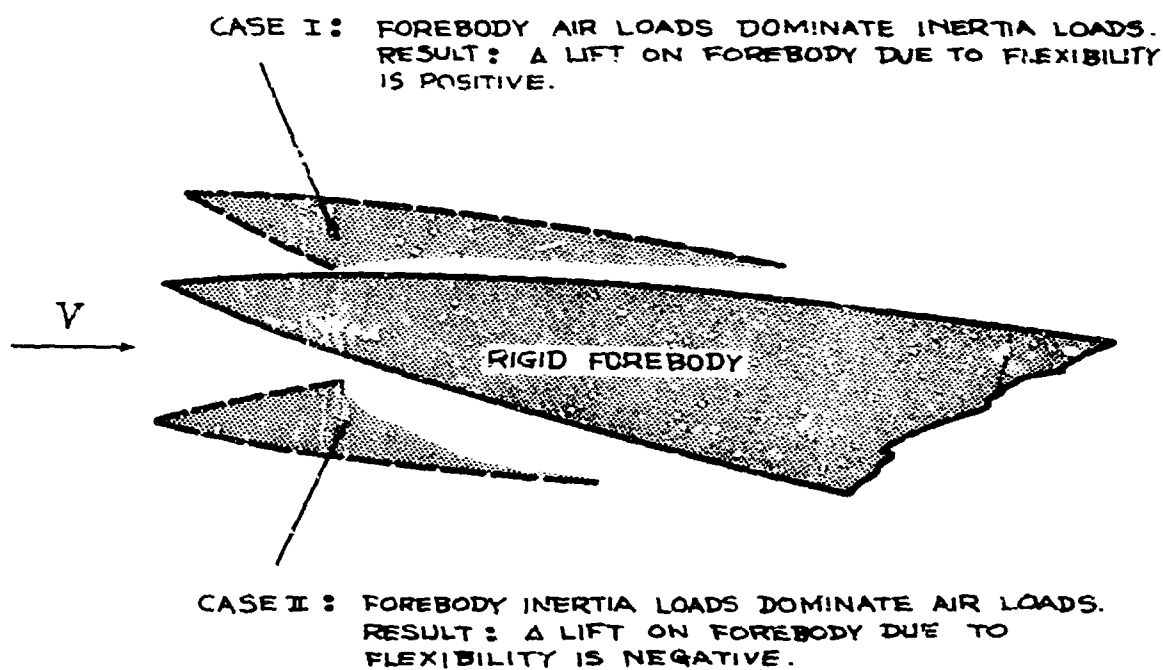


Figure 3-77. Typical Forebody Aeroelastic Deflections and Resulting Incremental Air Loads

currently working on a 2-yr research program to analyze methods for calculating stability characteristics of large elastic airplanes. This program is being carried out under the NASA Ames Contract NAS 2-3662. Applicable results are being integrated into the B-2707 program.

Two main computer programs were used in support of B-2707 design development and for preparation of proposal data. These programs calculate the aerodynamic influence coefficients for subsonic, transonic, and supersonic flow as a preliminary step to calculating the aeroelastic effects. The programs require inputs of airplane geometry, structural flexibility, mass distribution, and nacelle interference pressure distribution.

The geometric inputs define the airplane planform, camber lines, and the aerodynamic panel breakdown for the airplane. A typical panel breakdown is shown in Fig. 3-78. The paneling system is arranged to be consistent with the control surface planform shape so that effects of control surface angular position can be included in the calculations. This is done by adding the control surface angular position, relative to its zero position, to the basic camber slope of the surface.

The elastic properties of the wing, body, and tail are represented by two structural influence coefficient matrices (flexibility matrices). One matrix gives the change in position of each panel control point due to unit loads at the other panel control points. The other matrix gives the change in panel slope at each panel control point due to unit loads at the other panel control points.

The mass distribution is determined in accordance with the paneling of the airplane. A number of separate distributions are superimposed to permit convenient investigation of variations in fuel, cargo, and component mass distribution.

The aerodynamic properties of the wing, body, and tail are represented by an aerodynamic influence coefficient matrix. The elements of this matrix relate the lift on each panel to a unit angle of attack on the other panels. Interference effects are accounted for in the theory.

The computations are made for panel loads of the elastic airplane, P_E , for a load factor, η , dynamic pressure, q , and incidence, i .

$$\begin{bmatrix} P_E \end{bmatrix} = \begin{bmatrix} B \end{bmatrix}^{-1} q \left(\begin{bmatrix} A \end{bmatrix} \begin{bmatrix} 1 \end{bmatrix} + \begin{bmatrix} \theta \end{bmatrix} - \eta \begin{bmatrix} F \end{bmatrix} \begin{bmatrix} W \end{bmatrix} \right) + \begin{bmatrix} S \end{bmatrix} \begin{bmatrix} P_n \end{bmatrix}$$

where

$$\begin{bmatrix} B \end{bmatrix} = \begin{bmatrix} 1 \end{bmatrix} - q \begin{bmatrix} A \end{bmatrix} \begin{bmatrix} F \end{bmatrix}$$

and

$$\begin{bmatrix} \theta \end{bmatrix} = \text{initial panel slopes}$$

$$\begin{bmatrix} S \end{bmatrix} = \text{diagonal matrix of panel areas}$$

$$\begin{bmatrix} P_n \end{bmatrix} = \text{panel pressures due to nacelles}$$

$$\begin{bmatrix} F \end{bmatrix} = \text{slope flexibility matrix}$$

$$\begin{bmatrix} W \end{bmatrix} = \text{mass distribution matrix}$$

$$\begin{bmatrix} A \end{bmatrix} = \text{aerodynamic matrix}$$

The deflections at the control points, $\begin{bmatrix} \delta \end{bmatrix}$, are found as

$$\begin{bmatrix} \delta \end{bmatrix} = \begin{bmatrix} F_1 \end{bmatrix} \left(\begin{bmatrix} P_E \end{bmatrix} - \eta \begin{bmatrix} W \end{bmatrix} \right)$$

where

$$\begin{bmatrix} F_1 \end{bmatrix} = \text{deflection flexibility matrix}$$

Once the panel loads on the elastic airplane have been found, the forces and moments on the airplane are readily computed. For computation of stability derivatives that involve a variation in incidence angle such as roll damping, C_{l_p} , or

pitch damping, C_{m_q} , the proper distribution of

incidence is obtained by changing the column matrix $\begin{bmatrix} \theta \end{bmatrix}$.

Calculations to find the manufacturing jig shape are made by introducing the design condition elastic loads, dynamic pressure, load factor, incidence, and mass distribution into the above equations. They are then solved for the deflections which are subtracted from the design shape.

The experience of the company in using these methods to predict the aeroelastic characteristics of large airplanes has been generally successful. The structural influence coefficients have been accurately predicted and confirmed by full-scale

test. The aerodynamic coefficients have been more difficult to estimate accurately before full-scale test. For this reason, B-2707 aerodynamic data will be verified by pressure model tests. Means are being developed for the rapid inclusion of wind tunnel data into the aerodynamic matrices.

The major influence of elastic distortions on the dynamics of the airplane motion have been accounted for through modification of the aerodynamic derivatives. An exception to this approach was made for one study that included the dynamics of the forward fuselage. The excitation of the first cantilever mode was determined, including the aerodynamic perturbations. This analysis was carried out to ascertain the accelerations at the pilot's station as compared to center-of-gravity accelerations resulting from maneuvering gust and engine-out conditions.

3.3.2 Experimental Investigations

Considerable work has been done in exploring the effects of aeroelasticity by means of flexible model wind-tunnel testing. The tests, with supporting analyses, have been found to substantiate the analytical methods previously described.

The question of model scaling immediately arises in models simulating flexibility. True scaling for all conditions cannot be accomplished because of limitations on available model materials and the range of test facility conditions. The approach taken is to match directly the model and full-scale Mach number and dynamic pressure. The model structure is designed so that flexibilities (similar nondimensional deflections) between the model and full-scale airplane are simulated. Mass scaling to obtain the proper inertial loading has not been attempted because a model material with sufficient density is not available. Even if a suitable material were available, mass scaling would apply only for a single loading condition. The best procedure is to depend on analytical methods to account for inertial effects. These calculations are easy, accurate, and allow the investigation of any desired loading factor and mass distribution. They are also used to adjust the test results for the actual model mass distribution which in general is different than the desired airplane mass distribution. It is necessary to test at several facilities to cover the airplane flight envelope properly as a result of matching the model and airplane dynamic pressures and Mach numbers on a one-to-one basis, (See Figure 3-79).

The objectives of initial flexible model tests were to check the analytical methods and to develop advanced model construction techniques. For this reason, it was decided to build the model with a single fixed wing sweep angle and to make only the wing flexible. Features of the wing construction are shown in Fig. 3-80. Pictures showing the model during test are shown in Fig. 3-81. The rather large wing tip deflection at high angle of attack is easily seen by comparing the pictures.

Typical data for the tests are shown in Fig. 3-82. Also shown are data for a so-called rigid model which is found to be not perfectly rigid. The theory compares very closely with both the flexible model data and rigid model test data, thus substantiating the analytical methods.

A new model, now near completion and scheduled to begin tests in September 1966, was designed to represent the B-2707 configuration. This model is of more sophisticated design than earlier models. It has interchangeable flexible and rigid components to enable investigation of singular and combined component flexibility effects. It will be used to investigate:

- a. The effects of flexible wing and horizontal tail.
- b. The effects of wing to tail structural ties.
- c. The effect of wing sweep angle.
- d. The effect of flexible control surfaces; flaps, elevators, and elevons.

3.4 AERODYNAMIC DEVELOPMENT PROGRAM

The aerodynamic development program consists of analytical and experimental work that will insure that technological and state-of-the-art improvements are considered and incorporated in the refinement of the B-2707. It is discussed under two headings: cruise configuration and takeoff and landing configuration. This program is part of the overall Phase III program Integrated Test Program, V4B-2707-11.

3.4.1 Cruise Configuration

Boeing has worked closely with the NASA in the establishment of the present state of the art in supersonic aerodynamic research. Through the years, practical methods have been developed and these have been applied to the design of high

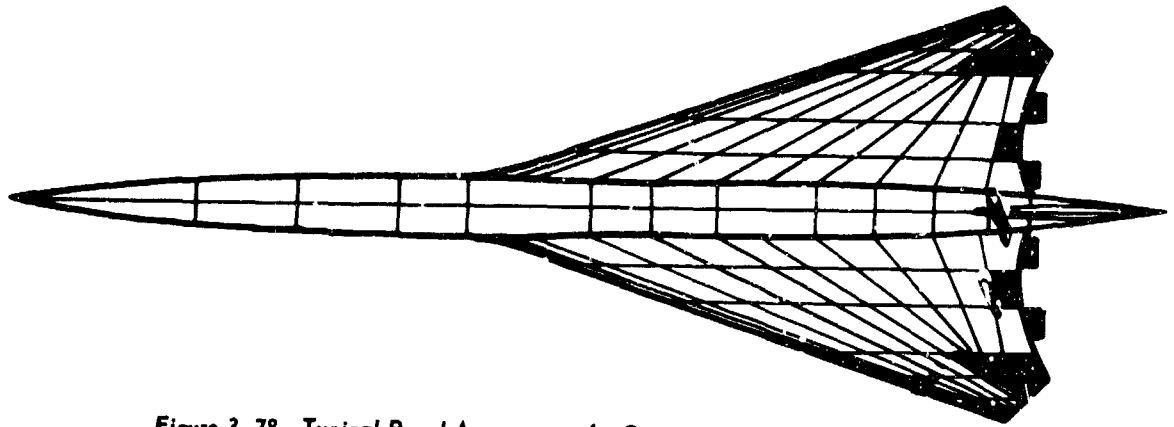


Figure 3-78. Typical Panel Arrangement for Computer Program Calculations

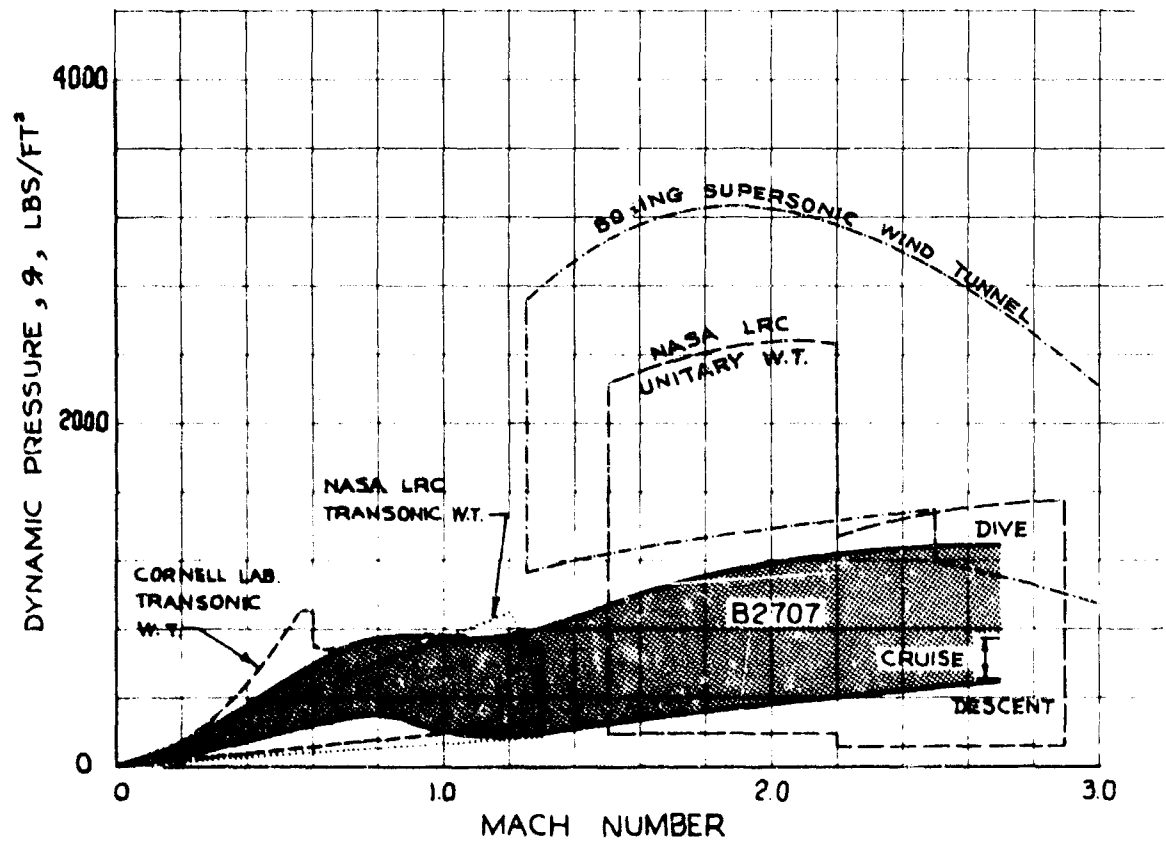


Figure 3-79. Test Condition Coverage For Flexible Model Testing

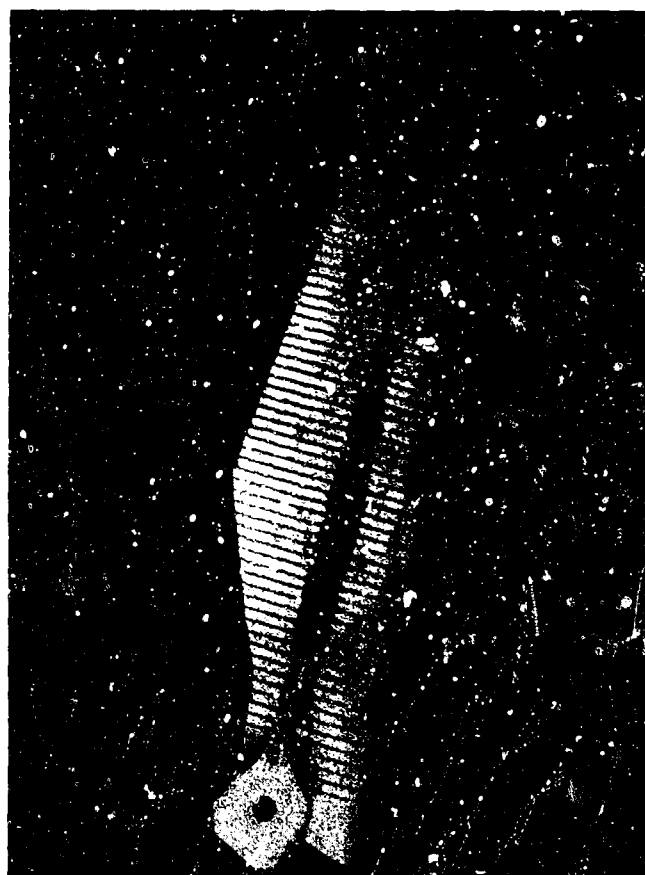


Figure 3-80. Typical Construction for Flexible Model Wing

V2-B2707-3

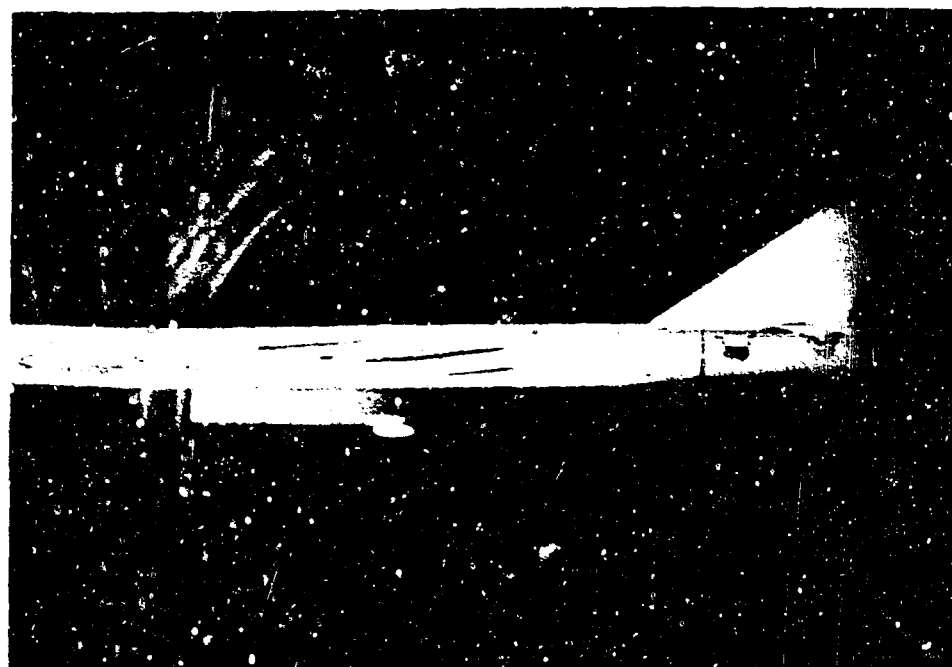
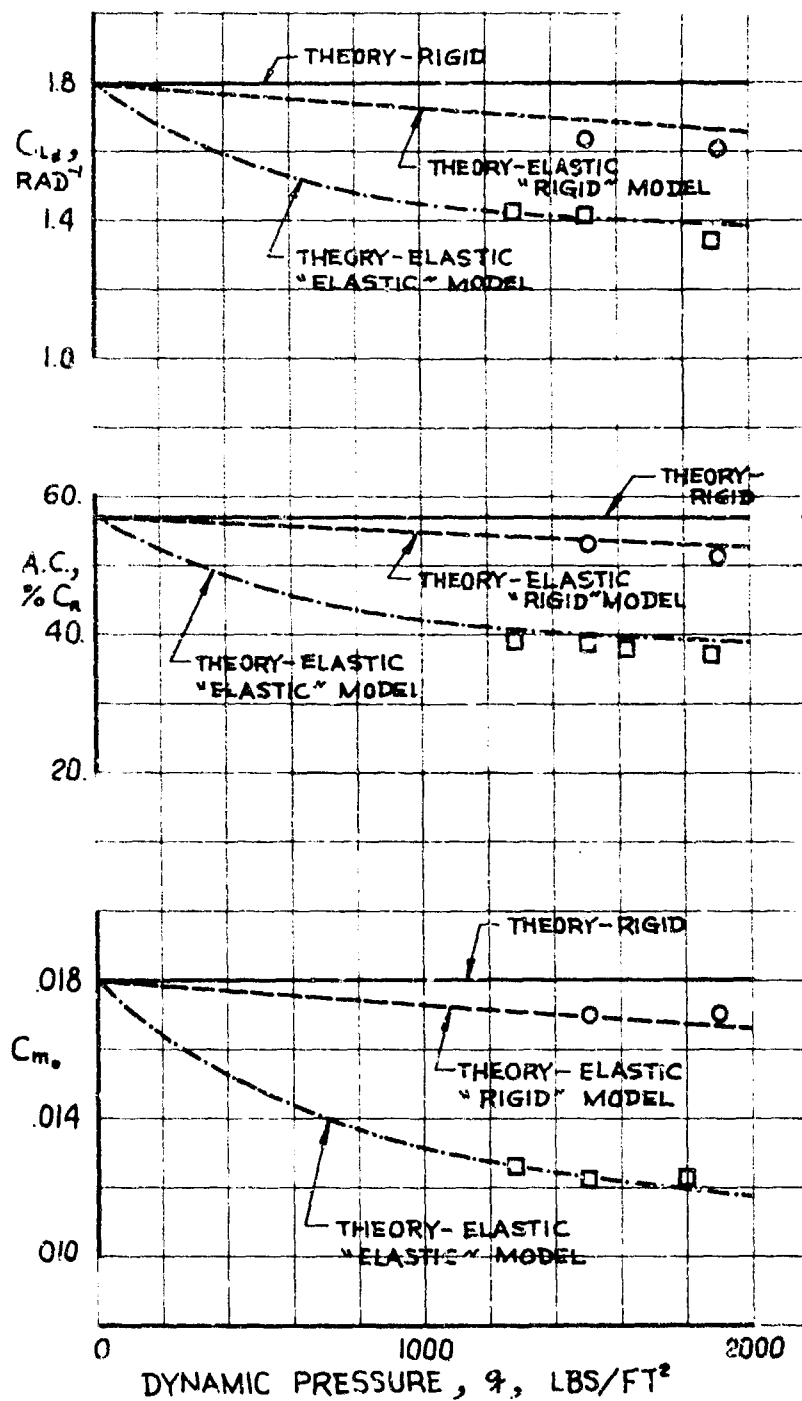


Figure 3-81. Wing Deflection on Model During Wind Tunnel Test

V2-B2707-3



MACH NO = 2.7
 $\angle LE = 72 \text{ DEG.}$

SYM WIND TUNNEL DATA
 O "RIGID" MODEL
 □ "ELASTIC" MODEL

Figure 3-82. Comparison of Flexible Model Test Data With Calculated Data

efficiency supersonic configurations. The methods will be refined through continued test correlations and used in future investigation. General areas of investigation will include continued development and improvement of wing camber surfaces for low drag, fuselage design studies to improve drag and sonic boom, and skin friction and base drag reduction studies. A comprehensive program of aeroelastic research will also be carried out.

a. Drag Due to Lift Reduction

Figure 3-83 compares the drag polar of the wind tunnel model of the B-2707 and a theoretical drag polar (as calculated by small disturbance theory) for a minimum drag wing of the identical planform. It is seen that large drag improvements are possible. Some part of this potential improvement is achievable through wing camber and twist refinement. Several computer programs have been developed and are now available. One of these uses combinations of up to 15 different loadings, on any given wing, and will allow the design of wing surfaces optimized with many arbitrary constraints. Already, experimental evidence is in hand to indicate that better drag-due-to-lift characteristics can be obtained through camber and twist development. Figure 3-84 shows that, at Mach 2.7, a wind-tunnel model has achieved drag-due-to-lift reduction equivalent to an increase of approximately 0.2 in lift-to-drag-ratio. This has been obtained with a camber surface designed for a three-loading optimum similar to that tested on the NASA SCAT 15F Model. Time did not permit incorporating this wing into the series of models designed to simulate the B-2707.

A novel approach to drag-due-to-lift reduction has been discussed in Ref. 24. In this approach, airplane wave drag is optimized at the lifting condition. A computer program that accomplishes this optimization using area rule concepts is in use at Boeing. Another program, using the classical approach to the lifting wing body problem is under continuous development. This latter work has been discussed in Ref. 16. These analysis methods are being applied to the detail design of the wing body combination.

Drag-due-to-lift reduction is possible not only by camber and twist design but also by wing planform changes. Such a planform change has been defined for the aerodynamic development model. Planform changes require, however, considerations of structural design and aerodynamic stability.

Careful tradeoff studies will be conducted to determine the overall effects of planform changes.

An extensive wind-tunnel test program has been defined to correlate analysis and to accomplish the necessary tailoring and refinement.

b. Fuselage Design Studies

Fuselage drag is an important percentage of the total airplane drag and the aerodynamic design of the fuselage requires careful attention. It is intended to carry out a number of fuselage design studies that will have the objectives of drag reduction and increase in useful volume. Different interior arrangements are being studied and a continuous contact with the airlines is being maintained in order to achieve a design that will combine a high aerodynamic efficiency with maximum passenger appeal.

Several alternate bodies for the B-2707 have already been designed and tested in the wind tunnel. These have a more nearly ideal longitudinal area variation that will allow a wider, deeper body forward, coupled with the minimum acceptable width aft (four- or five-abreast seating). Initial airline reaction has been enthusiastic because of the unusual interior arrangements that are possible, including such features as seven- or eight-abreast seating and two aisles with only one or two seats per seat unit. The body drag increments are equal to or less than that of the B-2707, depending on the minimum acceptable cross section. Refinement of these bodies will be continued.

c. Skin Friction Drag and Other Drag Studies

Skin friction drag is still the largest fraction of the airplane zero lift drag and it is necessary to carry out research in this area. It has been shown in Ref. 25, that surface flow injection is an effective means of drag reduction. Tradeoff studies will be carried out to examine the effects of local blowing on the airplane. In addition, it has been shown that small amounts of bleed air are powerful means for base drag reduction; this fact will be studied further. More data on skin friction will also be obtained through flight test measurements. Knowledge of skin friction coefficients and of the state of the boundary layer can also lead to indirect drag reduction by changes in the design of the camber surface. The design will thus benefit from these flight studies.

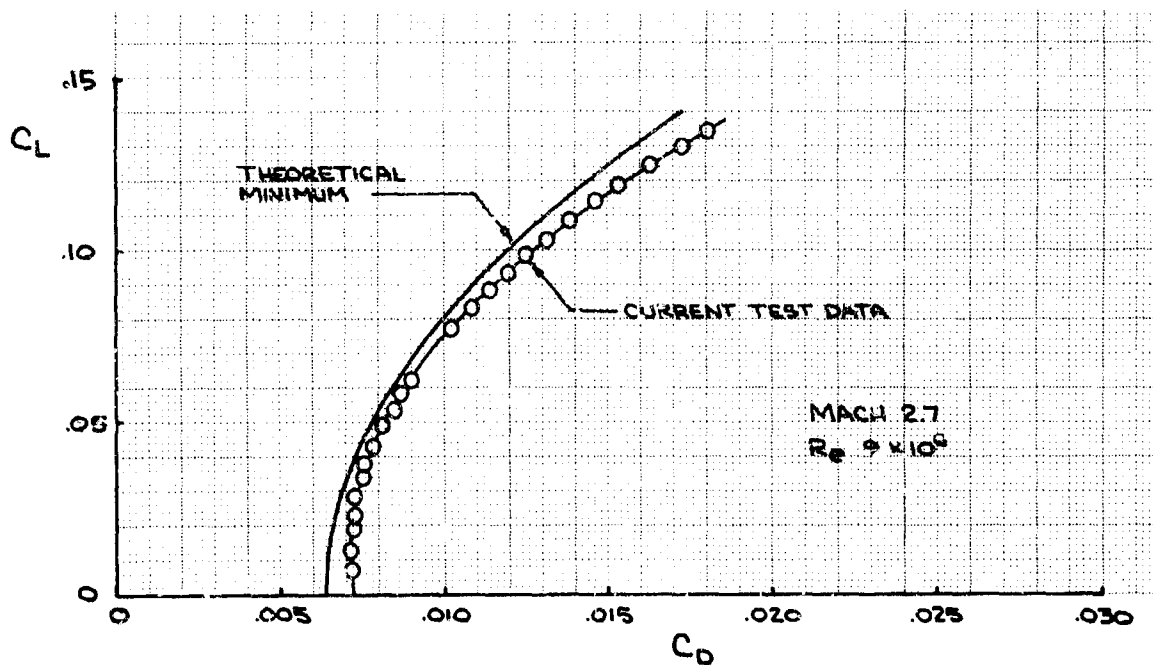


Figure 3-83. B-2707 - Drag Due To Lift Improvement

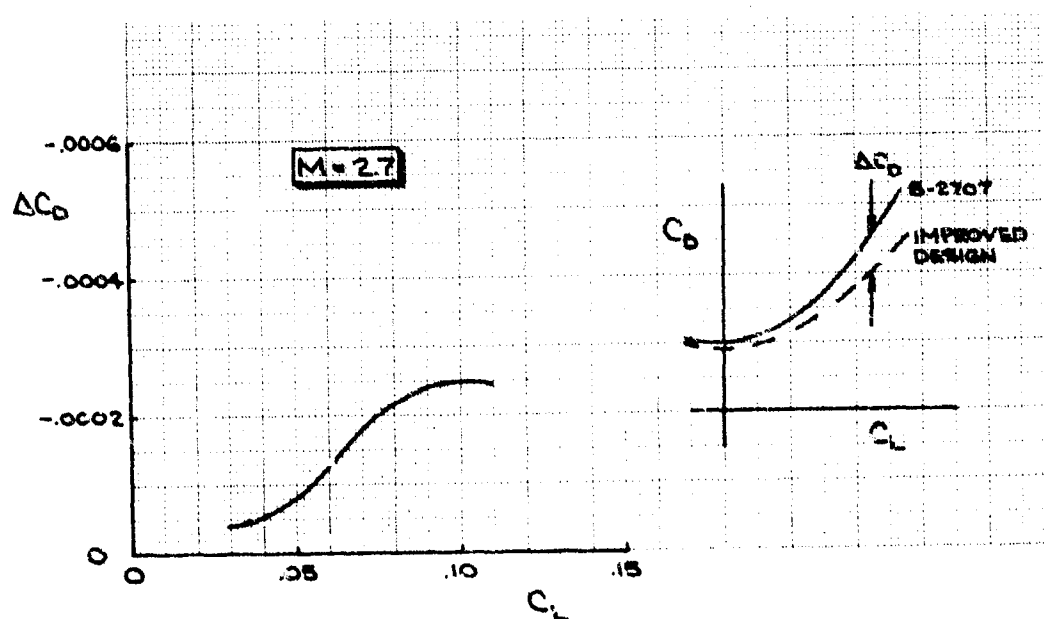


Figure 3-84. Effect of Camber Refinement on Drag Due to Lift

d. Aeroelastic Research

Aeroelastic research studies are being conducted to improve the design efficiency of the supersonic transport through evaluation of all the elastic benefits and penalties. Theoretical studies as well as experimental investigations with flexible wind tunnel models are being carried out. A detailed discussion of the aeroelastic program is in Par. 3.3.

3.4.2 Takeoff and Landing Configurations

The program is planned to achieve maximum trimmed lift and lift-to-drag ratios and to investigate the use of direct lift control for landing and takeoff operations. As already stated in Par. 3.2, one way to improve performance is to reduce the tail down load to trim the airplane, which has the further benefit of minimizing the horizontal stabilizer drag.

Careful control of center-of-gravity location and the wing sweep angle programmed for low-speed operations, contributes to performance optimization in all flight regimes. System design studies are being conducted in these areas.

Parallel studies to refine the airplane geometry for optimum aerodynamic efficiency will add to the airplane capability and will include:

a. Flap and slat development, using theoretical and test techniques to maximize effectiveness and minimize drags. Boundary layer control studies will be included.

b. Further wing lofting studies to optimize low-speed attitudes within the dictates of the required high-speed wing design.

c. The wing body tail optimization study will be a wind-tunnel test program supported by lifting surface theory. The approach is as follows:

- (1) Survey the flow field (downwash and dynamic pressure distributions).
- (2) Set up a vortex lattice system representing the wing body flap combination; adjust as necessary to match the experimental downwash field.
- (3) Add the horizontal tail representation to the vortex lattice system.
- (4) Make systematic variations to wing, flap, and tail geometry to study their effects and to minimize unfavorable wing tail interference.

	4.0	STABILITY AND CONTROL	Page
4.1		CONTROL AND TRIM	145
4.2		STATIC STABILITY	179
4.3		DYNAMIC STABILITY	210
4.4		CROSS-COUPLING CHARACTERISTICS	230
4.5		EMERGENCY OPERATIONS	231

4.0 STABILITY AND CONTROL

Tests and analyses conducted to date show that with normal systems development the production airplane will have stability and control characteristics that ensure the high levels of safety and the good handling qualities required for commercial transport operation.

The B-2707 design concept of integrated wing and horizontal tail, with the engines mounted aft below the tail, eliminates the tail temperature and the jet exhaust interference effects at the tail experienced by past configurations. Tail span and area are increased and the length is reduced (relative to past SST configurations) so that the same effective tail volume coefficient is maintained.

Substantial size increase over past configurations and the change in mass distribution, caused by aft-mounted engines, have caused the basic airplane to become quite sluggish. Stability and control studies indicate that increased reliance must be placed on stability and control augmentation to achieve good handling qualities as airplanes increase in size and inertia. Areas where current data show that stability and control improvements are required in order to achieve the desired characteristics throughout the flight envelope are indicated in the following paragraphs. New control concepts are being explored to improve this situation; for example, direct lift control holds promise of improving low speed airplane response to pilot inputs for high-inertia, close-coupled configurations.

The stability and control analysis presented herein is based on the B-2707 configuration. Areas where further improvements are expected during the development program are pointed out. Flight control and stability augmentation systems design and operation are described in detail in Systems Report, Part B, V2-B2707-11. Airplane control capabilities, stability, and handling qualities for normal and emergency operations are described in this section; the aerodynamic design requirements for the controls and augmentation system are discussed in Sec. 5.0.

The control system is illustrated in Sec. 5.0. Aerodynamic coefficients are based on the gross wing plus tail planform area, root chord, or span,

where the wing area is 9,000 sq ft, the root chord is 157.58 ft and the wing span is 105.67 ft. A detailed geometric description of the airplane and definitions of nomenclature are given in Appendix A.

4.1 CONTROL AND TRIM

The flight control system of the B-2707 combines the pitch and roll controls on the horizontal tail for wings-back operation. For the more critical low speed, wings-forward operation, the horizontal tail controls provide pitch control only. A conventional aileron and spoiler system provides the powerful roll control needed for the demanding landing approach task. The low speed control arrangement is thus similar to that of current jet transports. The control ability to maneuver and trim the airplane is discussed in the following paragraphs.

4.1.1 Longitudinal Control

The airplane is controlled longitudinally during all-flaps-up flight by segmented elevator surfaces on the tail between the engine nacelles, operating with large tail tip elevon surfaces that share roll and pitch control functions when the wings are fully swept. For wings-forward flight, the full authority of the tip elevons is assigned to pitch control. For flaps-down flight, the pitch control is augmented by large upward-moving elevator surfaces above the engine nacelles.

The critical design requirements for sizing the longitudinal controls are the forward cg limits, takeoff rotation, landing configuration stall, and landing flare control. High speed maneuvering flight dictates hydraulic system hinge moment capabilities and tail structural torsion and bending stiffness. Takeoff rotation is aided by a unique landing gear design that incorporates a manifolding system to maintain equal oleo pressures between the front main and aft main gears during the initial rotation. The manifolding system moves the location of the equivalent single reaction force well forward of the aft gear, relieving the pitch control requirements, and simultaneously preventing an overloading of the aft main gear struts and tires. Additional low speed pitch control capability is considered desirable for takeoff and landing at extreme forward center-of-gravity conditions; means of improving the control, such

as control surface modifications and small retractable canard surfaces far forward, are being explored.

Current data indicate that greater high speed control capability is required. Longitudinal control capability is affected by the variation of aeroelastic effects, aerodynamic center, and zero lift pitching moment with Mach number, altitude, and wing sweep and by hydraulic control power. Continuous design refinement with emphasis on the judicious tailoring of these effects will lead to a greatly improved control capability.

4.1.1.1 Takeoff Rotation

Control requirements for takeoff rotation are compared with longitudinal control capabilities in Fig. 4-1. Airplane loading for the normal mission will place the takeoff center of gravity at 61-1/2 percent of the wing root chord (C_R). Takeoff rotation control is seen to be adequate to meet the 169-kn design liftoff speed at this loading condition for the maximum takeoff gross weight. The most critical loading condition for takeoff control is the extreme forward cg loading case where the cg can

be as far forward as 59-1/2 percent C_R ; however, for this case the fuel can be transferred from the forward auxiliary tanks to the aft auxiliary tanks before takeoff thereby locating the cg at 61-1/2 percent C_R . For takeoff at the forward cg limit, either increased takeoff speed or improved pitch control are required. A 5-kn speed increase plus a modest increase in control provide adequate rotation control at the forward loading condition (59-1/2 percent C_R). Wind tunnel testing has shown

that one way to achieve this increase in control effectiveness is by adding a 20 percent chord split flap to the elevator and deflecting the leading edge of the tip elevon up at 10 percent of the chord. Analyses also show that reducing takeoff wing sweep to 20 degrees would permit rotation for takeoff at the forward cg limit at 174-kn liftoff speed with existing control capability.

Approximate takeoff rotation time histories are shown for comparison purposes in Figs. 4-2 and 4-3. The time histories, as well as the rotation summary in Fig. 4-1, employ normal control rotation techniques. A 5-sec interval was maintained between the rotation and liftoff speeds, to

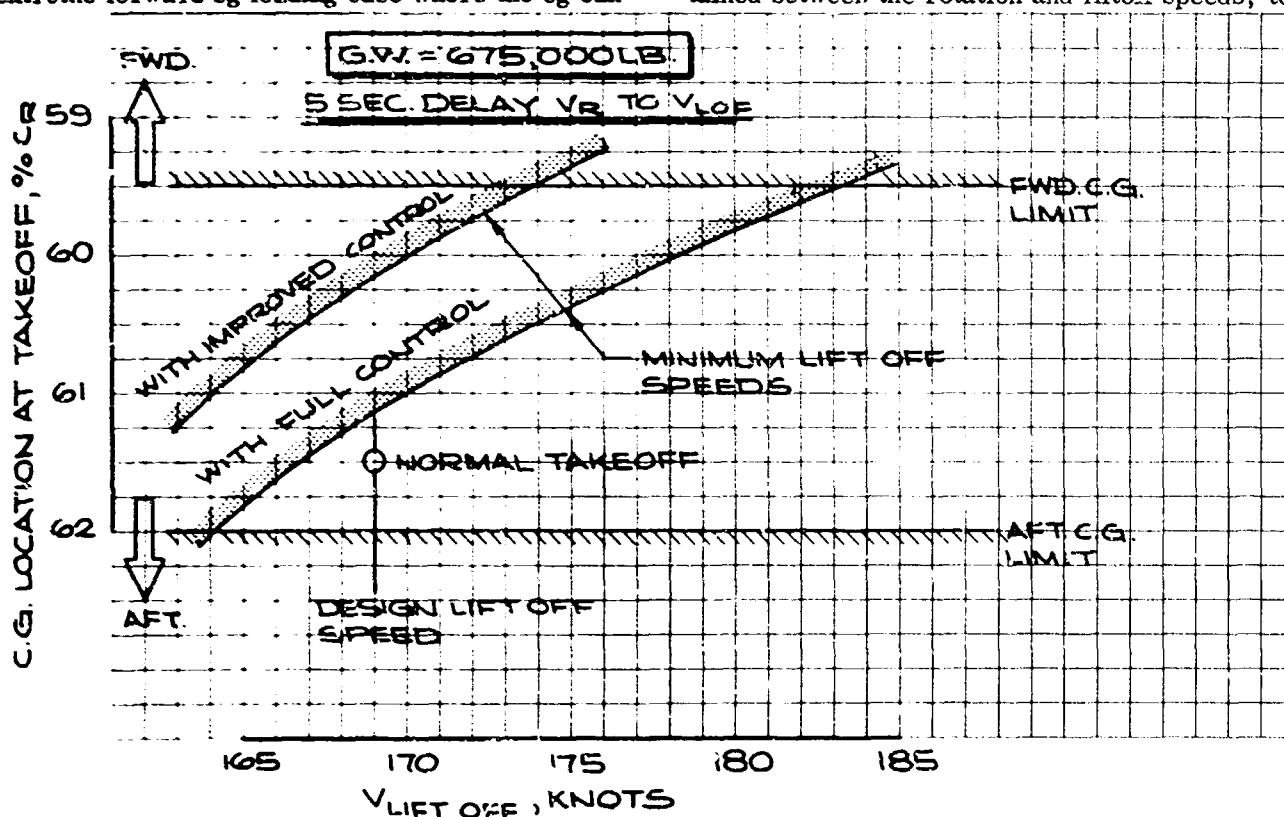


Figure 4-1. Takeoff Rotation Control Capability

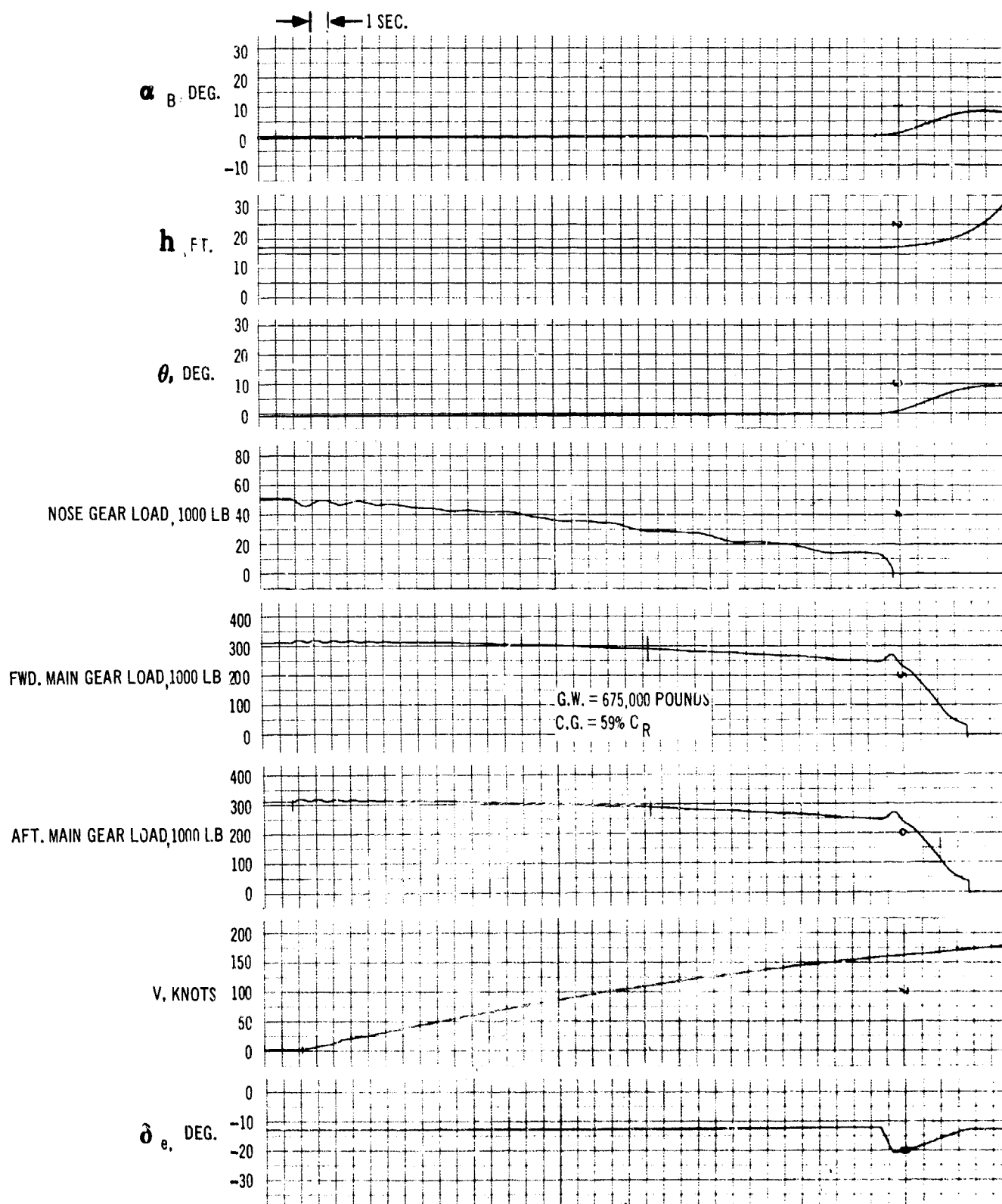


Figure 4-2. Takeoff With 4 Degrees Manifolded Main Gear

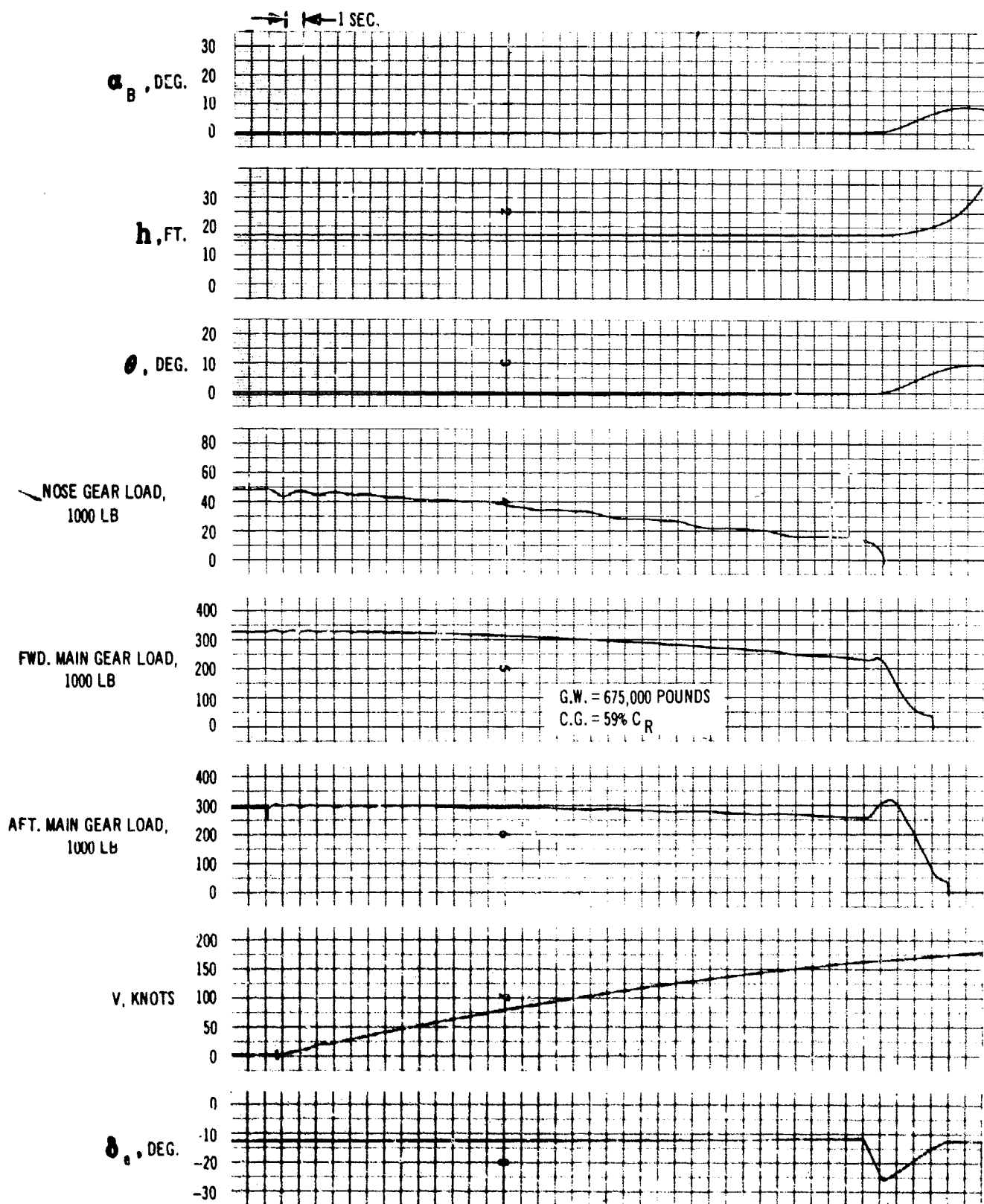


Figure 4-3. Takeoff Without Gear Manifold

V2-B2707-3

provide adequate time to allow an easily controllable pitch rate at the liftoff attitude; this eliminates any tendency for the pilot to overrotate or hunt for the desired attitude. A shorter time interval between liftoff and rotation speeds would require slightly less control for initial rotation, because of the higher dynamic pressure.

The effect of manifolding is illustrated by comparing Figs. 4-2 and 4-3. Manifolding reduces the amount of control required by 19 percent.

4.1.1.2 Landing Approach Control

Longitudinal control in the landing approach configuration is shown for two critical conditions in Fig. 4-4. Sufficient control is available to stall the airplane at forward cg, and to push over from well above the stall at aft cg. The nonlinear stability at high angle of attack shown in the figure is discussed in Par. 4.2. Longitudinal control in ground effect is shown in Fig. 4-5. Full nose up control remains adequate to compensate for the increased negative C_{M_0} in ground effect. The

24-ft cg height corresponds to the altitude just prior to touchdown. Little excess control power beyond trim is required in the landing flare because of the increase in total airplane lift from ground effect.

The variation of control moment with control deflection is shown in Fig. 4-6. Also included is the improved effectiveness due to the control, as discussed in Par. 4.1.1.1.

Landing flare capability has been evaluated to ensure that an adequate margin of control is available beyond normal static trim requirements. Time histories of landing flares are shown in Figs. 4-7 through 4-9 for normal and for very steep approaches. All flares were accomplished at the forward cg limit, using full elevator control. An unpiloted analog computer mechanization of the three longitudinal degrees of freedom similar to that employed in the takeoff rotation analysis was used to obtain the time histories. Aerodynamic characteristics in the simulation included the nonlinear influence of ground effect on lift, drag, and pitching moment, and gear reactions included damping and nonlinear spring rates. Satisfactory flare maneuvers were considered accomplished in the study when the following conditions were met at touchdown: sink rate was reduced to 2 to 4 fps, and the pitch rate and vertical acceleration were near zero. Flares shown in Figs. 4-7 and 4-8 were made with

throttle setting held at the level required to maintain the approach flight path before flare initiation. At a cg height of 25 ft thrust was reduced to zero. The thrust reduction, with accompanying speed loss, was used to simulate the most severe flare maneuver from the standpoint of control input. Flare from a normal 3-degree glide slope (Fig. 4-7) required a small nose up command to initiate the flare, followed by an increasing control deflection to counter the nose down moment from ground effect. Flares initiated from a high sink rate (Fig. 4-8) required more pitch command in the early part of the flare. The normal flare technique of adjusting thrust during the flare to maintain constant speed was employed for the time history in Fig. 4-9. This resulted in less pitch attitude buildup during the flare, and was accomplished with reduced control deflection.

Longitudinal control developed by the current wind tunnel model is marginal for landing flare; however, the control modifications discussed above, or a reduction in wing leading edge sweep to 20 degrees for landings, would provide a large margin of control for maneuver and flare.

Improved low speed pitch response is possible through the use of direct lift control. The B-2707 geometry is compatible with such a development.

The recent U. S. Navy tests using wing flaps for direct lift control on an F-8 airplane have shown marked improvement in pilot opinion of flying qualities and precision in accomplishing the very demanding carrier landing task. These results encourage applying direct lift control to the B-2707 or other large transport airplanes to improve landing approach and flare path control.

The data of Fig. 4-10, obtained during flap development testing, indicate the incremental lift that is readily obtainable. More important for direct lift consideration, the pitching moment curves indicate that the downwash change at the tail with flap deflection produces nearly complete self-trimming.

An alternate means of direct lift control would be to use symmetric spoiler deflection about some partially deflected position. Some preliminary experimentation has already been done by NASA Ames Research Center on the use of spoilers for direct lift control on a large subsonic transport, both in ground-based simulation and in actual flight. The results were promising. Figure 4-10

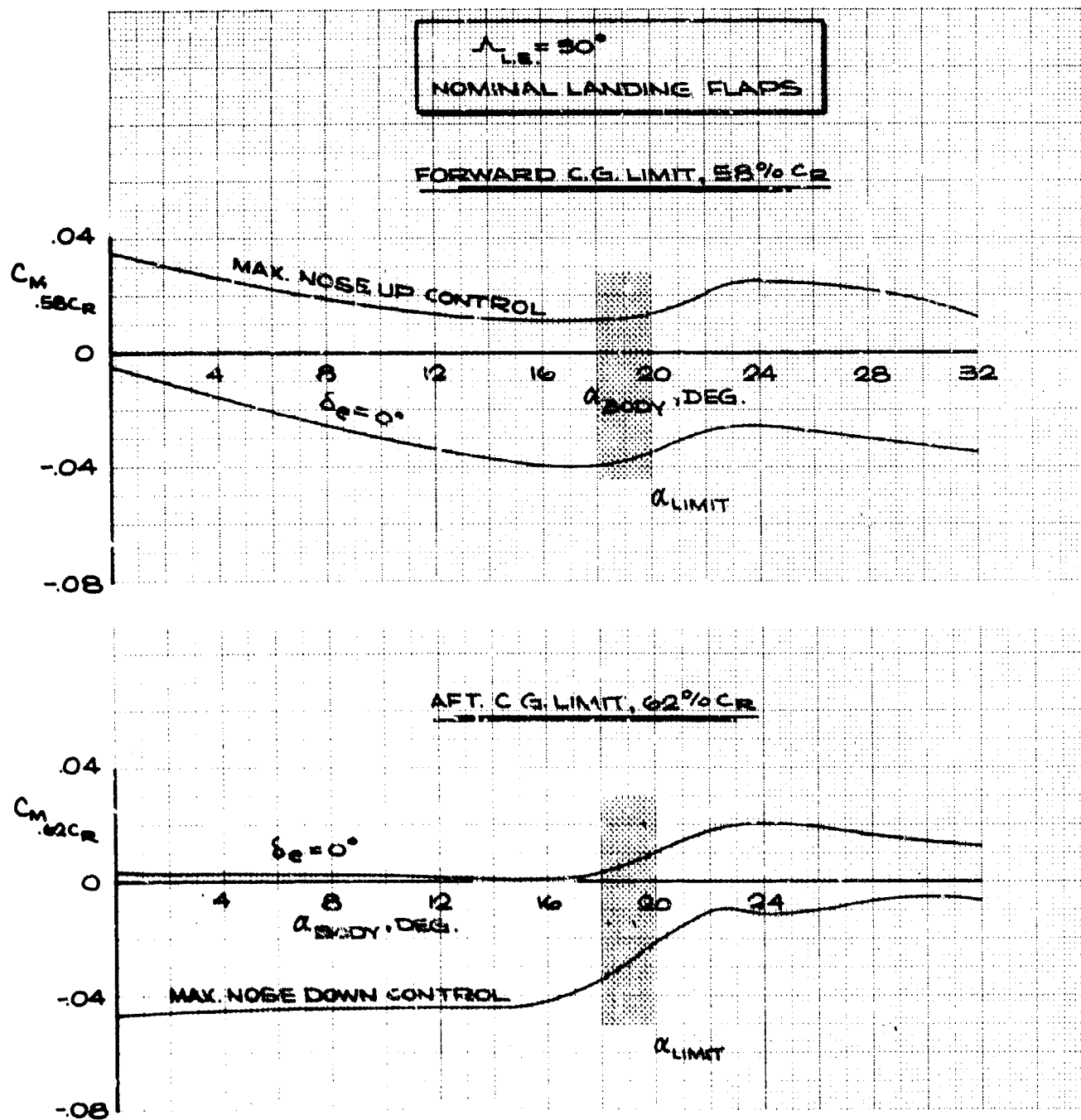


Figure 4-4. Landing Control, No Ground Effect

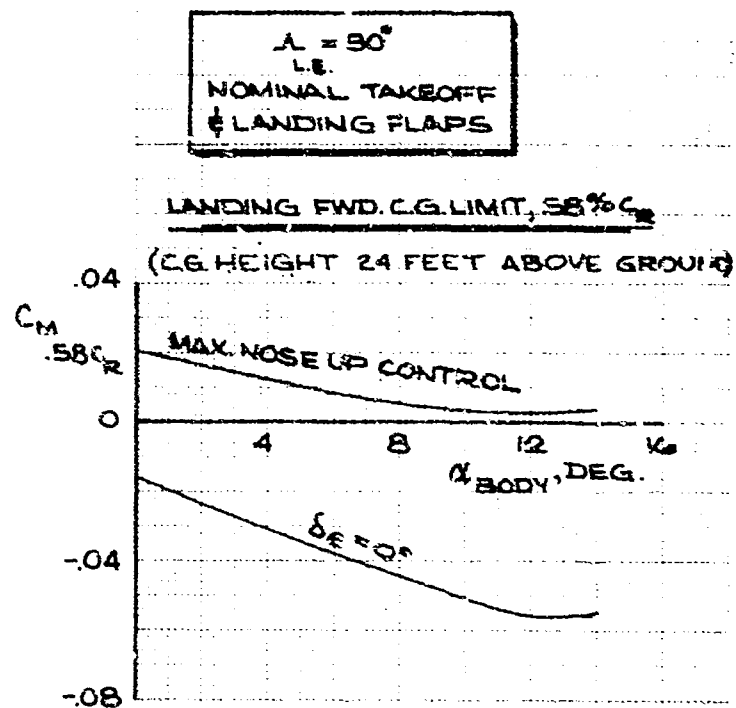


Figure 4-5. Landing Control, In Ground Effect

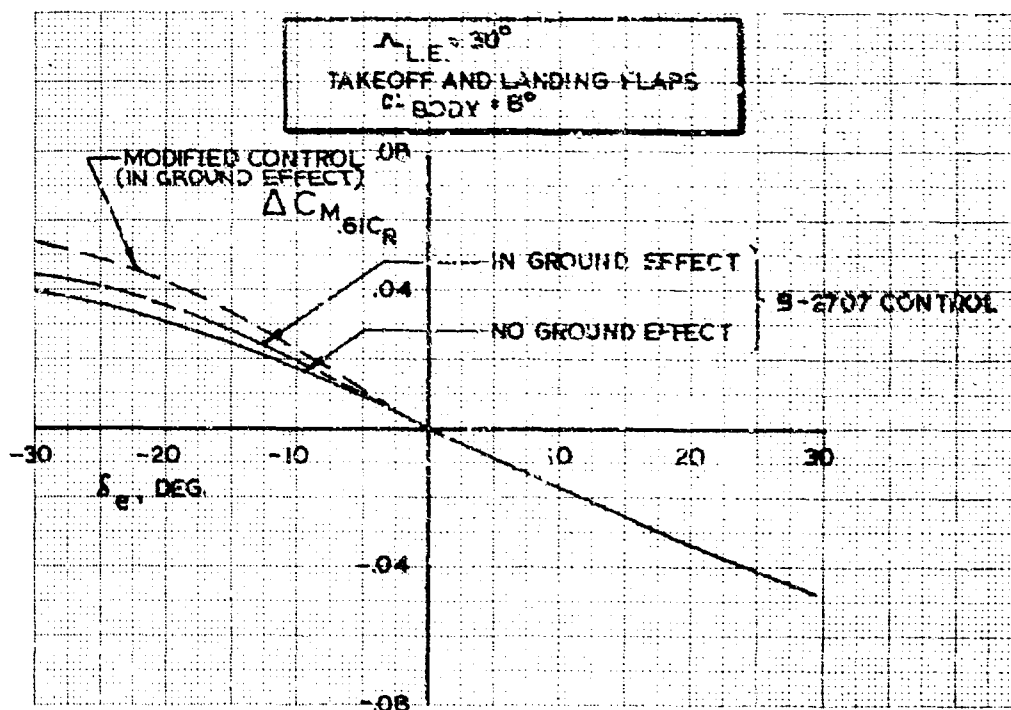


Figure 4-6. Low Speed Control Power

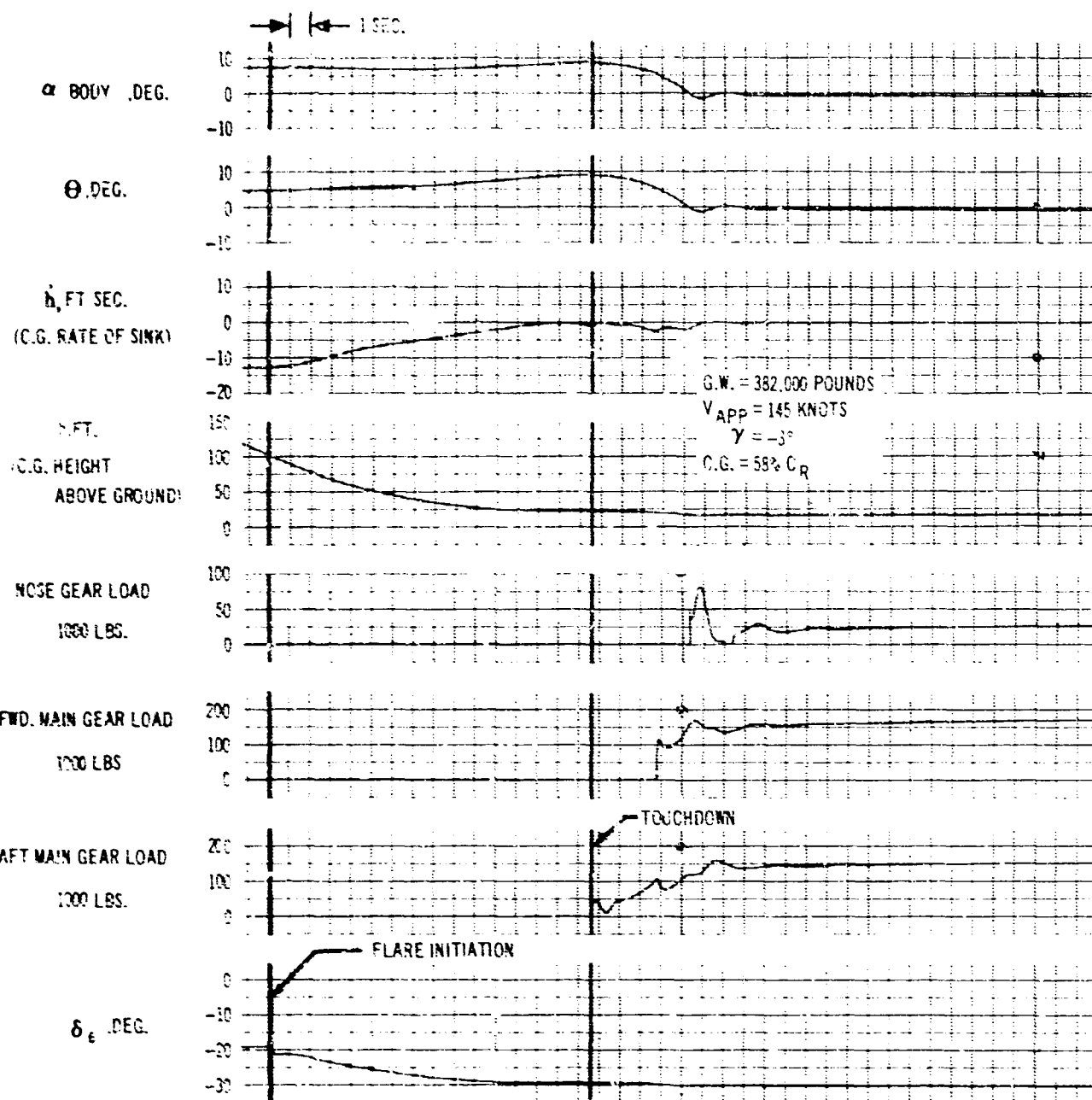


Figure 4-7. Landing Flare From Normal Approach

V2-B2767-3

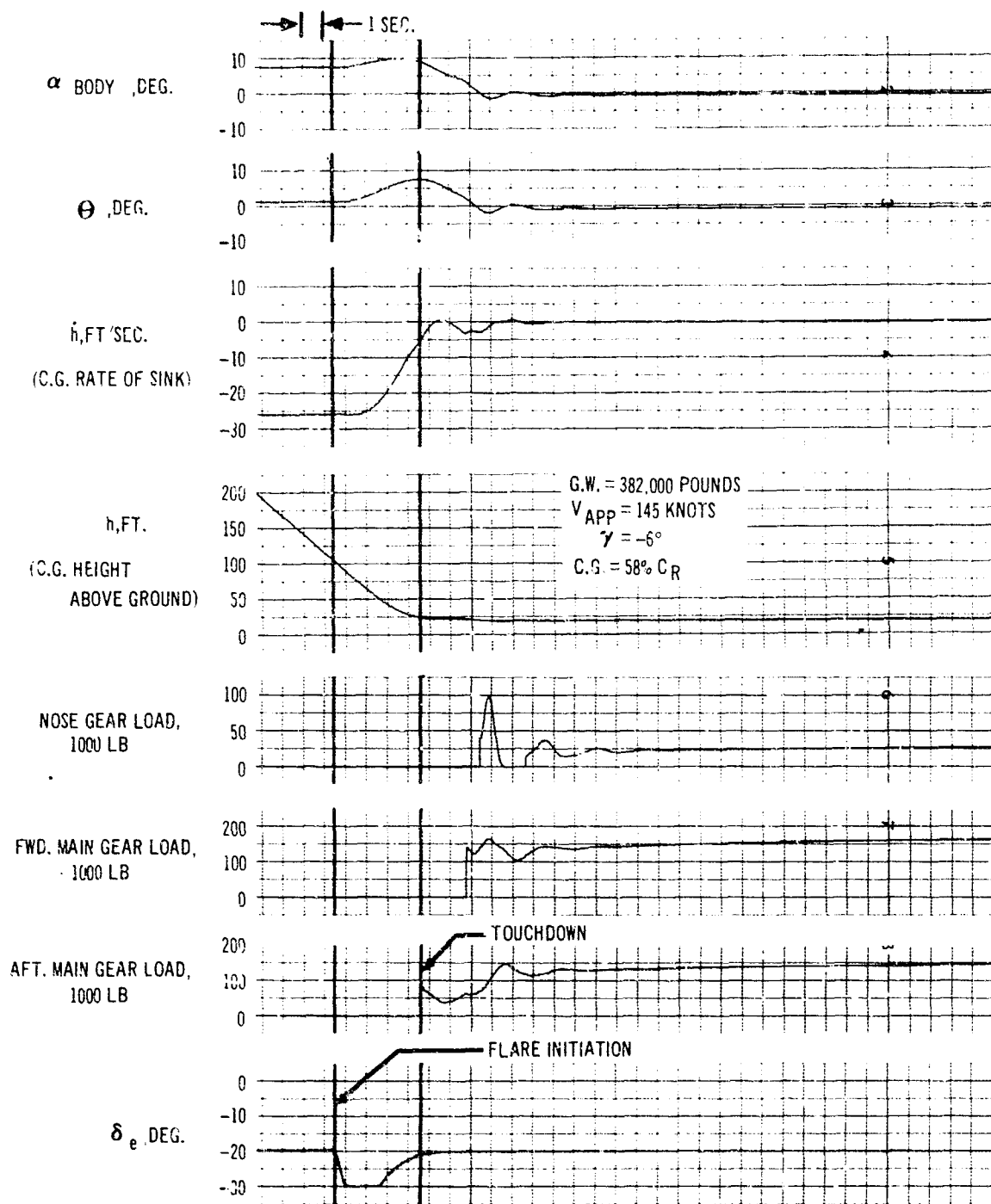


Figure 4-8. Landing Flare From Steep Approach

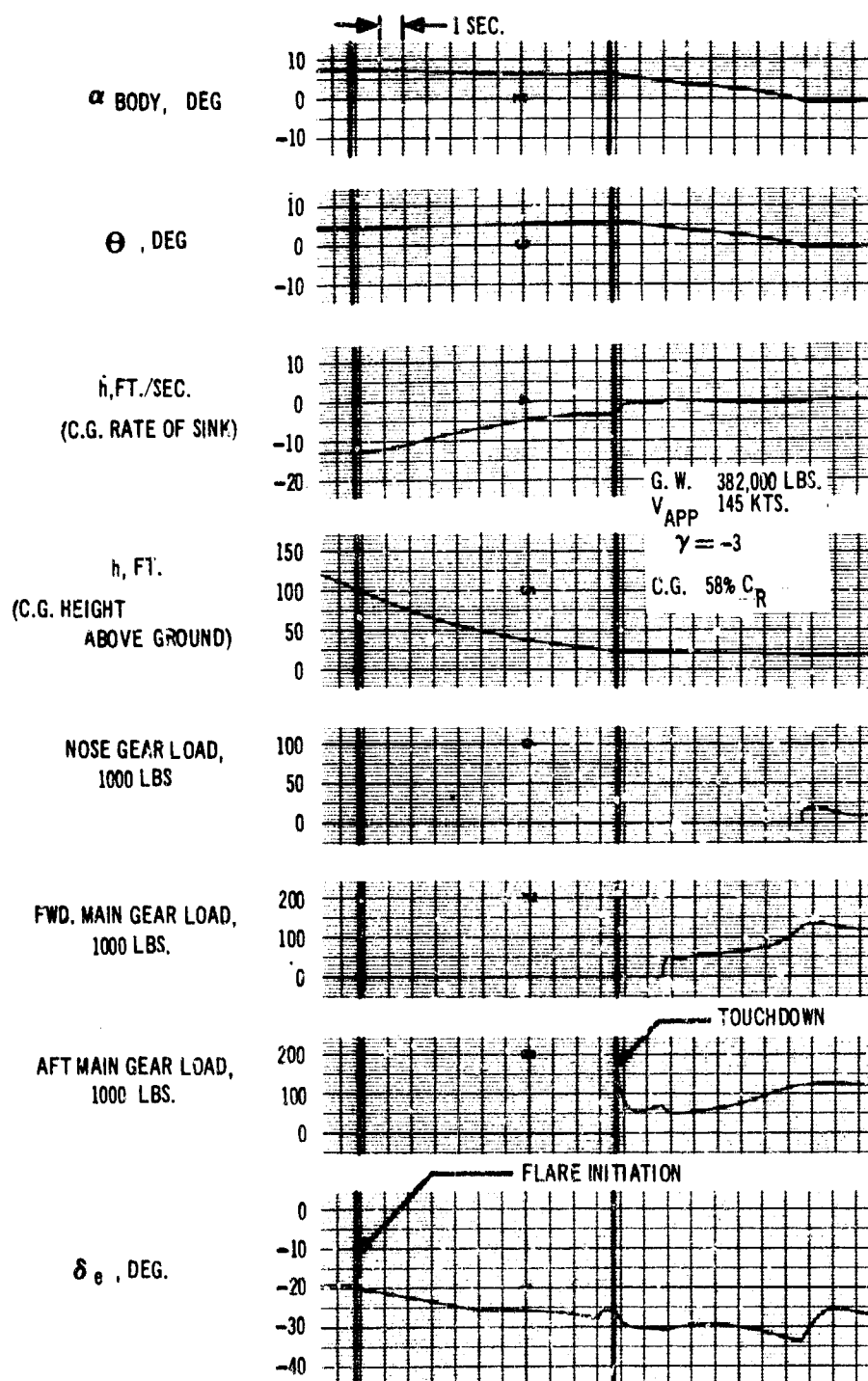


Figure 4-9. Landing Flare From Normal Approach, Constant Speed

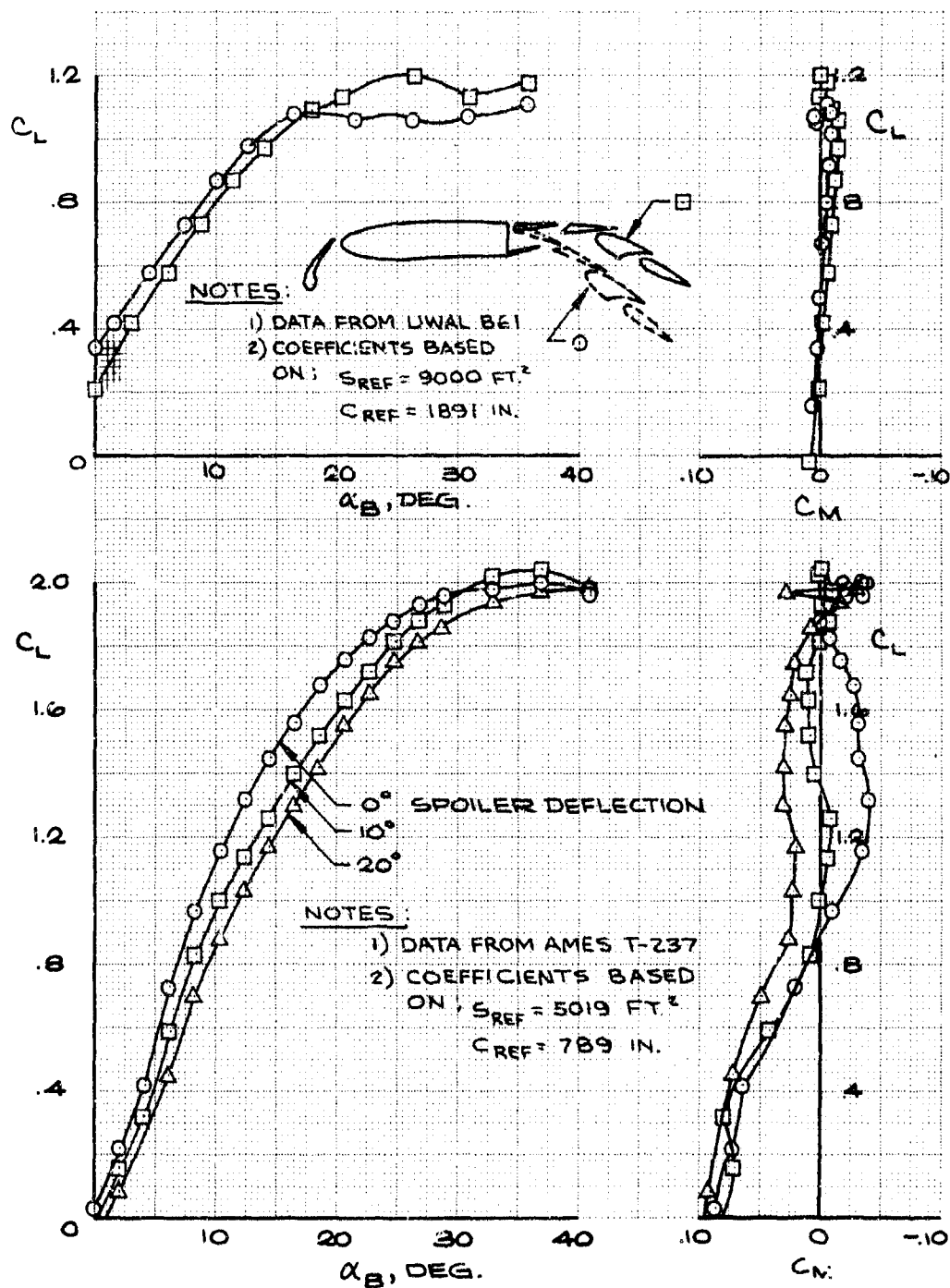


Figure 4-10. Effect of Spoiler and Flap Deflection on Lift and Trim

shows small spoiler deflection effects on an earlier SST configuration taken from large scale tests in the Ames Research Center 40-ft by 80-ft wind tunnel. Adequate lift increments for direct lift control are obtainable with moderate spoiler deflections, and the pitching moments are within the capability of a reasonable trim interconnect gearing. Direct lift control is being studied for the B-2707 as a possible improvement.

4.1.1.3 Low Speed Control, Flaps Up
Flaps up longitudinal control, Fig. 4-11, is adequate to stall the airplane at forward cg and push over from stall at aft cg. The moderate instability shown at aft cg is discussed in Par. 4.2. Longitudinal control for wings aft landing is shown in Fig. 4-12.

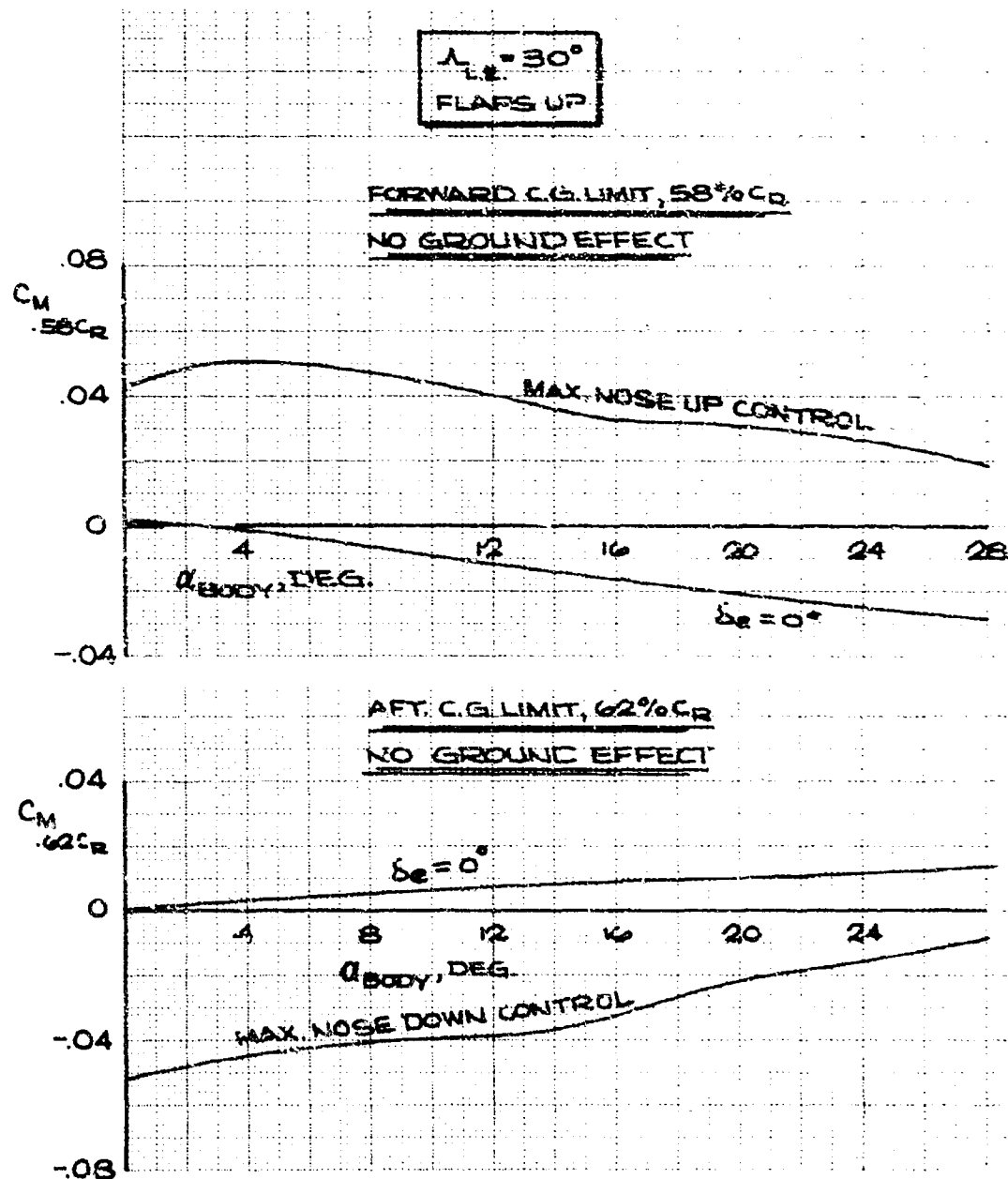


Figure 4-11. Low Speed Control, Flaps Up

V2-B2707-3

Table 4-A. Low Speed Trim Changes

Initial Trim Conditions				Configuration Change	Parameter Held Constant	$\Delta \delta_c$ Trim Change Degrees	
Configuration	Speed, Knots	Power	Flaps			Forward C.G. .58 C _R	Aft. C.G. .62 C _R
Maximum Landing Weight $\Lambda = 30^\circ$	1.4 Vs 189.5	Off	Up	Extend Landing Flaps	1.4 Vs	-10.4	-1.5
	1.4 Vs 157.0	Off	Takeoff Flaps	Retract Flaps	1.4 Vs	+10.4	+1.5
	1.4 Vs 189.5	Off	Up	Max. Aug. T.O. Power	1.4 Vs	+ 2.0	+2.0
	1.4 Vs 157.0	Off	Landing Flaps	Max. Aug. T.O. Power	1.4 Vs	+ 2.5	+2.5
	1.4 Vs 157.0	Off	Landing Flaps	Gear Down	Speed	Negligible	
	1.3 Vs 145.8	Off	Landing Flaps	Max Dry Thrust-Flaps Up, Max. L/D	Altitude	+12.2	+3.5
	1.4 Vs 157.0	Off	Landing Flaps	Speed Change To 1.1 Vs (123. KTS)	Altitude	- 5.4	-1.25
	1.4 Vs 157.0	Off	Landing Flaps	Speed Change To V _{F.E.} (195. KTS)	Altitude	+ 5.9	+0.25
G.W. = 627,000 LBS $\Lambda = 30^\circ$	1.4 Vs 230.0	On	Up	Sweep Wing To $\Lambda = 72^\circ$	Maintain Climbout Acceleration ($\Delta V=115. KTS$)	0 (C.G. At .59 C _R)	-2.5

4.1.1.4 Low Speed Trim Changes

Elevator deflections measured from initial trim required to control significant configuration changes are presented in Table 4-A. The trim changes are small for all conditions except those involving wing flap retraction or extension. Elevator trimming with flap actuation will be gradual due to the slow rate of operation for the flaps. No control force changes will be felt by the pilot because of the automatic trim feature in the stability augmentation system.

4.1.1.5 Flight Envelope Trim Requirements

The control surface deflections required to trim the airplane in steady level flight are shown in Fig. 4-12 for climb, V_{MO} descent and dive conditions throughout the flight envelope. Control

deflections for the elevator and tip elevon surfaces are shown at forward and aft center of gravity limits and also for the normal cg variations experienced during flight. The required trim

angles are moderate for all except transonic conditions at forward cg's where stability margins and C_{M_0} 's are at their maximum levels. Studies

are in progress to tailor the C_{M_0} variation with

Mach number to minimize the trim requirements at all conditions. These studies include experimentation with body shape variation, wing twist and camber, strake fairing, and the effects of a small canard trimming surface.

The control requirements for trim and maneuver shown herein are based on wind tunnel test data and not on tests of the models submitted for FAA evaluation. No accounting has been made for model control surface flexibility although subsequent analysis indicates that the effects of model flexibility may be significant. Estimates of control surface effectiveness based on these results may be somewhat conservative.

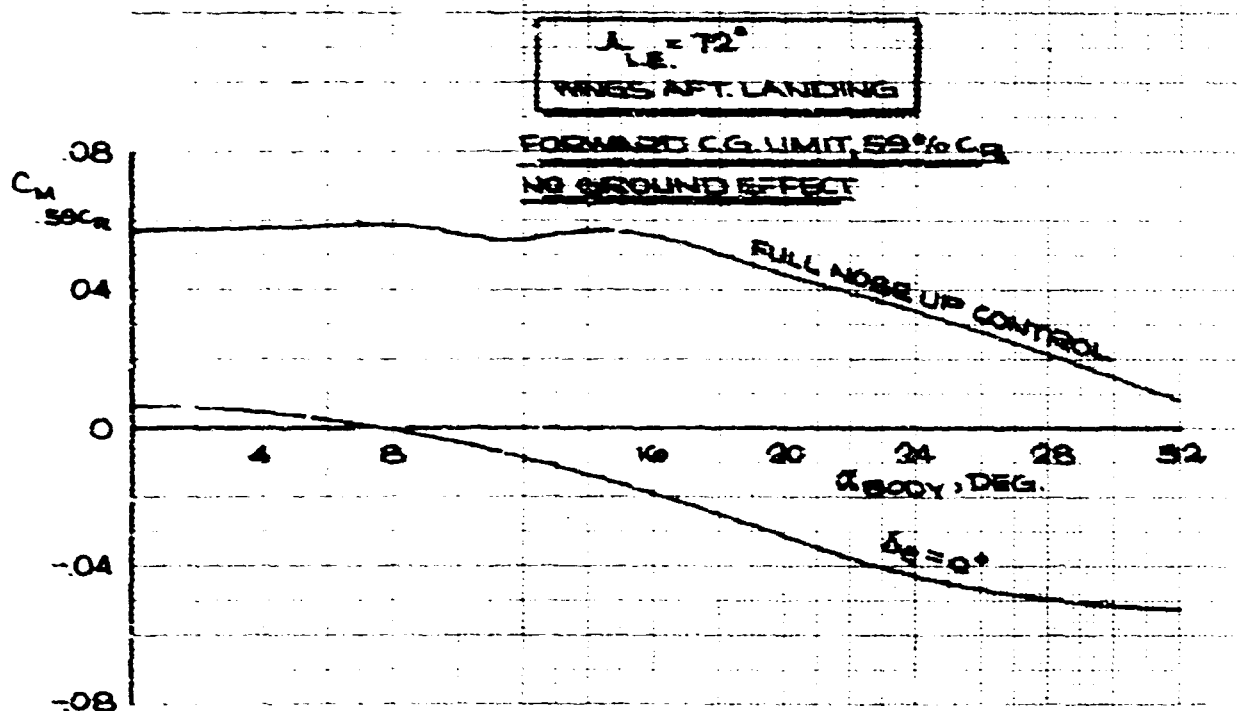


Figure 4-12. Low Speed Control, Wings Aft Landing

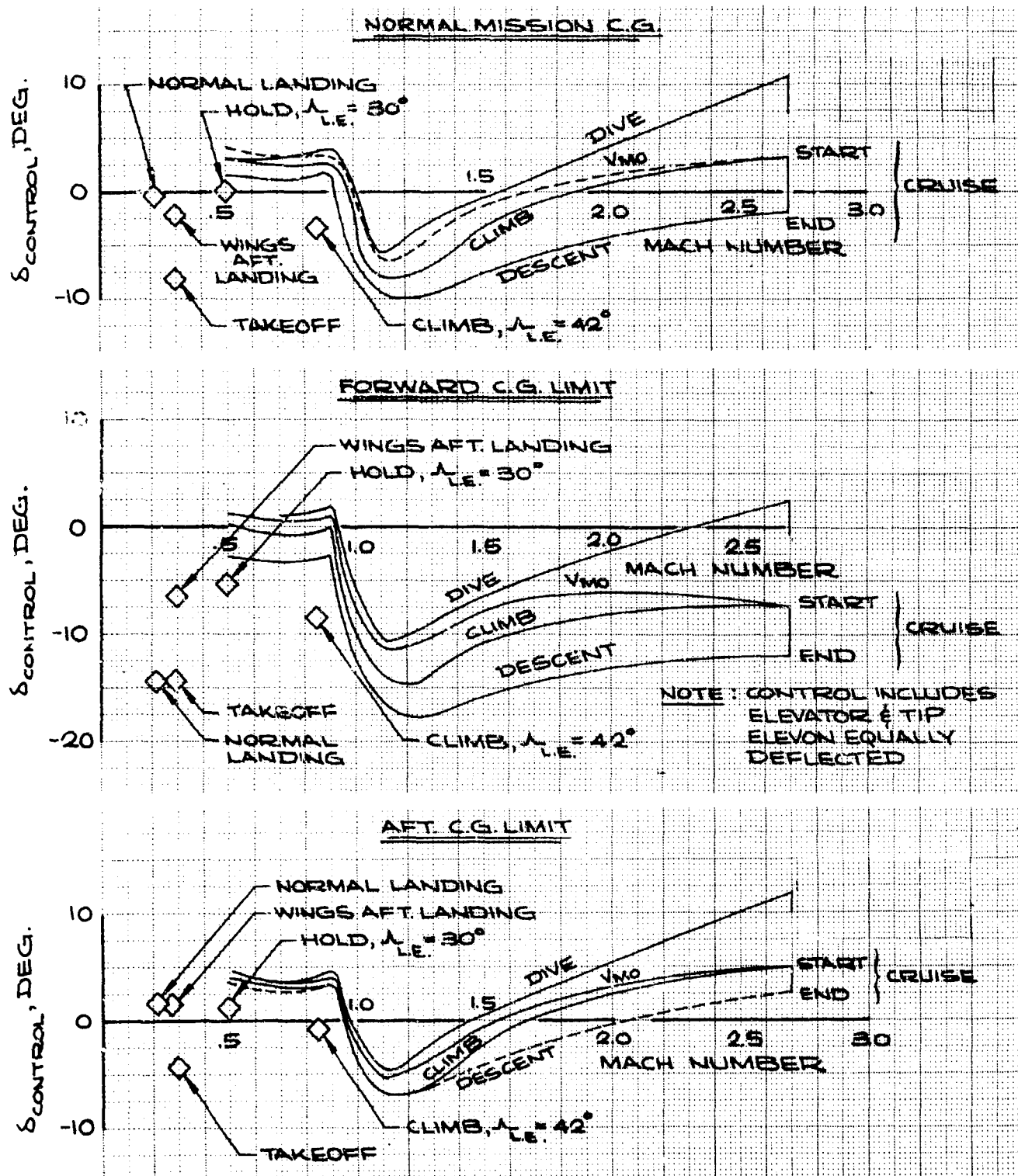


Figure 4-13. Longitudinal Trim Characteristics

The method of determining the control surface trim angles is as follows:

$$\delta = \frac{\Delta C_{M_{C.G.}}}{\left(C_{M_{\delta}} \right)_{\text{flexible}} \text{ constant } C_L} \quad \text{where,}$$

$$\left(C_{M_{\delta}} \right)_{\text{const. } C_L}^{\text{flex.}} = \left(C_{M_{\delta}} \right)_{\text{const. } \alpha}^{\text{rigid}} \left(\frac{M_E}{M_R} \right)_{\delta} + \left(C_{L_{\delta}} \right)_{\text{rigid}} \left(\frac{L_E}{L_R} \right)_{\delta} (X_S - .64),$$

$$X_S = X_{a.c.} \text{ (rigid aerodynamic center)} + \Delta X_{a.c.} \text{ (flexibility effect),}$$

$$\left(\frac{M_E}{M_R} \right)_{\delta} = \left(\frac{C_{M_{\delta}}}{C_{M_{\delta}}} \right)_{\text{flex.}}^{\text{flex.}}, \left(\frac{L_E}{L_R} \right)_{\delta} = \left(\frac{C_{L_{\delta}}}{C_{L_{\delta}}} \right)_{\text{flex.}}^{\text{flex.}} \text{ and}$$

$$\begin{aligned} \Delta C_{M_{C.G.}} = & \Delta C_M [\text{at flight } C_L \text{ from pitching} \\ & \text{moment data at mean reference point} \\ & - C_{L_{\text{flight}}} (.64 - X_{C.G.})] + \Delta C_{M_O} \\ & \text{(flexibility correction on } C_M \text{ at } C_L = 0) \\ & + \Delta C_M \text{ (flexibility corrections on aero-} \\ & \text{dynamic center)} + \Delta C_{M_{\text{thrust}}} \end{aligned}$$

The rigid aerodynamic centers, aeroelastic corrections, and thrust effects employed in the above calculations are presented in Par. 4.2.1.

The trim control requirements versus Mach number in Fig. 4-13 show negative speed stability (control versus M or V) for transonic operation. Acceptable control force versus speed characteristics will be provided throughout the flight envelope by the longitudinal stability augmentation system.

4.1.1.6 Maneuver Capability

The ability of the airplane to develop positive load factor is shown in Fig. 4-14. Good maneuver capability is seen to exist when operating at normal mission center of gravity. The airplane is capable of developing load factor in excess of the 2.5 g structural limit for most flight conditions. At forward cg's, however, the maneuver load factor capability shown is considered marginal, and will improve through the development refinement (Par. 4.1.1). Boeing flight simulator studies indicate requirement for 2.0 to 2.5 g load factor capability at maximum dive speeds for recovery from upset maneuvers. Consideration is also given to operating with failed hydraulic systems, where hinge moment limitation on control deflections will further restrict maneuverability, as discussed in Par. 4.5.

Studies are in progress to expand the longitudinal maneuver capabilities of the airplane considering both the normal operation and flight with single or dual hydraulic system failures. This work will investigate C_{M_O} tailoring and elimination of

control deflection restrictions imposed by large aerodynamic hinge moments and hydraulic power limitation.

Longitudinal control surface effectiveness is summarized in Figs. 4-15 through 4-21; aeroelastic corrections are shown in Par. 4.2.1. The following method is used to compute maneuver capability:

$$\frac{d\delta}{dn} = \frac{C_{L_{\text{trim}}} (X_M - X_{C.G.})}{\left(C_{M_{\delta}} \right)_{\text{flexible}} \text{ constant } C_L} \quad \text{where}$$

X_M = flexible airplane maneuver point, and

$$\begin{aligned} \left(C_{M_{\delta}} \right)_{\text{const. } C_L}^{\text{flex.}} &= \text{flexible control parameter} \\ &= \left(C_{M_{\delta}} \right)_{\text{const. } \alpha}^{\text{rigid}} \left(\frac{M_E}{M_R} \right)_{\delta} \\ &+ \left(C_{L_{\delta}} \right)_{\text{rigid}} \left(\frac{L_E}{L_R} \right)_{\delta} (X_M - .64) \end{aligned}$$

Maneuver capability equations continued on next page:

Maneuver capability equations concluded

$$\Delta n = \frac{(\Delta \delta)_{\text{effective}}}{\frac{d\delta}{dn}} \quad \text{where}$$

$$(\Delta \delta)_{\text{effect.}} = K_3(\Delta \delta)_{\text{tip elevon}} + K_4(\Delta \delta)_{\text{elevator}}$$

$$\text{and } (\Delta \delta)_{\text{tip elevon or elevator}} = \delta_{\text{available}}$$

(maximum deflection available as limited by hinge moments) - δ_{trim}

4.1.2 Lateral Control

A conventional aileron and spoiler system is used for roll control during wings-forward, flaps-down flight. The ailerons are phased out as wing flaps are retracted, and tail tip elevons are partially phased in. At low and intermediate sweep conditions, flaps up, roll control is provided by the segmented wing spoiler system and partial tip elevons. As the wings are swept aft, the outboard wing spoilers lose effectiveness and the tail tip elevon surfaces are phased fully into the lateral control system. The outermost wing wing spoiler segments are simultaneously phased out as lateral controls. The roll control system at wing sweep 72 degrees consists of the tip elevons, which also retain a longitudinal control function, and the four most effective wing spoiler segments. The large tip elevon surfaces provide between 75 percent and 90 percent of the effective rolling moment of the total lateral system. A mechanical rudder interconnect is incorporated into the design, operating with the elevons at all flaps-up conditions to minimize the adverse yaw characteristics of the elevons. The wing spoilers augment the elevon rolling moments and also reduce the adverse yaw effects of the roll control system. The pitch effects of both spoiler and elevons are negligible. Phasing of the various

elements in the lateral control system and the rudder interconnect are described in Sec. 5.9. Airplane dynamic response to roll control inputs and cross-coupling characteristics are discussed in Pars. 4.3 and 4.4 of this section.

4.1.2.1 Roll Performance

The lateral control surfaces have been sized to satisfy the roll control performance requirements developed in the Phase II-C studies. Figure 4-22 shows that the roll performance for coordinated (single degree of freedom) rolls meets the proposed requirements for representative flight cases which encompass the airplane's flight regime. The plot is in the form of maximum steady state roll rate attainable versus bank angle obtainable in 1 sec after application of full wheel by the pilot, using maximum lateral control deflections available from the 1g trim setting. Control surface rates are the maximum design values for all hydraulic systems operating. The airplane roll time constant which indicates the dynamic characteristics of the roll response is noted for each flight case. Long roll time constants, in excess of 2.0 sec, are typical at transonic and supersonic flight conditions for the unaugmented airplane. Roll response augmentation (Par. 4.3) is incorporated to improve roll damping and reduce overshoot to obtain satisfactory handling qualities at all flight conditions. At subsonic conditions, the variable sweep concept inherently provides short roll time constants and good control response characteristics.

For flight at high load factor conditions, pitch control authority for the elevons can restrict the available deflection for roll control. Figure 4-23 shows single degree of freedom rolls for the eight standard flight conditions for the airplane in a 1g maneuver ($n = 2$); at low speed where $n = 2$ is not possible, the case chosen is the stall. All conditions satisfy the emergency boundaries. Flight simulator testing will be conducted to evaluate roll performance in high-g maneuvers.

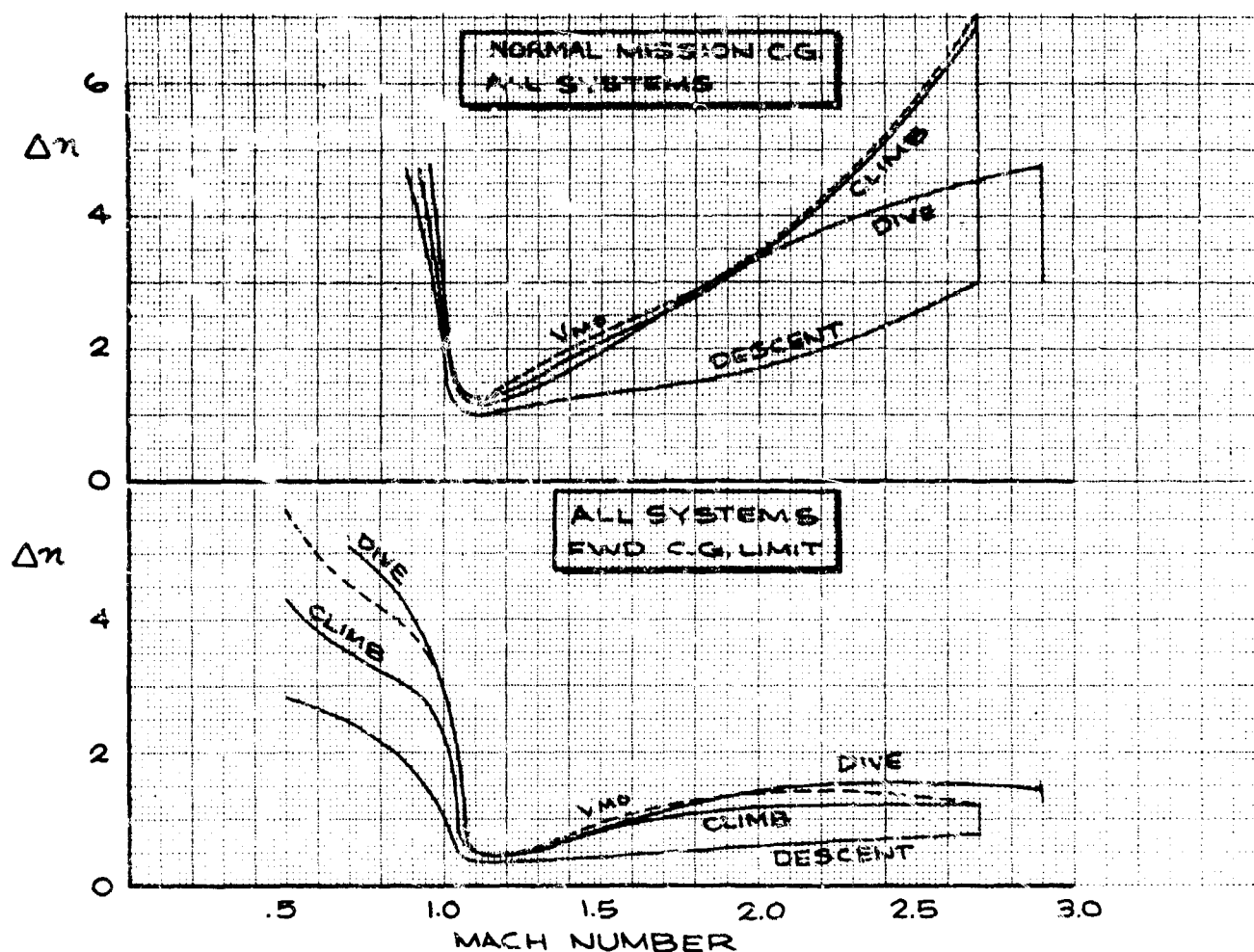


Figure 4-14. Maneuver Capability

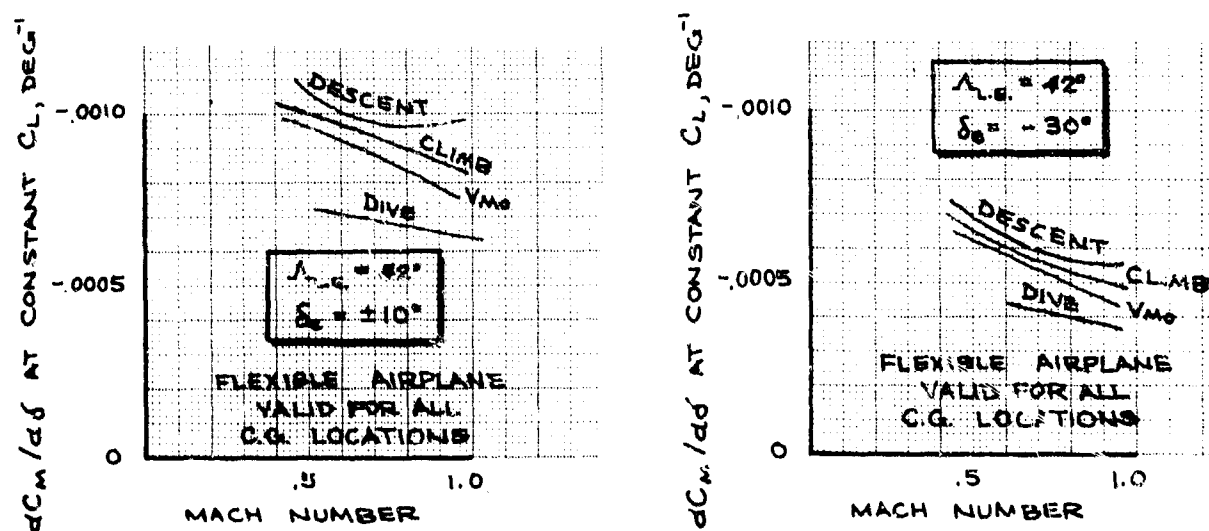


Figure 4-15. Longitudinal Control Effectiveness, $\Lambda = 42$ Degrees

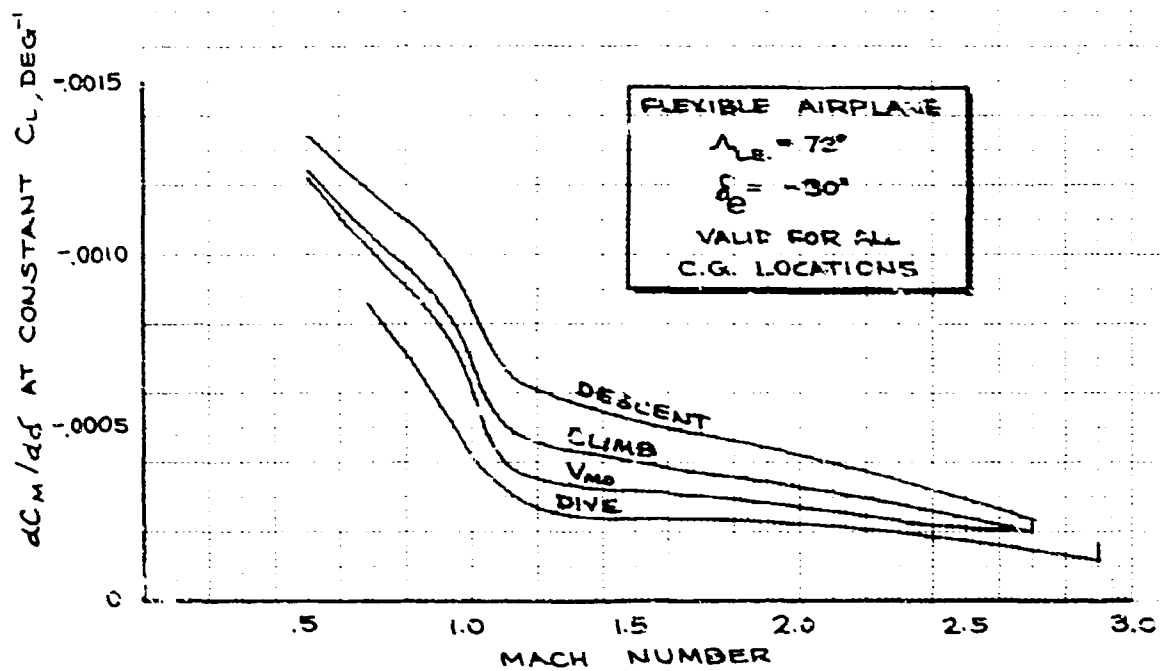
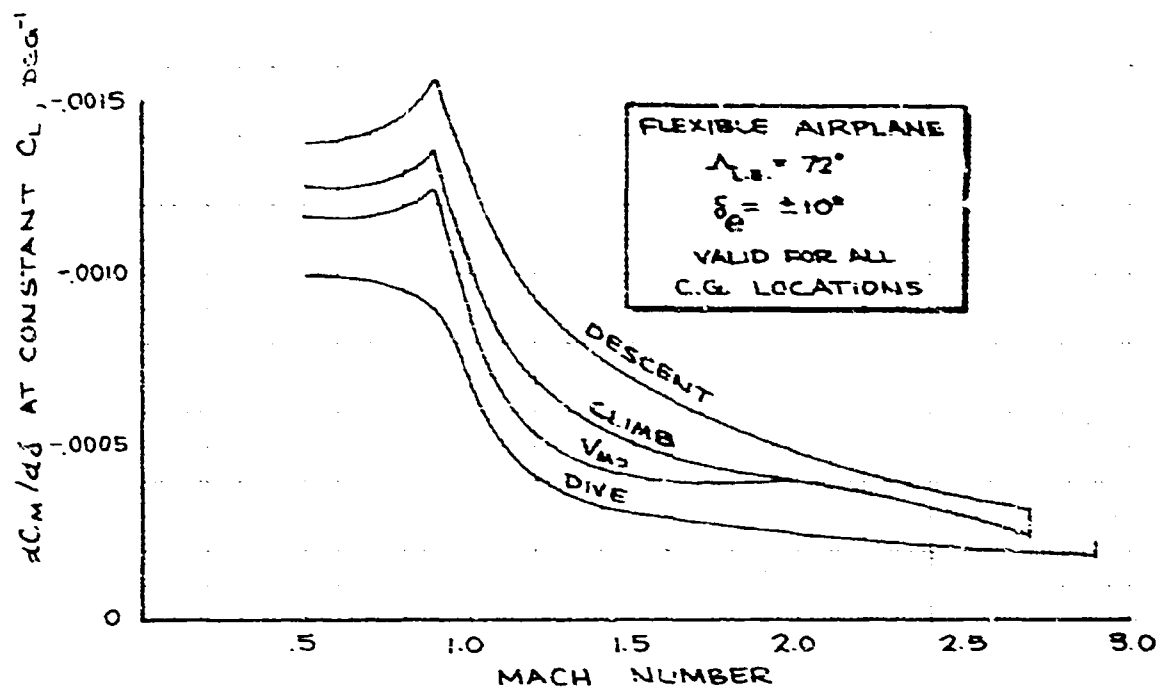


Figure 4-16. Longitudinal Control Effectiveness, $\Lambda = 72$ Degrees

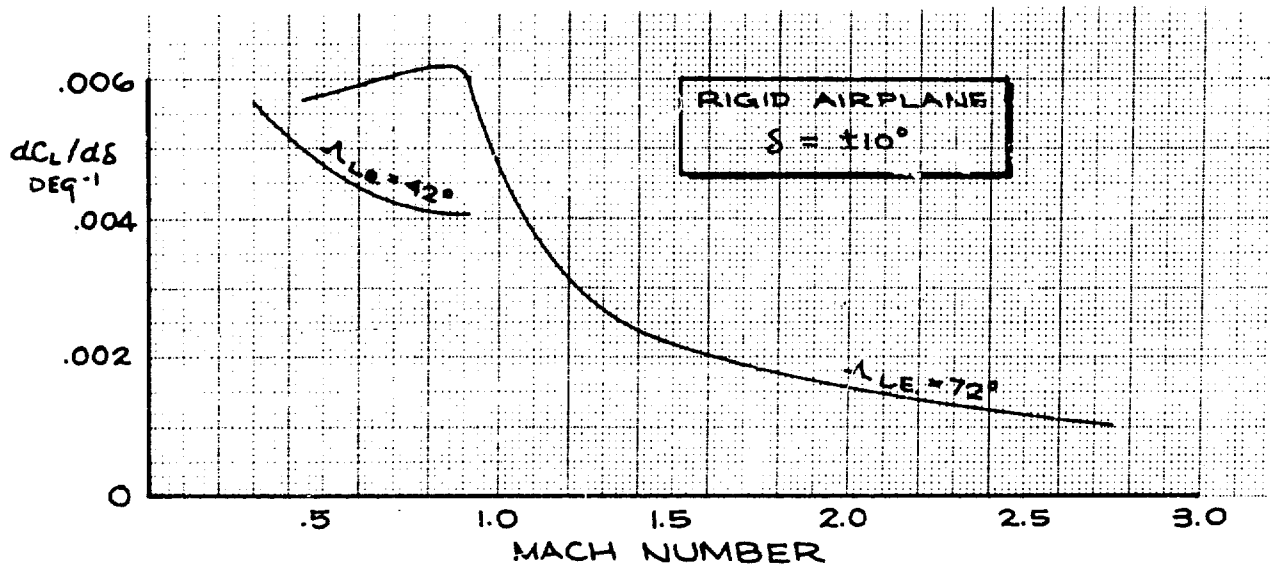
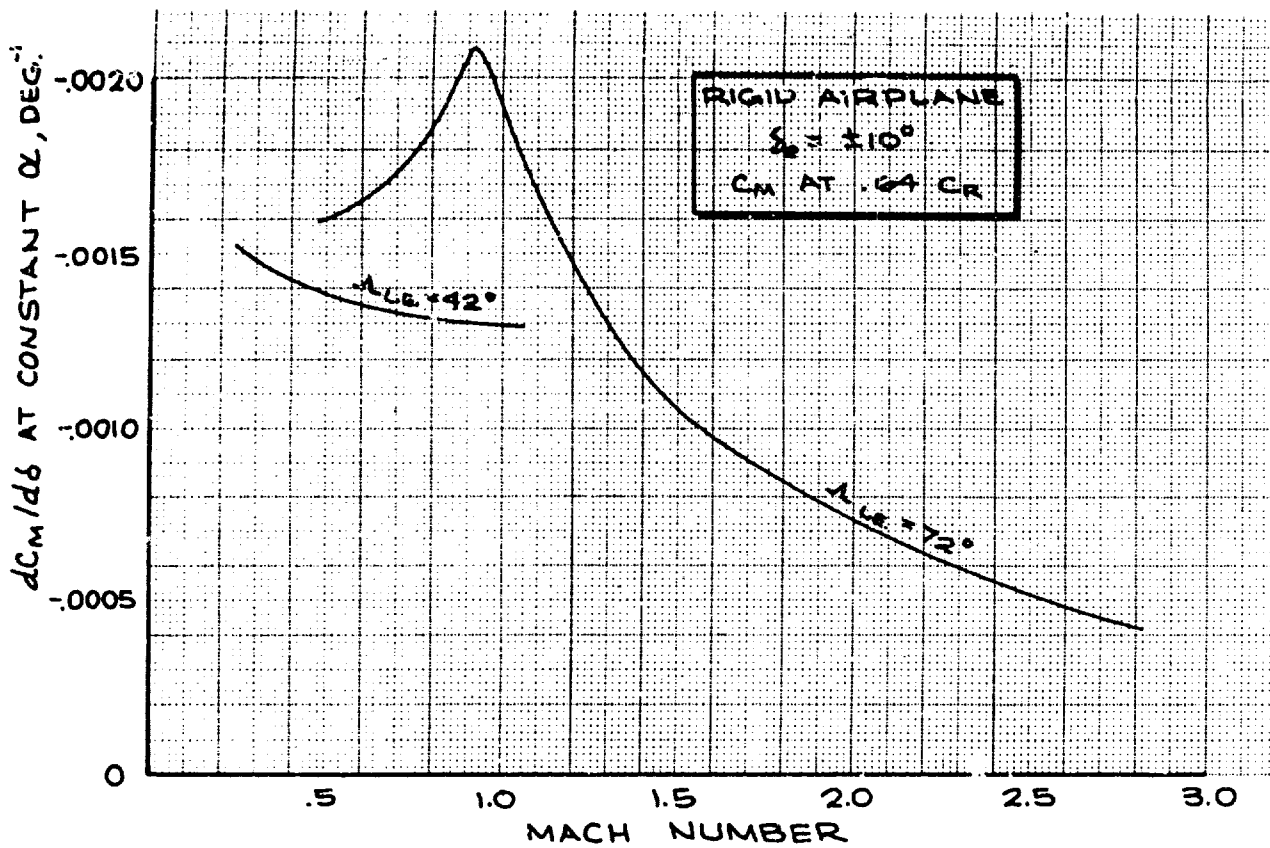


Figure 4-17. Longitudinal Control Effectiveness , Trim, Rigid Airplane

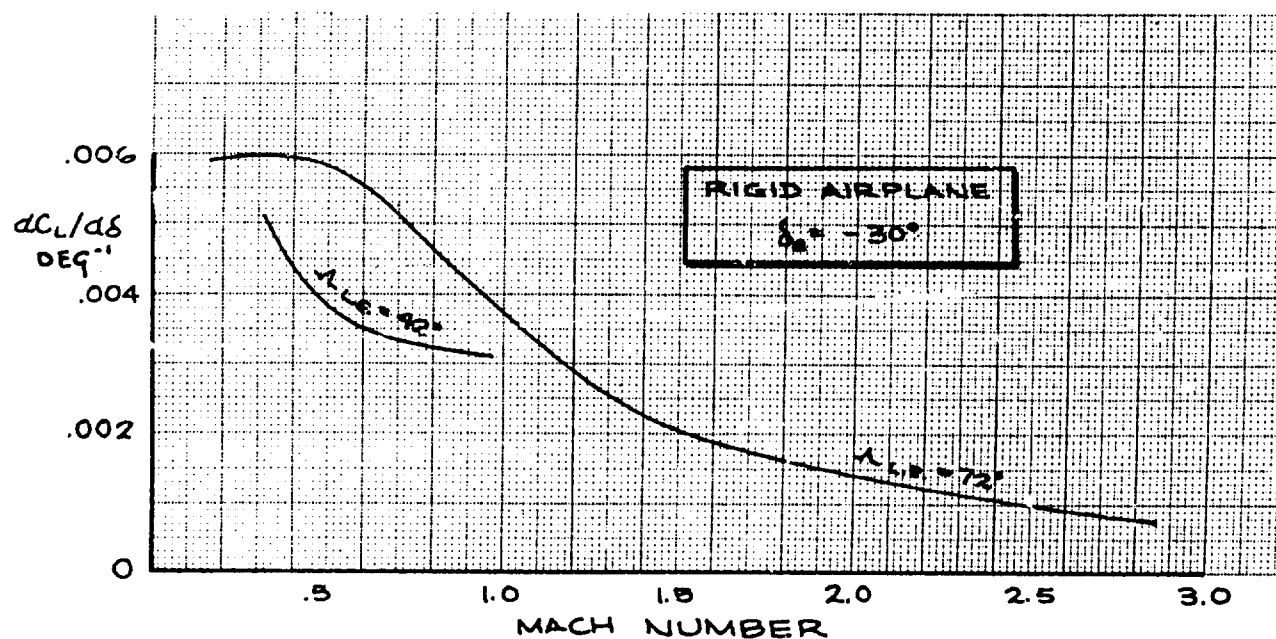
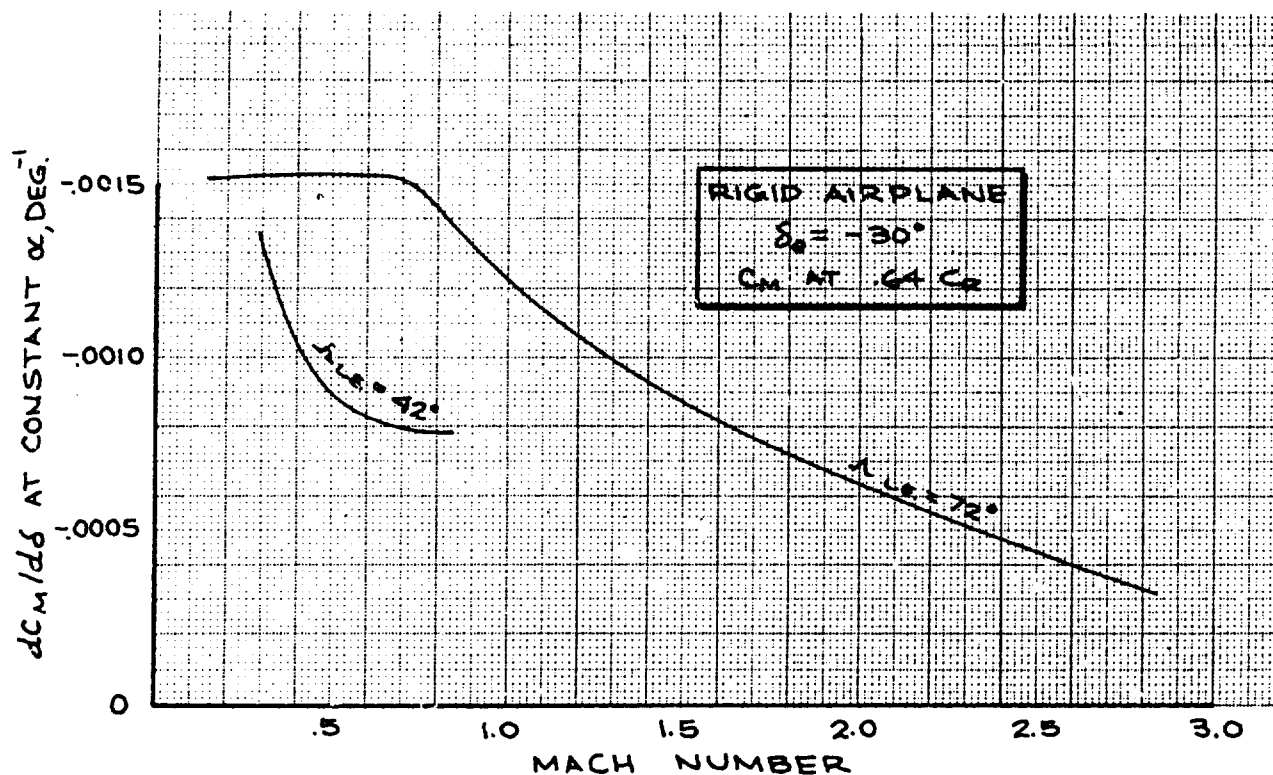


Figure 4-18. Longitudinal Control Effectiveness, Control, Rigid Airplane

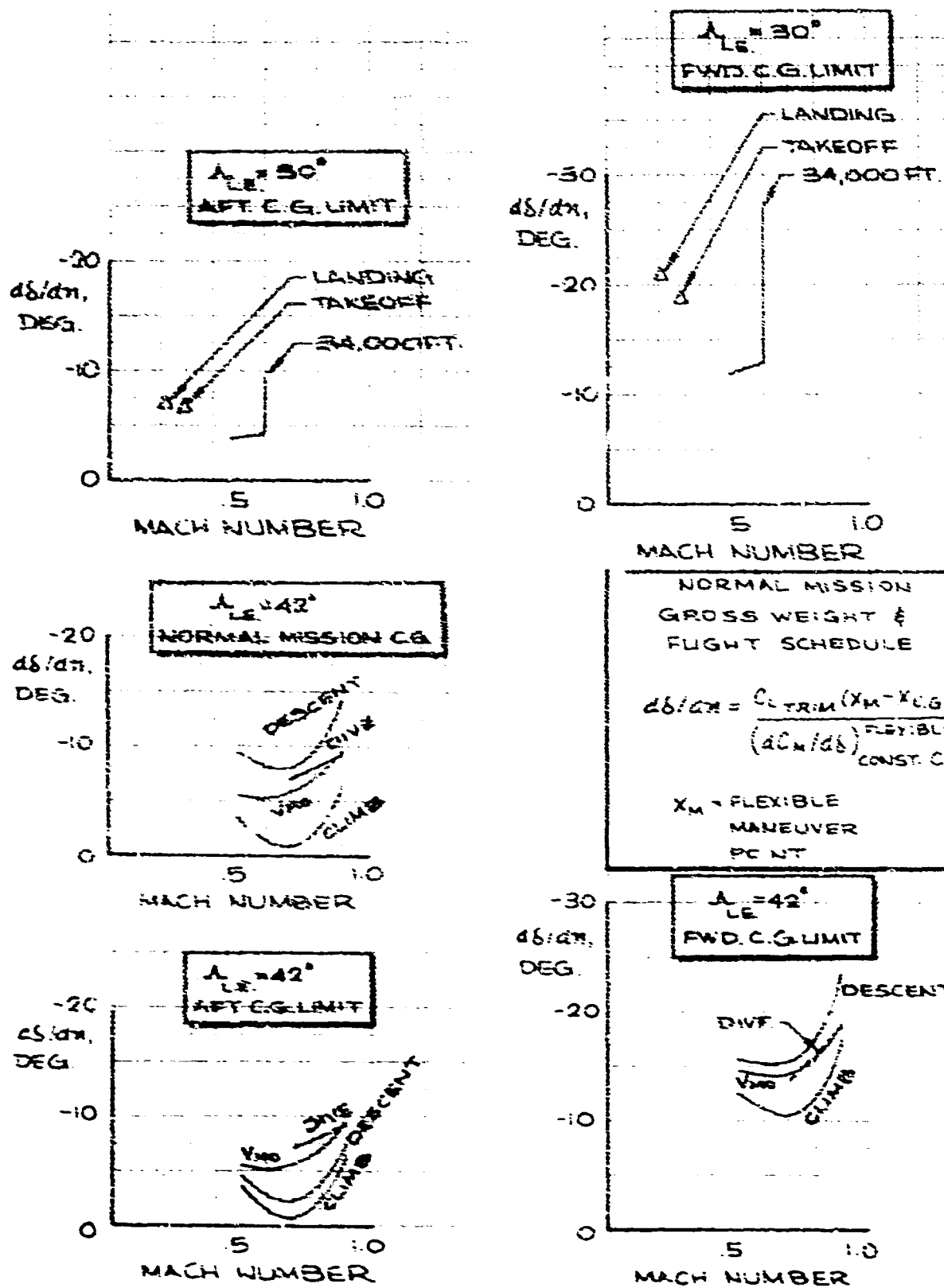


Figure 4-19. Longitudinal Control For α Wings Forward

W3-B2707-3

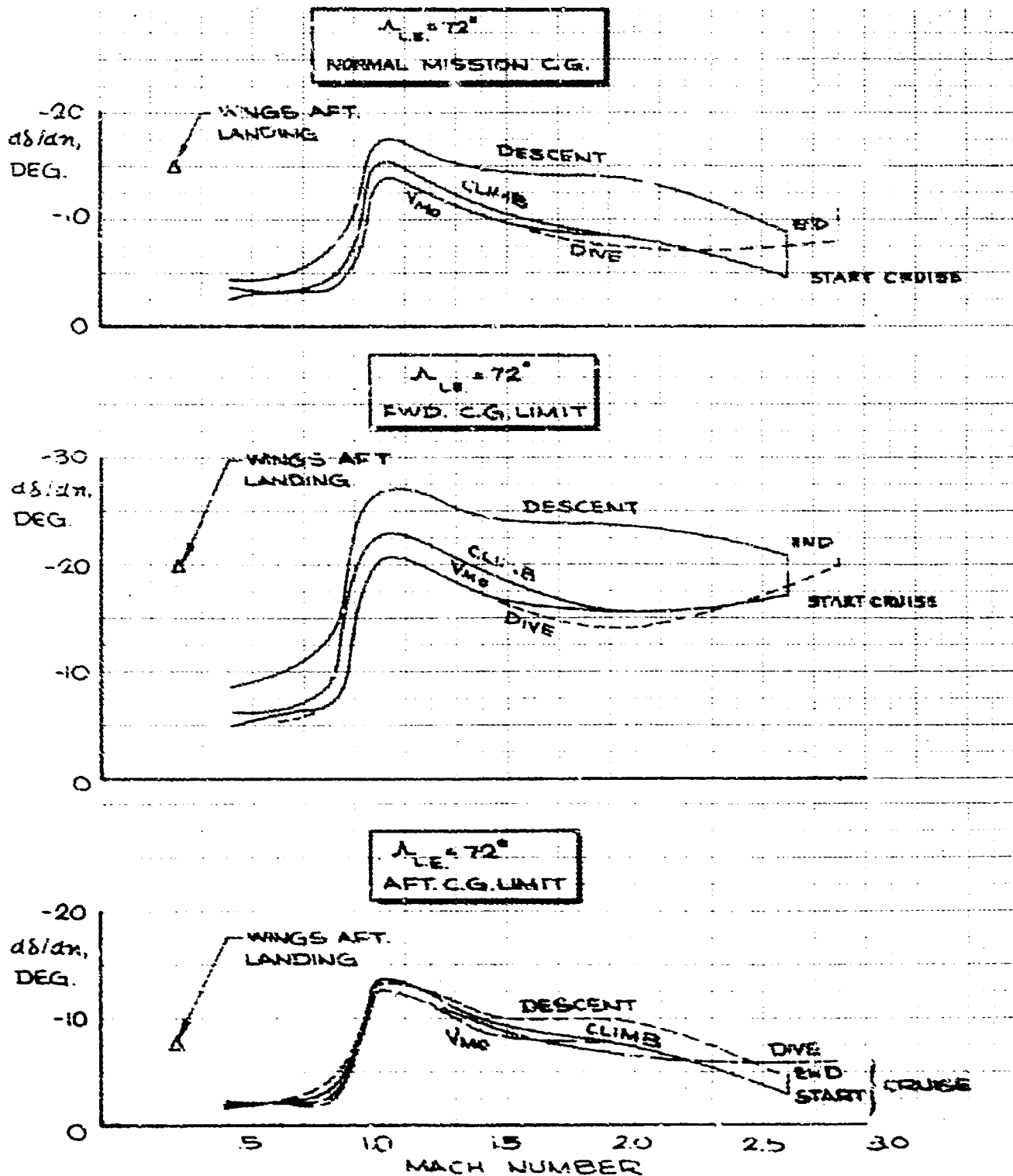


Figure 4-20. Longitudinal Control Per g, Wings Aft

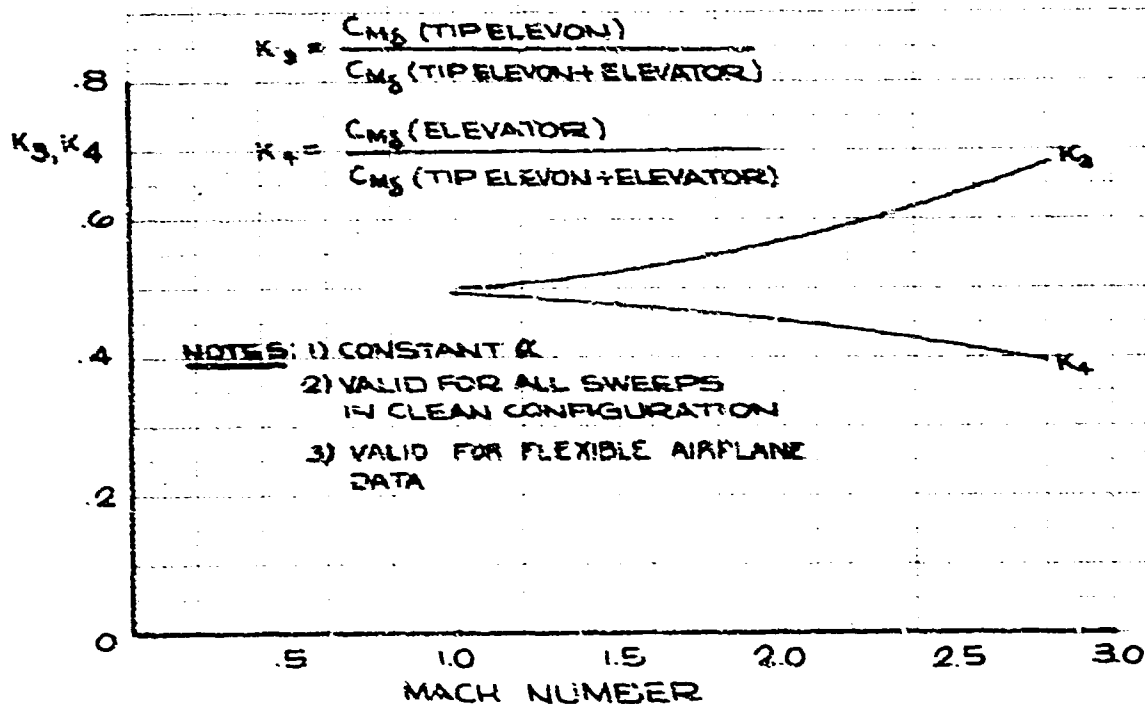
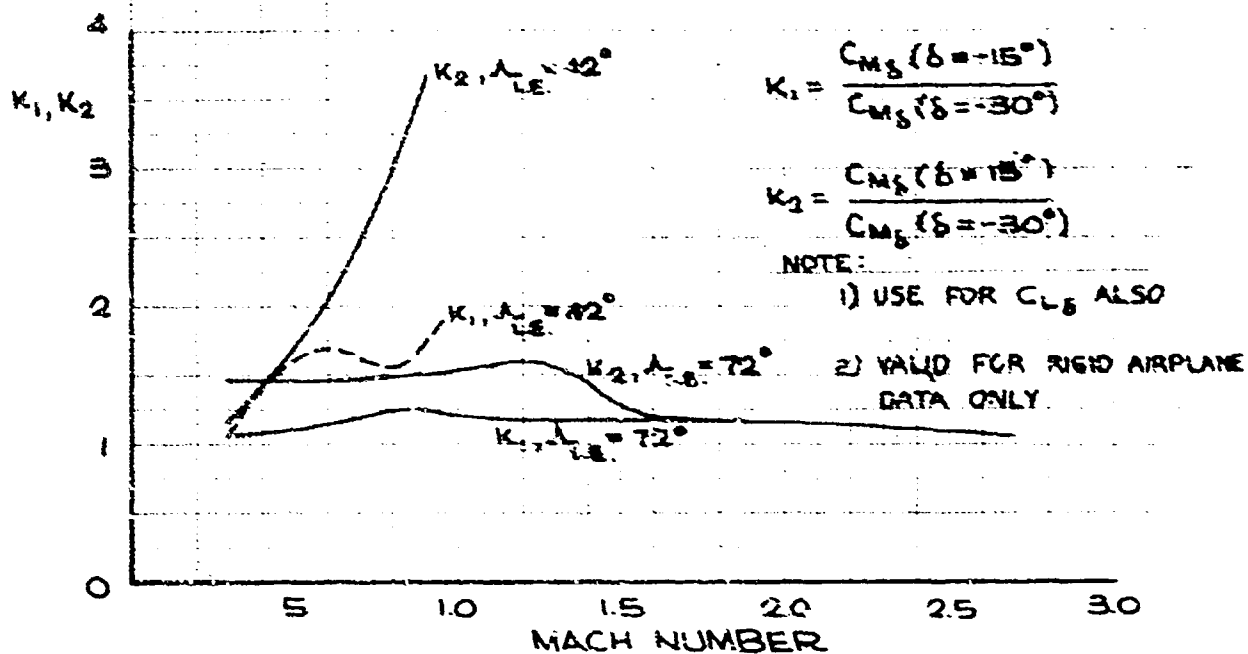


Figure 4-21. Longitudinal Control Effectiveness Factors

V2-R2707-3

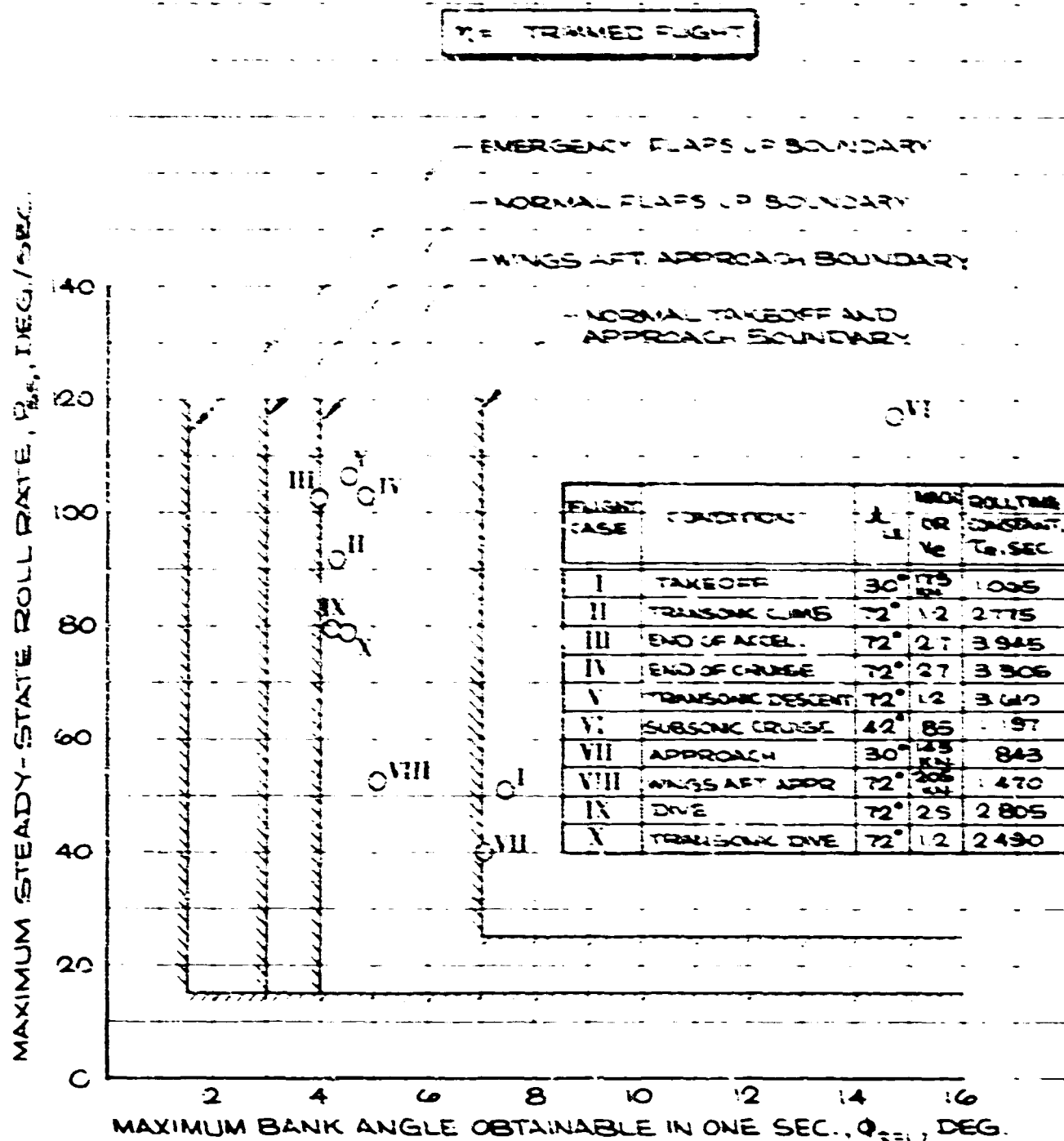


Figure 4-22. Roll Performance

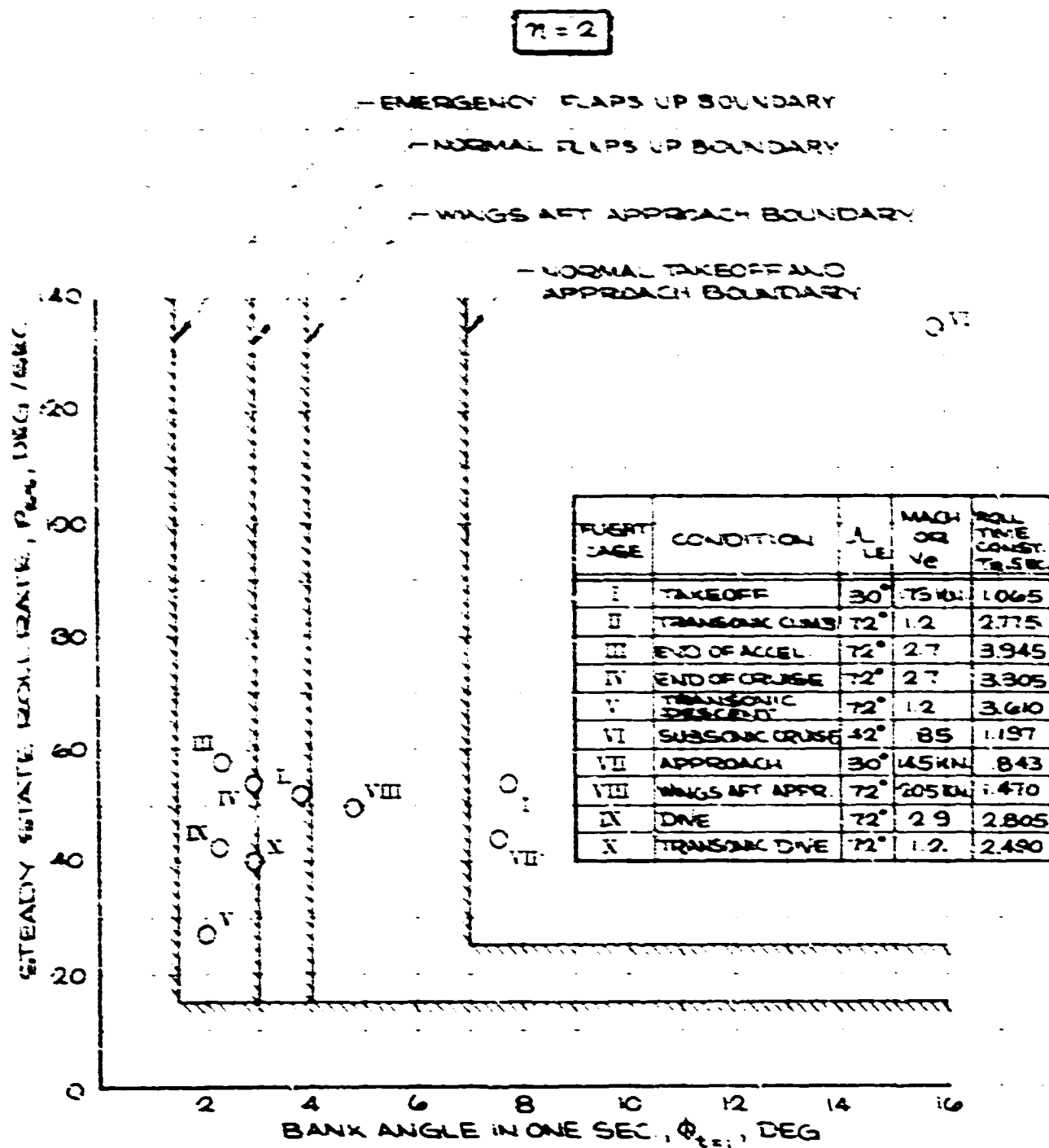


Figure 4-23. Roll Performance in Maneuvering Flight

V2-22707-3

Good lateral control capability in sideslip is associated with the lateral-directional stability characteristics inherent for the variable sweep airplane in the low sweep, large span, landing configuration shown in Fig. 4-24. Lateral controllability is not degraded appreciably up to the maximum sideslip angles attainable with full rudder deflection. This is caused by the combination of small dihedral effect, roll due to sideslip, and powerful lateral control provided in the low sweep configuration.

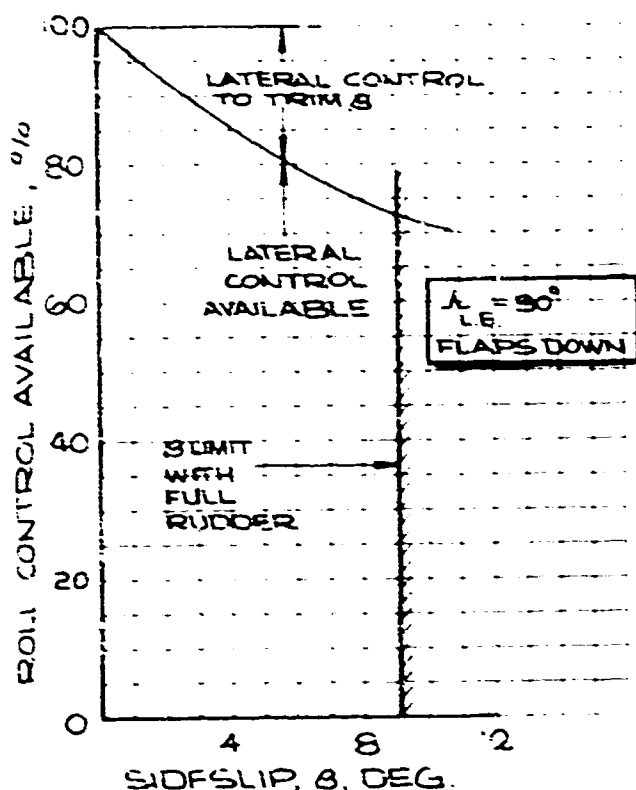


Figure 4-24. Roll Control in Sideslip

The rolling moment available per unit control wheel deflection is shown in Fig. 4-25 for the rigid and flexible airplane, along the V_{Y0} climb, cruise and descent profiles, at dive placard speeds, and in landing conditions. The damping in roll, $C_{l\dot{\beta}}$, is plotted versus Mach number for the rigid and flexible airplane for these same flight conditions in Fig. 4-26. Rigid airplane control effectiveness and yawing moment characteristics are shown in Figs. 4-27 through 4-29 as a function of angle of attack for representative Mach number and sweep conditions. The capability of main-

taining positive roll control well beyond stall or limit angle of attack is evident especially in the low speed, flaps down operation. These data show the adverse yaw characteristics of the tip elevon controls. Cross-coupling introduced by these adverse yaw characteristics is discussed in Par. 4.4.

Wind tunnel test results show that the elevon provides essentially linear effectiveness from zero deflection to large deflections. These data are shown in Fig. 4-30.

Figures 4-31 through 4-33 present the airplane aeroelastic corrections to be applied to the rigid controls data in the form:

$$(C_{l\delta})_{\text{flexible}} = (C_{l\delta})_{\text{rigid}} \left(\frac{R_E}{R_R} \right)_{\delta} \text{ for aileron,}$$

elevon and spoiler and

$$(C_{n\delta})_{\text{flexible}} = (C_{n\delta})_{\text{rigid}} \left(\frac{R_E}{R_R} \right)_{\delta} \text{ for aileron and}$$

elevon, where $\left(\frac{R_E}{R_R} \right)_{\delta}$ is the aeroelastic roll

factor for the control.

No aeroelastic corrections are applied to the side force terms which are assumed rigid for all controls. No aeroelastic correction is applied to the rigid spoiler yaw term $(C_{n\delta})$ since the reduc-

tion in parasite drag of the spoiler due to wing flexibility is approximately matched by increased induced wing drag with wing flexibility. Conversely, an aeroelastic correction is applied to the rigid aileron and elevon yaw effects $(C_{n\delta})$

since the yawing moment arises from the induced drag difference between left and right surfaces deflected antisymmetrically.

Roll damping equations are on next text page.

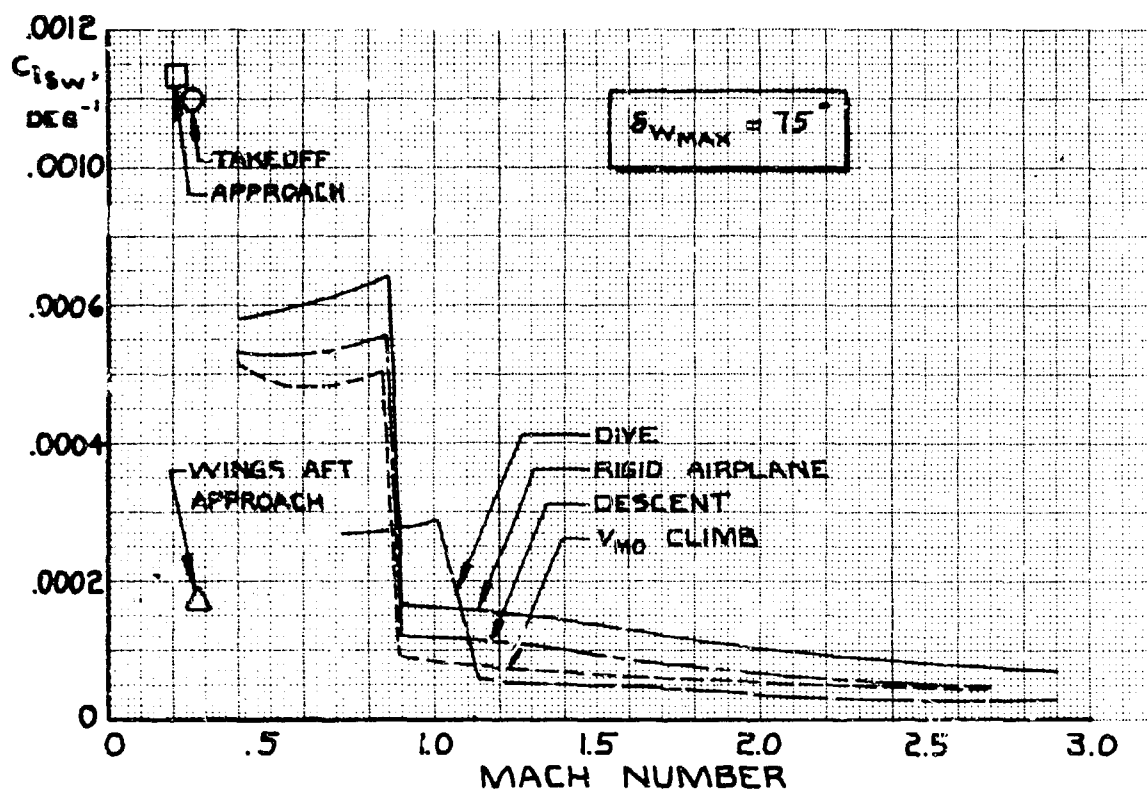


Figure 4-25. Rolling Moment Per Unit Wheel Deflection

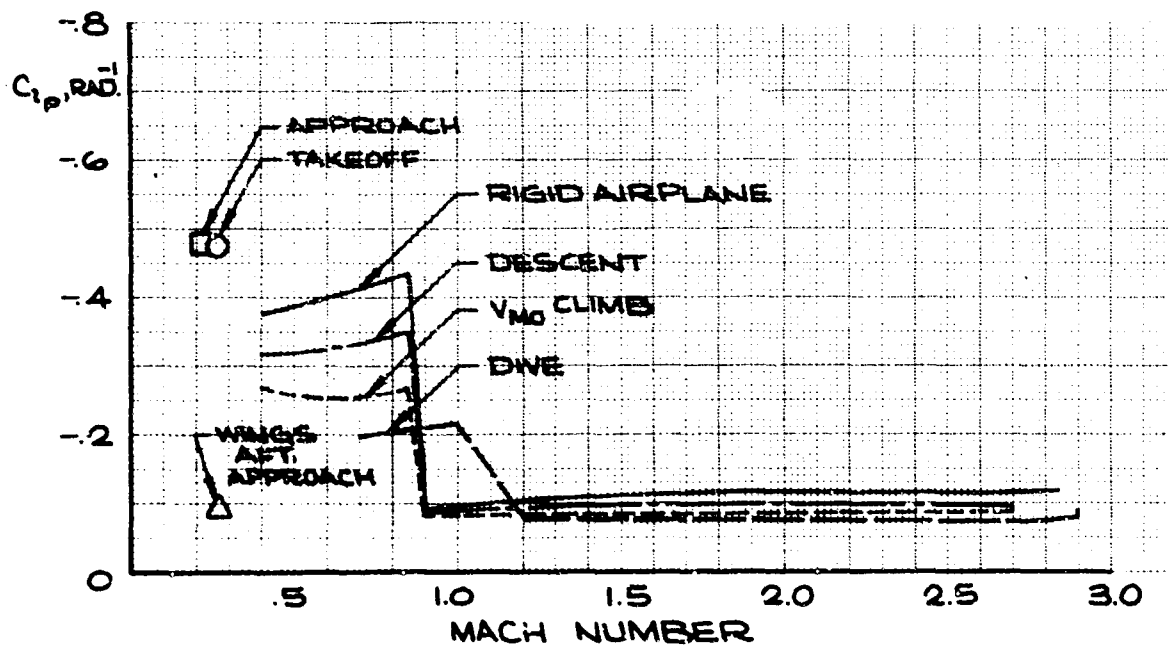


Figure 4-26. Roll Dampina Derivative

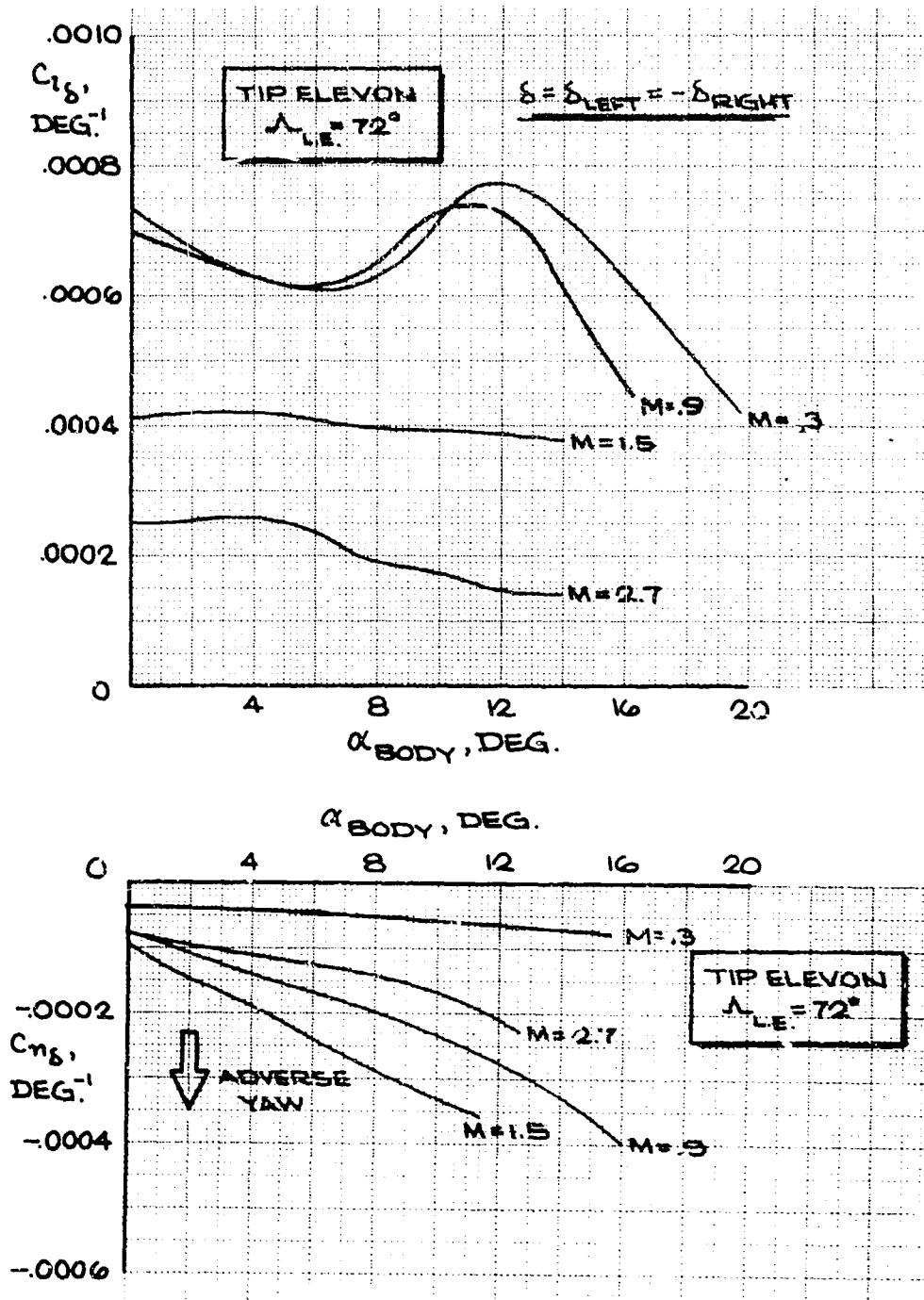


Figure 4-27. Tip Elevon Effectiveness, Rigid Airplane

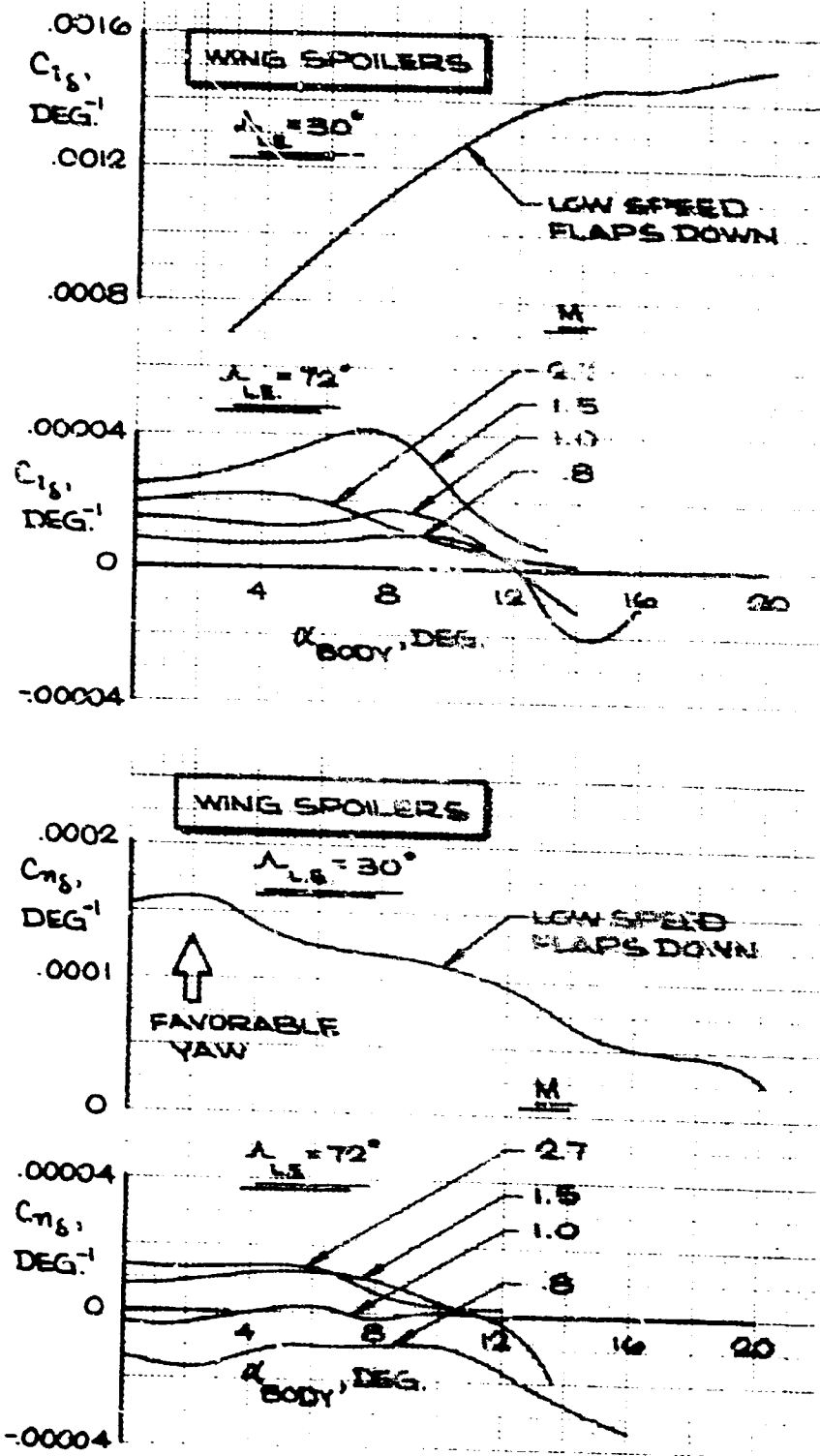


Figure 4-28. Wing Spoiler Effectiveness, Rigid Airplane

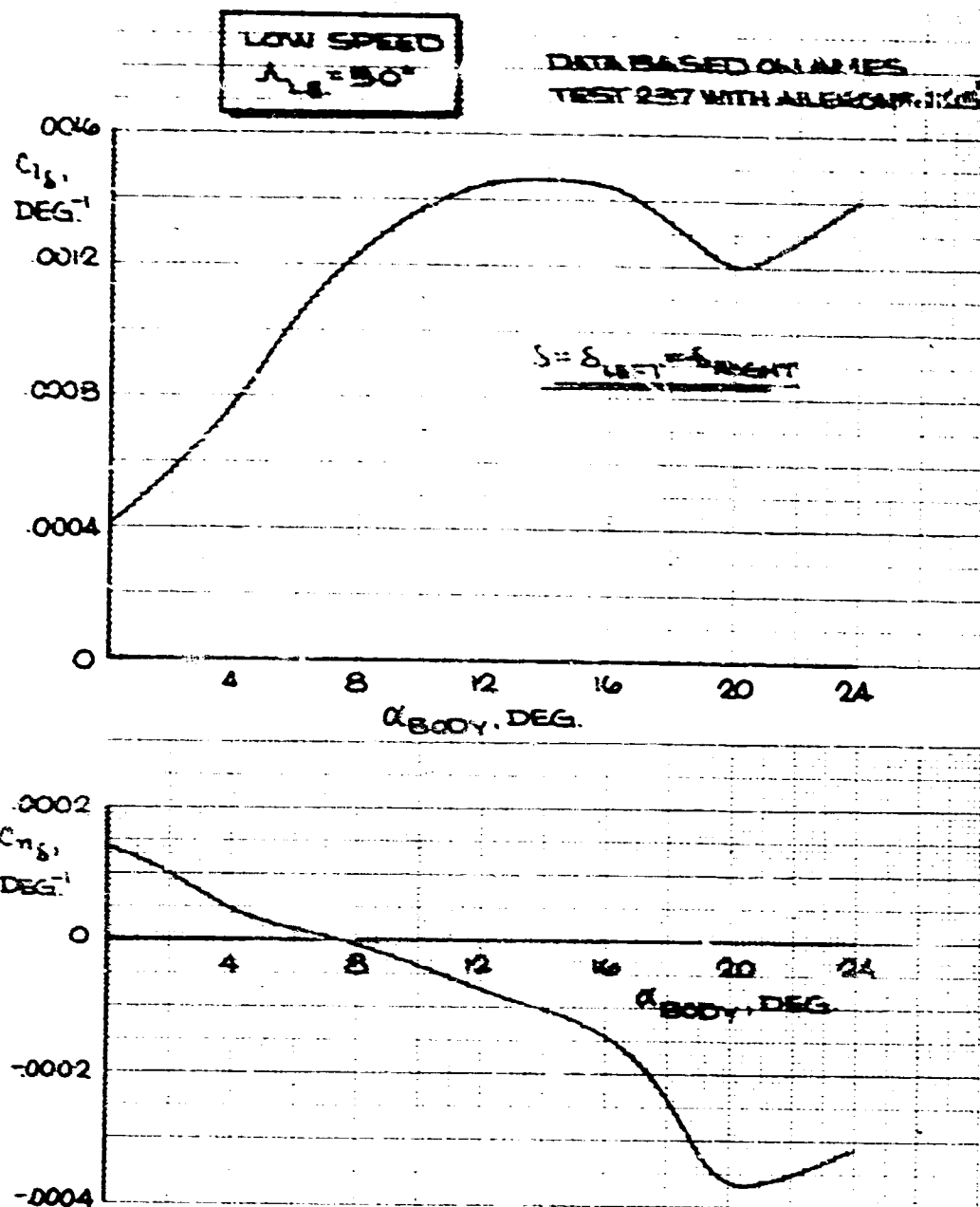


Figure 4-29. Wing Aileron Effectiveness, Rigid Airplane

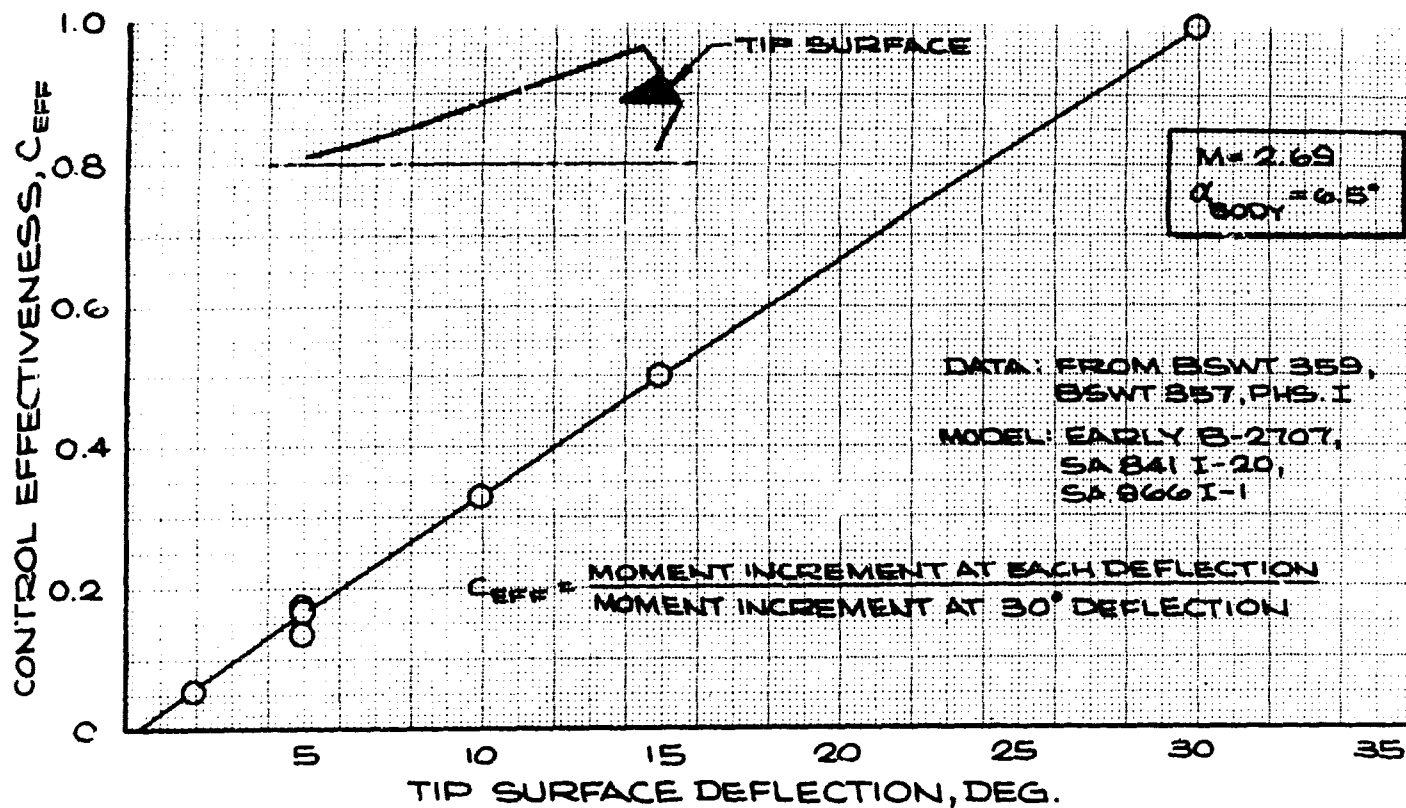


Figure 4-30. Tip Elevon Effectiveness

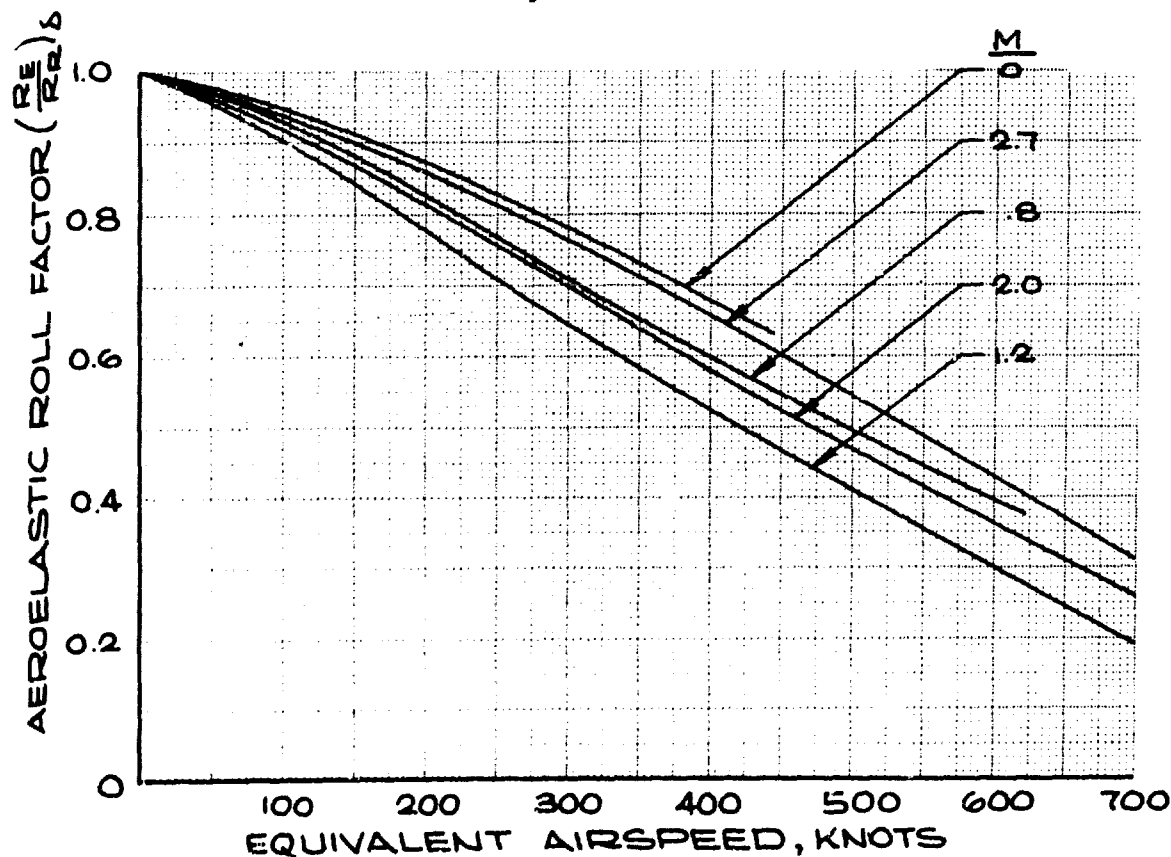


Figure 4-31. Aeroelastic Factor for Tip Elevon

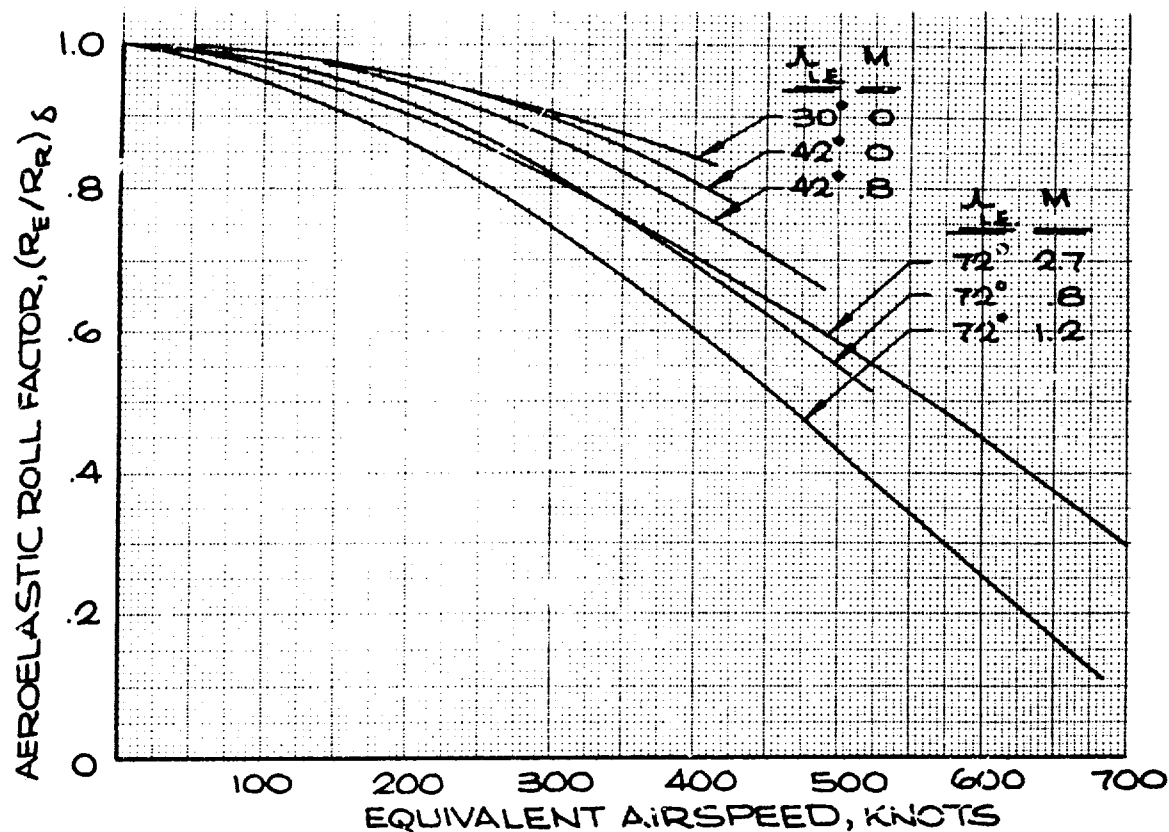


Figure 4-32. Aeroelastic Factor for Wing Spoilers

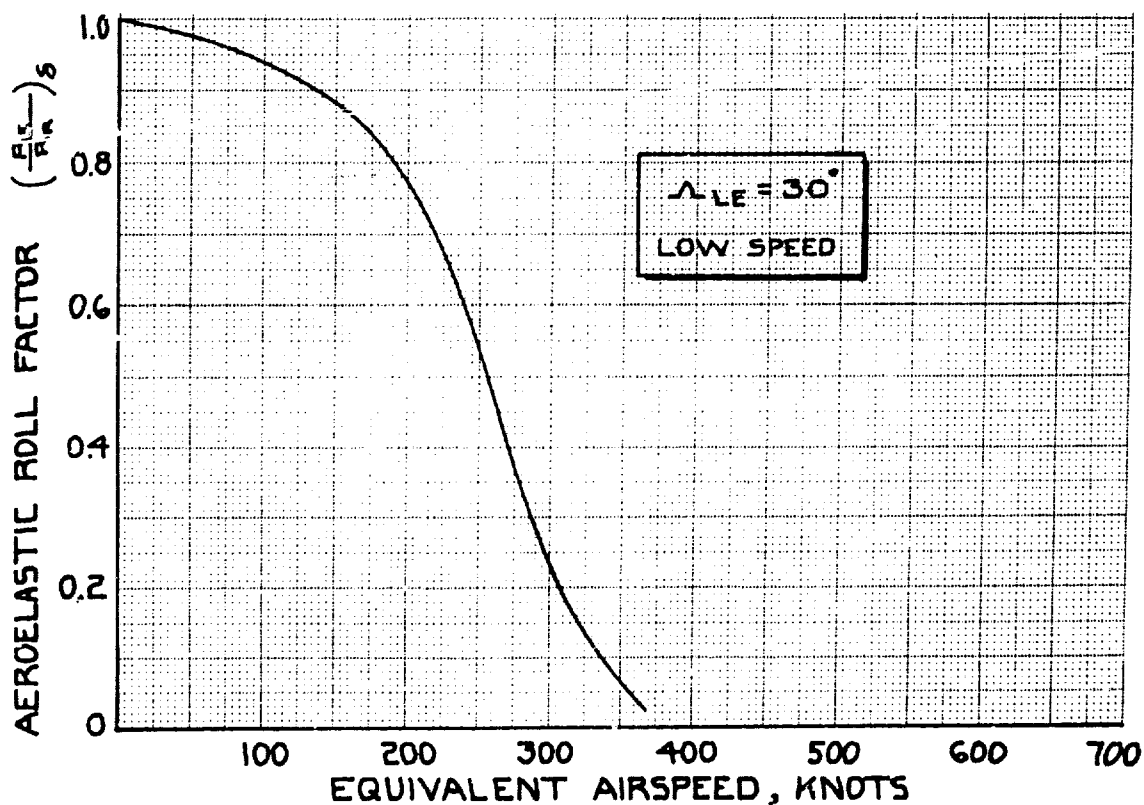


Figure 4-33. Aeroelastic Factor for Wing Ailerons

The rigid roll damping coefficient C_{l_p} is corrected as follows:

$$(C_{l_p})^{\text{flexible}} = (C_{l_p})^{\text{rigid}} \left(\frac{R_E}{R_R} \right)_p \text{ where}$$

$\left(\frac{R_E}{R_R} \right)_p$ is the aeroelastic factor on roll damping

and shown in Fig. 4-34

failure at takeoff, and has the capability of controlling landings in 90-degree crosswinds greater than 30 kn.

Figure 4-35 shows the ability of controls to handle the critical single engine failure at takeoff. Full rudder, applied to trim the asymmetric thrust and windmill drag, provides values for minimum control speed, V_{MC} (on ground, no nosewheel steering), of 132.5 kn for the B-2707 (GE) with engines at full afterburner thrust, and $V_{MC} = 115$ kn with maximum dry thrust. The V_{MC} speeds are 130kn and 115kn for the B-2707 (P&WA) with engines at maximum and 80 percent of maximum augmented thrust. A comparison with the FAR requirement shows that ample control

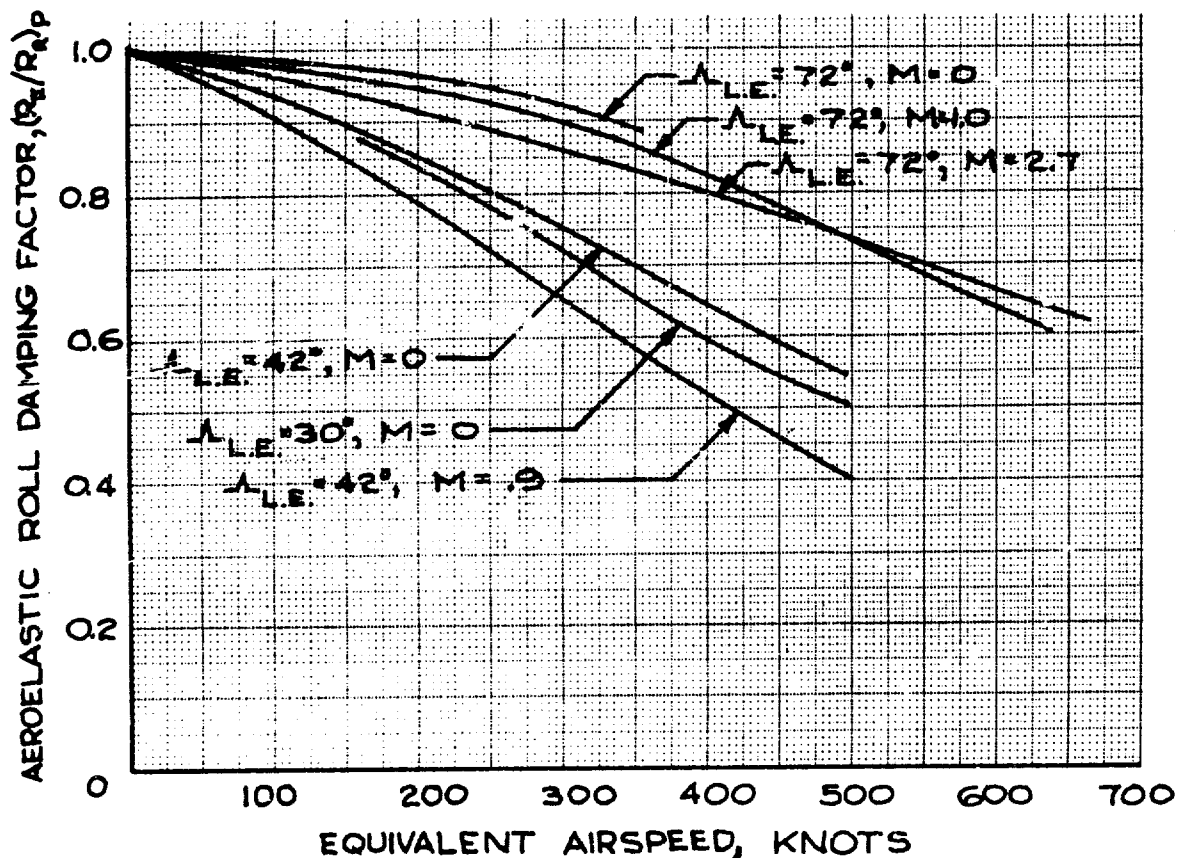


Figure 4-34. Aeroelastic Factor on Damping in Roll

4.1.3 Directional Control

Directional control is provided by a single piece rudder mounted on the low aspect ratio vertical tail. The rudder is powered by a triple hydraulic system and has control stops to limit rudder deflection. The deflection limits are controlled by wing flap position and wing sweep, as described in Sec. 5.0. The rudder is sized to provide adequate control for the critical single engine

margin is provided at normal takeoff weights. With maximum dry thrust B-2707 (GE) or 80 percent maximum augmented thrust with B-2707 (P&WA), adequate margins are provided for weights as low as 520,000 lb.

The crosswind landing capability is shown in Fig. 4-36. Full rudder produces 9.2 degrees of sideslip. About 30 percent of the lateral control

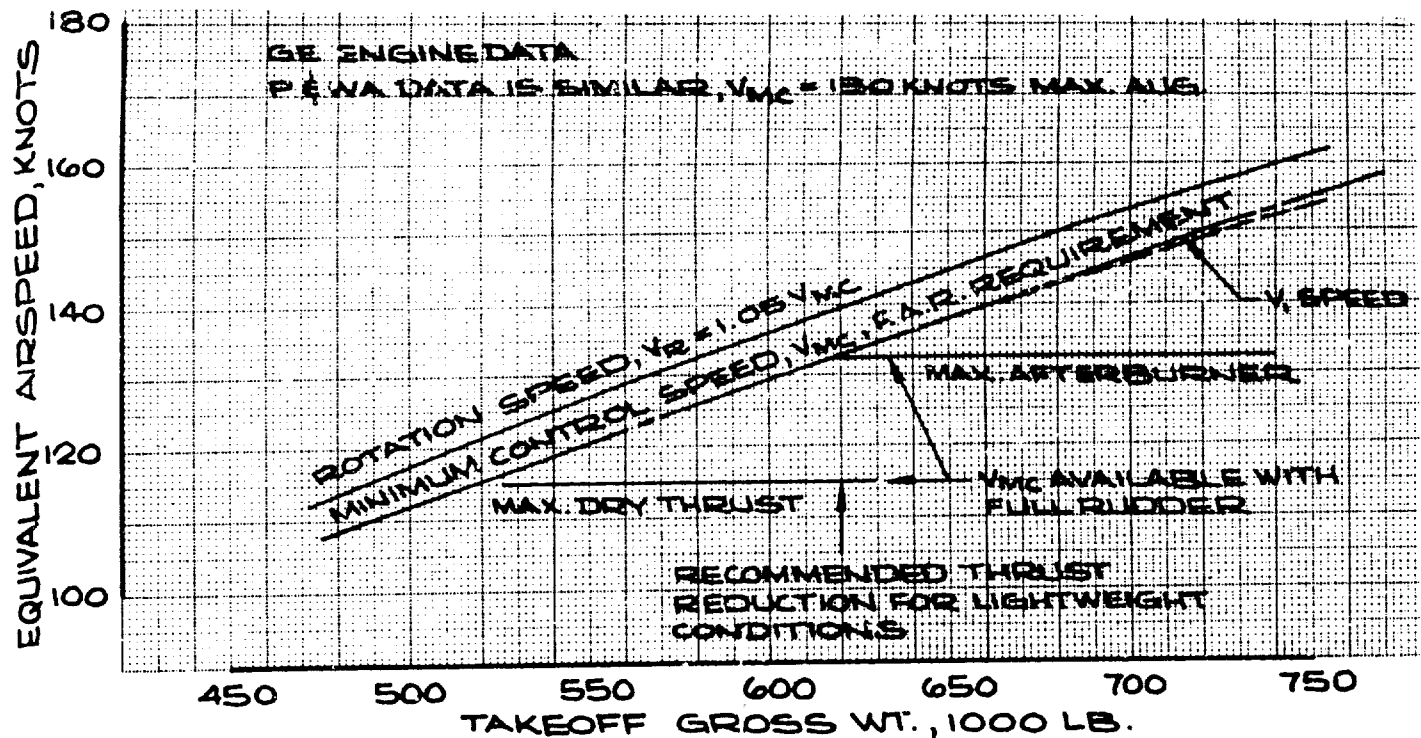


Figure 4-35. Takeoff Minimum Control Speeds

capability is required to maintain wings level (Par. 4.1.2). The 9.2-degree sideslip provides 33.1 kn, 90-degree crosswind capability equivalent to 13.2 degrees of sideslip, with the assumption that the airplane can be landed comfortably with degrees of crab remaining at touchdown. Crosswind velocities are normally quoted at the tower height of 50 ft; application of the standard FAR windshear correction (Fig. 4-37) gives a crosswind capability of 36.6 kn measured at tower elevation. The 36.6-kn, 90-degree crosswind capability quoted for the B-2707 follows the procedure of determining crosswind landing capabilities developed in certification of commercial jet transports. Crosswind control capability is determined by computing the maximum sideslip developed with full rudder and adding to this degrees of crab on the gear, which is the practical limit of crab that can be taken comfortably by the gear at touchdown. Boeing experience in demonstrating crosswind landings and the development of this criteria for establishing maximum crosswind landing capabilities are described in Ref. 26.

Rigid and elastic rudder effects are shown in Figs. 4-38 and 4-39. Figure 4-40 presents the rudder aeroelastic data that is used to correct the rigid data as follows:

$$\left[C_{\delta_r} \right]_{\text{flexible}} = \left[C_{\delta_r} \right]_{\text{rigid}} \left(\frac{M}{M_R} \right)_r (K_{BB})_{\text{vert.}}$$

where $\left(\frac{M_F}{M_R} \right)_r$ is the aeroelastic factor on rudder effectiveness due to vertical tail flexibility, and

K_{BB} vertical is the aeroelastic factor on rudder effectiveness due to body side bending,

$(K_{BB})_{\text{vertical}}$ is shown in Par. 4.2.2.

4.2 STATIC STABILITY

4.2.1 Longitudinal Static Stability

The large span, close-coupled tail arrangement of the airplane provides essentially linear stability characteristics for all flight conditions except low speed. At Mach numbers less than about 0.5, pitch instabilities exist at angles of attack near stall. An angle of attack warning and control system (Systems Report, Part B, V2-B2707-11) has been designed for the B-2707 to prevent inadvertent exposure to extreme attitudes at all flight conditions. Wing and strake leading edge slats eliminate instabilities for all wing sweeps, flaps up. However, moderate pitch up exists for

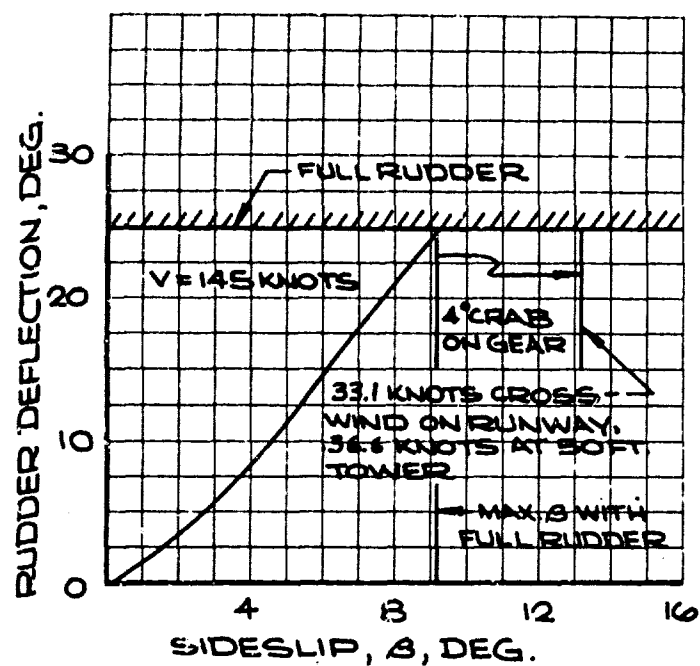


Figure 4-36. Rudder Control, Crosswind Landing

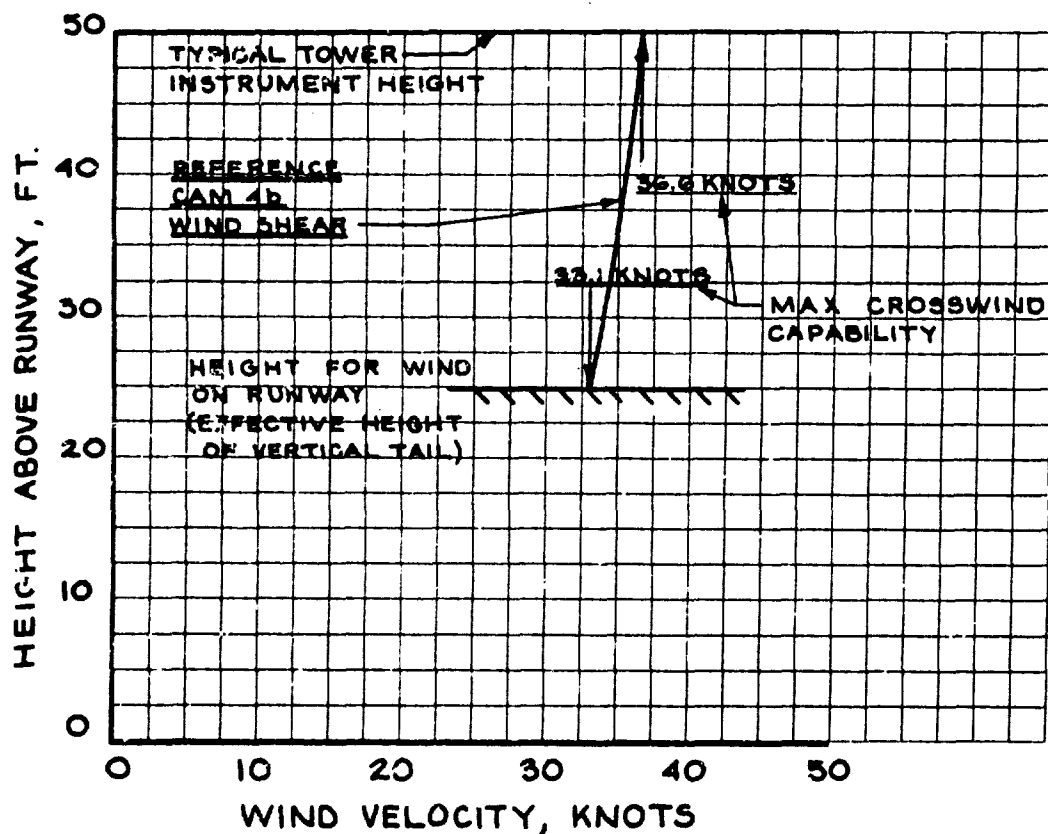


Figure 4-37. Wind Shear Effect

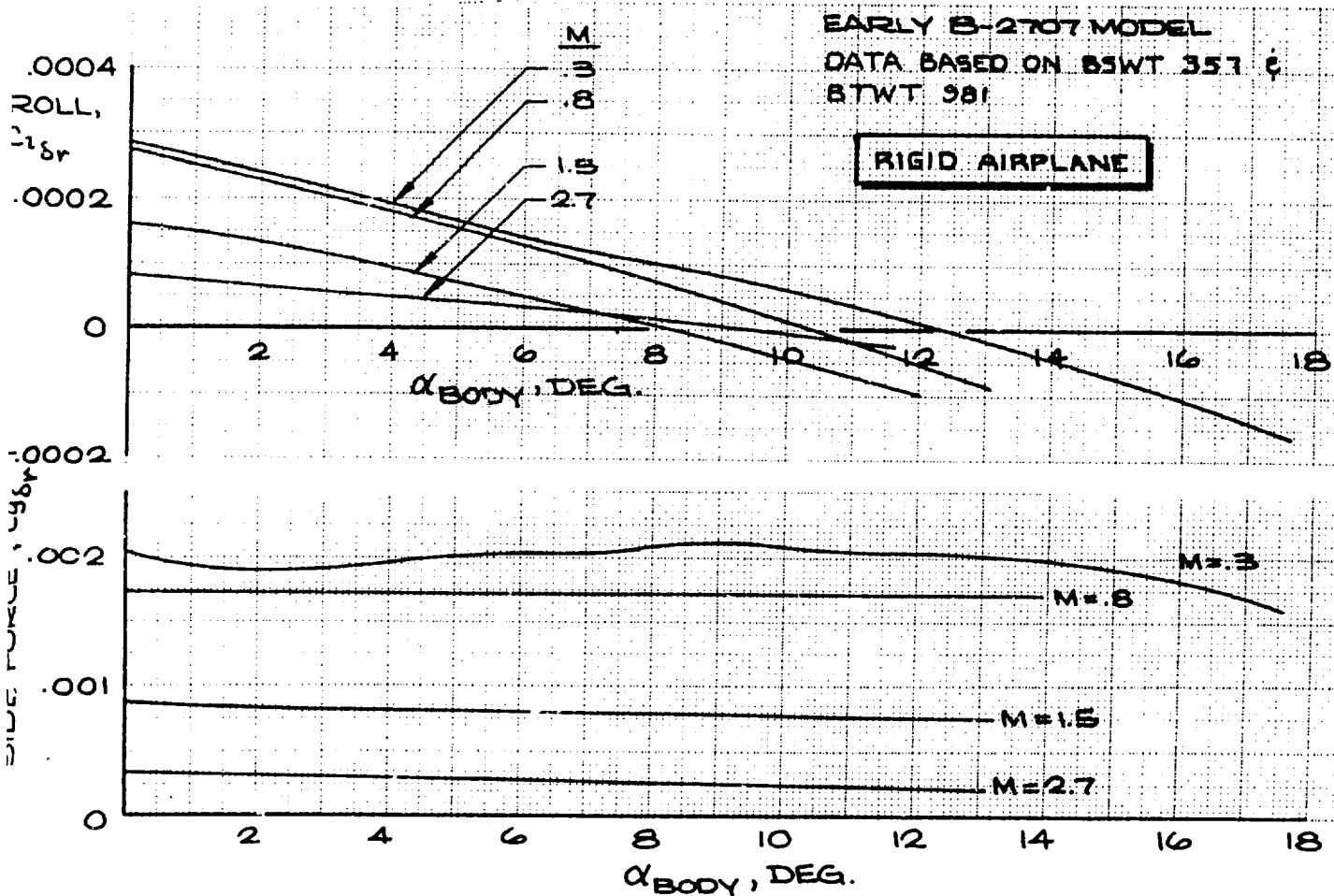
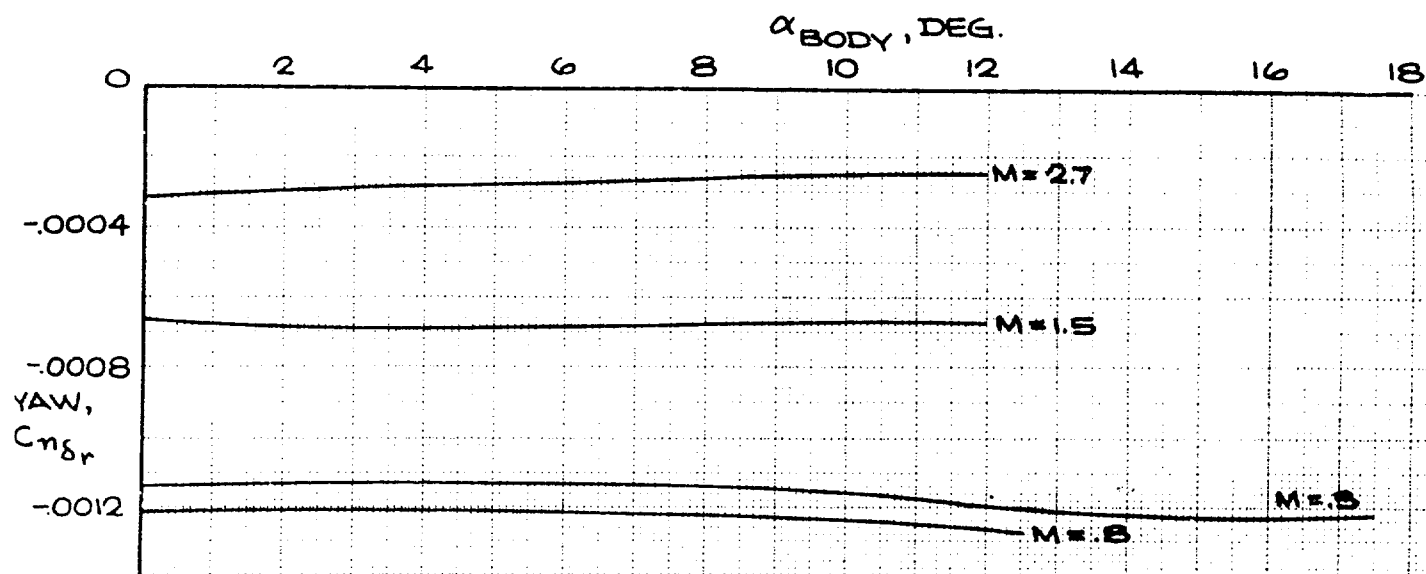


Figure 4-38. Rudder Effectiveness, Rigid Airplane

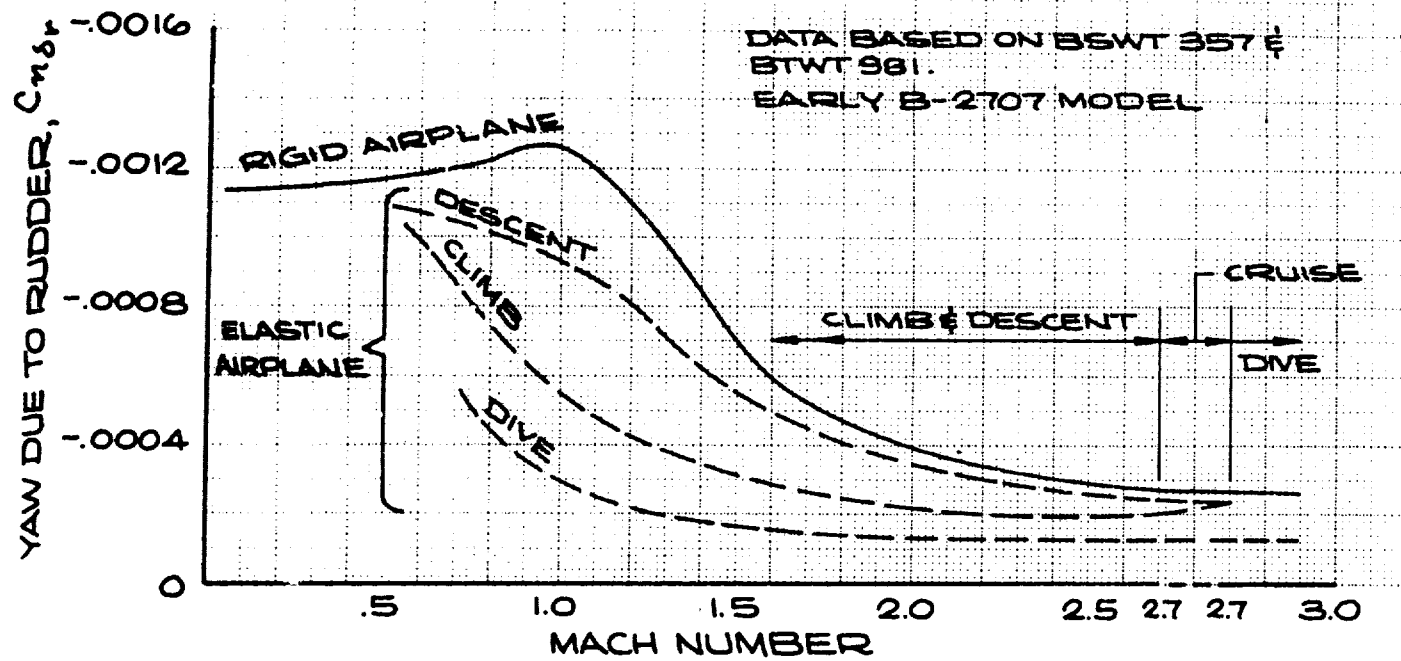


Figure 4-39. Rudder Effectiveness, Flexible Airplane

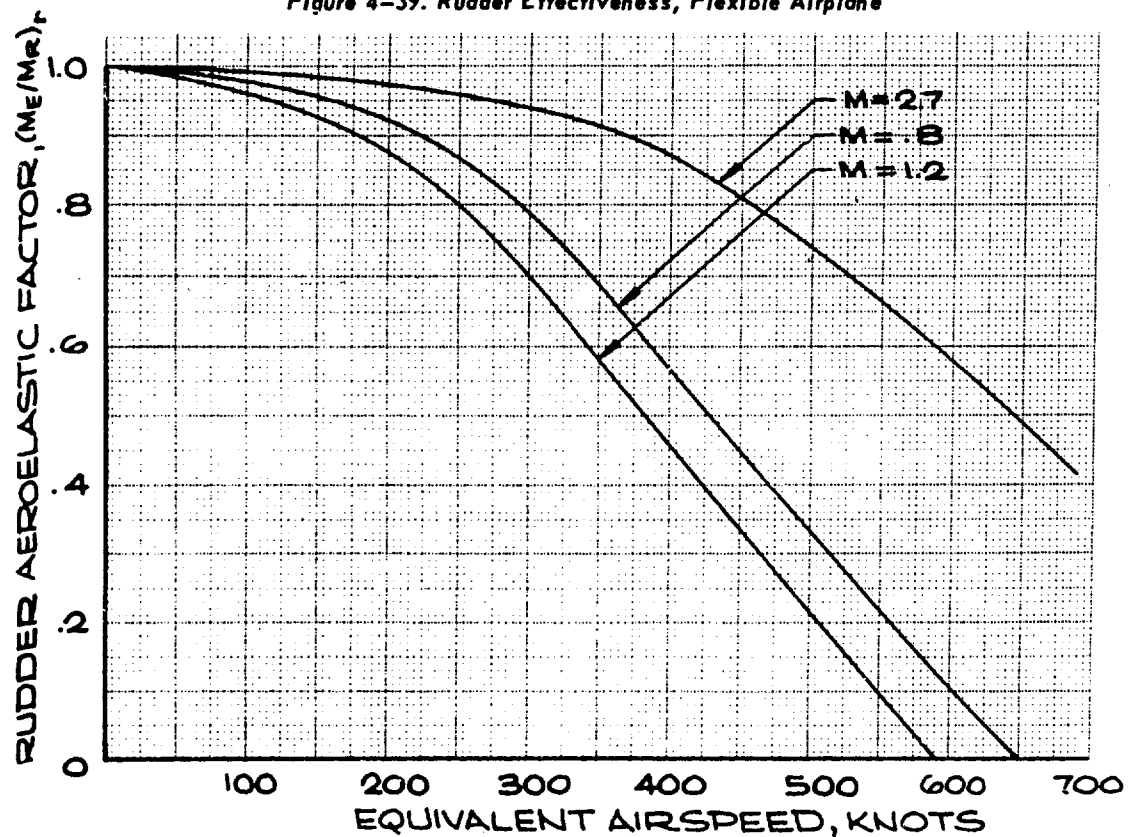


Figure 4-40. Aeroelastic Factor for Rudder

flaps down. Additional aerodynamic improvements will be explored in case they should be required to eliminate stall pitch up for flaps-down operation.

Placing engines aft on the B-2707 has caused a relatively far aft longitudinal balance. Considerable effort has been directed toward placing the stability center of gravity limits as far aft as possible to simplify airplane loading and fuel system management. The airplane has been balanced with low stability margins at subsonic conditions to achieve the desired longitudinal balance. Analytical studies and flight simulator testing have shown that acceptable airplane handling qualities are provided with these low stability margins. Handling qualities with and without stability augmentation are discussed in Par. 4.3 (See also Refs. 27 through 32).

4.2.1.1 Stability Margins

Figure 4-41 shows the flexible airplane static and maneuver neutral point computed for conditions of Mach number and dynamic pressure which are the most critical from the standpoint of minimum stability margins. The stability is compared with

the aft center of gravity limits which are 62 percent C_R for 30-degree sweep, 63 percent C_R for 42-degree sweep, and 64 percent C_R at 72-degree sweep.

The airplane is stable at all conditions except 30-degrees sweep, where static stability is about 1 percent C_R negative. This condition of instability is considered unsatisfactory and will be corrected. Available means of correction include adjusting airplane balance to move the aft cg limit forward, increasing the minimum flaps-up sweep to about 35 degrees, and improving the tail design. Subsonic operation below 0.6 Mach number at all wing sweeps requires that the strake leading edge slats be down to eliminate instabilities at moderate to high angles of attack. At low wing sweeps, the wing leading edge slats are down at Mach numbers less than 0.45 to provide satisfactory stability.

Figure 4-42 shows the variation of airplane center of gravity during the nominal mission. Figures 4-43 through 4-56 show longitudinal stability characteristics at various wing sweeps for representative Mach numbers.

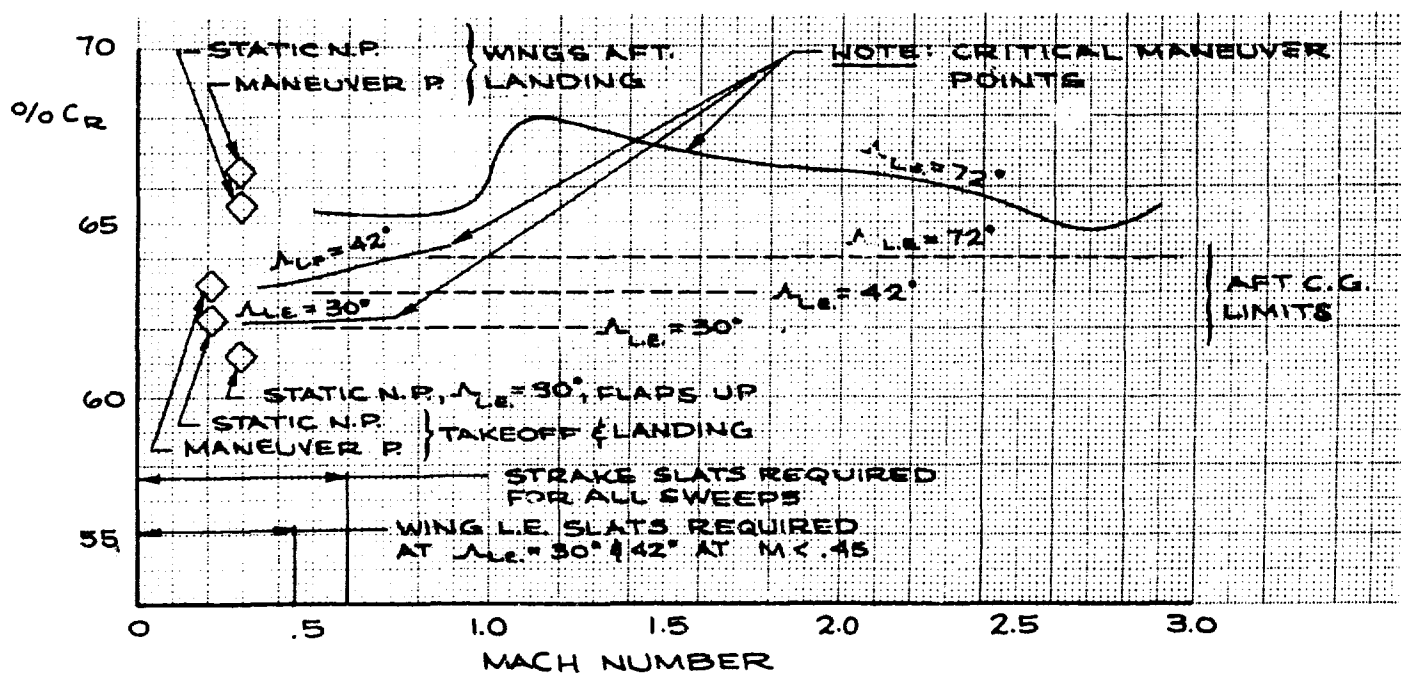


Figure 4-41. Longitudinal Stability Neutral Points

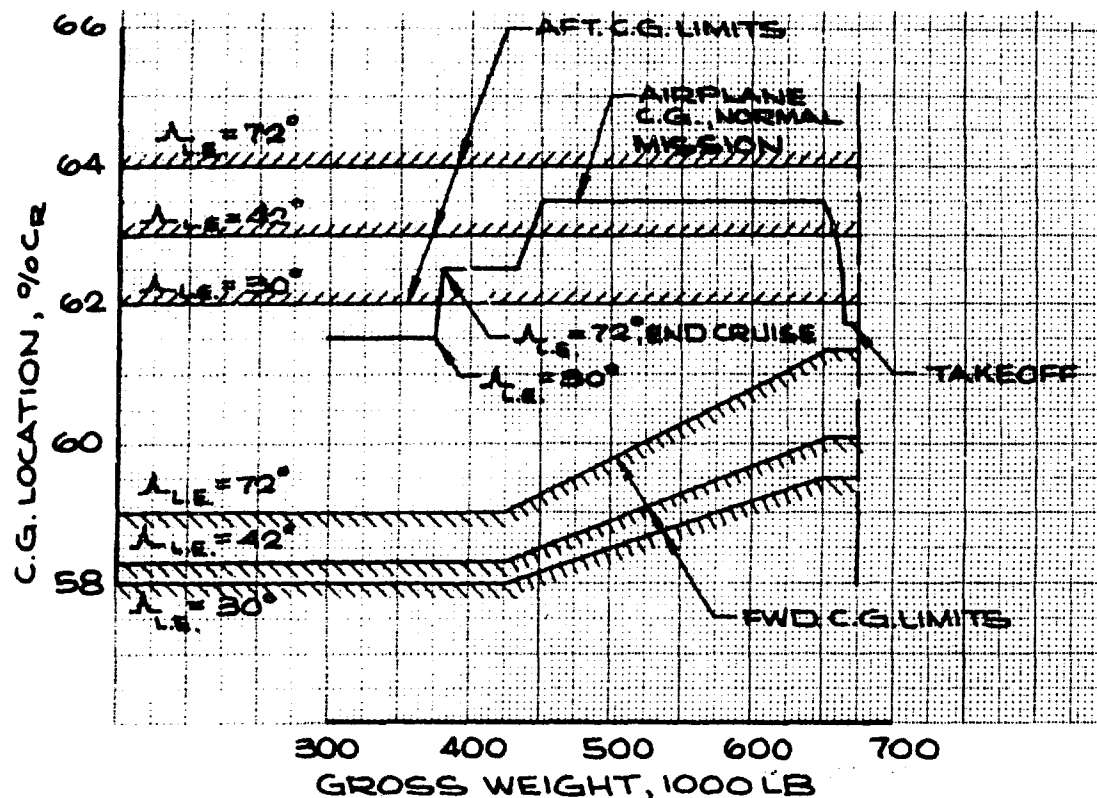


Figure 4-42. Center of Gravity Limits and Variations

The maneuver stability neutral points have been determined from model test data corrected for full-scale aeroelastic and wing body tail damping. The following equation is employed:

$$\begin{aligned}
 X_M &= \text{flexible airplane maneuver point} \\
 X_M &= X_{a.c.} \text{ (rigid aerodynamic center)} \\
 &+ \Delta X_{a.c.} \text{ (flexibility effect)} \\
 &+ \Delta X_{a.c.} \text{ (damping effect).}
 \end{aligned}$$

The aeroelastic corrections, damping effects, and thrust effects on stability are shown in Figs. 4-43 through 4-67.

4.2.1.2 Flaps-Down Static Stability
Stability characteristics in and out of ground effect are shown in Figs. 4-43 and 4-44 for the landing flap configuration. Low stability margins and moderate pitch up are evident. Handling

qualities analyses and flight simulator testing have demonstrated that handling characteristics are insensitive to static stability margin within the range of low margins that are practical for SST design. The airplane response in pitch is inherently sluggish because of the effect of high moment of inertia about the pitch axis. Increasing the static margin by the limited amounts that are practical from the standpoint of airplane balance and trim drag has no discernible effect on handling qualities. Stall demonstrations in the flight simulator have shown the airplane attitude to be controllable in the pitch up region for either slow or rapid stall entry rates. Dynamic longitudinal handling characteristics and stall testing in the simulator are discussed in Par. 4.3.

Recent wind tunnel testing has demonstrated methods to eliminate pitch up in the low speed region. Figures 4-45 and 4-46 show linear stability characteristics up to the maximum angle of attack tested, 33.5 degrees, which is about 14 degrees above the stall. This was accomplished through readjustment of the wing

lift distribution by retraction of outboard flaps, and by eliminating vortex flow development on the strake by folding up an outboard section of the strake. Design studies and wind-tunnel testing in this area are continuing in order to eliminate longitudinal instabilities. The angle of attack warning and control system will prevent inadvertent exposure to extreme attitudes at all flight conditions. The design goal, however, is to achieve inherent pitch down stability through and beyond stall.

4.2.1.3 Flaps Up Static Stability

Acceptable stability characteristics are provided with strake and wing leading edge slats down for all conditions except 30-degree sweep at the aft cg limit (62 percent C_R). Stability characteristics at 30-, 42- and 72-degree wing sweep at subsonic Mach numbers are shown in Figs. 4-47 through 4-53. Figure 4-47 shows the low speed 30-degree sweep stability at the aft cg limit with strake and wing slats down. The improvement in high angle of attack stability with wing and strake leading edge slats is shown in Figs. 4-49 and 4-50.

Good stability characteristics are provided at all wing sweeps for high subsonic and supersonic Mach numbers. Wind tunnel model test data for transonic and supersonic conditions are shown in Figs. 4-54 through 4-56.

4.2.1.4 Aeroelastic Corrections and Reference Flight Data

Structural aeroelastic effects on longitudinal stability and control effectiveness are substantially changed from those of previous configurations. The integration of wing and tail has provided deeper structure which has greatly reduced wing bending and twisting associated with the destabilizing forward shift of aerodynamic center. Forebody and aft body bending under inertia loading, during maneuvering flight, are stabilizing. The net effect of aeroelasticity at low and intermediate wing sweeps will increase the stability slightly.

Aeroelastic effects pertinent to longitudinal stability and control are summarized in Figs. 4-61 through 4-66. A detailed discussion of methods for determining structural aeroelastic effects is presented in Par. 3.3 of this document.

Reference data used in evaluating stability and control, such as operating lift coefficients, weights, and speed profiles, are presented in Figs. 4-67 through 4-71.

4.2.2 Lateral-Directional Static Stability

The low aspect ratio planform of the vertical tail has been selected to minimize aeroelastic stability losses at high airspeeds with minimum weight and drag. Tail size is dictated by the requirement for rudder control capability to ensure safe minimum control speed, V_{MC} , with critical engine failure on takeoff. This tail sizing has been found to provide ample static directional stability within the airplane flight envelope, with the possible exception of high angle of attack operation at Mach numbers in excess of 2.4. At high supersonic Mach numbers the stabilizing effect of top body-mounted vertical tails decreases as they become submerged in the forebody and wing wakes at high angles of attack. The level of $C_{n\beta}$ required at

high angle of attack is not clearly defined at this stage of the design development. Consideration of airplane dynamics indicates that the airplane will be dynamically stable even with unstable $C_{n\beta}$ due to the inertia characteristics and the

high level of positive dihedral effect, $C_{l\beta}$. Ex-

amination of the Dutch roll stability approximation parameter, $C_{n\beta \text{ dyn}}$, indicates that high levels

of dynamic directional stability will continue to exist at high angle of attack even where static $C_{n\beta}$ is negative: for example, at an angle of attack of 14 degrees and at Mach number 2.7.

$$C_{n\beta \text{ dyn}} = \frac{C_{n\beta} + \left(\frac{I_{xz}}{I_{xx}} \right) C_{l\beta}}{1 - \left(\frac{I_{xz}^2}{I_{xx} I_{zz}} \right)}$$

$$C_{n\beta \text{ dyn}} = 0.00248$$

The above approximation indicates positive Dutch roll damping. However, it does not consider the rotary derivatives or the effects introduced by the pilot in the control loop when attempting to hold wings level. If increased static directional stability is required, it will be provided by stabilizing surfaces mounted below the aft body, horizontal tail, or nacelles, or by location of top-mounted vertical tails outboard in good airflow regions on the horizontal tail. As previously discussed in Par. 4.2.1, the airplane is protected against inadvertent exposure to angles of attack greater than 12 degrees by an angle of attack warning and control system.

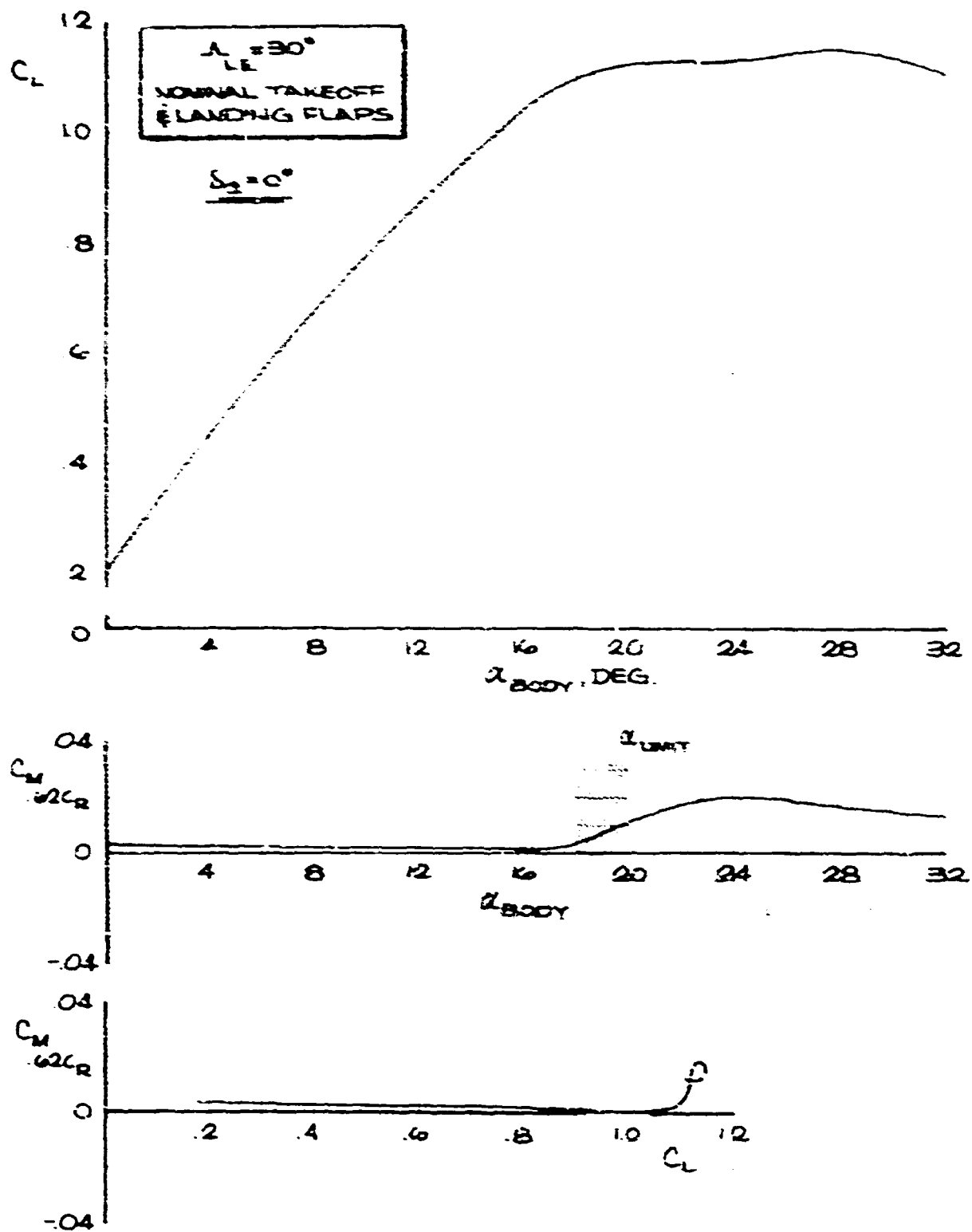


Figure 4-53. Landing Stability, No Ground Effect

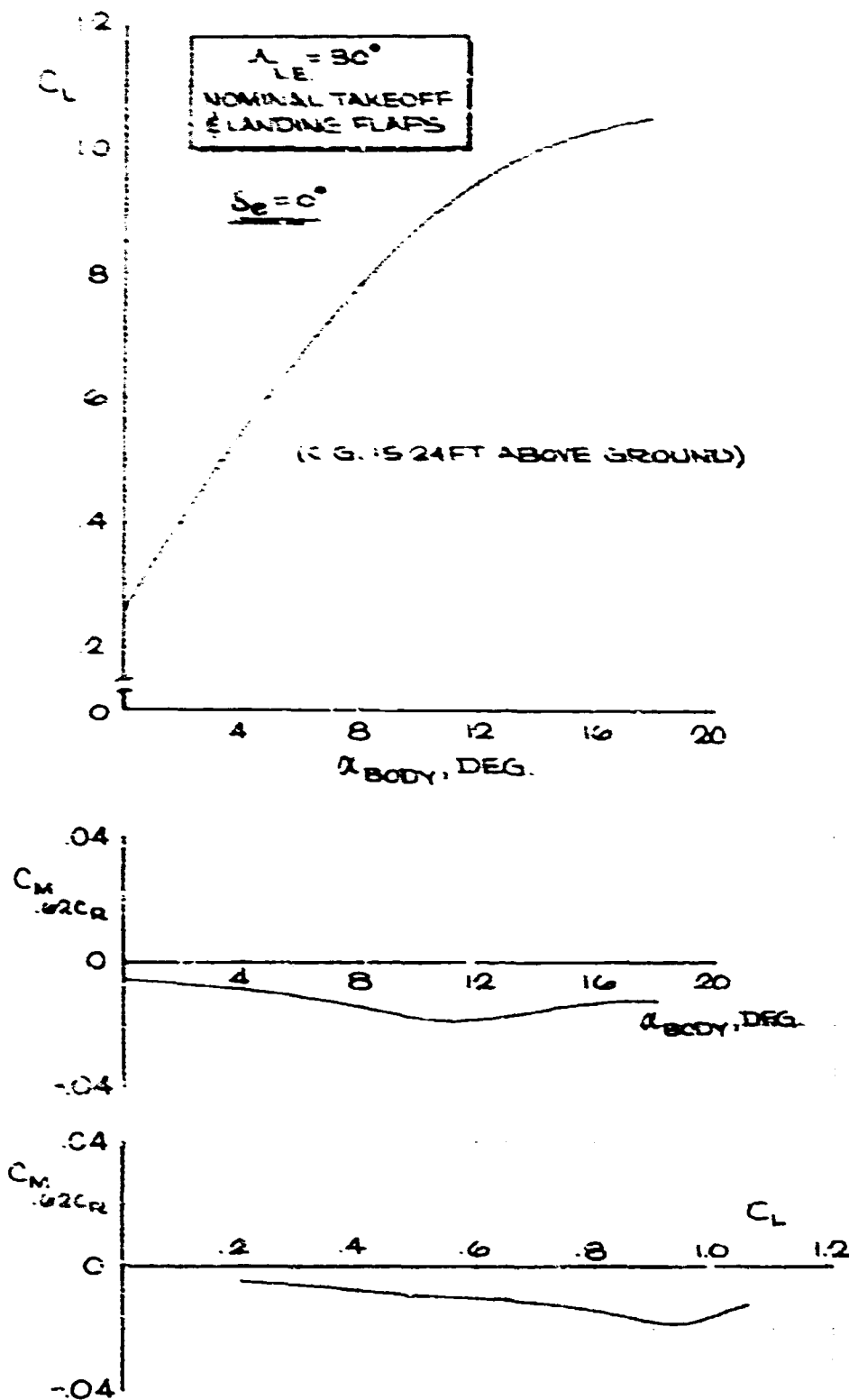


Figure 4-44. Landing Stability, in Ground Effect

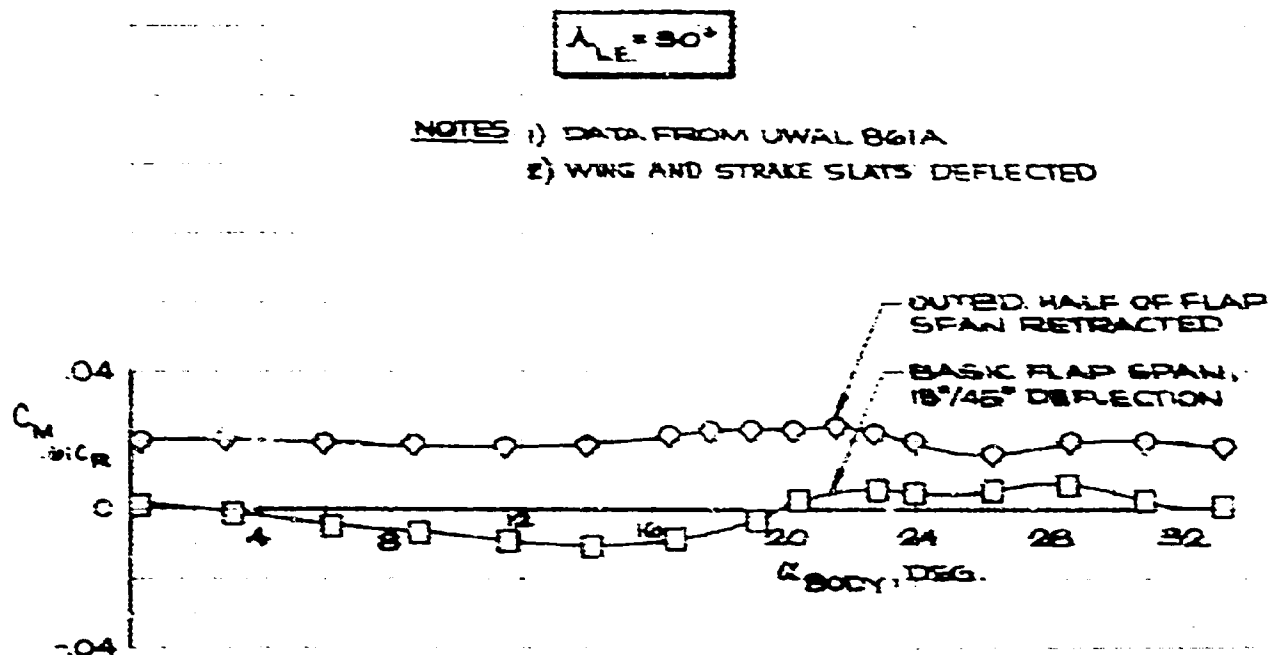


Figure 4-45. Effect of Flap Span

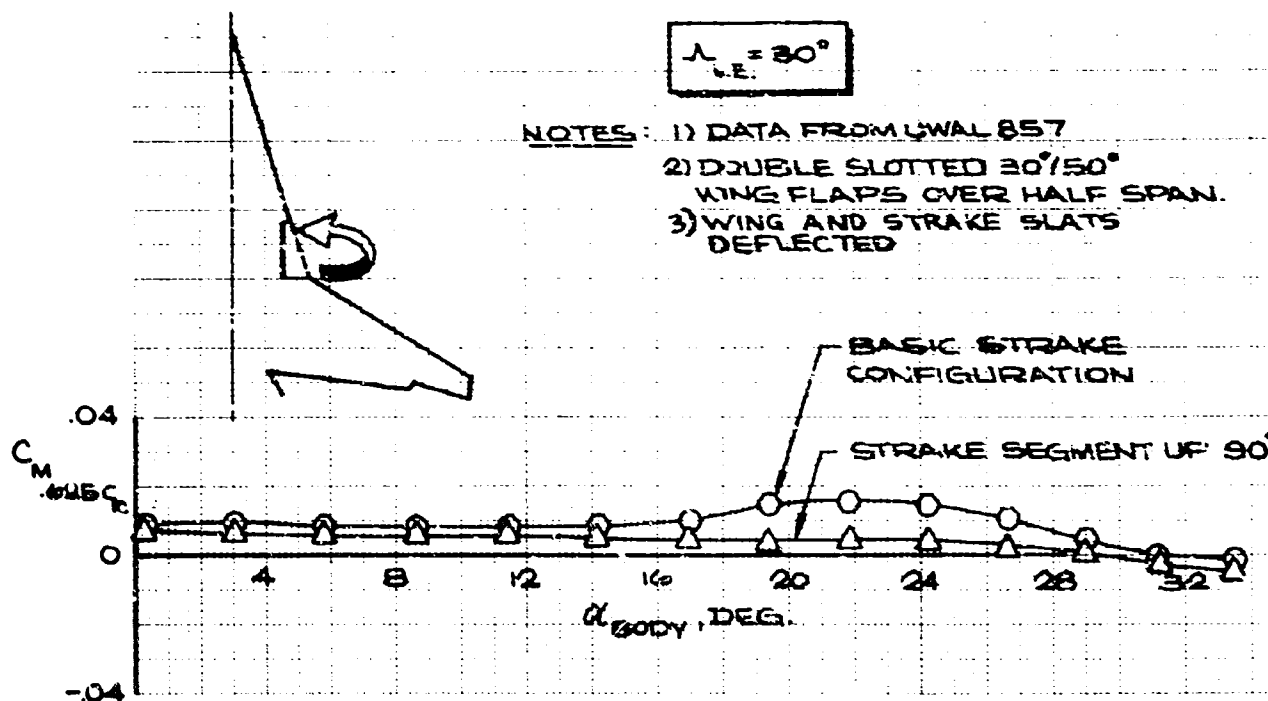


Figure 4-46. Effect of Strake Segment Rotation

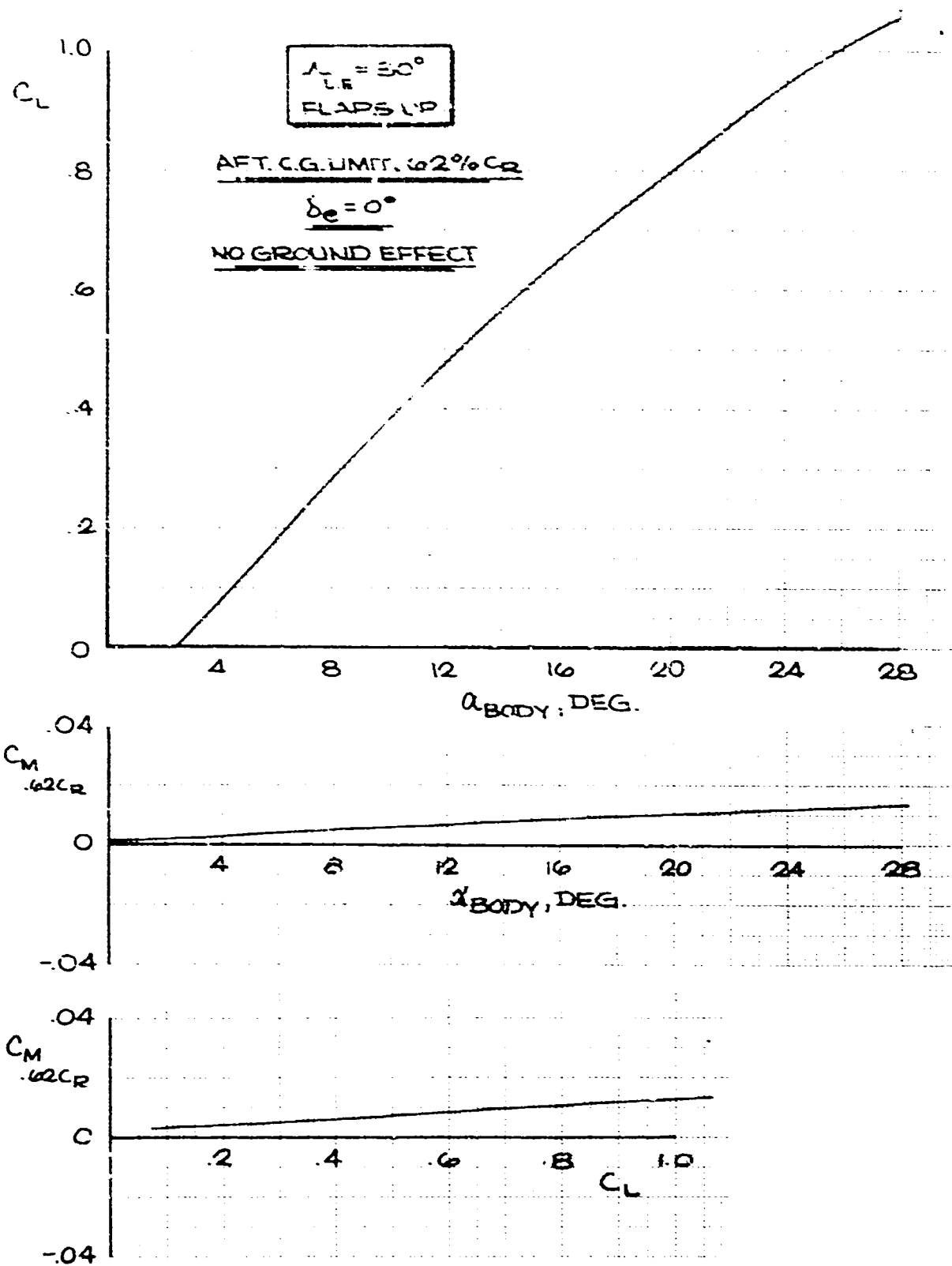


Figure 4-47. Low Speed Stability, Flaps Up, No Ground Effect

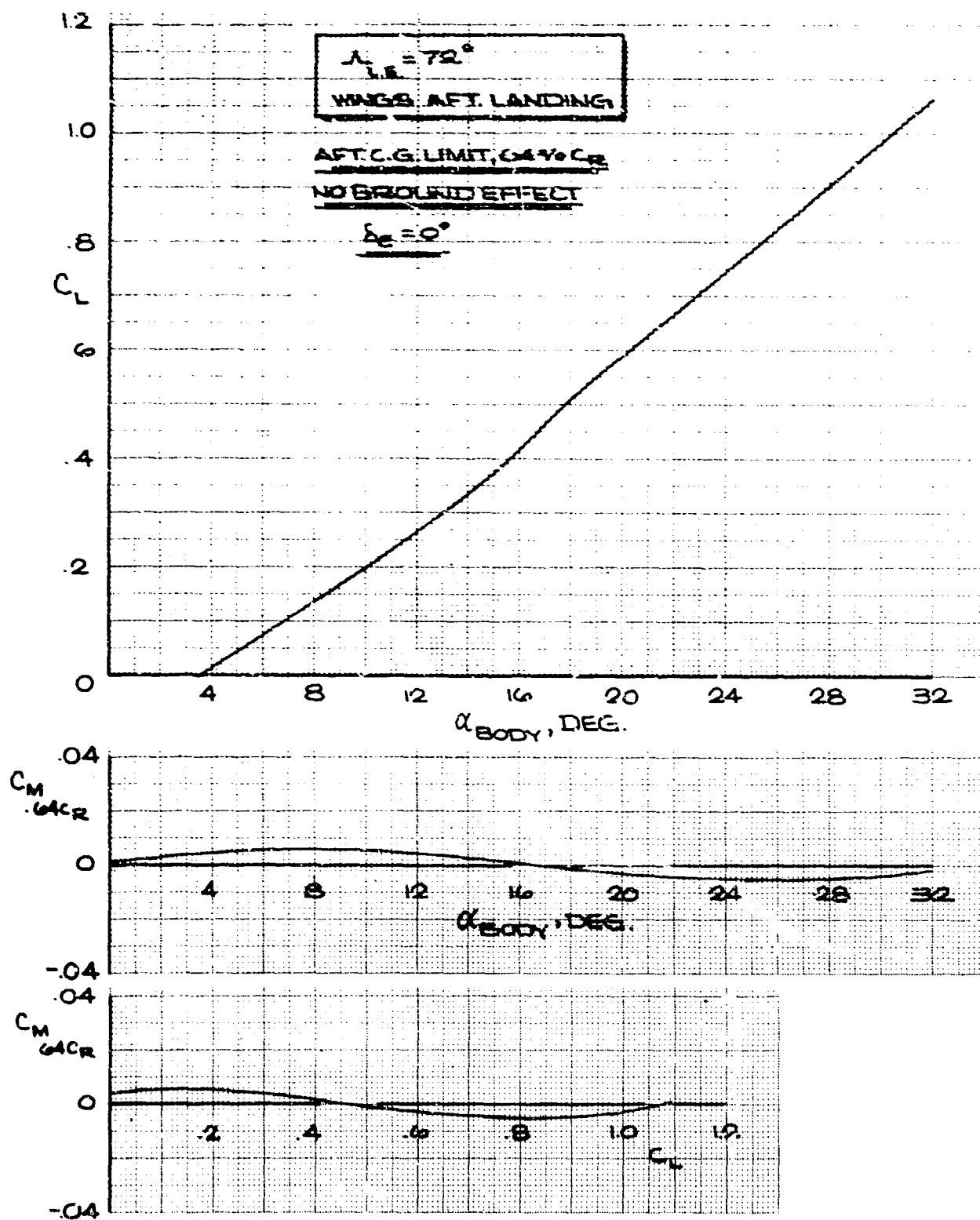


Figure 4-18. Low Speed Stability, Wings Aft Landing

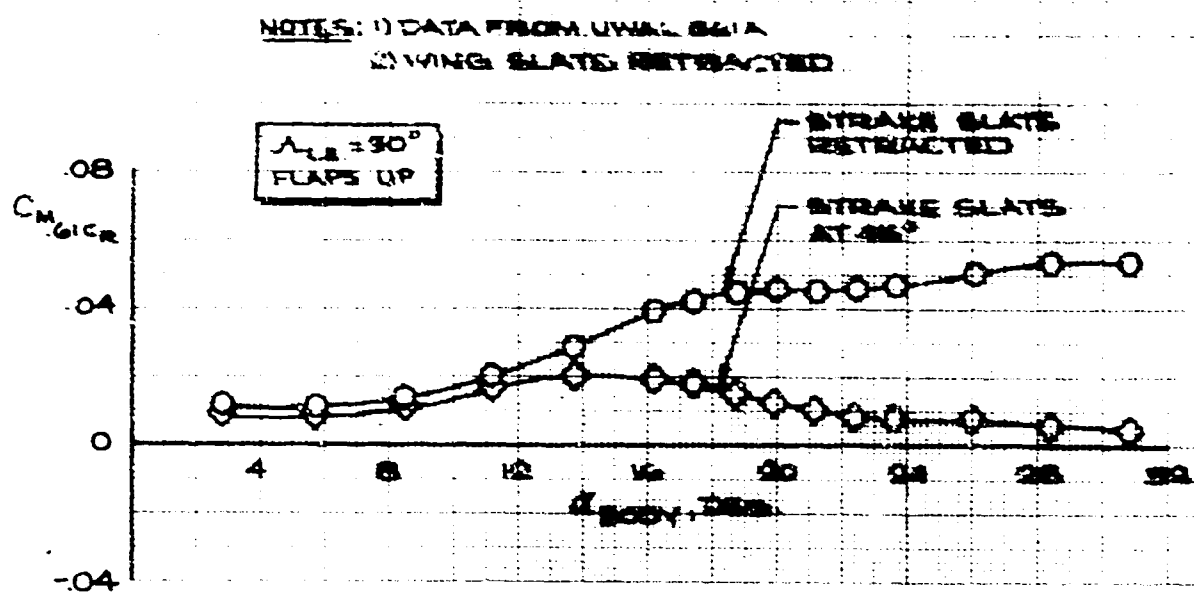


Figure 4-49. Effect of Strake Slats

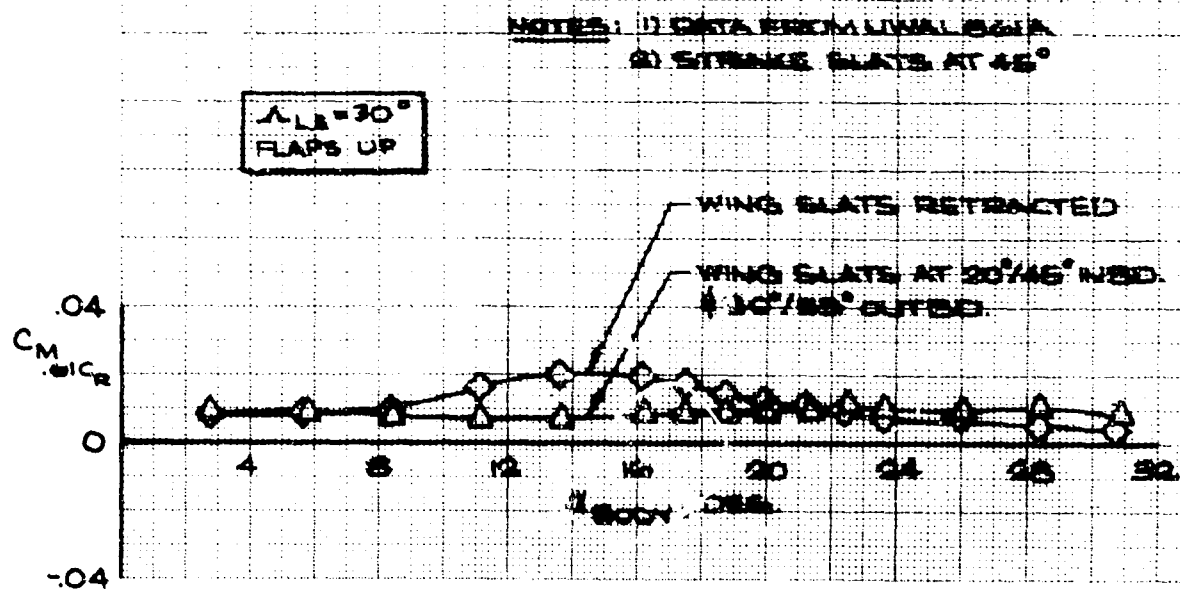


Figure 4-50. Effect of Wing Slats

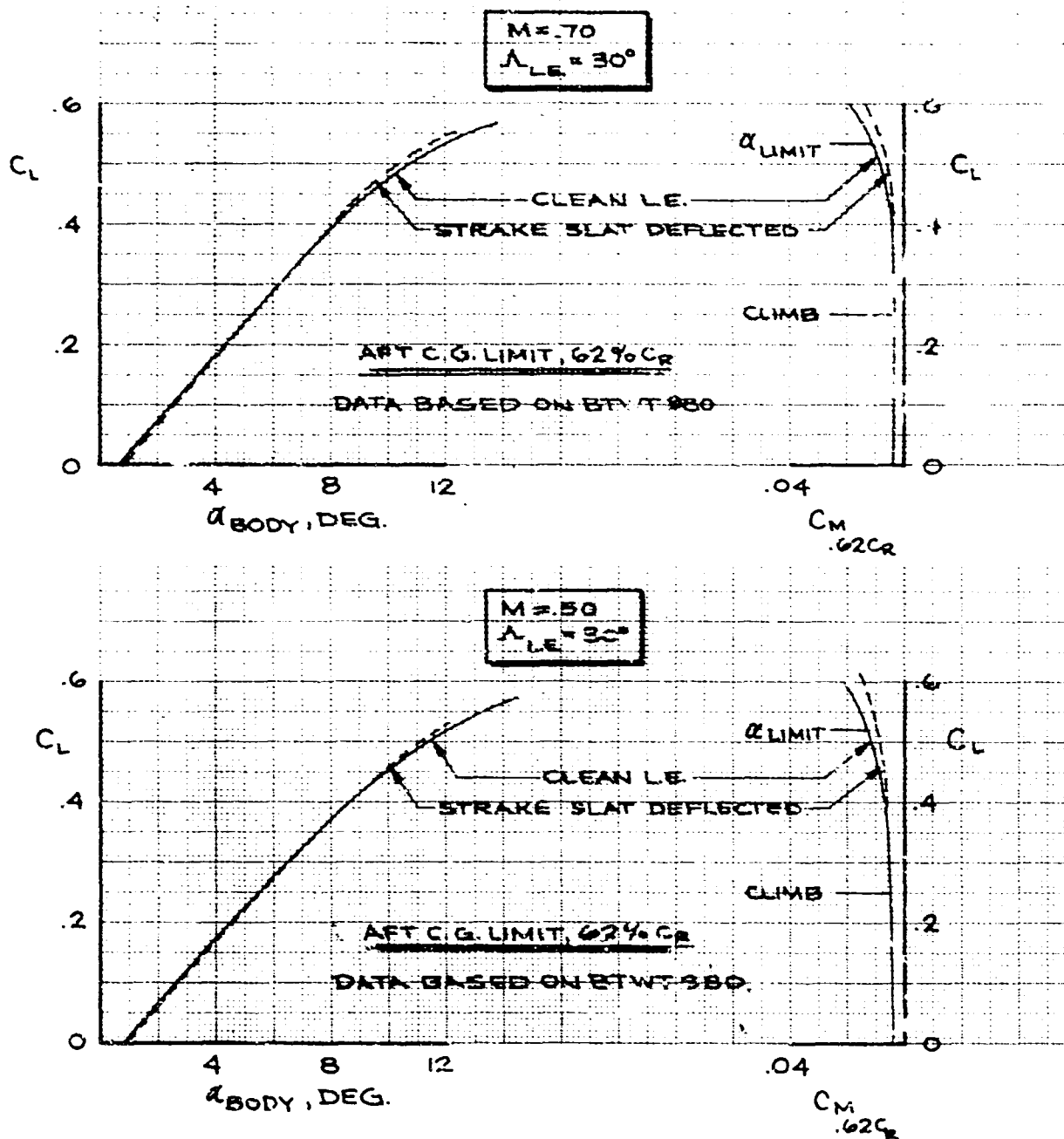


Figure 4-51. Longitudinal Stability Characteristics, $\Lambda = 30$ Degrees

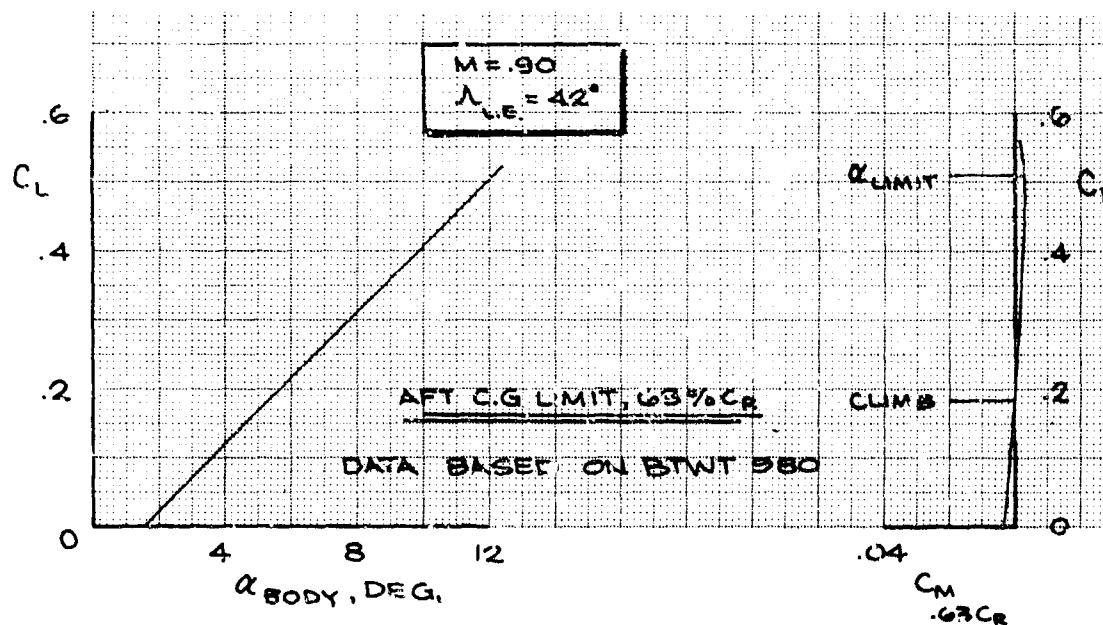
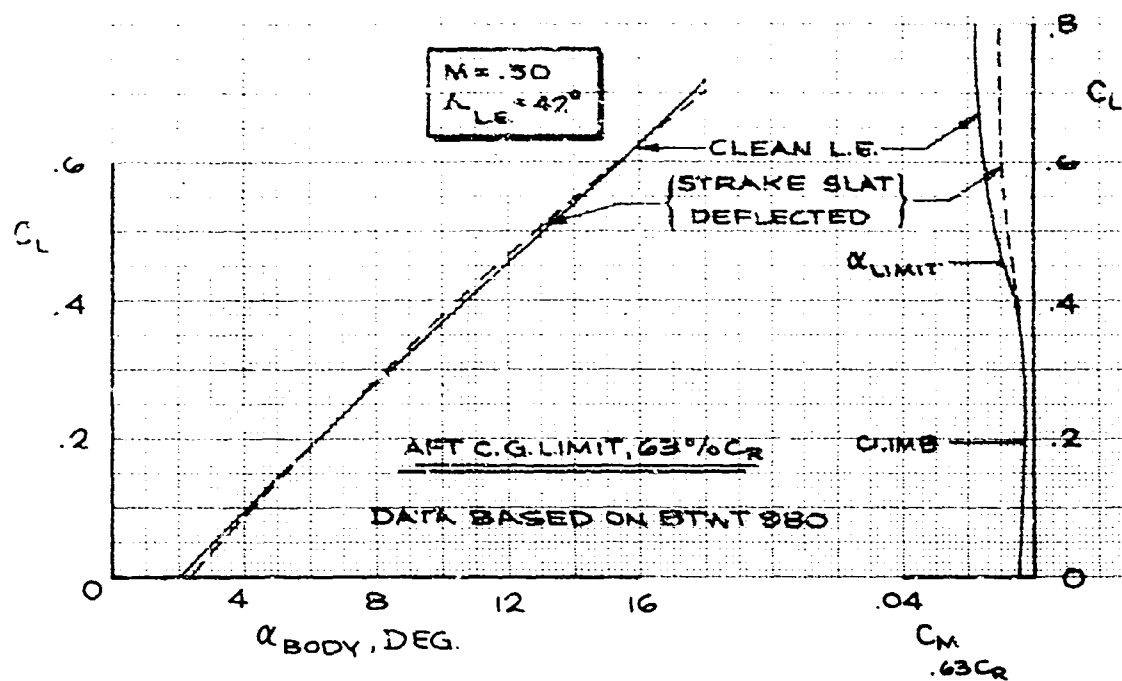


Figure 4-52. Longitudinal Stability Characteristics, $\Lambda = 42$ Degrees

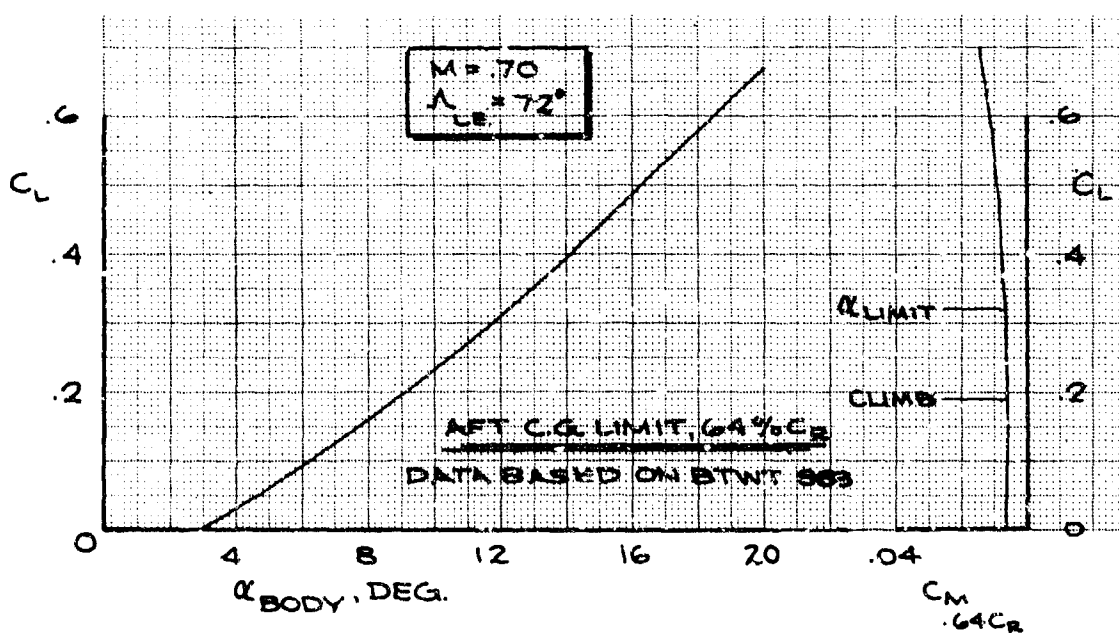
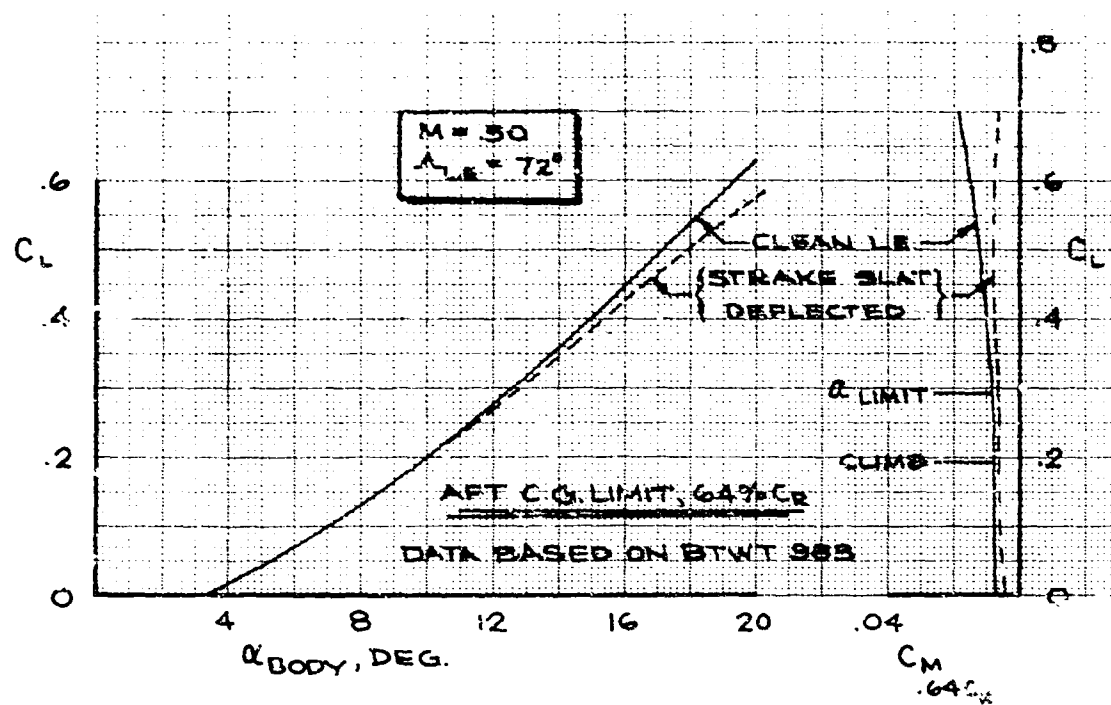


Figure J-53. Longitudinal Stability Characteristics, $\Lambda = 72$ Degrees, $M = .5, .7$

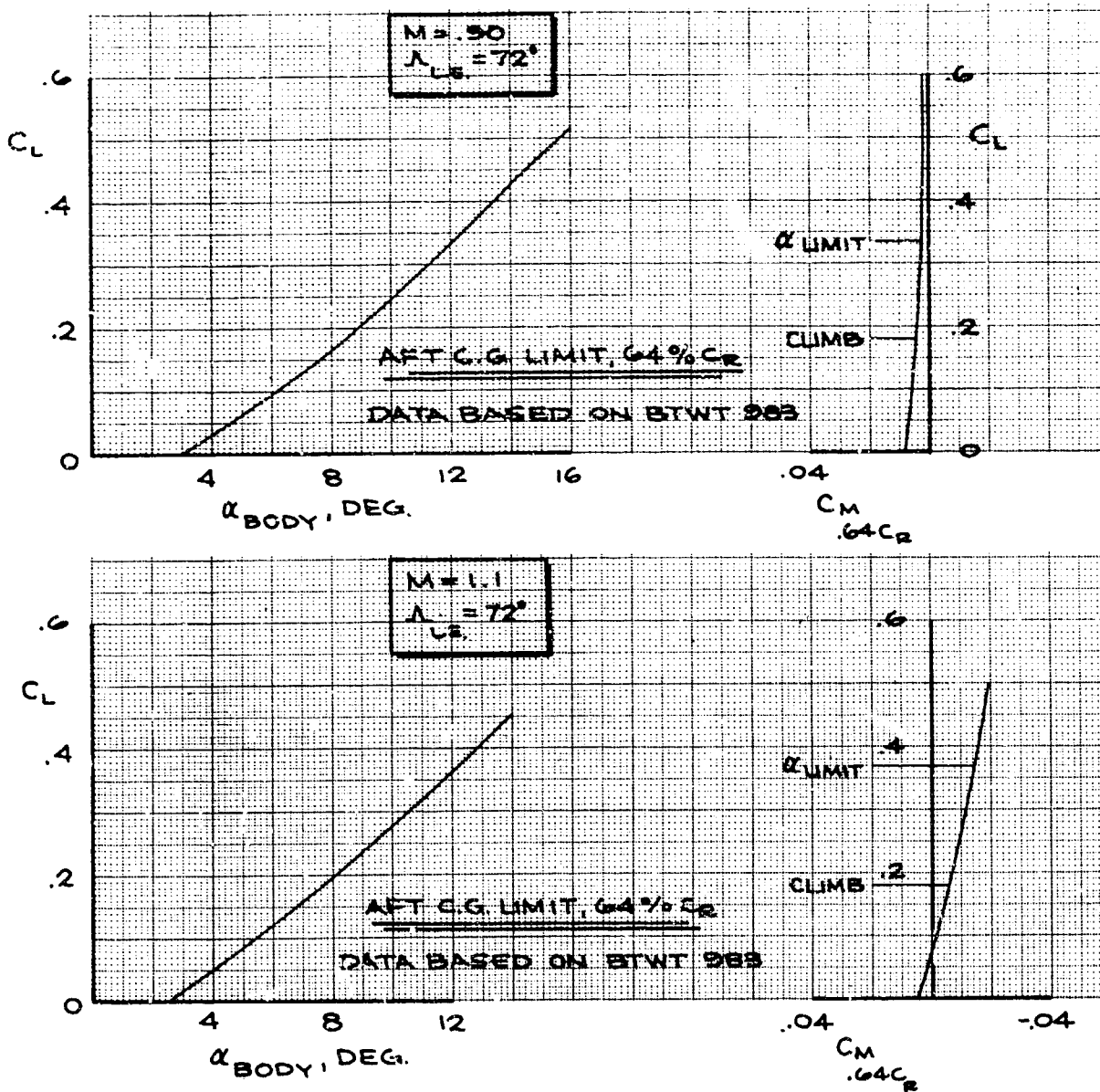


Figure 4-54, Longitudinal Stability Characteristics, $\Lambda = 72$ Degrees, $M = .9, 1.1$

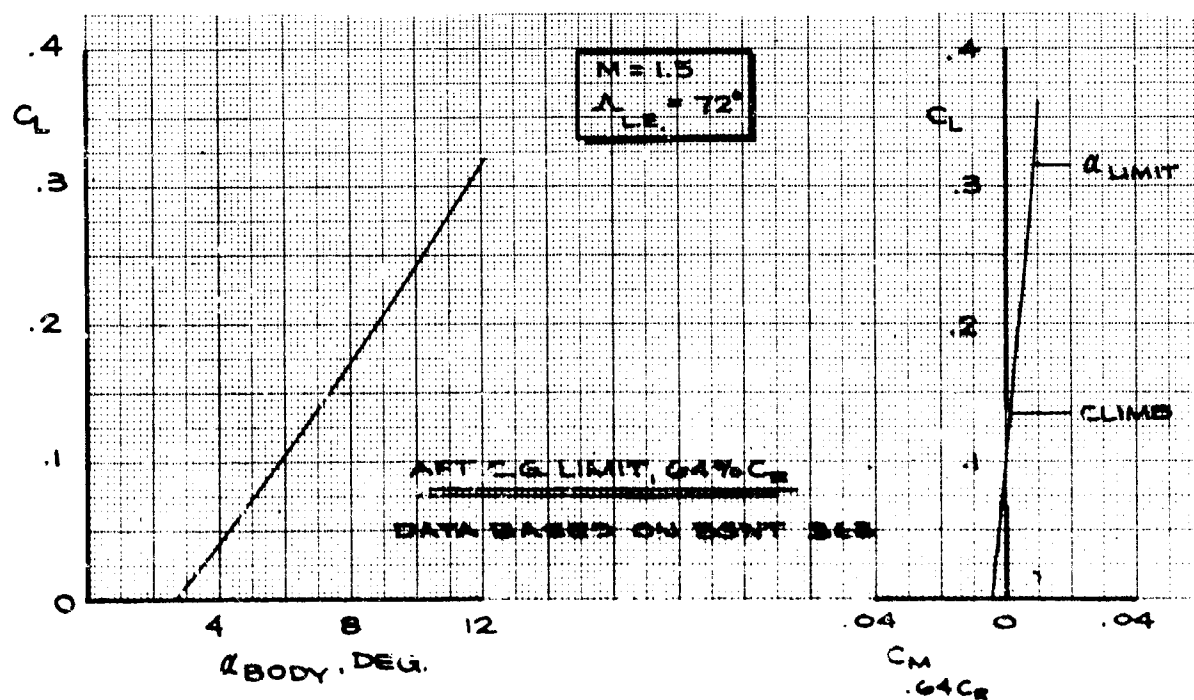
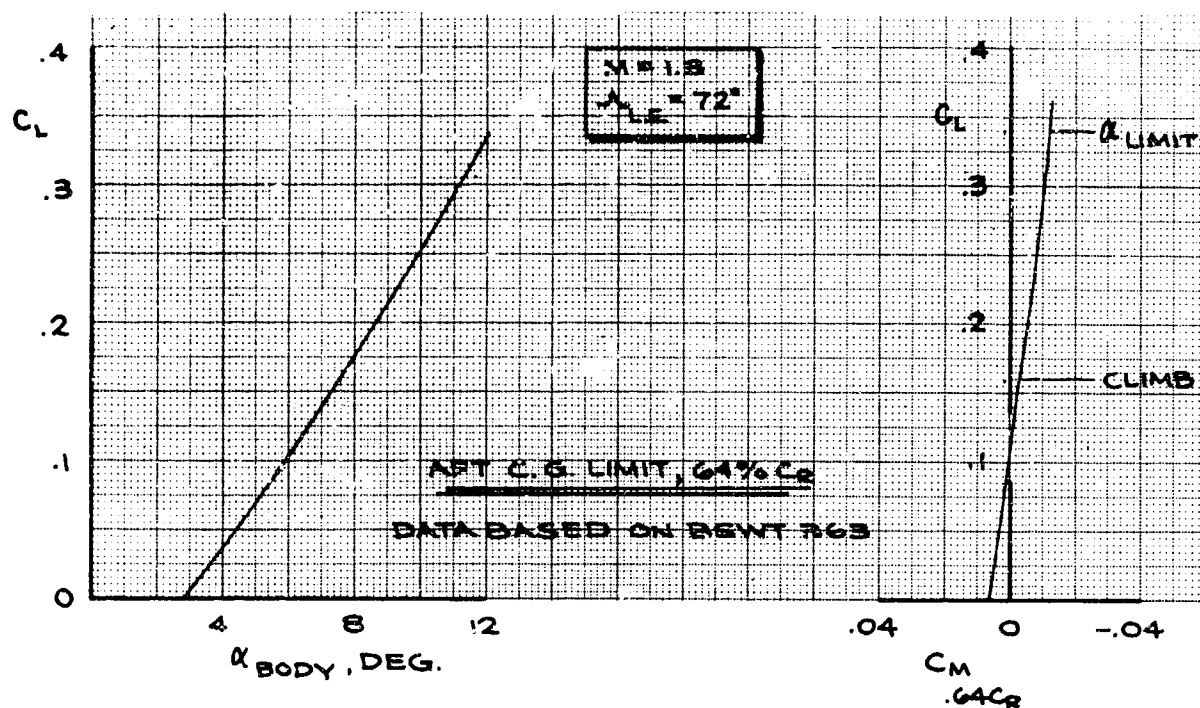


Figure 4-55. Longitudinal Stability Characteristics, $\Lambda_{LE}=72$ Degrees, $M=1.3, 1.5$

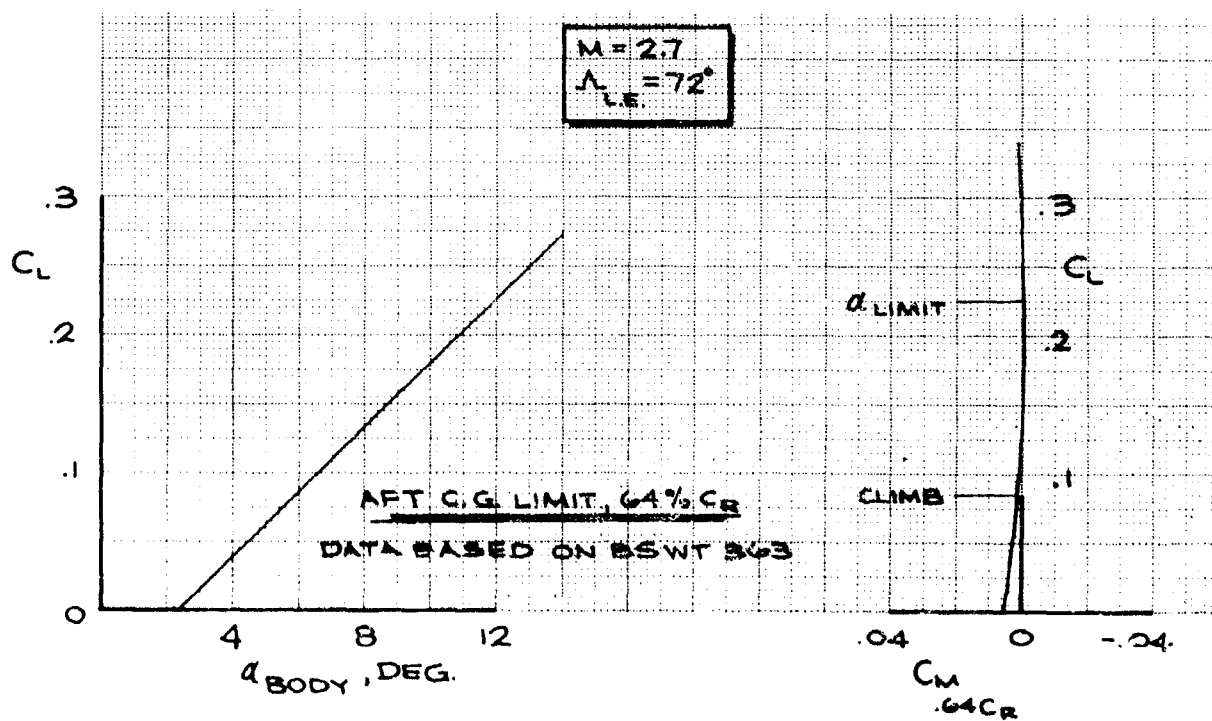
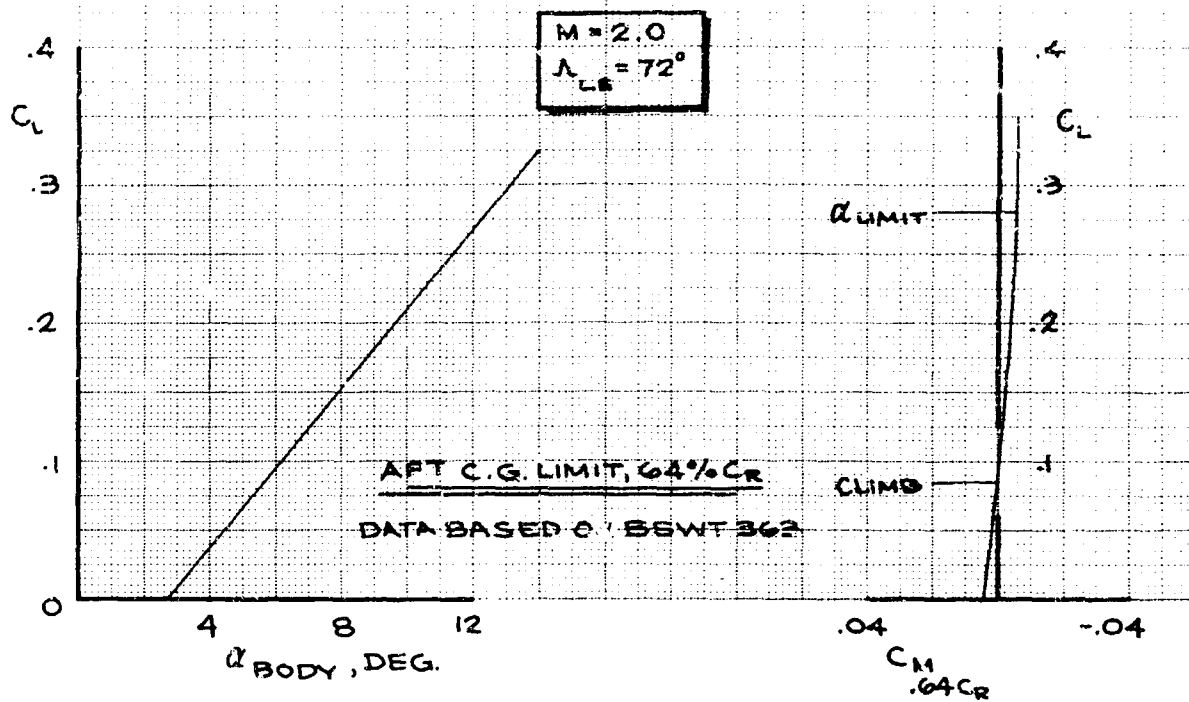


Figure 4-56. Longitudinal Stability Characteristics, $\Lambda = 72$ Degrees, $M = 2.0, 2.7$

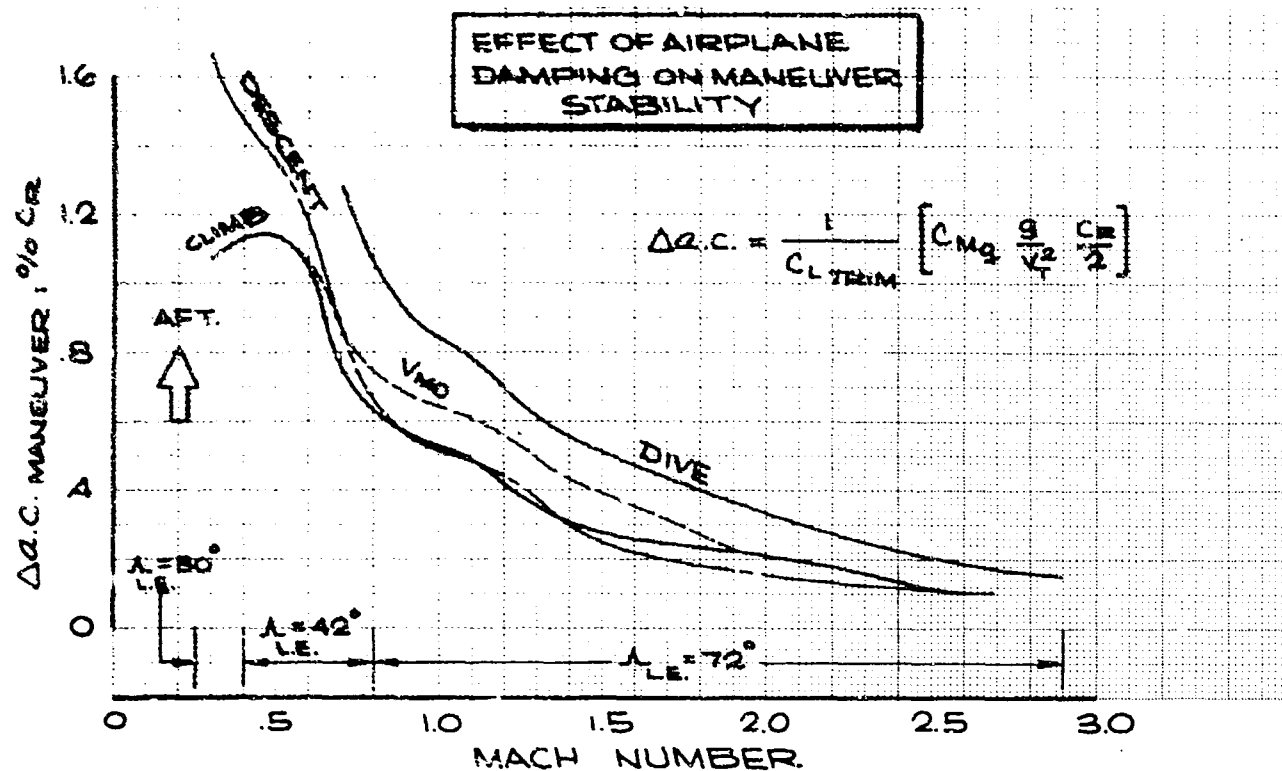


Figure 4-57. Aerodynamic Center Shift Due to Pitch Damping

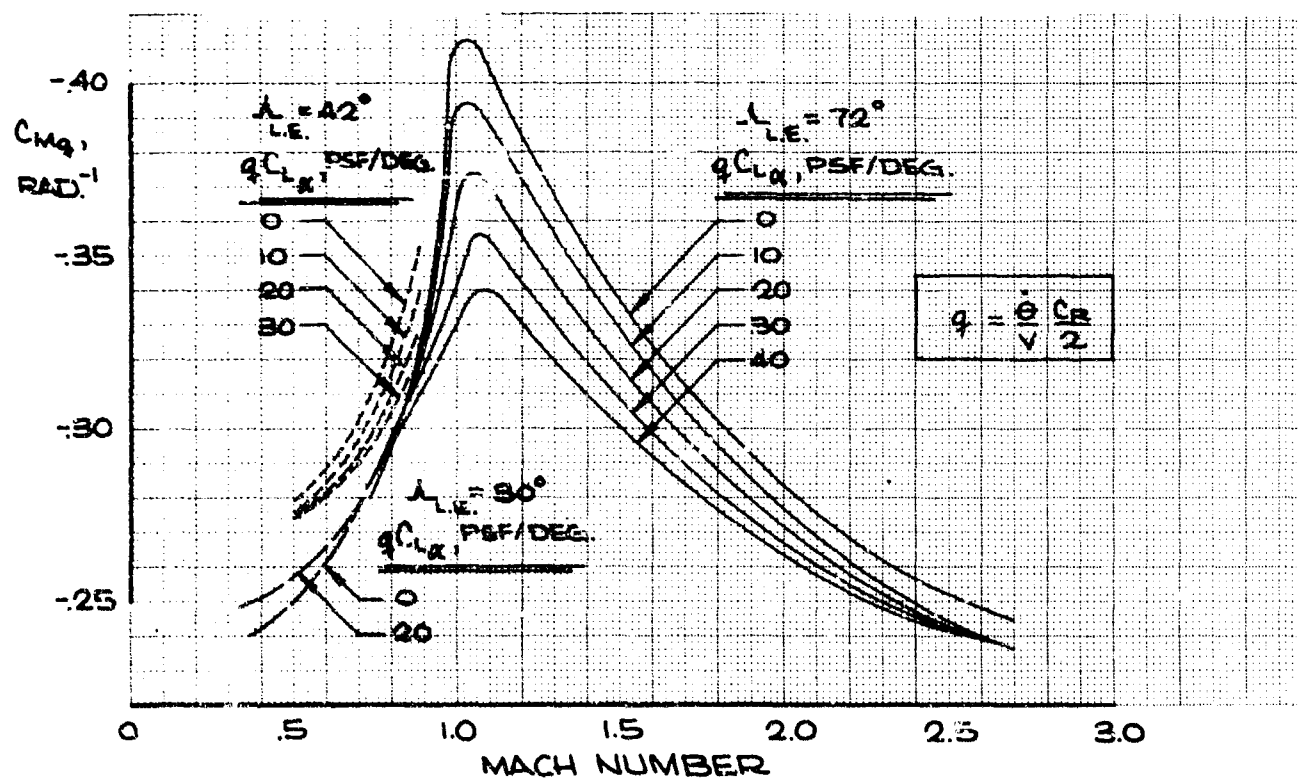


Figure 4-58. Pitching Moment Due to Pitch Rate

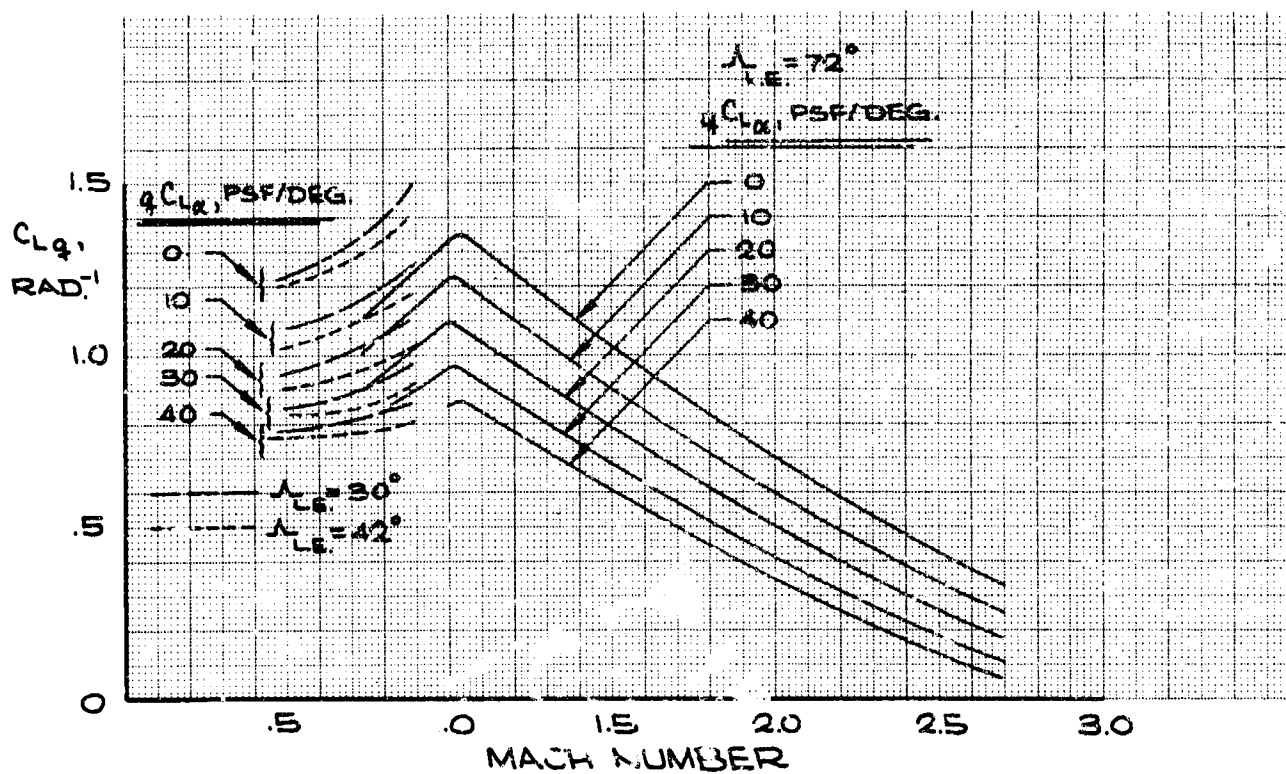


Figure 4-59. Lift Due to Pitch Rate

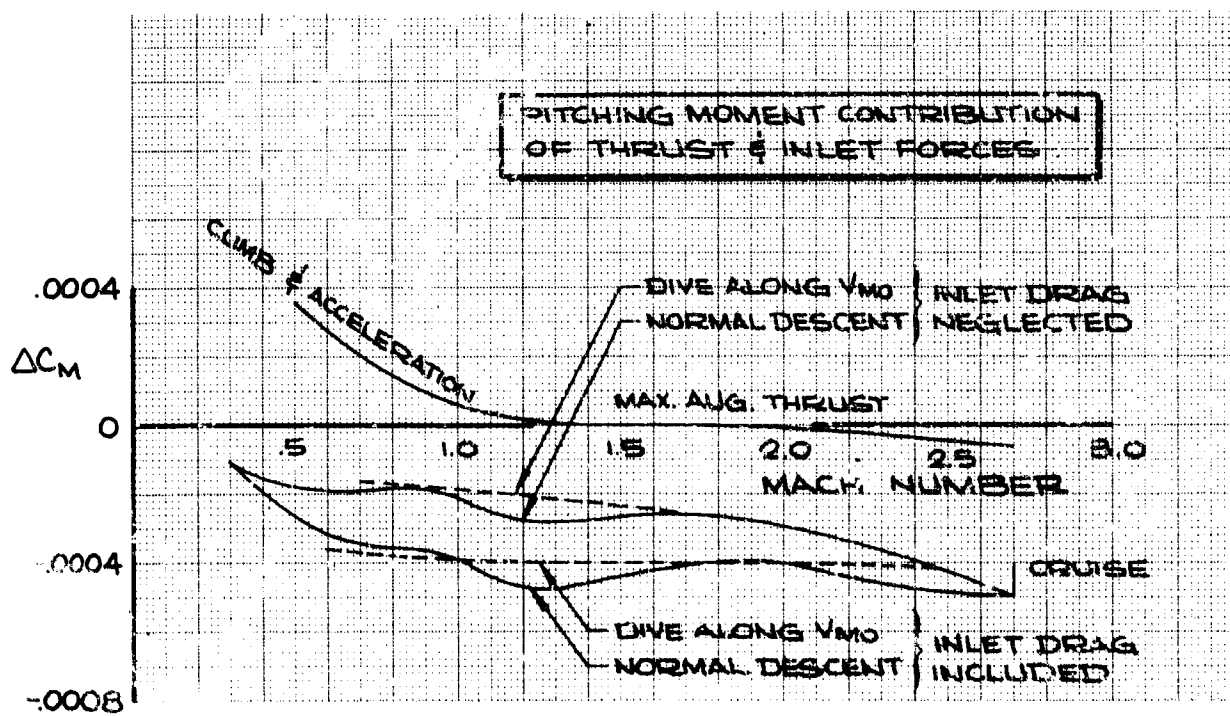


Figure 4-60. Pitching Moment Contribution of Thrust and Inlet Forces

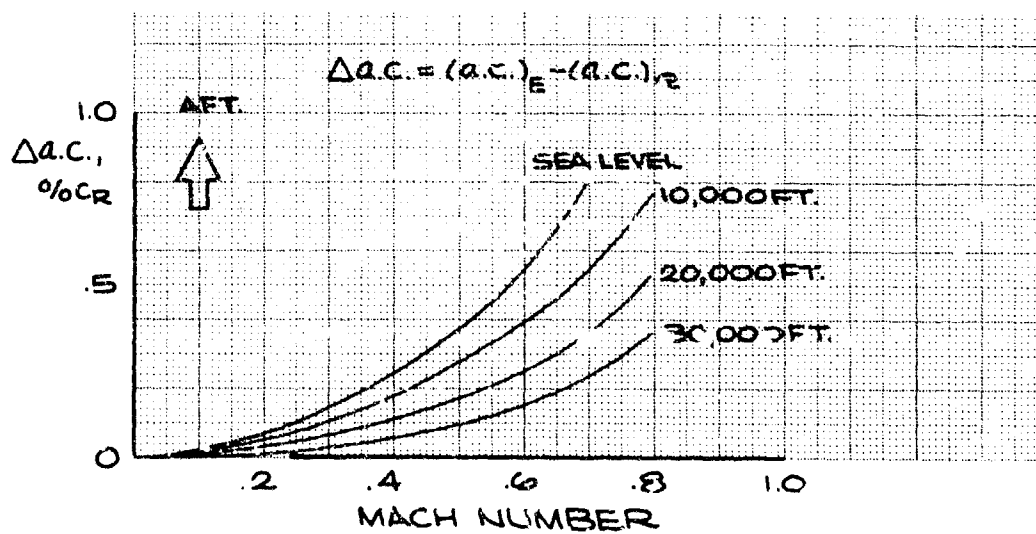
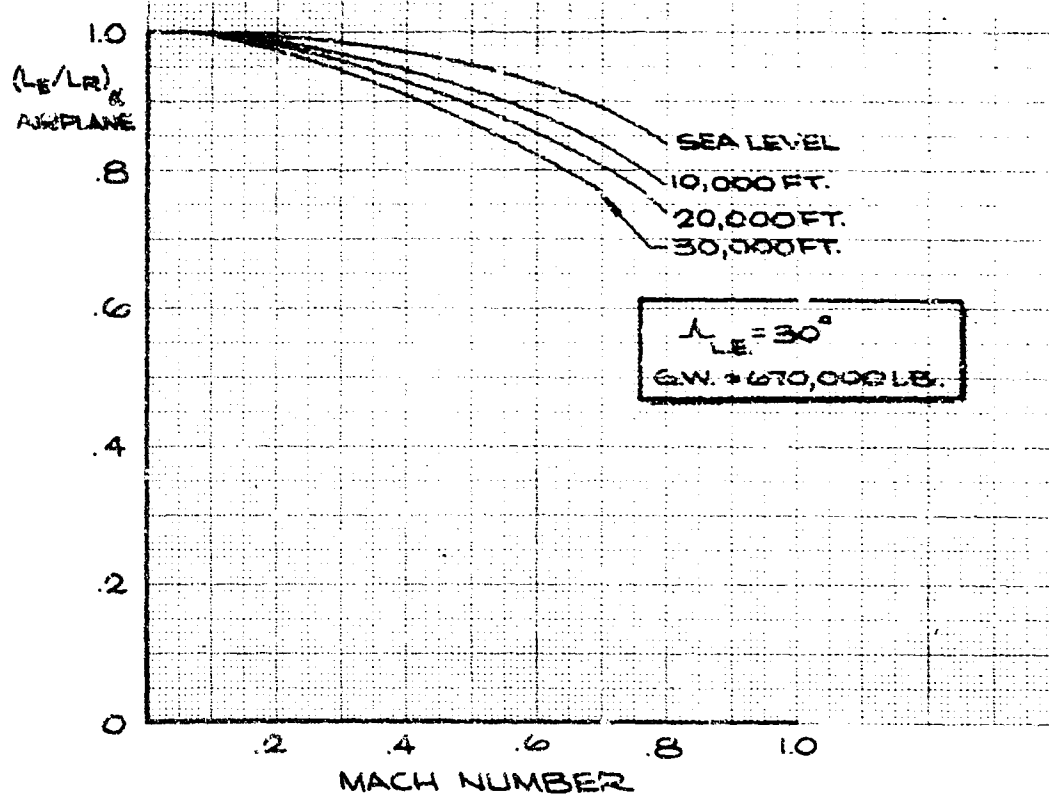


Figure 4-61, Aeroelastic Effects, $\Lambda = 30$ Degrees

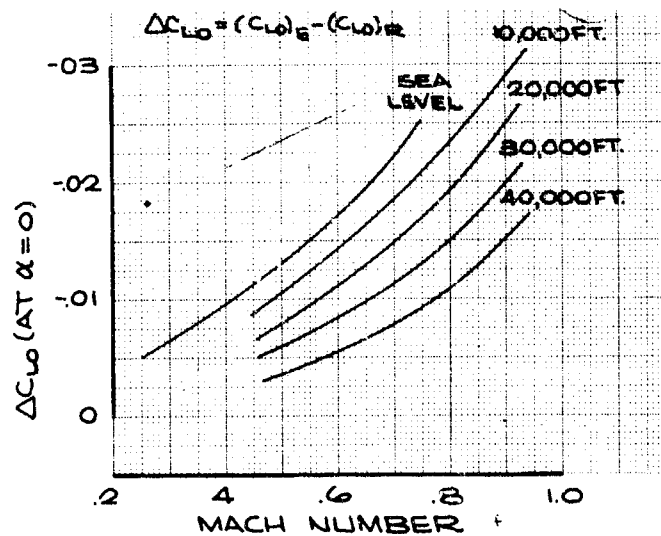
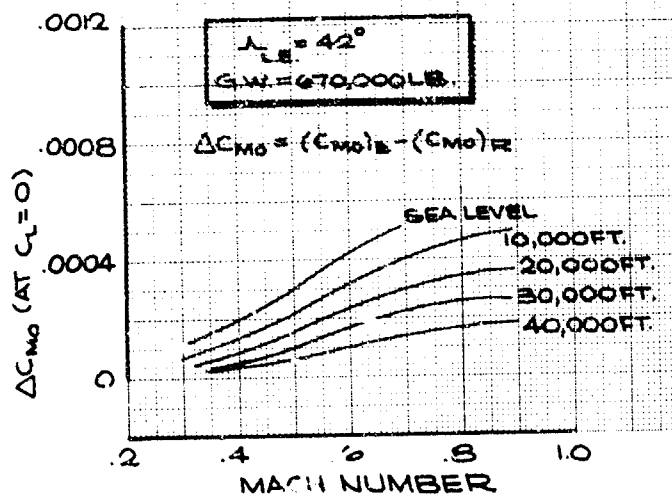
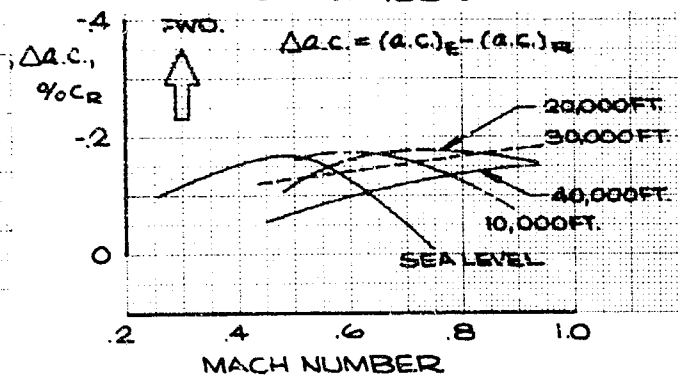
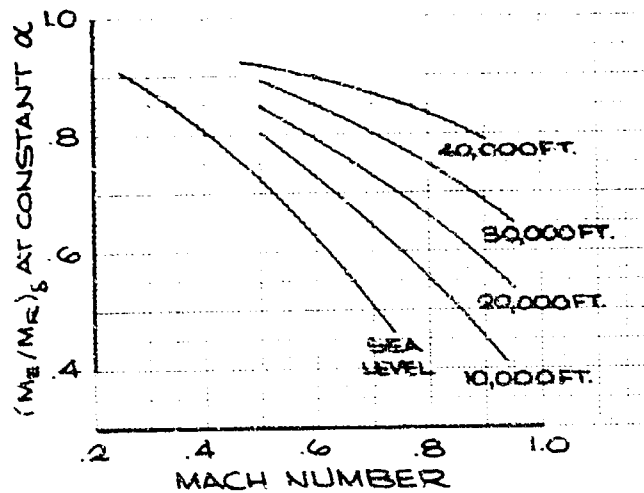
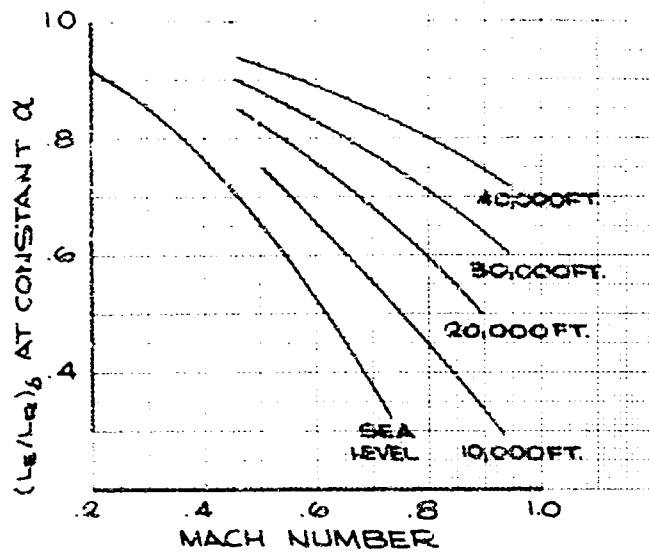
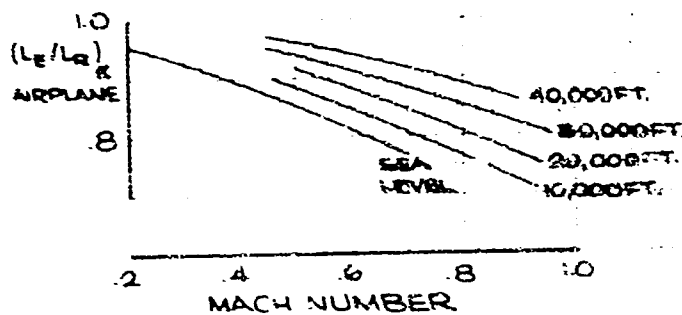


Figure 4-62. Aeroelastic Effects, $\Lambda = 42$ Degrees

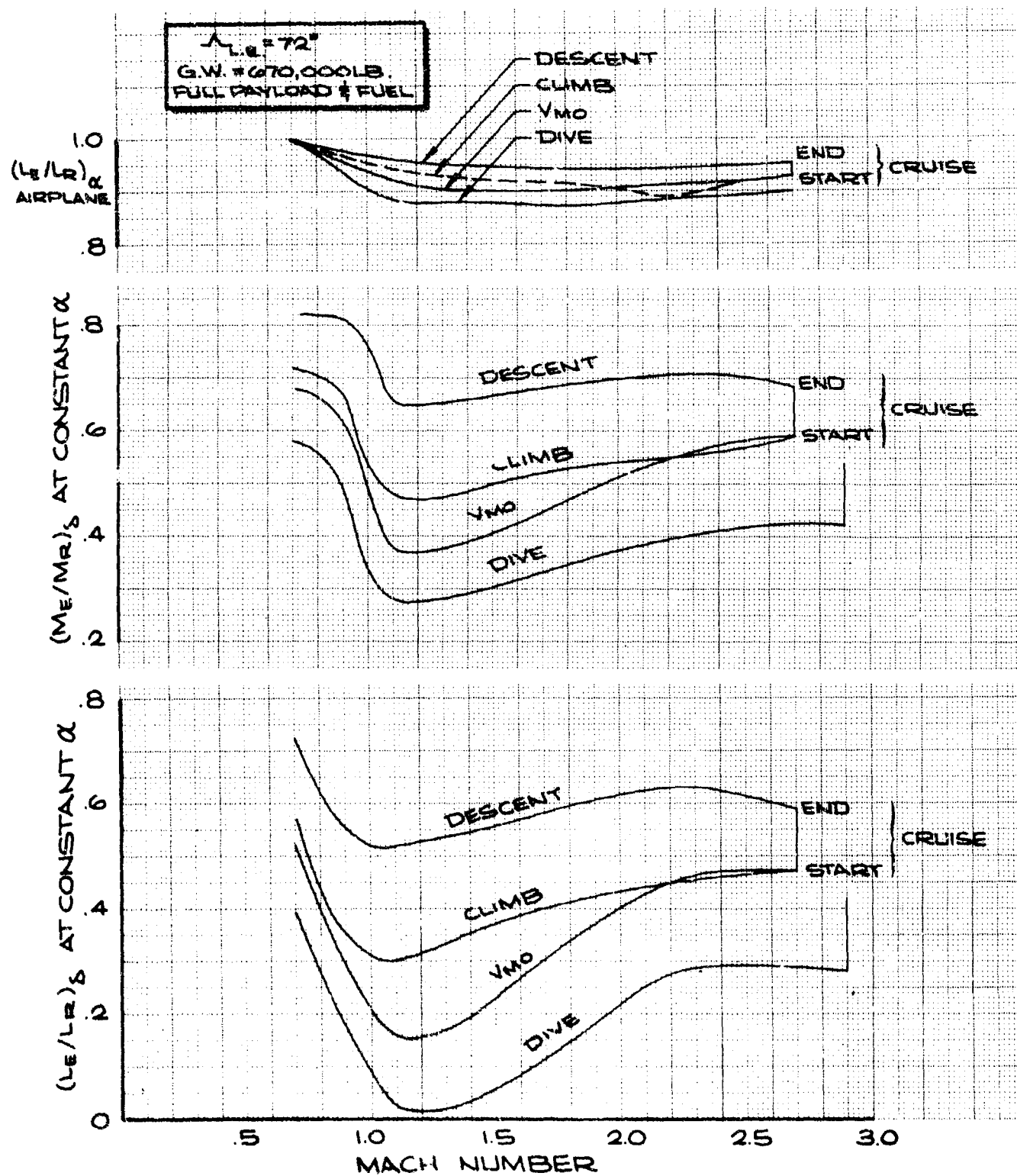


Figure 4-63. Aeroelastic Effects, $\Lambda = 72$ Degrees, Factors

V2-B2707-3

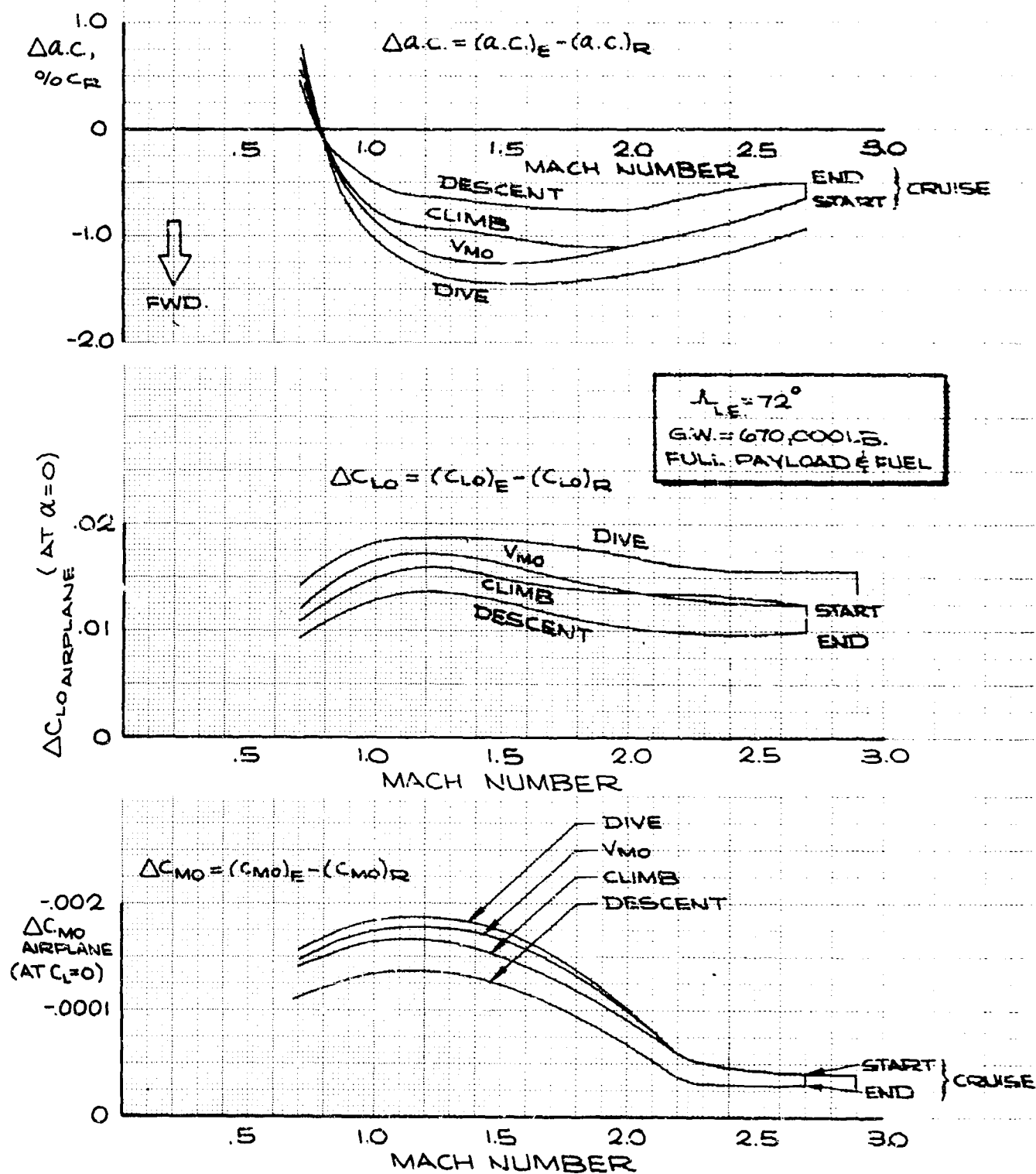


Figure 4-64. Aeroelastic Effects, $\Lambda = 72$ Degrees, Increments

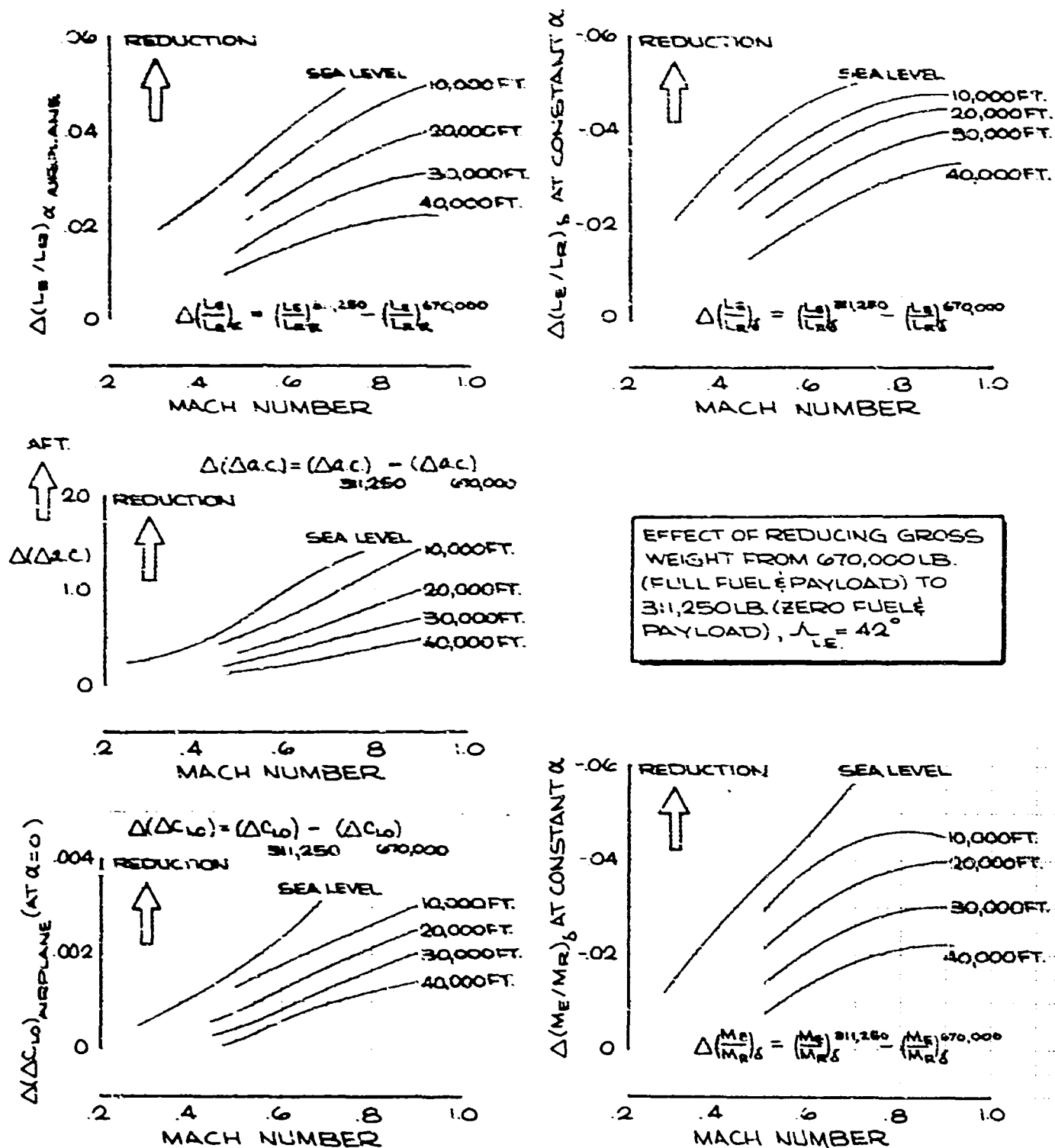


Figure 4-65. Effect of Changing Airplane Weight on Aeroelastic Effects, $\Lambda = 42$ Degrees

EFFECT OF REDUCING GROSS WEIGHT FROM 670,000 LB. (FULL PAYLOAD & FUEL) TO 311,250 LB. (ZERO PAYLOAD & FUEL), $\Lambda_{LE} = 72^\circ$

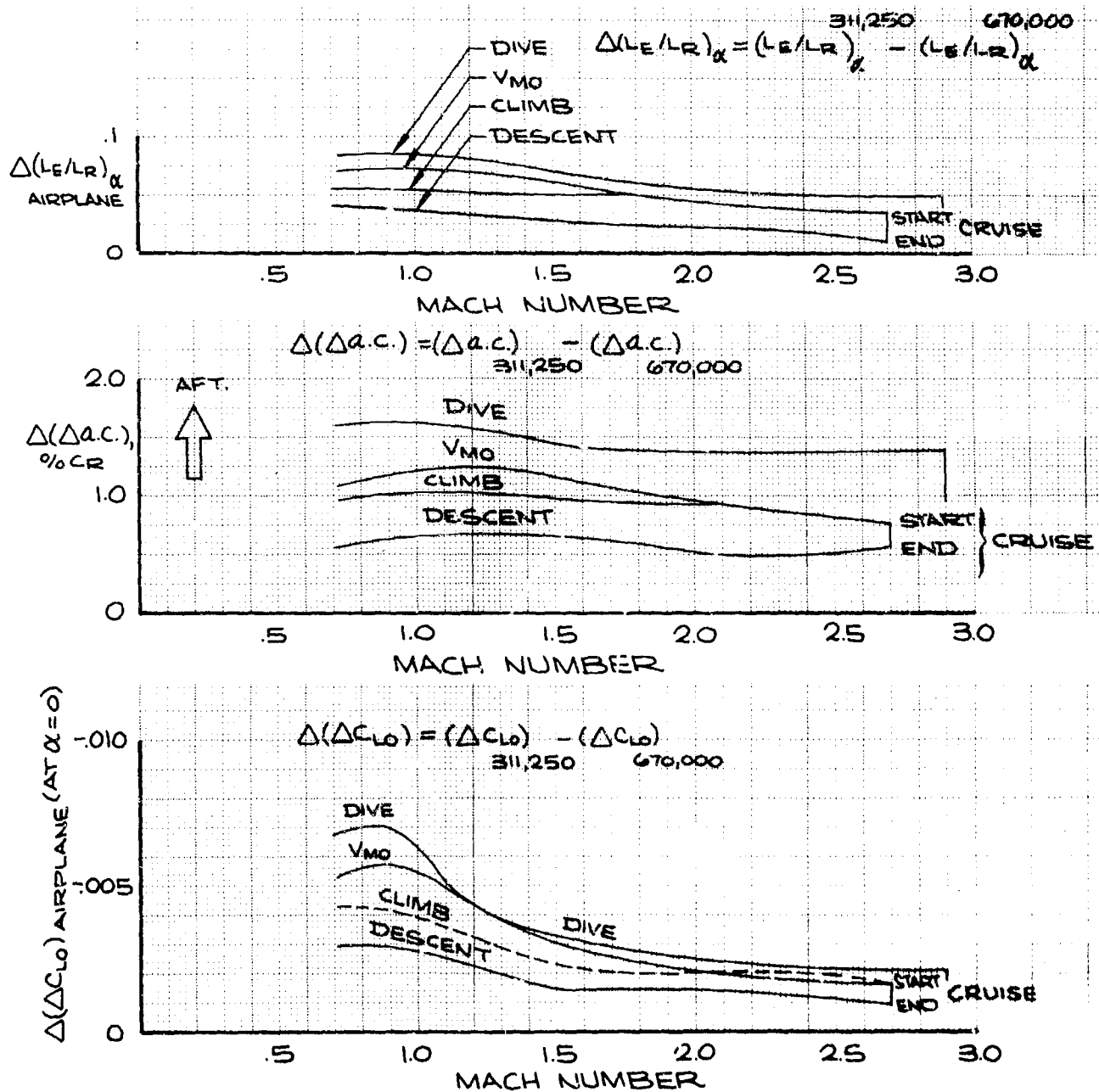


Figure 4-66. Effect of Changing Airplane Weight on Aeroelastic Effects, $\Lambda = 72$ Degrees

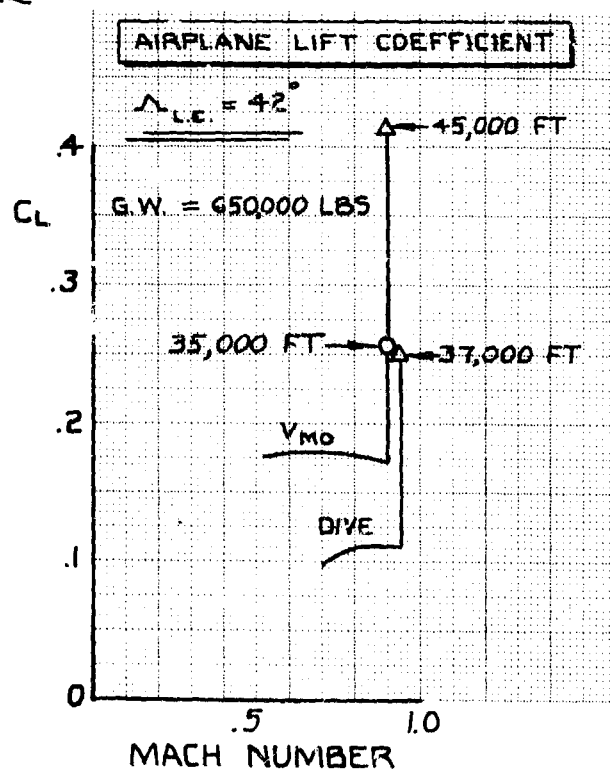
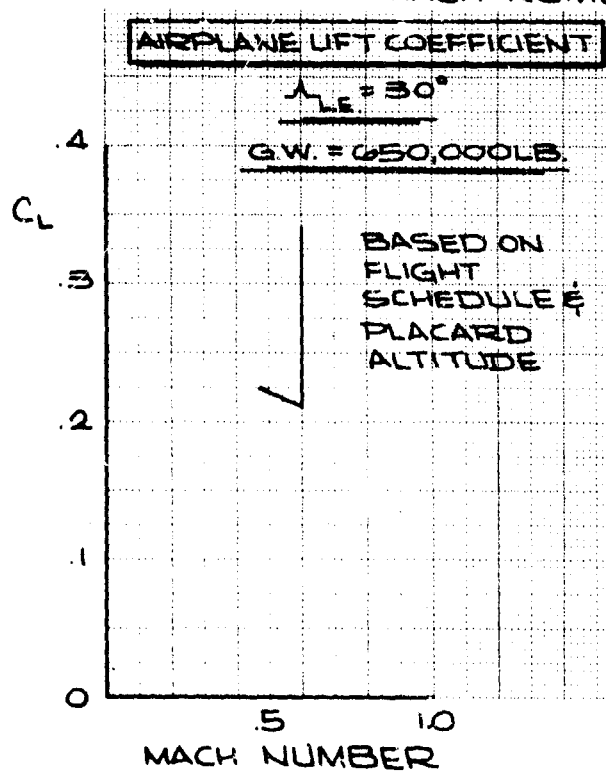
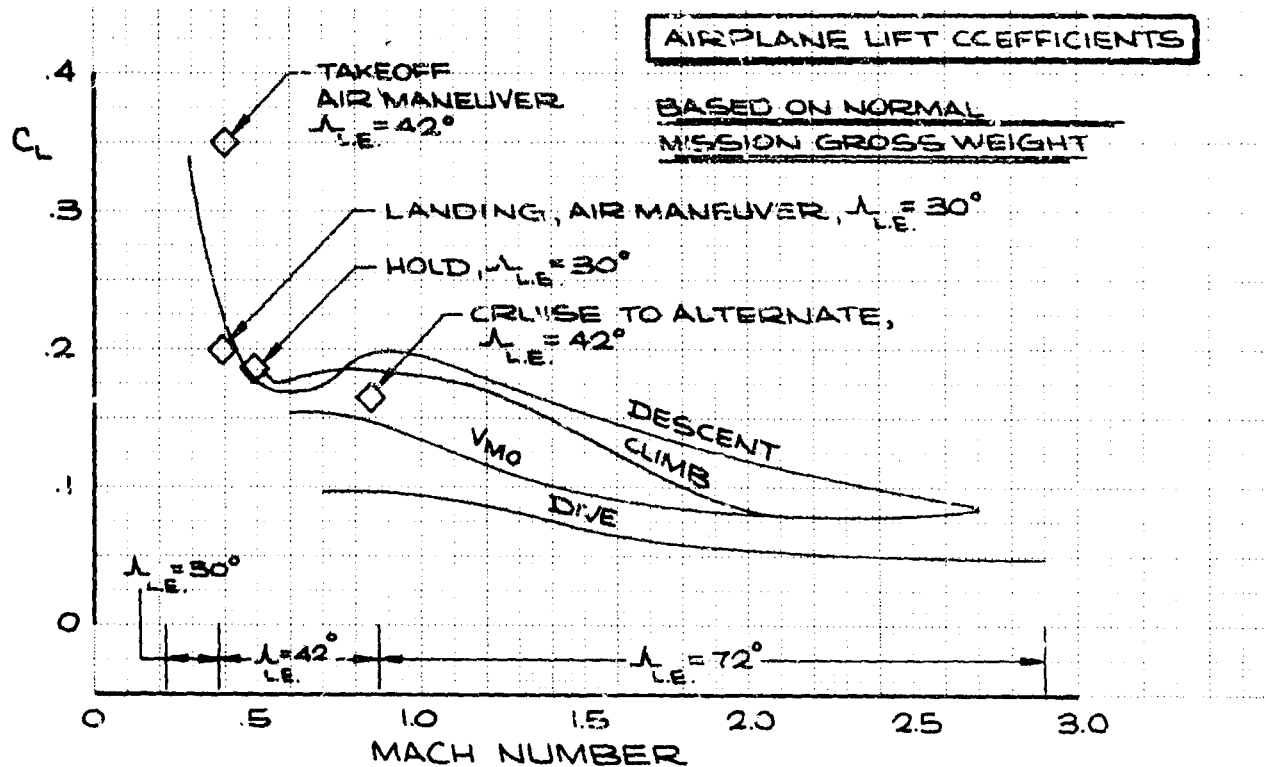


Figure 4-67. Flexible Airplane Lift Coefficients

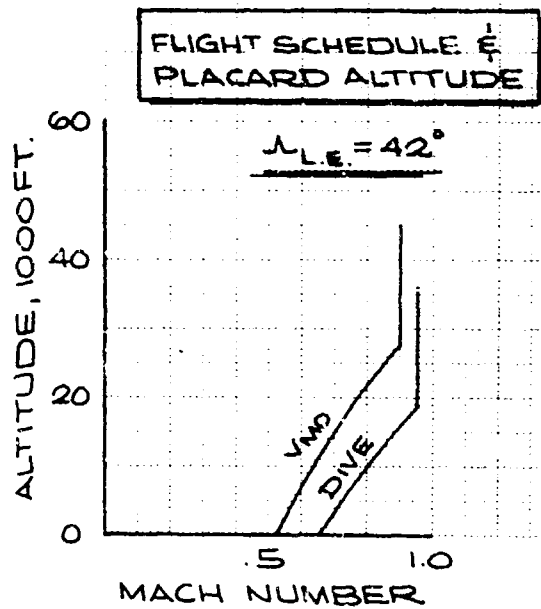
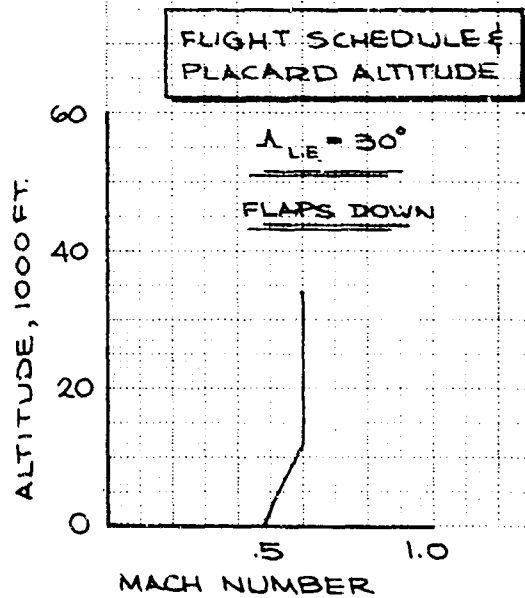
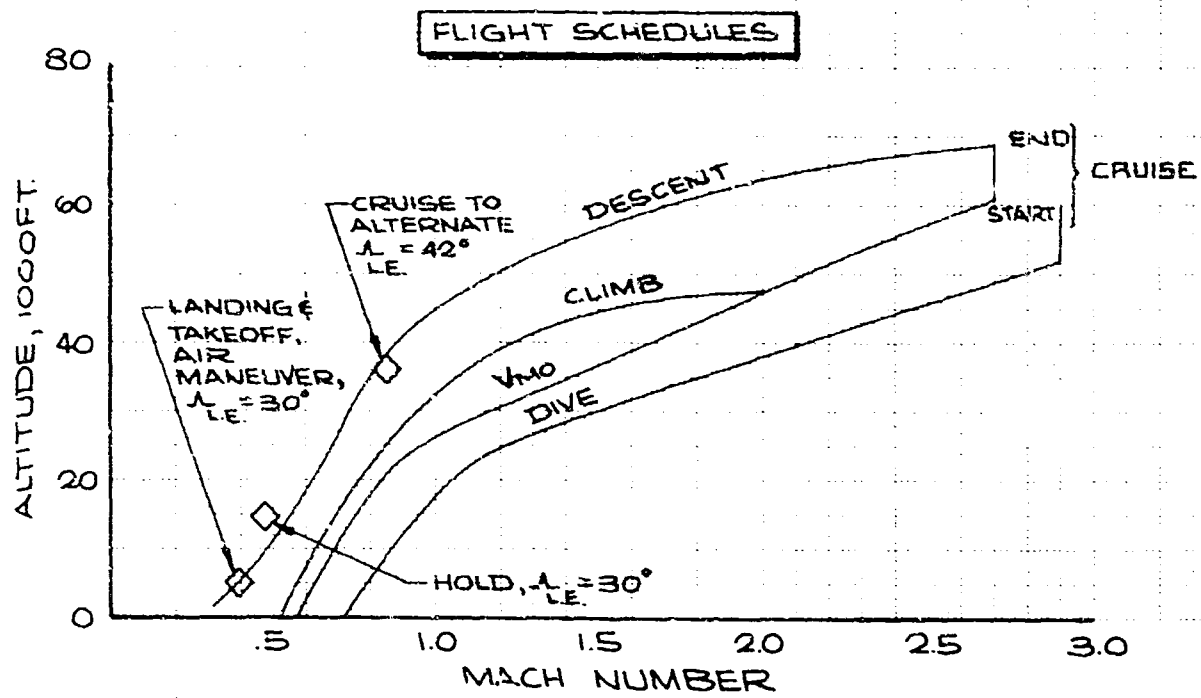


Figure 4-68. Airplane Flight Schedules

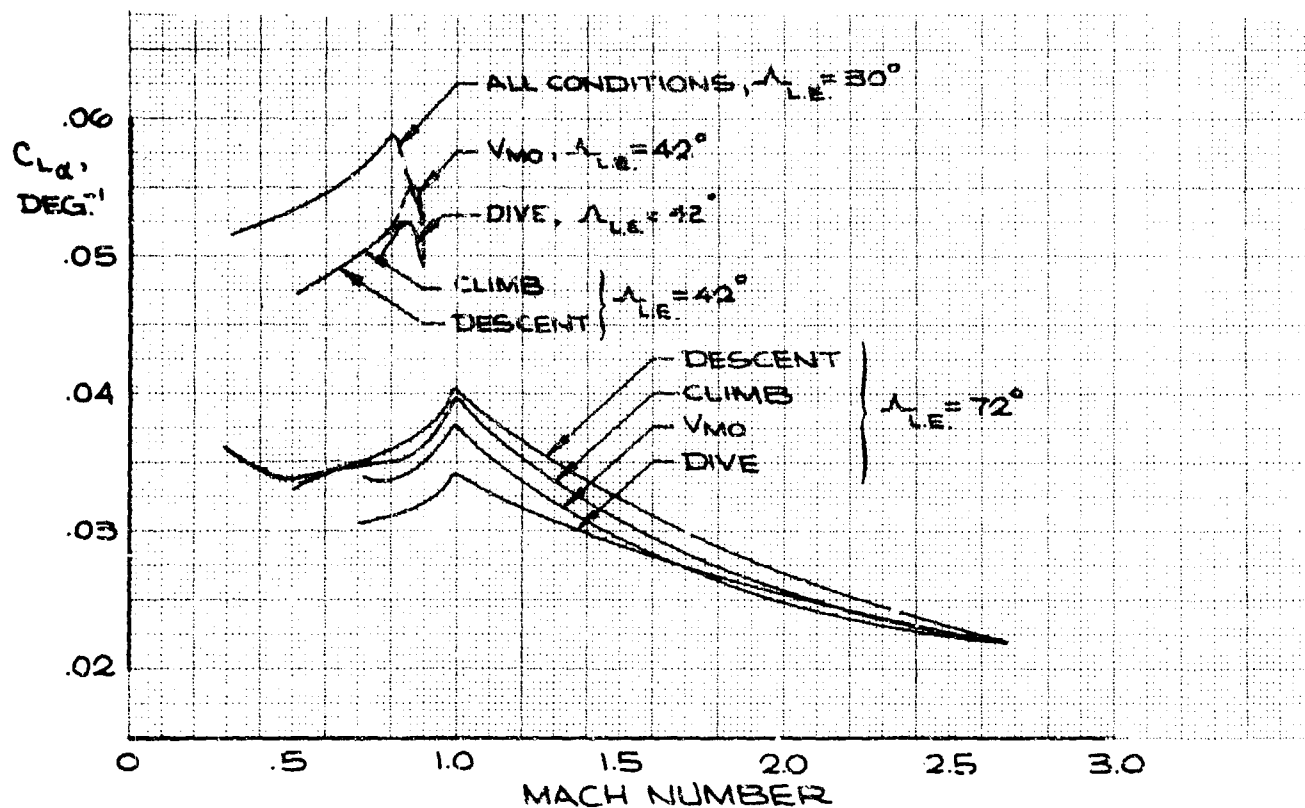


Figure 4-69. Lift Curve Slope, Rigid Airplane

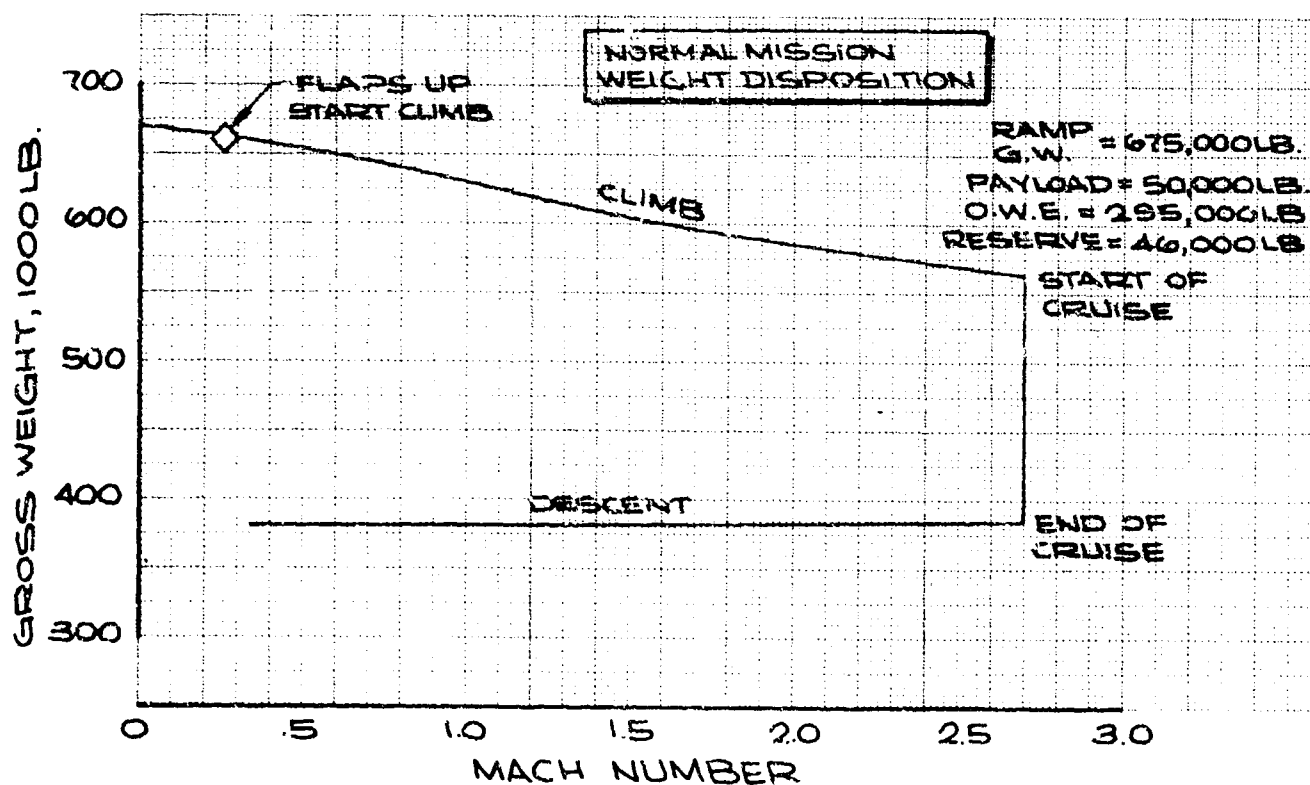


Figure 4-70. Normal Mission Weight Disposition

V2-B2707-3

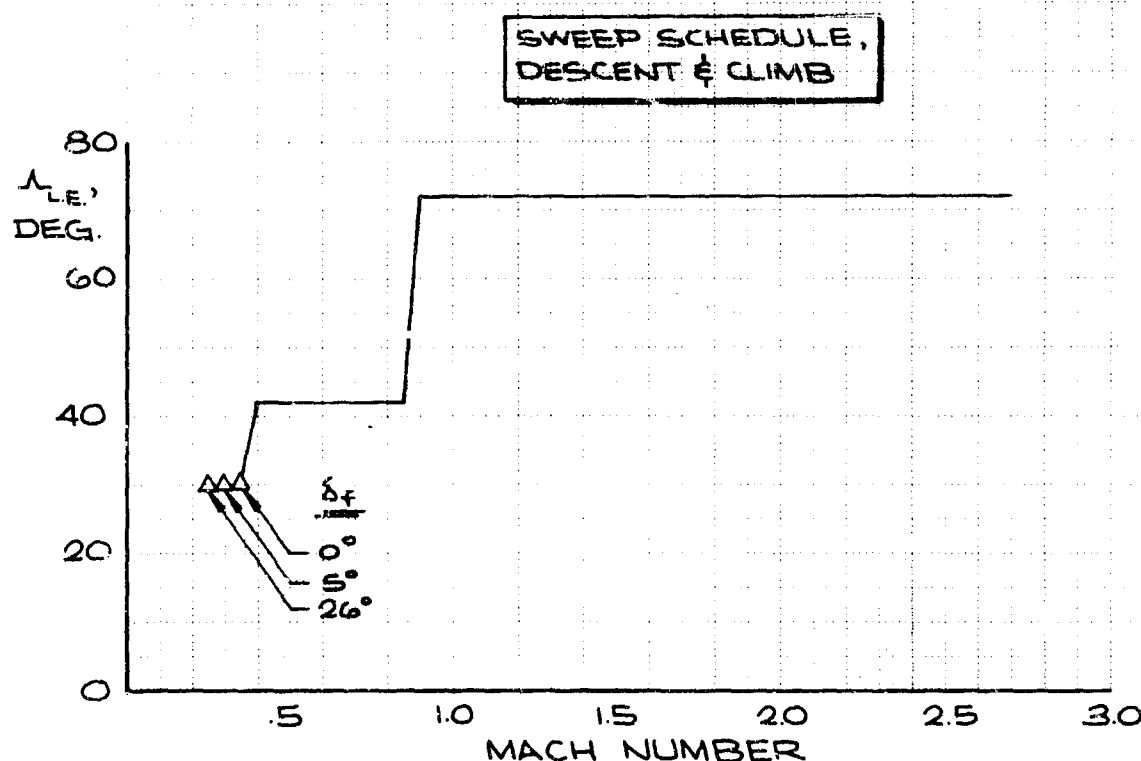


Figure 4-71. Wing Sweep Schedule

Directional stability at the 2.7 M_{MO} placard altitude is shown for the flexible airplane in Fig. 4-72 as a function of airplane angle of attack. This flight condition is the most critical from the standpoint of $C_{n\beta}$ deterioration with angle of

attack. A folding vertical fin has been wind tunnel tested and can provide positive directional stability to attitudes above 2.5 load factor as shown in Fig. 4-72.

Studies are in progress to evaluate the dynamic transients with the estimated control cross-coupling characteristics and the elevon rudder interconnect. These will include nonlinearities of $C_{n\beta}$ with both angle of attack and sideslip angle.

The results of these studies will be available for the onsite evaluation.

Directional stability in the 30-degree sweep landing configuration is shown in Fig. 4-73. Good characteristics exist up to very high angles of attack, well beyond wing stall. These test data were obtained at low Reynolds number, and therefore may change at full scale Reynolds

number due to differences in forebody flow separation. Correlation with flight Reynolds number characteristics will be provided by testing small models in pressure tunnels and by testing the large 1/5 scale model in the NASA Ames 40-ft by 80-ft wind tunnel. If directional stability problems exist at full scale conditions, they probably can be corrected by proper placement of small forebody strakes to induce flow separation similar to that occurring at low Reynolds number.

Figure 4-74 shows the airplane directional stability versus Mach number over the normal flight range. The effect of flexibility is seen to be small, due to the stiff vertical tail and aft body.

Lateral stability, $C_{l\beta}$, is shown over the Mach

range in Fig. 4-75 for the flexible airplane at 1-g normal load factor conditions. These characteristics are based on rigid model data without aeroelastic corrections, since tests of a 72-degree sweep model with a flexible wing have shown little effect of wing flexibility on $C_{l\beta}$ for a wide range

of dynamic pressures. The changes in wing dihedral due to wing bending were evidently com-

compensated for by the unloading of the wing tip through bending. Figure 4-76 shows the wind tunnel data for the elastic model.

The variation of lateral stability with angle of attack is shown in Fig. 4-77 for several combinations of Mach number and wing sweep. Directional stability and side force characteristics are shown in Figs. 4-78 and 4-79. It is seen that directional stability at Mach 2.7 is a function of both angle of attack and side slip.

The aeroelastic correction factors for the rigid lateral-directional stability data are presented in Figs. 4-80 and 4-81. The following equations indicate the manner of application of the aeroelastic data to obtain flexible airplane effects.

$$\left(\Delta C_{n\beta}\right)_{\text{vertical tail}}^{\text{flexible}} = \left(\Delta C_{n\beta}\right)_{\text{vertical tail}}^{\text{rigid}} \left(\frac{L_E}{L_R}\right)_v (K_{BB})_{\text{vert.}}$$

$$\left(\Delta C_{n\beta}\right)_{\text{ventral fin}}^{\text{flexible}} = \left(\Delta C_{n\beta}\right)_{\text{ventral fin}}^{\text{rigid}} (K_{BB})_{\text{ventral}}$$

$$\left(\Delta C_{Y\beta}\right)_{\text{vertical tail}}^{\text{flexible}} = \left(\Delta C_{Y\beta}\right)_{\text{vertical tail}}^{\text{rigid}} \left(\frac{L_E}{L_R}\right)_v (K_{BB})_{\text{vert.}}$$

No aeroelastic corrections were applied to the body, nacelles, and horizontal tail contributions to airplane directional stability or side force effects. In addition, no aeroelastic corrections were applied for the wing and ventral fin contributions to side force, or for the wing contribution to directional stability.

4.3 DYNAMIC STABILITY

Preliminary dynamic analyses and flight simulator evaluations of the B-2707 have been conducted to evaluate unaugmented airplane handling qualities, control capabilities, stability augmentation systems, and emergency operations. These studies have shown that there are practical solutions available for all cases in which control problems exist or where improvements in handling characteristics are desired. The airplane has demonstrated that it is sufficiently tractable to permit safe deceleration, descent, and landing in the event of complete failure of the stability augmentation systems. However, the simulator tests have emphasized the need for stability and control response augmentation and improved instrument displays to ensure good handling qualities at all flight conditions.

4.3.1 Longitudinal Dynamics

Longitudinal handling qualities of the unaugmented airplane are characterized by sluggish pitch response which is well damped at low speeds and lightly damped at high speeds. These character-

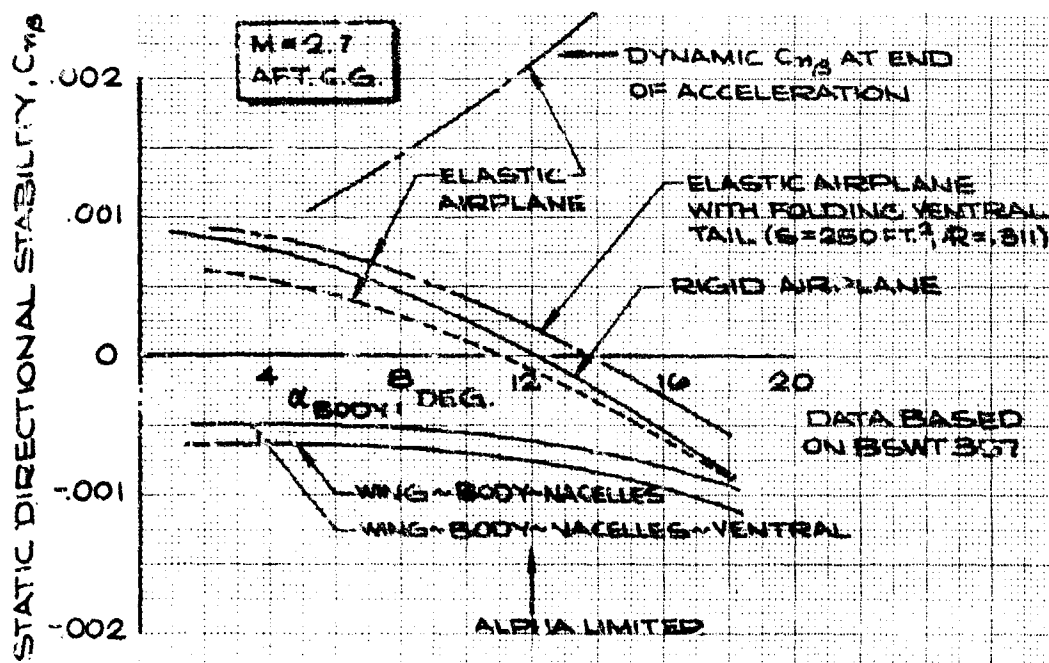


Figure 4-72 Mach 2.7 Directional Stability

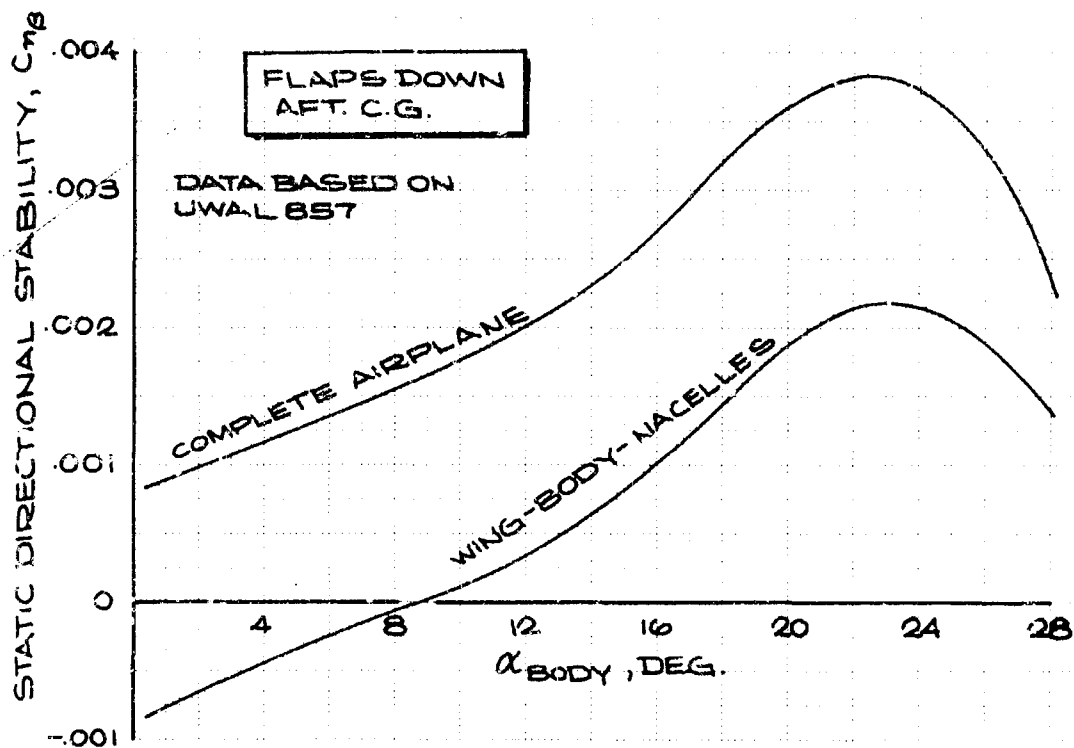


Figure 4-73. Directional Stability, Landing

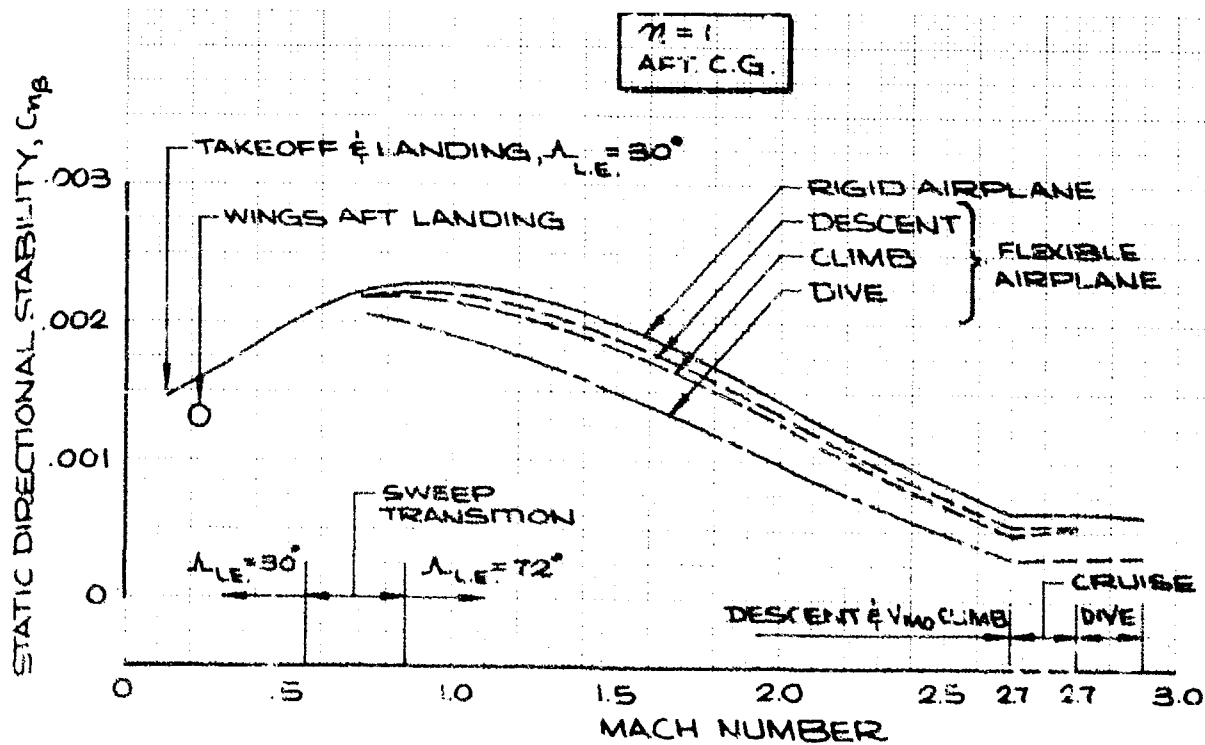


Figure 4-74. Directional Stability Vs. Mach Number

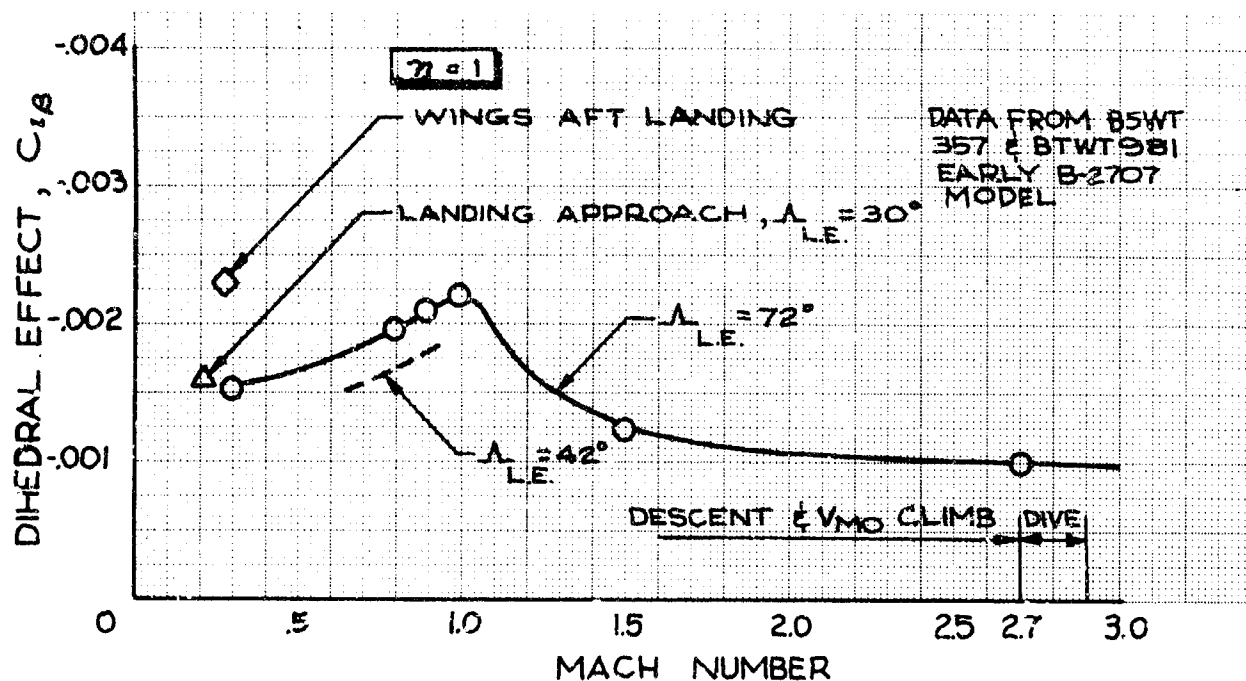


Figure 4-75. Dihedral Effect

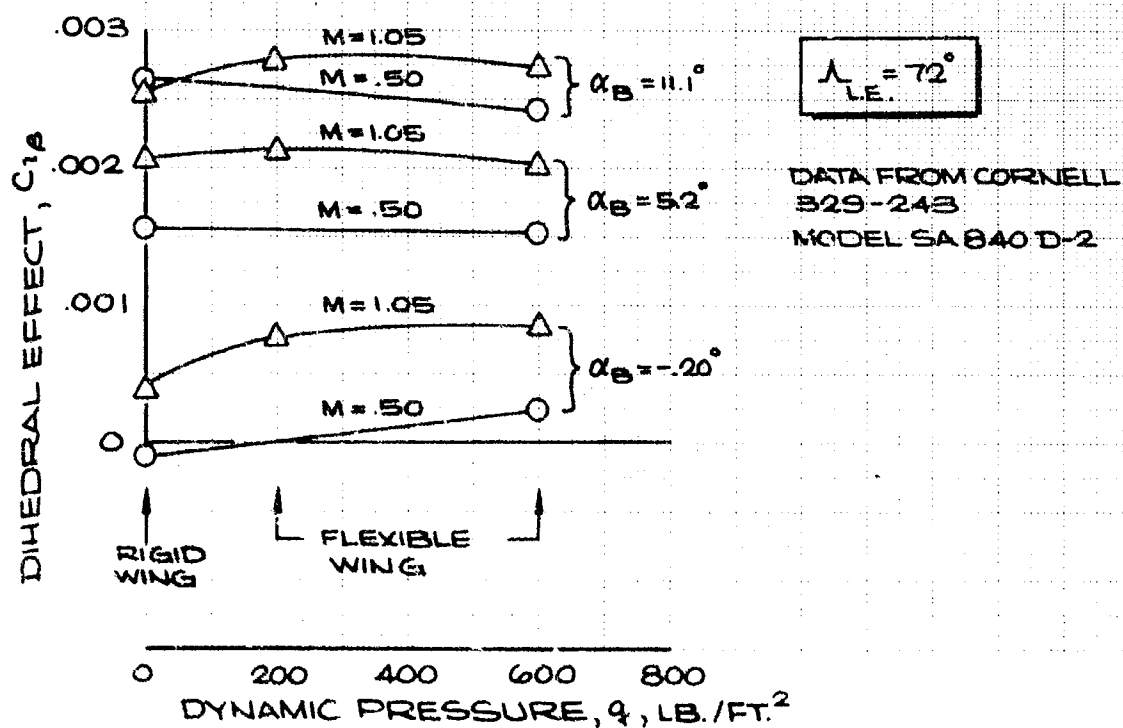


Figure 4-76. Effect of Wing Flexibility on Dihedral Effect

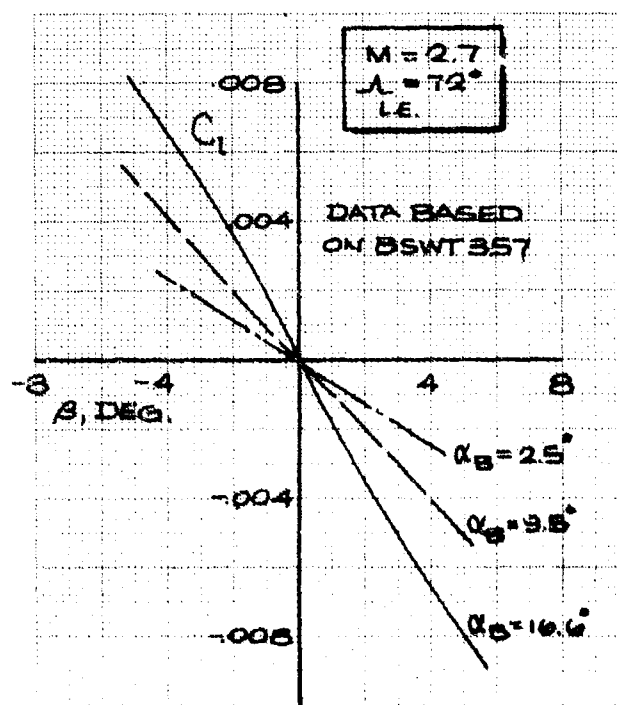
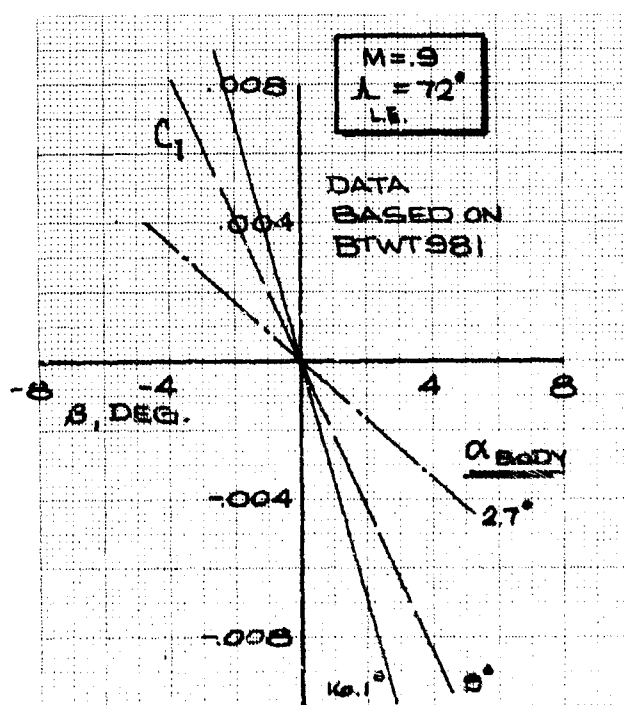
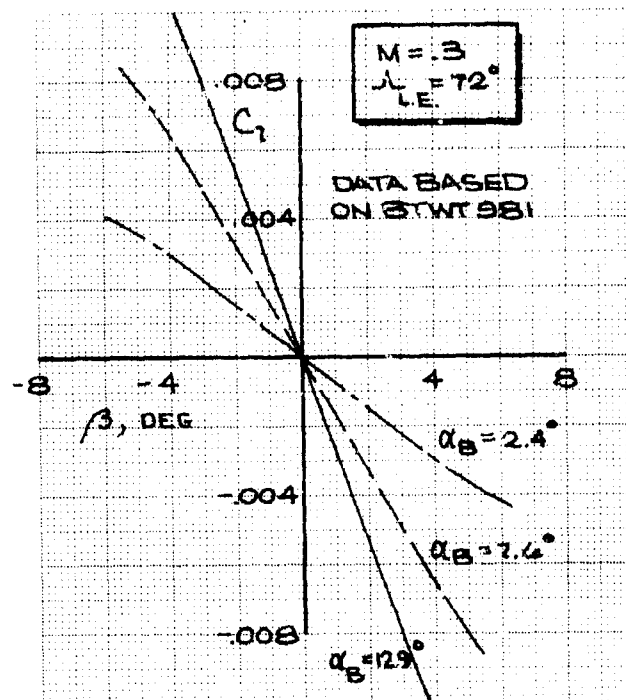
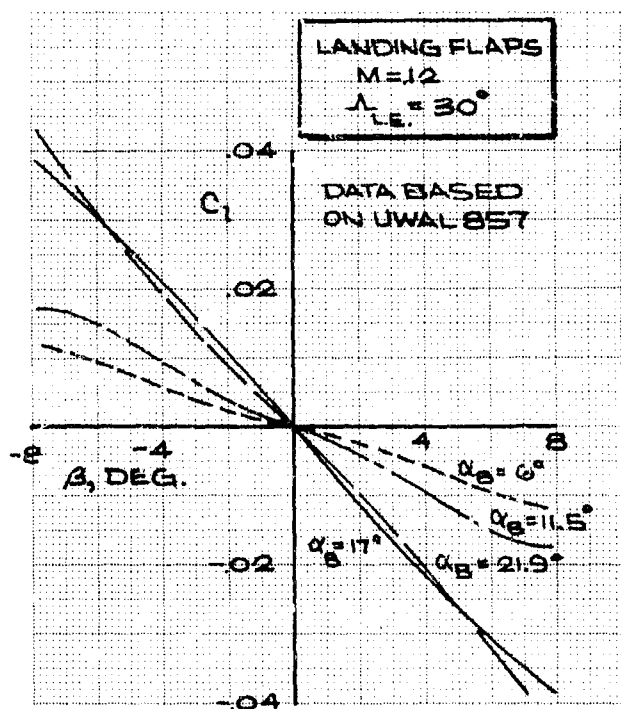


Figure 4-77. Rigid Airplane Dihedral Effect

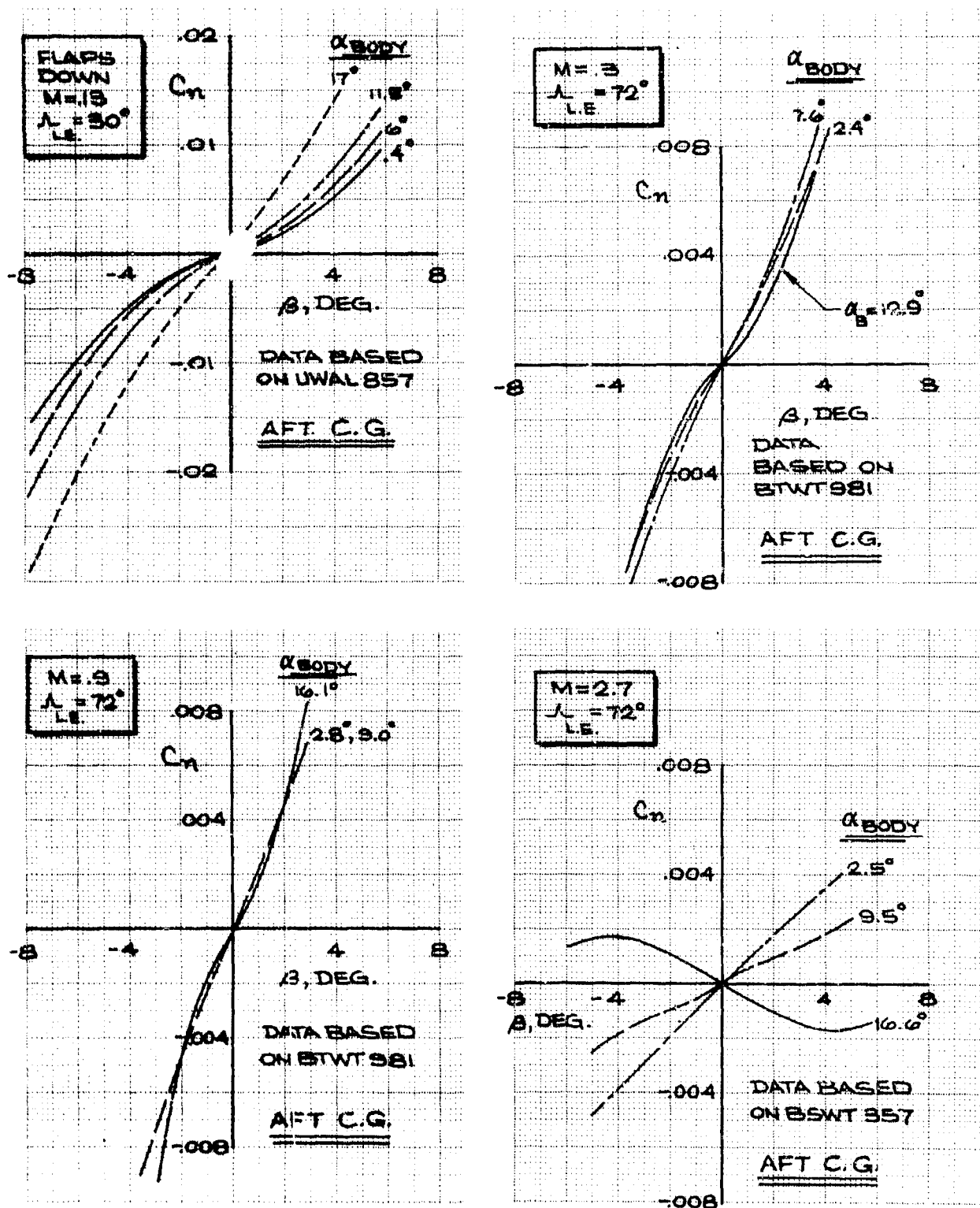


Figure 4-78. Rigid Airplane Directional Stability

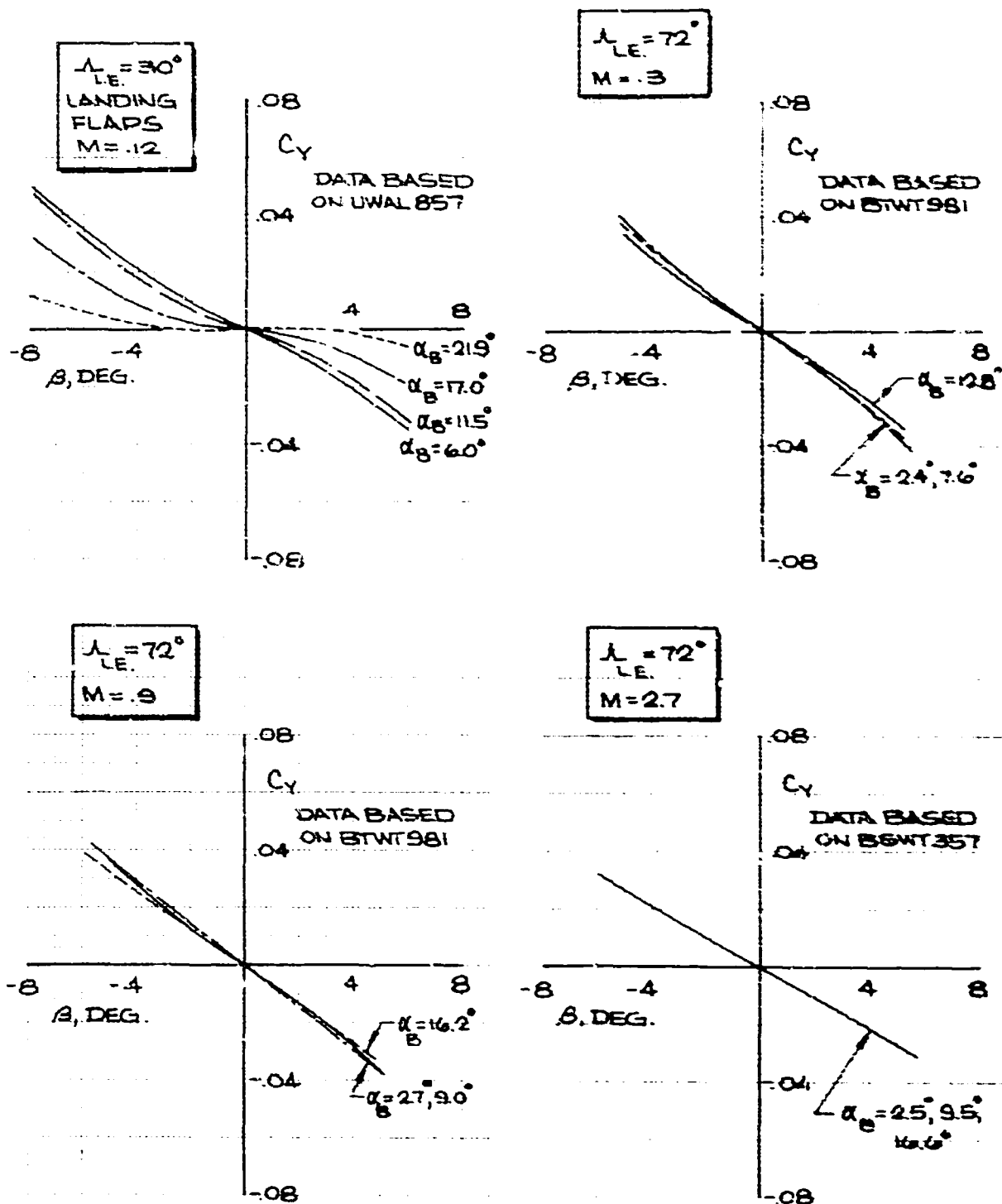


Figure 4-79. Rigid Airplane Side Force Characteristics

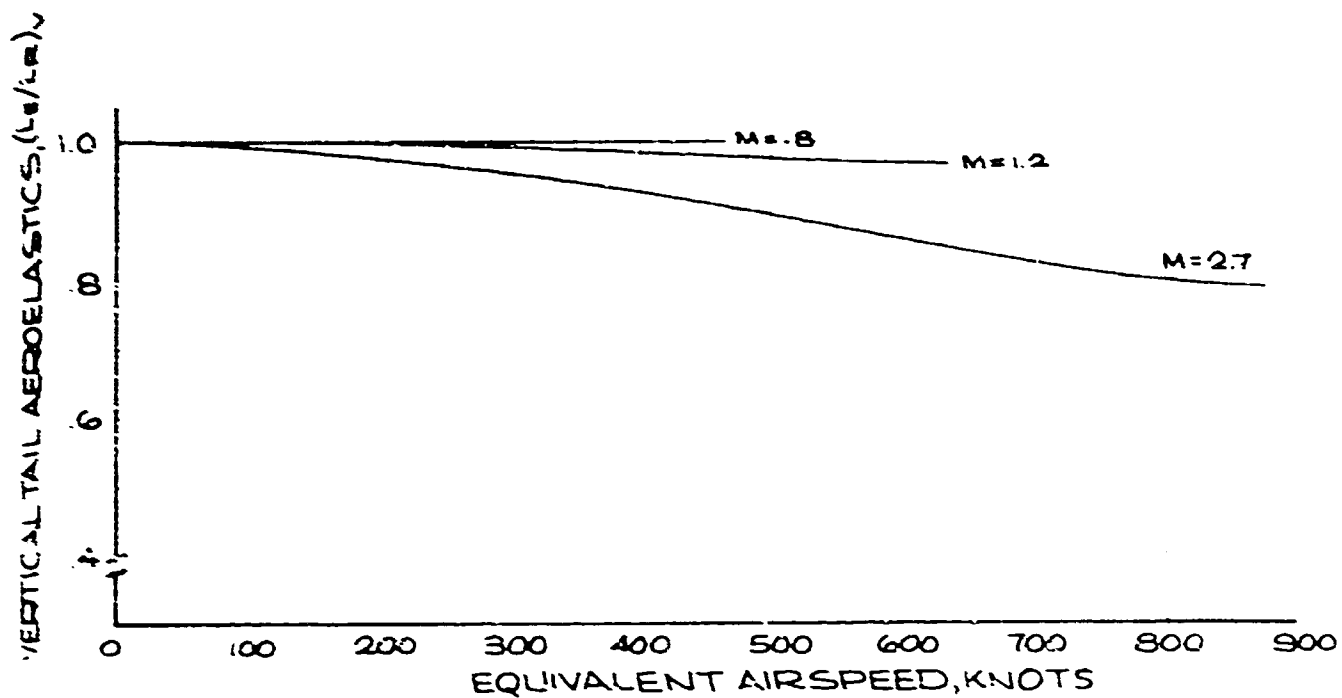


Figure 4-30. Aeroelastic Factor for Vertical Tail

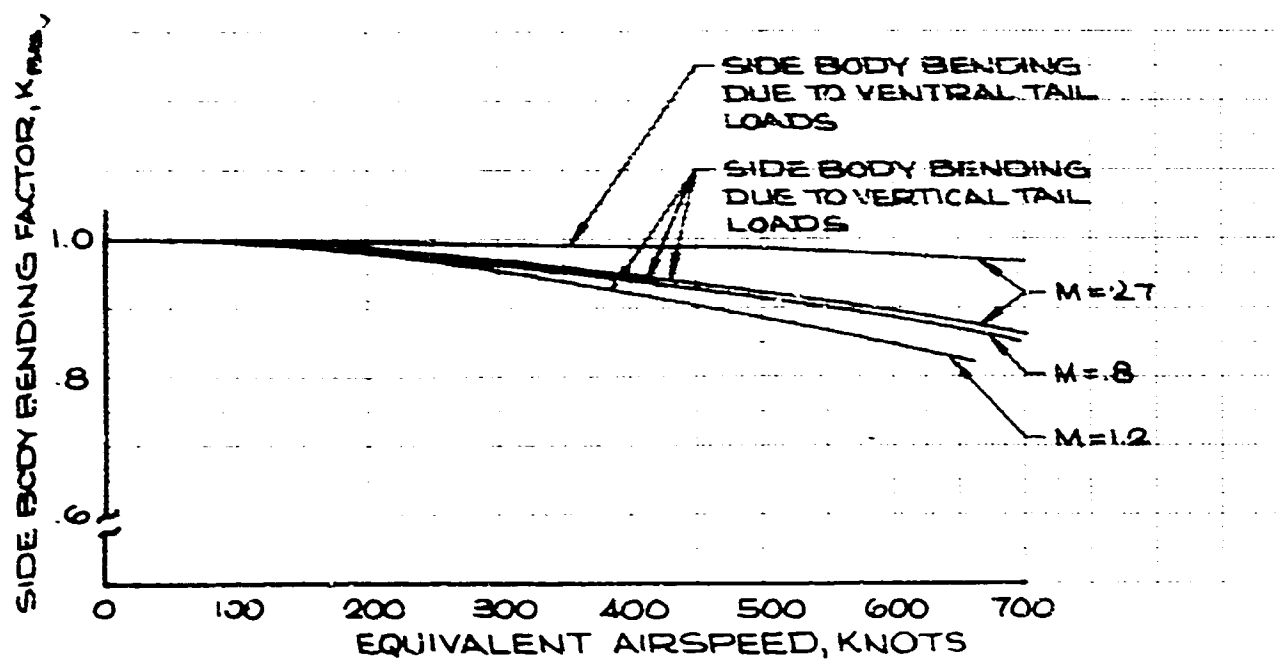


Figure 4-81. Body Bending Due to Vertical Tail Loads

istics are inherent in high-inertia configurations. Good handling qualities will be provided by pitch response augmentation and improved attitude display. Pilot effort is high without pitch response augmentation; however, the low frequency character of the motion eliminates any tendency toward pilot induced oscillations or other undesirable characteristics. There is some concern that, for low speed operation, better flight path response to control input may be required than that which can be attained with the conventional elevator controls and the stability augmentation system. Direct lift control is being studied as a possible method of providing further improvement in low speed flight path control (Par. 4.1.1.2). The dynamic characteristics of the airplane with conventional control system, with and without stability augmentation, are discussed in the following paragraphs.

4.3.1.1 Unaugmented Airplane

The longitudinal dynamic characteristics of the unaugmented B-2707 at eight significant flight conditions are presented in the form of Bode plots of the pitch rate to elevator deflection transfer function in Fig. 4-82. The significance of this

form of presentation in terms of the more conventional static and dynamic stability parameters is shown in Fig. 4-83. This format was chosen to be compatible with the discussion of the augmented airplane characteristics. It is also consistent with the stability augmentation system design objectives shown in the preliminary procurement specification for the automatic flight control system. A great deal of analytical and flight simulator work has been done to establish and present airplane handling qualities criteria in the way most useful to groups within and outside the company who are engaged in the analysis, synthesis, and design of the automatic flight control system. The results have shown the desirability of presenting dynamic stability and response criteria in the frequency domain.

Figure 4-82 shows that the airplane short period frequencies remain essentially constant throughout the normal flight range, but the damping varies from heavy at the landing approach condition (VII) to light at the end of cruise condition (IV). The light damping at the high speed flight conditions is apparent to the pilot as a pitch rate overshoot. There is general agreement among pilots

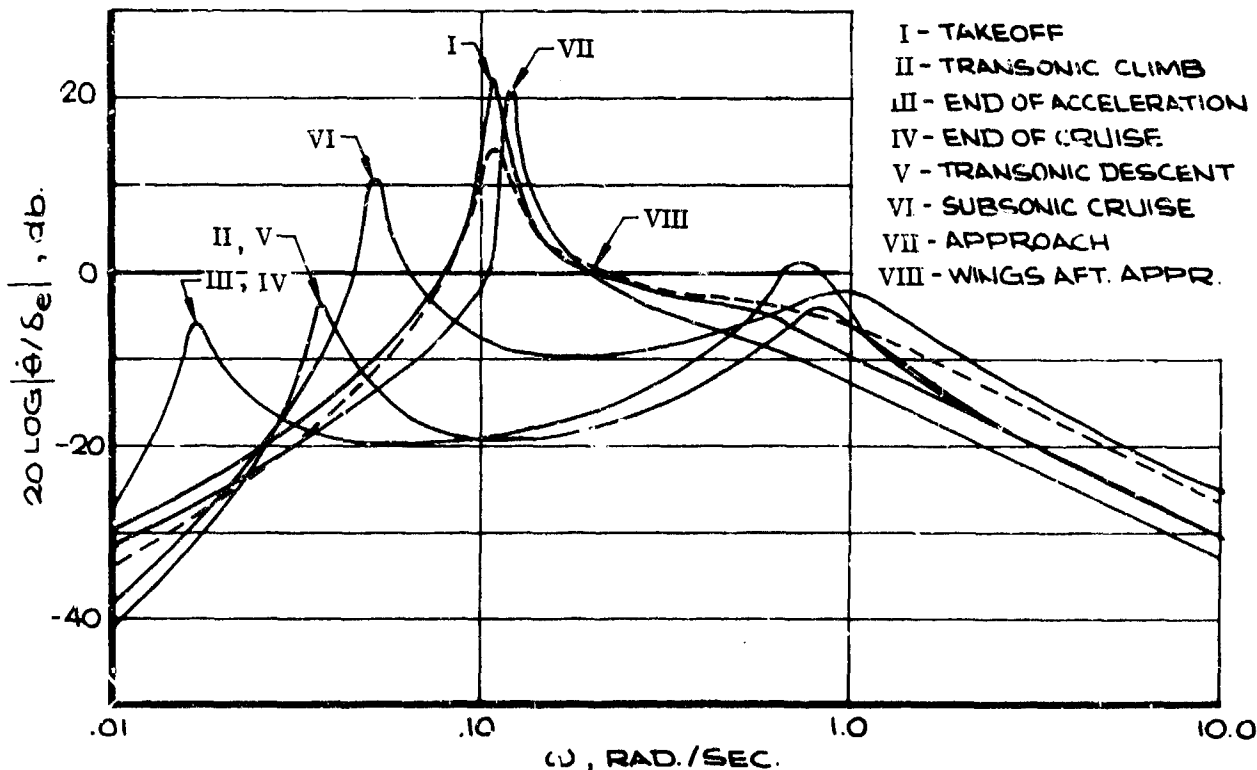


Figure 4-82. Frequency Response Diagrams, Unaugmented Airplane

who have flown the simulator that the unaugmented airplane is sluggish and lightly damped at high speeds and overdamped at low speeds. The low frequency portion of the curves exhibit the typical lightly damped phugoid characteristic with the break frequency of the mode varying roughly as a function of true airspeed. The low damping of this mode does not present any particular problem but does add to the pilot workload when the task is to arrive at a precise pitch attitude.

4.3.1.2 Augmented Airplane

Figure 4-84 presents the criterion on which the pitch axis portion of the stability augmentation system has been synthesized. This criterion has several important features:

- a. The maximum deviation allowable up to the high frequency break point is 2.5 db, which precludes any lightly damped modes in the closed-loop control response.
- b. The high frequency break point which establishes the effective short period frequency was selected at 1.6 rad/sec (0.255 cps). Flight simulator experience has shown this to be a good compromise value for jet transport operation since it provides adequate response characteristics without imposing a severe requirement for control system rates.

c. At the low frequency end of the diagram the solid lines represent the criterion for high speed operation. The criterion demands a constant pitch rate output to control input down to very low frequencies. This characteristic suppresses the airplane's natural phugoid mode or speed stability characteristics as, in the absence of pilot command, the pitch rate is held near zero. Flight simulator studies showed a requirement for a moderate level of static stability at low speeds. The dashed lines on Fig. 4-84 represent the change made to the criterion at the low frequency portion of the diagram to achieve this end; the low frequency component of the commanded pitch rate is washed out and a fixed control input is required to hold the airplane at an attitude different from trim. When a control input is released the attitude returns to trim without overshoot. The location of the low frequency break point fixes the level of apparent static stability.

The response due to control input is not the same as the response due to external disturbances. It is also specified that airplane oscillations due to these disturbances should damp to 0.2 amplitude in one cycle. This also has the effect of greatly reducing trim changes due to configuration changes.

An augmentation system approximating the above criterion was tested on the flight simulator at

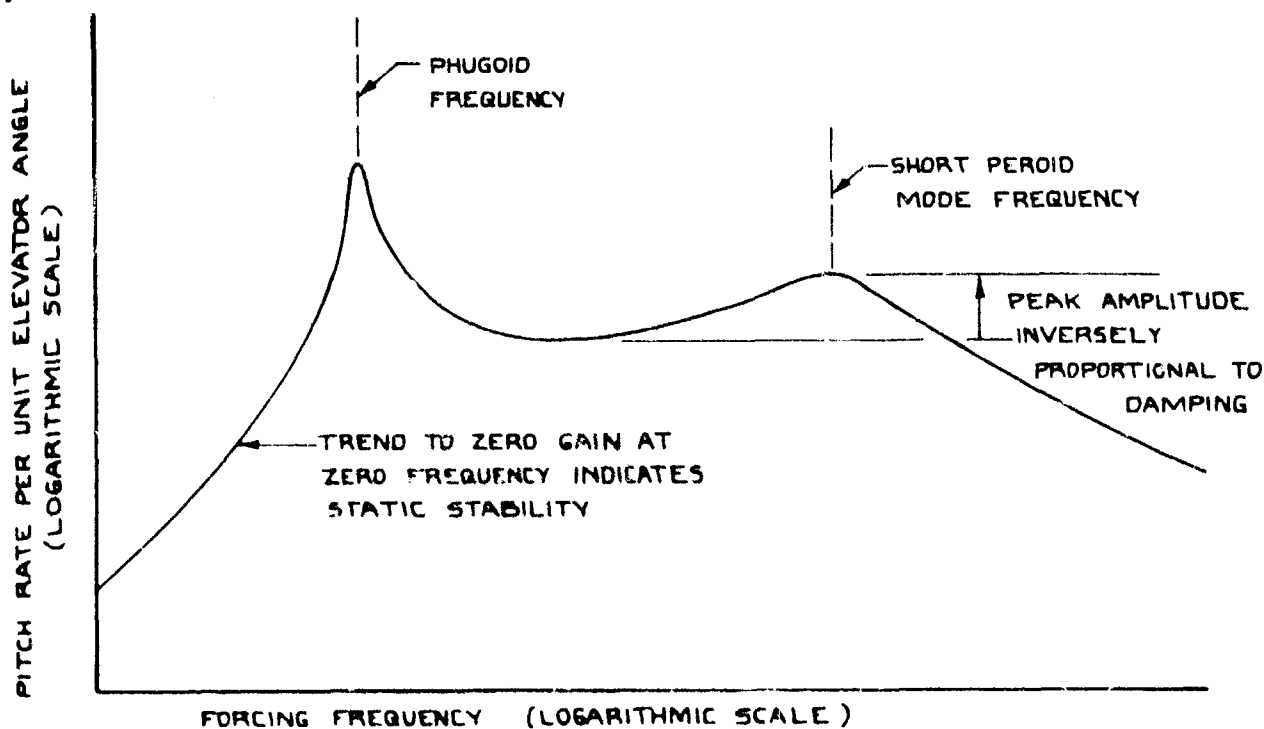


Figure 4-83. Frequency Response Sample Diagram

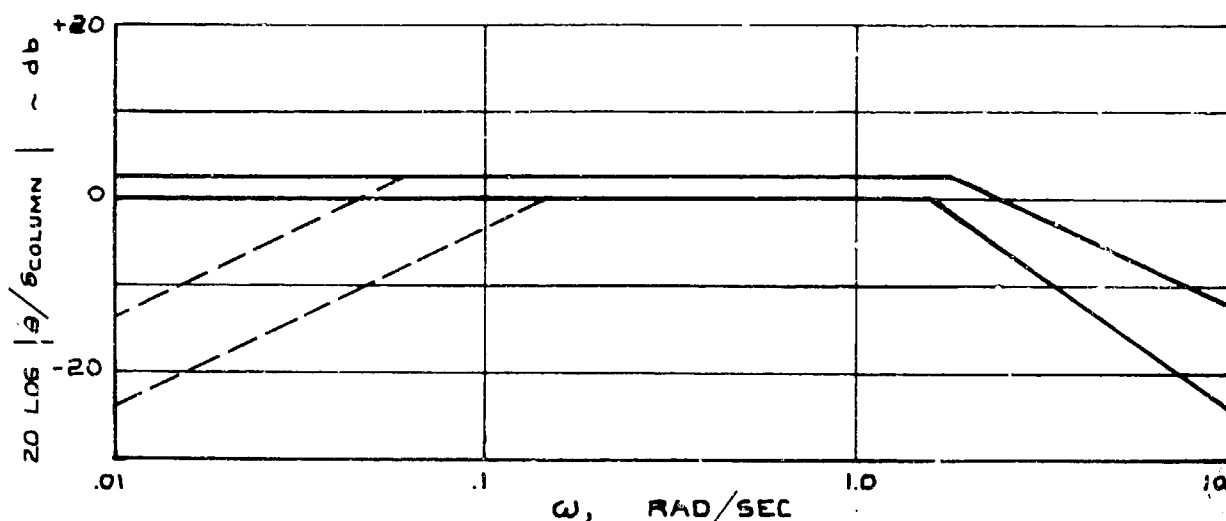


Figure 4-84. Pitch Axis Augmentation Design Criteria

various flight conditions. The resulting airplane response characteristics were satisfactory. Flight simulator and analytical studies are continuing in order to improve the criterion and to ensure that the airplane will possess good control response characteristics throughout the flight envelope.

4.3.1.3 Flight Simulation of Stalls

A series of stalls was performed in a flight simulator evaluation of the flaps down pitching moment characteristics of the airplane at high angles of attack without the angle of attack warning and control system operative. The simulation included the complete nonlinear lift, drag, pitching moment, and elevator characteristics as a function of angle of attack. Time histories of two stalls are presented in Figs. 4-85 and 4-86. The first figure presents the unaugmented airplane and shows that the small nonlinearity in the pitch curve is easily controllable through the stall and that there is not a large increase of pitch rate or of angle of attack rate as the minimum speed point is traversed. The second trace for the airplane with the pitch axis augmented shows about the same characteristics, except for the increase in elevator activity ordered by the SAS to improve the airplane response to control input. In either case, the stall speed could be demonstrated with no unusual control action required to complete the recovery.

4.3.2 Lateral-Directional Dynamics

The lateral-directional oscillatory characteristics

of the B-2707 are illustrated in Figs. 4-87 and 4-88. Figure 4-88 presents time histories of sideslip releases for the eight representative flight conditions tabulated in Par. 4.3.3. The B-2707 is inertially a very slender airplane and, unaugmented, exhibits the mode shape (ϕ/β) typical of such an inertia distribution. The ratio ϕ/β varies from about 2 in the transonic flight conditions to near 5 at the end of cruise.

The large yaw inertia of the airplane produces a lateral-directional oscillation natural frequency that is somewhat lower than that exhibited by current large jet transports.

There is no generally accepted criterion at present for the damping of lateral-directional oscillations for this class of airplane. However, this mode is primarily a nuisance motion and its acceptability is best determined in terms of the time to damp. A tentative criterion of 5 sec to one-half amplitude has been selected for the augmented airplane. The time required to damp to some specified amplitude is proportional to the product $\zeta_d \omega_d$, and the handling quality of the airplane is approximately constant along a line of constant time to damp, i.e., constant $\zeta_d \omega_d$. Figure 4-87 shows the frequency and damping ratio for each of the eight representative flight conditions with lines of 10 sec to one-half amplitude ($\zeta_d \omega_d = 0.069$) and 5 sec to one-half amplitude ($\zeta_d \omega_d = 0.0139$).

The time histories of Fig. 4-88 illustrate the improvement in time to damp provided by the

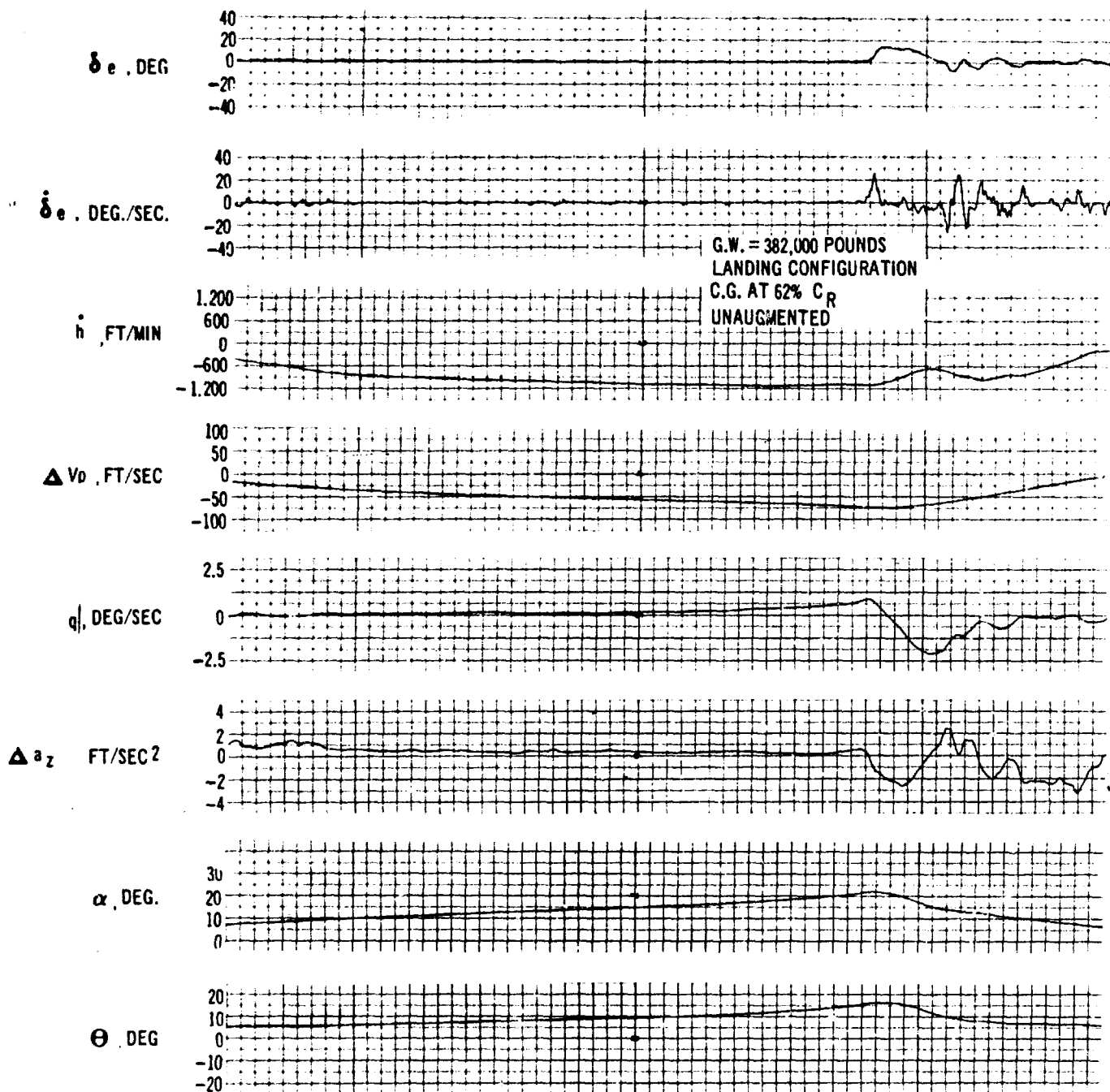


Figure 4-85. Stall Demonstration, Unaugmented Airplane

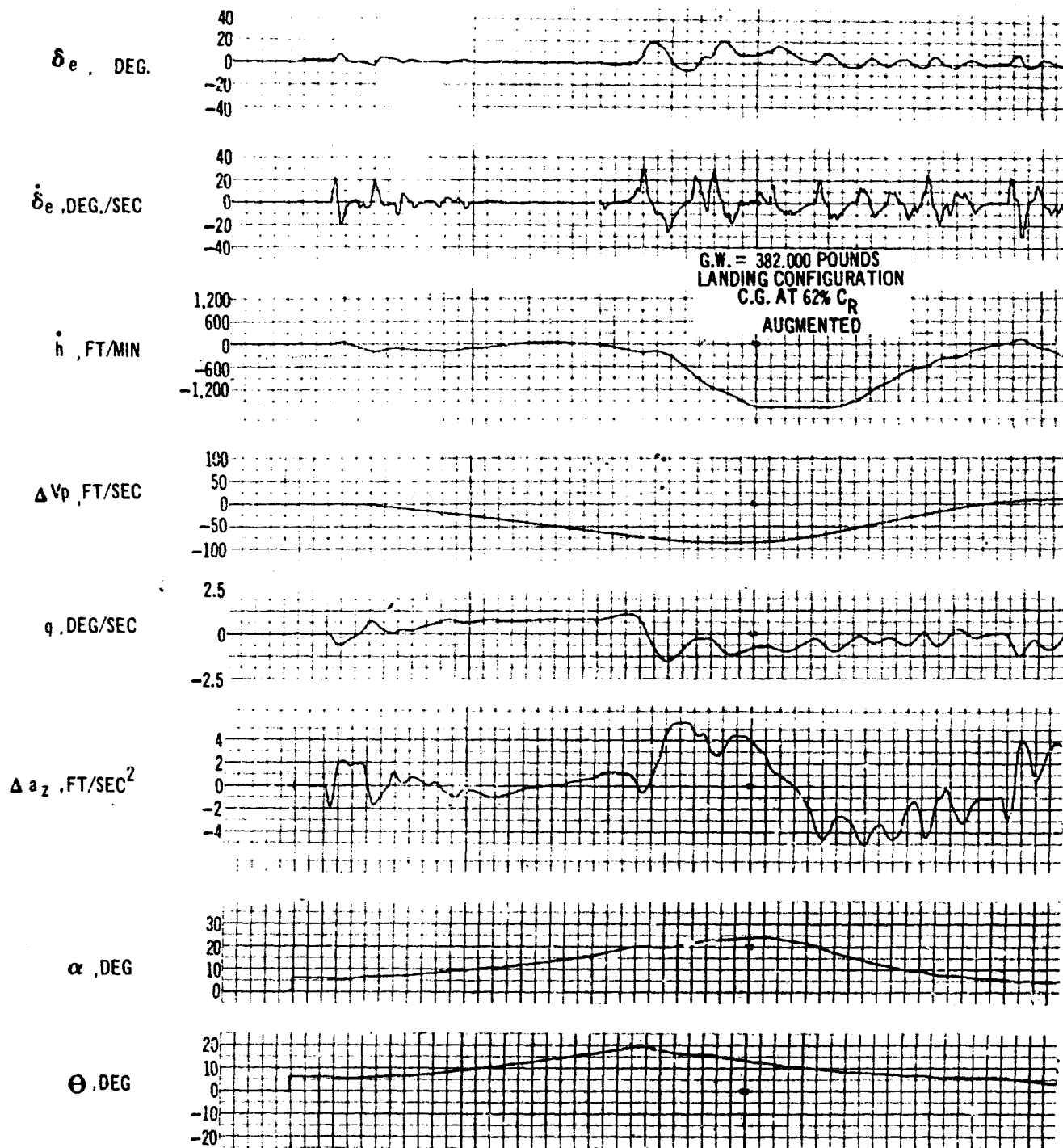


Figure 4-86. Stall Demonstration, Augmented Airplane

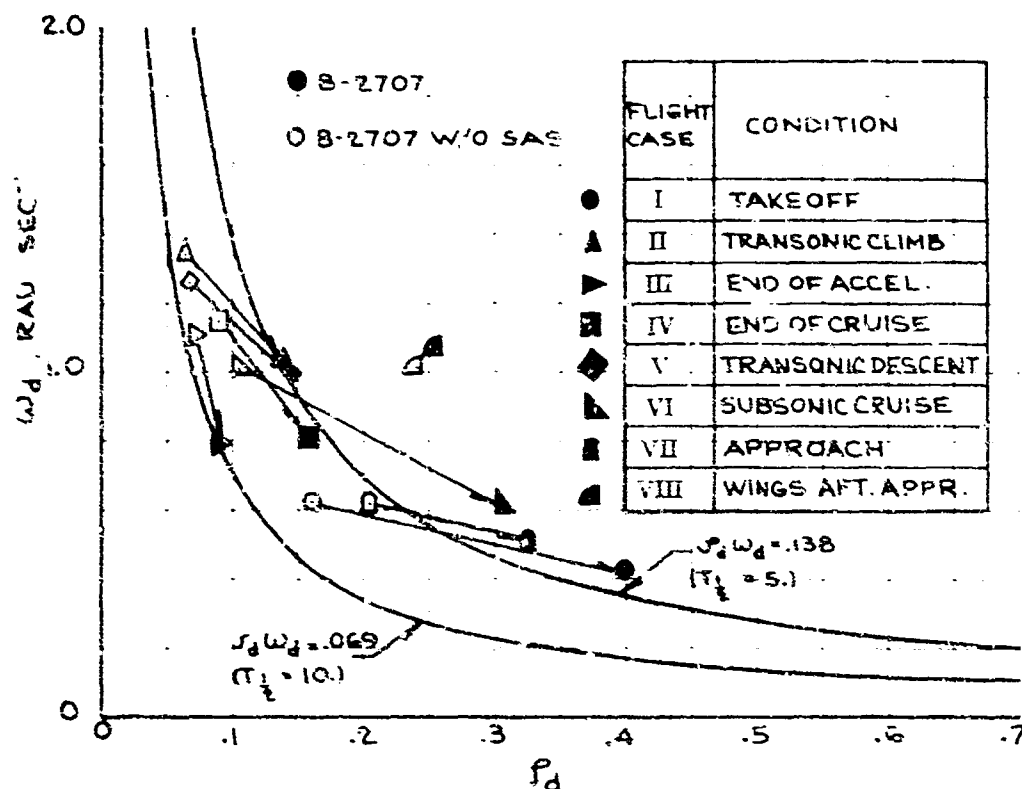


Figure 4-87. Lateral-Directional Oscillatory Characteristics

present mechanization of the SAS. The system changes the period as well as the damping ratio. The shaded symbols of Fig. 4-87 represent the B-2707 with SAS operating, and as observed on the time histories, exhibit lower frequencies and higher damping ratios than the airplane with SAS off. Continuing development of the SAS will produce satisfactory characteristics at all flight conditions.

4.3.3 Response to Lateral Control

Figure 4-89 illustrates the response of the B-2707 in supersonic cruise, and transonic descent, to a step application of the pilot's wheel to less than maximum deflection, i.e., normal control operation, and to maximum deflection. Normal use of the control allows the SAS to utilize the elevons

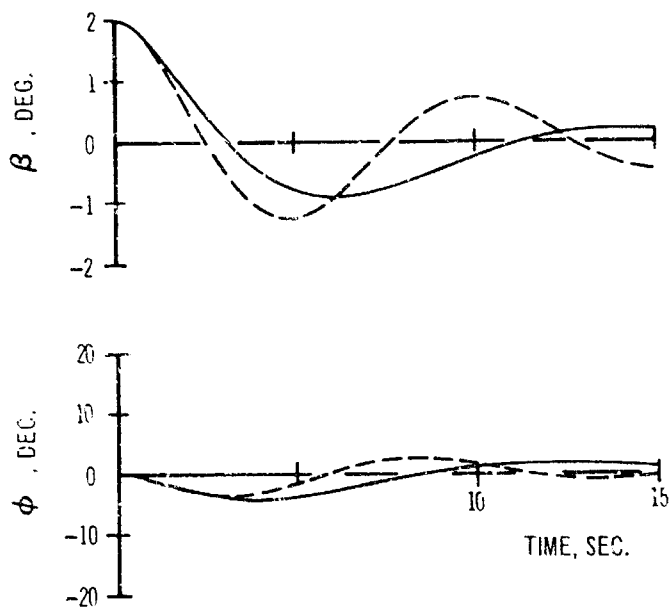
to increase the damping, which improves the quality of the bank angle response. However, full control is available at maximum deflection, and provides the greater roll response shown.

Figure 4-90 shows the bank angle response for subsonic cruise (42-degree sweep) and landing approach (30-degree sweep, flaps down). This is response to partial control and illustrates the powerful lateral control available at these flight conditions.

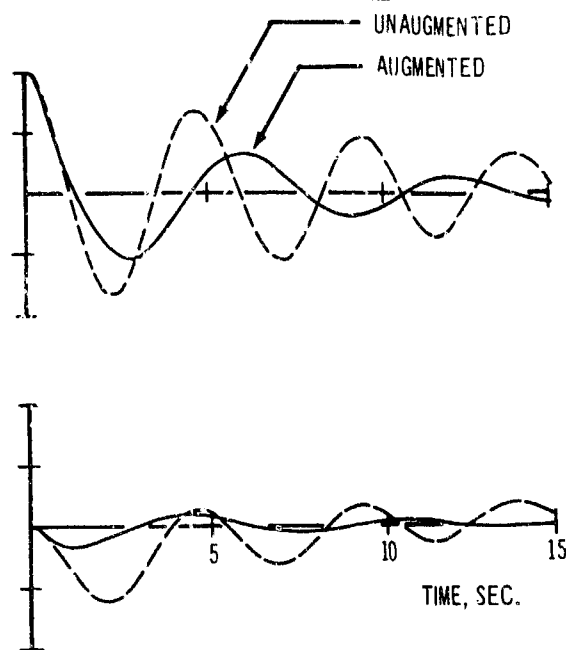
4.3.4 Dynamic Stability Data

Tables 4-B and 4-C summarize dynamic stability characteristics and stability derivative data applicable to the eight flight conditions selected for analysis.

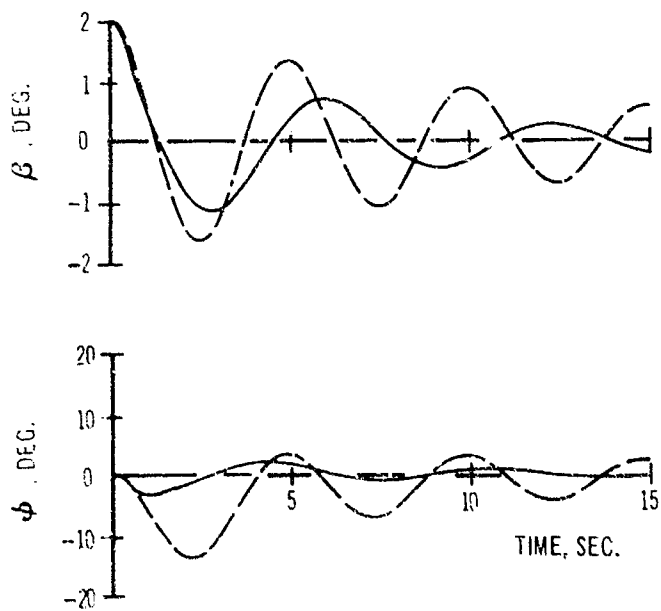
TAKEOFF



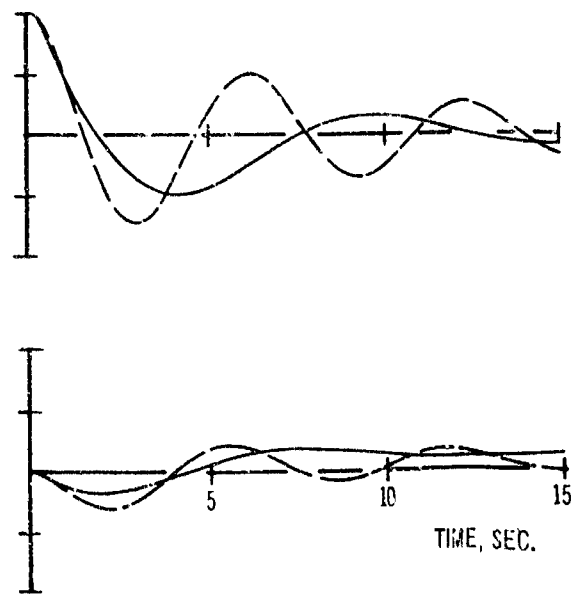
TRANSONIC CLIMB



TRANSONIC DECELERATION



SUPERSONIC CRUISE



A

MENTED
MENTED

TIME, SEC.

TIME, SEC.

END OF ACCELERATION

END OF CRUISE

LANDING APPROACH

WINGS AFT LANDING APPROACH

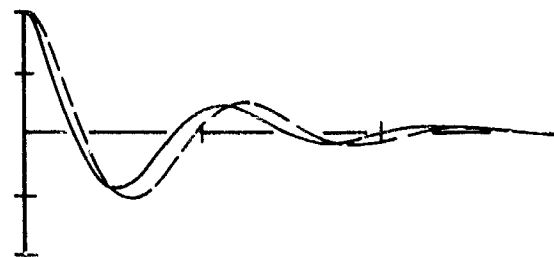
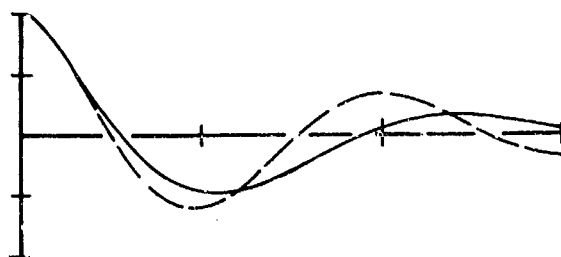
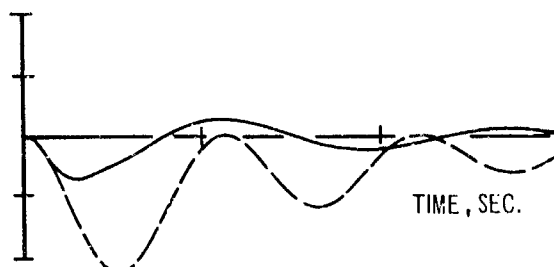
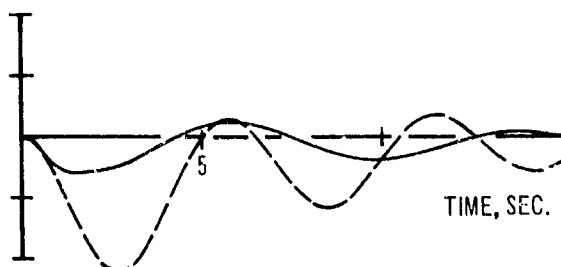
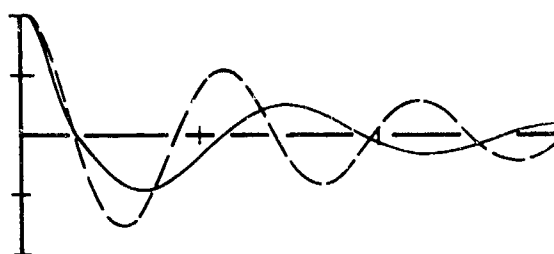
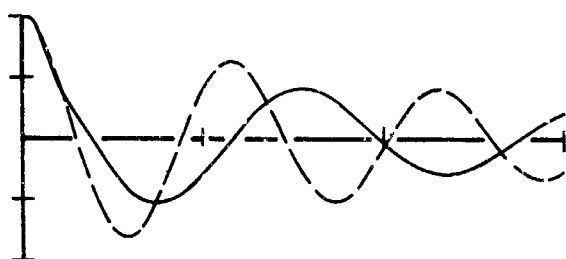
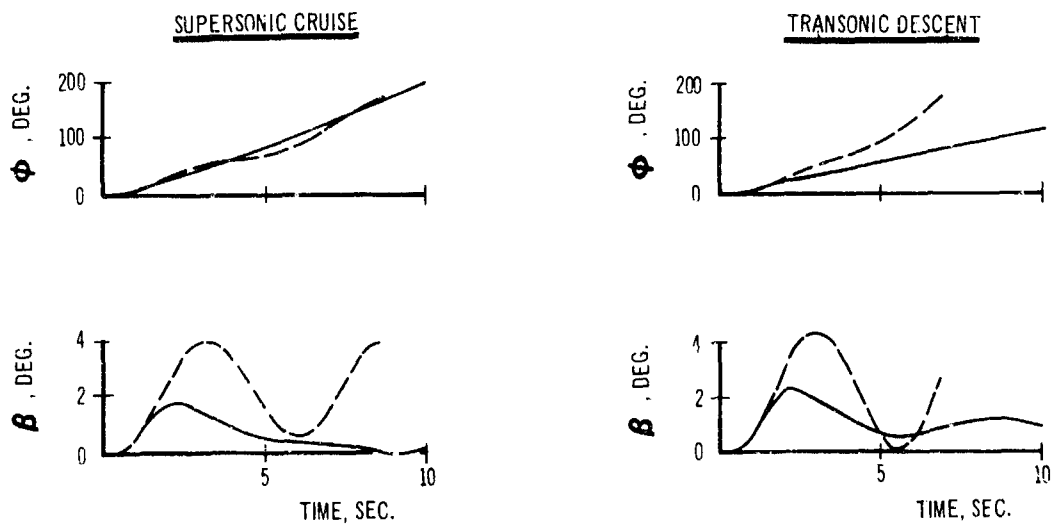


Figure 4-88. β -Releases, Augmented and Unaugmented Airplane

V2-B2707-3

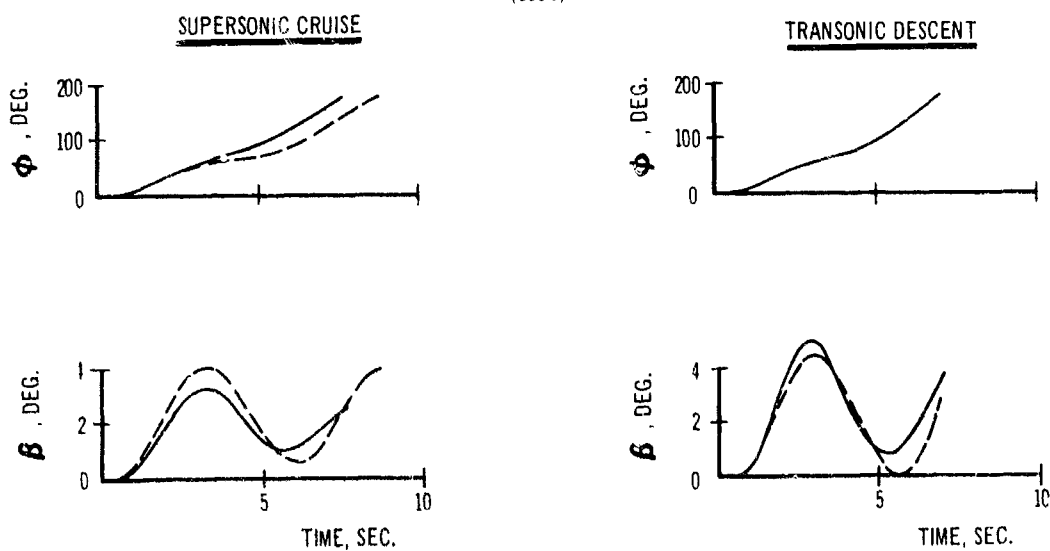
PARTIAL WHEEL DEFLECTION

(50%)



MAXIMUM WHEEL DEFLECTION

(100%)



- NOTES:
1. CRUISE CONFIGURATION
 2. RUDDER PEDALS FIXED
 3. AIRPLANE WITH LATERAL-DIRECTIONAL SAS
 4. AIRPLANE WITHOUT LATERAL-DIRECTIONAL SAS

Figure 4-89. Response to Control Wheel Deflection, Cruise Configuration

PARTIAL WHEEL DEFLECTION

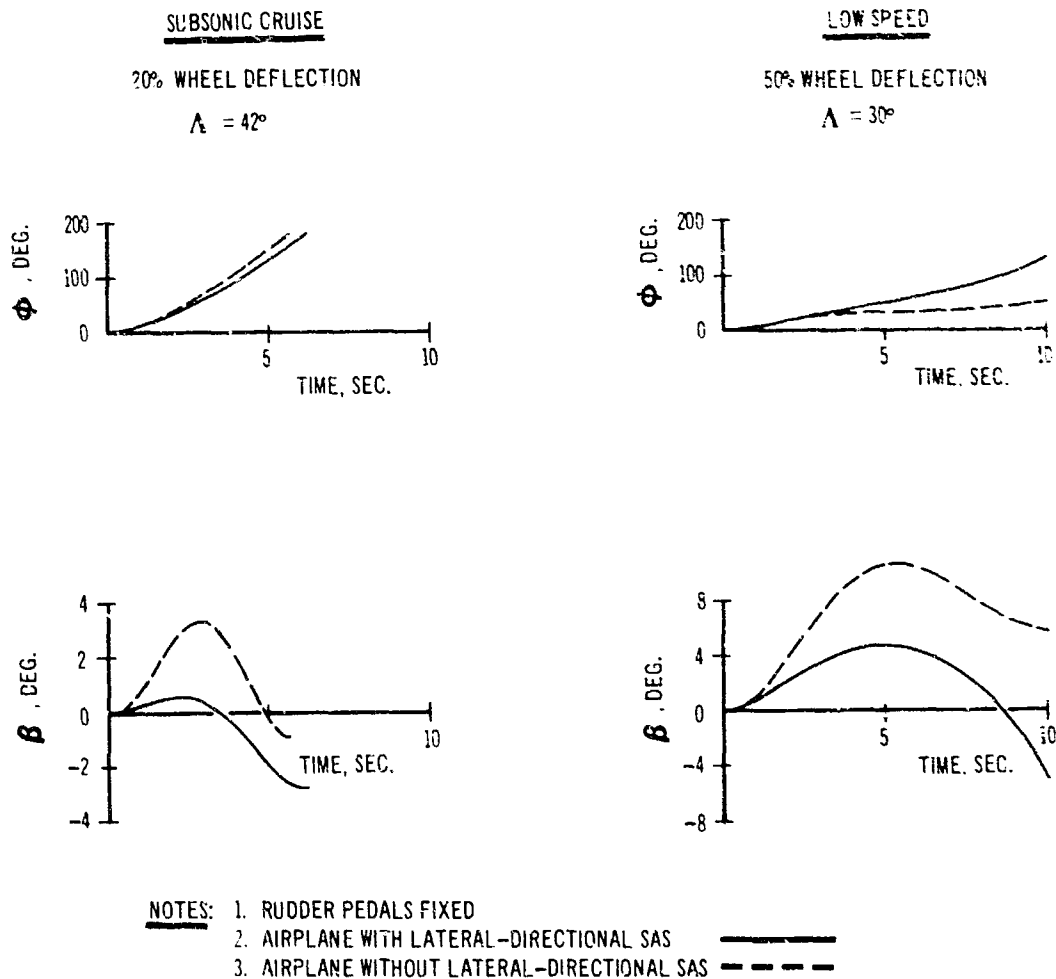


Figure 4-20. Response to Control Wheel Deflection, Wings Forward

FLIGHT CONDITION	GW 1000 LB	A.G. 100 % CR	Λ L.E. DEG	ALTITUDE FT	V_{T_0} FT SEC	Q LBS FT ²	MACH NO.	AX	AY
I	678	61.7	30	Sea Level	347	113	.275	1.113	5.1
II	614.8	62.5	72	40,513	1,162	387	1.2	5.13	8.1
III	574.1	62.5	72	51,217	2,621	735.3	2.7	4.52	7.1
IV	388.2	62.1	72	71,377	2,630	473.3	2.7	2.81	4.3
V	387.6	62.1	72	52,600	1,163	216.3	1.2	2.81	4.1
VI	650	62.3	42	34,000	845	320	.85	3.81	7.2
VII	581	61.1	30	Sea Level	244	71	.219	4.27	4.1
VIII	340	62.2	72	Sea Level	346	142	.312	2.61	3.1

FLIGHT CONDITION	C_L β RAD. ⁻¹	C_{L_P} RAD. ⁻¹	C_{L_T} RAD. ⁻¹	$C_{L_{\delta W}}$ RAD. ⁻¹	$C_{L_{\delta R}}$ RAD. ⁻¹	$C_{L_{\delta A}}$ RAD. ⁻¹	$C_{L_{\delta SP}}$ RAD. ⁻¹	$C_{L_{\delta TIP}}$ RAD. ⁻¹	C_{L_p} RAD.
I	-.159	-.530	.531	.0682	0	.0682	.9738	-	.837
II	-.095	-.0969	.0385	.00539	.00097	-	.00135	.0180	.117
III	-.0573	-.0832	.0105	.00229	.00126	-	.00063	.00739	.03
IV	-.0579	-.0903	.0110	.00264	.00149	-	.00092	.00831	.31
V	-.095	-.101	.0384	.00641	.00132	-	.00120	.0212	.127
VI	-.0091	-.278	.338	.0309	.00430	-	.00441	.0249	.127
VII	-.159	-.547	.211	.0647	.00312	.0693	.0696	-	.03
VIII	-.0888	-.112	.115	.0103	.00103	-	.000229	.0384	.03

H

MACH NO.	\dot{X}_X	\dot{X}_Y	\dot{X}_Z	\dot{X}_N	α_{TRIM}	δ_{TRIM}	$C_{D\alpha}$	$C_{L\alpha}$	$C_{L\delta}$	$C_{L\delta}^{elev. aux}$	$C_{L\delta}^{elev. aux}$
	X: 10 ⁻⁵ SLUG-FT ²				DEG	DEG	RAD. ⁻¹	RAD. ⁻¹	RAD. ⁻¹	RAD. ⁻¹	RAD. ⁻¹
.276	10.05	46.6	36.0	.70	12.0	-8.0	.297	3.152	.135	.060	
1.2	8.23	43.0	32.6	.65	8.4	-8.0	.193	2.040	.0266	-	
2.7	4.62	40.6	31.6	.62	6.6	-3.25	.093	1.215	.0108	-	
3.7	3.80	41.9	44.1	.31	6.9	-2.0	.101	1.238	.0135	-	
1.2	2.97	41.9	44.1	.30	6.5	-10.0	.227	2.103	.0453	-	
.65	6.60	47.2	55.0	.70	6.9	-3.2	.181	2.521	.087	-	
.219	4.27	41.2	44.2	.25	9.8	-.5	.29	3.152	.132	.0625	
.312	3.61	39.7	41.0	.29	11.5	-2.0	.35	1.948	.152	.0693	

$C_{L\delta_{SP}}$	$C_{L\delta_{TIP}}$	$C_{Y\beta}$	$C_{Z\beta}$	C_{Zr}	C_{δ_W}	C_{δ_R}	C_{δ_A}	$C_{\delta_{SP}}$	$C_{\delta_{TIP}}$	$C_{Y\beta}$	$C_{Z\beta}$
RAD. ⁻¹	RAD. ⁻¹	RAD. ⁻¹	RAD. ⁻¹	RAD. ⁻¹	RAD. ⁻¹	RAD. ⁻¹	RAD. ⁻¹	RAD. ⁻¹	RAD. ⁻¹	RAD. ⁻¹	RAD. ⁻¹
.0758	-	.0837	-.072	-.226	-.00206	-.063	-.00355	+.0054	-	-.201	
.00103	.0180	.117	-.0111	-.210	-.00052	-.0298	-	-.00029	-.00860	-.350	
.00063	.00739	.029	-.0069	-.182	-.00011	-.0115	-	-.00069	-.00430	-.275	
.00092	.00831	.0315	-.0066	-.187	-.000057	-.0138	-	+.00080	-.00493	-.287	
.00120	.0212	.122	-.0115	-.219	-.000057	-.0458	-	+.00029	-.0101	-.355	
.00441	.0249	.127	-.0231	-.196	-.00424	-.0524	-	+.00613	-.00722	-.327	
.0696	-	.0837	-.0812	-.239	-.00315	-.0630	-.00178	+.0630	-	-.229	
.000229	.0384	.00	-.0172	-.186	-.00195	-.0615	-	-.000802	-.00298	-.344	

3

Table 4-B. Airplane Stability Derivatives

$C_{L\delta}$ RAD. ⁻¹	$C_{L\delta_{\text{elev. aux}}}$ RAD. ⁻¹	$C_{L\delta_{\text{TIP}}}$ RAD. ⁻¹	$C_{M\alpha}$ RAD. ⁻¹	$C_{M\dot{\alpha}}$ RAD. ⁻¹	C_{Mq} RAD. ⁻¹	$C_{M\delta_{\text{elev.}}}$ RAD. ⁻¹	$C_{M\delta_{\text{aux}}}$ RAD. ⁻¹	$C_{M\delta_{\text{TIP}}}$ RAD. ⁻¹
.135	.060	.189	-.0258	-.08	-.255	-.0361	-.0160	-.0504
.0266	-	.0266	-.105	0	-.38	-.0189	-	-.0189
.0103	-	.0175	-.0447	0	-.236	-.00510	-	-.00963
.0135	-	.0220	-.0619	0	-.238	-.00596	-	-.0113
.0453	-	.0453	-.147	0	-.390	-.0261	-	-.0261
.037	-	.0702	-.0636	0	-.33	-.0281	-	-.0264
.132	.0625	.156	-.0430	-.10	-.33	-.0363	-.0172	-.0430
.152	.0692	.152	-.0573	0	-.26	-.0458	-.0210	-.0458

$C_{n\delta_{\text{IF}}}$ RAD. ⁻¹	$C_{Y\beta}$ RAD. ⁻¹	C_{Y_P} RAD. ⁻¹	C_{Y_r} RAD. ⁻¹	$C_{Y\delta_W}$ RAD. ⁻¹	$C_{Y\delta_R}$ RAD. ⁻¹	$C_{Y\delta_{\text{SP}}}$ RAD. ⁻¹		
-	-.201	.202	.009	-.00007	.115	-.00011		
-.00860	-.350	.435	.153	-.00007	.0315	-.00011		
-.00430	-.275	.189	.0773	-.00010	.0120	-.00017		
-.00493	-.287	.190	.0825	-.00010	.0149	-.00017		
-.0101	-.355	.435	.151	-.00007	.0544	-.00011		
-.00722	-.327	.147	.051	-.00029	.0802	-.00046		
-	-.229	.177	.054	-.00007	.120	-.00011		
-.00298	-.344	.0938	.0737	-.0021	.115	-.00355		

Table 4-C. Dynamic Parameters

FLIGHT CONDITION	DUTCH ROLL					SPIRAL
	ζ_d	$T_{1/2}$	f_{nd}	$\frac{ \phi }{ \beta }$	$\frac{\omega_\phi}{\omega_d}$	$T_{1/2} (\Gamma_2)$
I	.154	7.46	.096	2.56	.691	(86.4)
II	.0638	8.29	.209	4.26	.658	30.8
III	.0905	6.81	.179	7.26	.541	20.3
IV	.0995	5.97	.186	7.14	.481	27.0
V	.0742	7.26	.205	4.78	.591	40.1
VI	.0946	6.89	.169	3.05	.903	(38.7)
VII	.131	8.99	.0940	2.32	.646	31.9
VIII	.265	2.46	.169	3.92	.589	36.1

FLIGHT CONDITION	SHORT PERIOD		PHUGOID	
	$f_{n.s.p.}$	$\zeta_{s.p.}$	P_d	ζ_p
I	.0743	.880	67.8	.0738
II	.179	.270	166.6	.0836
III	.162	.167	375.5	.0875
IV	.163	.143	355.1	.0869
V	.170	.231	164.7	.0854
VI	.136	.421	128.9	.0302
VII	.091	.950	58.4	.107
VIII	.115	.715	64.8	.0975

4.4 CROSS-COUPLING CHARACTERISTICS

The lateral control system is described in Sec. 5. The tip elevons, employed as the primary roll control surfaces at large wing sweep angles, exhibit adverse yaw characteristics. Figure 4-91 illustrates the C_n/C_l ratio of the tip elevon at Mach 2.7. The addition of the spoiler improves the control system yaw characteristics by providing additional rolling moment as well as favorable yawing moment. At moderate to low angles of attack the improvement is significant. The further

addition of 4 degrees of rudder (rudder-elevon interconnect) provides a C_n/C_l ratio of approximately zero for the Mach 2.7 cruise condition. The C_n/C_l ratio is essentially constant with wheel deflection. Modifications to the control system such as an unswept spoiler on the wing or additional rudder interconnect will improve the C_n/C_l variation with angle of attack.

The lateral control for low speed, flaps-down flight consists of ailerons and spoilers. Fig. 4-91

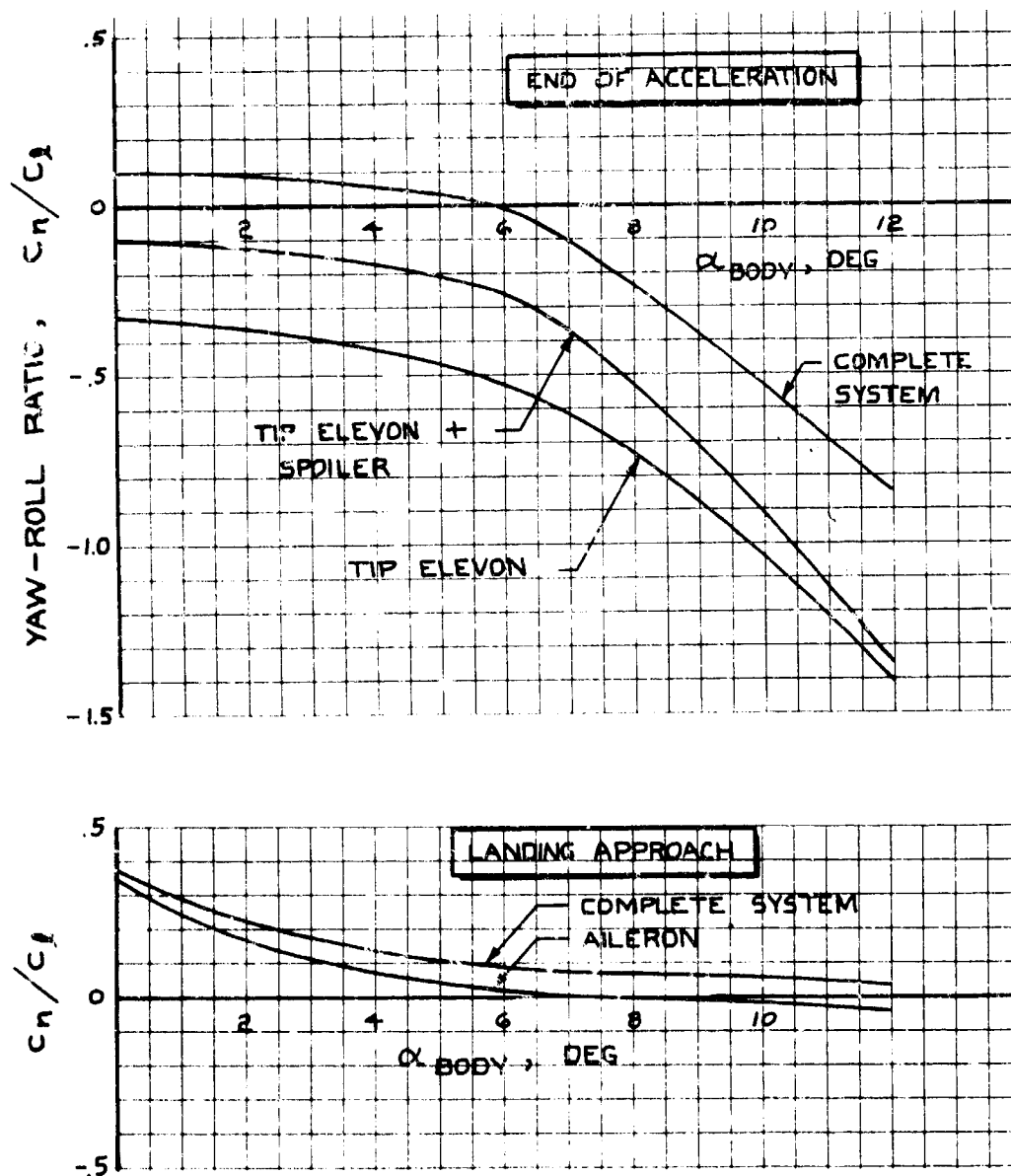


Figure 4-91. Yaw Due to Lateral Control

V2-B2707-3

shows a favorable C_n/C_l ratio for a wide range of angle of attack. The data shown correspond to full wheel deflection; as at cruise, C_n/C_l is essentially invariant with wheel deflection.

The roll-yaw parameter, ω_ϕ/ω_d , is shown for maximum lateral control at the eight representative flight conditions in Fig. 4-92. The characteristics illustrated are considered satisfactory but not optimum at all flight conditions. Further studies will be directed toward improving the basic roll-yaw coupling.

4.5 EMERGENCY OPERATIONS

A high level of reliability is provided in critical airplane systems through design concepts and redundancy. The flight control system will provide a margin of controllability to ensure safe operation in the event of system failures that affect airplane handling characteristics. These include single or multiple engine or inlet failures, flight control and trim system failures, stability augmentation failures, fuel system failures, and failures of the wing sweep system.

4.5.1 Engine Failure on Takeoff

Sufficient rudder control has been provided to ensure a safe margin between the minimum control speed, V_{MC} , and takeoff rotation speed. Rudder control for safe V_{MC} speed is the critical design point for sizing the rudder surface area, and as such it is discussed in Par. 4.1.5.

4.5.2 Steady State Engine Failures, Enroute

The rudder deflection range has been selected to provide complete trim of the asymmetric yawing moment associated with the failure of two engines on one side (engine windmilling, inlets started, bypass doors open). Figure 4-93 shows the capability of the rudder to trim the airplane in these conditions throughout the normal flight envelope.

4.5.3 Abrupt Engine Inlet Failures, Supersonic Speeds

The severity of the engine inlet failure problem at supersonic speeds is governed by several factors: the level of asymmetric thrust, the aerodynamic forces and moments generated by shock expulsion in supersonic flight, and the

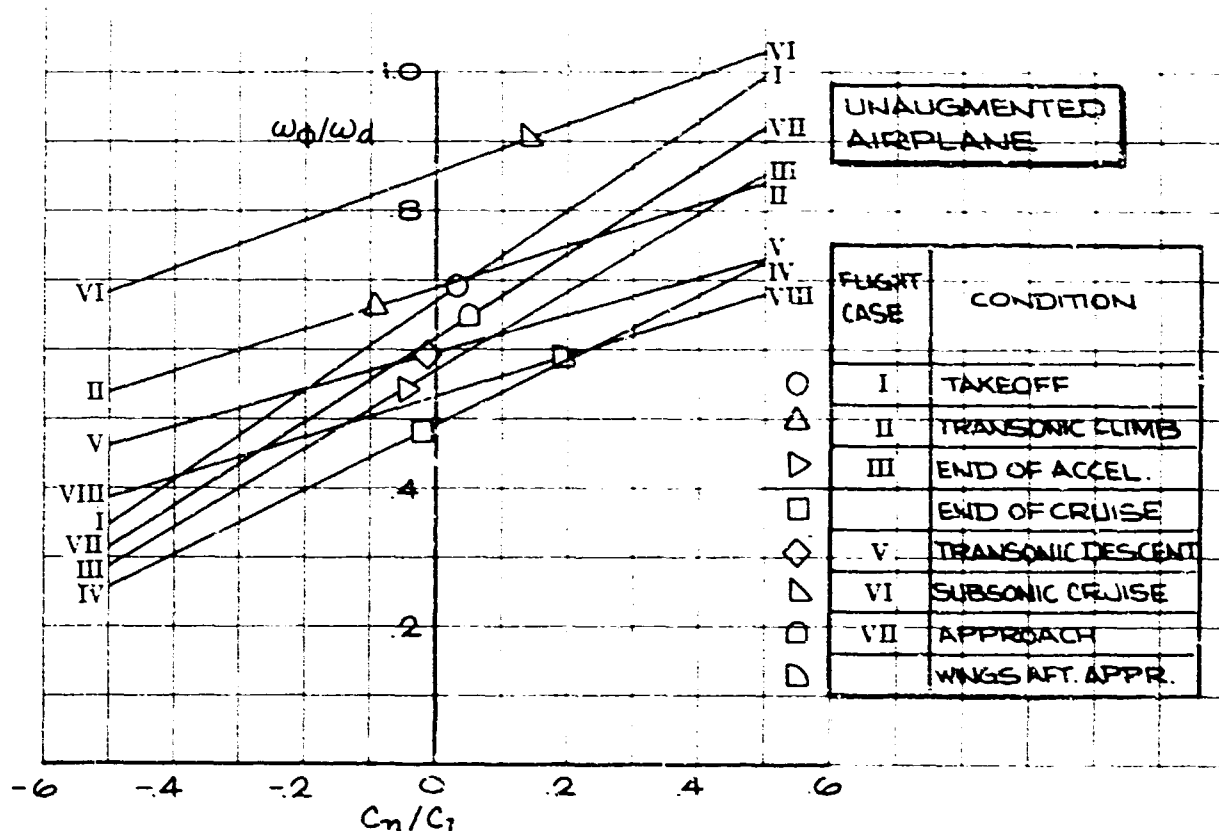


Figure 4-92 Roll - Yaw Coupling Parameter, Eight Flight Conditions

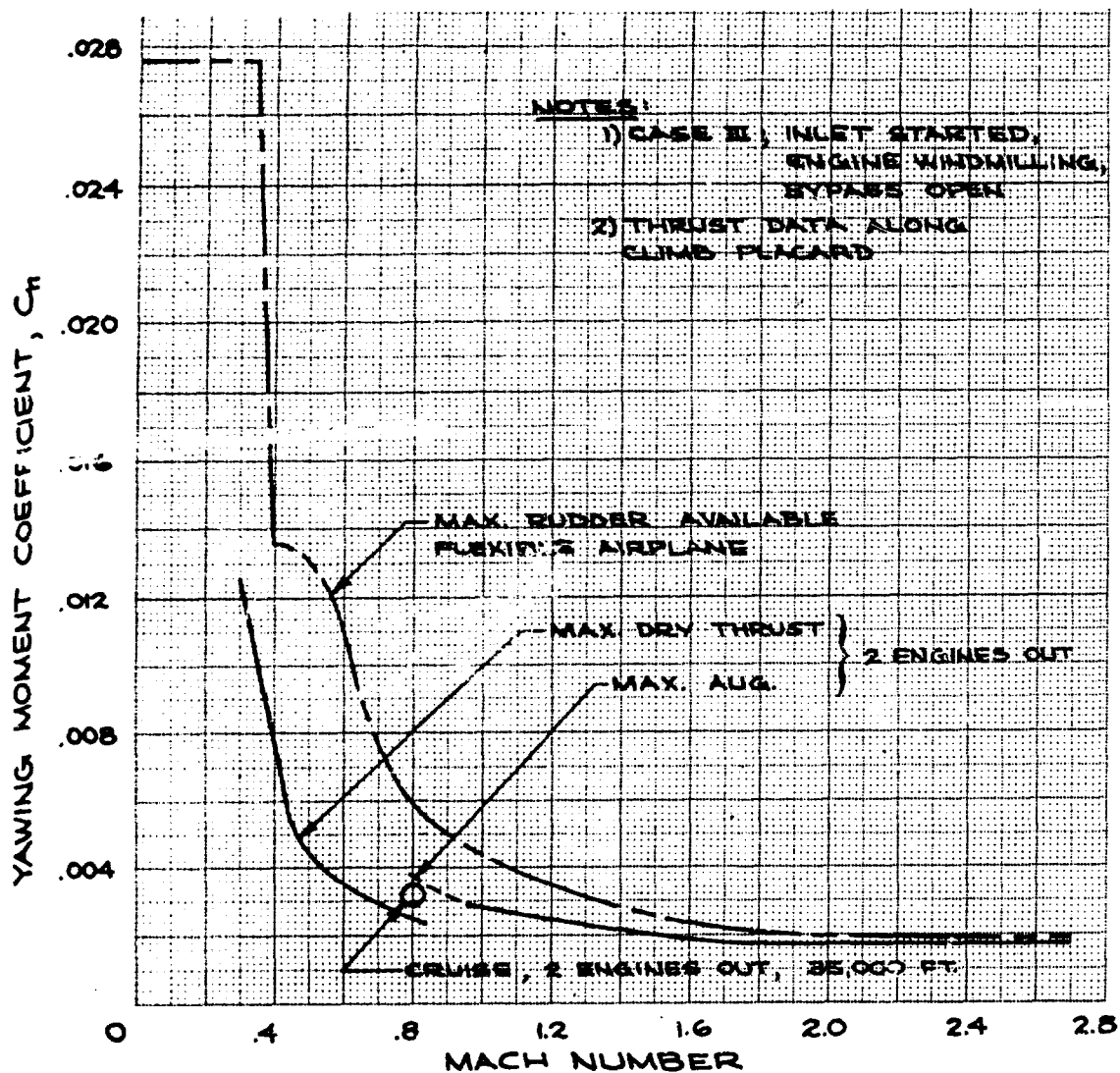


Figure 4-93. Rudder Capability to Trim Asymmetric Thrust

lateral control capabilities and cross-coupling characteristics.

The aerodynamic forces and moments associated with partial or complete engine/inlet failure were measured in the Boeing supersonic wind tunnel at the critical Mach 2.7 condition and at Mach 2.0. Additional testing is scheduled at other flight conditions.

Aerodynamic data from wind tunnel tests are shown in Fig. 4-94 for 2.7 Mach number. The

data have been adjusted to include the effects of recent inlet changes. Four cases are presented:

- a. Case I, inlet unstarted and buzzing
- b. Case II, inlet started, bypass open, engine running.
- c. Case III, inlet started, bypass open, engine windmilling.
- d. Case IV, inlet unstarted, bypass open, engine rotor stopped.

CASE I ~ INLET UNSTARTED AND BUZZING, ENGINE RUNNING
CASE II ~ INLET STARTED, BYPASS OPEN, ENGINE RUNNING
CASE III ~ INLET STARTED, BYPASS OPEN, ENGINE WINDMILLING
CASE IV ~ INLET UNSTARTED, BYPASS OPEN, ENGINE ROTOR STOPPED

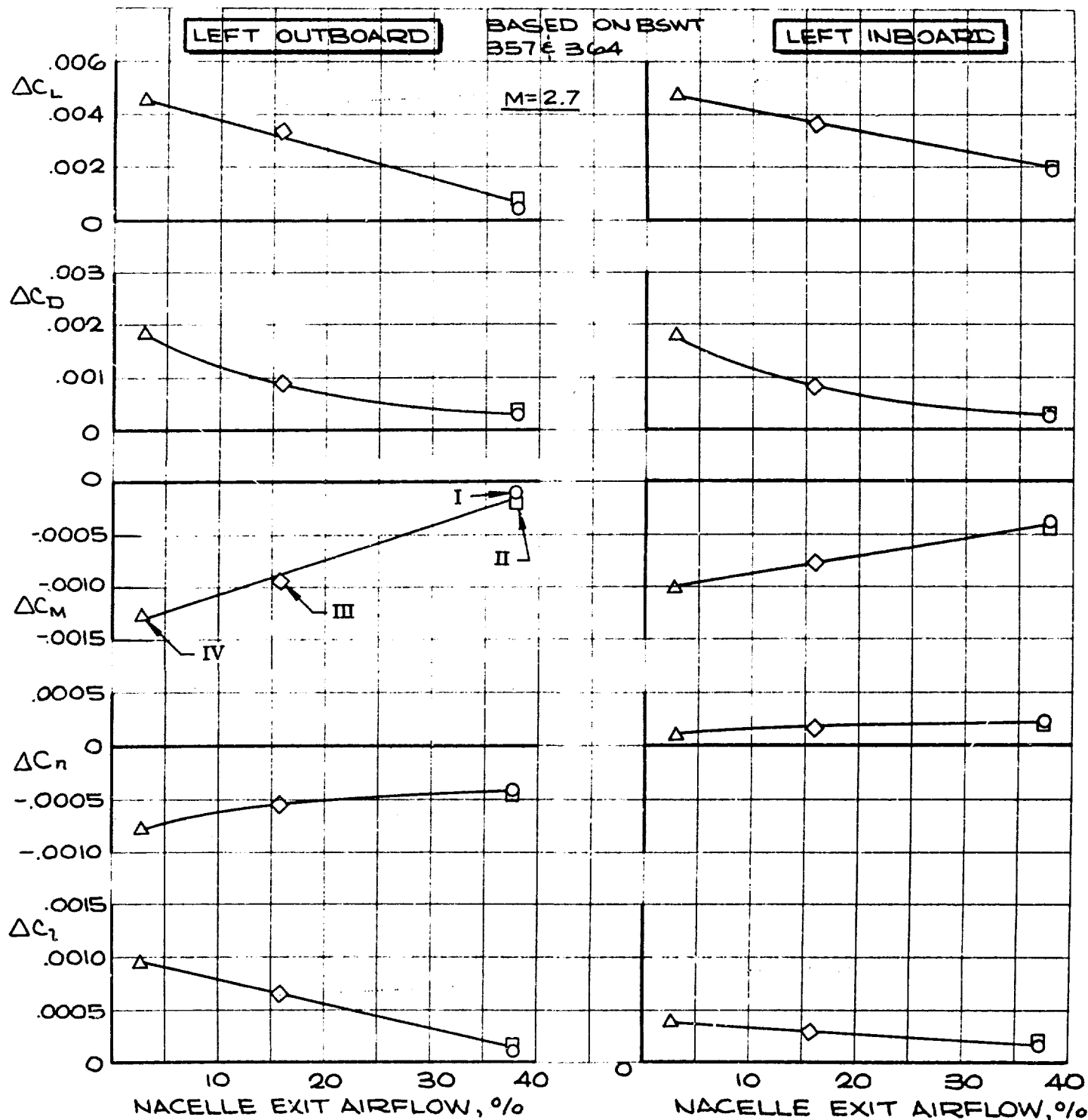


Figure 4-94. Wind Tunnel Test Data, Propulsion Failure Effects

4.5.3.1 Propulsion Failures

Four propulsion system failures were chosen for analysis of airplane handling problems following engine/inlet failure at Mach 2.7. These four failures are described as follows:

- a. Failure A. Inlet unstart followed by automatic restart. This is a normal operational response of the inlet control to some excessive internal or external disturbance. Single and multiple failures were examined with the most extreme case being a simultaneous unstart of all four engines.
- b. Failure B. Inlet unstart with no restart, followed by engine shutdown. A malfunction in the inlet control could cause an unstart which, if the pilot could not obtain a manual restart, would result in engine shutdown to windmill 10 sec after unstart.
- c. Failure C. Engine shutdown. This condition represents an engine malfunction with the inlet remaining started.
- d. Failure D. Engine failure followed by the rotor stopping and inlet unstart. This is the most extreme failure case in which a massive mechanical failure causes almost complete blocking of engine airflow and the inlet is forced into an unstarted condition. Both single and multiple failures were examined for this case.

The most critical failure conditions are those resulting in asymmetric thrust and drag forces acting to yaw the airplane. Single and double engine failures on one side produce strong yawing moments toward the failed engine. The resulting sideslip induces rolling moments toward the failed engine due to the large dihedral effect of the highly swept wing. The pilot is sensitive to bank angle change and will apply lateral wheel control in the proper direction to level the wings. If the lateral control provides strong rolling moment and very little cross-coupling in yaw, the airplane is readily brought under control. The B-2707 lateral control system with rudder interconnect is being designed to provide the desired roll response characteristics to ensure safe operation for the most extreme engine/inlet failure conditions.

Fixed base simulator testing was conducted to examine both the uncontrolled and the piloted transient response of the airplane to propulsion system failure. The responses of the augmented

airplane to each of the failures are shown in Fig. 4-95, for cases where no corrective control is applied. For the most severe case (Failure D) the bank angle reaches 20 degrees in 12.3 sec following the complete failure of the outboard engine.

Simulated engine failures with the pilot applying corrective control are shown in Fig. 4-96. These were single outboard engine failures with stability augmentation operative. In each case, the pilot easily controlled the airplane disturbance with the lateral control; no rudder pedal inputs or thrust retarding on opposite engines was required.

Simulator tests showed difficulty in handling the Dutch roll oscillations created by engine failure disturbance. Directional stability was increased by the addition of increased ventral surface area (folding ventral fin) as discussed in Par. 4.2.2. Simulator testing of the most severe engine failure cases showed that this increase in directional stability enabled the pilot to control the airplane satisfactorily without the aid of the SAS. As shown in Fig. 4-97 for the worst double engine failure case, the pilot was able to control the bank angle to within ± 8 degrees and sideslip to ± 1 degree.

Engine/inlet failure studies are continuing with wind tunnel testing, computer studies, and flight simulator tests. The Boeing criterion for satisfactory airplane handling in these emergencies is that the pilot must be able to control the most severe cases with lateral control only, with or without the assistance of the stability augmentation system.

4.5.4 Wing Sweep Failure

The inability to sweep the wings forward for landing is an extremely remote possibility. In this case the ability to correct for crosswinds during landing is limited by the large dihedral effect and low roll control power. Figure 4-98 summarizes the roll performance available for a crosswind landing with the wings fully swept. With 4 degrees of crab on the landing gear, the maximum tolerable 90-degree crosswind velocity is 21 kn at tower height. The roll performance in this condition is based on attaining 4 degrees bank angle in 1 sec. The wind shear correction for tower height is shown in Fig. 4-99.

4.5.5 Control System Failures

4.5.5.1 Longitudinal Control

The ability to maneuver the airplane with single

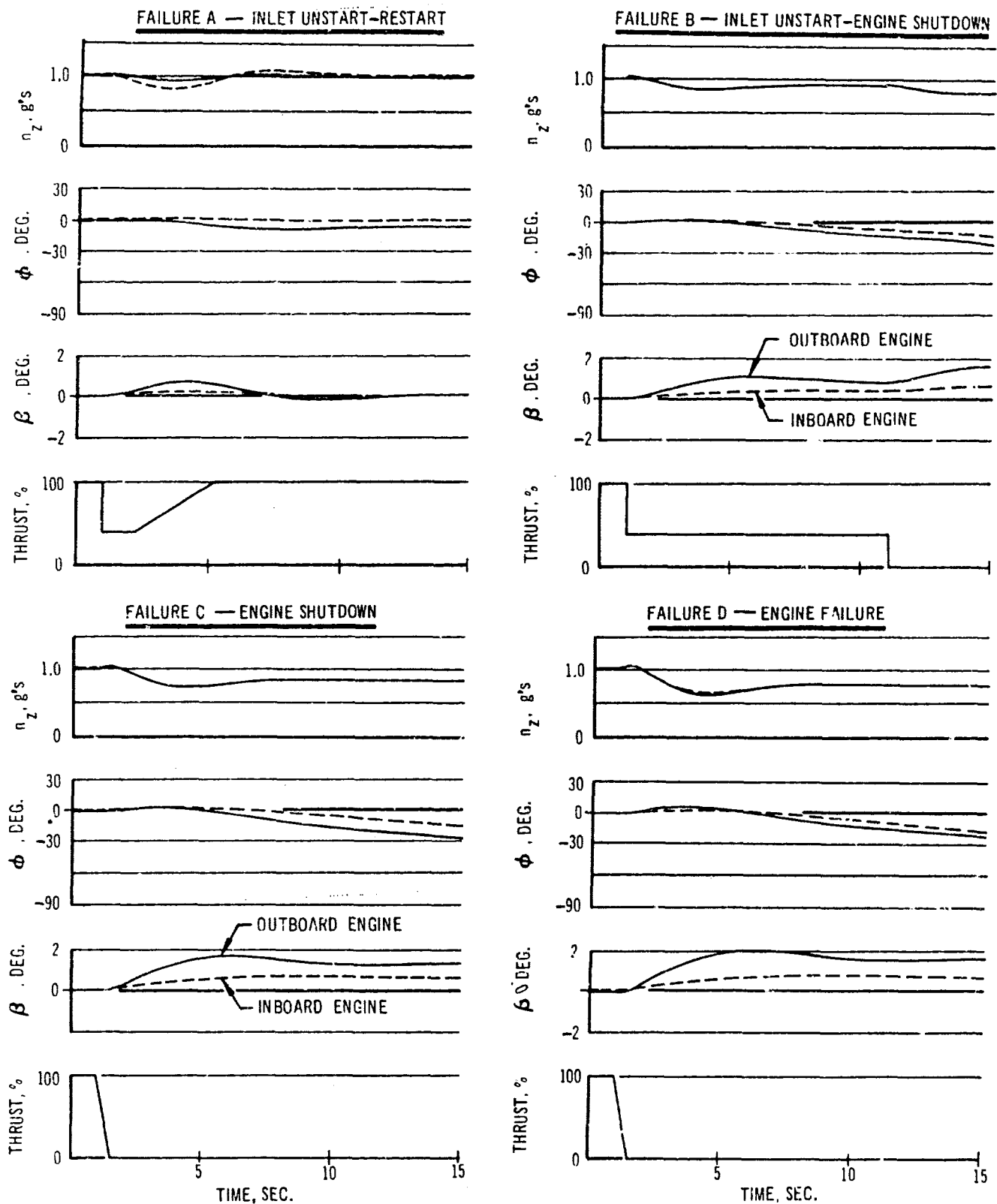


Figure 4-95. Response to Single Propulsion Failure, No Pilot Correction, Augmented

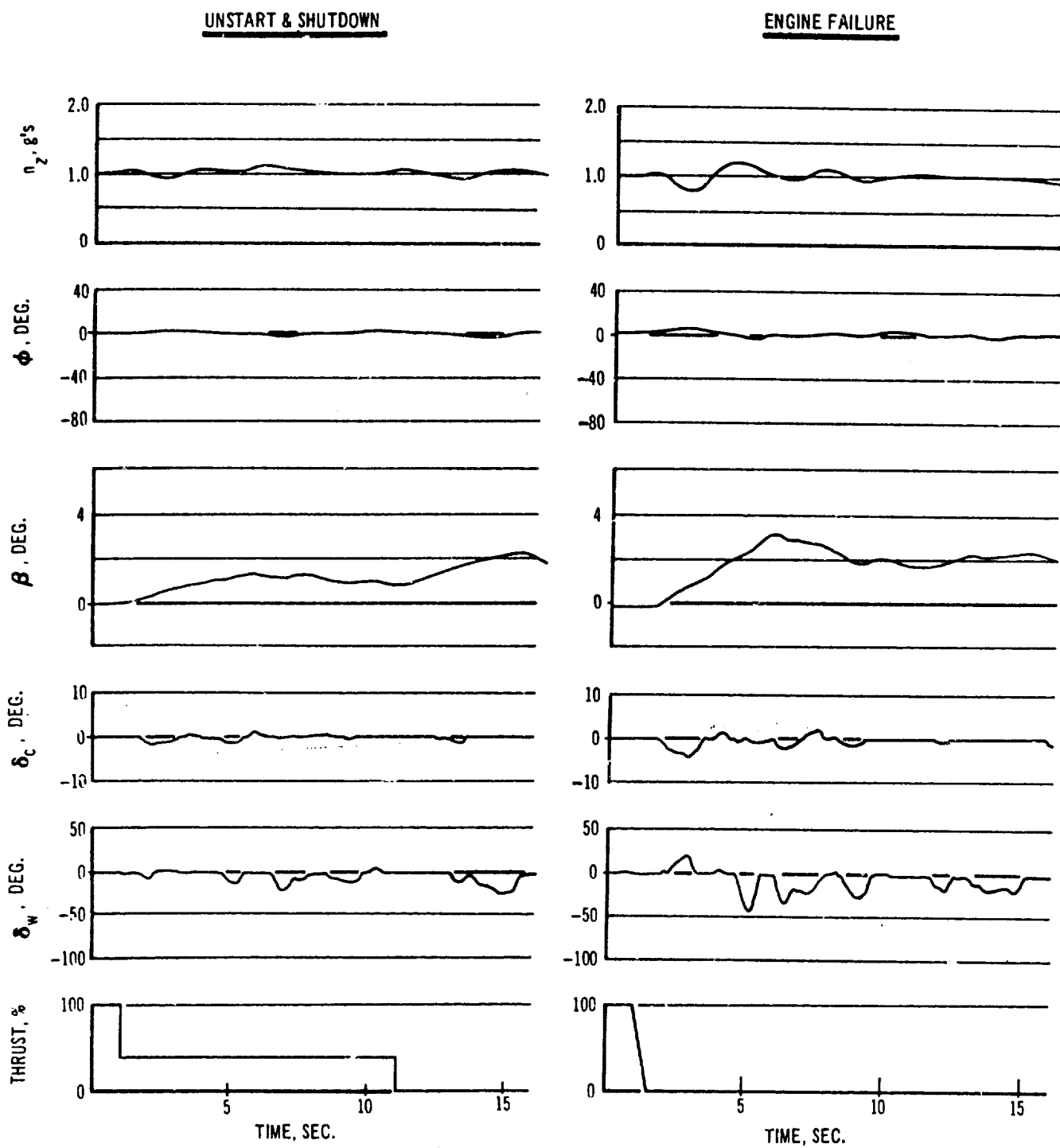
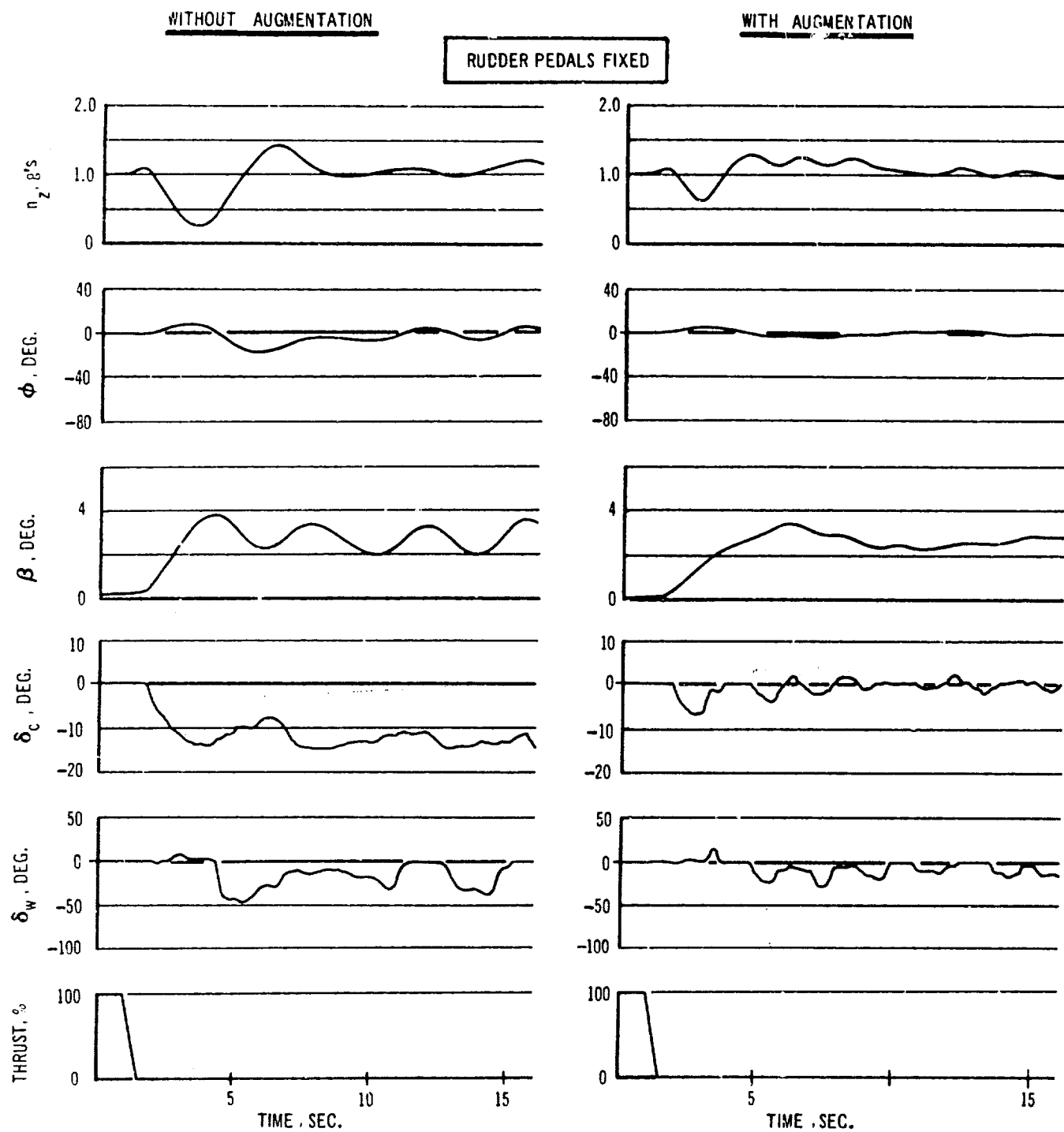


Figure 4-96. Single Propulsion Failure, With Pilot Corrective Action



**Figure 4-97. Double Engine Failure, With Pilot Corrective Action,
Improved Directional Stability**

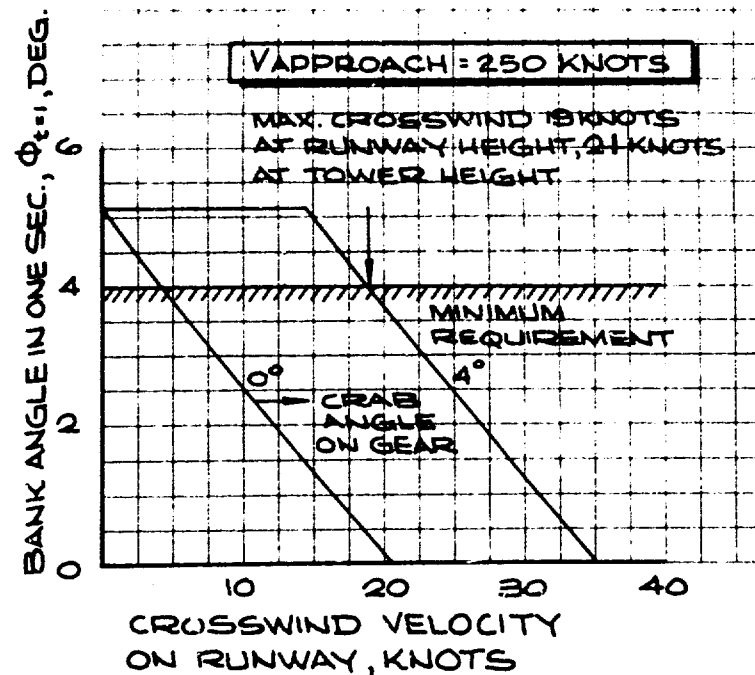


Figure 4-98. Roll Performance, Wings Aft Landing

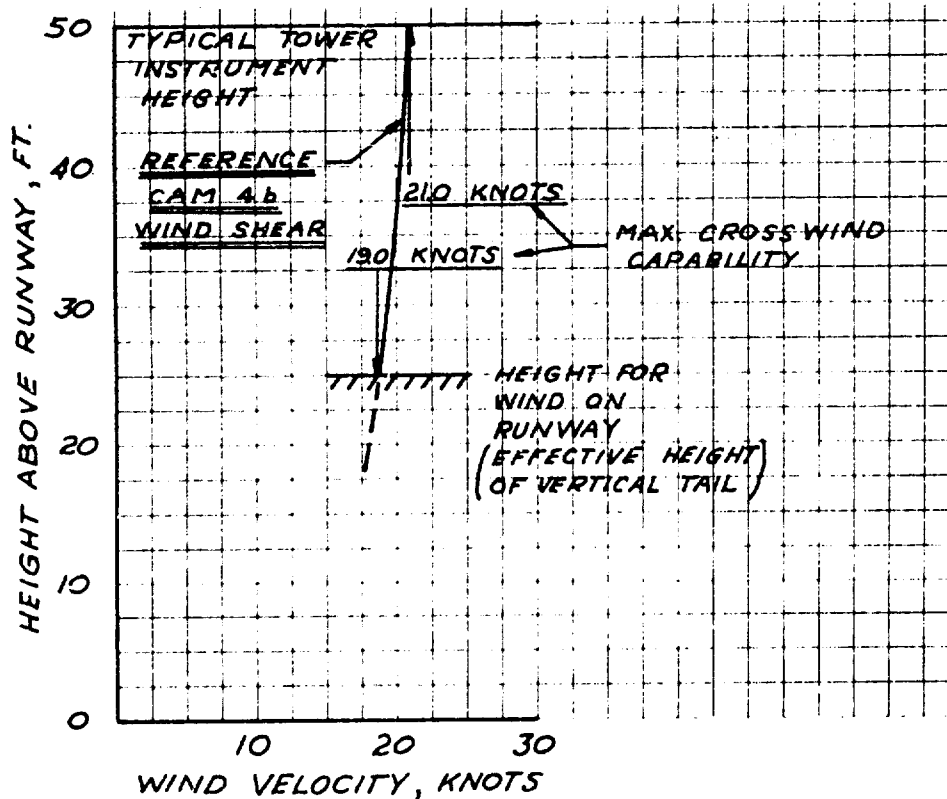


Figure 4-99. Wind Shear Effect

and dual hydraulic system failures is shown in Figs. 4-100 and 4-101. Adequate maneuver capability is seen to exist for all conditions except operations with forward cg's at supersonic Mach numbers. The existing hydraulic control power partially limits elevator travel with all hydraulic systems operating, and severely limits surface deflection with one or two systems failed (Sec. 5.0). Thus, maneuver capability becomes marginal at extreme forward cg's with system failures. Improved maneuver capabilities will be developed to provide a substantial margin of safety for operating with failed hydraulic systems. The design goal is to provide the ability to continue supersonic cruise following a single system failure, with the assurance that a safe deceleration and descent can be made following a subsequent, second, hydraulic system failure. It is considered that adequate maneuver capability will be provided with the ability to develop 1.5 g normal acceleration at V_D with only one hydraulic system operative while at the most critical center of gravity loading.

4.5.5.2 Lateral Control

Lateral control performance under single and double hydraulic system failure is summarized in Fig. 4-102, which shows steady state roll rate and bank angle in 1 sec capabilities for coordinated single degree of freedom rolls. The selected roll performance requirements for emergency conditions are shown compared with the roll performance provided for the failure conditions for eight flight conditions. Adequate roll control is provided in all cases for either two systems operating or one system operating.

4.5.5.3 Directional Control

No limitation in available rudder deflection occurs up to Mach 0.85 with either single or double system failure (Fig. 4-103). At higher speeds the available rudder deflection is limited by reduced hydraulic power following system failure. However, sufficient directional control capability remains to trim sideslip to zero with one hydraulic system failed and an outboard engine inoperative with maximum thrust on the other engines. With two engines failed and maximum thrust on the remaining engines, a small residual sideslip (less than 1 degree) remains with full available rudder trim for either two hydraulic systems failed or one system failed. Directional control capabilities for these emergency operations are considered satisfactory.

4.5.5.4 Trim Systems

The parallel trim system design precludes runaway trim about any control axis, Systems Report, Part B, V2-B2707-11. Even if failures of this nature could occur, pilots control forces are such that the runaway trim could be overpowered.

4.5.5.5 Fuel System Failure

The fuel system is described in Propulsion Report Part B, V2-B2707-13. Unbalance of the airplane due to fuel system failures is an extremely remote possibility because of the fuel transfer system redundancy. Fuel transfer is not employed to maintain the airplane within stability limits in any case, but only to ensure minimum trim drag.

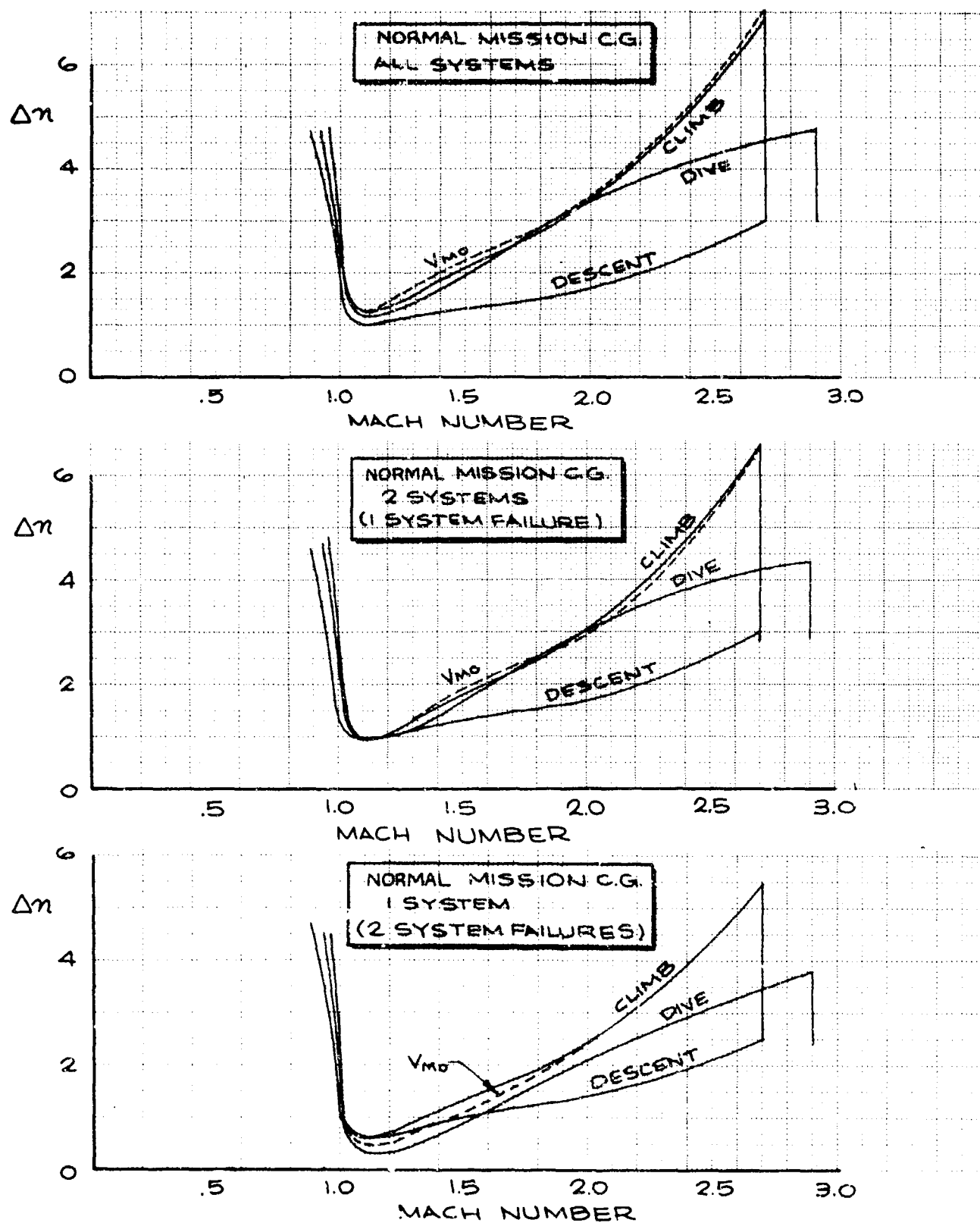


Figure 4-100. Manuever Capability With Control System Failures, Normal Mission C.G.

V2-B2707-3

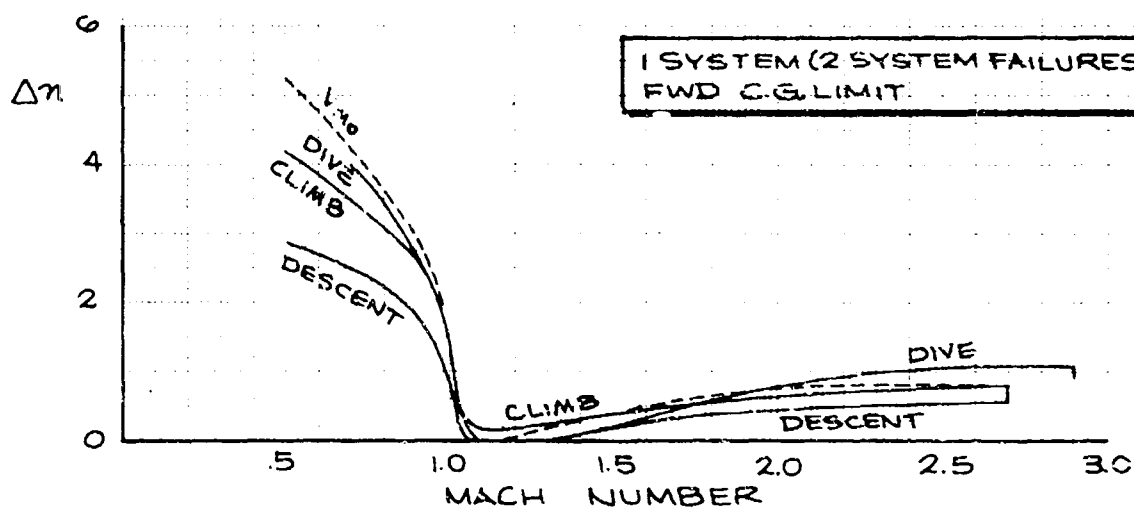
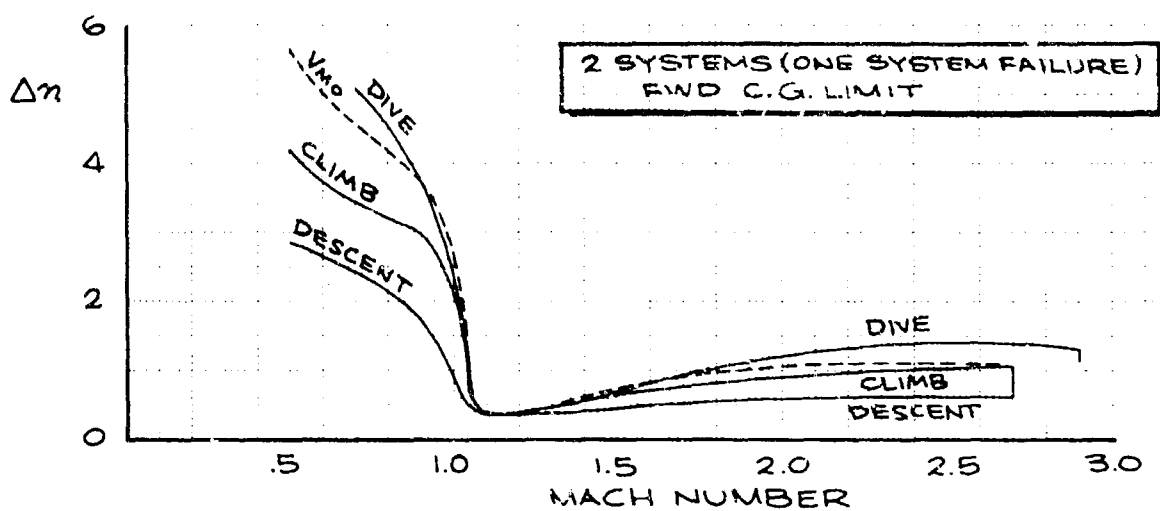
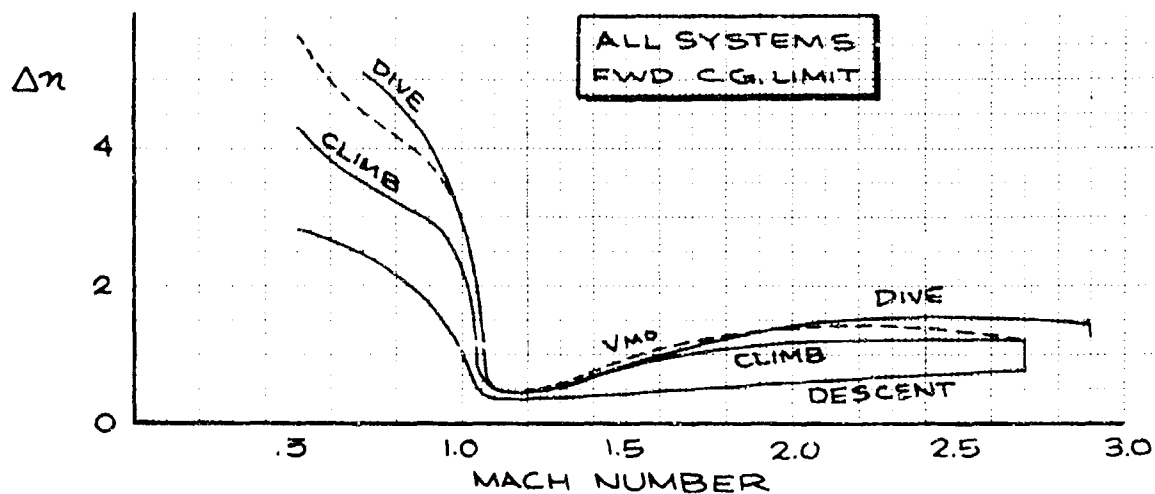


Figure 4-101. Maneuver Capability With Control System Failures, Forward C.G. Limit

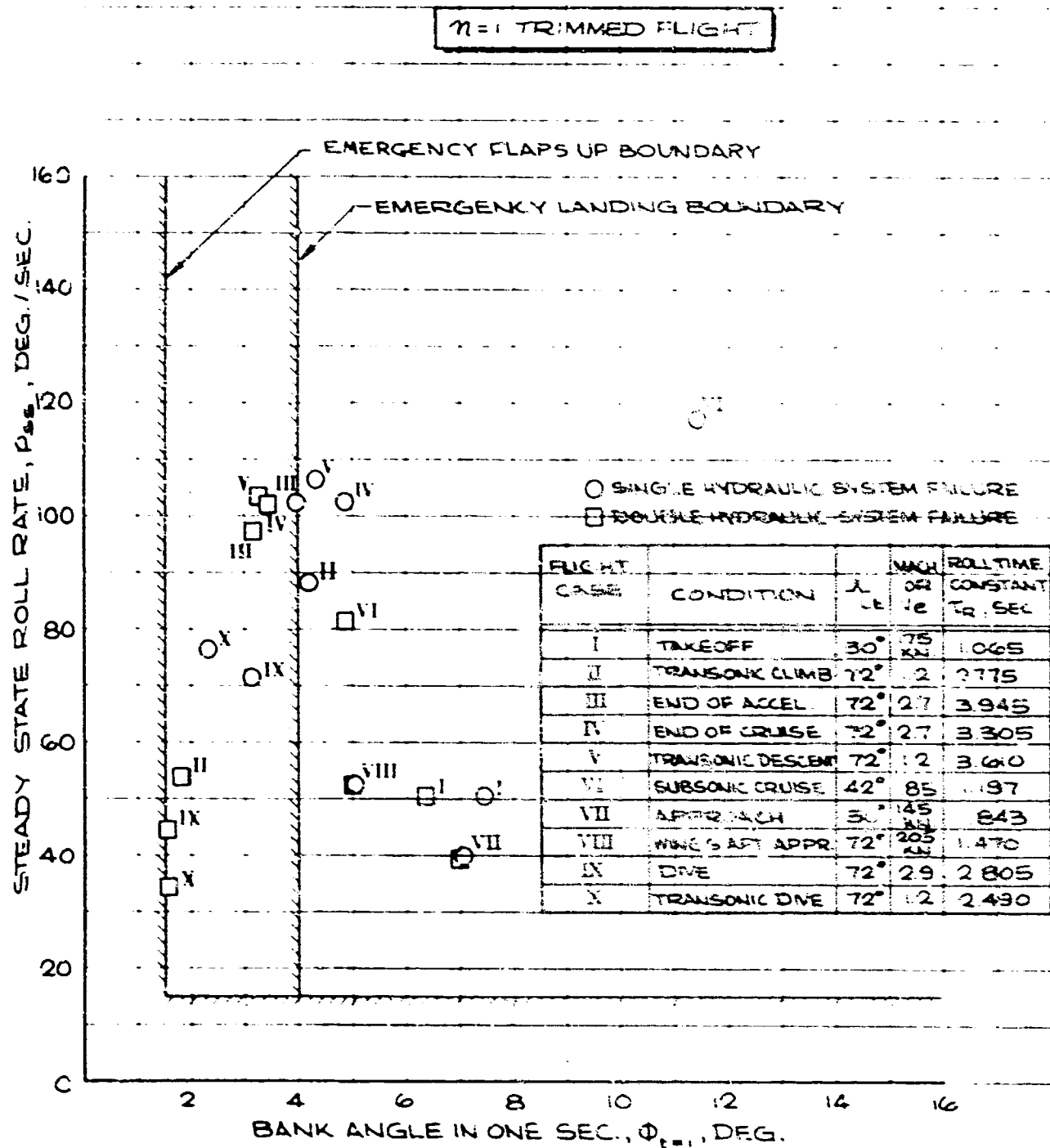


Figure 4-102. Roll Performance with Control System Failures

V2-B2707-3

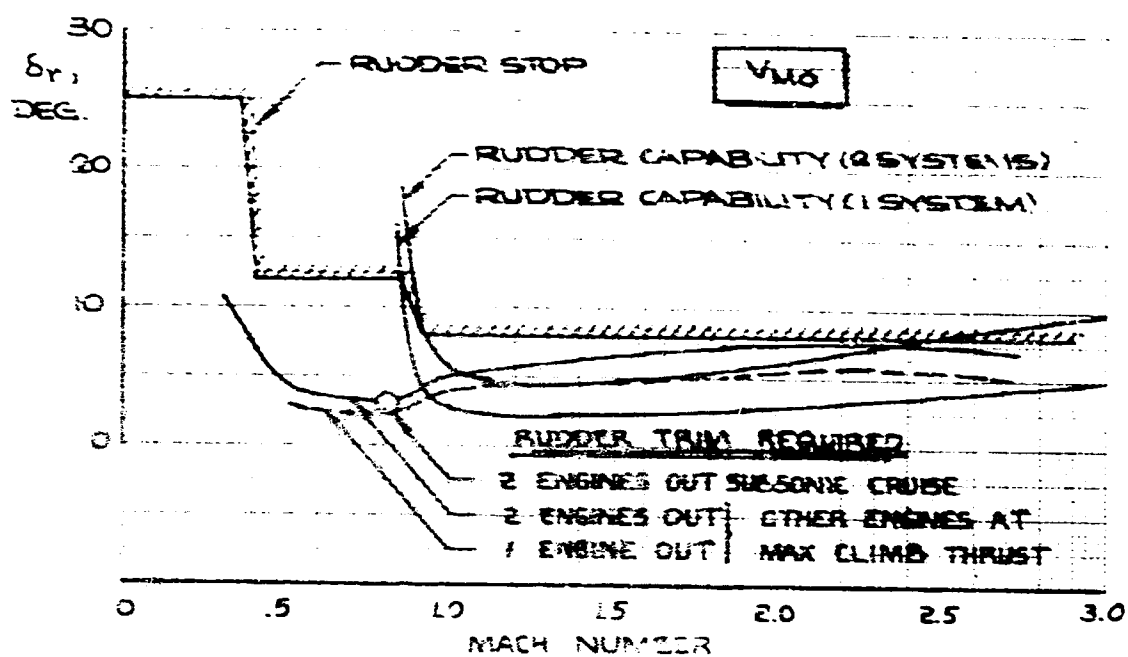


Figure 4-103. Rudder Capability With Control System Failures

5.0	FLIGHT CONTROLS AND STABILITY AUGMENTATION SYSTEM	
5.1	PRIMARY FLIGHT CONTROL SYSTEM	245
5.2	SECONDARY FLIGHT CONTROL SYSTEM	254
5.3	STABILITY AUGMENTATION SYSTEM	254

5.0 FLIGHT CONTROLS AND STABILITY AUGMENTATION SYSTEM

The basic features of the B-2707 flight controls subsystem are determined by the large size and variable geometry characteristics of the airplane and by the requirements for high safety and reliability. These requirements are met through the inclusion of such items as the electric command system, triplicated hydraulic actuation of the primary control surfaces, and multichannel SAS on all control axes. The functional characteristics and aerodynamic design requirements of the flight control system are described in this section. Systems Report, Part B (V2-B2707-11) provides a detailed description of the design features of the control systems. The control surfaces and their high speed and low speed functions are shown in Fig. 5-1.

5.1 PRIMARY FLIGHT CONTROL SYSTEM

Primary flight control is obtained from aerodynamic control surfaces driven by hydraulic power control packages in response to pilot inputs through conventional control columns and rudder pedals. The aerodynamic control surfaces consist of elevons, elevators, and auxiliary elevators for longitudinal control, ailerons and spoilers for low speed lateral control, elevons and spoilers for high speed lateral control, and a rudder for directional control. The normal mode of operation of the longitudinal and lateral axes employs an electric command system. If the electric command system becomes inoperative, a backup mechanical cable system will take over the control functions. Pilots' rudder input is transmitted to the rudder surface actuator by mechanical cables. Various hydraulic, electronic, and mechanical redundancy arrangements are used to achieve a fail-operational design.

5.1.1 Electric Command System, Pitch and Roll Axes

An electric command system is provided to compensate for the compliance, inertia, hysteresis, and friction associated with mechanical cable systems. The electric command is the normal control mode for the primary flight control longitudinal and lateral axes and is backed up by a mechanical cable system. Electric signals proportional to the force applied to the control column are produced by force transducers. After filtering and gain scheduling, these electric signals are fed to the hydraulic master servos. The master

servos drive the surface actuators and also back drive the mechanical cable system which repositions the control columns. Triple redundant electric command channels in each axis ensure fail-operational capability upon the first failure and fail-passive upon the second failure. A control panel for the electric command system is located in the flight deck which allows separate axis and channel selection and engagement. Trimming is accomplished by electrically biasing the center point of the master servo and simultaneously biasing the center point of the mechanical feel and centering spring. The trim motor drives the trim screw which positions the mechanical feel spring center point. A position transducer provides an electrical input to the master servo, thus providing coordination between the electrical and mechanical system trim points.

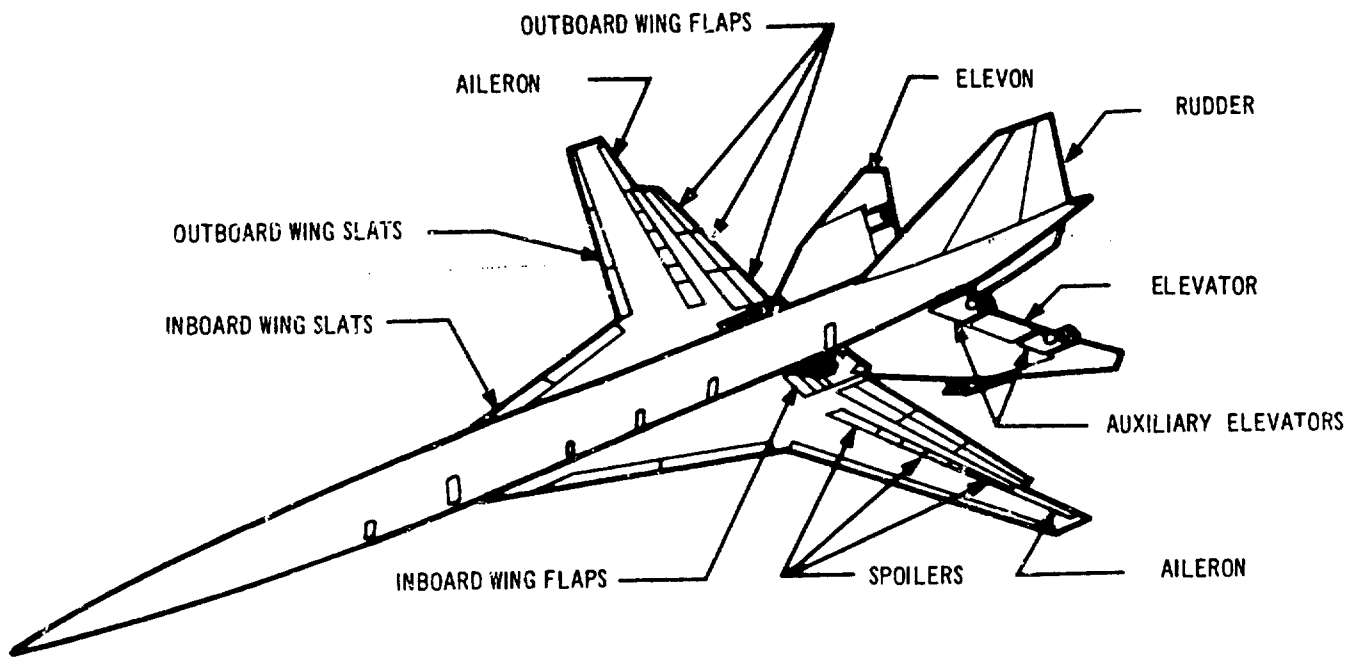
5.1.2 Longitudinal Control System

The output action of the longitudinal master servo is mechanically transmitted to the actuator valves of the elevators, auxiliary elevators, and, through a mixer unit which combines longitudinal and lateral inputs, to the elevons. The auxiliary elevators are operative only when the flaps are in the takeoff or landing position. Longitudinal SAS signals from the SAS servo are combined mechanically with pilot inputs by a summing linkage.

5.1.3 Lateral Control System

The lateral master servo output is transmitted to the elevons through the mixer unit which combines the lateral and longitudinal inputs. The lateral master servo output also drives the actuators of the four inboard spoiler panels on each wing; when the wings are at sweep angles less than 60 degrees, it drives all spoiler panels. When the wing flaps are extended to takeoff or landing position, the ailerons are also driven by the lateral control system. Gearing of the lateral control surfaces as a function of wing sweep and flap position is shown in Fig. 5-2. The relative longitudinal and lateral control gearing of the elevons is shown in Fig. 5-3. The longitudinal input to the elevon always has priority over the lateral input; i. e. if a control position is commanded outside the boundary of Fig. 5-3, the longitudinal deflection commanded is produced and the lateral command uses the remaining surface deflection to the maximum of 30 degrees.

Low Speed Configuration



Cruise Configuration

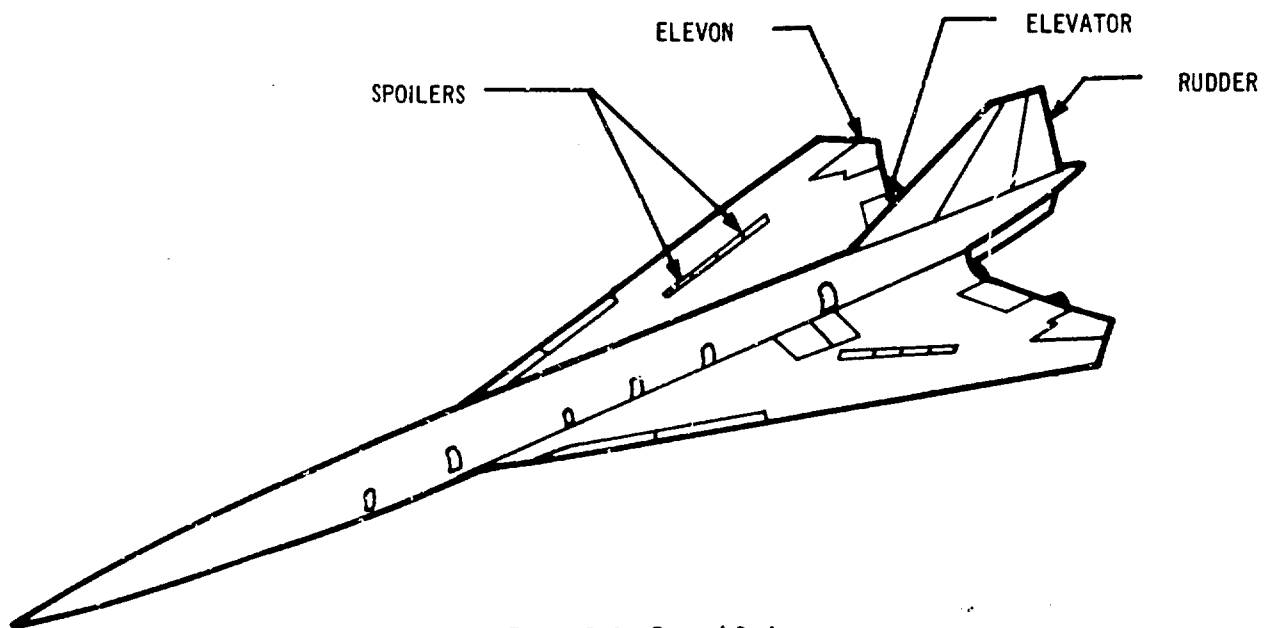


Figure 5-1. Control Surfaces

V2-B2707-3

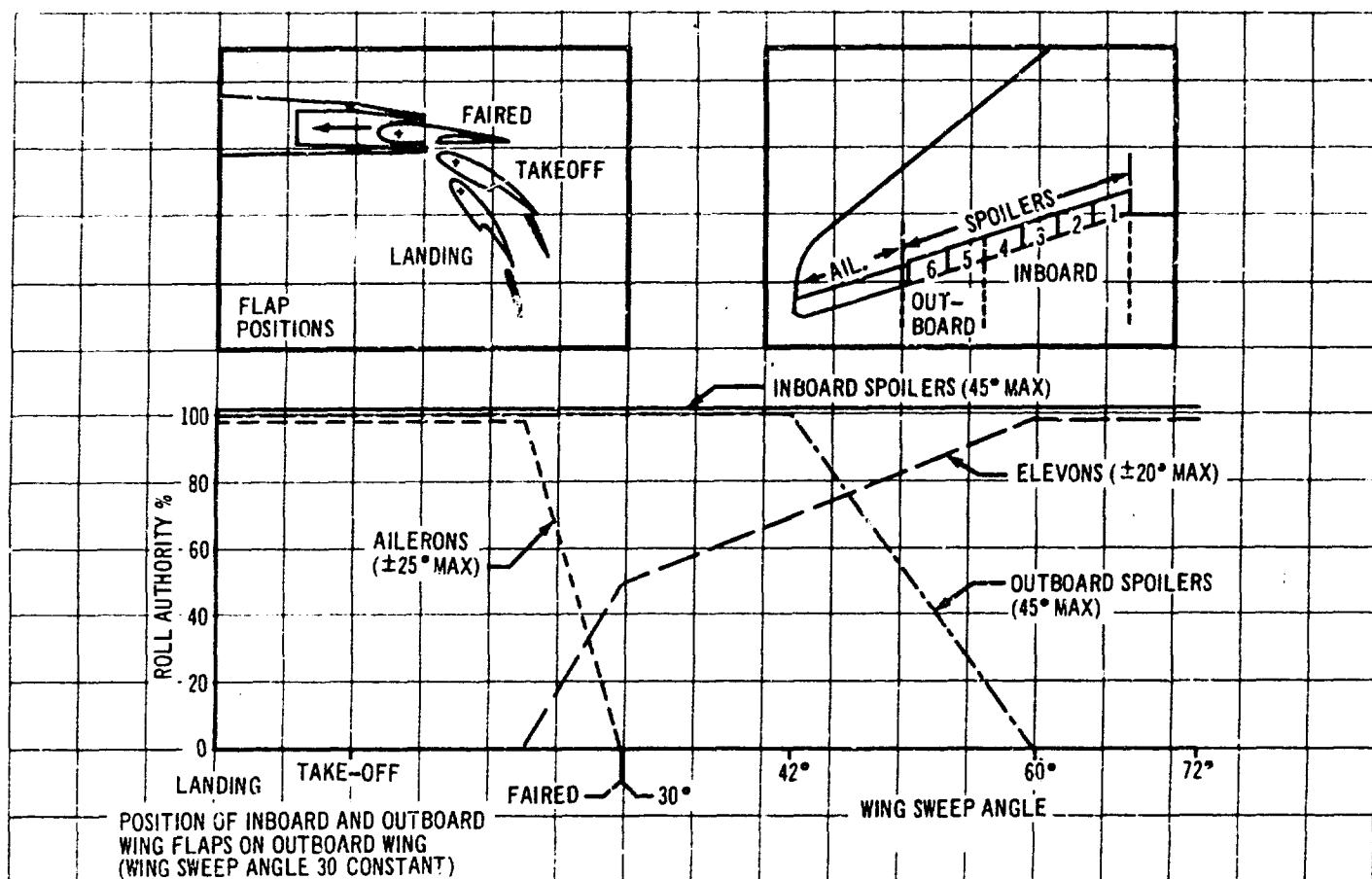


Figure 5-2. Lateral Control Programming

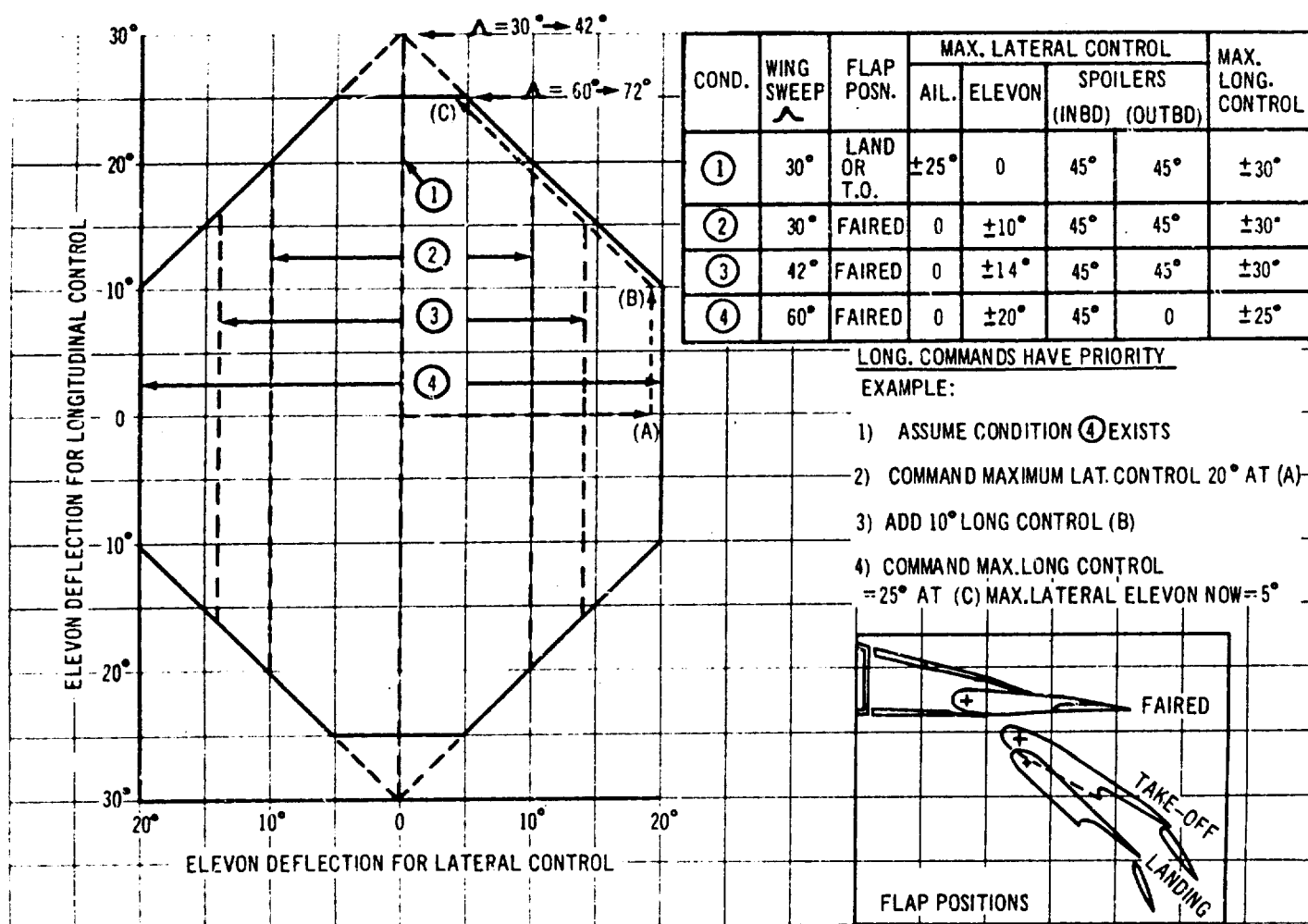


Figure 5-3. Elevon Mix-Longitudinal / Lateral Control

Lateral SAS servo signals are transmitted only to the elevon surfaces; thus the lateral SAS effectiveness is faded to zero when the flaps are extended and the lateral input to the elevons is zeroed. As described in Par. 5.1.1, trimming is accomplished by biasing the center point of the lateral master servo. The control output of the master servo to the spoilers has a trim cancelling input introduced to avoid deflecting the spoiler panels for trim.

5.1.4 Directional Control System

The directional control system is mechanically controlled and hydraulically powered. Commands to the rudder actuator package are received from flight deck controls, the stability augmentation system, and the lateral control system. Rudder trim is provided by moving the location of the centering point for the artificial feel spring. Rudder authority is limited by mechanical stops in the control linkage to the actuators which are introduced as a function of flap position and wing sweep. The stability augmentation system inputs and turn coordination commands from the lateral control system are added to the pilot control inputs in the mechanical mixer. SAS and turn coordination inputs do not produce flight deck control motion.

5.1.5 Control Surfaces

The primary control surfaces are shown in Fig. 5-1. Pitch control is obtained from the elevators, elevons, and, in takeoff and landing configuration, from the auxiliary elevators. Lateral control is produced by differential deflection of the elevons and by the eight inboard wing spoiler panels in the supersonic cruise configuration. As the wings are extended to the subsonic cruise position, the remaining wing spoilers become operative. When the wings are fully forward to the 30-degree sweep position and the high lift devices extended, the elevons revert to pitch control only and the ailerons are operated for additional low speed lateral control. Table 5-A tabulates the control surface deflections, rates, and actuation. The pitch and roll control surfaces have fixed deflection limits, unless otherwise limited by actuator hinge moment capability. To limit the maneuver loads, the rudder deflection is limited by mechanical stops in the actuator input linkage which are adjusted as a function of flap and wing sweep as shown in Fig. 5-4. The high speed deflection limit can be withdrawn by a pilot operated override for the emergency wings aft landing condition.

Control surface deflection rate requirements have been estimated from various dynamic analyses and simulation studies. Lateral control surface rates are determined by high speed roll response requirements, longitudinal surface rates by landing approach maneuver, and rudder rates by control of abrupt engine failure. The specified rates are conservative and further refinement will be made.

Control surface hinge moments have been estimated for all primary control surfaces to establish the actuation component sizing and power requirements. These hinge moment values are preliminary and further refinement and wind tunnel testing will be performed in Phase III to establish final design values. No aerelastic corrections have been applied to the hinge moment data presented herein; this is a conservative approach.

Elevator hinge moments shown in Fig. 5-5 are based on National Advisory Committee for Aeronautics data (Ref. 34) for the Mach No. range 0.75 to 1.96 and Boeing wind tunnel data (BSWT 357) at $M = 1.5$ and 2.7. The NACA data are for a 60-degree delta wing configuration with a mid-span elevator and the Boeing data for a configuration closely approximating the B-2707. The agreement between the two sets of data is good, shown in Fig. 5-5. For zero elevator deflections, the hinge moment is zero at an approximately 6-degree angle of attack for the B-2707 configuration at $M = 1.5$ and 2.7. This angle of attack for zero hinge moment has been assumed for all Mach numbers since angle of attack effects are relatively unimportant in determining the maximum surface hinge moments which occur in the $M = 1.2$ region. Hinge moments for the low speed auxiliary elevators are assumed to be similar to the elevator moments.

Data from several sources on tip control surfaces have been correlated to estimate the elevon hinge moments. These data are for a variety of hinge line locations and tip shapes, shown in Fig. 5-6. The correlating parameter used for these data was S_{11}/S_c ; the ratio of area forward of the hinge line to total control surface area. Zero hinge moment is assumed to occur at a 6-degree angle of attack and at zero deflection which is the case for the elevator. The effect of unporting the tip control from behind the wing at low deflections on the hinge moments is unknown at this time, but as is shown in

Table 5-A. Primary Flight Controls, Travels, Rates, and Power

Wing Sweep	Flap	Longitudinal Control			Speed Brakes	Lateral Control			Directional Control
		Primary Elevator	Aux Elevators	Elevons	Spoilers	Spoilers	Ailerons	Elevons	Rudder
30°	T.O. or Landing	±30°	0 - 30°	±30°	0 - 45° (All Panels)	0 - 45° (All Panels)	±25°	0	±25°
30°	Faired	±30°	0	±30°	0 - 45° (All Panels)	0 - 45° (All Panels)	0	±10°	±12°
42°	Faired	±30°	0	±30°	0 - 45° (All Panels)	0 - 45° (All Panels)	0	±14°	±12°
72°	Faired	±30°	0	±25°	0 - 45° (8 Inboard Panels)	0 - 45° (8 Inboard Panels)	0	±20°	± 8°
Maximum Surface Rate (Deg/Sec)	1.5	25	25	25	60	60	50	25	25
1 Max. Design Hinge Mom. (In. Lb.)		2,840,000	514,000	3,200,000	980,000	490,000	340,000	3,200,000	1,250,000
Control Surface Actuators	Total Number	18	10	6	36	36	6	6	3
	Bore (In.)	4.33	3.14	7.225	2.5	2.5	—	7.225	6.88
	Stroke (In.)	6.25	3.1	18.0	5.42	5.42	—	18.0	11.0
Flow/Hyd System (GPM)		108.0	17.6	115.2	110.4	55.2	27.0	115.2	50.5

1 Max. Design Hinge Moment with One Hydraulic System

2 Total for Inboard & Outboard Auxiliary Elevators

3 Total for 12 Spoilers

4 Total for 6 Spoilers

5 Each Actuator has Two Cylinders & Pistons

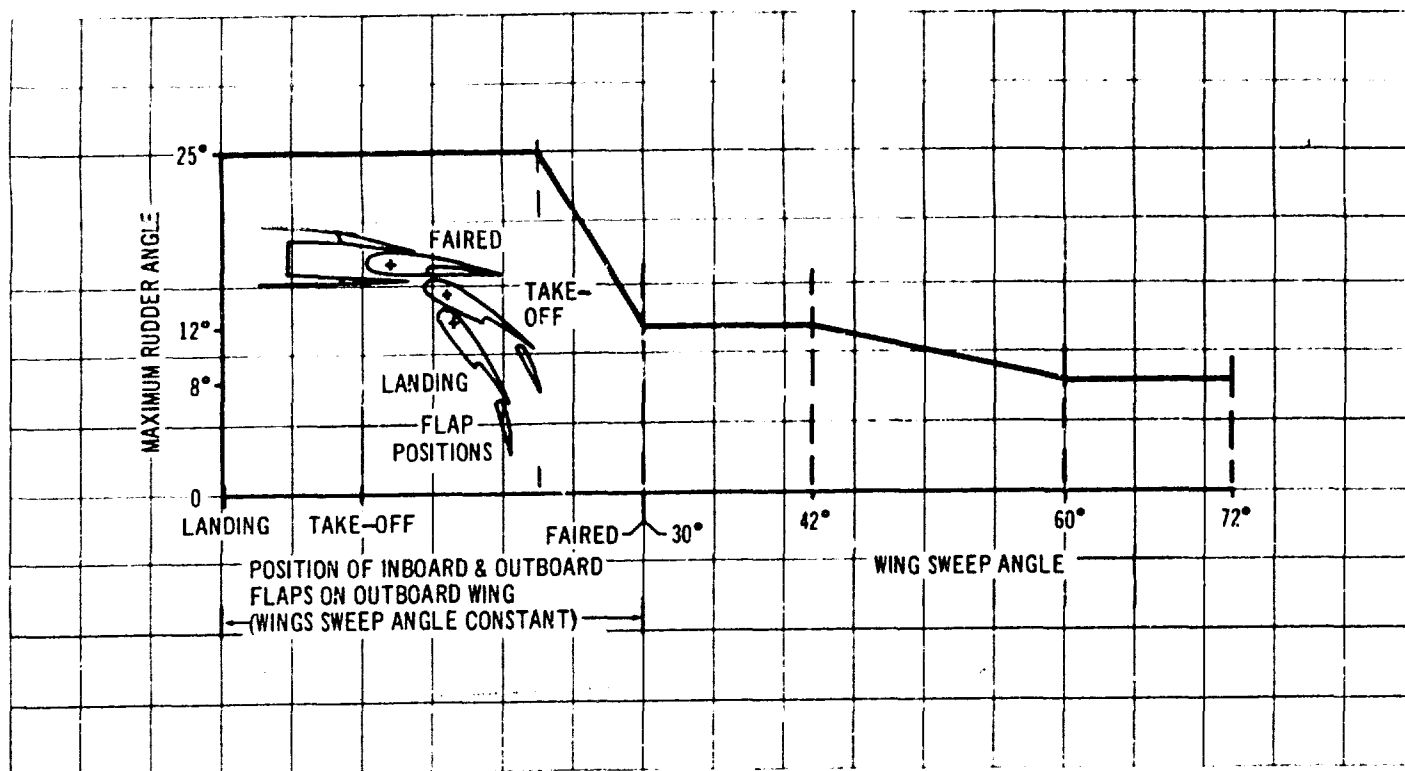


Figure 5-4. Rudder Travel Limiting

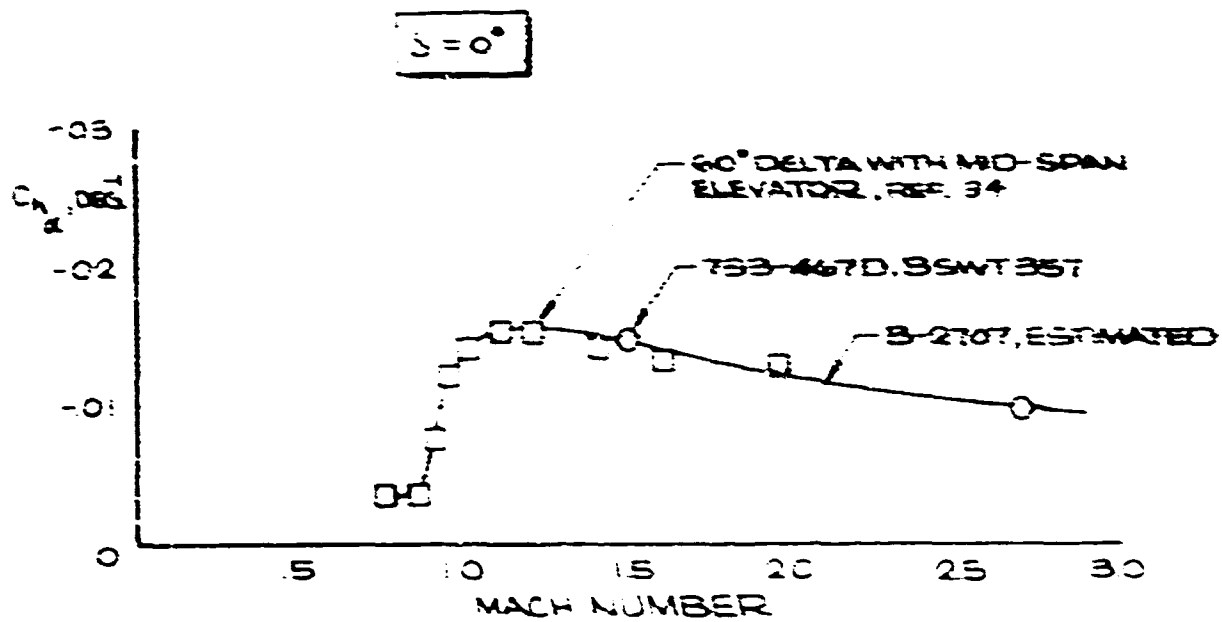
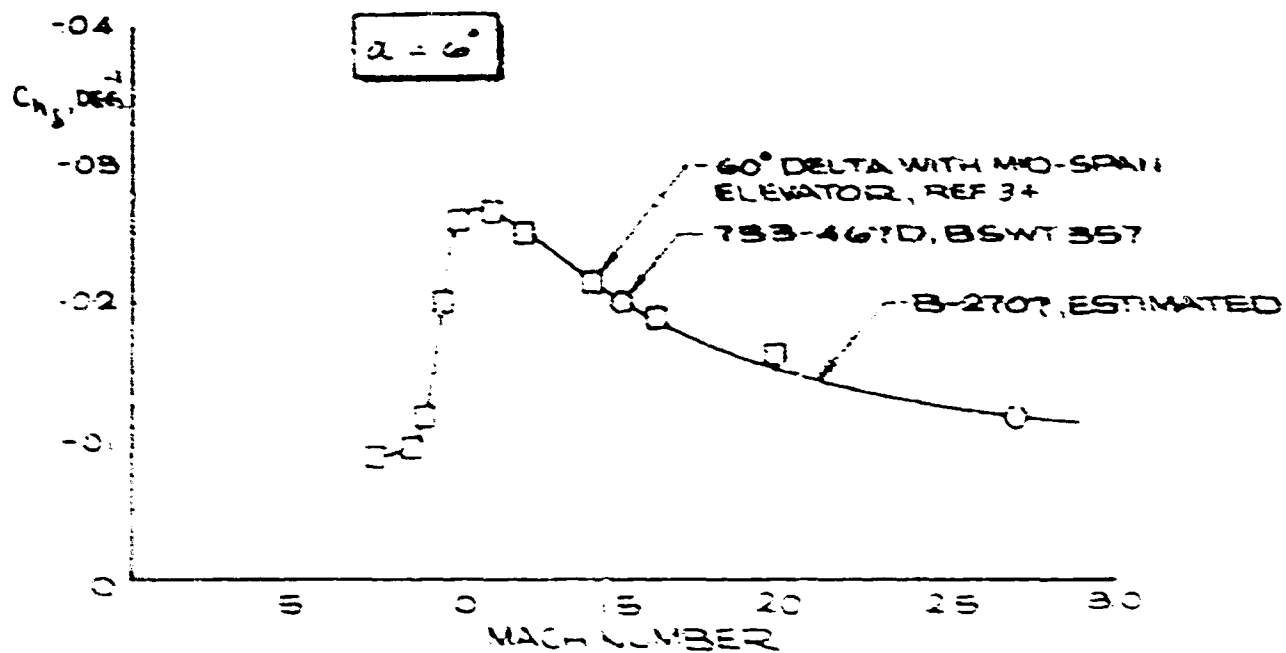


Figure 3-5. Elevator Hinge Moment Characteristics

V2-R0707-3

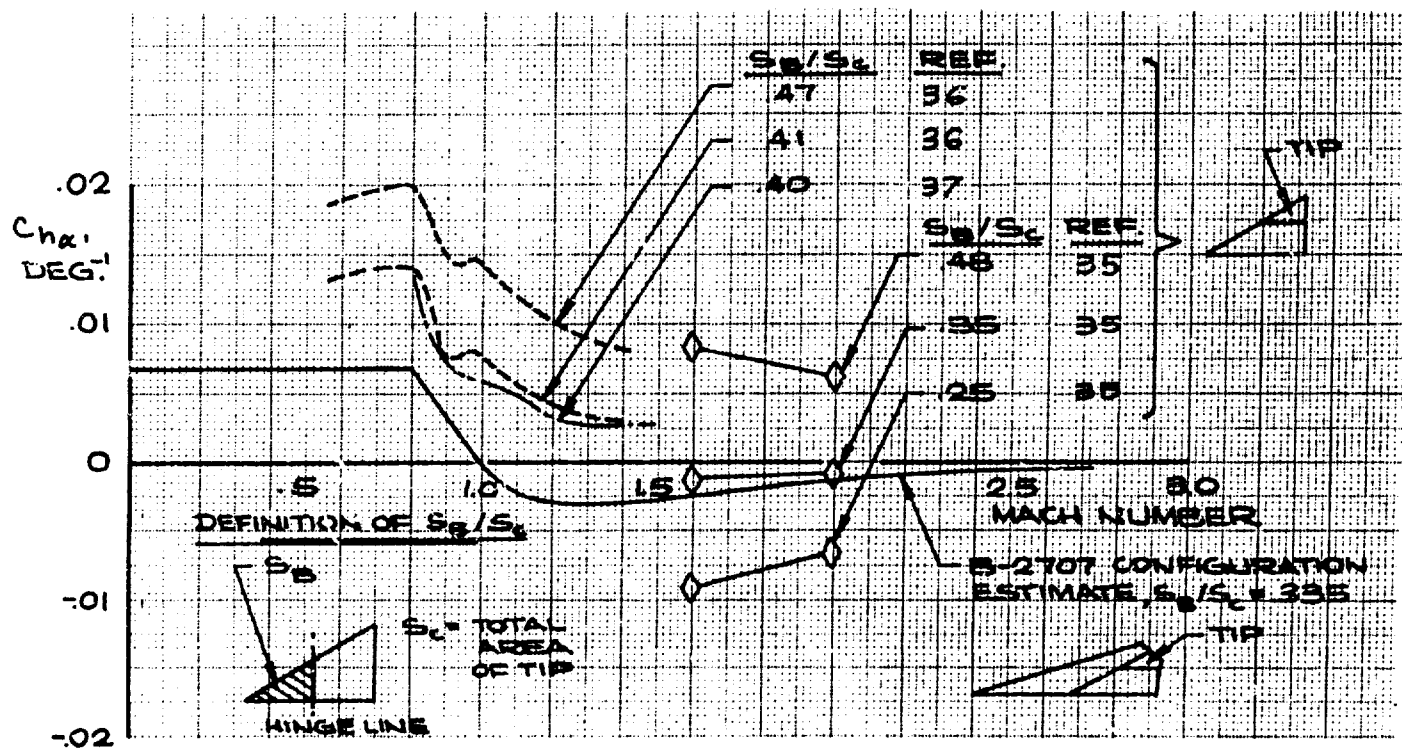
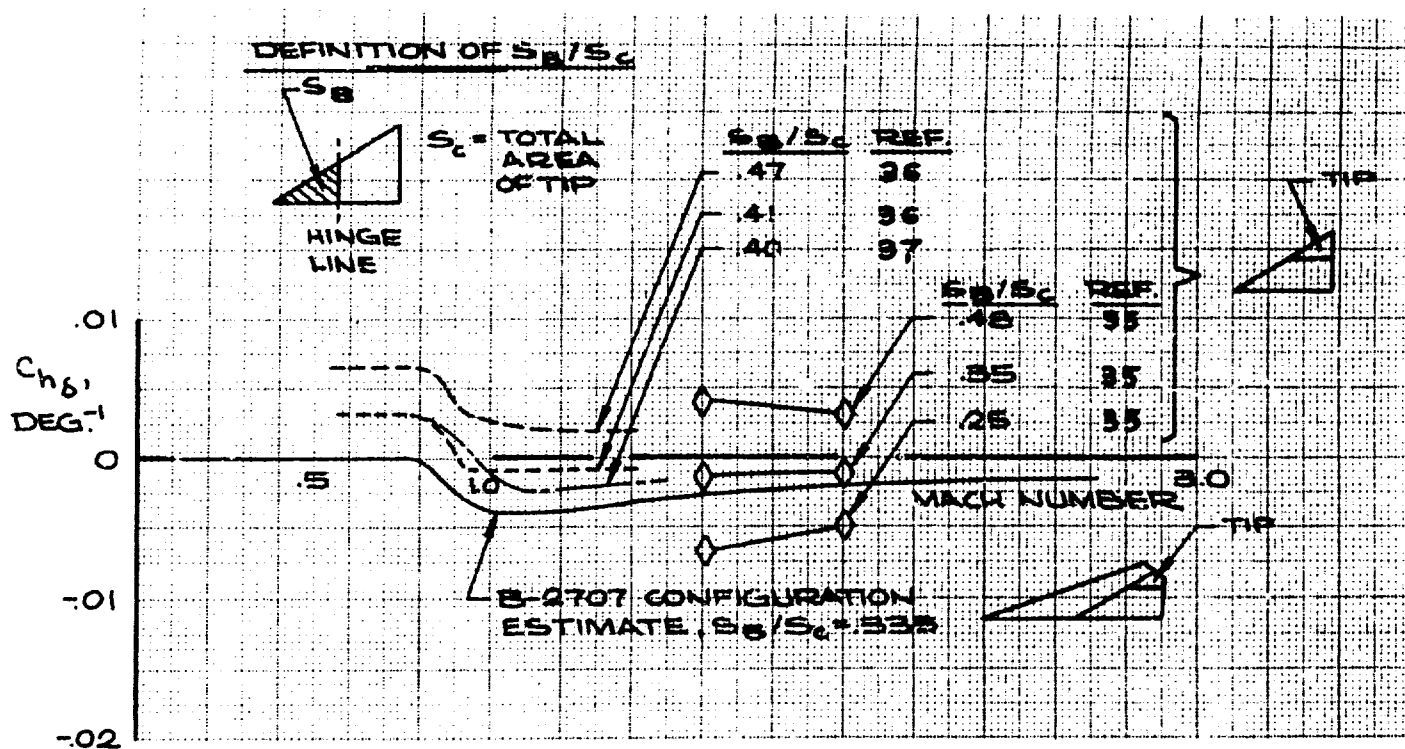


Figure 5-6. Elevon Hinge Moment Characteristics

Sec. 4.0 the surface effectiveness is substantially linear in the small deflection range, and the hinge moment characteristics would be expected to be fairly linear. In any event, little effect is expected on the maximum hinge moments at large deflection.

The spoiler and aileron hold-down hinge moment coefficients and hinge moment coefficients caused by deflection are shown in Fig. 5-7. Spoiler deflection hinge moment characteristics are based on NACA data and Boeing wind tunnel test data referenced in Fig. 5-7. Low speed, flaps down spoiler, and aileron, and flaps up spoiler characteristics are based on model 727 wind tunnel test data (UWAL 692) adjusted for sweep angle changes. High speed spoiler characteristics are based on wind tunnel tests (BSWT 320) with spoilers similar to the current B-2707 configuration. Hold-down hinge moment requirements for the spoilers and ailerons are based on low speed, flaps down model 727 wind tunnel data (UWAL 692) and high subsonic pressure model data on the 733-290 configuration, from NASA Ames Unitary test 143. The large hold-down loads indicated are caused by high local negative pressures caused by high circulation with flaps down at low speeds and by the leading edge vortex at high speed and high angles of attack with the wings at 72-degree sweep.

The estimated rudder hinge moment data shown in Fig. 5-8 are based on the referenced NACA data and low speed estimates using the methods of Ref. 22.

Elevon and elevator deflection capability is shown along V_{MO} and V_D placards in Fig. 5-9 and also along normal climb and descent schedules in Fig. 5-10. Full control surface deflection is available with all systems operating within the normal flight envelope. Moderate loss in maximum deflection occurs if one hydraulic system fails. At the maximum operating speed (V_{MO}), the ability of the airplane to maneuver to its structural limits is only slightly restricted by control hinge moments in the low supersonic speed range; maneuver capability, although reduced, appears adequate with a failed system. Analysis based on current data indicates that the control surface deflections available are marginal for upset recovery at V_D with forward CG. Improvements in control effectiveness will be developed as discussed in Section 4.0.

Spoiler control deflection capabilities are shown in Fig. 5-11 at V_{MO} and V_D at wing sweeps of 42

degrees and 72 degrees. At design dive speed, the deflection capability is only slightly limited at 72 degrees sweep and about half deflection is available at 42-degree sweep where full deflection is not needed to meet requirements. Single system capability (two failures) is shown in Fig. 5-12. Sufficient spoiler deflection is available for lateral balance and bank angle corrections for all conditions.

Rudder hinge moment, adequate to give essentially full deflection to the surface stops, is available at all speeds as shown in Fig. 5-13. The two-engine-out enroute directional control requirement is not compromised by rudder actuation power.

5.2 SECONDARY FLIGHT CONTROL SYSTEM

5.2.1 Wing Sweep Control

The wing sweep control mechanism is described in Systems Report, Part B, V2-B2707-11. Wing sweep rates are 0.7 degree per second for increasing sweep and 0.35 degree per second for decreasing sweep. These rates were chosen to be compatible with the airplane accelerations and decelerations along normal flight profiles. Trim changes with wing sweep are moderate, as shown by the data in Sec. 4.0 and in normal operation are compensated by the SAS. The system has multiple power sources and load paths for safety and reliability of operation as described in V2-B2707-11.

5.2.2 High Lift Devices

The high lift devices consist of leading edge slats and trailing edge flaps on both the inboard fixed portion and outboard variable sweep portion of the wing. The details of flap and slat drive mechanisms are described in V2-B2707-11. The leading and trailing edge flap extension is scheduled with wing sweep as shown in Fig. 5-14. An override mechanism allows inboard slat extension with the wings at 72-degree sweep for the emergency wings aft landing condition.

5.3 STABILITY AUGMENTATION SYSTEM

5.3.1 General Description

A stability augmentation system is provided on all three primary control axes to improve handling qualities and reduce the variation in airplane response characteristics with loading and flight condition. Besides improving the handling qualities, the SAS provides gust loads alleviation, turn coordination, and inner loop damping for the autopilot. The stability augmentation system

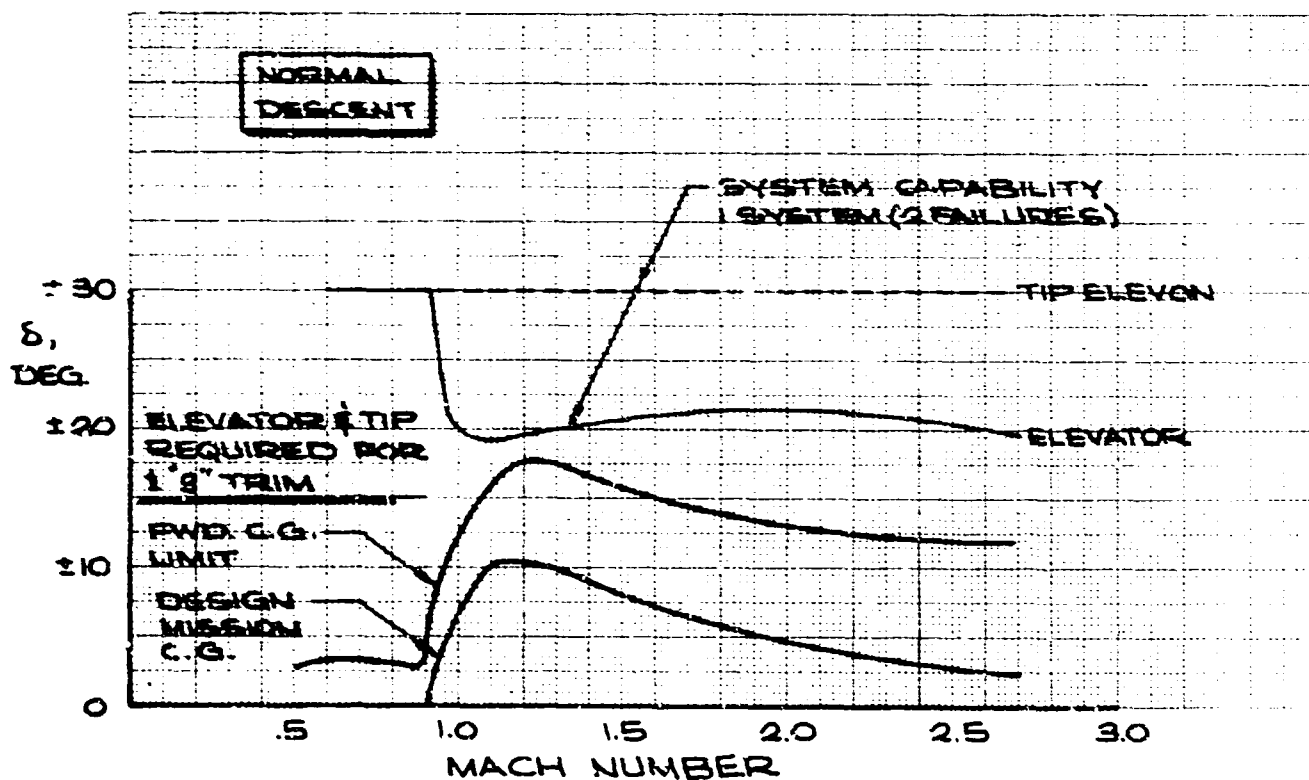
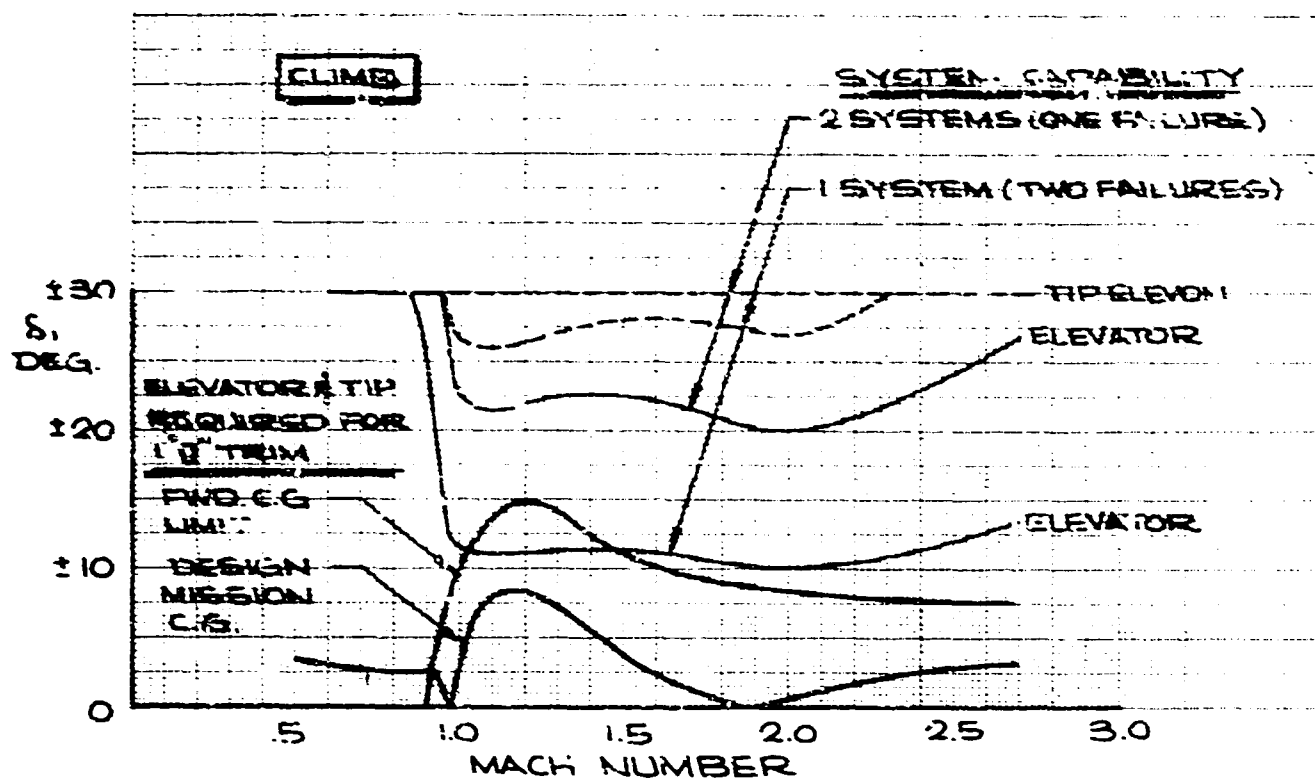


Figure 5-10. Elevator and Elevon Deflection Capability (Climb and Descent)

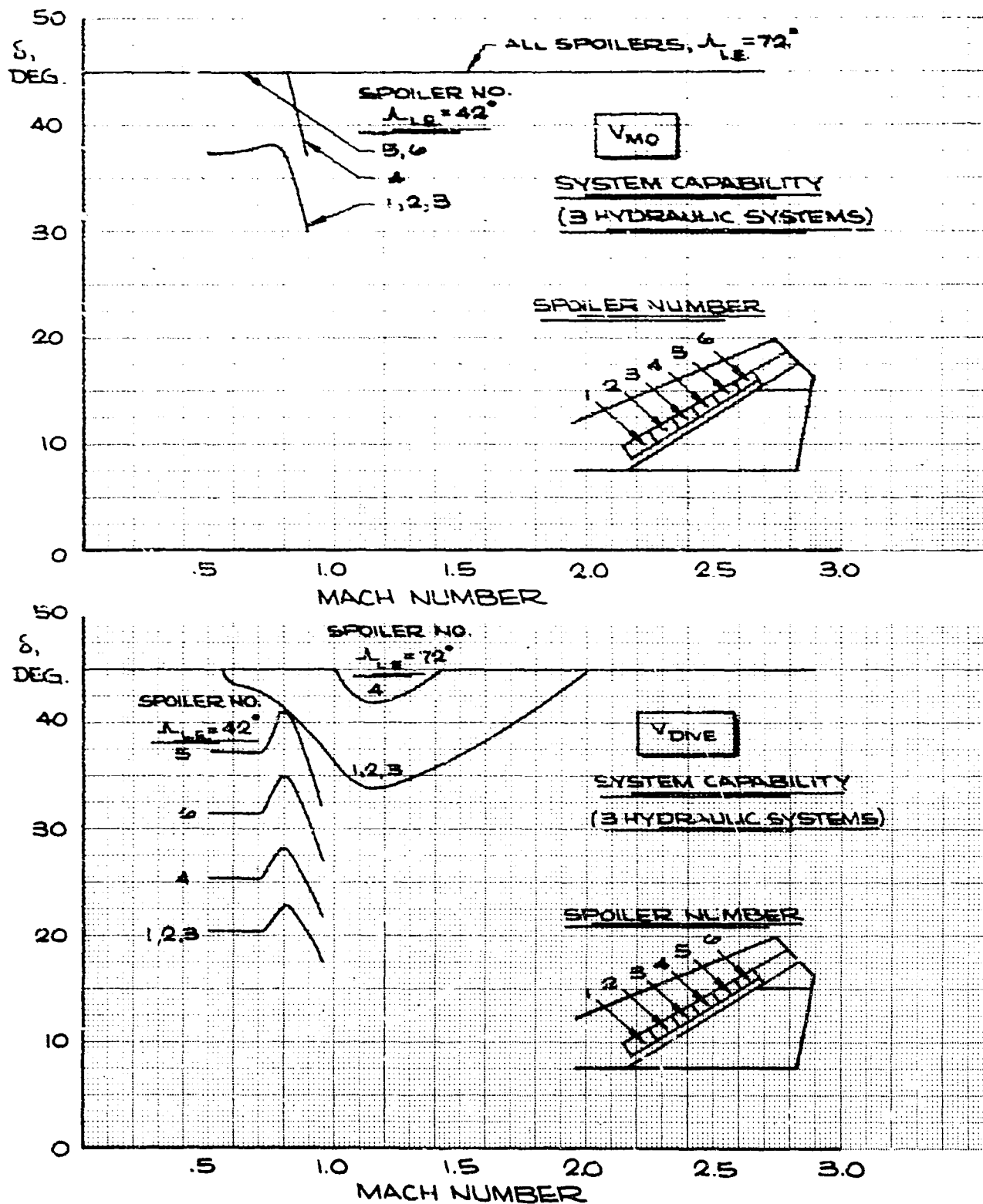


Figure 5-11. Spoiler Deflection Capability (All Systems)

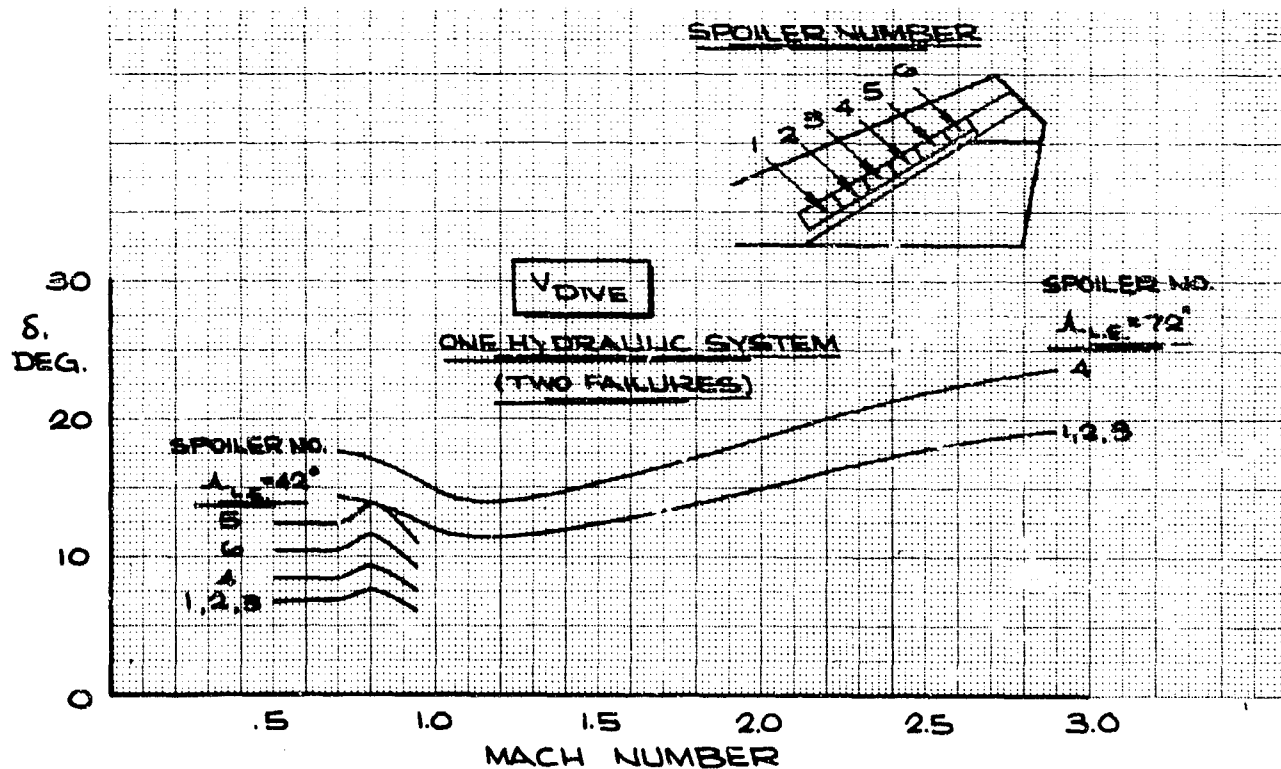
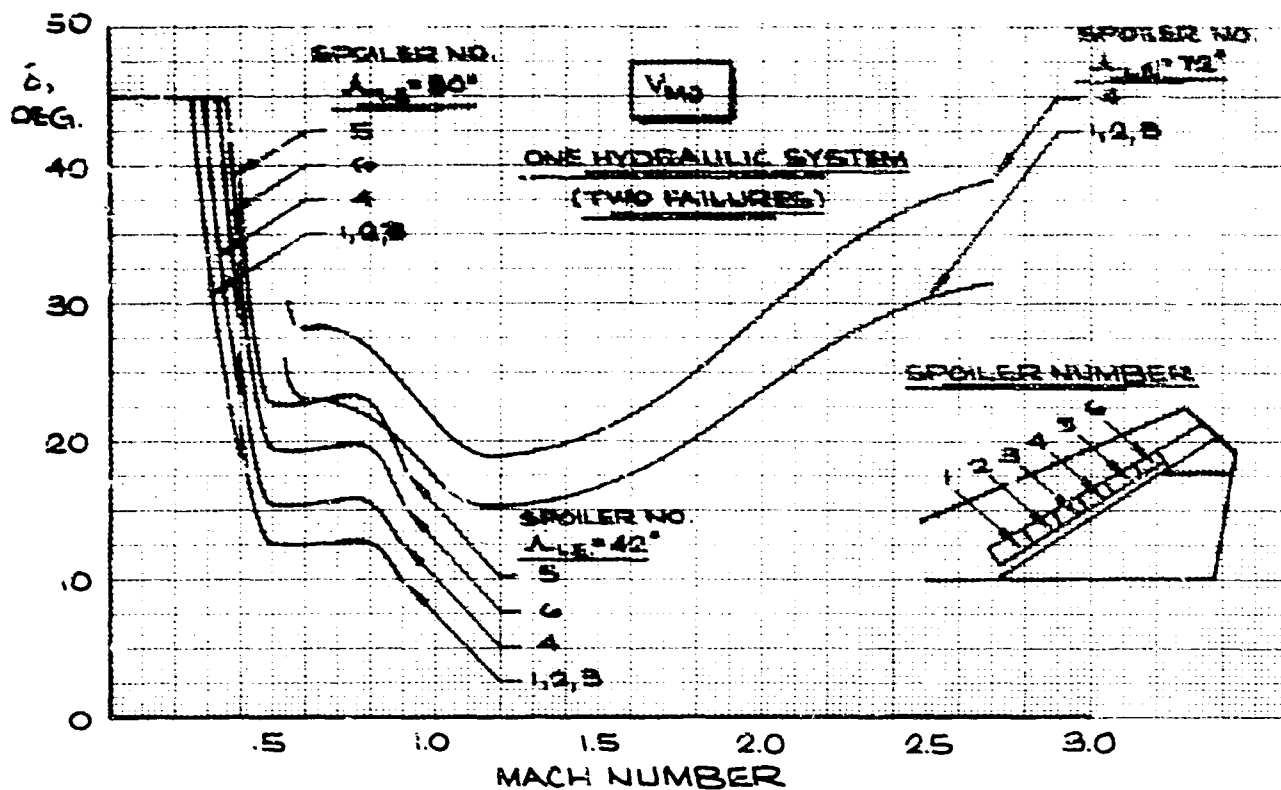


Figure 5-12. Spoiler Deflection Capability (One System)

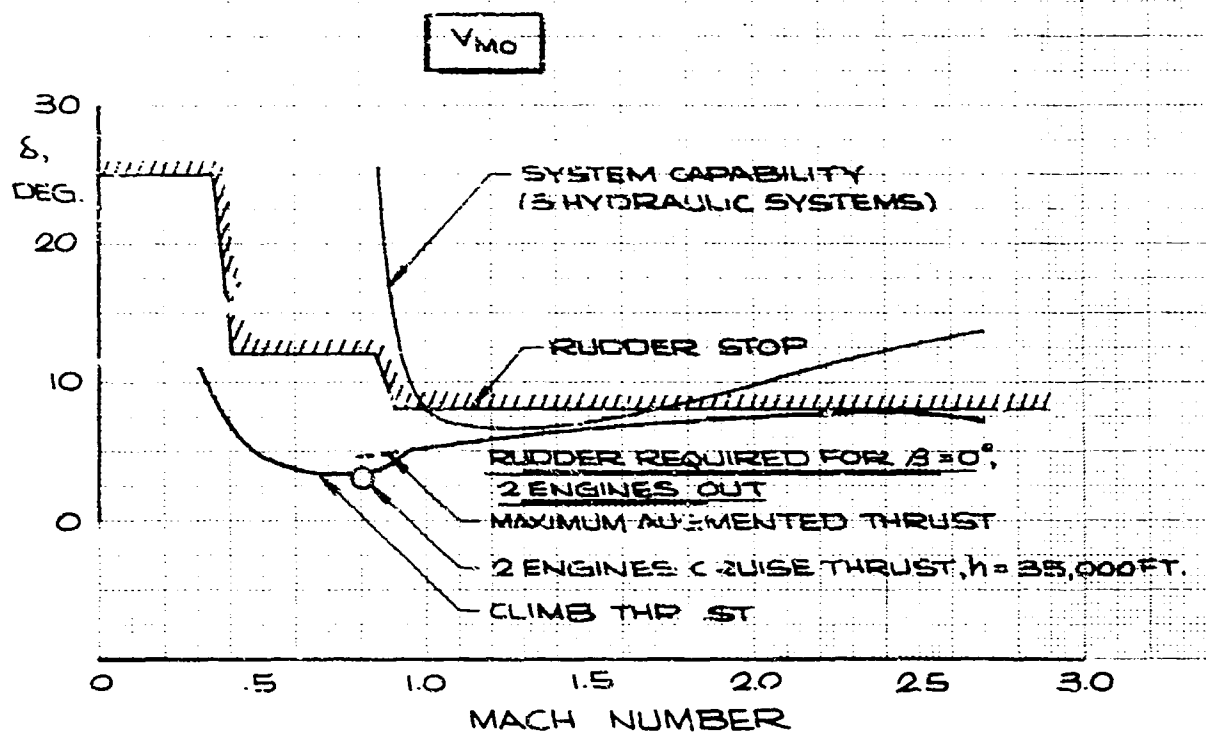


Figure 5-15. Rudder Deflection Capability

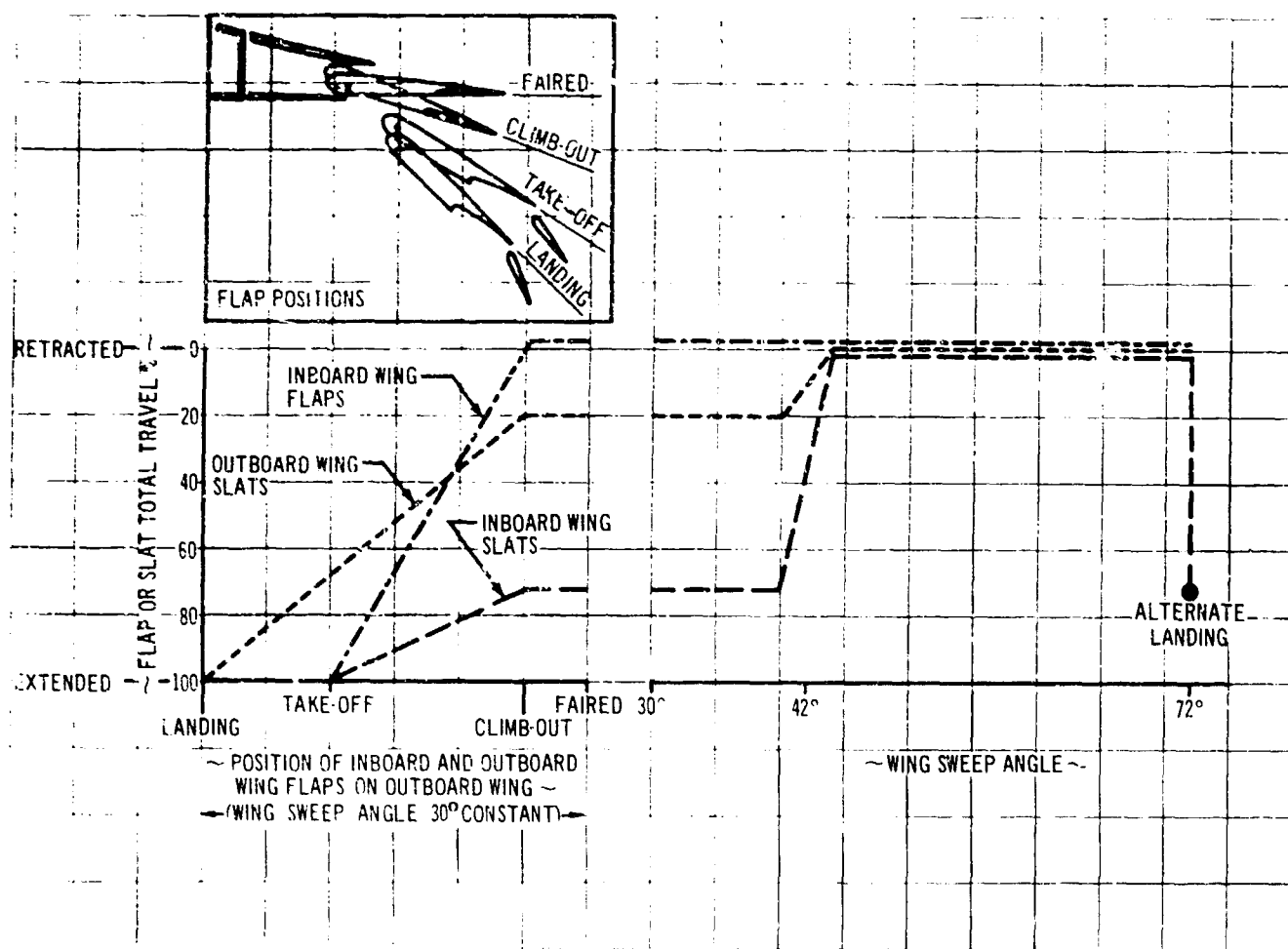


Figure 5-14. Slat and Flap Programming

pitch and roll axes provide series inputs to the elevators and elevons, and the yaw axis provides a series input to the rudder. The SAS pitch axis also provides an automatic trim signal which positions the control column. Triple force summed series actuators are used in each axis to provide fail-operational characteristics. The pitch and the yaw axes have four separate channels of sensors and electronics, and a servo monitor. This provides fail-operational characteristics after both the first and the second failure. The roll axis has three separate channels and is fail-operational after the first failure.

5.3.2 Pitch Axis

5.3.2.1 System Functional Characteristics

Figure 5-15 is a functional block diagram of the pitch axis of the SAS which also shows the relationship with the electric command and trim systems. The pitch axis of the SAS is essentially a pitch rate feedback system with command augmentation. The SAS feedback and electric command combine to give an airplane response to control input which is heavily damped and has minimum variation with flight condition. When the applied control force is reduced to zero, the pitch rate command is zero and the airplane remains at the new attitude. This characteristic is referred to as platform stability.

Pilot command inputs to the SAS are measured at the output position of the pitch master servo and are shaped by the prefilter to give a pitch rate command signal. Body mounted rate gyros measure the airplane pitch rate, resulting in a pitch rate error signal. This signal is then shaped by the compensation filter to give a SAS pitch axis servo position command. This servo provides a series input which is added mechanically to the pitch master servo position. The resulting servo output linkage movement then positions the pitch control surfaces by means of the surface actuators.

The steady pitch rate developed for a given change in pitch master servo position is fixed for all flight conditions. This simplifies the gain scheduling in the electric command system required to give near constant stick force per g characteristics. Scheduling for CG shift and variation in control effectiveness is therefore not required. Electric command system gain scheduling and the

resultant stick force per g characteristics are shown in Fig. 5-16.

Because the augmented airplane has platform stability, the pitch axis of the SAS produces a control deflection to balance moment changes caused by flap deflection or wing sweep. To minimize the SAS servo authority required, automatic trimming is provided within the SAS and therefore a slow drift in attitude occurs if the SAS is providing a balancing moment. Automatic trimming minimizes this drift.

Manual trim commands move the feel center and the pitch master servo is positioned accordingly. This master servo position change is sensed by the SAS pitch axis command augmentation and interpreted as a pitch rate command. Whether the column is controlled by the force sensors or by the trim system the airplane responds in the same manner.

To prevent the automatic trim being interpreted as manual trim command, an electronic counterpart is generated within the SAS computer to balance the change in the master servo position signal. The components of the automatic trim function are a threshold detector, a pulse generator to command the trim stepping motor, and an electronic model of the trim motor and master servo. The same pulses are integrated by the trim stepping motor and the pulse counting circuitry of the electronic model so that the two systems track identically. This integrator is also used for pre-engage synchronization. The basic platform stability mode of the pitch axis of the SAS has characteristics similar to those of a stick steering system. It exhibits neutral speed stability, i.e. changes in speed do not cause pitch attitude changes and do not require the pilot to hold a steady force proportional to the speed change. For many modes of flight, neutral speed stability simplifies the control problem; however, for landing approach and low speed operation, it may be desirable to have positive speed stability. A separate speed stability mode is provided within the pitch SAS which may be selected for these cases. When this mode is engaged, an airspeed error signal with an airspeed rate damping signal is introduced which opposes the command augmentation signals and provides ideal speed stability characteristics.

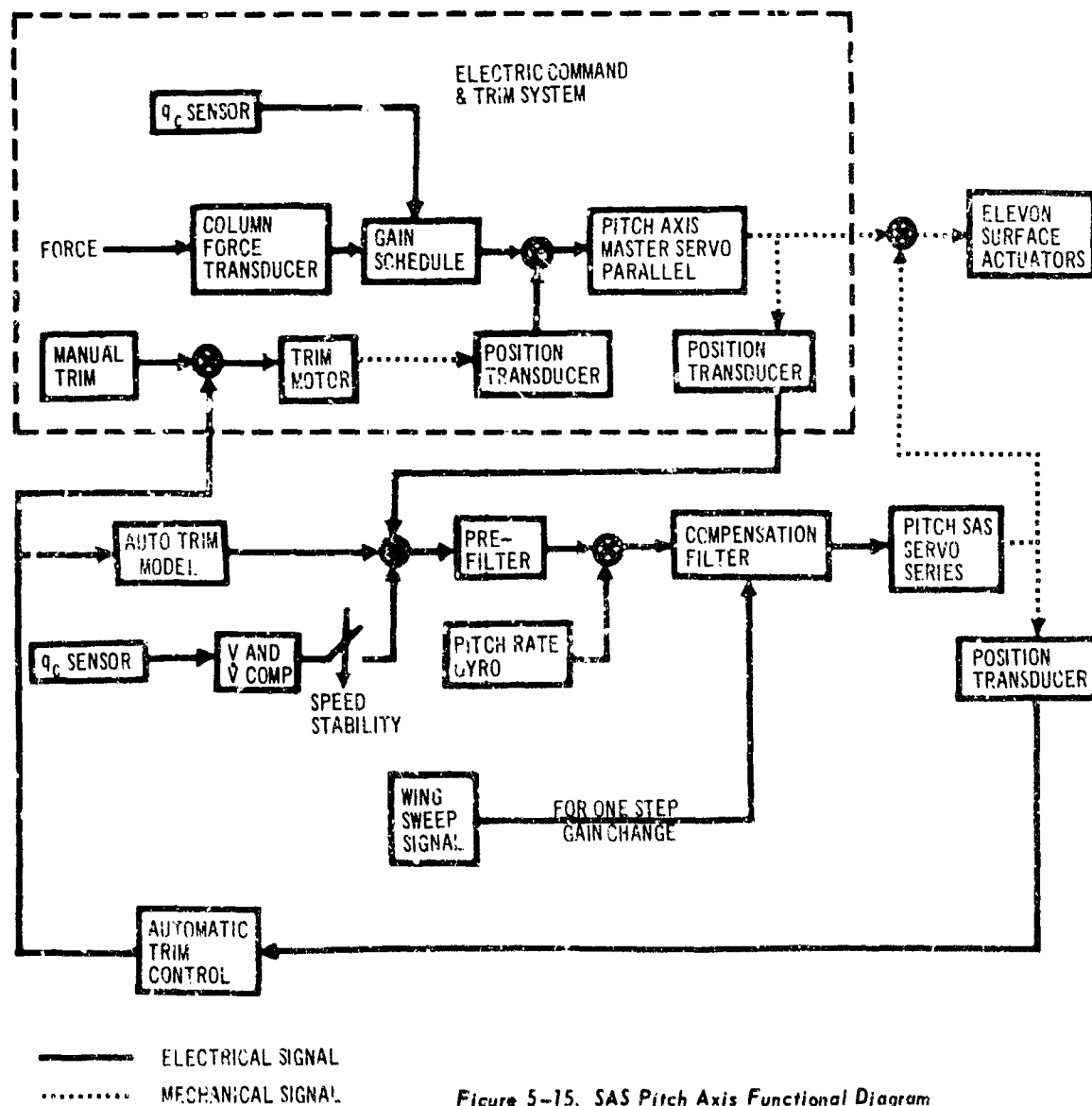


Figure 5-15. SAS Pitch Axis Functional Diagram

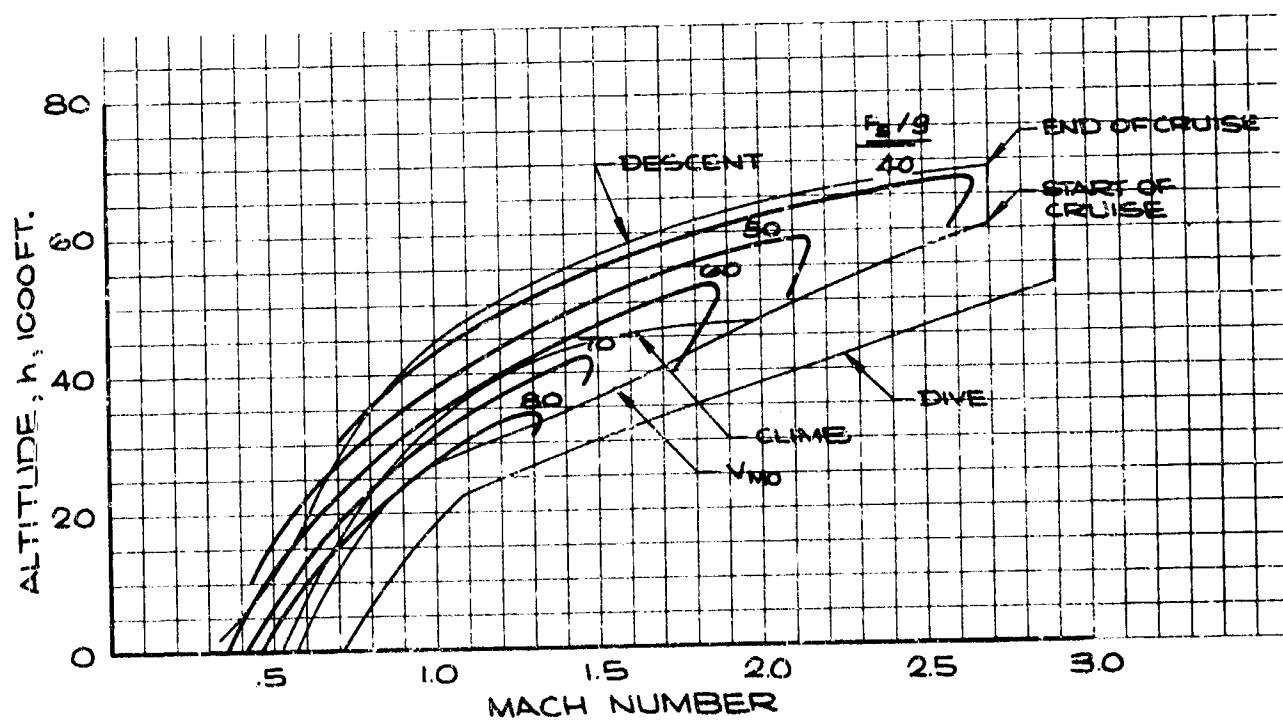
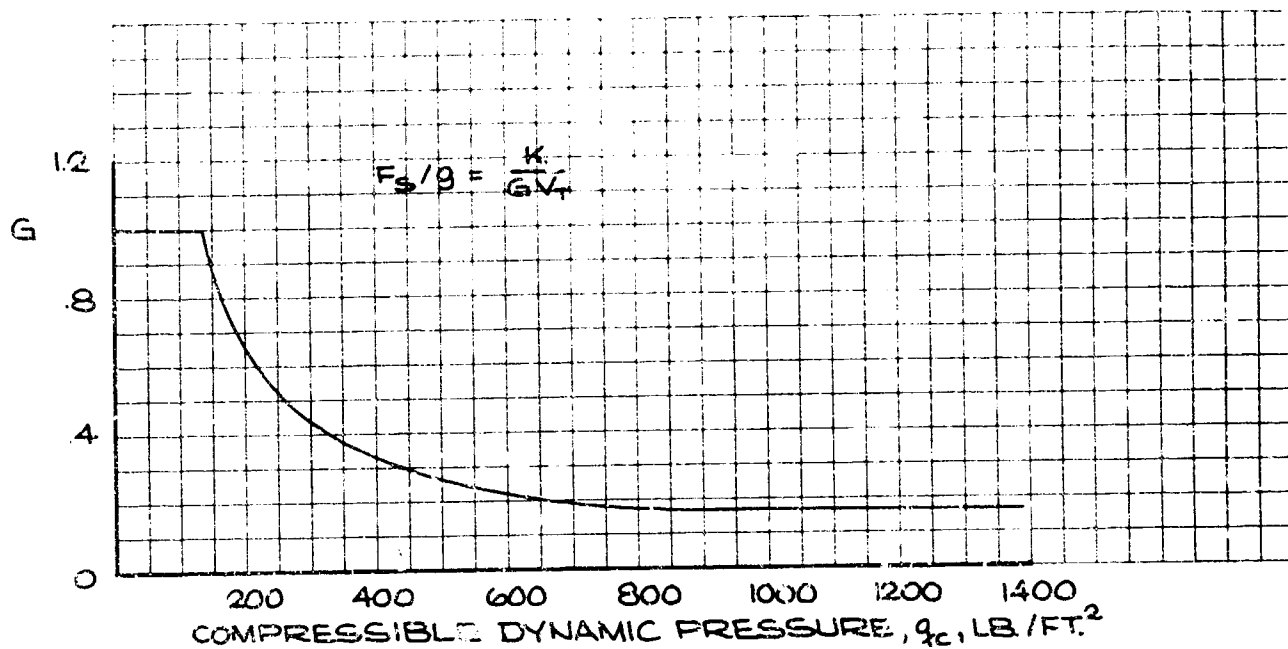


Figure 5-16. Stick Force Per g

The air data required for this mode are computed within the SAS using the same dynamic pressure signals as used for electric command gain scheduling. This part of the system will be fail-operational upon the first failure and fail-passive for the second failure.

Loads alleviation is provided by the SAS pitch axis through damping of the short period. By eliminating the large pitch rate overshoot, which is characteristic of the unaugmented airplane response to a step command, a slow well damped normal acceleration response is obtained at high speed. This reduces the maneuver loads induced by the pilot when he is making small path corrections. Structural loads for design maneuver cases are considered for both SAS on and off (Airframe Design Report, Part C, V2-B2707-7).

Electronic filtering of the SAS feedback loops is relied upon to prevent excitation of the flexible body modes. An initial attempt to provide one compensation filter suitable for all flight conditions resulted in too much gain at high frequencies. With two compensation filters, one for the wings forward flight conditions and another for the wings aft conditions, the desired high-frequency cutoff is attained. This transition is made as a function of wing sweep position.

5.3.2.2 Response to Command and Disturbance
The longitudinal response of the augmented airplane to step command inputs and to step vertical gusts is shown in Figs. 5-17 and 5-18. Unaugmented airplane responses are shown for comparison. These traces show the master servo and series servo position responses as well as the surface deflection. Note that the pitch rate response to step command for the augmented airplane has similar characteristics at all flight conditions. The large pitch rate overshoot of the unaugmented airplane response at high speed is eliminated by the SAS. The longitudinal SAS authority is determined by the requirements of the landing approach flight condition to be ± 15 degrees at 30-degree sweep and is reduced to ± 8 degrees at sweep angles greater than 40 degrees. SAS actuators have a 30 radian per second break frequency and will have rate capability for full-stroke operation at this frequency.

The pitch axis SAS design resulted from the synthesis of a fixed-gain system providing good handling qualities at all flight conditions. The design method was developed by Horowitz. As applied to the Boeing SST, the design causes the

pitch rate due to command input to approach a specified ideal amplitude frequency response for all flight conditions and all frequencies.

The basic assumption is that an ideal pitch rate transfer function is known and may be expressed as a Bode plot. In the actual synthesis, a band or envelope of a specified width in decibels is used as the criterion rather than a single curve. If the amplitude responses for all flight conditions of the augmented airplane lie inside the envelope at all frequencies, the airplane will exhibit satisfactory handling qualities at all flight conditions.

In order to avoid flexible mode coupling, it is necessary to reduce the gain at the higher frequencies. This is achieved by dividing the flight conditions into two groups, one group for the wings forward flight condition and another group for the wings aft conditions. An analysis of the airframe SAS structural coupling, including five flexible modes, has been completed using aerodynamic and structural data from an earlier configuration with satisfactory results. This analysis is presently being repeated with B-2707 aerodynamic and structural characteristics and will be reported in Development Data Document D6A-10339-1.

5.3.3 Roll Axis

5.3.3.1 System Functional Characteristics
Figure 5-19 is a functional block diagram of the roll axis of the SAS. The roll axis of the SAS is a roll rate feedback system with command augmentation. The electric command and SAS work together so that in response to an applied wheel force a steady roll rate is developed. Roll rate feedback and command augmentation are included to produce good roll command response.

No gain change is required in the roll axis command because the control gains are varied by the mechanical programming of elevons, spoilers, and ailerons with wing sweep and flap extension as described in Par. 5.1.3.

5.3.3.2 Response to Command and Disturbance
The lateral-directional responses of the augmented and unaugmented airplane to step wheel inputs are shown in Fig. 5-20. These traces are obtained with the longitudinal SAS operating. Response to an initial value of sideslip is shown in Fig. 5-21.

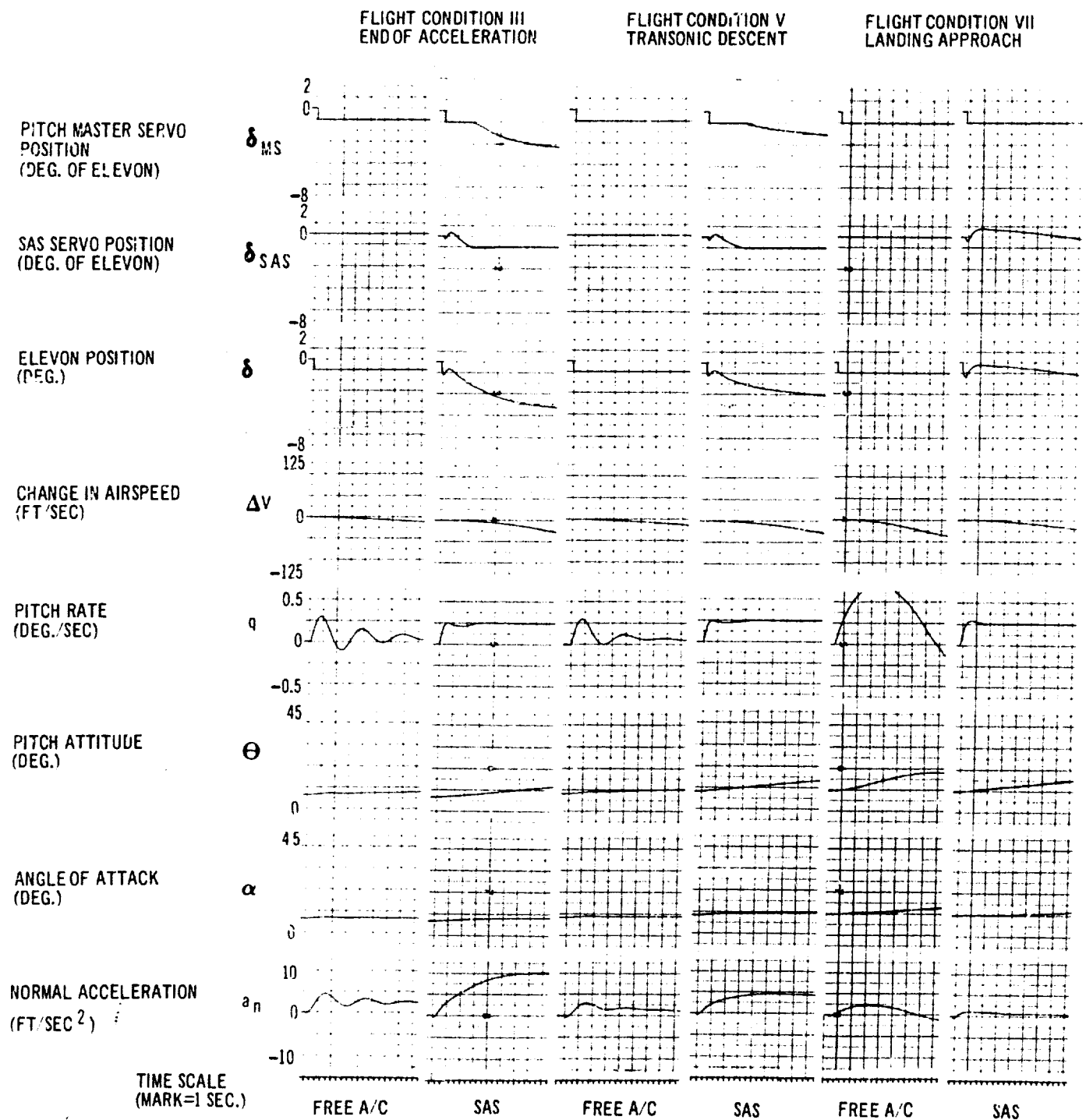


Figure 5-17. Longitudinal Response to Step Command

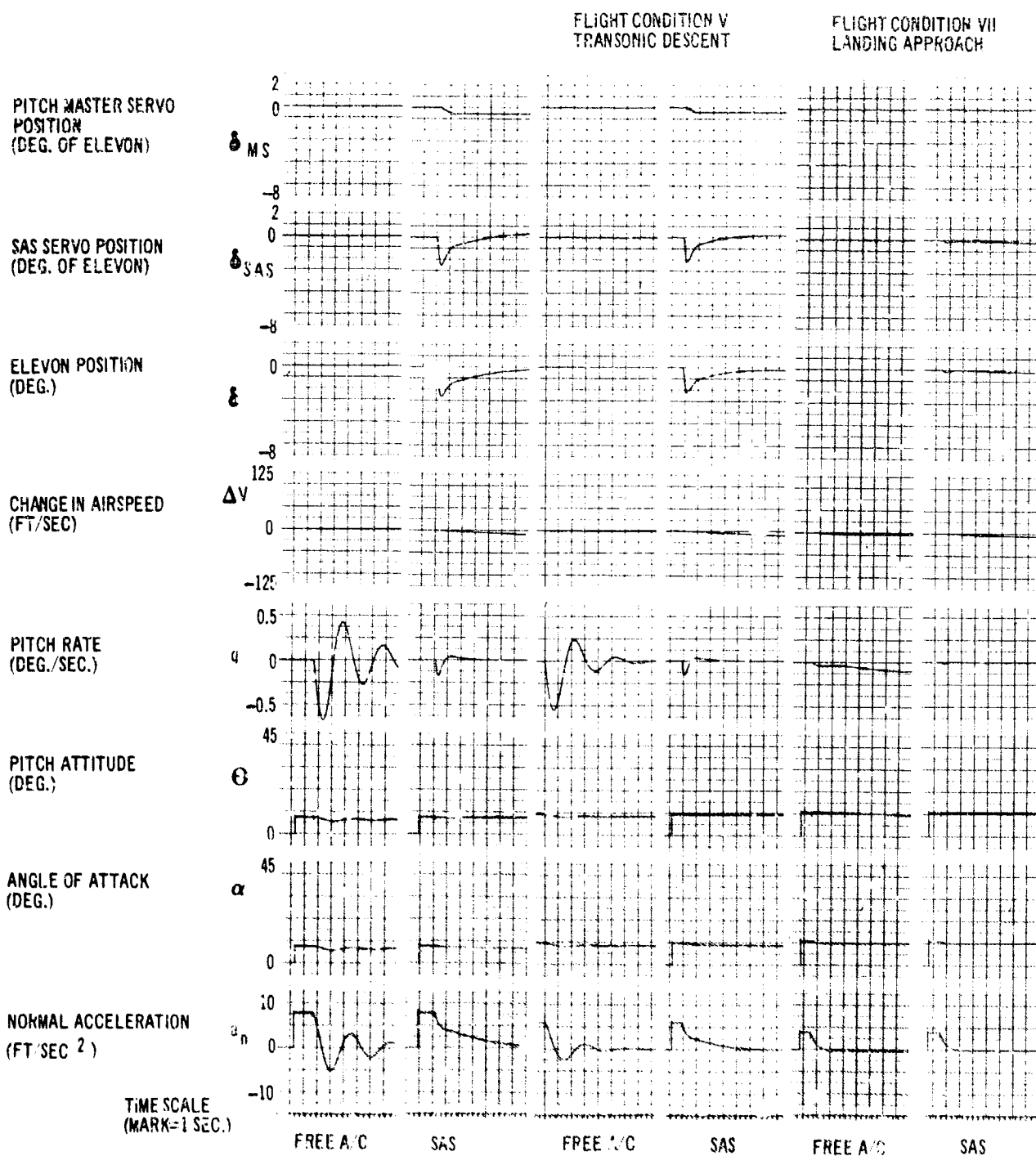


Figure 5-18. Longitudinal Response to Step Gusts

V2-B2707-3

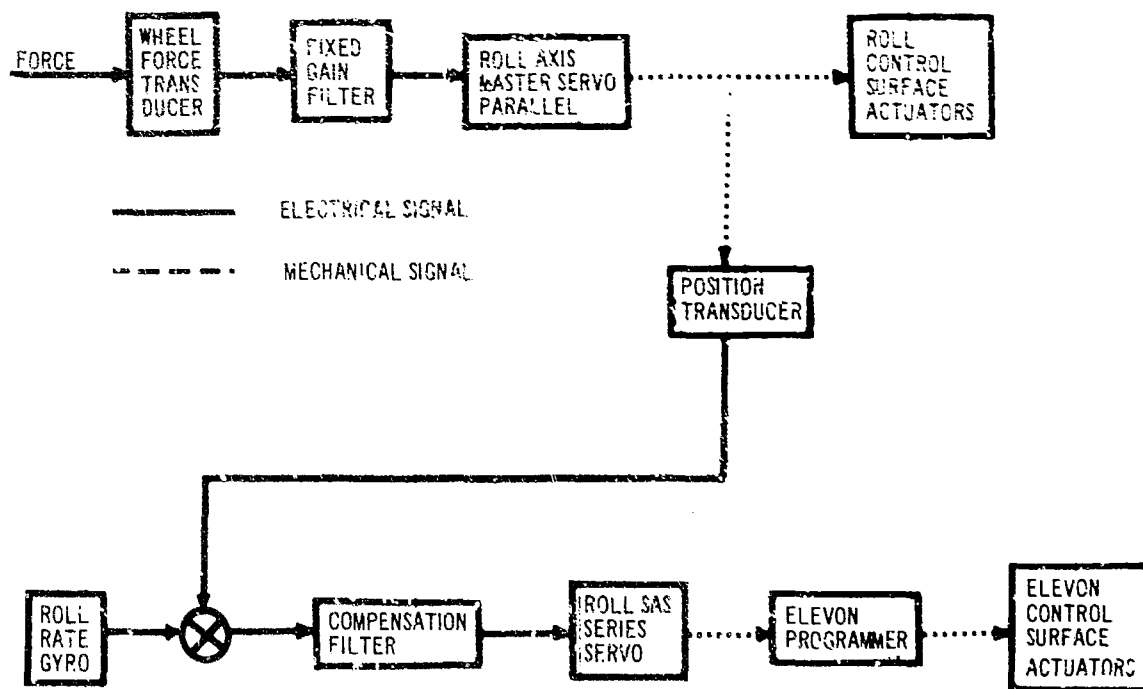


Figure 5-19. SAS Roll Axis Functional Diagram

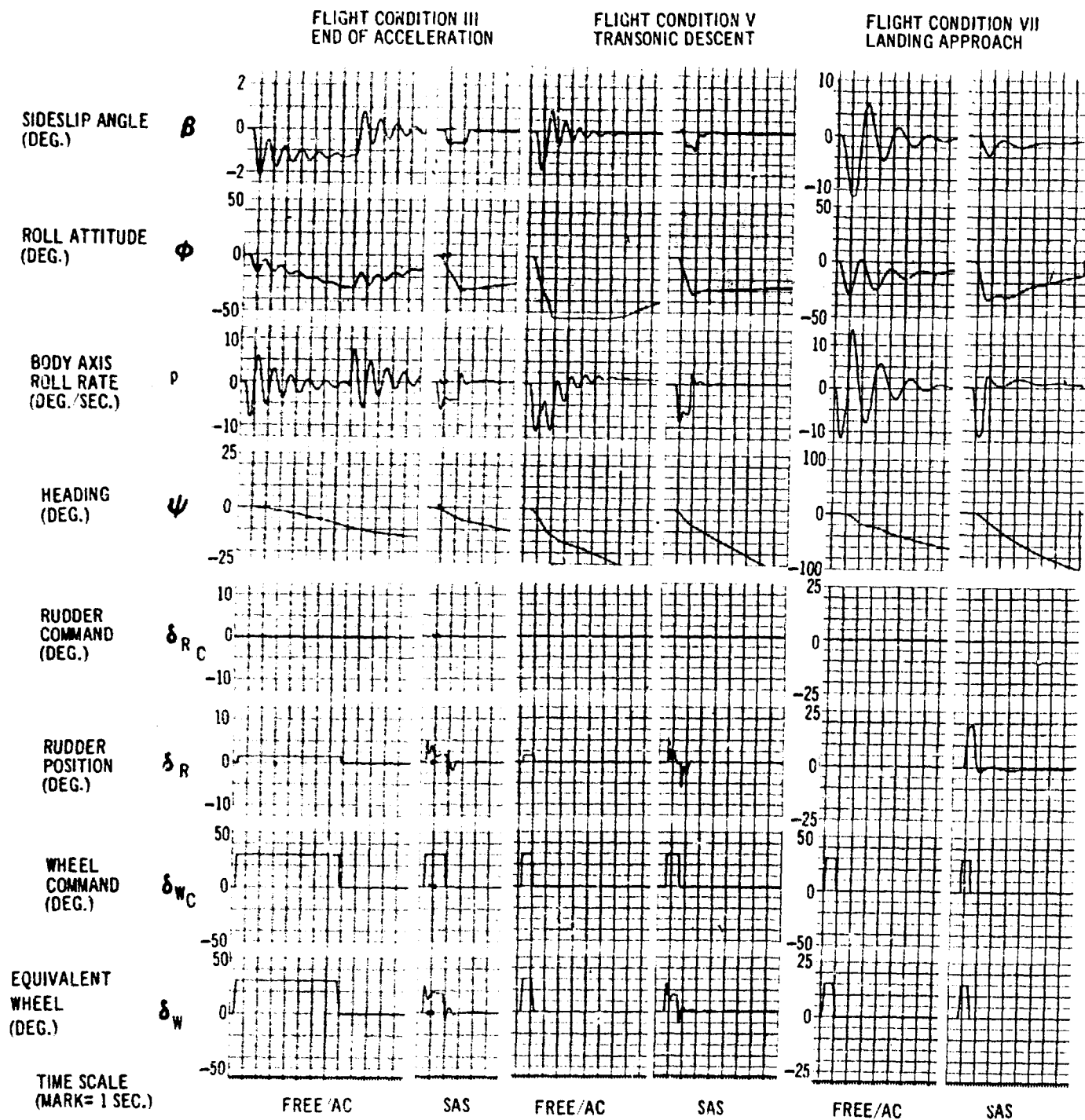


Figure 5-20. Lateral - Directional Response to Step Command

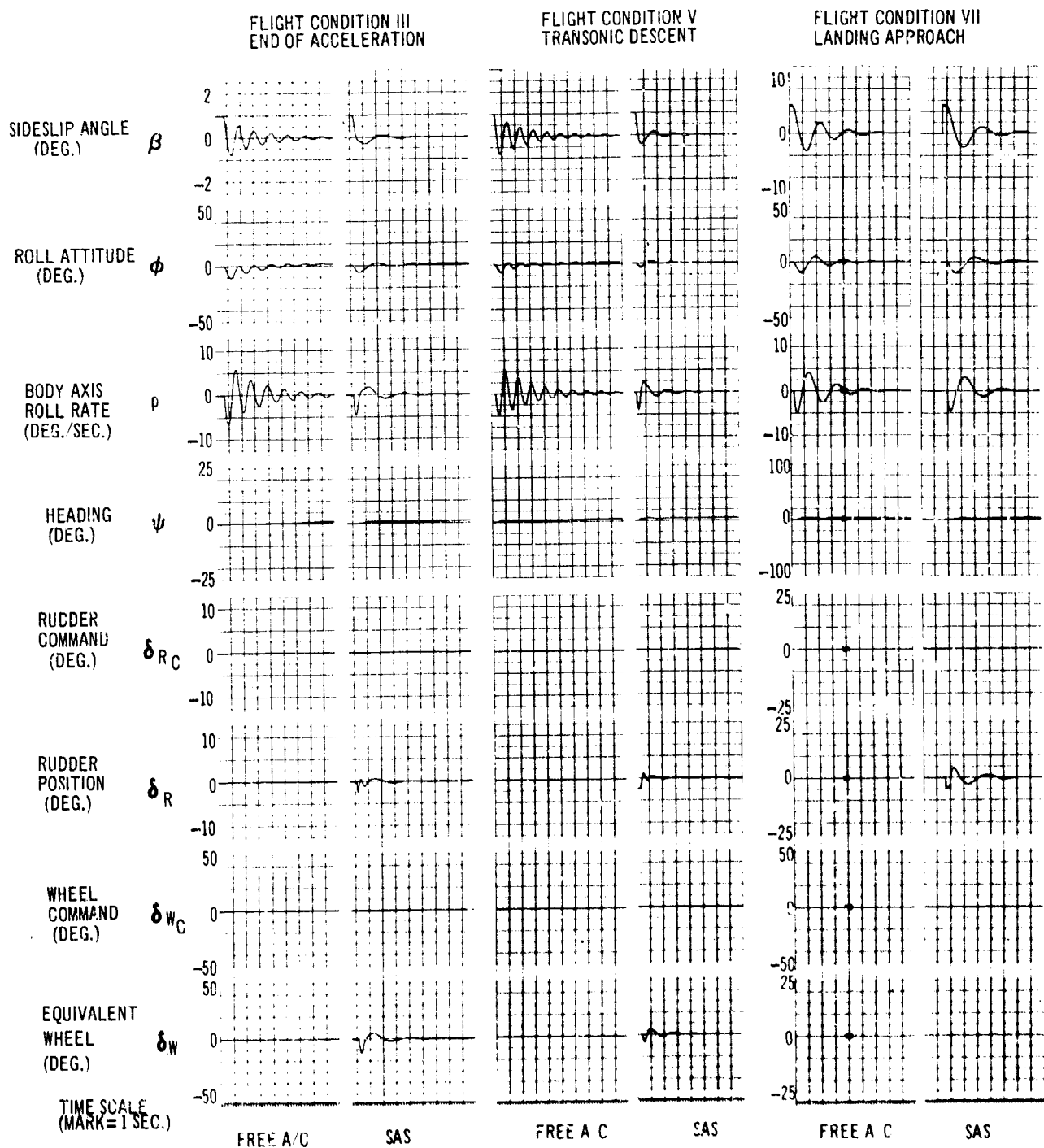


Figure 5-21. Lateral - Directional Response to Step Sideslip

5.3.4 Yaw Axis

5.3.4.1 System Functional Characteristics

Figure 5-22 is a functional block diagram of the yaw axis of the SAS. Suitably filtered roll rate feedback results in good Dutch roll damping and a substantial decrease in roll time constant. This roll rate signal is gain scheduled as a function of compressible dynamic pressure (q_c). A limited signal from a body-mounted lateral accelerometer provides directional static augmentation and reduces sideslip angles in maneuvers. The mechanical gearing between elevons and rudder deflection is augmented in the SAS by a shaped electrical signal. This signal, like the

mechanical interconnection, is gain scheduled by wing sweep.

Improvement in Dutch roll damping by the use of roll rate feedback into rudder is demonstrated by the root locus diagram shown in Fig. 5-23. By filtering roll rate with a washout and lag network, the position of the spiral mode is moved toward the origin (neutral spiral stability) and the roll time constant is reduced.

5.3.4.2 Response to Command

The sideslip angle developed in the response to a pulse wheel command is shown in Fig. 5-24.

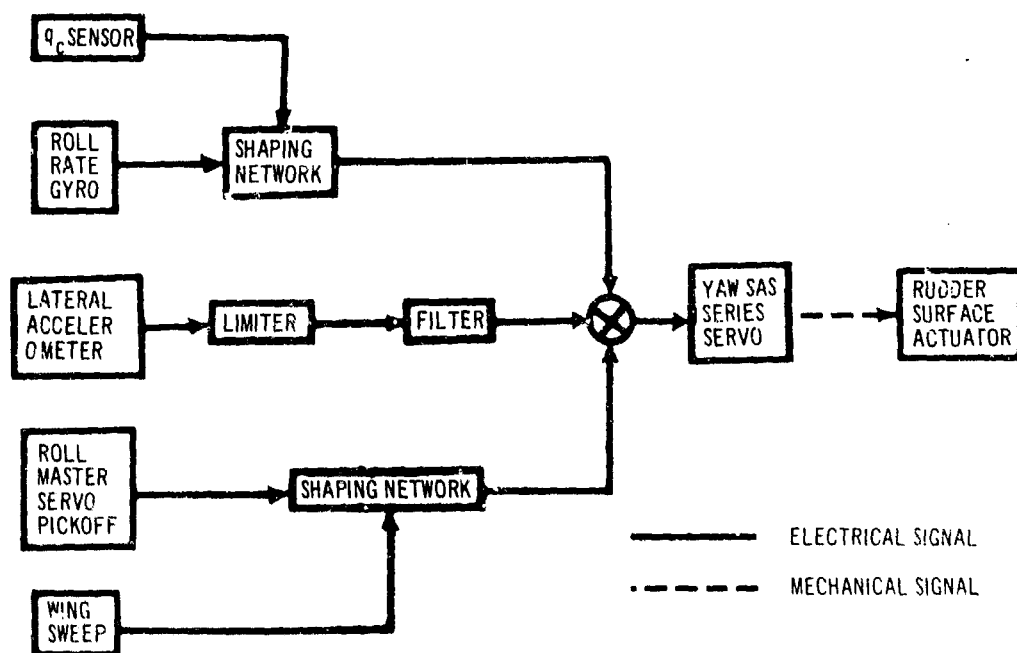


Figure 5-22. SAS Yaw Axis Functional Diagram

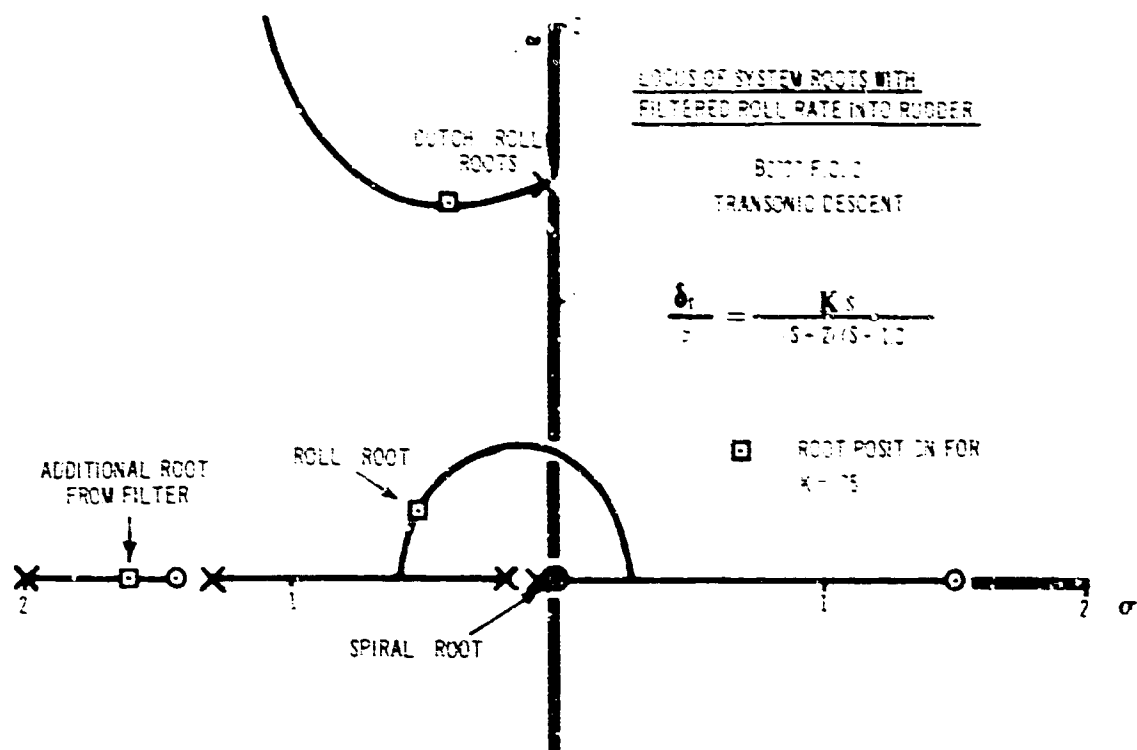


Figure 5-23. Root Locus Roll-Yaw SAS

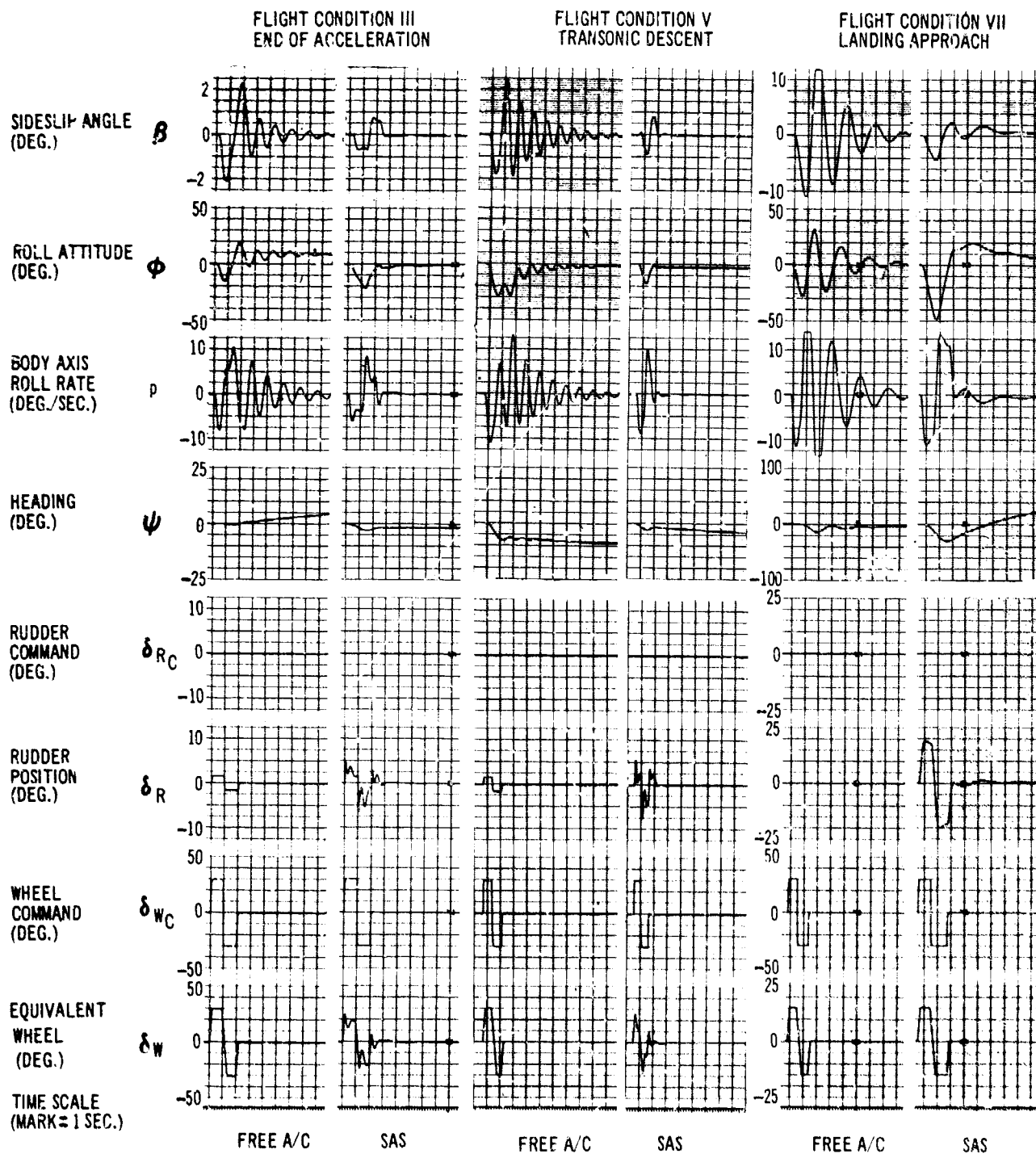


Figure 5-24. Yaw Response in Abrupt Roll Maneuvers

SYMBOLS

Coefficients and Derivatives

C_D	Drag coefficient, drag/qS
C_h	Hinge moment coefficient, H. M. /qS c_c
C_L	Lift coefficient, Lift/qS
C_l	Rolling moment coefficient, rolling moment/qSb
C_m, C_M	Pitching moment coefficient, pitching moment/qSc
C_n	Yawing moment coefficient, yawing moment/qSb
C_Y	Side-force coefficient, side force/qS
C_{h_α}	Hinge moment coefficient due to angle of attack, $\partial C_h / \partial \alpha$
C_{h_δ}	Hinge moment coefficient due to surface deflection, $\partial C_h / \partial \delta$
C_{L_α}	Lift-curve slope, $\partial C_L / \partial \alpha$
C_{L_δ}	Lift coefficient due to surface deflection, $\partial C_L / \partial \delta$
C_{l_β}	Effective dihedral derivative, $\partial C_l / \partial \beta$
C_{l_δ}	Roll control power derivative, $\partial C_l / \partial \delta$
C_{l_p}	Rolling moment coefficient due to rolling velocity, $\partial C_l / \partial (pb/2V)$
C_{l_r}	Rolling moment coefficient due to yawing velocity, $\partial C_l / \partial (rb/2V)$
C_{m_α}	Static longitudinal stability derivative, $\partial C_m / \partial \alpha$
$C_{m_{\dot{\alpha}}}$	Pitching moment coefficient due to angle-of-attack rate $\partial C_m / \partial (\dot{\alpha}c/2V)$
C_{m_δ}	Pitch control power derivative, $\partial C_m / \partial \delta$
C_{m_q}	Pitching moment coefficient due to pitching velocity, $\partial C_m / \partial (qc/2V)$
C_{n_β}	Static directional stability derivative, $\partial C_n / \partial \beta$
C_{n_δ}	Yawing moment coefficient due to surface deflection, $\partial C_n / \partial \delta$
C_{n_p}	Yawing moment coefficient due to rolling velocity, $\partial C_n / \partial (pb/2V)$

C_{n_r}	Yawing moment coefficient due to yawing velocity, $\partial C_n / \partial (rb/2V)$
C_{Y_β}	Side-force derivative, $\partial C_Y / \partial \beta$
C_{Y_δ}	Side-force coefficient due to surface deflection, $\partial C_Y / \partial \delta$
C_{Y_p}	Side-force coefficient due to rolling velocity, $\partial C_Y / \partial (pb/2V)$
C_{Y_r}	Side-force coefficient due to yawing velocity, $\partial C_Y / \partial (rb/2V)$
\dot{h}	Rate of change of altitude
$\dot{\delta}$	Rate of change of surface deflection
$\dot{\theta}$	Pitch rate, $d\theta/dt$
$\ddot{\theta}$	Pitch acceleration, $\frac{d^2\theta}{dt^2}$

General

a	Acceleration
a.c.	Aerodynamic center
AR	Aspect ratio b^2/S
b	Wing span
BSWT	Boeing supersonic wind tunnel
BTWT	Boeing transonic wind tunnel
c	Chord
C_R	Reference chord: root chord at basic 72° sweep wing planform
$C_{1/2}$	Cycles to half amplitude
C.G.; CG;cg	Center of gravity
db	Decibels
F_s	Stick force, pounds
f_n	Undamped natural frequency
g	Gravitational constant, 32.2 fps^2
G.W.	Gross weight
H.M.	Control surface hinge moment
h	Altitude
I	Moment of inertia, slug-feet ²

K	Control surface effectiveness parameter
K_{BB}	Body aeroelastic factor
LE	Leading edge
L_E/L_R	Aerodynamic surface aeroelastic factor
M	Mach number, moment
M_E/M_R	Aerodynamic surface aeroelastic factor
M_D	Mach number, dive placard
M_{MO}	Mach number, maximum operating
n	Load factor, g's
n_{z_α}	Change in load factor per degree of angle of attack
N. P.	Neutral point
P	Damped period, pressure
PNdb	Perceived noise, decibels
p	Rolling velocity
q	Dynamic pressure, pitching velocity
q_c	Compressible dynamic pressure
r	Yawing velocity, rotation
R_E/R_R	Aerodynamic surface aeroelastic factor
S	Area
s	Laplace operator
SAS	Stability augmentation system
SST	Supersonic transport
TE	Trailing edge
UWAL	University of Washington Aeronautical Laboratory
V	Velocity
V_{APP}	Velocity during landing approach
V_D	Velocity at dive placard
V_e	Equivalent airspeed
V_{LOF}	Liftoff speed
V_{LNDG}	Velocity at touchdown
V_{MC}	Minimum control velocity
V_{MCG}	Minimum control speed with critical engine failed, on ground

V_{MO}	Maximum operating velocity
V_{MU}	Minimum approach velocity
V_P	Path velocity
V_R	Velocity at start of rotation
V_S	Velocity at stall
\bar{V}_H	Horizontal tail volume coefficient, $\frac{l_H S_H}{b S_W}$
\bar{V}_V	Vertical tail volume coefficient, $\frac{l_V S_V}{b S_W}$
\bar{V}_u	Ventral volume coefficient, $\frac{l_{VEN} S_{VEN}}{b S_W}$
V_2	Takeoff speed at 35 feet height above runway, with critical engine failed
V_{35}	Takeoff speed at 35 feet height, all engines operating
α	Angle of attack of horizontal reference line
β	Sideslip angle
Δ	Increment
δ	Surface deflection
ζ	Damping ratio
θ	Angle between the horizontal reference line and the horizon, panel slope
$\Lambda_{LE}; \wedge$	Leading edge sweep angle
λ	Taper ratio, c_t/c_r
ρ	Air density
σ	Density ratio, ρ_h/ρ_o
τ	Time constant
ϕ	Roll angle
ψ	Yaw angle
ω_ϕ	Undamped natural frequency derived from the numerator of the bank angle to aileron transfer function
ω_d	Dutch roll undamped natural frequency

Subscripts

a	Aileron
aux.	Auxiliary
B	Body
c	Control column; control surface
d	Dutch roll
E	Elastic
f	Flap
H	Horizontal stabilizer
ILS	Instrument landing system
MAX	Maximum
O	Reference; free stream; at zero lift
P	Phugoid
r	Rudder, root
R	Rigid, reference
S	Stall
s	Spoiler
ss	Steady state
S. P.	Short period
t	Tip
T	Tail
trim	Trim condition
V	Vertical
VEN	Ventral
w	Wing; wheel
XX, YY, ZZ, XZ	Moment of inertia axis designation
z	
	Along z -axis

Other nomenclature is defined in text.

REFERENCES

1. FAA Letter to Mr. M. L. Pennell from Mr. Gordon Bain, "Sonic Boom Calculation Methods to be Used for Phase II-A Evaluation", September 8, 1964
2. Boeing Document, D6A10368-1, Aerodynamic Smoothness and Alignment Requirements, Vents, and Protuberances, 1966
3. Commercial Supersonic Transport Program, Phase II-A Comprehensive Report, The Boeing Company, Volume V-A, Book 1, Aerodynamics
4. Jay Fox, "Surface Pressure and Turbulent Airflow in Transverse Rectangular Notches", NASA TN D-2501, November 1964
5. R. L. Roensch, Investigation of Skin Friction Drag on Practical Construction Surfaces for Supersonic Transport, Douglas Aircraft Company, FDL-TDR 64-74, August 1964
6. John B. Peterson Jr. and Albert L. Braslow, "Implications of the Effects of Surface Temperature and Imperfections on Supersonic Operations", NASA SP-83, May 1965, pp. 227-233
7. K. R. Czarnecki, "The Problem of Roughness Drag at Supersonic Speeds", NASA SP-124, May 1966, pp. 455-468
8. A. R. Vick, An Investigation to Determine the Discharge and Thrust Characteristics of Auxiliary-Air Outlets for Stream Mach Number of 3.25, NASA TN D-1478, October 1962
9. P. E. Dewey and A. R. Vick, An Investigation of the Discharge and Drag Characteristics of Auxiliary-Air Outlets Discharging into a Transonic Stream, NACA TN 3466, July 1955
10. D. C. Anderson, Efficiency of Flush and Protruding Oblique Exhaust Nozzles with and without External Flow, United Aircraft Corp., Report R-0955-22, October 1957
11. J. E. Broadwell, "Analysis of the Fluid Mechanics of Secondary Injection for Thrust Vector Control", AIAA Journal, Vol. 1, No. 5, May 1963
12. J. E. Broadwell, "Correlation of Rocket Nozzle Gas Injection Data", AIAA Journal, Vol. 1, No. 8, August 1963
13. J. J. Janos, Loads Induced on a Flat Plate Wing by an Air Jet Exhausting Perpendicularly Through the Wing and Normal to a Free Stream Flow, NASA TN D-649, March 1961
14. W. E. Stoney, Collection of Zero-Lift Drag Data on Bodies of Revolution from Free Flight Investigations, NACA TN 42-1, January 1958
15. Nash, Quincey, and Callinan, Experiments on Two-Dimensional Base Flow at Subsonic and Transonic Speeds, ARC 25 070, January 1963
16. F. A. Woodward, A Method of Optimizing Camber Surfaces for Wing-Body Combinations at Supersonic Speeds - Theory and Applications, D6-10741, The Boeing Company, prepared under NASA Contract NASA-2282, October 1965
17. S. Lampert, Some Applications of Conical Flow Methods to Subsonic Lifting Surface Problems, NACA TN 2262, 1950
18. H. Carlson and W. Middleton, A Numerical Method of Estimating and Optimizing the Supersonic Aerodynamic Characteristics of Wings of Arbitrary Planform, AIAA Preprint No. 64-590, August 1964

19. A. L. Courtney, "A Collection of Data on Lift-Dependent Drag of Uncambered Slender Wings at Supersonic Speeds", Aeronautical Research Council Current Paper, C. P. 757, 1964
20. W. P. Henderson, "Studies of Various Factors Affecting Drag Due to Lift at Subsonic Speeds", NASA SP-124, May 1966, pp. 327-339
21. G. B. Whitham, "The Flow Pattern of a Supersonic Projectile", Communications on Pure and Applied Mathematics, Vol. V, pp. 301 to 348, 1952
22. Royal Aeronautical Society Data Sheets, Vol. IV
23. Tentative Airworthiness Standards for Supersonic Transports, Federal Aviation Agency, Flight Standards Service, November 1, 1965
24. Roy V. Harris Jr., "A Numerical Technique for Analysis of Wave Drag at Lifting Conditions", NASA SP-124, May 1966, pp. 399-409
25. John B. Peterson Jr. and William J. Monta, "Considerations Regarding the Evaluation and Reduction of Supersonic Skin Friction", NASA SP-124, May 1966, pp. 437-455
26. Report No. NADC-ED-6282, Proposal for Revised Military Specification, "Flying Qualities of Piloted Airplanes" (MIL-F-8785ASG), with Substantiating Test, Bureau of Naval Weapons
27. "Design Objectives for Flying Qualities of Civil Transport Aircraft," ARP 842, Society of Automotive Engineers
28. USAF Stability and Control Handbook (DATCOM)
29. USAF Stability and Control Handbook (M-03671)
30. B. Etkin, Dynamics of Flight, John Wiley and Sons, 1959
31. Bruce R. Wright and Benjamin J. Averett, Transonic Aerodynamic Damping and Oscillatory Stability in Yaw and Pitch for a Model of a Variable Sweep Supersonic Transport Airplane, NASA TM X-1207, March 1966
32. C. J. W. Meles and K. B. Bridgman, "Measurements of the Direct Pitching Oscillation Derivatives for Three Cropped Delta and Three Arrowhead Planforms at Subsonic and Transonic Speeds," British R & M No. 3397, 1965
33. R. Middleton, R. R. Larson, and J. Waddell, Crosswind Landings, The Boeing Company, D6-11455
34. Lawrence D. Guy, and Hoyt V. Brown, "Effects of an Inset Tab on the Hinge-Moment and Effectiveness Characteristics of an Unswept Trailing-Edge Control on a 60° Delta Wing at Mach Numbers from 0.75 to 1.96," NACA RM L54K16a, February 1955
35. Douglas R. Lord and E. R. Czarnecki, "Hinge-Moment Characteristics for a Series of Controls and Balancing Devices on a 60° Delta Wing at Mach Numbers of 1.61 and 2.01," NACA RM L57B01, April 1957
36. William C. Martz, James D. Church, and John W. Goslee, "Rocket-Model Investigation to Determine the Force and Hinge-Moment Characteristics of a Half-Delta Tip Control on a 56° Sweptback Delta Wing Between Mach Numbers of 0.55 and 1.43," NACA RM L52H06, January 1952
37. David G. Stone, "Recent Data on Controls," NACA RM L52A10, January 1952

APPENDIX A

CONFIGURATION DESCRIPTION

The geometric and basic weight data required to determine aerodynamic characteristics of the configuration are presented in this Appendix.

Geometric Data

General Arrangement Drawing	Fig. A-1	285
Wing Planform	Fig. A-2	287
High Lift Devices	Fig. A-3	289
M 1.0 Area Plot, GE	Fig. A-4	291
M 1.0 Area Plot, P&WA	Fig. A-5	292
Wing Section Definition at Various Leading Edge Sweep Angles	Fig. A-6	293
Wing Geometry	Table A-A	294
Airfoil Ordinates, Leading Edge Sweep, 72 Degrees	Table A-B	295
Airfoil Ordinates, Leading Edge Sweep, 42 Degrees	Table A-C	297
Airfoil Ordinates, Leading Edge Sweep, 30 Degrees	Table A-D	298
High Lift Devices	Table A-E	299
Lateral Control Surfaces	Table A-F	301
Horizontal Stabilizer	Table A-G	302
Vertical Tail and Rudder	Table A-H	303

Weight Data

Design Weights	Table A-I	304
Moment of Inertia, Pitch and Yaw	Fig. A-7	305
Moment of Inertia, Roll and Product	Fig. A-8	306

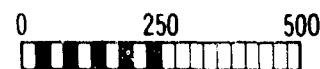
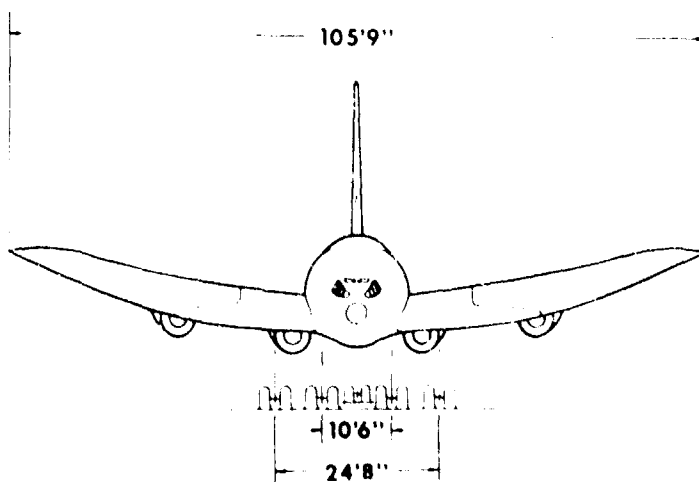
DATA MODEL B-2707

	G.E.	P&WA
POWER PLANTS (4)	G.E. 4/J5P	JTF 17A-21B
TOTAL ENGINE AIRFLOW	2480 LBS/SEC	2748 LBS/SEC
MAX. DESIGN TAXI WEIGHT	675,000 LBS	675,000 LBS
NOMINAL PAYLOAD	50,000 LBS	50,000 LBS
OPERATIONAL EMPTY WEIGHT	287,500 LBS	285,000 LBS
FUEL	374,700 LBS	374,700 LBS

MAIN GEAR 16 - 45 x 19.2 TIRES TYPE VIII
 NOSE GEAR 2 - 34 x 16 TIRES TYPE VIII
 MAX. DESIGN TAXI WEIGHT C.G. - LIMITS, GEAR DOWN
 MOST FORWARD C.G. 59.57 REF. LENGTH - WINGS FWD
 MOST AFT C.G. 64.07 REF. LENGTH - WINGS AFT

9 AIRPLANE

STA. 200



SCALE (INCHES)

A

2WA

7A-21B

5/SEC

00 LBS

00 LBS

00 LBS

00 LBS

AIRPLANE

103' 4"

15' 8"

STA. 1440

158' 1"
REF. LENGTH

STA. 200

294' 9"

MAX. GROSS WEIGHT C.G.

15' 7"

12' 6"

8' 3"

13' 11"

122' 10"

306' 0"

STA. 1189

82' 5"

4' 0"

250

500

SCALE (INCHES)

B

697 REF. LENGTH

607 REF. LENGTH

43'6"

MAC 4

52'9"

15'8"

72

124

048

27'8"

10'0"

93'4"

174'3"

31'3"

30

158'1"
REF. LENGTH

5'10"

647 REF. LENGTH

MAC/4

14'6"

62'7"

STA. 2650

10'10"

23'2"

AX. GROSS WEIGHT C.G.

48'3"

8 1/4

STATIC GROUND LINE

THESE DIMENSIONS ARE MEASURED
IN THE WING DESIGN PLANE

306'0"

14'10"

STA. 2663

G.E. 4 JSP

JTF 17A-21B

Figure A-1. General Arrangement Model B-2707

V2-B2707-3

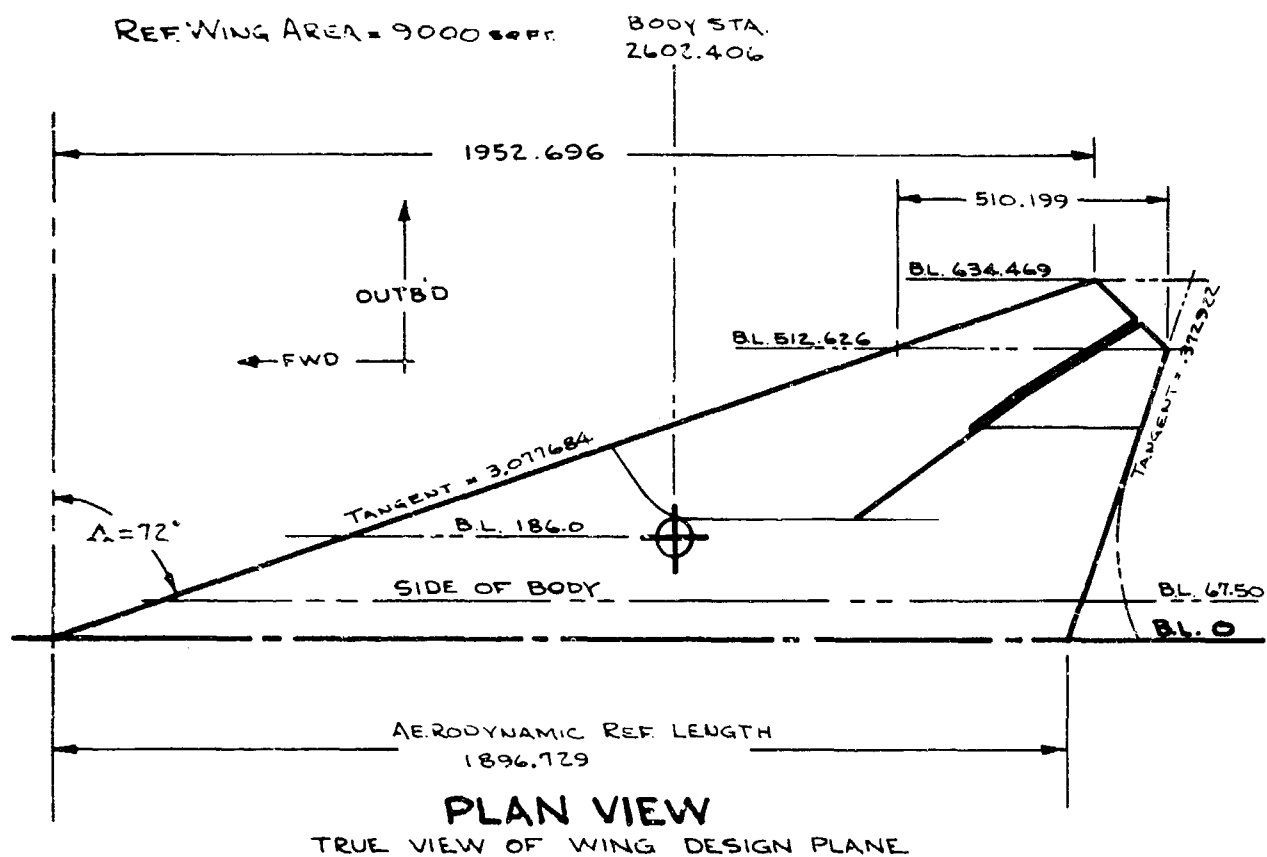
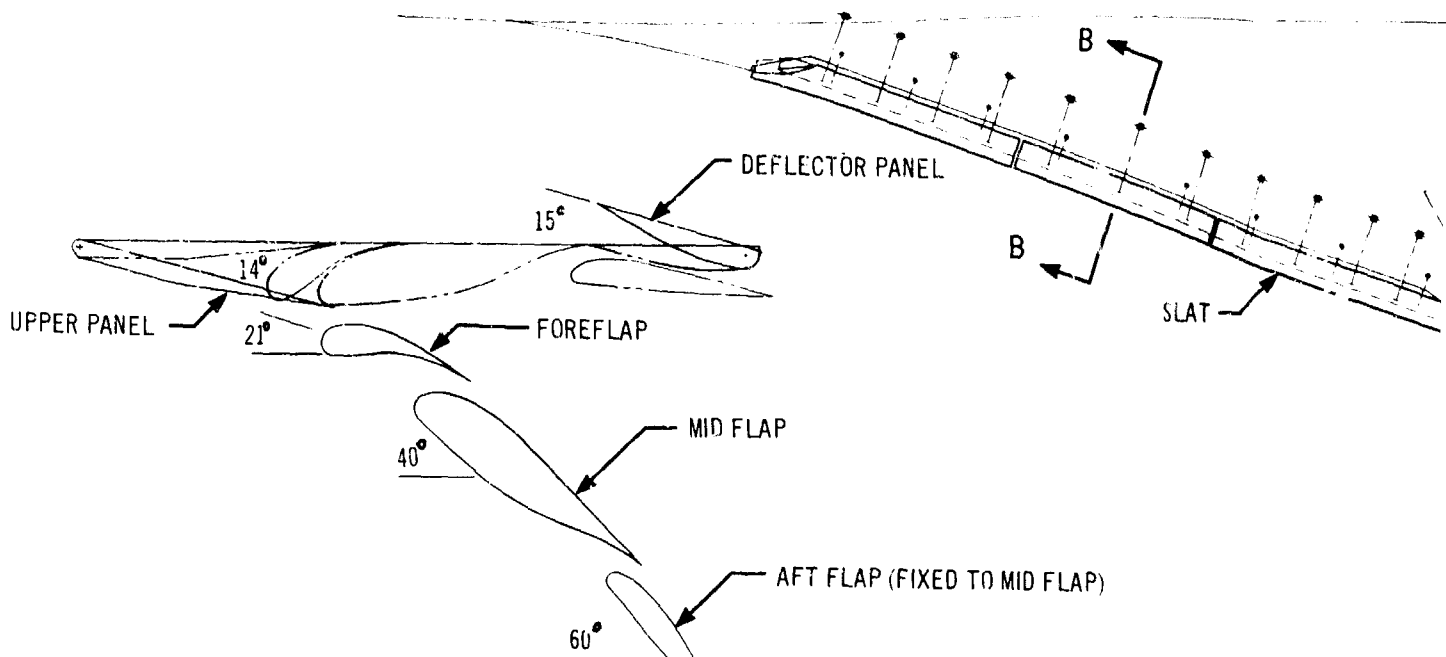
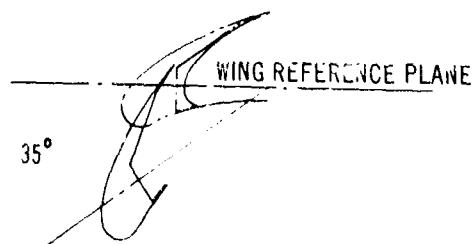


Figure A-2. Wing Planform



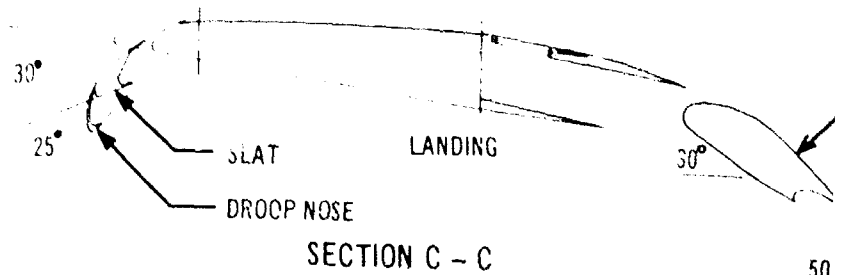
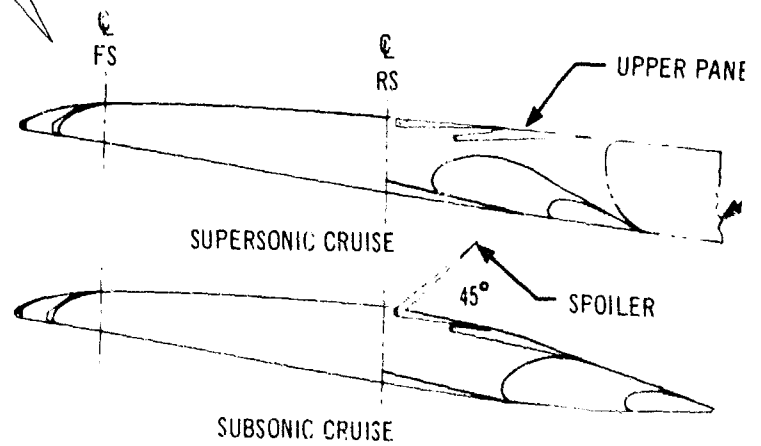
SECTION D - D



SECTION B - B



SECTION A - A



SECTION C - C

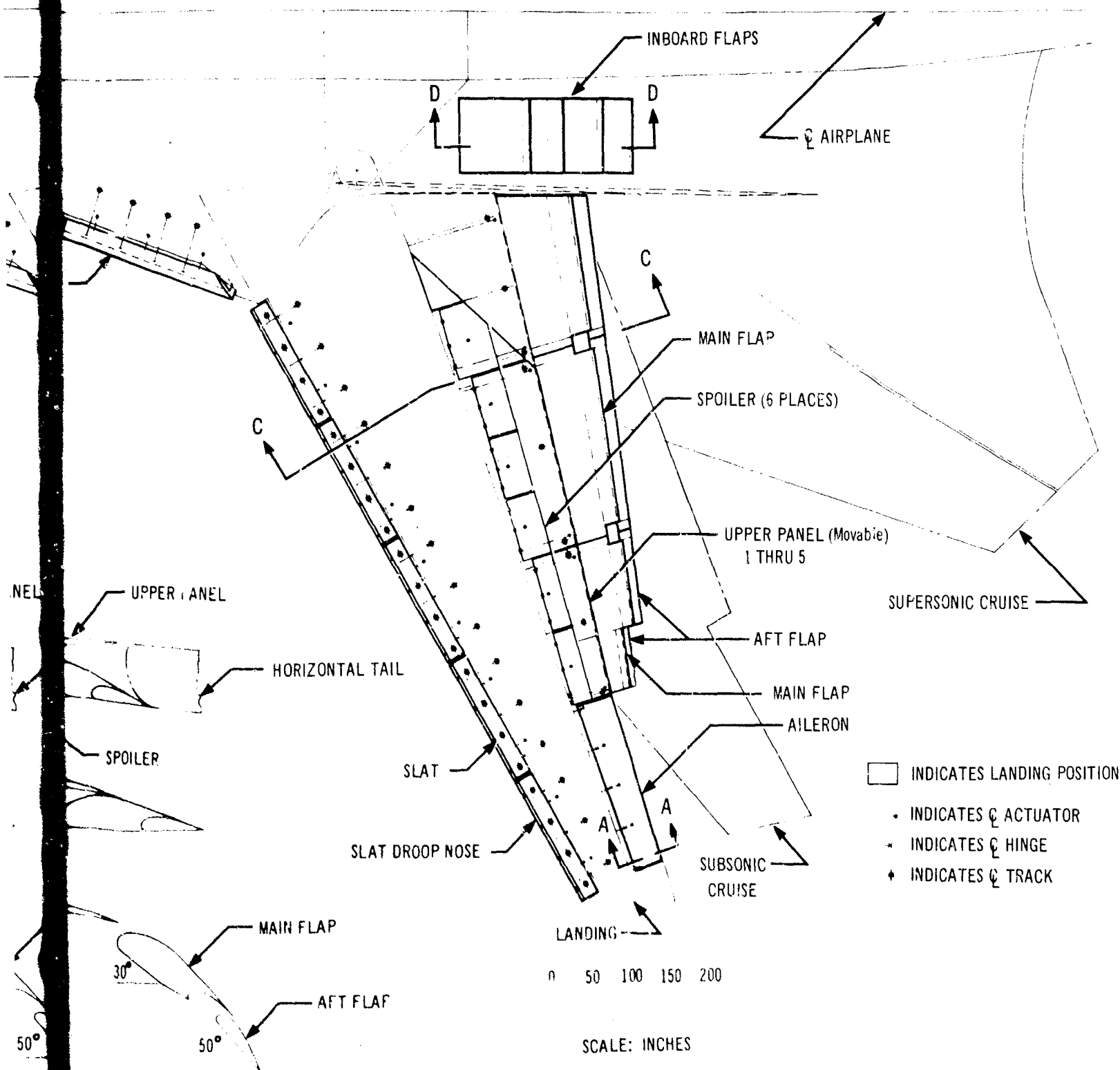


Figure A-3. High Lift Devices

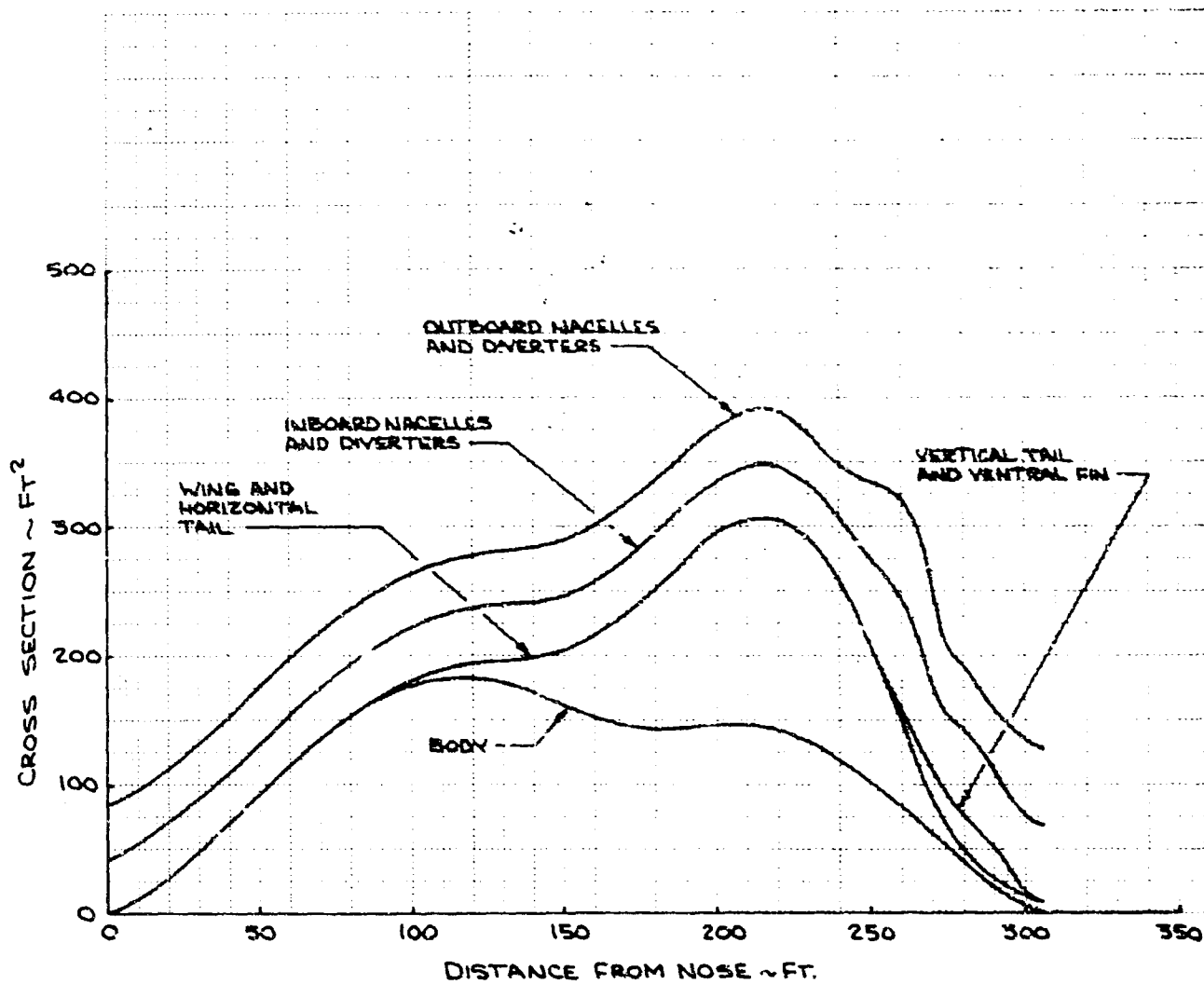


Figure A-4. M 1.0 Area Plot - G E

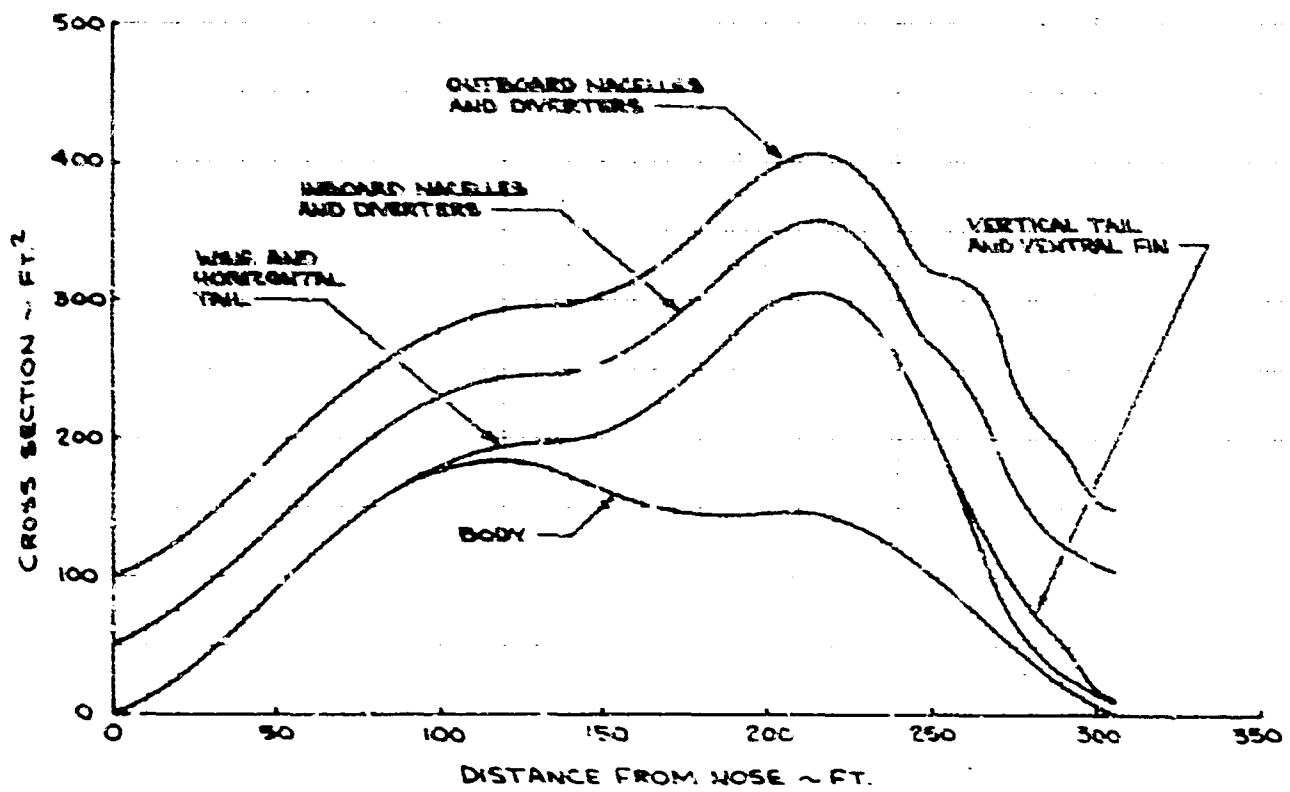
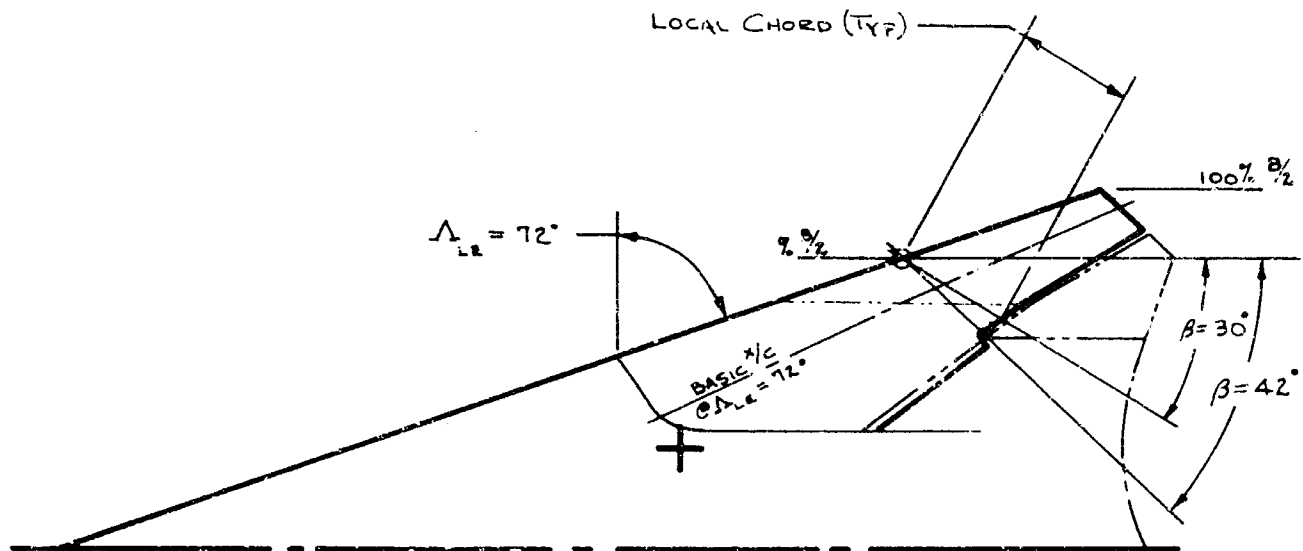


Figure A-5. M.T.O. Area Plot - P3WA

V8-B2707-3



L.E. SWEEP	β
72°	0°
42°	30°
30°	42°

PIVOT AXIS NORMAL TO
WING DESIGN PLANE.

Figure A-6. Wing Section Definition at Various Leading Edge Sweep Angles

Table A-A. Wing Geometry

Reference wing area, ft ²	9000
Aerodynamic reference length, ft (see Fig. A-2)	158.06
Leading edge sweep, degrees	72°00'
Aspect Ratio @ $\Lambda_{LE} = 72^\circ$ degrees	1.24
Sweep @ 0.25 Chord	
Wing aft, degrees	69°58'
Dihedral, degrees	0
Angle of incidence of root chord to fuselage	
Ref. line (wing aft), degrees	-0.718°
Angle of incidence of chord @ 100% semi-span	
to fuselage ref. line (wing aft), degrees	-4.958°
Span, ft	
Wings aft	105.74
Wings fwd	174.28

Table A-B. Airfoil Ordinates - Leading Edge Sweep, 72 Degrees

	10.6388 % B/2 Chord = 1804.8307		18.6460 % B/2 Chord = 1636.8416		29.3159 % B/2 Chord = 1422.9724		47.3680 % B/2 Chord = 1086.4714	
X/C %	Z/C % Upper	Z/C % Lower	Z/C % Upper	Z/C % Lower	Z/C % Upper	Z/C % Lower	Z/C % Upper	Z/C % Lower
0	1.6095	1.6095	1.1514	1.1514	0.4384	0.4384	-0.6233	-0.6233
5	2.3177	0.9657	1.9390	0.6268	1.2752	-0.0094	0.3087	-0.9493
10	2.5265	0.7313	2.1771	0.3711	1.5697	-0.1915	0.7308	-1.0252
15	2.5902	0.4848	2.2073	0.0751	1.6873	-0.4351	0.9775	-1.1375
20	2.4700	0.1374	2.1068	-0.2636	1.6646	-0.7108	1.1109	-1.2673
30	2.0046	-0.5996	1.7482	-0.8922	1.4420	-1.2312	1.1598	-1.5462
40	1.3862	-1.3176	1.2121	-1.5247	1.0479	-1.7379	0.9940	-1.8186
50	0.6494	-2.0322	0.5560	-2.1748	0.5439	-2.2305	0.7594	-2.0386
60	-0.1230	-2.6052	-0.1179	-2.6325	-0.0070	-2.5510	0.4399	-2.1701
70	-0.8632	-2.9686	-0.7618	-2.8512	-0.5656	-2.6444	0.0422	-2.1058
80	-1.5736	-3.0140	-1.4540	-2.8836	-1.1441	-2.5467	-0.3878	-1.8598
90	-2.1824	-2.8950	-2.3887	-3.0973	-1.6577	-2.3605	-0.8295	-1.5635
100	-2.6999	-2.6999	-3.4415	-3.4415	-2.1100	-2.1100	-1.2469	-1.2469

$\beta = 0^\circ$ (See Fig. A-6)

Table A-B. (concluded)

	51.6000 % B/2 Chord = 1012.4744		59.1045 % B/2 Chord = 882.4438		68.4204 % B/2 Chord = 468.3027		88.9317 % B/2 Chord = 294.0694	
X/C %	Z/C % Upper	Z/C % Lower	Z/C % Upper	Z/C % Lower	Z/C % Upper	Z/C % Lower	Z/C % Upper	Z/C % Lower
0	-0.6880	-0.6880	-0.8128	-0.8128	-0.4951	-0.4951	5.5369	5.5369
5	+0.2463	-1.0133	+0.1100	-1.1469	+0.5051	-0.8145	6.6078	5.3820
10	0.6776	-1.0784	0.5763	-1.1759	1.0382	-0.7964	7.2946	5.4594
15	0.9469	-1.1667	0.8952	-1.2161	1.4715	-0.7342	7.7695	5.5626
20	1.0997	-1.2773	1.0892	-1.2815	1.7888	-0.6888	8.1361	5.6565
30	1.1931	-1.5065	1.2665	-1.4237	2.2017	-0.6389	8.7655	5.9228
40	1.0812	-1.7284	1.2729	-1.5232	2.4339	-0.5517	9.2117	6.2239
50	0.0961	-1.8877	1.2210	-1.5549	2.5398	-0.4557	9.4695	6.4726
60	0.6328	-1.9694	1.0737	-1.5022	2.5385	-0.3366	9.8113	6.9355
70	0.2670	-1.8670	0.7849	-1.3109	2.4098	-0.1060	9.9265	7.4101
80	-0.3783	-1.8341	0.3922	-1.0215	2.1603	+0.2436	9.9024	7.9855
90	-1.1055	-1.8317	0.0123	-0.6916	1.7720	0.6940	9.7425	8.6642
100	-1.8173	-1.8173	-0.3559	-0.3559	1.2501	1.2501	9.4692	9.4692

$\beta = 0^\circ$ (See Fig.A-6)

Table A-C. Airfoil Ordinates, Leading Edge Sweep, 42 Degrees

59.2622 % B/2 Local Chord = 417.8800			63.4037 % B/2 Local Chord = 347.1133			90.5270 % B/2 Local Chord = 160.7600			95.3553 % B/2 Local Chord = 137.3333		
Local X/C %	Z/C % Upper	Z/C % Lower	Local X/C %	Z/C % Upper	Z/C % Lower	Local X/C %	Z/C % Upper	Z/C % Lower	Local X/C %	Z/C % Upper	Z/C % Lower
0	-1.7181	-1.7181	0	-0.3715	-0.6715	0	11.2603	11.2603	0	16.8211	16.8211
4.7944	+0.4462	-2.3395	4.5523	+0.9288	-1.4423	5.5352	13.3603	10.5746	5.5353	18.8837	16.0618
9.8777	1.5504	-2.4277	9.6448	1.7246	-1.7641	9.3578	14.1108	10.4319	9.3578	19.6920	16.0185
13.4403	2.0377	-2.5914	13.3893	2.1053	-2.0412	15.3020	14.7317	10.1609	15.3021	20.4814	15.9141
21.0223	2.6470	-3.0886	21.0223	2.8367	-2.4654	19.4127	15.0605	10.0283	19.4126	20.8129	15.7873
29.2815	3.0549	-3.5740	29.2815	3.2841	-2.7900	28.0124	15.4930	9.8356	28.0125	21.2185	15.5620
38.3129	3.0653	-4.2492	38.3129	3.1350	-3.4280	41.9504	15.4389	9.3914	41.9504	21.3139	15.2664
48.2302	2.7281	-5.0861	48.2302	3.0637	-4.3795	52.0153	15.1853	9.1884	52.0151	21.2739	15.2808
59.1703	2.0569	-5.9816	59.1704	2.7974	-5.1972	62.7728	14.5165	9.0803	62.7730	20.8139	15.3849
71.3002	0.5908	-6.4979	71.3002	1.5421	-5.1828	68.4341	14.0463	9.1074	68.4343	20.4575	15.5245
77.8736	-0.4901	-6.3950	77.8736	0.5399	-5.0651	80.3733	12.7347	9.2436	80.3734	19.3377	15.8568
92.1879	-3.5099	-5.9153	92.1879	-2.4747	-4.6099	93.2115	10.9394	9.5784	93.2115	17.5930	16.2405
100.000	-5.4773	-5.4773	100.0000	-4.2629	-4.2629	100.0000	9.8369	9.8369	100.0000	16.4991	16.4991

$\beta = 30^\circ$ (See Fig. A-6)

Table A-D. Airfoil Ordinates, Leading Edge Sweep, 30 Degrees

59.2622 % B/2 Local Chord = 394.2800			68.4037 % B/2 Local Chord = 327.5066			90.6270 % B/2 Local Chord = 146.2800			100.0000 % B/2 Local Chord = 104.7400		
Local X/C %	Z/C % Upper	Z/C % Lower	Local X/C %	Z/C % Upper	Z/C % Lower	Local X/C %	Z/C % Upper	Z/C % Lower	Local X/C %	Z/C % Upper	Z/C % Lower
0	-1.8209	-1.8209	0	-0.7117	-0.7117	0	12.3750	12.3750	0	26.9944	26.9944
4.3794	+0.4680	-2.5093	5.6896	+1.2297	-1.7034	5.2366	14.6153	11.5441	5.2354	29.0113	25.8479
9.0647	1.6587	-2.6202	8.9291	1.7551	-1.9865	10.7357	15.6491	11.2157	10.7348	30.3368	25.9040
15.8454	2.5819	-3.0617	15.9454	2.5341	-2.6345	14.5578	16.0003	10.9324	14.5565	30.9872	25.9292
19.4902	2.8751	-3.3551	19.4902	2.9237	-2.8923	18.5119	16.3137	10.7210	18.5112	31.3044	25.7266
31.6081	3.3980	-4.2632	31.6081	3.5644	-3.6447	31.2406	16.6938	10.1525	31.2396	31.7583	25.2175
40.8420	3.2330	-5.1287	40.8421	3.3662	-4.6155	40.5299	16.4373	9.6286	40.5287	31.7437	24.9355
51.1965	2.7354	-6.2204	51.1965	3.1545	-5.6508	50.5505	15.9753	9.1838	50.5503	31.7486	24.9631
62.8886	1.5519	-7.0751	62.8886	2.2044	-6.3985	61.3930	15.0103	8.8129	61.3926	31.2408	25.0581
69.3200	0.5534	-7.3258	69.3201	1.3364	-6.4399	67.1542	14.3539	8.7044	67.1537	30.8384	25.2018
83.5628	-2.3866	-7.3506	83.5629	-1.4726	-6.3250	79.4320	12.5847	8.5609	79.4320	29.5072	25.5068
91.4766	-4.4537	-7.2823	91.4766	-3.5071	-6.2660	92.8311	10.2446	8.6618	92.8311	27.3473	25.7847
100.0000	-6.8044	-6.8044	100.0000	-5.9412	-5.9412	100.0000	8.8191	8.8191	100.0000	25.9865	25.9863

$\beta = 42^\circ$ (See Fig. A-6)

Table A-E. High Lift Devices

Buttock lines and percent chord are streamwise to 30 degrees, leading edge		
Outboard Flaps	Landing & T/O (30° LE)	Subsonic Cruise (42° LE) (Streamlining Only)
Distance from centerline airplane (to trailing edge)		
To inboard edge, ft	18.3	--
To outboard edge, ft	68.2	--
Maximum deflection (main/auxiliary)	30/50°	0° (20% wing chord extend)
Takeoff deflection	As required	0°
Chord, % wing chord	30	20
Percent wing area affected (2,245 ft ²)	57	--
Area, ft ² (total)	684	--
Strake Flaps		
Distance from \mathcal{C}_l airplane		
To inboard edge, ft	8.5	--
To outboard edge, ft	16.0	--
Maximum deflection (fore, main/aft)	20°, 40° & 60°	0
Area, ft ² (total)	210	--
Chord, % wing & strake chord	15°	--
Strake & wing area affected	1200 ft ²	--

Table A-E. (concluded)

Leading Edge Slats	Wing	Strake
Distance from ∇ airplane (to leading edge)		
To inboard edge, ft	28.8	10.8
To outboard edge, ft	87.2	28.0
Chord, ft	3.0	4.0
Area, ft ² (total)	393	420
Takeoff deflection	20°/37.5°	35°
Landing deflection	20°/37.5°	35°

Table A-F. Lateral Control Surfaces

Aileron (subsonic only)	
Area, ft ²	120
Span, ft	17.2
Chord, percent	34
Deflection	
Down	25°
Up	25°
Spanwise location from ϕ airplane	
Inboard edge - ft	68.2
Outboard edge - ft	84.5
Spoilers	
Area, ft ² (total)	236
Chord, ft	4.3, 3.0, 2.0
Span, ft (along hinge line)	12.1, 18.8, 15.3
Spanwise loc, from ϕ airplane	41.3
Inboard edge - ft	29.1
Outboard edge - ft	68.2
Deflection	45°
Elevons (supersonic only)	
See horizontal tail for specification.	

Table A-G. Horizontal Stabilizer

Horizontal tail	Wings out			
Area (exposed), ft ²	2478			
Span (total), ft	95.2			
Aspect ratio	3.52			
Taper ratio	0.15			
Leading edge sweep angle	55°/60°			
MAC ft	36.4			
Location of LEMAC from leading edge root, ft	21.9			
Dihedral angle (effective)	+7.5°			
Pitch control	Inboard auxiliary		Outboard auxiliary	
	Stabilizer	Stabilizer	Stabilizer	Elevon
Area, ft ² (893 ft ² total)	211	149	111	422
Chord, % stabilizer chord (ave)	23	30	30	100
Dist. from \bar{C}_L airplane				
To inboard edge, ft	13.0	6.0	23.8	31.0
To outboard edge, ft	23.8	13.0	31.0	46.7
Deflection (max)	±30°	+30°, -0°	+30°, -0°	±30°
Airfoil section	---	---	---	Modified double wedge

Table A-H. Vertical Tail and Rudder

<u>Vertical Tail (exposed)</u>	
Area, ft ²	575
Span, ft	23.2
Taper ratio	0.238
Aspect ratio	0.615
Sweep $\pm 25^\circ$ degrees	39°
MAC, ft	42.75
Location of LEMAC	
From leading edge root, ft	15.6
From thrust line, ft (of outboard engine)	27.7
Airfoil section	Modified double wedge
Tail arm (measured from 0.64 wing ref length to 0.25 MAC Tail), ft	62.58
<u>Rudder</u>	
Area, ft ² (30% total area)	262.5
Span, ft.	23.9
Chord, Avg ft (30%)	11.6
Deflection	$\pm 25^\circ$

Table A-1. Design Weights

	GE (lb)	P & W (lb)
Maximum design taxi weight	675,000	675,000
Maximum design takeoff weight (flaps down)	672,000	672,000
Maximum design flt weight (flaps down)	668,000	668,000
Maximum design flt weight (flaps up)	666,000	666,000
Maximum design landing weight	420,000	430,000
Maximum zero fuel weight	360,000	362,500
Minimum flying weight	310,000	314,000
Operational empty weight	285,000	287,500
Manufacturer's empty weight	274,250	276,750
Max. usable fuel - pounds	367,100	367,100
Gallons at 6.7 lb/gal	54,790	54,790

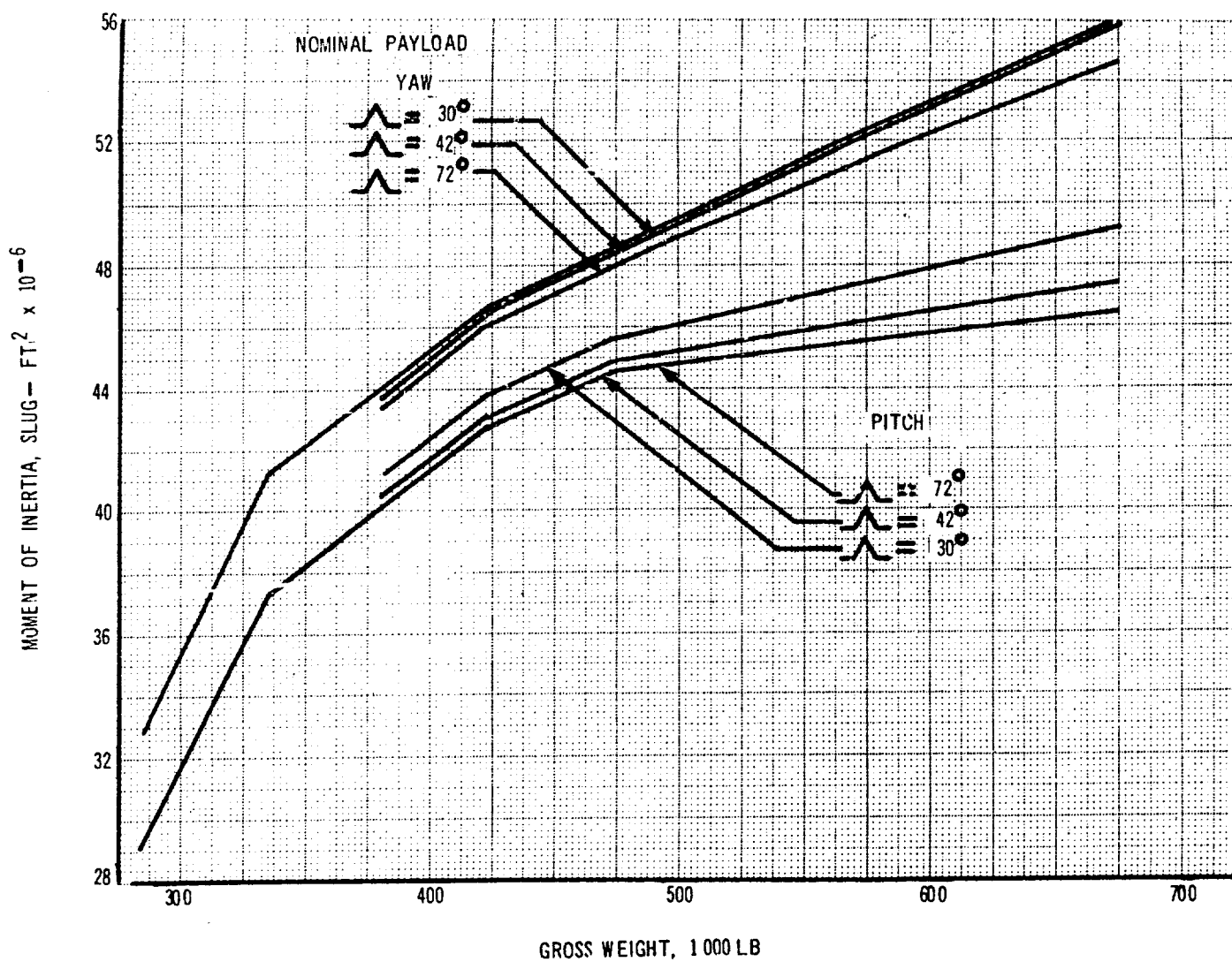


Figure A-7. Moment of Inertia - Pitch and Yaw

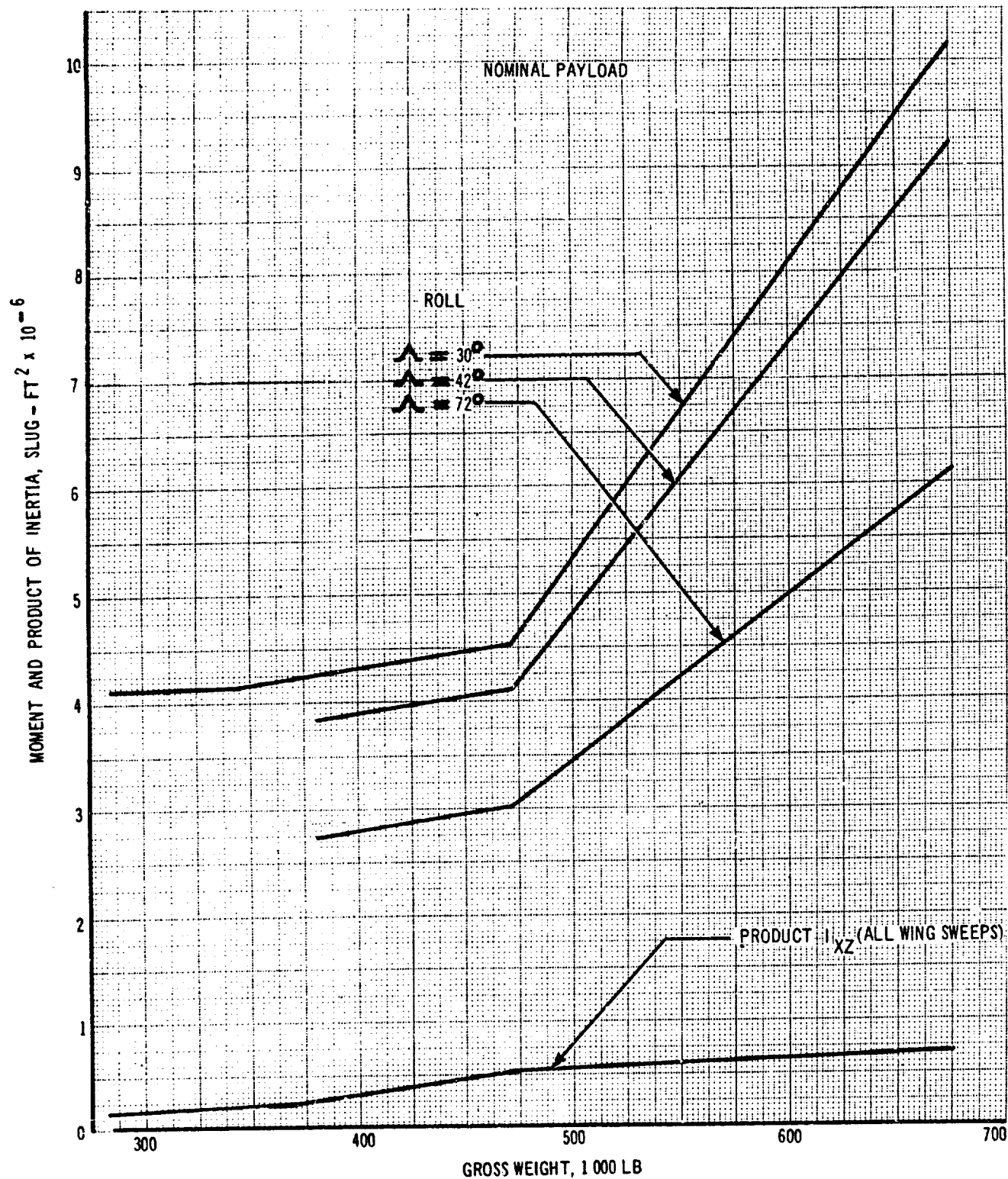


Figure A-8. Moment of Inertia - Roll and Product

ADDENDUM

SUMMARY REPORT - 8 AUGUST 1966 ENGINE PERFORMANCE DATA

The foregoing document is based upon engine performance data received prior to 15 July 1966.

Because there was insufficient time available to completely revise the B-2707 performance after receiving the 3 August 1966 firm technical engine data, the following summary is provided to show the major effect of the firm data on the airplane performance shown in the Phase III proposal documents. Only the most important figures have been provided herein.

If additional or supplemental data is needed, a request to The Boeing Company, SST Division, will receive immediate attention.

8/10/66
10/1/66

APPENDIX B
ADDENDUM
AERODYNAMIC DESIGN

CONTENTS

		<u>Page</u>
1.0	INTRODUCTION AND SUMMARY	1
1.1	ENGINE DIFFERENCES	1
1.2	AIRPLANE PERFORMANCE	2
2.0	ENGINE CHANGES	5
2.1	PERFORMANCE	5
2.2	INSTALLATION	5
2.3	NOISE	5
3.0	AIRPLANE WEIGHT EFFECTS	13
4.0	AIRPLANE PERFORMANCE	15

SECTION 1.0 INTRODUCTION AND SUMMARY

The Boeing SST Proposal is prepared on the basis of engine manufacturer technical data received prior to July 15, 1966. On August 8, 1966, firm technical data was received from General Electric and Pratt & Whitney Aircraft which differed in some respects from the data received prior to July 15, 1966. The purpose of this addendum is to describe the significant differences and to summarize effects on performance of the Boeing Model 2707 airplane.

All information in the proposal is based on the July 15, 1966 engine data with the exception of the Phase III Proposal Summary, V1-B2707-1, Propulsion Report - Part C, Engine Evaluation, V2-B2707-14, and this addendum. These documents are based on engine data received from the engine manufacturers as of August 8, 1966.

1.1 ENGINE DIFFERENCES

The General Electric GE4/J5P engine data received on August 8, 1966, provided lower airport and community noise levels for all engine operating conditions. These lower noise levels were the result of redesign of the exhaust nozzle and noise suppression data obtained from J-93 engine testing. Acoustic data provided by General Electric also indicated reduced turbine noise from that being predicted by Boeing for the GE4/J5P engine. These changes provide significantly improved takeoff and approach noise for the B-2707 (GE). An improvement in transonic thrust was also provided. Updated installed engine weight, including optional equipment has resulted in a 112-lb weight increase for the GE4/J5P engine installation. Engine changes have not affected the installed pod configuration.

In the case of Pratt & Whitney Aircraft JTF17A-21B engine, a 2-percent reduction in specific fuel consumption (SFC) at essentially all operating conditions was the principal change. This improvement reduces B-2707 (P&WA) fuel consumed over the design mission and lowers the reserve fuel requirements. Updated installed engine weight including optional equipment has resulted in a 190-lb weight increase for the JTF17A-21B engine installation. Engine changes have not affected the installed pod configuration.

1.2 AIRPLANE PERFORMANCE

The major effects of these engine changes on airplane performance are summarized in Table 1-A for the international B-2707 with a maximum design taxi weight of 675,000 lb and in Table 1-B for the domestic airplane with a maximum design taxi weight of 575,000 lb. The improved hot day range capability and noise characteristics of the B-2707 (GE) are apparent, as is the improved range capability of the B-2707 (P&WA).

Table 1-B. Performance Changes, Domestic Mission

		Domestic B-2707 (GE)		Domestic B-2707 (P&WA)	
Maximum Taxi Gross Weight = 575,000 lb		July 15, 1966 Basis	Aug. 8, 1966 Basis	July 15, 1966 Basis	Aug. 8, 1966 Basis
Operational Empty Weight lb		275,500	275,500	273,000	273,760
<u>Range with 50,000 lb Payload</u>					
<u>ΔP_{\max} = 2.0 psf Climb; 1.5 psf Cruise</u>					
Standard Day, nmi		2,450	2,465	2,442	2,493
Standard Day + 10° C, nmi		2,295	2,368	2,268	2,307
<u>M = 0.85 Cruise</u>					
Standard Day, nmi		2,571	2,571	3,042	3,100
<u>Takeoff Noise, PNdb</u>		Maximum Dry Thrust		80% Maximum Aug. Thrust	
Standard Day	Airport Noise	117	115	114	114
	Community Noise				
	eg at 0.595 CR	99	93	103	103
	eg at 0.615 CR	98	92	102	102
Standard Day 15° C	Airport Noise	116	114	114	114
	Community Noise eg at 0.595 CR	107	99	108	108
<u>Landing Approach Noise, PNdB</u>					
Standard Day					
Landing Weight, lb		410,000	410,000	400,000	400,000
20° - 10° Flaps	eg at 0.595 CR	112	104	115	115
	eg at 0.615 CR	110	102	114	114
30° - 50° Flaps	eg at 0.615 CR	112	106	116	116
Decelerating Approach		108	98	111	111

Table 1-8. Performance Changes, Domestic Mission

		Domestic B-2707 (GE)		Domestic B-2707 (P&WA)	
Maximum Taxi Gross Weight = 575,000 lb		July 15, 1966 Basis	Aug. 8, 1966 Basis	July 15, 1966 Basis	Aug. 8, 1966 Basis
Operational Empty Weight lb		275,500	275,500	273,000	273,760
<u>Range with 50,000 lb Payload</u>					
<u>$\Delta P_{\max} = 2.0$ psf Climb; 1.5 psf Cruise</u>					
Standard Day, nmi		2,450	2,465	2,442	2,493
Standard Day + 10° C, nmi		2,295	2,368	2,268	2,307
<u>M = 0.85 Cruise</u>					
Standard Day, nmi		2,571	2,571	3,042	3,100
<u>Takeoff Noise, PNdb</u>		Maximum Dry Thrust		80% Maximum Aug. Thrust	
Standard Day	Airport Noise	117	115	114	114
	Community Noise eg at 0.595 CR	99	93	103	103
	eg at 0.615 CR	98	92	102	102
Standard Day 15° C	Airport Noise	116	114	114	114
	Community Noise eg at 0.595 CR	107	99	108	108
<u>Landing Approach Noise, PNdB</u>					
Standard Day					
Landing Weight, lb		410,000	410,000	400,000	400,000
20° - 40° Flaps	eg at 0.595 CR	112	104	115	115
	eg at 0.615 CR	110	102	114	114
30° - 50° Flaps	eg at 0.615 CR	112	106	116	116
Decelerating Approach		108	98	111	111

SECTION 2.0 ENGINE CHANGES

2.1 PERFORMANCE

2.1.1 General Electric GE4/J5P Engine

A 6-percent improvement in transonic thrust was provided as well as increased transonic hot day thrust by means of higher engine rpm and increased airflow for an incremental 50-lb weight increase. Figure 2-1 shows the change in hot day transonic thrust for a 2.5 PSF sonic boom overpressure climb path. Reduced transonic inlet drag due to lower bypass airflow is also shown.

2.1.2 Pratt & Whitney Aircraft JTF17A-21B Engine

The two percent SFC reduction for the JTF17A-21B engine at all power settings except idle power is listed in Table 2-A for important B-2707 operating points. This improvement is provided as a result of increased component efficiencies demonstrated in primary burner, duct burner, and nozzle component development programs.

2.2 INSTALLATION

Pod configuration and external contours for both engine installations are unchanged. The final installed pod weights for both engines including added weight for optional equipment are listed in Table 2-B.

2.3 NOISE

The noise characteristics of the JTF17A-21B remain unchanged from those data presented in the body of the Boeing SST proposal. The remainder of the discussion concerns the GE4/J5P engine.

2.3.1 Engine Noise Characteristics GE4/J5P

The engine noise characteristics of the GE4/J5P engine have been predicted from the engine data and jet noise suppression as supplied by General Electric. Additional engine noise suppression achieved through inlet choking by use of the sonic throat principle as described in the Airport and Community Noise Program report, V4-B2707-4, has also been included. The jet noise suppression values used in the calculation of noise levels for the GE4/J5P engine are shown in Fig. 2-2. These values have been determined by General Electric through acoustic tests that have been conducted on a J-93 engine.

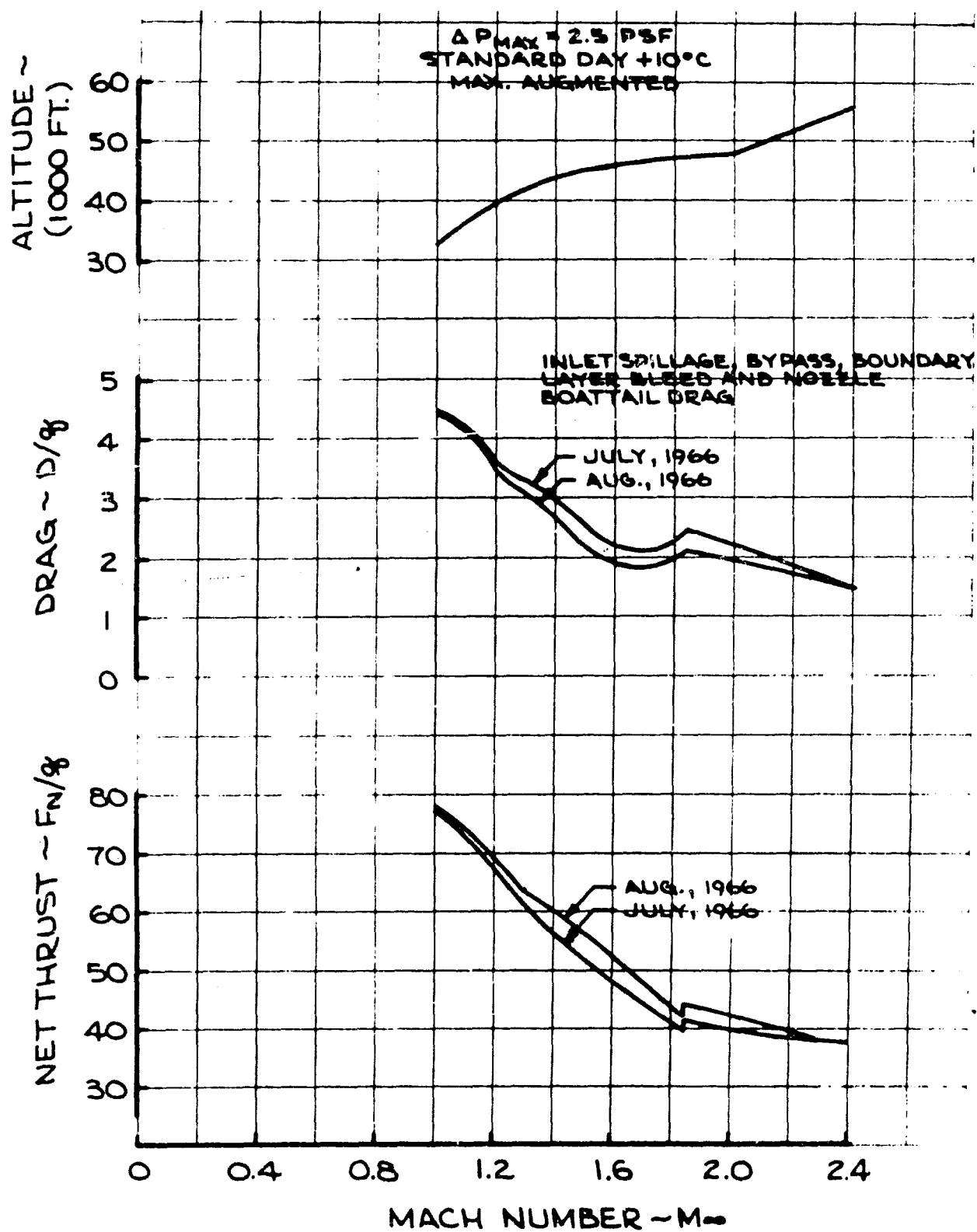


Figure 2-1. GE4/J5P Climb Performance, Standard Day +10°C

Table 2-A. JTF17A-21B Performance Summary

Power Setting	Pressure Altitude ft	Temperature	Mach No	Net Thrust lb	July-1966 SFC lb/hr/lb	August-1966 SFC lb/hr/lb
Max Augmented	0	Std	0	56,740	1.86	1.83
Max Non-Augmented	0	Std	0	35,490	0.77	0.76
Max Augmented	45,000	Std	1.2	19,630	1.94	1.90
Max Augmented	45,000	Std + 10°C	1.2	18,140	2.00	1.96
Partial Augmented	65,000	Std	2.7	15,000	1.57	1.54
Partial Augmented	65,000	Std + 10°C	2.61	15,000	1.66	1.63
Partial Non-Augmented	36,150	Std	0.85	5,000	1.07	1.06
Partial Non-Augmented	15,000	Std	0.5	5,000	1.10	1.08

2.3.1 (Continued)

The unsuppressed noise levels for the GE4/J5P engine for ground and flight operations are shown in Figs. 2-3 and 2-4. Also shown in these figures are the predicted noise levels with all suppression included. The effect of the open-nozzle concept wherein the nozzle throat area is maintained on a maximum area schedule is included in the suppressed noise level predictions. The predicted noise spectra for a series of engine operating conditions have also been predicted and are presented in Table 2-C.

Noise levels beneath and to the side of the airplane flight path have been determined from the revised noise data. These levels have been integrated into contours of Perceived Noise Level for takeoff. These contours are shown for the B-2707 (GE) international airplane in Fig. 4-12 and the B-2707 (GE) domestic airplane in Fig. 4-14.

The landing noise characteristics of the B-2707 (GE) have changed significantly due to the noise data presented on August 8, 1966. These data indicated that turbine noise would not contribute significantly to the total noise from the airplane even at landing approach power settings. Boeing had been predicting very significant noise increases due to turbine noise contribution. The predictions were based on the J-75 engine acoustic test results. Since the GE data were obtained on an engine more closely resembling the SST turbojet offering, these data should be more representative of the noise characteristics of the SST engine. Therefore the B-2707 landing noise levels have been revised to conform to the August 8, 1966 data inputs. The results of these revisions are shown in Figs. 4-17 and 4-18.

Table 2-B. Installed Pod Weight

	B-2707 (GE)	B-2707 (P&WA)
Engine weight	11,125	9,910
Optional equipment	112	730
Total	11,237	10,640
Inlet	2,070	2,485
Cowl panels		
Forward	325	225
Aft	150	---
Structure	495	480
Miscellaneous	35	35
Total	14,312	13,865

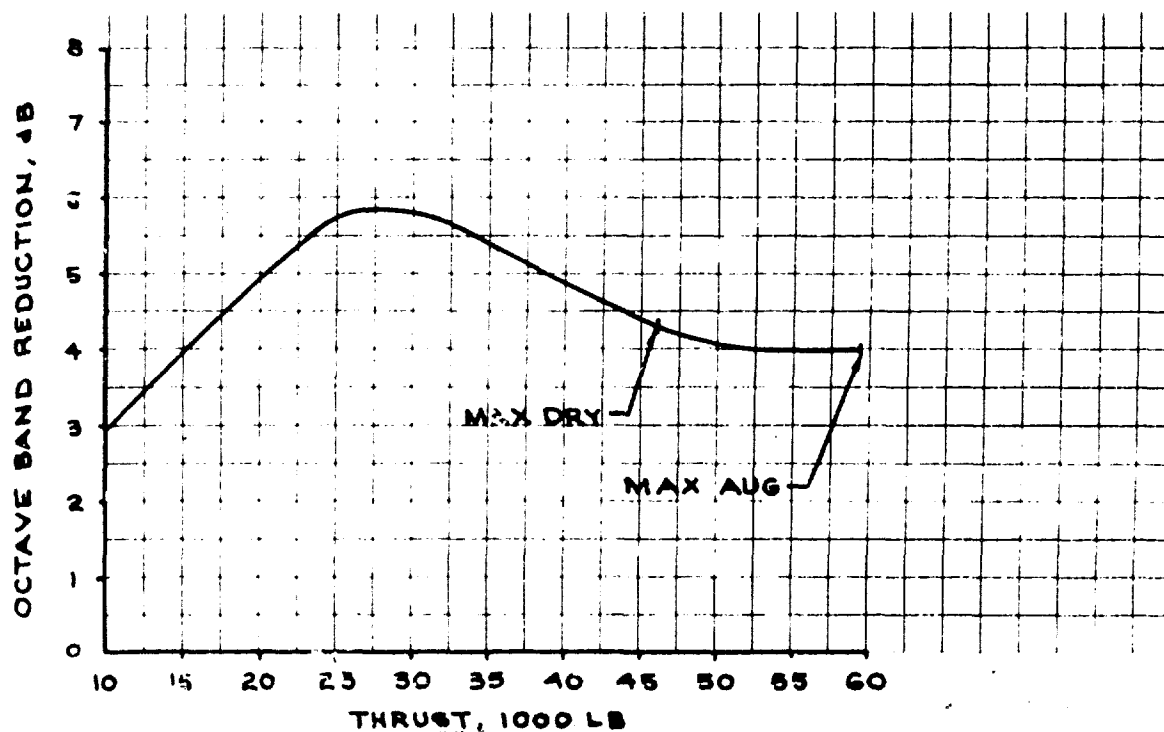


Figure 2-2. Predicted GE4/JSP Jet Noise Suppression

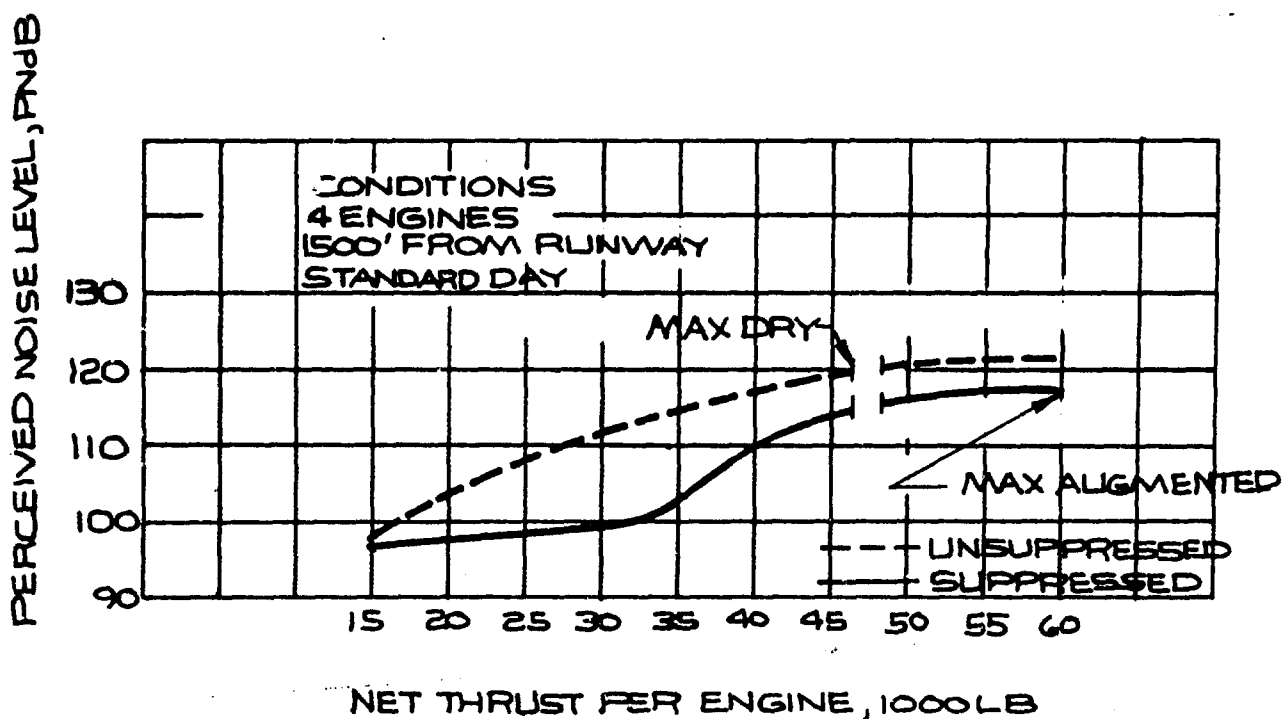
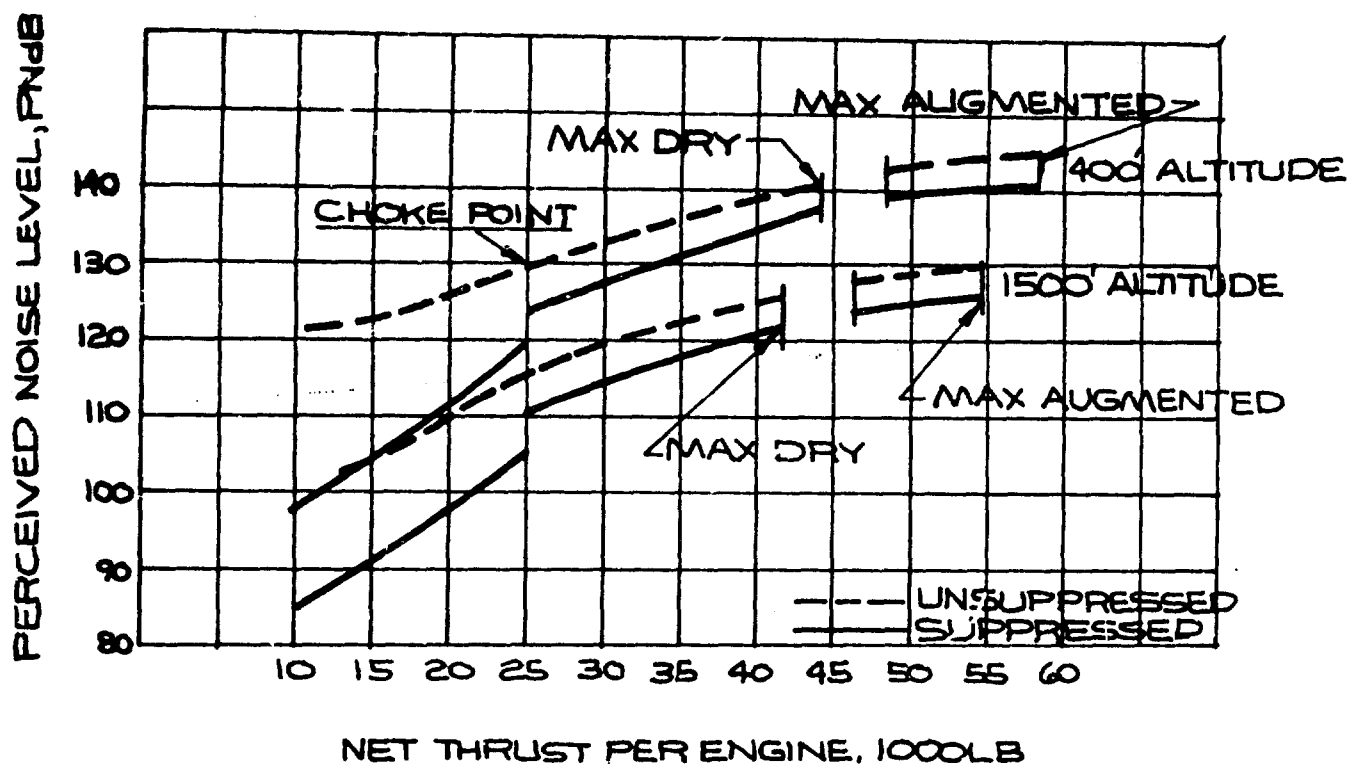


Table 1 - Noise Spectra For GE4 15P Engine

Operating Conditions (4 Engines)	Overall dB	Takeoff Band Bandwidth (dB)								Landing Band Bandwidth (dB)				Per ceived Noise Metric (PNM)
		1	2	3	4	5	6	7	8	9	10	11	12	
Ground Idle 1,500 ft														
Max Avg Unsuppressed	116.5	113	115	113	109	107	102	95	76	44	61	62	62	121.0
Suppressed	114.5	109	111	109	105	103	98	91	74	44	61	62	62	117.0
Max Dry Unsuppressed	117.0	111	113	111	107	105	100	93	76	44	61	62	62	119.0
Suppressed	115.0	107	109	107	103	101	96	89	72	44	61	62	62	114.5
Taxi (5,000 lb/ft) 200 ft														
Unsuppressed	106.5	85	86	82	80	76	70	60	60	60	60	60	60	119.0
Suppressed	97.0	85	86	82	80	76	70	60	60	60	60	60	60	111.0
Flight (0.5 ft) 1,500 ft Alt														
Max Avg Unsuppressed	125.5	113	116	121	116	114	108	97	86	66	77	74	74	130
Suppressed	121.0	109	114	117	114	110	104	97	91	66	77	74	74	126
Max Dry Unsuppressed	122.0	110	116	117	115	111	106	97	90	66	77	74	74	128.5
Suppressed	118.0	106	112	112	111	107	100	97	86	66	77	74	74	112.0
10,000 lb/ft Unsuppressed	99.0	93	94	93	89	83	76	66	61	66	44	46	46	97
Suppressed	95.0	89	90	89	84	78	70	61	61	60	44	46	46	97
10,700 lb/ft Unsuppressed	96.0	90	91	90	86	80	72	62	60	61	41	41	41	105
Suppressed	92.5	86	87	86	81	75	68	57	54	56	37	43	43	94
Landing (0.23 ft) 320 ft Alt														
Unsuppressed	111.5	101	100	98	94	89	84	80	79	107	74	103	103	124
Suppressed	101.5	97	96	94	90	86	80	77	76	82	70	78	78	106

SECTION 3.0 AIRPLANE WEIGHT EFFECTS

The Airframe Design Report - Part A, Weight and Balance, gives an Operating Empty Weight breakdown of the GE and P&WA powered airplanes. Table 3-A lists these comparative weights as they are modified by the August 8, 1966 engine data and other related airplane changes.

The 760-lb weight change in the P&WA powered airplane increases the Manufacturer's Empty Weight, Operating Empty Weight and Zero Fuel Weight of the following P&WA powered airplanes:

- a. 635,000-lb gross weight design point airplane
- b. 675,000-lb gross weight production international airplane
- c. 635,000-lb gross weight prototype airplane
- d. 575,000-lb gross weight production domestic airplane

TABLE 3-A
OPERATING EMPTY WEIGHT

GROUP	GE	P&WA
Engines	44,950	42,560
Nacelle	12,300	12,900
Horizontal Tail	20,400	20,460
Engine Accessories - ADS	1,100	1,160
Anti-Icing and Anti-Fogging	280	330
Starting System	400	430
Fuel System	7,400	7,510
Hydraulic System	3,600 ⁽¹⁾	3,420
Body Structure	47,300 ⁽¹⁾	47,220
Other	<u>149,770</u>	<u>149,770</u>
Operational Empty Weight (Max. design taxi weight 675,000 lb)	287,500	285,760
Original Operating Empty Weight	<u>287,500</u>	<u>285,000</u>
Weight Change	0	+760 lb

⁽¹⁾ Includes effect of ram air turbine - B-2707 (GE) only

SECTION 4.0

AIRPLANE PERFORMANCE

The effect of the changes in engine data on the standard day payload-range capability are illustrated in Fig. 4-1 for the international B-2707 and Fig. 4-2 for the domestic airplane. As noted, there is no significant effect on the standard day range of the B-2707 (GE). The improved specific fuel consumption of the Pratt & Whitney Aircraft engine results in slightly less than 2 percent increase in range. The effect of temperature changes from standard day on range are shown in Fig. 4-3 for the B-2707 (GE) and Fig. 4-4 for the B2707 (P&WA). There is no change for the B-2707 (P&WA) curve since the effect of temperature on the engine data did not change.

Figures 4-5 and 4-6 show the off-loaded supersonic range capability and corresponding transonic thrust margins for the airplanes. The range performance with a mixed subsonic and supersonic mission is shown in Fig. 4-7. Figures 4-8 and 4-9 show fuel, time, and distance breakdowns for a nominal, standard day, intercontinental mission at a maximum sonic-boom overpressure of 2.5 psf for both airplanes.

Summaries of takeoff performance, using maximum augmented thrust, are shown in Figs. 4-10 and 4-11. The significant change in takeoff performance is in the airport and community noise of the B-2707 (GE). The changes in noise characteristics are shown in more detail by the noise contours around the airport in Figs. 4-12 through 4-15.

The noise data shown on the preceding curves are based on the engines as proposed by the engine contractors with the use of a sonic throat in the inlet at reduced powers. With the Boeing noise suppressor, the August 8, 1966 General Electric engine data have resulted in an additional 1 PNdb reduction in the airplane's noise characteristics at maximum augmented thrust. Noise contours with the Boeing jet suppressor are compared in Fig. 4-16 for the B-2707 (GE).

The only change in landing performance for the airplanes caused by the changed engine data is in the approach noise for the B-2707 (GE) as shown in Figs. 4-17 and 4-18. Figure 4-19 shows the B-2707 (P&W) landing performance.

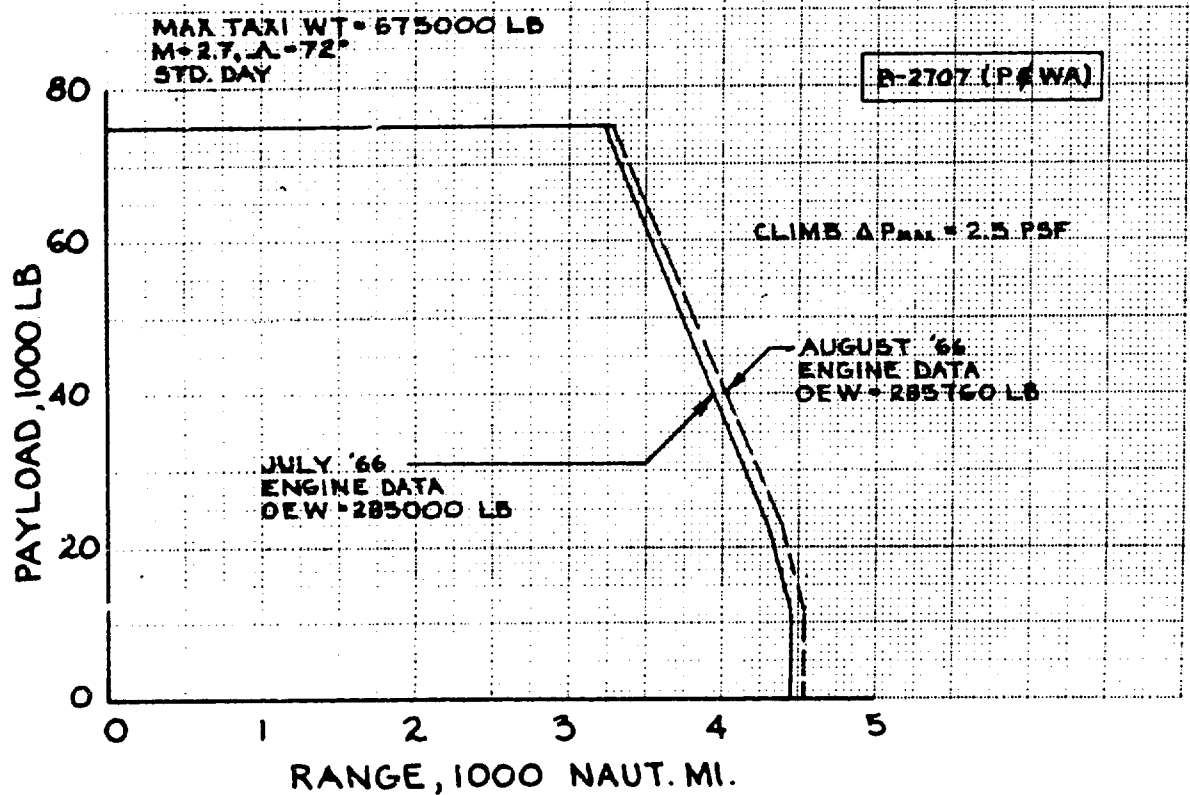
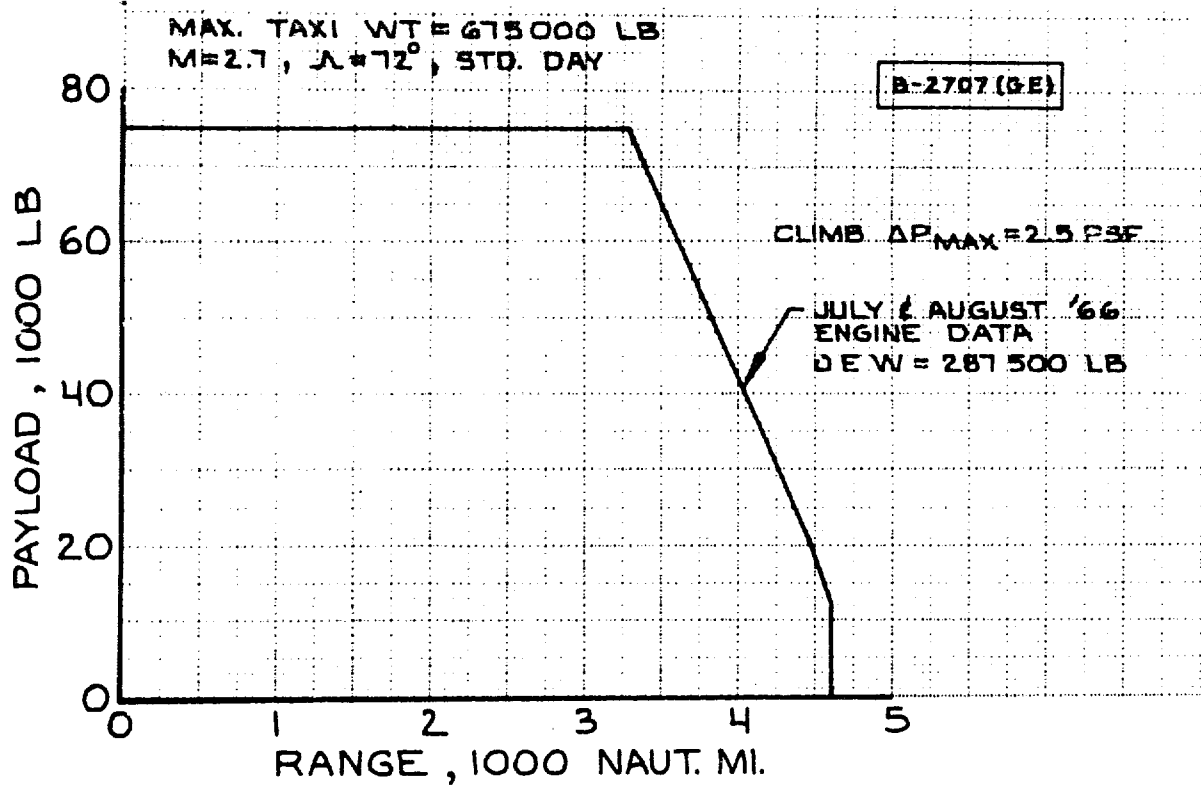


Figure 4-1. Payload-Range, International Model B-2707

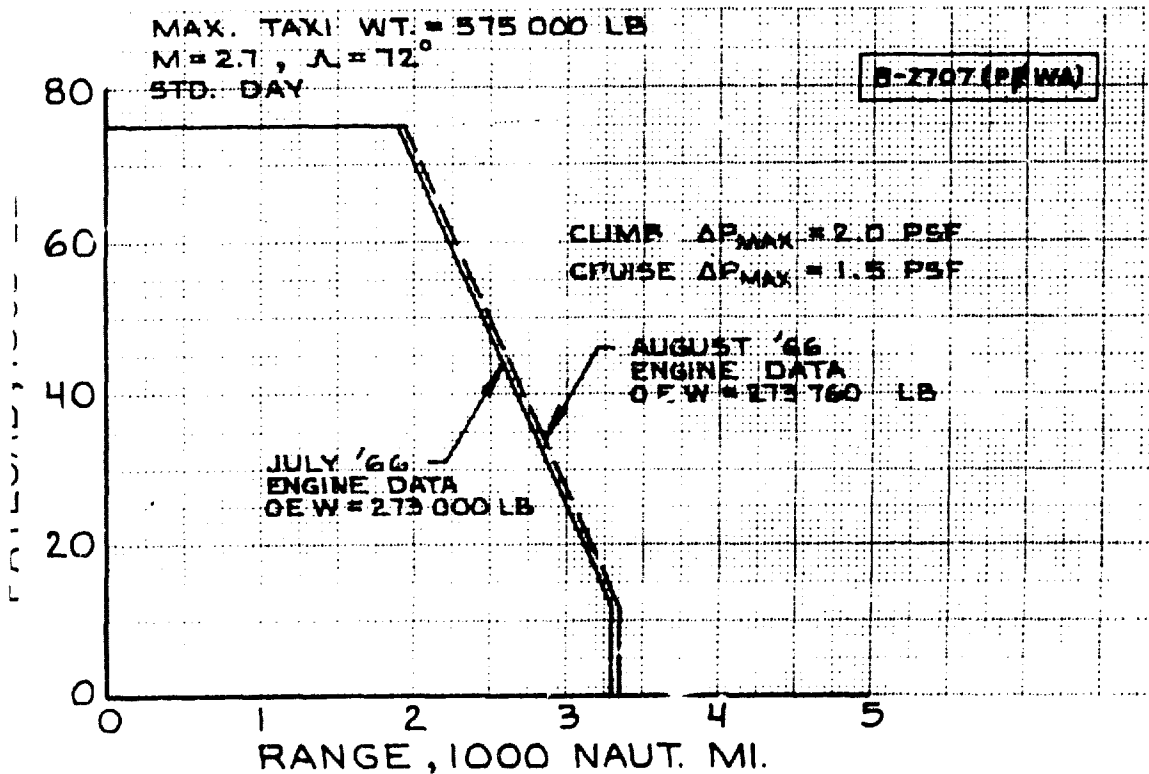
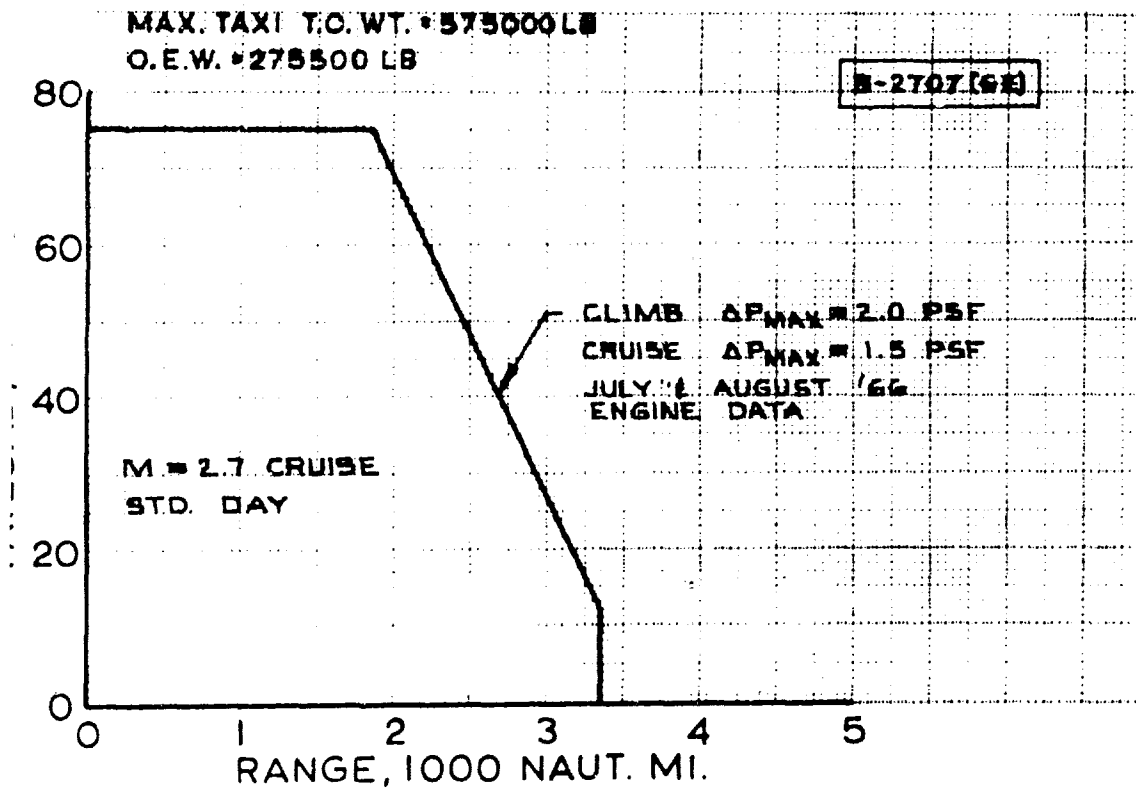


Figure 4-2. Payload-Range, Domestic Model B-2707

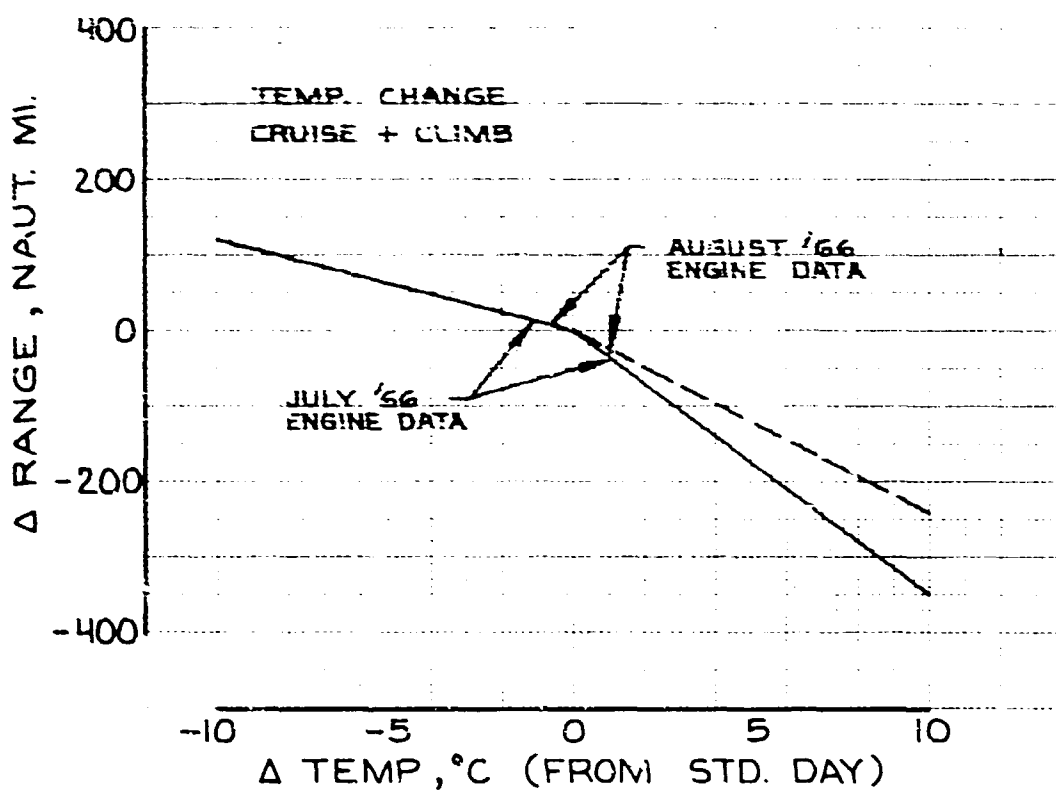
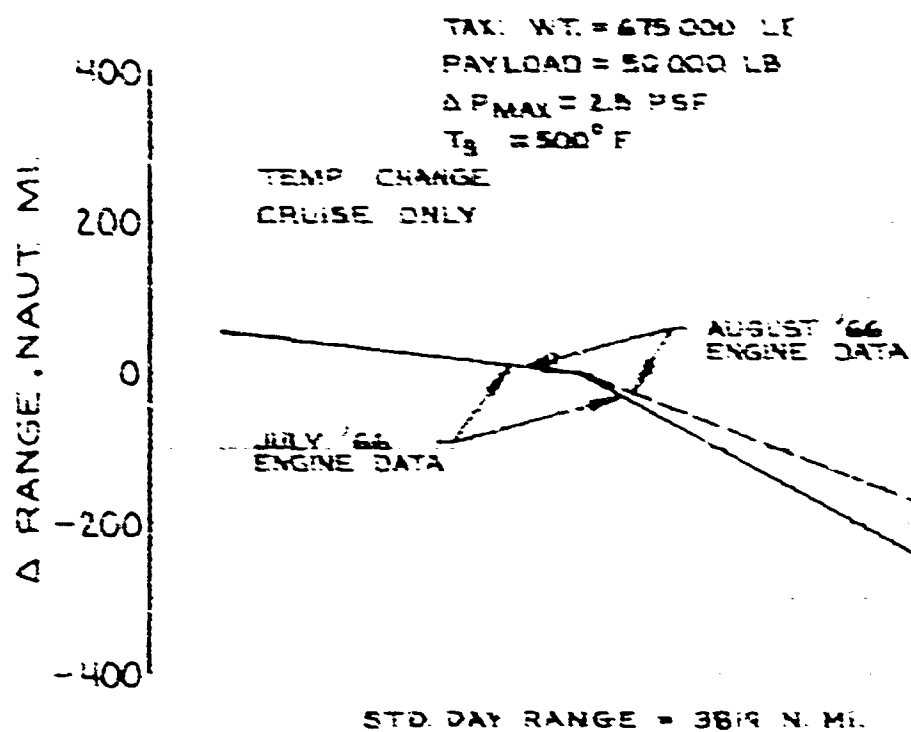


Figure 4-3. Effect of Temperature Change on Range Model B-2707 (GE)

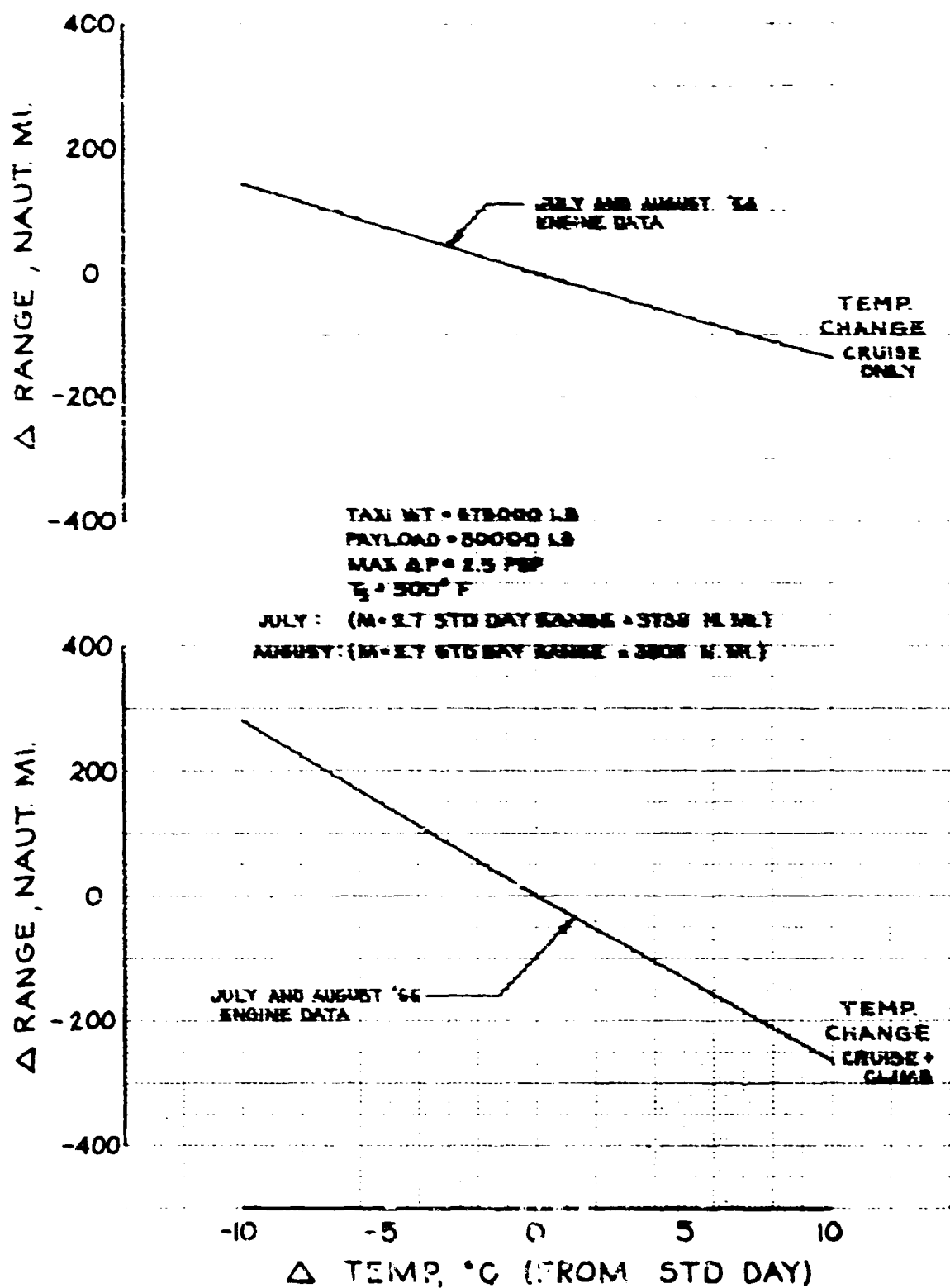


Figure 4-4. Effect of Temperature Change on Range Model B-2707 (P&WA)

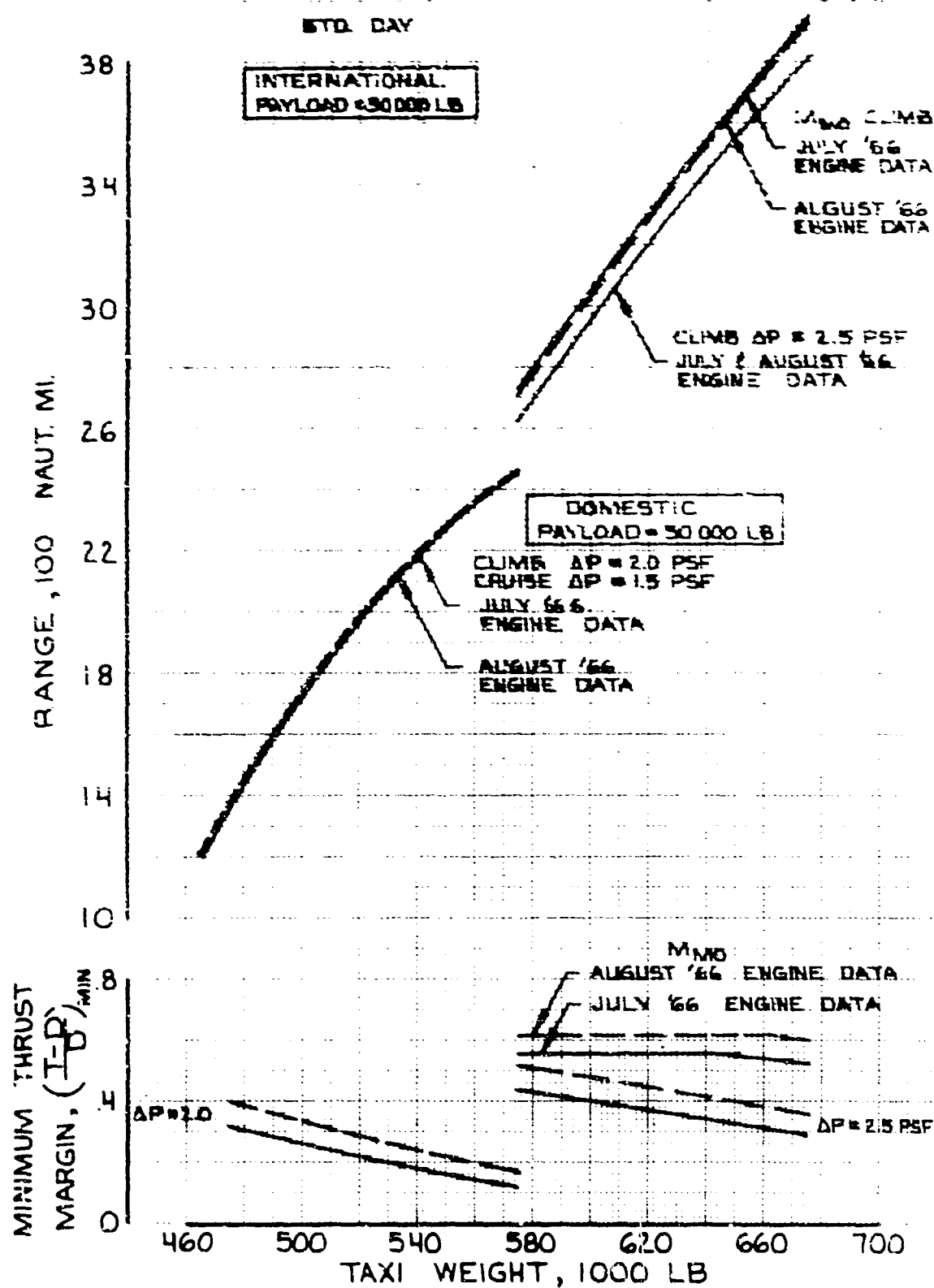


Figure 4-5. Off-Loaded Airplane Performance Model B-2707 (GE)

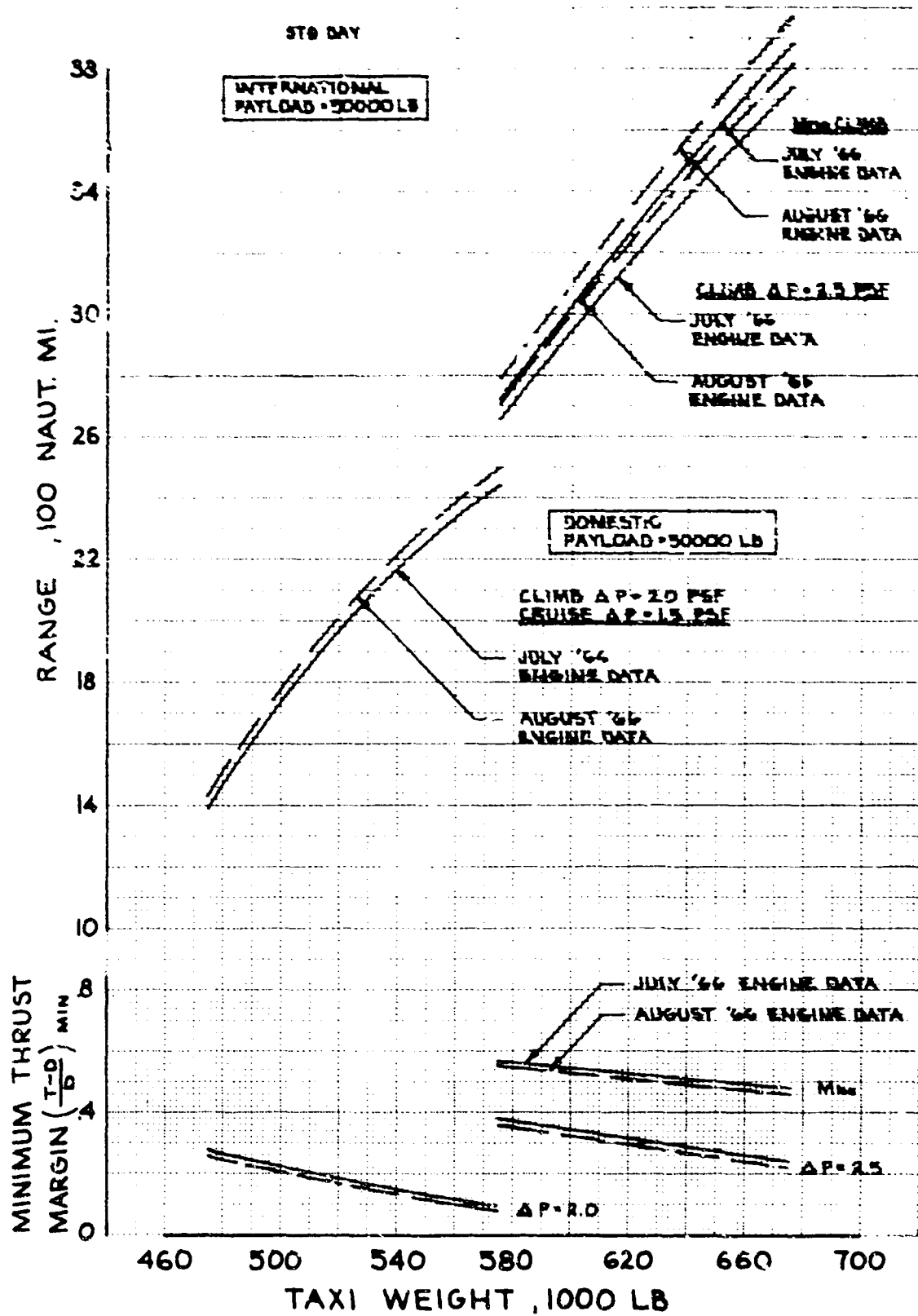


Figure 4-6. Off-Loaded Airplane Performance Model B-2707 (P&WA)

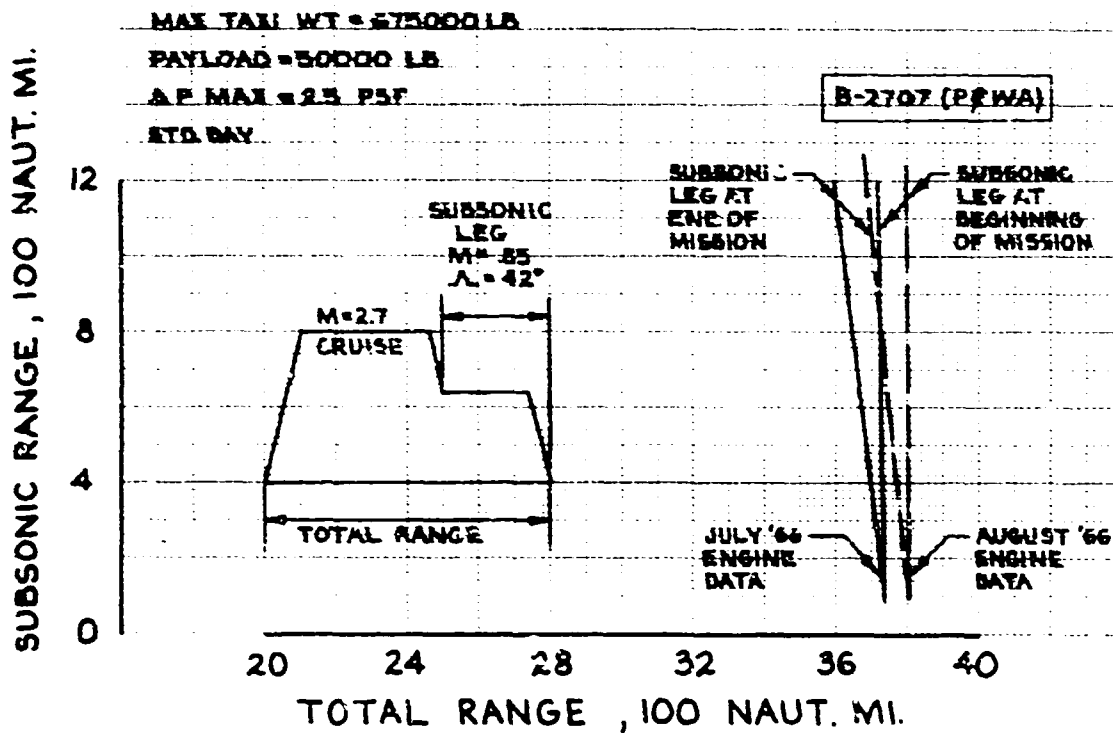
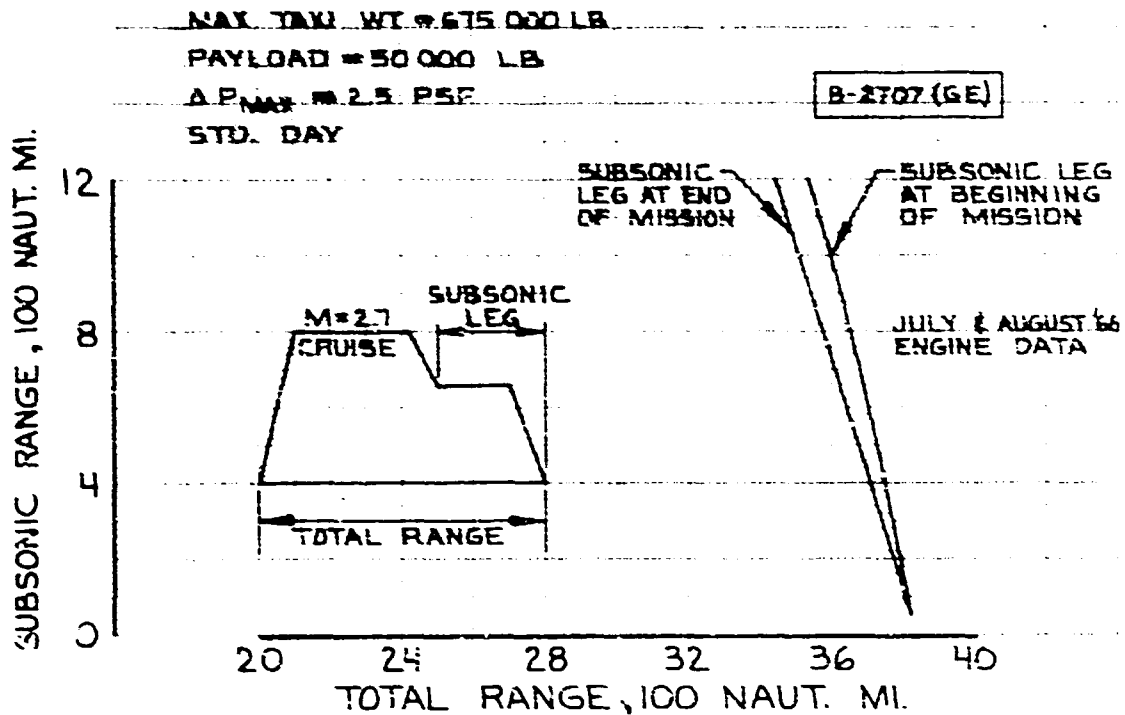


Figure 4-7. Operational Versatility Model B-2707

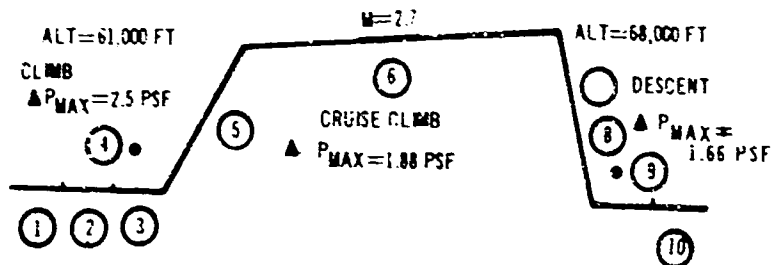
Max. Design

Taxi Weight - 675,000 lb
 OEW - 287,500 lb
 Payload - 50,000 lb
 Wing Area - 9,000 ft²
 Engine - GE4/J5P
 Airflow - 620 lb/sec

Std Day, Zero Wind

Phase III Rules

Block Time - 3.290 hr
 Block Fuel - 292,191 lb



	Fuel Burned (lb)	Fuel Remaining (lb)	Weight At End of Operation (lb)	Time (hr)	Distance (nmi)
1. Taxi-out	4,060	333,440	670,940	0.167	—
2. Takeoff (Sea level to 35 ft)	4,150	329,290	666,790	0.010	—
3. Acceleration to climb speed	4,790	324,500	662,000	0.024	5.0
4. Departure air maneuver allowance (250 kts EAS & 5,000 ft)	4,000	320,500	658,000	0.0673	—
5. Acceleration and climb	81,400	238,800	576,600	0.411	337
6. Supersonic cruise climb	186,791	52,309	369,809	2.112	3271
7. & 8. Deceleration and descent (cruise altitude to 1,500 ft)	2,330	49,979	387,479	0.333	206
9. Destination air maneuver (Approach & Landing Allow- ance, 250 kts EAS at 5,000 ft) WT = WT at (8) = 5% block fuel	2,940	47,039	384,539	0.083	—
10. Taxi-in	(1,720)*			0.083	—
TOTAL MISSION	290,461			3.290	3819
Reserves					
A. 5 percent block fuel	14,609		369,930		
B. Missed approach (climb sea level to 1,500 ft)	2,510		367,420		
C. Climb from 1,500 ft subsonic cruise, descent to sea level at altn (300 at mi)	20,070		347,350		
D. 20 min hold at 15,000 ft over alternate	9,850		337,500		
TOTAL RESERVES	47,039				
TOTAL FUEL	337,500				

* Fuel burned not included in mission fuel; for D.O.C. only

Figure 4-8 B-2707 (GE) International Supersonic Cruise Mission

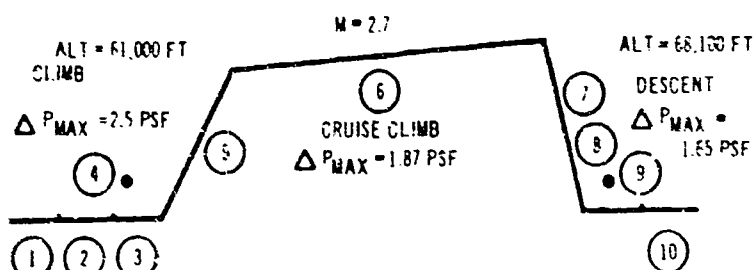
Max Design

Taxi Weight 675,000 lb
 OEW - 285,760 lb
 Payload 50,000 lb
 Wing Area = 9,000 sq ft
 Engine PWAJTF17A-21B
 $W_n = 687 \text{ lb/sec}$

Std Day, Zero Wind

Phase III Rules

Block Time 3.400 hr
 Block Fuel 297,890 lb



	Fuel Burned (lb)	Fuel Remaining (lb)	Weight At End of Operation (lb)	Time (hr)	Distance (nmi)
1. Taxi-out	2,880	336,360	672,120	0.167	—
2. Takeoff (Sea level to 35 ft)	4,385	331,975	667,735	0.010	—
3. Acceleration to climb speed	4,880	327,095	662,855	0.043	10
4. Departure air maneuver allowance (250 kts EAS to 5,000 ft)	3,160	323,935	659,695	0.067	—
5. Acceleration and climb	95,400	228,535	564,295	0.570	422
6. Supersonic cruise climb	181,626	46,909	382,669	2.051	3,180
7. & 8. Deceleration and descent (cruise altitude to 1,500 ft)	2,070	44,839	380,599	0.326	196
9. Destination air maneuver (Approach & Landing Allowance, 250 kts EAS at 5,000 ft) WT = WT at (8) = 5% block fuel	2,234	42,605	378,365	0.083	—
10. Taxi-in	(1,255)*			0.083	—
TOTAL MISSION	296,635			3.400	3,808

Reserves

A. 5 percent block fuel	14,895	363,470
B. Missed approach (climb sea level to 1,500 ft)	2,200	361,270
C. Climb from 1,500 ft subsonic cruise, descend to sea level at altn (300 at mi)	17,670	343,600
D. 20 min hold at 15,000 ft over alternate	7,840	335,760
TOTAL RESERVES	42,605	
TOTAL FUEL	339,240	

* Fuel burned not included in mission fuel; for D.O.C. only

Figure 4-9 B-2707 (P&WA) International Supersonic Cruise Mission

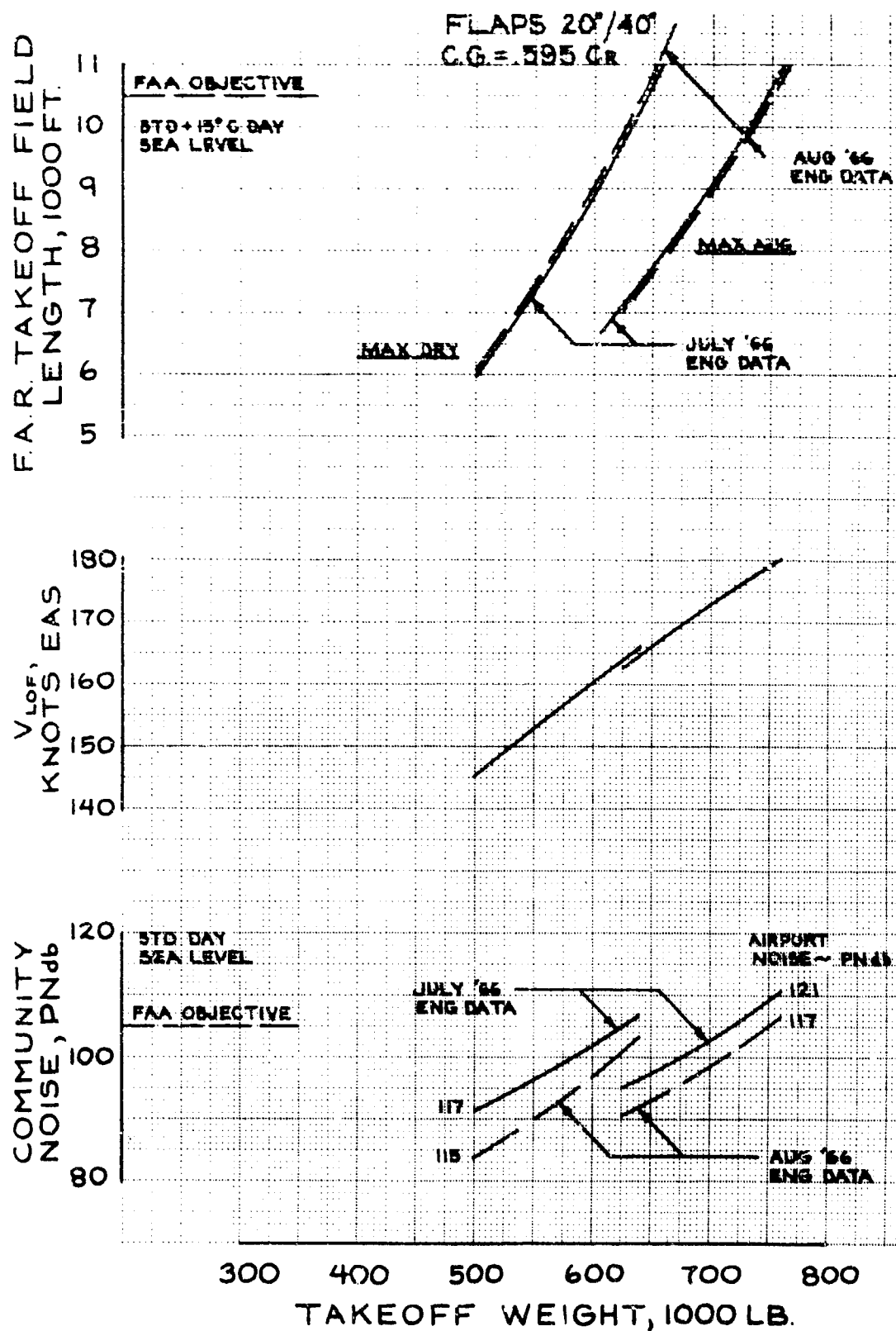


Figure 4-10. Takeoff Performance Model B-2707 (GE)

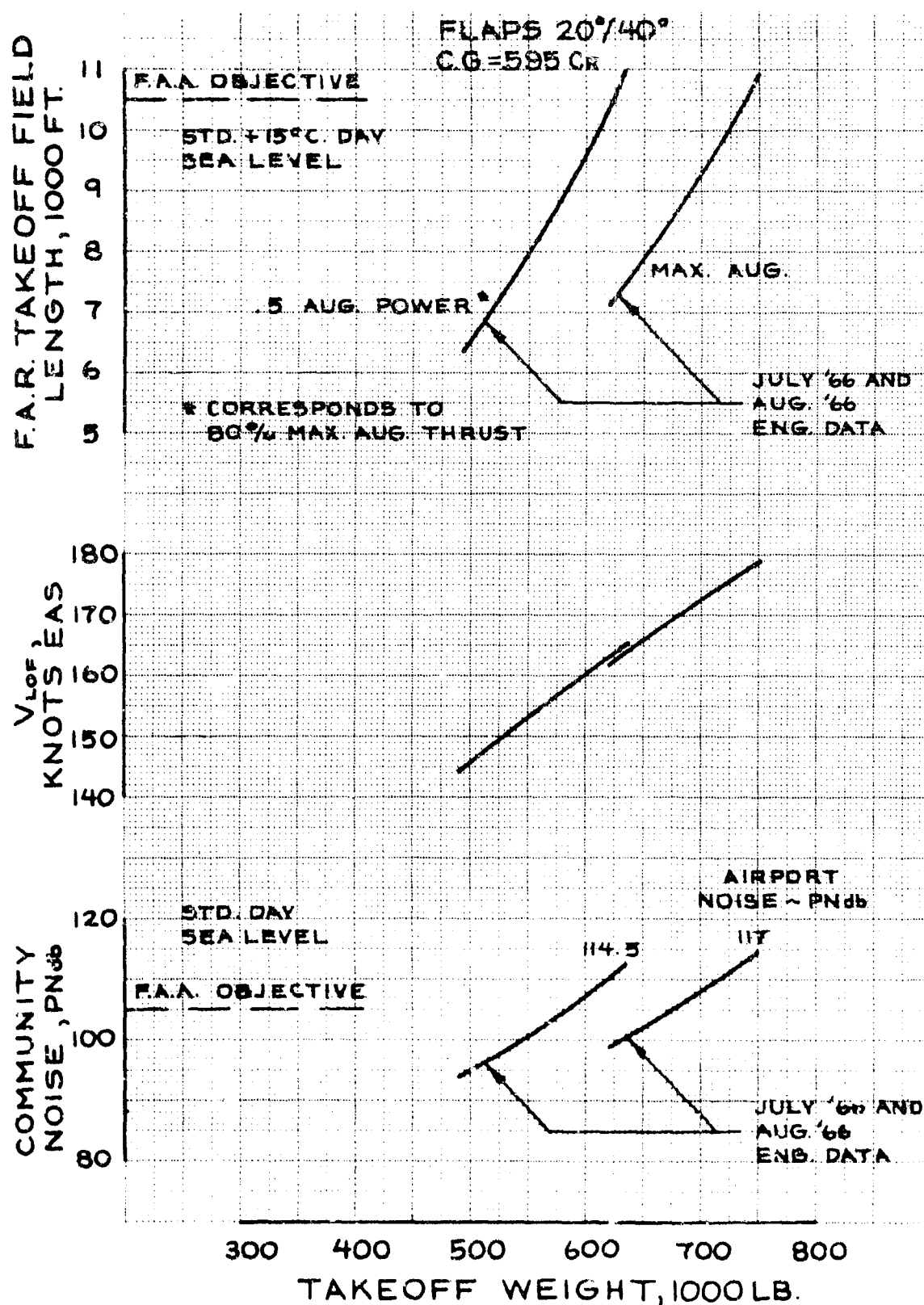


Figure 4-11. Takeoff Performance Model B-2707(P&WA)

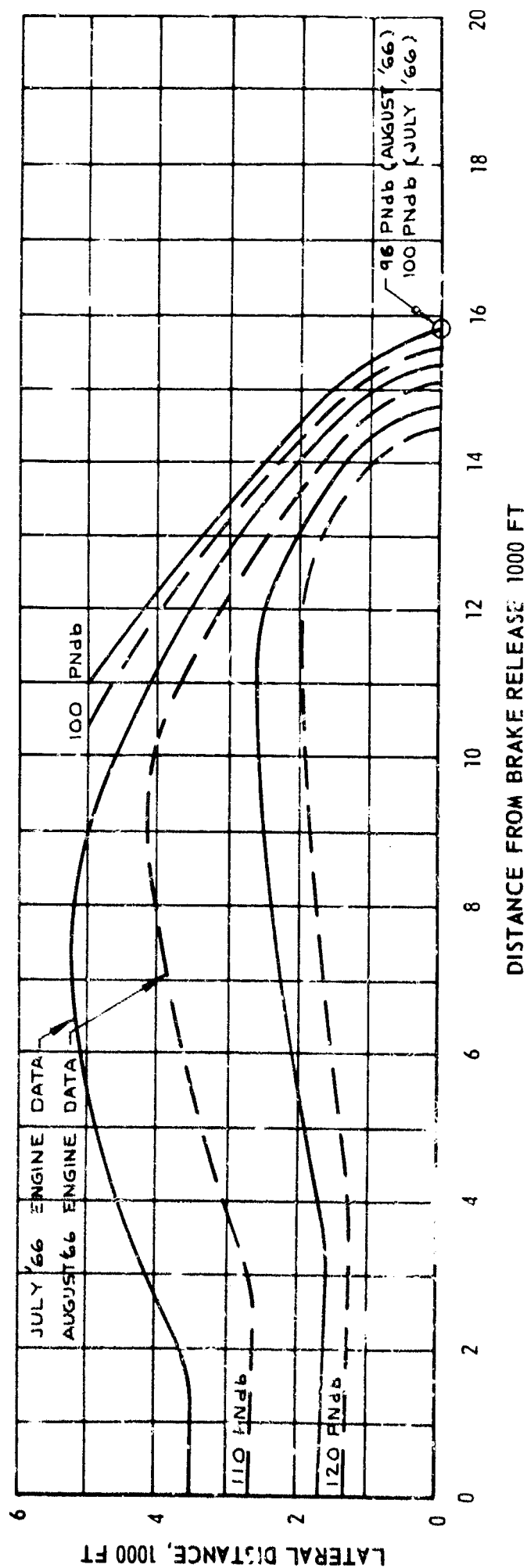
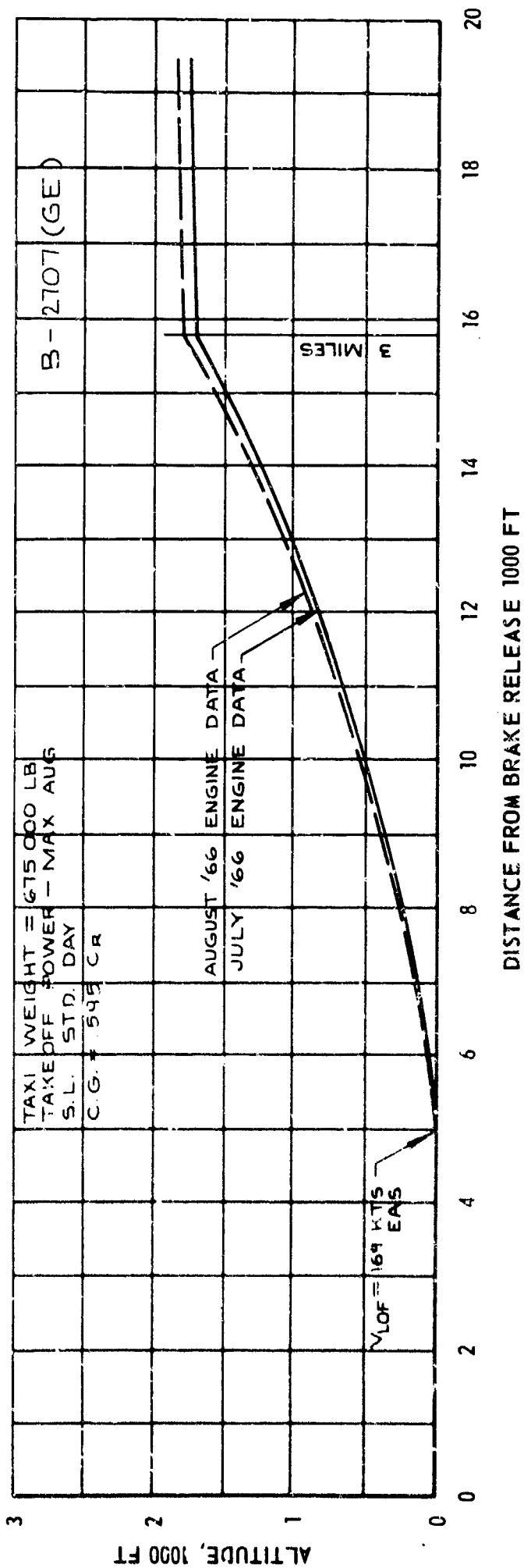
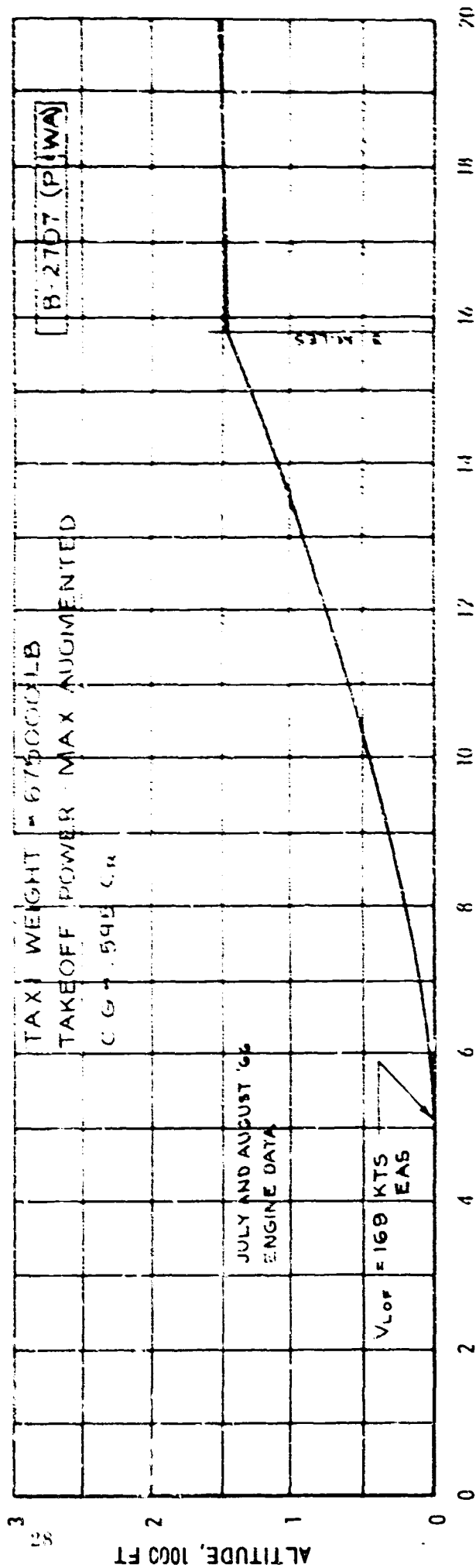
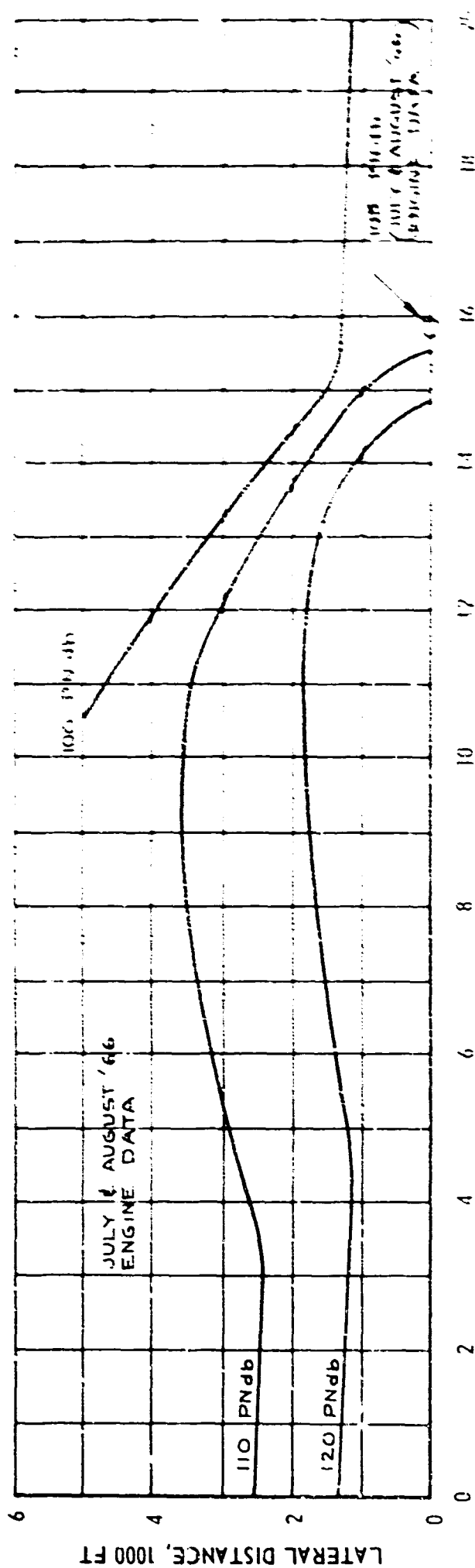


Figure 4-12. Noise Contours, International Mission, Standard Day Model B-2707 (GE)



DISTANCE FROM BRAKE RELEASE 1000 FT



DISTANCE FROM BRAKE RELEASE 1000 FT

Figure 4-13. Noise Contours, International Mission, Standard Day Model B-2707 (P) (WA)

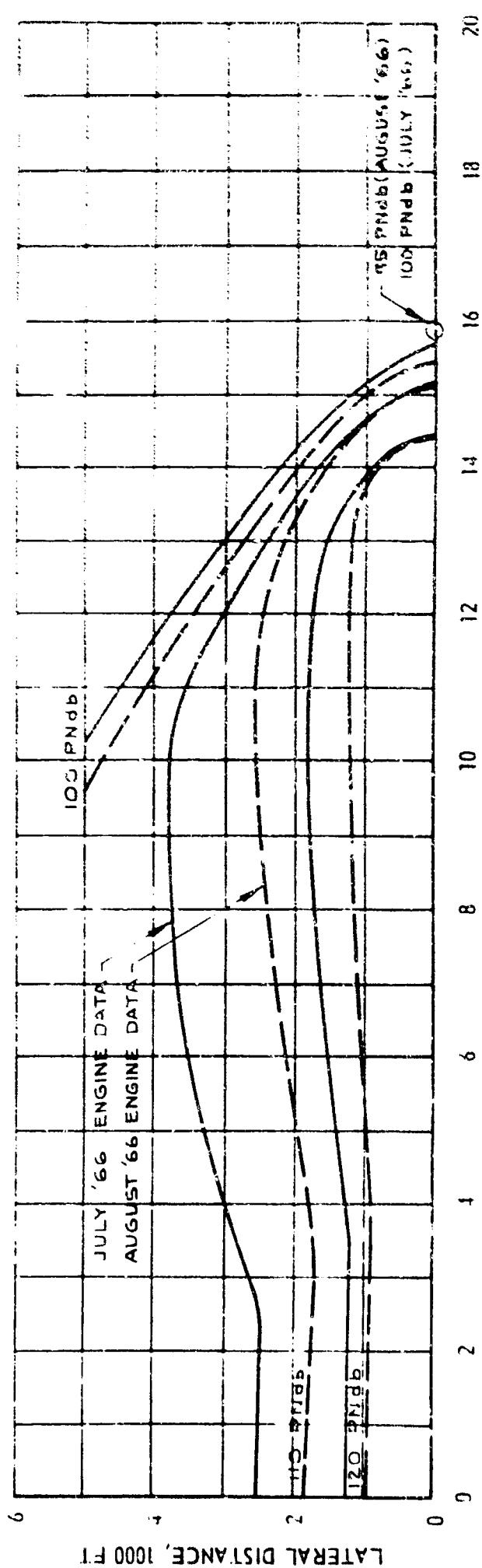
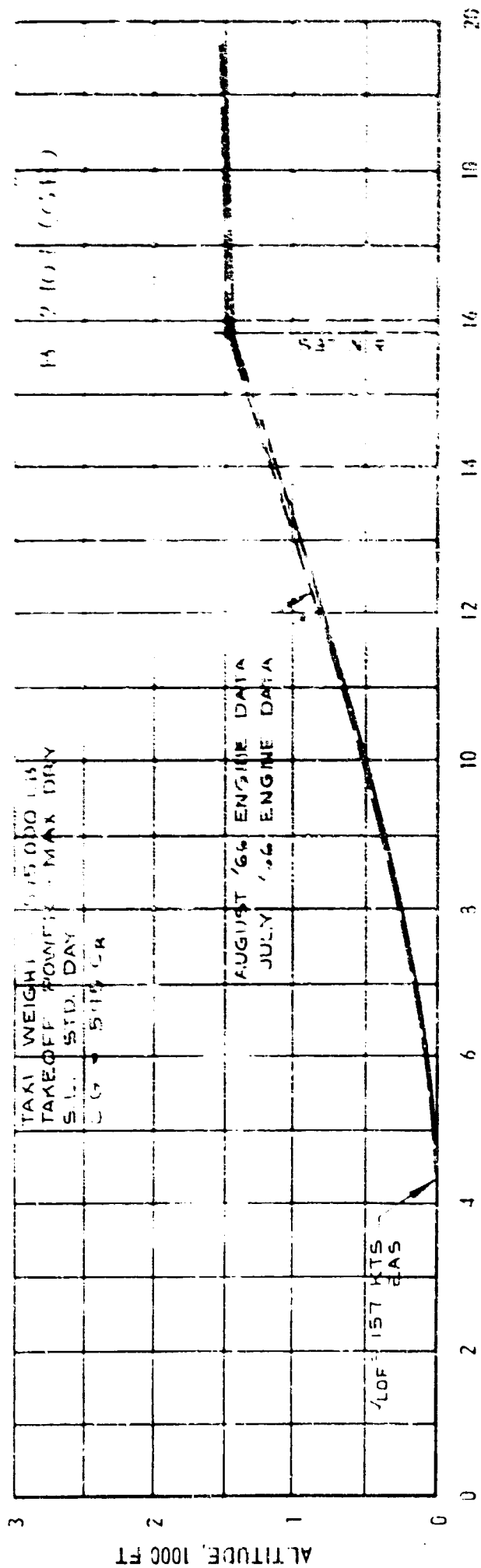


Figure 1-11. Noise Contours, Domestic Mission, Standard Day Model 8-2707 (GE)

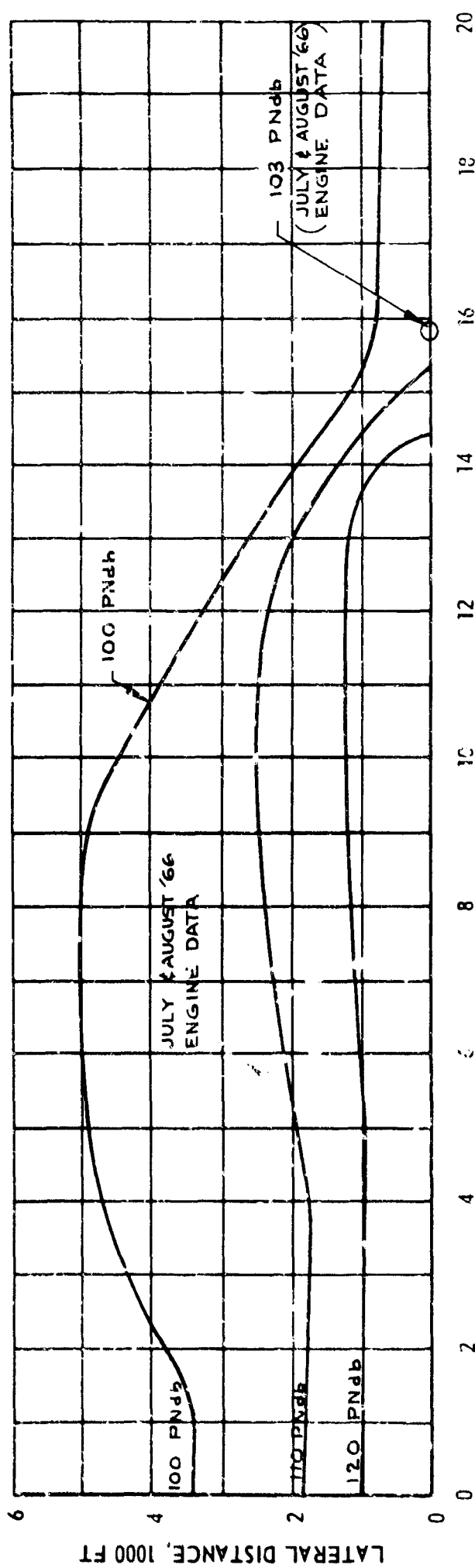
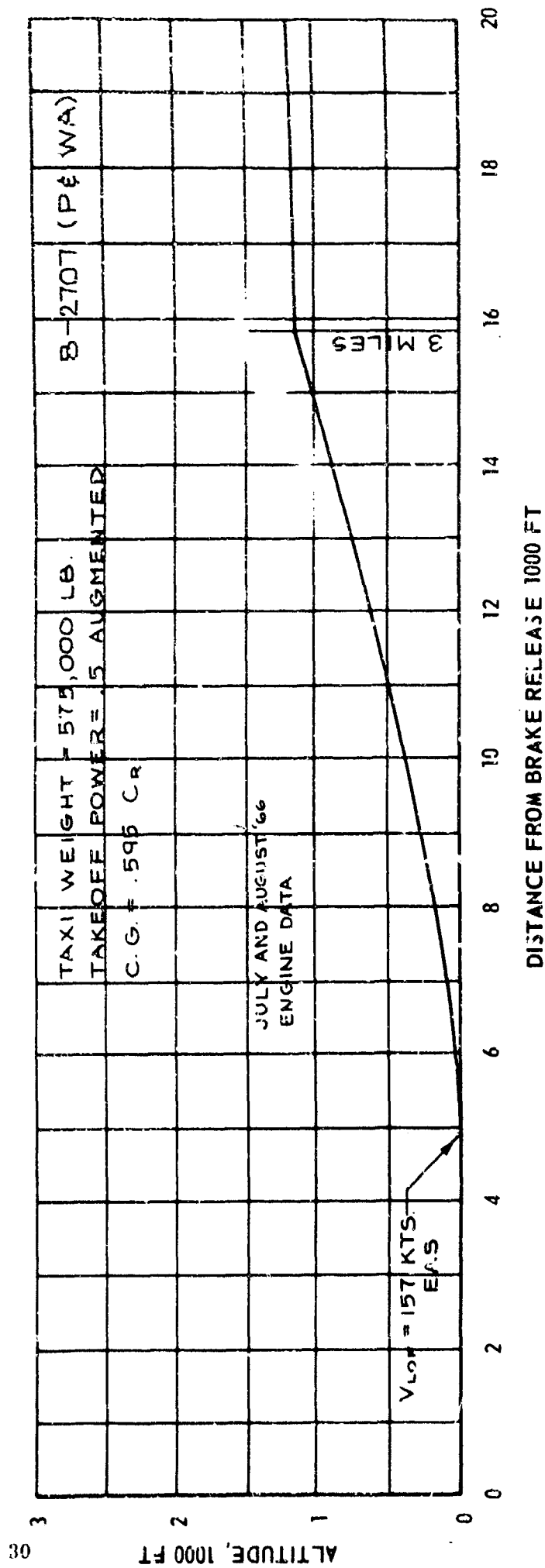


Figure 4-15. Noise Contours, Domestic Mission Standard Day Model B-2707 (P & WA)

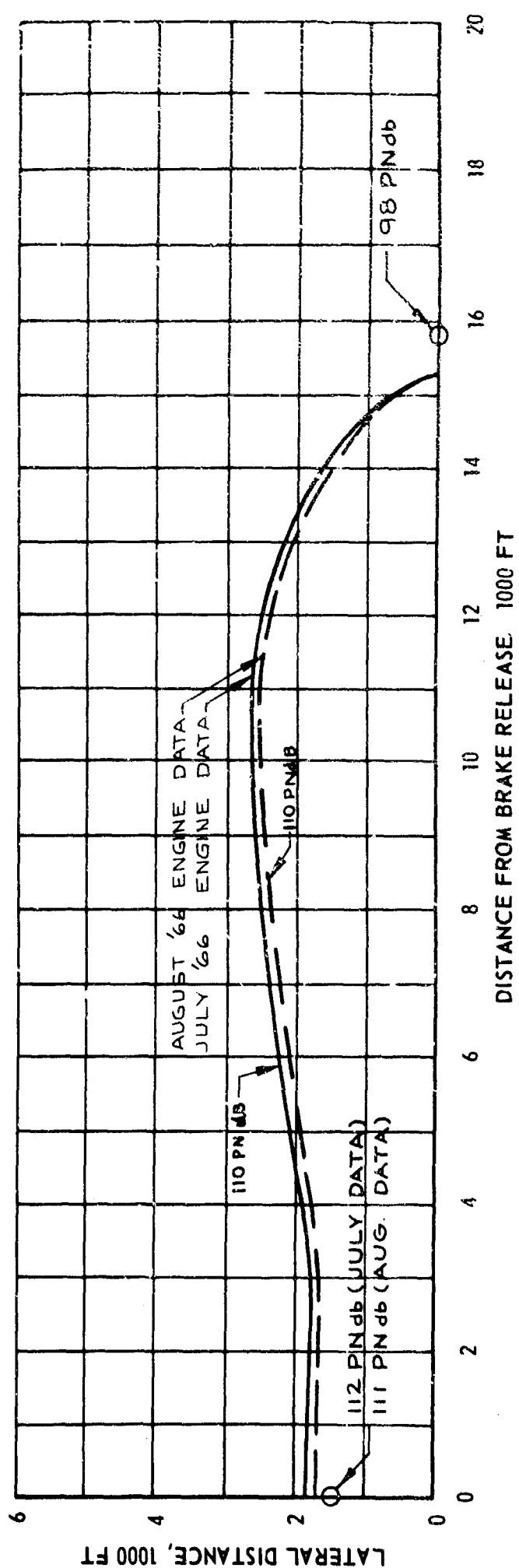
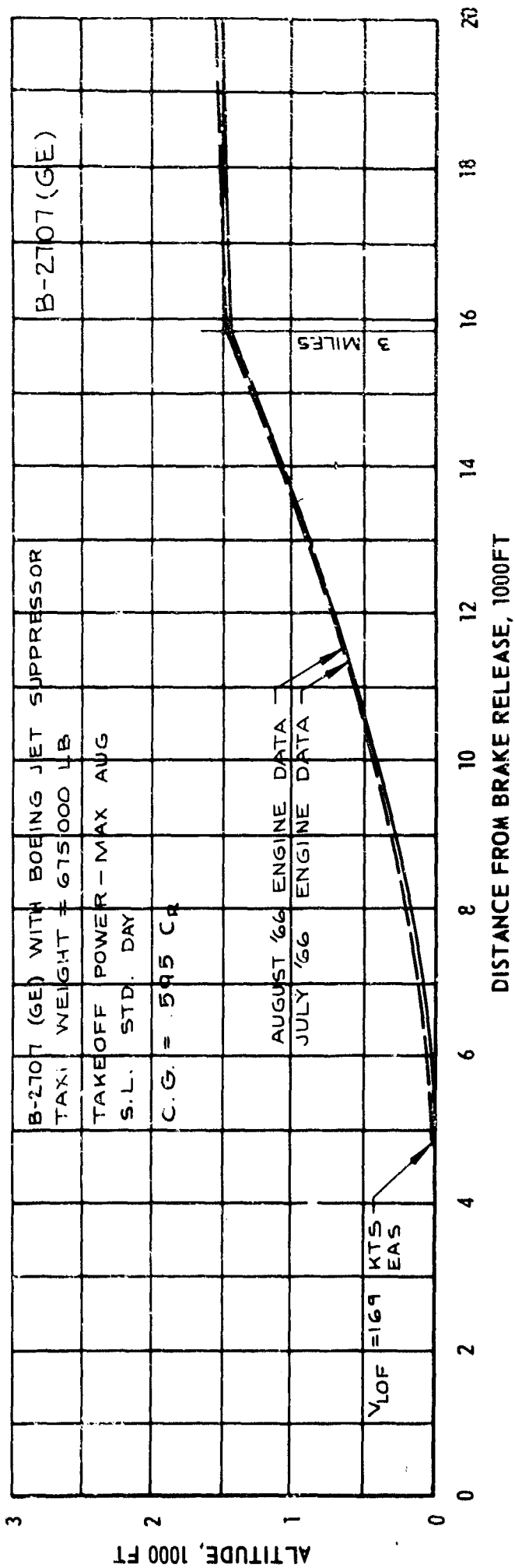


Figure 4-16. Noise Contours, Boeing Jet Suppressor, Model B-2707 (GE)

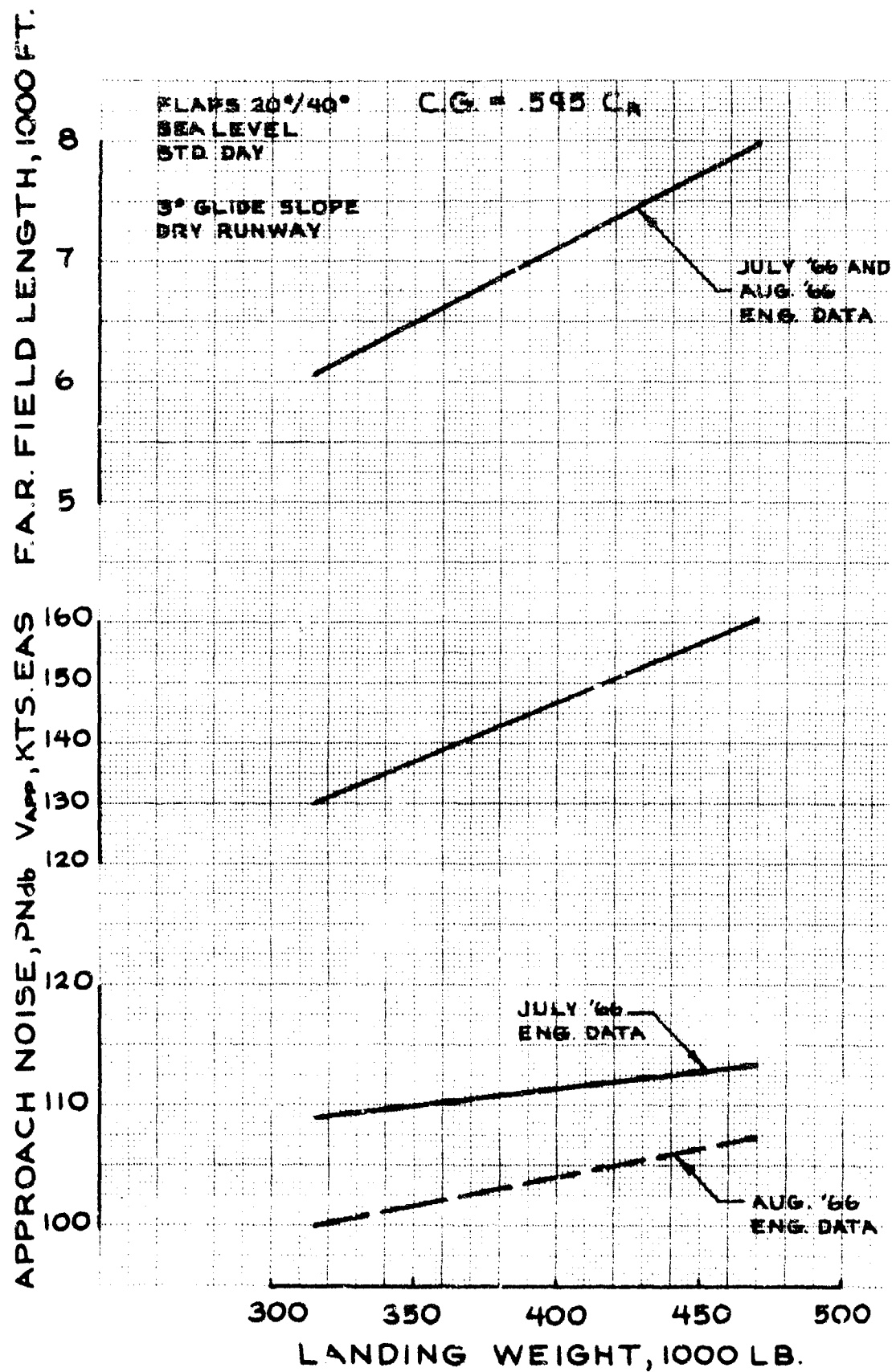


Figure 4-17. Landing Performance Model B-2707 (GE)

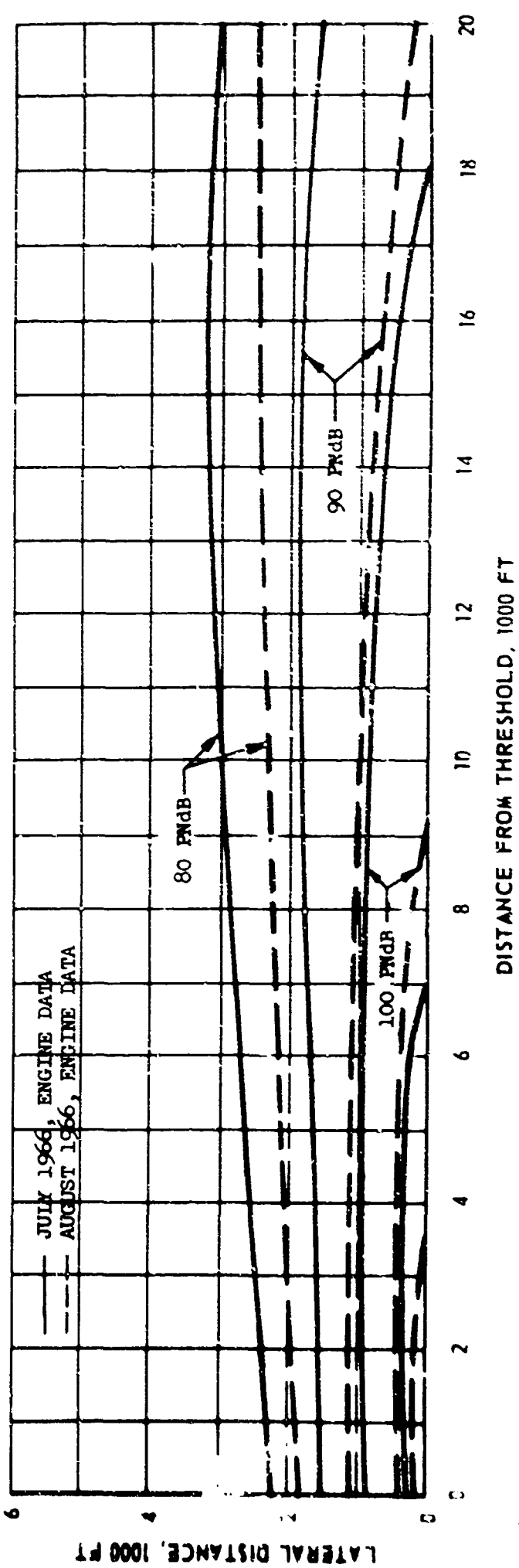
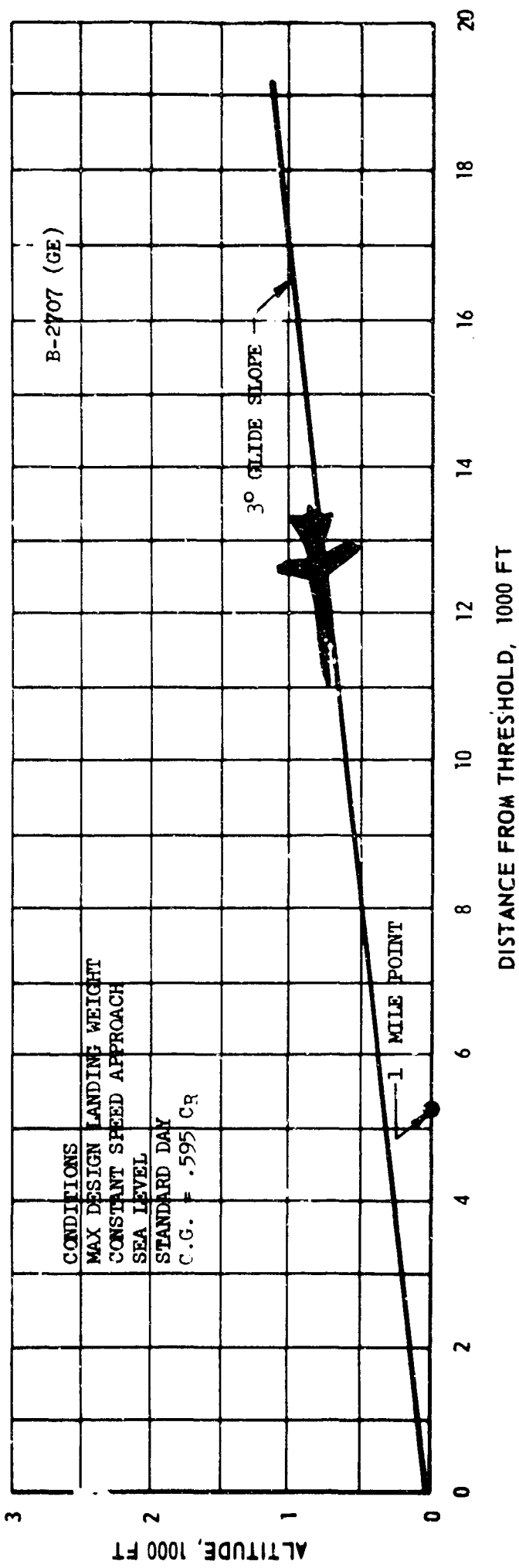


Figure 4-18. Landing Noise Contours, International Mission B-2707 (GE)

